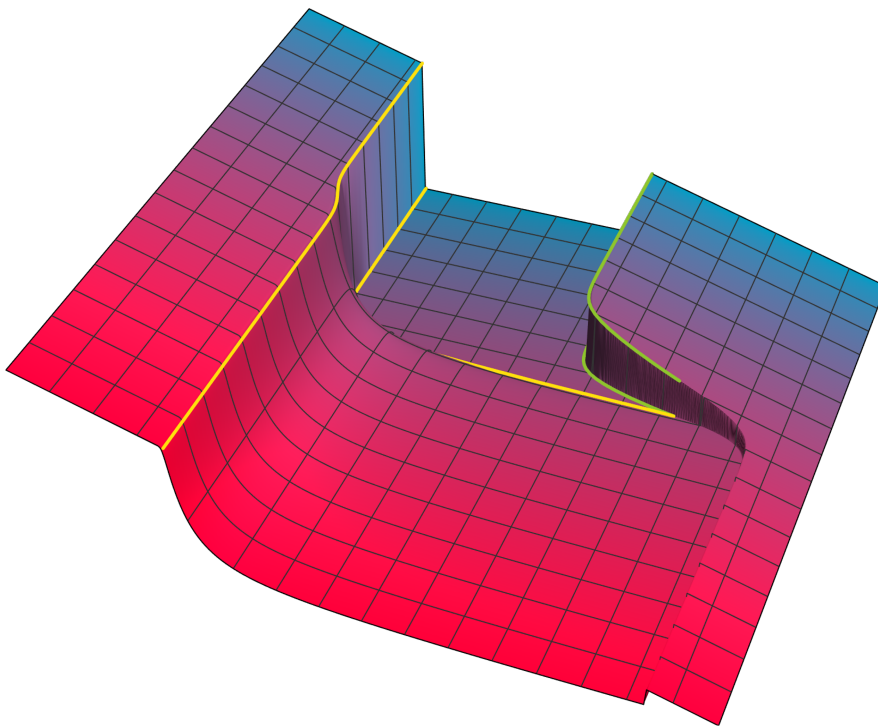

From zero-dimensional theories to inhomogeneous phases with the functional renormalization group

Von null-dimensionalen Theorien zu inhomogenen Phasen mit der funktionalen Renormierungsgruppe

Zur Erlangung des Grades eines Doktors der Naturwissenschaften (Dr. rer. nat.)
Genehmigte Dissertation von M.Sc. Martin Jakob Steil geboren in Offenbach a. M.
Tag der Einreichung: 12.12.2023, Tag der Prüfung: 15.05.2024

1. Gutachten: Priv.-Doz. Dr. Michael Buballa
2. Gutachten: Prof. Dr. Jens Braun
Darmstadt, Technische Universität Darmstadt



TECHNISCHE
UNIVERSITÄT
DARMSTADT

Fachbereich Physik
Institut für Kernphysik
Theoriezentrum
NHQ Group

From zero-dimensional theories to inhomogeneous phases with the functional renormalization group

Von null-dimensionalen Theorien zu inhomogenen Phasen mit der funktionalen Renormierungsgruppe

Accepted doctoral thesis by M.Sc. Martin Jakob Steil

Date of submission: 12.12.2023

Date of thesis defense: 15.05.2024

Darmstadt, Technische Universität Darmstadt

Bitte zitieren Sie dieses Dokument als:

URN: urn:nbn:de:tuda-tuprints-273801

URL: <https://tuprints.ulb.tu-darmstadt.de/27380>

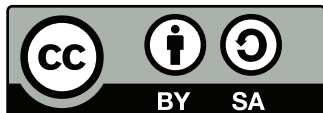
Jahr der Veröffentlichung auf TUpriints: 2024

Dieses Dokument wird bereitgestellt von tuprints,

E-Publishing-Service der TU Darmstadt

<https://tuprints.ulb.tu-darmstadt.de>

tuprints@ulb.tu-darmstadt.de



Die Veröffentlichung steht unter folgender Creative Commons Lizenz:

Namensnennung – Weitergabe unter gleichen Bedingungen 4.0 International

<https://creativecommons.org/licenses/by-sa/4.0/>

This work is licensed under a Creative Commons License:

Attribution–ShareAlike 4.0 International

<https://creativecommons.org/licenses/by-sa/4.0/>

Cover picture: Functional renormalization group flow of an instructive toy model in the zero-dimensional $O(N)$ model in the limit $N \rightarrow \infty$. Adapted from figure 3.34a, i.e., Fig. 6 of Ref. [3].

“McKay (David Hewlett): Yeah, I-I recorded some of my reflections on some of my more ground-breaking accomplishments and theories . . . uh, just a couple hours worth.

Teyla (Rachel Luttrell): You should not have gone to so much trouble.”

Stargate Atlantis S4E18 “The Kindred Part 1” written by Joseph Mallozzi and Paul Mullie

Erklärungen laut Promotionsordnung

§ 8 Abs. 1 lit. c PromO

Ich versichere hiermit, dass die elektronische Version meiner Dissertation mit der schriftlichen Version übereinstimmt.

§ 8 Abs. 1 lit. d PromO

Ich versichere hiermit, dass zu einem vorherigen Zeitpunkt noch keine Promotion versucht wurde. In diesem Fall sind nähere Angaben über Zeitpunkt, Hochschule, Dissertationsthema und Ergebnis dieses Versuchs mitzuteilen.

§ 9 Abs. 1 PromO

Ich versichere hiermit, dass die vorliegende Dissertation selbstständig und nur unter Verwendung der angegebenen Quellen verfasst wurde.

§ 9 Abs. 2 PromO

Die Arbeit hat bisher noch nicht zu Prüfungszwecken gedient.

Rodgau Weiskirchen, 12.12.2023



Martin Jakob Steil

Abstract

In this work, we study strongly interacting quantum field theories using the functional renormalization group (FRG) as our primary computational method. The goal is to facilitate FRG computations in the context of quantum chromodynamics (QCD) to study the phase structure of dense strong-interaction matter. The main part of this work is split into three chapters, differing in the space-time dimension of the theories under consideration.

We begin by studying zero-dimensional theories, which ultimately involves solving ordinary integrals with complicated FRG flow equations. Initially, this might seem like an unnecessarily convoluted way to solve a simple problem. However, it is this very fact – applying the FRG to such simple theories – that allows us to gain enormous insights into the FRG in a rigorous manner. Arguably, the most relevant development is the novel understanding of FRG flow equations in a fluid-dynamic context. This allows for the application of methods and concepts from the highly developed field of computational fluid dynamics (CFD) to the FRG. Two key findings are the identification of bosonic (fermionic) fluctuations as convective (source- or sink-like) contributions to the FRG flow and the resulting link between the CFD concept of numerical entropy and the irreversibility of non-perturbative renormalization group (RG) flows. These developments serve as a vital stepping stone facilitating the following applications.

We proceed with computations in the (1+1)-dimensional Gross-Neveu (GN) model. We use it to study spontaneous chiral symmetry breaking (χ SB) – a phenomenon vital to the understanding of QCD. Using the previously established CFD methods for the FRG, we study the effects of fermionic and crucially bosonic quantum and thermodynamic fluctuations on spontaneous χ SB. The main result of this part of our research is that thermal bosonic fluctuations prevent χ SB in the (1+1)-dimensional GN model. We further study inhomogeneous χ SB indirectly using a stability analysis in mean-field (MF) approximation, *i.e.*, considering only fermionic fluctuations. Our research helps to establish this method as a robust tool for both qualitative and quantitative statements about inhomogeneous χ SB.

We conclude the main part of this thesis with our studies of the (3+1)-dimensional Quark-Meson (QM) model, which we primarily consider as a low-energy effective theory of QCD. We focus on inhomogeneous chiral condensates by studying the QM model within the FRG framework, using a position-dependent ansatz for the chiral condensate, *viz.* the chiral density wave (CDW) for which we have been able to derive explicit FRG flow equations. We again investigate the effects of fluctuations on spontaneous χ SB by solving those flow equations in RG-consistent MF calculations. Thus establishing contact with existing literature results for the QM model with CDW condensates. These computations – incorporating only fermionic fluctuations – are a first step towards a complete solution of the derived flow equations using our established CFD methods.

Zusammenfassung

In dieser Arbeit untersuchen wir stark wechselwirkende Quantenfeldtheorien unter Verwendung der funktionalen Renormierungsgruppe (FRG) als unsere primäre Rechenmethode. Das Ziel ist es, FRG-Rechnungen im Kontext der Quantenchromodynamik (QCD) zu ermöglichen, um die Phasenstruktur von dichter, stark wechselwirkender Materie zu studieren. Der Hauptteil dieser Arbeit ist in drei Kapitel unterteilt, die sich in der Raumzeitdimension der betrachteten Theorien unterscheiden.

Wir beginnen mit dem Studium von null-dimensionalen Theorien, was letztendlich bedeutet, gewöhnliche Integrale mit komplizierten FRG-Flussgleichungen zu lösen. Dies mag zunächst wie eine unnötig umständliche Methode erscheinen, um ein einfaches Problem zu lösen. Es ist jedoch genau diese Tatsache – die Anwendung der FRG auf solch einfache Theorien – die es uns auf rigorose Weise ermöglicht, enorme Einblicke in die FRG zu gewinnen. Die wohl relevanteste Entwicklung ist das neuartige Verständnis der FRG-Flussgleichungen im Kontext der Fluidodynamik. Dies ermöglicht die Anwendung von Methoden und Konzepten aus dem hochentwickelten Bereich der numerischen Strömungsmechanik (CFD) auf die FRG. Zwei Schlüsselerkenntnisse sind die Identifizierung von bosonischen (fermionischen) Fluktuationen als konvektive (Quellen- oder Senken-artige) Beiträge zum FRG-Fluss und die daraus resultierende Verknüpfung des CFD-Konzepts der numerischen Entropie und der Irreversibilität von nicht-perturbativen Renormierungsgruppen (RG) Flüssen. Diese Entwicklungen stellen einen entscheidenden Schritt zur Ermöglichung der folgenden Anwendungen dar.

Wir fahren fort mit Berechnungen im $(1+1)$ -dimensionalen Gross-Neveu (GN) Modell. Wir verwenden es, um spontane chirale Symmetriebrechung (χ SB) zu untersuchen – ein Phänomen, das für das Verständnis von QCD von entscheidender Bedeutung ist. Mit den zuvor etablierten CFD-Methoden für die FRG untersuchen wir die Auswirkungen von fermionischen und insbesondere bosonischen Quanten- und thermodynamischen Fluktuationen auf spontane χ SB. Das Hauptergebnis dieses Teils unserer Forschung ist, dass thermische bosonische Fluktuationen χ SB im $(1+1)$ -dimensionalen GN Modell verhindern. Wir untersuchen des Weiteren inhomogene χ SB indirekt mittels einer Stabilitätsanalyse in *Mean-Field* (MF) Näherung, d.h. nur unter Berücksichtigung fermionischer Fluktuationen. Mit unserer Forschung tragen wir dazu bei, diese Methode als robustes Werkzeug für sowohl qualitative als auch quantitative Aussagen über inhomogene χ SB zu etablieren.

Wir schließen den Hauptteil dieser Arbeit mit unseren Studien zum $(3+1)$ -dimensionalen Quark-Meson (QM) Modell ab, welches wir hauptsächlich als eine effektive Niederenergietheorie von QCD betrachten. Wir konzentrieren uns auf inhomogene chirale Kondensate, indem wir das QM Modell im Rahmen der FRG untersuchen und dabei einen positionsabhängigen Ansatz für das chirale Kondensat verwenden, namentlich die chirale Dichtewelle (CDW), für die wir

explizite FRG-Flussgleichungen ableiten konnten. Wir untersuchen erneut die Auswirkungen von Fluktuationen auf spontane χ_{SB} , indem wir diese Flussgleichungen im Rahmen von RG-konsistenten MF Rechnungen lösen. Dadurch stellen wir eine Verbindung zu bestehenden Literaturergebnissen für das QM Modell mit CDW Kondensaten her. Diese Berechnungen – die derzeit nur fermionische Fluktuationen berücksichtigen – sind ein erster Schritt hin zu einer vollständigen Lösung der abgeleiteten Flussgleichungen unter Verwendung unserer etablierten CFD-Methoden.

Contents

Erklärungen laut Promotionsordnung	iv
Abstract	v
Contents	viii
1. Introduction	1
1.1. Outline	10
1.2. Publications and disclaimers	12
2. Theoretical background and methods	14
2.1. The functional renormalization group	14
2.1.1. Scale-dependent generating functionals	16
2.1.2. Scale-dependent effective average action	18
2.1.3. Quantum equation of motion and propagator	19
2.1.4. The Wetterich equation	21
2.1.5. Higher-order flow equations and their combinatorics in field space	33
2.1.6. Renormalization group consistency	38
2.1.7. Renormalization group equations as functional flow equations	42
2.2. Conservation laws, hydrodynamics, and the finite volume method	43
2.2.1. The finite volume method	45
2.2.2. The KT/KNP scheme and the MUSCL reconstruction	47
2.2.3. Advection and shocks	54
2.2.4. Diffusion and the heat equation	62
2.2.5. Sources and the heat equation	66
2.2.6. Euler equations – the KT scheme showing its MUSCLes	67
2.3. Quantum chromodynamics and low-energy effective theories	71
2.3.1. Quantum chromodynamics	72
2.3.2. Asymptotic freedom, confinement, and chiral symmetry (breaking)	76
2.3.3. χ SB and the emergence of LEFTs from QCD	81
2.4. Inhomogeneous (chiral) condensates	89
2.4.1. Technical challenges and methods	91
2.4.2. Literature results	92

3. Models in zero dimensions	95
3.1. Quantum field theory in zero dimensions	97
3.1.1. The partition function	98
3.1.2. Solving integrals with flow equations	100
3.1.3. The functional renormalization group equation	104
3.2. The $O(N)$ model – strongly interacting scalars	111
3.2.1. Symmetry restoration during the FRG flow	114
3.2.2. Exact FRG flow equation of the zero-dimensional $O(N)$ model	115
3.2.3. The $O(N)$ model at finite N	135
3.2.4. The $O(1)$ model – entropy production and irreversibility of RG flows	163
3.2.5. The $O(N)$ model in the large- N limit	185
3.3. A $SU(2)$ model – strongly interacting Grassmann numbers	211
3.3.1. Construction of the $SU(2)$ Grassmann-scalar theory	212
3.3.2. System of FRG flow equations	219
3.4. Conclusion and outlook	225
4. Gross-Neveu model in two dimensions	230
4.1. The Gross-Neveu(-Yukawa) model	231
4.1.1. The models in vacuum and at non-zero T and μ	233
4.2. The FRG in LPA for the Gross-Neveu-Yukawa model	237
4.2.1. The GNY model in LPA truncation	237
4.2.2. LPA flow equation as non-linear diffusion-source/sink equation	243
4.3. Infinite- N analysis of homogeneous phases	249
4.3.1. The mean-field vacuum potential and asymptotic freedom	251
4.3.2. The mean-field phase diagram in the renormalized limit $\Lambda \rightarrow \infty$	254
4.3.3. Ginzburg-Landau analysis and Landau’s theory of phase transitions	256
4.4. Infinite- N analysis of inhomogeneous phases	262
4.4.1. The inhomogeneous phase diagram of the Gross-Neveu model	265
4.4.2. Stability analysis of the spatially homogeneous \mathbb{Z}_2 -symmetric phase	266
4.4.3. Generalized Ginzburg-Landau analysis	279
4.5. The Gross-Neveu-Yukawa model at finite N	282
4.5.1. To break or not to break – \mathbb{Z}_2 symmetry at finite N	283
4.5.2. UV initial condition for FRG flows at variable N	285
4.5.3. Bosonic quantum fluctuations in the GNY model	289
4.6. Conclusion and outlook	303
5. Quark meson model in four dimensions	306
5.1. Deriving a LPA flow equation for the chiral density wave	307
5.2. RG-consistent mean-field results	310
5.2.1. Renormalized mean-field, parameter fitting, and Poincaré invariance	312
6. Summary and outlook	315

A. Digital auxiliary files and used software	318
A.1. Digital auxiliary files and online repository	318
A.2. Used software	319
B. Units, conventions, and notations	320
B.1. Compact notations	320
B.2. Units	320
B.3. The (special) unitary group	321
B.3.1. $SU(2)$ and $U(2)$ algebras	322
B.4. Field space notation	323
B.5. Fourier transformations and functional derivatives	325
B.6. Spinor degrees of freedom	328
B.6.1. Clifford algebra in two dimensions	329
B.6.2. Clifford algebra in four dimensions	330
C. Thermal quantum field theory	331
C.1. Grand canonical partition function	331
C.2. Selected Matsubara sums and identities for distribution functions	333
C.3. Momentum integrals and related notations	337
C.4. Series expansion for the medium part of the MF thermodynamic potential	337
C.4.1. Ginzburg-Landau series for $\mathcal{V}_{f;med}^{s=1}(\mu, T; \Delta)$ in one spatial dimension	340
C.4.2. Ginzburg-Landau series for $\mathcal{V}_{f;med}^{s=3}(\mu, T; \Delta)$ in three spatial dimension	341
C.5. Zero temperature limit of the medium part of the MF thermodynamic potential	341
D. Models in zero dimensions	343
D.1. $O(N)$ model	343
D.1.1. Selected vertices, propagators, and regulator insertions	343
D.1.2. Numerical derivatives	344
D.1.3. Additional expressions for the $O(N)$ model in the $N \rightarrow \infty$ limit	345
D.2. $SU(2)$ model	351
D.2.1. Selected vertices, propagators, and regulator insertions	351
E. Gross-Neveu model in two dimensions	354
E.1. Selected vertices, propagators, and regulator insertions	354
E.2. The LPA flow equation	355
E.3. The bosonic two-point function in the limit $N \rightarrow \infty$	356
Bibliography	358
Acronyms	394
Curriculum vitae	396
Acknowledgments	399

1. Introduction

The strong interaction, one of the four established fundamental interactions and one of three cornerstones of the *Standard Model of particle physics*, governs the confinement of quarks into protons, neutrons, and other more exotic states of strongly interacting matter. Quarks are fundamental, massive spin- $\frac{1}{2}$ particles [10–17], which carry color charge [18–20]. Colored quarks are not directly observable but their bound states – most notably protons and neutrons – are observable and form the building blocks of ordinary matter. The established fundamental quantum field theory (QFT) describing the strong interaction is quantum chromodynamics (QCD) [21], which describes the interaction of color-charged quarks and gluons. Gluons are the color-charged gauge bosons of quantum chromodynamics (QCD) and mediate the strong force. The strong interaction is crucial for the binding of protons and neutrons in atomic nuclei as it is able to overcome the electrostatic repulsion between protons at short range. It is also important for the understanding of matter at extreme conditions, *i.e.*, at temperatures $T \gtrsim 10^{10}$ K ≈ 1 MeV and densities $n \gtrsim n_0$, above nuclear saturation density $n_0 = 1.6 \cdot 10^{44}$ m $^{-3}$ = 0.16 fm $^{-3}$ [22]. Such extreme conditions are expected in the early universe, see, *e.g.*, Refs. [23, 24], studied in experimental high-energy particle physics, see, *e.g.*, Refs. [25–42], and are present in extreme astrophysical environments like neutron stars, see, *e.g.*, Refs. [43–46].

Computing observables of strongly interacting systems in QCD is technically extremely challenging due to the complicated nature of QCD as a non-Abelian gauge theory [47], which becomes non-perturbative, *i.e.*, strongly coupled at low energies – at macroscopic scales ~ 1 GeV in the context of high-energy physics. The phase structure and thermodynamics of QCD matter at especially intermediate densities and temperatures ($2n_0 \lesssim n \lesssim 10n_0$ and $T \lesssim 150$ MeV) is still very poorly understood both from experiment and theory. It is however of profound importance especially in extreme astrophysical environments like isolated neutron stars, neutron star mergers, and supernovae explosions, which are important sites of nucleosynthesis, see, *e.g.*, Ref. [48]. We humans and nature surrounding us are truly made of “star dust” including the “dust” of neutron stars.

The phase diagram of QCD – Here be dragons

In figure 1.1 we show a sketch of the conjectured phase diagram of QCD including information from experiment and theory, see, *e.g.*, Refs. [49, 50, 52, 58–63] for more details on the rich phase structure of strongly interacting matter. At low temperatures and densities we encounter nuclear matter where quarks and gluons are confined to baryons, *e.g.*, protons and neutrons, and the chiral symmetry of QCD is broken spontaneously [64, 65]. This chiral symmetry breaking (χ SB) is signaled by a non-zero expectation value $\langle \bar{q}q \rangle \neq 0$ for the anti-quark-quark condensate – the *chiral condensate*. The mechanism of spontaneous chiral symmetry breaking

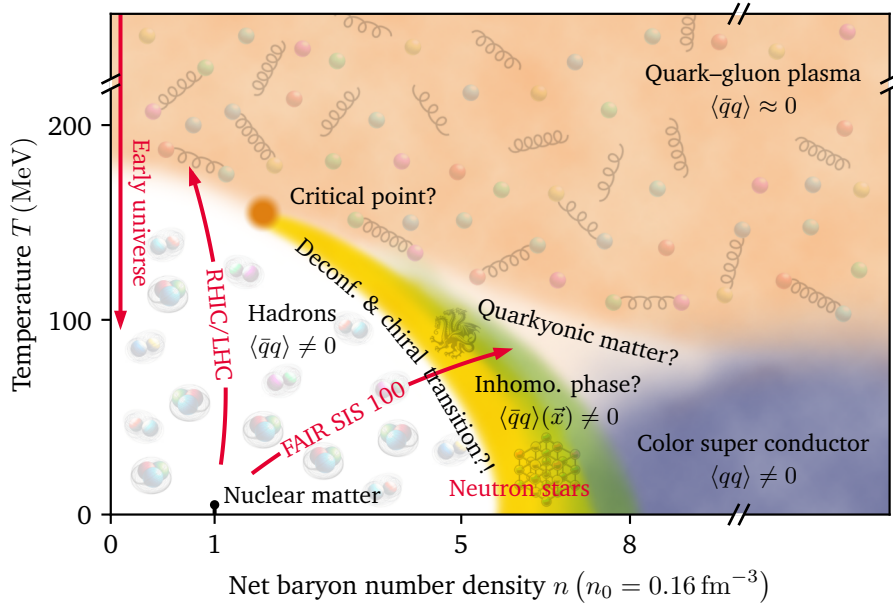


Figure 1.1.: Conjectured QCD phase diagram with various states of strongly interacting matter including chiral symmetry breaking patterns in black and experimental laboratories, *cf.* Refs. [23, 24, 37–46], in red. Note that both the T - and n -axis are cut and especially the n -axis is non-linear. It should also be noted that a representation in n - T should include mixed phases, *i.e.*, regions with phase coexistence around first-order phase transitions, *cf.* figure 4.7. This figure is meant to introduce the relevant phases and their rough location in the phase diagram while the shapes and boundaries should not be interpreted literally. The visualization of phase boundaries and shapes is reminiscent of a diagram in the temperature and quark/baryon chemical potential plane, *cf.* figures 2.13 and 2.16b. We settled for a presentation using net baryon number density instead for quark chemical potential in this introduction since it is arguably more intelligible for non-experts. *Based on Fig. 1. of Ref. [49] and including information from Fig. 1 of Ref. [50], Fig I.8 of Ref. [51], and Fig. 2 of Ref. [52]. Elements of the background were generated using Axodraw version 2 [53, 54] and DALL-E [55]. The final figure has been composed by hand using Matplotlib [56] and Photoshop CS6 [57].*

(χ SB) [64, 65] plays a critical role for the generation of masses of QCD bound states, like protons and neutrons. In fact about 99% of the proton’s (neutron’s) mass of 938.27 MeV (939.57 MeV) is generated dynamically in QCD since the quarks themselves are incredibly light (compared to typical scales in QCD) with $m_u \approx 2$ MeV and $m_d \approx 5$ MeV in the $\overline{\text{MS}}$ -scheme at a renormalization scale of 2 GeV [36]. Throughout this work we focus on the dynamics of the two light quark flavors – up and down – hence $\langle \bar{q}q \rangle$ denotes the anti-quark-quark condensate of the light quarks. Furthermore we limit most discussions to the chiral limit, *i.e.*, neglecting the small masses of the up and down quark: $m_u = m_d = 0$.

At high temperatures and/or densities, *i.e.*, high momenta, QCD becomes asymptotically free [66–68]: the interaction strength between quarks and gluons decreases with increasing momentum transfer allowing a perturbative treatment of QCD in this extreme high-energy regime. The quarks and gluons at high temperatures are deconfined and present thermody-

namically as a quasi-free, ultrarelativistic gas called the *quark–gluon plasma* (QGP). Chiral symmetry is approximately restored in the QGP, $\langle \bar{q}q \rangle \approx 0$, meaning that the only breaking of χ SB is due to quark masses. In the chiral limit $m_u = m_d = 0$ chiral symmetry gets completely restored $\langle \bar{q}q \rangle = 0$.

The existence of a (strongly coupled) QGP is established theoretically (experimentally) in high-energy particle physics. The existence of nuclear matter – bound protons and neutrons – is nowadays a well-established fact in physics, supported by extensive experimental evidence and theoretical understanding. This poses an interesting question for the phase diagram of QCD: how do we get from hadrons – bound states of confined quarks and gluons – to the QGP – deconfined quarks and gluons – or in terms of chiral symmetry: how does chiral symmetry get restored as temperature and density increase? This is one of the major open research questions in both experimental and theoretical high-energy physics. The closely related and unsolved *Yang-Mills & The Mass Gap* problem [69] was stated as a major mathematical challenge as one of the seven *Millennium Prize Problems*. At low densities and quark chemical potentials existing collider experiments, see, e.g., Refs. [70–75], and theoretical first principle computations in QCD (especially but not exclusively from the field of lattice QCD, see, e.g., Refs. [49, 76–78]) have basically established that chiral symmetry gets approximately restored as temperature increases in a smooth crossover, which in the chiral limit manifests as a second-order phase transition.

At higher densities ($n \gtrsim 2 n_0$) and associated quark chemical potentials the experimental situation remains unclear since this region is notoriously difficult to probe in colliders. Indirect experimental access to this region is provided by the study of isolated and merging neutron stars. With the recent advances in direct gravitational wave detection this experimental, astrophysical laboratory is gaining more and more attention in high-energy physics. The established major theoretical instrument of lattice QCD can not access the region of the QCD phase diagram at non-vanishing chemical potential directly due to the notorious *QCD sign-problem*: a conceptual and computational algorithmic limitation preventing simulation at $\mu > 0$, see, e.g., the review [79]. Extrapolations of lattice QCD results to non-zero chemical potential start to become unreliable at $3\mu/T \equiv \mu_B/T \gtrsim 2$ [77, 78, 80]. Hence the phase structure at intermediate densities and temperatures is not fully understood both from a theoretical and experimental perspective. The center of figure 1.1 – the QCD phase diagram at intermediate temperatures and densities – is still to an extent a *terra incognita* of challenges and mysteries: “*Here be dragons*” and maybe even three-headed ones.

Accessing the QCD phase diagram at intermediate temperatures and densities to study chiral symmetry restoration and the confinement-deconfined transition requires non-perturbative methods for strongly-interacting QCD. Functional methods – like the functional renormalization group (FRG) – and effective models – especially chiral low-energy effective theorys (LEFTs) of QCD like the Nambu–Jona-Lasinio (NJL) model and related quark-meson (QM) model – are important tools to theoretically study QCD in this regime. The functional renormalization group (FRG) is a non-perturbative functional method, which implements Wilson’s non-perturbative renormalization group (RG) approach exactly by introducing momentum and renormalization group (RG)-scale-dependent regulator terms. It effectively maps the problem of solving complicated functional integrals, which lattice QCD tackles directly by discretization in position space,

onto the problem of solving complicated functional differential equations. Those so-called RG-flow equations describe the evolution of microscopic theories defined at high momentum scales – in the ultraviolet (UV) – towards macroscopic theories at low momentum scales – in the infrared (IR). At its core the FRG is based on successively integrating out quantum and thermodynamic fluctuations.

Those are the methods and the part of the QCD phase diagram relevant for our explicit research.

Inhomogeneous chiral condensates – the quark-meson (QM) model in $d = 3 + 1$

Several model calculations especially in the $(3+1)$ -dimensional QM model with the FRG (incorporating both bosonic and fermionic quantum and thermodynamic fluctuations), see, *e.g.*, Ref. [81], and in mean-field (MF)/large- N_c approximation (including only fermionic fluctuations), see, *e.g.*, Ref. [82], predict a first-order phase transition ending in a critical point (CP) as the mechanism of chiral symmetry restoration. In figure 1.1 the possible location of the CP is marked as a diffuse orange dot and the first-order phase transition (with the corresponding phase coexistence region) would be located in the yellow band. This finding however is based on the – often tacit – assumption of homogeneous chiral condensation. Allowing for inhomogeneous, *i.e.*, explicitly position-dependent, expectation values $\langle \bar{q}q \rangle(\vec{x})$, computations using mean-field (MF)/large- N_c approximation, see, *e.g.*, Refs. [83–86], and to an extent also existing FRG computations, see, *e.g.*, Refs. [80, 87], predict that such an inhomogeneous phase can be energetically favored over a homogeneous one. This preference typically occurs at or around the previously predicted location of the homogeneous first-order phase transition.

One major research question regarding this exotic state of strongly interacting matter is its stability against bosonic Quantum and thermodynamic fluctuations. Inhomogeneous phases are established in MF/large- N_c approximation in $(3+1)$ -dimensional chiral LEFTs of QCD like the NJL model and QM model, see, *e.g.*, the reviews [63, 88]. But those computations only incorporate the effects of fermionic fluctuations. Using the FRG we originally set out to study the effects of bosonic quantum and thermal fluctuations on inhomogeneous phases in the QM model. Both a direct computation with explicitly position-dependent expectation values $\langle \bar{q}q \rangle(\vec{x})$ and an indirect approach using a stability analysis of the homogeneous ground state have been planned. I have focused on the first while my colleague Adrian Koenigstein has focused on the latter.

Using a specific ansatz for the expectation values $\langle \bar{q}q \rangle(\vec{x})$, *viz.* the chiral density wave (CDW), I have been able to derive FRG flow equations including this explicitly inhomogeneous condensate using the established local potential approximation (LPA) as truncation [6]. As a first step we have solved the derived FRG/LPA flow equations with CDW condensates neglecting bosonic fluctuations. In the resulting RG-consistent MF computations we made contact with various existing mean-field results in literature studying the QM model both as a renormalizable quantum field theory (QFT) and as a chiral LEFT of QCD [6].

FRG flow equations as convection equations and computational fluid dynamics

At this point we turned our attention at the role of bosonic fluctuations and set out to solve our derived flow equations without the simplifying assumption of neglecting bosonic contributions.

The flow equations for the CDW in the QM model present as generalizations of the well known FRG/LPA flow equations for homogeneous chiral condensates and include those in the limit of vanishing position-dependence. Those flow equations are non-linear partial differential equations (PDEs) for scale depended interaction potentials $U(k, \varrho)$ in two variables: RG scale (k) and the magnitude of the chiral condensate ($\propto \varrho$). The FRG community employs a multitude of numerical methods to solve such PDEs which have been constructed for the problems at hand by various authors with varying mathematical rigor – often based on a fair degree of *a posteriori* insight. Those methods include

- **local (Taylor) expansions**, see, *e.g.*, Refs. [80, 89–109],
- **collocation methods** – which are often referred to in FRG literature as just “*grid methods*” – like finite difference (FD), see, *e.g.*, Refs. [81, 87, 93, 100, 110–144], and related spline methods, see, *e.g.*, Refs. [145–152], and
- **global pseudo-spectral methods** like an expansion in Chebyshev polynomials, see, *e.g.*, Refs. [109, 153–160].

For our studies involving spontaneous χ SB and restoration including first- and second-order phase transitions a local Taylor expansion of the potential is both *a priori* and *a posteriori* ill-suited, so we focused on the established FD methods and on the less common pseudo-spectral (Chebyshev) collocation methods.

However we – especially Adrian Koenigstein and I – soon had to realize that the seemingly well established numerical methods in the FRG community to solve truncated flow equations, *i.e.*, PDEs, turned out to be numerically rather unstable. Varying just numerical discretization parameters yielded qualitatively differing results all while being incredibly inefficient and numerically unstable in terms of RG-scale evolution. With this came the realization that published, peer-reviewed literature using and in some cases seemingly establishing those methods included only sparse information about boundary conditions, subtleties in the implementation of the numerical schemes, numerical parameters (number of discretization points, size of the computational domain, *etc.*), numerical IR cutoffs of RG-scale evolution, and rigorous tests of numerical convergence of the employed methods¹. The problem with those schemes is that they ultimately rely on smoothness or technically even analyticity of the underlying potentials. The encountered PDEs however can include (*e.g.*, caused by the quark chemical potential) and

¹I have chosen not to highlight specific publications for criticism. The issue is, in my opinion, not confined to a few isolated instances but is rather a somewhat systemic one. I must express concern regarding the wide spread use of seemingly suboptimal numerical methods for PDEs, without sufficient exploration and reflection on their limitations. I think the FRG community could benefit tremendously from a more judicious approach when it comes to choosing, adapting, testing, and/or designing numerical methods. Although these issues are by no means ubiquitous, their presence in the field should, in my opinion, warrant more attention. I will end this remark on a more positive note by citing Max Planck: “Even a disappointment, if it is only thorough and final, represents a step forward, and the sacrifices associated with resignation would be amply compensated by the gain in treasures of new knowledge.” (translated from the original quote in German [161] which I saw first in a talk of Dr. Johannes Weber).

dynamically generate (e.g., due to dynamical, spontaneous symmetry breaking in the IR²) discontinuities in the derivative of the studied potentials.

Eduardo Grossi and Nicolas Wink, two colleagues from Heidelberg encountered the same problems with the established methods and were able to ultimately identify the root cause in a mathematically and conceptually rigorous manner: the LPA flow equation/FRG flow equations in general are convection/conservation equations [162] since the involved PDEs manifest as advection-diffusion-(source/sink) equations. This is not a new concept in the context of the RG – it originally informed the term “*flow equations*” when talking about RG evolution equations – but the consequences of this connection were not realized in the broader FRG community prior to Ref. [162] and our extensive follow up collaboration and research in Refs. [1–4]. Adrian Koenigstein and I decided to apply finite volume (FV) methods from computational fluid dynamics (CFD) to FRG flow equations, *viz.* as a first test to the LPA flow equation of $O(N)$ models. We reproduced the results from Ref. [162] and inspired by the superb publication [163] of Jan Keitel and Lorenz Bartosch, started studying $O(N)$ models in zero dimensions with the FRG and our new CFD perspective on it.

Zero-dimensional field theories – A gift that keeps on giving in $d = 0$

At the Mini-Workshop “QCD & beyond with the FRG” in Heidelberg (July 17, 2019), I presented first results that Adrian Koenigstein and I obtained with the FV method for the LPA flow equation of the three- and zero-dimensional $O(N)$ model at infinite and finite N in a talk titled “Solving ~~QFTs~~ convection–diffusion equations with finite volume methods Kurganov and Tadmor (KT) $O(x^2)$ central scheme - An appetizer” [164], which sparked the collaboration of Adrian Koenigstein and myself with Eduardo Grossi, Nicolas Wink, Jens Braun, Dirk Rischke and Michael Buballa leading to the series of publications [1–3]. We decided to research the implications of the identification of FRG flow equations as convection equations/conservation laws in detail. Especially with regard to the application and adaptation of concepts and numerical methods from the highly-developed field of CFD to the FRG, which at that point in time was clearly lacking rigorously developed and tested numerical tools for PDEs. Particularly Eduardo Grossi and Dirk Rischke with their background in relativistic hydrodynamics have brought much needed CFD-expertise to the project.

Zero-dimensional $O(N)$ models describe the interaction of N scalars in a single point in space-time. Due to $O(N)$ symmetry and the complete absence of a notion of space-time in zero dimensions, such theories can be described using ordinary, one-dimensional integrals like the one shown in Eq. (1.1). One might ask the question: how are there three publications [1–3], two doctoral theses (Ref. [165] and this document), and ongoing research projects [7, 8] studying one-dimensional integrals? One could make the completely valid argument that computing numerical values for (converging) integrals like

$$Z_S(J) \equiv \int_{-\infty}^{+\infty} d\phi e^{-S(\phi)+J\phi} \quad (1.1)$$

²Symmetry breaking is signaled during FRG flow by a non-zero expectation value, *i.e.*, non-trivial minimum in ϱ of $U(k, \varrho)$, but we know as we approach the physical IR limit $k \rightarrow 0$, $U(k, \varrho)$ has to turn convex $\lim_{k \rightarrow 0} \partial_\varrho U(k, \varrho) \geq 0$, which necessitates a kink at/around a non-trivial minimum.

has been practically possible at the very least since the development of integral calculus by Isaac Newton and Gottfried Wilhelm Leibniz in the late 17th century and Leonhard Euler’s work on exponential functions in the 18th century. With the advent of computers (including here actually the occupation *computer* – a person performing mathematical calculations) and numerical methods over the centuries, computing the integral (1.1) numerically for a given real function S and real number J – for which $Z_S(J)$ converges – is a simple exercise today. Especially modern computer algebra systems capable of arbitrary precision arithmetic, like MATHEMATICA [166], can compute Eq. (1.1) to high numerical precision in literally milliseconds. So how did we go from a *Millennium Prize Problem*, viz. the *Yang-Mills & The Mass Gap* problem of page 3, to the integral (1.1) on page 6?

The answer is simple: one can learn an almost shocking amount about QFTs and more precisely about methods used in the study of QFTs from simple integrals like (1.1). The integral (1.1) is the zero-dimensional analogue of the partition function: replacing the ordinary with a functional integral, identifying S with the action, ϕ with a fluctuating quantum field $\phi(x)$, and J with a source $J(x)$ (introduced to extract correlation functions from Z using derivatives with respect to (w.r.t.) $J(x)$), we arrive at the text book expression for the partition function of an $O(1)$ model. Computing partition functions and related moments to gain access to observables is at the very core of QFT and its methods. In “*The zero-dimensional $O(N)$ vector model as a benchmark for perturbation theory, the large- N expansion and the functional renormalization group*” [163] Jan Keitel and Lorenz Bartosch illustrate beautifully and in a self-contained manner how all three methods (perturbation theory, the large- N expansion, and the FRG Taylor expansion) can be applied to zero-dimensional $O(N)$ models. The mentioned QFT methods – FRG among them – are by no means mathematically trivial in zero dimensions. The concepts and diagrammatic techniques of all three methods can be studied without encountering diverging momentum integrals, complicated functional integrals and calculus of functionals. Results and working principles can be visualized by just plotting the involved expressions. It is truly a didactic dream: zero-dimensional applications of QFT techniques should be part of any introductory lecture or at the very least of accompanying exercises.

Academic, didactic, and conceptual insight into the FRG framework can be gained by extending the work in Ref. [163] to the study of the untruncated FRG flow equation in zero dimensions. The governing equation of the FRG – the Wetterich equation – is for theories in non-zero dimensions a functional differential equation. Tools for the direct solution of non-trivial, functional differential equations are non-existent. Any practical FRG computation in non-zero dimensions includes a truncation: a method to project from the Wetterich equation onto a finite set of ordinary differential equations (ODEs) and PDEs. As a truly non-perturbative method it is often *a priori* very difficult to construct a good truncation/projection strategy for a given research problem. Established truncation schemes for certain classes of models/computations are usually established *a posteriori*. In zero dimensions the FRG flow equation manifests directly as a PDE which can be studied without the need for truncations.

Just as their higher-dimensional counter parts the flow equation encountered for the zero-dimensional $O(N)$ model are advection-diffusion equations, which can be conceptually and

numerically treated with methods from CFD. Leveraging existing concepts of CFD we have been able to identify pion-like contributions of massless modes in FRG flows as non-linear advective contributions, while contributions from massive radial σ -modes act as diffusive contributions [1]. The irreversibility of non-perturbative RG transformations – FRG flows from high to low energies/RG scales – can be understood in this context and can be linked to the concept of numerical entropy in CFD [2]. In the large- N limit of infinitely many scalars FRG flow equations become purely advective with the absence of diffusion allowing for unique features clearly distinguishing scenarios at finite and infinite N [3].

Extending the discussion from the $O(N)$ model to an $SU(2)$ model including Grassmann numbers, we can identify fermionic contributions to FRG flows as source and sink terms [7]. Furthermore, such more involved zero-dimensional models allow interesting insights into truncations and conservative formulations of more involved systems of FRG flow equations [7].

Numerical precision test and benchmarks are especially easy to construct in zero-dimensional models. The fact that we can compute integrals like (1.1) to arbitrary precision using just numerical integration provides us with basically exact reference values. Any QFT method applied to compute Eq. (1.1) can be benchmarked against the exact results: we do not have to wonder if and/or when a perturbative series converges, whether a saddle-point expansion in the spirit of the large- N limit makes sense for a theory at hand, talk about apparent convergence of the FRG Taylor expansion, or wonder if our numerical scheme for the solution of the full untruncated FRG flow equation produces a meaningful result – we have exact reference values for all conceivable observables in zero dimensions for any action S to compare to. There are only very few exact solutions for non-trivial, interacting QFTs in non-zero dimensions but in zero dimensions we can study any action S we desire and just compute any observable in milliseconds on a laptop. This allows us to construct a series of very illuminating and challenging *test cases* in form of specific choices for S . There is no discussion to be had if a truncation is valid, a simplification justified, or a numerical scheme suited: their quality can be quantified by just comparing the results obtained from them with the exact reference values. In zero dimensions there is no room to hide. We test the FV method of our choosing, *viz.* the *Kurganov-Tadmor* (KT) scheme [167, 168], for the numerical solution of FRG flow equations extensively with the zero-dimensional $O(N)$ model and our set of test cases. We investigate the role of boundary conditions, the spatial discretization, the size of the computational interval, the role of UV and IR cutoffs, and limitations of the FRG Taylor expansion extensively [1–3].

The Gross-Neveu model – a testing ground in $d = 1 + 1$

At this point we hope to have convinced the reader that studying zero-dimensional models is worthwhile for didactic, conceptual, and methodological reasons. But the valid question arises: can the developments in zero dimensions for the FRG be used in non-zero dimensions? We argue and demonstrate in the following that our work in zero dimensions extends beyond mere academic theory, having profound implications and applications beyond the realm of scalars and Grassmann numbers.

Instead of applying our new found understanding of the FRG and our, at this point rigorously tested adaptation of the KT scheme, directly to the QM model in $3 + 1$ dimensions, we choose

a more incremental approach. The QM model is a rather involved theory at the very least when compared with the Gross-Neveu (GN) model [169] in 1+1 dimensions. The Gross-Neveu (GN) model is a simple four-fermi theory of N chiral fermions in 1+1 space-time dimensions which is frequently used as a toy model in the context of theoretical high-energy physics to study spontaneous χ SB. Like QCD the GN model is asymptotically free [169–179] and at the classical level – at large RG scales in the UV – conformal. Notably, it exhibits dimensional transmutation, a phenomenon where studying quantum fluctuations leads to the emergence of a mass scale/gap in a theory initially free of dimensionful couplings, see, e.g., Refs. [176, 178]. The asymptotic freedom of the GN model makes constructing an explicit, initial action at varying number of fermion flavor N rather simple. We study the GN model both at an infinite number of fermion flavors (considering only fermionic fluctuations) and at a finite number of flavors (considering both fermionic and bosonic fluctuations) at non-zero temperature and chemical potential/density.

At infinite- N we study both homogeneous and inhomogeneous chiral condensates from an FRG perspective. In the context of theoretical high-energy physics and inhomogeneous chiral condensates the GN model is renowned for a dominant inhomogeneous phase in its phase diagram in the infinite- N limit. The phase diagram allowing for inhomogeneous chiral condensates in this limit has been computed by Micheal Thies and others [180–183] revising in some cases longstanding homogeneous infinite- N results [184–192]. We use those literature results for a qualitative and quantitative evaluation of the stability analysis of the homogeneous phase [5, 80, 87, 180, 182, 193–208] as a tool to detect inhomogeneous condensation [5].

At finite- N we use the homogeneous infinite- N results to construct an appropriate initial condition for FRG computations at varying N . We study the Gross-Neveu-Yukawa (GNY) model as a variant of the GN model in the LPA truncation. The encountered flow equation falls directly into the category of flow equations we studied extensively in zero dimensions. Employing our adapted numerical methods from zero dimensions to this problem, we were able to study the effect of bosonic fluctuations at finite N . In doing so we have been able to address a long-standing question for the GN model: is there χ SB in the GN model in 1+1 dimensions? There are various – almost exclusively *a priori* arguments – which predict no χ SB, *i.e.*, the complete disappearance of a broken phase at finite N . Using explicit FRG computations in LPA we found no χ SB at non-zero temperature, indications for χ SB at zero temperature and a quantum phase transition (chiral symmetry restoration driven by density fluctuations induced by the chemical potential) at finite N in the GNY model [4].

A disclaimer about physics

The goal of physics is understanding nature and the laws that govern it. Theoretical physics, as a branch of physics, is tasked with using mathematical models to describe nature, focusing on identifying and theoretically understanding the governing laws and mechanisms of nature. In the context of this work, this means using the microscopic theory of QCD to describe the macroscopic phase structure of strongly interacting matter which our colleagues can probe using collider experiments, astrophysical objects (like neutron stars), and indirect experiments aimed at understanding the states of matter in the early universe. To compute macroscopic observables from the microscopic theory of QCD, we have to employ non-perturbative techniques from

the field of QFT. For us the non-perturbative tool of choice is the FRG. Of the many open research questions regarding the phase diagram of strongly interacting matter at intermediate temperatures and densities, we set out to focus on the question whether inhomogeneous chiral condensates exist in this phase diagram. We are particularly interested in the role of bosonic quantum and thermal fluctuations, which, so far, is poorly understood.

We will not provide an answer to this question in this work since the application of the developed numerical methods to the relevant LEFT, *viz.* the QM model, is subject to further research. In fact, throughout this entire thesis, we will not claim that our results have any direct implications for nature as we observe it. Our zero-dimensional models have no real tangible role in describing physical systems. The GN model in 1+1 dimensions has some applications in solid-state physics, but frankly, we are not qualified to comment on the possible implications of our results for physical systems in this context. We use the GN model in the context of high-energy physics, *i.e.*, purely as a toy model to study χ SB and as a stepping stone for computations in 3+1 dimensions. Our explicit results in the QM model in 3+1 dimensions are not novel but rather a reproduction of mean-field literature results with the FRG framework. Disregarding bosonic fluctuations in mean-field approximation or justifying this approximation by considering an infinite number of colors in a large- N_c limit is *a priori* by no means a valid approach to describe nature at $N_c = 3$.

Probably the closest we ever come to describing nature is our discussion of the heat equation and classical Euler equations of ideal fluid dynamics in our methodological introduction of CFD.

This work is therefore almost entirely focused on technical developments within the framework of the FRG. With our research we aim at improving the conceptual understanding of FRG flow equations and the role of inhomogeneous condensates in this context. Furthermore, we aim to establish robust numerical methods within the FRG framework, methods which have been rigorously developed and tested by the CFD community for the type of PDEs encountered. All these incremental developments have the goal to help facilitate first principle FRG computations of QCD with qualitative and quantitative predictive power at intermediate temperatures and quark chemical potentials, see, *e.g.*, Refs. [80, 209, 210]. Such computations are currently one of the most promising candidates to access these regimes of the phase diagram theoretically.

1.1. Outline

For this thesis we adopt a somewhat modified IMRaD (Introduction, Methods, Results, and Discussion) structure to present our research. Chapter 1 serves as an overall introduction to our research, which includes remarks about its chronological development in the context of my PhD studies and thus also already includes some remarks about key findings which shaped our research.

In chapter 2 we introduce overarching methods and concepts which are relevant for the main part of this thesis. We introduce the FRG as the main method employed in our studies in section 2.1. To discuss, study, and numerically solve FRG flow equations we employ the tools

and language established in section 2.2 from the field of CFD. In section 2.3 we briefly introduce QCD as the fundamental theory governing the strong force and motivate the LEFT, *viz.* the QM model, we use in this work. The notion of inhomogeneous phases in strongly-interacting matter and related computational challenges are discussed in section 2.4.

Chapters 3–5 constitute the main part of our research. Each chapter includes its own introduction and conceptualization, our research, and concluding remarks – incorporating a summary and outlook. For the presentation here I have chosen to order results by space-time dimension rather than by their chronological development within my PhD studies.

In chapter 3 we present and discuss our extensive research of zero-dimensional theories in the context of the FRG. This includes our studies of zero-dimensional $O(N)$ models in sections 3.1 and 3.2, which are already published in the series [1–3]. In section 3.3 we discuss first steps of an extension of this work to fermionic, *i.e.*, Grassmann-valued, degrees of freedom in zero dimensions which is based on the manuscript and material surrounding Ref. [7].

Chapter 4 is based on our research of the GN model and its variants. This discussion includes our study [5] of inhomogeneous phases in the GN model at infinite- N with a stability analysis in subsection 4.4.2 and our FRG-based study [4] of homogeneous phases at finite N in section 4.5. The latter is a direct application of our research and development in zero dimensions to a model in non-zero, *viz.* $1+1$ dimensions.

Chapter 5 is based on our research of the QM model in $3+1$ dimensions surrounding the draft [6]. The focus of this research is the novel and explicit study of inhomogeneous phases within the FRG framework. We discuss the derivation of the novel LPA flow equation for the CDW in the QM model in section 5.1 and related mean-field results in the subsequent section 5.2.

We give a brief, final summary and outlook in chapter 6. Technical details, conventions, and supplementary material can be found in the printed [Appendices](#) and in the accompanying digital auxiliary files, see App. A.1. The following backmatter includes the [Bibliography](#), a list of [Acronyms](#), my [Curriculum vitae](#), and [Acknowledgments](#).

The focus of our research on technical developments in the FRG might be off-putting to a reader not familiar and not invested into the framework. For readers unfamiliar with the FRG, I suggest a non-linear approach to reading this thesis to facilitate a more accessible entry into the subject matter. The methodological introduction to the FRG in section 2.1 begins at, and maintains, a very technical level, making it likely ill-suited for “*first-contact*” on its own.

I recommend initially skipping section 2.1 and, arguably, the entirety of chapter 2, and instead start with sections 3.1 and 3.2, as these sections are more accessible and didactic in nature. The reader then may use the included cross-references to jump back to relevant parts of sections 2.1 and 2.2 as and when needed. The remainder of chapter 3 should become accessible after that. Before continuing with chapter 4, I would advise reading section 2.4. For the study of chapter 5, I recommend reading the last remaining part of chapter 2, *viz.* section 2.3, since it is particularly relevant for the QM model.

I decided against structuring the thesis in this way to maintain a clearer split between methods and our research (results/discussion).

1.2. Publications and disclaimers

This thesis has been composed by me independently. No source materials or aids other than those mentioned have been used in accordance with the affidavit – [Erklärungen laut Promotionsordnung](#). However, most results have been obtained in collaboration with colleagues. Sections of this thesis dealing with results and ideas which are directly related to those collaborations have corresponding declarations at their beginning. Those declarations refer to the following publications, preprints, drafts, and notes:

- [1] A. Koenigstein, M. J. Steil, N. Wink, E. Grossi, J. Braun, M. Buballa, and D. H. Rischke, “Numerical fluid dynamics for FRG flow equations: Zero-dimensional QFTs as numerical test cases. I. The $O(N)$ model”, *Phys. Rev. D* **106** (2022) 065012, arXiv: [2108.02504 \[cond-mat.stat-mech\]](#),
- [2] A. Koenigstein, M. J. Steil, N. Wink, E. Grossi, and J. Braun, “Numerical fluid dynamics for FRG flow equations: Zero-dimensional QFTs as numerical test cases. II. Entropy production and irreversibility of RG flows”, *Phys. Rev. D* **106** (2022) 065013, arXiv: [2108.10085 \[cond-mat.stat-mech\]](#),
- [3] M. J. Steil and A. Koenigstein, “Numerical fluid dynamics for FRG flow equations: Zero-dimensional QFTs as numerical test cases. III. Shock and rarefaction waves in RG flows reveal limitations of the $N \rightarrow \infty$ limit in $O(N)$ -type models”, *Phys. Rev. D* **106** (2022) 065014, arXiv: [2108.04037 \[cond-mat.stat-mech\]](#),
- [4] J. Stoll, N. Zorbach, A. Koenigstein, M. J. Steil, and S. Rechenberger, “Bosonic fluctuations in the $(1 + 1)$ -dimensional Gross-Neveu(-Yukawa) model at varying μ and T and finite N ” (2021), arXiv: [2108.10616 \[hep-ph\]](#),
- [5] A. Koenigstein, L. Pannullo, S. Rechenberger, M. J. Steil, and M. Winstel, “Detecting inhomogeneous chiral condensation from the bosonic two-point function in the $(1 + 1)$ -dimensional Gross-Neveu model in the mean-field approximation*”, *J. Phys. A* **55** (2022) 375402, arXiv: [2112.07024 \[hep-ph\]](#),
- [6] M. J. Steil, M. Buballa, and B.-J. Schaefer, “Inhomogeneous chiral condensates in the quark-meson model with the functional renormalization group”, Draft, 2024, in preparation,
- [7] M. J. Steil, A. Koenigstein, and J. Braun, “Numerical fluid dynamics for FRG flow equations: Zero-dimensional QFTs as numerical test cases - Part IV: A fermion-boson model”, Draft, 2021, in preparation,
- [8] A. Koenigstein and M. J. Steil, “Absence of global fixed-point solutions in the zero-dimensional $O(N)$ -model”, 2021, unpublished notes, private communication,
- [9] A. Koenigstein and M. J. Steil, “Comment on the “grid methods” and other numerical schemes”, 2021, unpublished notes, private communication.

Figures and data taken or adapted from those joint publications are individually and explicitly marked and declared as such, while adapted formulations and equations are not marked individually.

Although I am not the sole author of the aforementioned material, I have been a major contributor to all of it. Further details regarding the publications and the use of material from them can be found in subsequent declarations – indented and typeset in italic, these disclaimers are placed under headings.

Information on digital auxiliary files, software packages, and tools relevant to this thesis can be found in Apps. [A.1](#) and [A.2](#). The digital material is available in the online repository

<https://github.com/MJSteil/PhD-Thesis>.

2. Theoretical background and methods

In this chapter we introduce the theoretical background and the methods used throughout this work.

In section 2.1 we begin with a discussion and summary of the key concepts of the FRG³, which we use as the main theoretical framework to compute observables for the models and theories studied in this thesis. The central equations of the FRG framework manifest as flow (conservation) equations, which we will discuss in general in section 2.2 with a special focus on CFD. In the subsequent section 2.3 we give a brief introduction of QCD as the fundamental theory of the strong interaction, which includes a discussion of LEFTs and their emergence from QCD in the FRG framework. We conclude this chapter with section 2.4, where we provide a concise introduction to inhomogeneous phases (condensates), focusing on computational challenges, employed methods, and selected literature results.

2.1. The functional renormalization group

The functional renormalization group (FRG) [211–216] and Dyson-Schwinger equations (DSEs) [217–219] are two major functional methods used to study QFTs. Related two-particle irreducible (2PI) and n -particle irreducible (n PI) techniques, see, *e.g.*, Refs. [220–224] as well as the lecture notes [225], are also popular for certain applications. Those functional methods are used to compute correlation functions (or their generating functionals) using non-perturbative loop equations.

Within this work we will primarily work with the FRG which we will introduce on a technical level in the following subsections. For more details we refer the interested reader to the lecture notes [93, 226–228] as well as to the following Refs. [95, 222, 229–231]. For details regarding DSEs, see, *e.g.*, Ref. [232] and references therein. The FRG was developed in the early 1990s by Christof Wetterich [211, 212] and others, including notable early developments by Martin Reuter, Tim R. Morris, Nikolaos Tetradis, and Ulrich Ellwanger [213–216].

Before a discussion of the FRG on a technical level (culminating in the derivation and discussion of the central Wetterich equation (2.37) in subsection 2.1.4), we will outline the idea behind this powerful non-perturbative method. The FRG implements Kenneth G. Wilson’s non-perturbative continuum RG approach [233–235] in momentum space and thus by extension the discrete equivalent – position space based – RG concept of Leo P. Kadanoff’s

³Sometimes also referred to as exact renormalization group (ERG) due to the fact that its central RG evolution equation, *viz.* the Wetterich Eq. (2.37), is formally an exact equation. This is in contrast to earlier non-perturbative RG evolution equations, which often times included approximations.

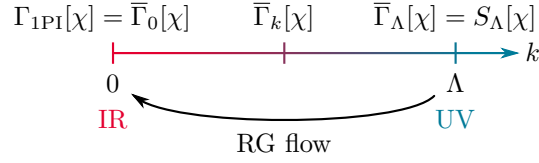


Figure 2.1.: Sketch of the FRG flow of the EAA $\bar{\Gamma}_k[\chi]$ from its initial condition $S_\Lambda[\chi]$ in the UV ($k = \Lambda$) towards the full quantum EA in the IR ($k \rightarrow 0$).

block-spin transformations [236]. The conceptual idea behind the RG is the study of physical systems/theories at different scales. The (functional) renormalization group ((F)RG)⁴ can be used to study the scale evolution of a theory from a microscopic scale – where the theory is initially defined using microscopic interactions – to a macroscopic scale – where we can compute macroscopic observables and correlation functions of the physical system under consideration. The changes during scale evolution in the correlation functions and observables of a field theory are governed by quantum and/or thermodynamic fluctuations. Considering a functional formulation of QFT based on a suitable functional integral, Wilson’s RG approach is based on integrating out fluctuations step by step – momentum shell by momentum shell. This incremental study of successive RG steps facilitates the practical computation of the underlying functional integral, which is usually not possible when trying to incorporate all fluctuations at once.

The FRG describes the RG-scale evolution of a scale-dependent effective average action (EAA) $\bar{\Gamma}_k[\chi]$ as a series of infinitesimal RG steps in form of a so-called RG flow. See figure 2.1 for a pictographic sketch of this process. In the following we use k to denote the RG scale. The starting point of the FRG flow is $\bar{\Gamma}_\Lambda[\chi]$ which is based on an Euclidean action $S_\Lambda[\chi]$ at a RG UV initial scale $k = \Lambda$. The action at this scale is considered “classical” in a sense that either Λ is asymptotically large or $S_\Lambda[\chi]$ includes all quantum fluctuations with momenta $|p| > \Lambda$. Starting at the initial scale Λ the idea is to integrate out fluctuations successively in a Wilsonian manner by splitting the quantum fields based on their momenta. In the FRG this is achieved by introducing a suitable regulator which ultimately implements and facilitates this process. The RG-scale evolution in the FRG is governed by one central non-perturbative one-loop equation – the so-called *Wetterich* flow equation [211–216]. This non-linear functional differential equation is exact given a suitable regulator choice and thus maps the problem of solving the functional integral to solving a corresponding flow equation. Using this flow equation, one can track the change of a microscopic theory with a given action $\bar{\Gamma}_\Lambda[\chi] = S_\Lambda[\chi]$ in the UV ($k = \Lambda$) towards a macroscopic theory with a full quantum effective action $\bar{\Gamma}_0[\chi] = \Gamma_{1PI}[\chi]$ in the IR ($k \rightarrow 0$). The FRG is inherently non-perturbative and thus allows the study of both weakly and strongly coupled systems. Using the scale-dependent EAA $\bar{\Gamma}_k[\chi]$ it is in principle possible to study the ground state, realized symmetries, thermodynamic properties, and correlation functions of a theory at varying RG scales k . This makes the FRG an immensely powerful tool to study the effect of quantum and/or thermodynamic fluctuations in a wide range of physical systems at

⁴We use (F)RG when making statements which apply for the functional renormalization group as well as for the non-perturbative renormalization group in general.

different scales in a controlled and unified framework.

2.1.1. Scale-dependent generating functionals

We begin our technical discussion of the FRG by introducing two auxiliary scale-dependent generating functionals.

For the following discussion we consider a quantum field theory with the Euclidean action $S_\Lambda[\tilde{\chi}]$, where $\tilde{\chi}$ is a multi component fundamental quantum field which includes the entire field content of the theory under consideration in the field space (FS) notation of App. B.4. In the subsequent derivation we consider a generic theory in which $\tilde{\chi}$ collects scalar (mesonic) fields $\tilde{\varphi}$ and Grassmann-valued (fermionic) fields $\tilde{\psi}$ and $\tilde{\bar{\psi}}$:

$$(\tilde{\chi}_a) \equiv (\tilde{\varphi}, \tilde{\psi}, \tilde{\bar{\psi}}). \quad (2.1)$$

We further introduce $\hat{\chi}$ as a RG-scale-dependent multi component composite field of the fundamental fields

$$(\hat{\chi}_a) \equiv (\hat{\chi}_{k;a}[\tilde{\chi}]). \quad (2.2)$$

For readability we will usually suppress the scale and functional dependency in the notation. We introduce corresponding sources

$$(\hat{J}_a) \equiv (\hat{J}_\varphi, \hat{J}_{\tilde{\psi}}, \hat{J}_\psi) \quad (2.3)$$

in the generating functional to extract correlation functions and to study condensation. Working with such scale-dependent composite fields as degrees of freedom is more elegant and efficient since the fundamental fields of a theory are not necessary suitable degrees of freedom at all scales. A prime example for this is QCD, where the fundamental fields are quarks and gauge fields which are excellent degrees of freedom in the UV (at some UV reference scale Λ) due to asymptotic freedom. In the IR ($k \rightarrow 0$) however – due to confinement and chiral symmetry breaking – a description in terms of hadrons is desirable, since baryons and mesons are the relevant degrees of freedom. Introducing those hadrons as composite fields of the fundamental fields has proven highly effective and elegant in FRG studies of QCD, see, *e.g.*, Refs. [80, 109, 237] and references therein and subsection 2.3.3.

To implement Wilson's RG approach we introduce a RG-scale-dependent regulator term $\Delta S_k[\hat{\chi}]$ in the Euclidean generating functional of the theory under consideration

$$Z_k[\hat{J}] = \exp\left(-\Delta S_k\left[\frac{\delta}{\delta \hat{J}}\right]\right) Z[\hat{J}] = \int \mathcal{D}[\tilde{\chi}] \exp\left(-S_\Lambda[\tilde{\chi}] - \Delta S_k[\hat{\chi}] + \hat{J}^m \hat{\chi}_m\right), \quad (2.4)$$

where $S_\Lambda[\tilde{\chi}]$ is the Euclidean, classical action prescribing kinematics and interactions of the fundamental fields $\tilde{\chi}$. $\mathcal{D}[\tilde{\chi}]$ is a suitable functional integral measure including a possible normalization factor \mathcal{N} and appropriate boundary conditions for the fields when working at non-zero temperature, see App. C for details. Such a normalization factor \mathcal{N} is arbitrary, since

it does not affect observables and thus varies depending on the conventions used for $Z[\hat{J}]$. General expectation values in presence of \hat{J} and $\Delta S_k[\hat{\chi}]$ are given by

$$\langle O[\hat{\chi}] \rangle_{k;\hat{J}} = \frac{1}{Z_k[\hat{J}]} \int \mathcal{D}[\tilde{\chi}] O[\hat{\chi}] \exp \left(-S_\Lambda[\tilde{\chi}] - \Delta S_k[\hat{\chi}] + \hat{J}^{\mathbf{m}} \hat{\chi}_{\mathbf{m}} \right). \quad (2.5)$$

From Eq. (2.5) one obtains the useful identity

$$\frac{\delta}{\delta \hat{J}^{\mathbf{a}}} \langle O[\hat{\chi}] \rangle_{k;\hat{J}} = - \langle \hat{\chi}_{\mathbf{a}} \rangle_{k;\hat{J}} \langle O[\hat{\chi}] \rangle_{k;\hat{J}} + \langle \hat{\chi}_{\mathbf{a}} O[\hat{\chi}] \rangle_{k;\hat{J}}. \quad (2.6)$$

For practical computations in the scope of this work it is convenient to choose a regulator term $\Delta S_k[\hat{\chi}]$ which is quadratic in the fields

$$\Delta S_k[\hat{\chi}] \equiv \Delta S[\hat{\chi}, R_k] \equiv \frac{1}{2} R_k^{\mathbf{mn}} \hat{\chi}_{\mathbf{n}} \hat{\chi}_{\mathbf{m}}, \quad (2.7)$$

where we introduced the regulator $R_k^{\mathbf{mn}}$ ⁵. $\Delta S_k[\hat{\chi}]$ should appear as a scalar in the exponent under the functional integral. This implies a bilinear form of the regulator for Grassmann-valued FS components with

$$R_k^{\mathbf{mn}} = (-1)^{\mathbf{nm}} R_k^{\mathbf{nm}} \quad (2.8)$$

and a non-trivial structure in its internal spaces. A quadratic regulator leads to one-loop flow equations for all n -point functions [222, 238]. Higher-order regulators are possible, see, e.g., Ref. [222], but will not be discussed in our work. With the definition (2.7) the second FS derivative of the regulator term is given by

$$\Delta S[\hat{\chi}, R_k]_{,\mathbf{ab}} = \frac{1}{2} \frac{\delta}{\delta \hat{\chi}_{\mathbf{a}}} \frac{\delta}{\delta \hat{\chi}_{\mathbf{b}}} R_k^{\mathbf{mn}} \hat{\chi}_{\mathbf{n}} \hat{\chi}_{\mathbf{m}} = \frac{1}{2} \frac{\delta}{\delta \hat{\chi}_{\mathbf{a}}} \left(R_k^{\mathbf{mb}} \hat{\chi}_{\mathbf{m}} + (-1)^{\mathbf{bn}} R_k^{\mathbf{bn}} \hat{\chi}_{\mathbf{n}} \right) = R_k^{\mathbf{ab}}. \quad (2.9)$$

We will discuss further constraints on the regulator related to the proper implementation of Wilson's RG approach in subsection 2.1.4.1.

The scale-dependent Schwinger functional $W_k[\hat{J}]$ is given by

$$W_k[\hat{J}] = \ln Z_k[\hat{J}]. \quad (2.10)$$

Considering functional derivatives of the Schwinger functional leads to connected n -point functions, see, e.g., Refs. [177, 178, 226, 239, 240]. The one-point function – the expectation value of $\hat{\chi}$ in presence of $\Delta S_k[\hat{\chi}]$ and \hat{J} – is simply given by

$$\frac{\delta}{\delta \hat{J}^{\mathbf{a}}} W_k[\hat{J}] = \frac{1}{Z_k[\hat{J}]} \frac{\delta Z_k[\hat{J}]}{\delta \hat{J}^{\mathbf{a}}} = \langle \hat{\chi}_{\mathbf{a}} \rangle_{k;\hat{J}}. \quad (2.11)$$

⁵We have chosen $\frac{1}{2} R_k^{\mathbf{mn}} \hat{\chi}_{\mathbf{n}} \hat{\chi}_{\mathbf{m}}$ and not $R_k^{\mathbf{nm}} \hat{\chi}_{\mathbf{n}} \hat{\chi}_{\mathbf{m}}$ like in Ref. [222] out of personal preference especially related to the form of Eq. (2.9).

To study the RG scale evolution of $W_k[\hat{J}]$ and by extension $Z_k[\hat{J}]$ we consider the total RG-scale derivative⁶ of $W_k[\hat{J}]$. It is convenient to study and discuss the scale evolution from $k = \Lambda$ to $k \rightarrow 0$ using a dimensionless RG/flow time t which we define⁷ as

$$t \equiv -\ln\left(\frac{k}{\Lambda}\right) = \ln\left(\frac{\Lambda}{k}\right), \quad t \in [0, \infty). \quad (2.12)$$

The evolution equation for $W_k[\hat{J}]$ is given by

$$\frac{dW_k[\hat{J}]}{dt} = \frac{d}{dt} \ln Z_k[\hat{J}] = \frac{1}{Z_k[\hat{J}]} \frac{dZ_k[\hat{J}]}{dt} = \quad (2.13a)$$

$$= \frac{1}{Z_k[\hat{J}]} \int \mathcal{D}[\tilde{\chi}] \frac{d}{dt} \exp\left(-S_\Lambda[\tilde{\chi}] - \frac{1}{2} R_k^{\text{mn}} \hat{\chi}_n \hat{\chi}_m + \hat{J}^m \hat{\chi}_m\right) = \quad (2.13b)$$

$$= \hat{J}^m \langle \partial_t \hat{\chi}_m \rangle_{k; \hat{J}} - \frac{1}{2} (\partial_t R_k^{\text{mn}}) \langle \hat{\chi}_n \hat{\chi}_m \rangle_{k; \hat{J}} - R_k^{\text{mn}} \langle \hat{\chi}_n \partial_t \hat{\chi}_m \rangle_{k; \hat{J}}, \quad (2.14)$$

where we considered $k = k(t) \equiv \Lambda e^{-t}$. Eq. (2.14) is the generalization of the Polchinski equation [241] for composite fields with IR regularization [226]⁸. We will discuss the scale-dependent Schwinger functional further in subsection 3.1.3.1 in the context of zero-dimensional QFTs.

2.1.2. Scale-dependent effective average action

While working with RG equations (2.14) for the Schwinger functional is possible, it is more convenient for most practical computations to work with the scale-dependent EAA $\bar{\Gamma}_k[\chi]$ which is given by the modified Legendre transform of the Schwinger functional

$$\bar{\Gamma}_k[\chi] \equiv \Gamma_k[\chi] - \Delta S_k[\chi] \equiv \sup_{\hat{J}} \left(\hat{J}^m \chi_m - W_k[\hat{J}] \right) - \Delta S_k[\chi], \quad (2.15)$$

$$\bar{\Gamma}_k[\chi] + \Delta S_k[\chi] = \Gamma_k[\chi] = J^m \chi_m - W_k[J], \quad (2.16)$$

where we denote J^m as the source \hat{J}^m which realizes the supremum for a given so-called mean-field χ_m and $\Delta S_k[\chi] = R_k^{\text{mn}} \chi_n \chi_m / 2$ in analogy to Eq. (2.7). The modification of the Legendre transform with $\Delta S_k[\chi]$ is necessary in order to implement $\bar{\Gamma}_k \rightarrow S_\Lambda$ in the UV limit $k \rightarrow \Lambda$, see subsection 3.1.3.2 for a detailed discussion of this subtle point. $\bar{\Gamma}_k[\chi]$ is only

⁶Total derivatives w.r.t. the RG scale (RG time) will be frequently abbreviated by ∂_k (∂_t) in the following. We denote RG scale-dependence with either k or t depending on the element and context. In terms of derivatives both are always understood as $k(t)$ and $t(k)$. The reasoning behind this mixed use of k and t in formulas is that for the discussion of flow/evolution we like t while for denoting IR and UV we prefer k .

⁷We adopt a sign convention for the RG flow time resulting in a positive time evolution from the UV ($k = \Lambda \Leftrightarrow t = 0$) to the IR ($k \rightarrow 0 \Leftrightarrow t \rightarrow \infty$).

⁸However, in the original work [241] an effective action $L(\Lambda, \phi)$ takes the role of $W_k[\hat{J}]$ and it is formulated in terms of the fields ϕ instead of the sources \hat{J} . For relations between the original Polchinski equation and the flow equations studied in this work and selected applications of the Polchinski equation, see, e.g., Refs. [109, 242–245].

guaranteed to be convex in the IR ($k \rightarrow 0$)⁹, where $\Delta S_k[\chi] \rightarrow 0$. In this limit the EAA reduces to the canonically known effective action (EA) $\Gamma_0[\chi] \equiv \Gamma_{\text{1PI}}[\chi]$, see, e.g., Ref. [177]. The EAA $\bar{\Gamma}_k[\chi]$ is the scale-dependent generating functional of scale-dependent one-particle irreducible (1PI) correlation functions, see, e.g., Refs. [177, 178, 226, 239, 240], which in the IR limit $k \rightarrow 0$ reduce to the canonical 1PI correlation functions of the full quantum field theory. As such $\bar{\Gamma}_k[\chi]$ encodes the entire information of a theory without diagrammatic redundancies. In the IR it also encodes the thermodynamic *grand potential* $\tilde{\Omega}$, see App. C.1 and especially Eq. (C.7) for details, and thus can be used to study thermodynamic properties, phase transitions, and symmetry breaking, cf. chapters 4 and 5 for explicit applications.

By construction Eq. (2.16) implies

$$\frac{\delta}{\delta \hat{J}^{\mathbf{a}}} \left(\bar{\Gamma}_k[\chi] + \Delta S_k[\chi] \right) = 0 = \frac{\delta}{\delta \hat{J}^{\mathbf{a}}} \sup_{\hat{J}} \left(\hat{J}^{\mathbf{m}} \chi_{\mathbf{m}} - W_k[\hat{J}] \right) = \sup_{\hat{J}} \left(\chi_{\mathbf{a}} - \frac{\delta W_k[\hat{J}]}{\delta \hat{J}^{\mathbf{a}}} \right), \quad (2.17)$$

which at the supremum $\hat{J} = J$ is equivalent to

$$\chi_{\mathbf{a}} = \left. \frac{\delta W_k[\hat{J}]}{\delta \hat{J}^{\mathbf{a}}} \right|_{\hat{J}=J} \equiv \frac{\delta W_k[J]}{\delta J^{\mathbf{a}}} \quad (2.18)$$

in accordance to Eq. (2.11).

The source realizing the supremum in Eq. (2.15) is a scale-dependent functional of the mean-field, $J^{\mathbf{a}} \equiv J_k^{\mathbf{a}}[\chi]$, and in turn the mean-field as the expectation value of $\hat{\chi}_{\mathbf{a}}$ in presence of $\Delta S_k[\hat{\chi}]$ and J is a scale-dependent functional of the source J : $\chi_{\mathbf{a}} \equiv \chi_{k;\mathbf{a}}[J] \equiv \langle \hat{\chi}_{\mathbf{a}} \rangle_{k;J}$. We suppress the scale and functional-dependencies of $J^{\mathbf{a}}$ and $\chi_{\mathbf{a}}$ in our notation only for readability while still considering them in our computations, if not stated explicitly otherwise. In the following we will mainly work with the source J and expressions evaluated at it. Functionals and functional derivatives of J are to be understood as functionals and functional derivatives w.r.t. \hat{J} evaluated at $\hat{J} = J$ like in Eq. (2.18).

2.1.3. Quantum equation of motion and propagator

Using the identity (2.18) together with Eq. (2.16) we derive the scale-dependent quantum equation of motion (QEOM)

$$\frac{\delta}{\delta \chi_{\mathbf{a}}} \left(\bar{\Gamma}_k[\chi] + \Delta S_k[\chi] \right) = \frac{\delta}{\delta \chi_{\mathbf{a}}} \left(J^{\mathbf{m}} \chi_{\mathbf{m}} - W_k[J] \right) = \quad (2.19a)$$

$$= \frac{\delta J^{\mathbf{m}}}{\delta \chi_{\mathbf{a}}} \chi_{\mathbf{m}} + (-1)^{\mathbf{a}\mathbf{m}} J^{\mathbf{m}} \frac{\delta \chi_{\mathbf{m}}}{\delta \chi_{\mathbf{a}}} - \frac{\delta J^{\mathbf{m}}}{\delta \chi_{\mathbf{a}}} W_{k,\mathbf{m}}[J] = \quad (2.19b)$$

$$= (-1)^{\mathbf{a}\mathbf{m}} \delta_{\mathbf{m}}^{\mathbf{a}} J^{\mathbf{m}} = \quad (2.19c)$$

$$= \gamma_{\mathbf{m}}^{\mathbf{a}} J^{\mathbf{m}} \quad (2.20)$$

⁹For certain theories and initial conditions for the RG-scale evolution in a given truncation $\bar{\Gamma}_0[\chi] = \Gamma_0[\chi]$ is only locally convex in the IR. For details, see, e.g., Refs. [246, 247]. In this work we only consider theories with a convex effective action in the IR limit.

relating sources $J^{\mathbf{a}}$ to their respective mean-fields $\chi_{\mathbf{a}}$.

Taking one additional derivative of $\chi_{\mathbf{b}} = W_{k,\mathbf{b}}[J]$ w.r.t. $J^{\mathbf{a}}$ leads to the connected two-point function – the full scale-dependent propagator – in presence of the source J and regulator ΔS_k :

$$G_{k;\mathbf{ab}}[\chi] \equiv W_{k,\mathbf{ab}}[J] \quad (2.21)$$

$$= \frac{\delta}{\delta J^{\mathbf{a}}} W_{k,\mathbf{b}}[J] = \frac{\delta}{\delta J^{\mathbf{a}}} \langle \chi_{\mathbf{b}} \rangle_{k;J} \equiv \chi_{\mathbf{b},\mathbf{a}} = \quad (2.22a)$$

$$= \left(\frac{\delta}{\delta J^{\mathbf{a}}} \frac{1}{Z_k[J]} \right) \int \mathcal{D}[\tilde{\chi}] \hat{\chi}_{\mathbf{b}} \exp(\dots) + \frac{1}{Z_k[J]} \int \mathcal{D}[\tilde{\chi}] \frac{\delta}{\delta J^{\mathbf{a}}} \hat{\chi}_{\mathbf{b}} \exp(\dots) = \quad (2.22b)$$

$$= -\langle \hat{\chi}_{\mathbf{a}} \rangle_{k;J} \langle \hat{\chi}_{\mathbf{b}} \rangle_{k;J} + (-1)^{\mathbf{ab}} \langle \hat{\chi}_{\mathbf{b}} \hat{\chi}_{\mathbf{a}} \rangle_{k;J} = \quad (2.22c)$$

$$= \langle \hat{\chi}_{\mathbf{a}} \hat{\chi}_{\mathbf{b}} \rangle_{k;J[\chi]} - \chi_{\mathbf{a}} \chi_{\mathbf{b}}. \quad (2.23)$$

The scale-dependent propagator $G_{k;\mathbf{ab}}[\chi]$ is a fundamental object in the FRG due to its relation to the scale-dependent two-point function and since it connects functional derivatives w.r.t. J to the ones w.r.t. χ via a chain rule

$$\frac{\delta}{\delta J^{\mathbf{a}}} = \frac{\delta \chi_{\mathbf{m}}}{\delta J^{\mathbf{a}}} \frac{\delta}{\delta \chi_{\mathbf{m}}} = G_{k;\mathbf{am}}[\chi] \frac{\delta}{\delta \chi_{\mathbf{m}}}, \quad (2.24)$$

which, when applied to $\chi_{\mathbf{a}}$, yields

$$\frac{\delta \chi_{\mathbf{b}}}{\delta J^{\mathbf{a}}} = G_{k;\mathbf{ab}}[\chi] = \langle \hat{\chi}_{\mathbf{a}} \hat{\chi}_{\mathbf{b}} \rangle_{k;J} - \chi_{\mathbf{a}} \chi_{\mathbf{b}} \quad (2.25)$$

in accordance to Eq. (2.6).

Taking one additional J derivative of the QEOM (2.20) and using the chain rule (2.24) leads to the following relations between the scale-dependent propagator and the EAA:

$$\frac{\delta}{\delta J^{\mathbf{a}}} \frac{\delta (\bar{\Gamma}_k[\chi] + \Delta S_k[\chi])}{\delta \chi_{\mathbf{b}}} = \gamma_{\mathbf{m}}^{\mathbf{b}} \frac{\delta J^{\mathbf{m}}}{\delta J^{\mathbf{a}}}, \quad (2.26a)$$

$$G_{k;\mathbf{am}}[\chi] \frac{\delta}{\delta \chi_{\mathbf{m}}} \frac{\delta (\bar{\Gamma}_k[\chi] + \Delta S_k[\chi])}{\delta \chi_{\mathbf{b}}} = \gamma_{\mathbf{m}}^{\mathbf{b}} \delta_{\mathbf{a}}^{\mathbf{m}}, \quad (2.26b)$$

$$G_{k;\mathbf{am}}[\chi] \left(\bar{\Gamma}_k^{\mathbf{mb}}[\chi] + R_k^{\mathbf{mb}} \right) = \gamma_{\mathbf{a}}^{\mathbf{b}}, \quad (2.27)$$

$$G_{k;\mathbf{ac}}[\chi] = \gamma_{\mathbf{a}}^{\mathbf{n}} \left(\bar{\Gamma}_k[\chi] + \Delta S_k[\chi] \right)_{\mathbf{nc}}^{-1}, \quad (2.28a)$$

$$\gamma_{\mathbf{a}}^{\mathbf{n}} G_{k;\mathbf{nc}}[\chi] = \left(\bar{\Gamma}_k[\chi] + \Delta S_k[\chi] \right)_{\mathbf{ac}}^{-1}, \quad (2.28b)$$

with

$$\left(\bar{\Gamma}_k^{\mathbf{an}}[\chi] + R_k^{\mathbf{an}} \right) \left(\bar{\Gamma}_k[\chi] + \Delta S_k[\chi] \right)_{\mathbf{nb}}^{-1} \equiv \delta_{\mathbf{b}}^{\mathbf{a}}. \quad (2.29)$$

The relation between the full scale-dependent propagator and the inverse Hessian of $\bar{\Gamma}_k[\chi] + \Delta S_k[\chi]$ includes a contraction with $\gamma_{\mathbf{a}}^{\mathbf{n}}$ which results in a minus sign for the propagators of Grassmann-valued fields¹⁰.

¹⁰It is very common in literature to absorb this minus sign in a so-called super-trace denoted by STr . We will retain the minus sign for Grassmann-valued fields in their propagators.

2.1.4. The Wetterich equation

Using the expressions derived in the previous subsections we are now able to derive the central equation of the FRG – the Wetterich flow equation governing the RG-scale/RG-time evolution of the EAA. The total RG time derivative of the EAA can be computed by combining Eqs. (2.14) and (2.16):

$$\frac{d}{dt} \bar{\Gamma}_k[\chi] = \frac{d}{dt} (J^{\mathbf{m}} \chi_{\mathbf{m}} - W_k[J] - \Delta S_k[\chi]) = \quad (2.30a)$$

$$= (\partial_t J^{\mathbf{m}}) \chi_{\mathbf{m}} + J^{\mathbf{m}} \partial_t \chi_{\mathbf{m}} - \partial_t|_J W_k[J] - (\partial_t J^{\mathbf{m}}) W_{k,\mathbf{m}}[J] - \frac{1}{2} (\partial_t R_k^{\mathbf{mn}}) \chi_{\mathbf{n}} \chi_{\mathbf{m}} - R_k^{\mathbf{mn}} \chi_{\mathbf{n}} \partial_t \chi_{\mathbf{m}} = \quad (2.30b)$$

$$= (\partial_t J^{\mathbf{m}}) (\chi_{\mathbf{m}} - W_{k,\mathbf{m}}[J]) + J^{\mathbf{m}} \partial_t \chi_{\mathbf{m}} - J^{\mathbf{m}} \langle \partial_t \hat{\chi}_{\mathbf{m}} \rangle_{k;J} + \frac{1}{2} (\partial_t R_k^{\mathbf{mn}}) \langle \hat{\chi}_{\mathbf{n}} \hat{\chi}_{\mathbf{m}} \rangle_{k;J} + R_k^{\mathbf{mn}} \langle \hat{\chi}_{\mathbf{n}} \partial_t \hat{\chi}_{\mathbf{m}} \rangle_{k;J} - \frac{1}{2} (\partial_t R_k^{\mathbf{mn}}) \chi_{\mathbf{n}} \chi_{\mathbf{m}} - R_k^{\mathbf{mn}} \chi_{\mathbf{n}} \partial_t \chi_{\mathbf{m}} = \quad (2.30c)$$

$$= J^{\mathbf{m}} \left(\partial_t \chi_{\mathbf{m}} - \langle \partial_t \hat{\chi}_{\mathbf{m}} \rangle_{k;J} \right) + \frac{1}{2} (\partial_t R_k^{\mathbf{mn}}) G_{k;\mathbf{nm}}[\chi] + R_k^{\mathbf{mn}} \left(\langle \hat{\chi}_{\mathbf{n}} \partial_t \hat{\chi}_{\mathbf{m}} \rangle_{k;J} - \chi_{\mathbf{n}} \partial_t \chi_{\mathbf{m}} \right) = \quad (2.30d)$$

$$= \frac{1}{2} (\partial_t R_k^{\mathbf{mn}}) G_{k;\mathbf{nm}}[\chi] + J^{\mathbf{m}} \left(\partial_t \chi_{\mathbf{m}} - \langle \partial_t \hat{\chi}_{\mathbf{m}} \rangle_{k;J} \right) + R_k^{\mathbf{mn}} \left(\frac{\delta}{\delta J^{\mathbf{n}}} \langle \partial_t \hat{\chi}_{\mathbf{m}} \rangle_{k;J} + \chi_{\mathbf{n}} \left(\langle \partial_t \hat{\chi}_{\mathbf{m}} \rangle_{k;J} - \partial_t \chi_{\mathbf{m}} \right) \right) \quad (2.30e)$$

$$\frac{d}{dt} \bar{\Gamma}_k[\chi] = \frac{1}{2} (\partial_t R_k^{\mathbf{mn}}) G_{k;\mathbf{nm}}[\chi] + (J^{\mathbf{m}} + R_k^{\mathbf{mn}} \chi_{\mathbf{n}}) \left(\partial_t \chi_{\mathbf{m}} - \langle \partial_t \hat{\chi}_{\mathbf{m}} \rangle_{k;J} \right) + R_k^{\mathbf{mn}} G_{k;\mathbf{nl}}[\chi] \frac{\delta \langle \partial_t \hat{\chi}_{\mathbf{m}} \rangle_{k;J}}{\delta \chi_{\mathbf{l}}}, \quad (2.31)$$

where we used the identities (2.18) and (2.25) in Eq. (2.30d), the identity (2.6) in Eq. (2.30e), and the chain rule (2.24) to ultimately obtain Eq. (2.31). Enforcing the constraint

$$\langle \partial_t \hat{\chi}_{\mathbf{m}} \rangle_{k;J} = \partial_t \chi_{\mathbf{m}} \quad (2.32)$$

on the composite field $\hat{\chi}_{\mathbf{m}}$ simplifies the scale evolution equation for $\bar{\Gamma}_k$ significantly. Eq. (2.32) introduces additional constraints which resolve the scale evolution of $\hat{\chi}$ in terms of the $\tilde{\chi}$ [222]. Working with the evolution equation for $\bar{\Gamma}_k[\chi]$ does not require an explicit resolution of the evolution $\partial_t \hat{\chi}_{t;\mathbf{a}}[\tilde{\chi}]$ of the composite quantum fields $\hat{\chi}_{t;\mathbf{a}}[\tilde{\chi}]$ in terms of the microscopic, fundamental fields $\tilde{\chi}$, see Refs. [80, 109, 222, 226, 248] for more details. Therefore we encode the theory in $\bar{\Gamma}_k[\chi]$ completely in terms of mean-fields χ , consider Eq. (2.32) as the defining property of $\hat{\chi}_{k;\mathbf{a}}[\tilde{\chi}]$, and eliminate all dependencies on $\partial_t \hat{\chi}_{\mathbf{m}}$ on the level of the EAA using Eq. (2.32). Using the constraint (2.32) simplifies the scale evolution (2.31) for $\bar{\Gamma}_k$ to

$$\frac{d}{dt} \bar{\Gamma}_k[\chi] = \partial_t|_{\chi} \bar{\Gamma}_k[\chi] + \bar{\Gamma}_k^{\mathbf{m}}[\chi] \partial_t \chi_{\mathbf{m}} = \frac{1}{2} (\partial_t R_k^{\mathbf{mn}}) G_{k;\mathbf{nm}}[\chi] + R_k^{\mathbf{mn}} G_{k;\mathbf{nl}}[\chi] \frac{\delta \partial_t \chi_{\mathbf{m}}}{\delta \chi_{\mathbf{l}}}. \quad (2.33)$$

This is the RG evolution/Wetterich equation of $\bar{\Gamma}_k[\chi]$ for general scale-dependent mean-fields χ_k , cf. Refs. [104, 227, 248], sometimes also referred to as *Flow Equation with Dynamical Hadronization* [97, 226] in the context of QCD. To close the system (2.33) the (flow of) the composite field $(\partial_t)\chi_{\mathbf{m}}[\chi]$ has to be specified. This generalized version of the Wetterich equation for composite fields is an extremely powerful tool to study strongly interacting theories with emerging, relevant degrees of freedom – like QCD – cf. Refs. [80, 109, 237, 249] and subsection 2.3.3.

For our computational studies within this work, which do not include explicit composite fields, this general equation can be simplified further by considering only linear scale-dependencies in $\partial_t\chi_{k;\mathbf{m}}$ solely governed by an appropriate, field-independent wave-function renormalization:

$$\chi_{k;\mathbf{m}} = (Z_{k;\mathbf{m}}^\chi)^{1/2} \chi_{0;\mathbf{m}} \Rightarrow \partial_t\chi_{k;\mathbf{m}} = \eta_{k;\mathbf{m}}^\chi \chi_{k;\mathbf{m}}, \quad (2.34)$$

with the anomalous dimension

$$\eta_{k;\mathbf{m}}^\chi \equiv \frac{1}{2} \partial_t \ln Z_{k;\mathbf{m}}^\chi = \frac{1}{2} \frac{\partial_t Z_{k;\mathbf{m}}^\chi}{Z_{k;\mathbf{m}}^\chi}. \quad (2.35)$$

Using Eq. (2.34) the general evolution Eq. (2.33) simplifies to

$$\begin{aligned} \frac{d}{dt} \bar{\Gamma}_k[\chi] &= \partial_t|_\chi \bar{\Gamma}_k[\chi] + \bar{\Gamma}_k^{\mathbf{m}}[\chi] \eta_{k;\mathbf{m}}^\chi \chi_{\mathbf{m}} = \frac{1}{2} (\partial_t R_k^{\mathbf{mn}}) G_{k;\mathbf{nm}}[\chi] + R_k^{\mathbf{mn}} G_{k;\mathbf{nl}}[\chi] \eta_{k;\mathbf{l}}^\chi = \\ &= \left(\partial_t|_\chi + \eta_{k;\mathbf{m}}^\chi \chi_{\mathbf{m}} \frac{\delta}{\delta \chi_{\mathbf{m}}} \right) \bar{\Gamma}_k[\chi] = \frac{1}{2} G_{k;\mathbf{mn}}[\chi] \left(\partial_t + 2\eta_{k;\mathbf{n}}^\chi \right) R_k^{\mathbf{nm}}, \end{aligned} \quad (2.36)$$

which we refer to as the Wetterich equation for the scale-dependent mean-field $\chi_{k;\mathbf{m}}$. The simple scale-dependence of Eq. (2.34) can be absorbed into the EAA by switching variables from $\chi_{k;\mathbf{m}}$ to $\chi_{0;\mathbf{m}}$ (which we will denote as $\chi_{\mathbf{m}}$ in the following for simplicity/readability) thus considering an EAA for the bare mean-fields with the wave-function renormalizations $Z_{k;\mathbf{m}}^\chi$ absorbed into the couplings within $\bar{\Gamma}_k[\chi_0 \equiv \chi]$. This simplifies Eq. (2.36) even further to the Wetterich equation [211–216] in its well known form

$$\partial_t \bar{\Gamma}_k[\chi] = \frac{1}{2} G_{k;\mathbf{mn}}[\chi] \partial_t R_k^{\mathbf{nm}} \equiv \mathcal{F}_k[\chi] = \frac{1}{2} \text{⊗}, \quad (2.37)$$

where we still use FS notation (instead of a super-trace) for a unified treatment of fermionic (Grassmann-valued) and bosonic (non-Grassmann-valued) fields collected in χ as well as our RG time derivative with $k = k(t) \equiv \Lambda e^{-t} \Rightarrow \partial_t \rightarrow -k\partial_k$.

Recalling Eq. (2.27) we note that the propagator $G_{k;\mathbf{ab}}[\chi]$ on the right-hand side (r.h.s.) of the Wetterich equation (2.37) depends on the inverse Hessian of $\bar{\Gamma}_k[\chi] + \Delta S_k[\chi]$ and thus on the second functional derivatives of $\bar{\Gamma}_k[\chi]$. Therefore the Wetterich equation manifests as a non-linear functional differential equation for the EAA. The r.h.s. of Eq. (2.37) is a non-perturbative one-loop equation since it involves the full scale-dependent propagator $G_{k;\mathbf{ab}}[\chi]$ (solid black line in diagrams) of the theory contracted with the regulator insertion $\partial_t R_k^{\mathbf{ba}}$ (black cross

within a circle in diagrams). In Eq. (2.37) we further introduced the symbolic abbreviation $\mathcal{F}_k[\chi]$ ¹¹ for the FRG flux on the r.h.s., which will be particularly useful in subsection 2.1.6. The Wetterich equation (2.37) is the governing master equation of the FRG framework and it can be used as a generating equation for explicit flow equations for higher-order n -point functions, see subsection 2.1.5 for details.

2.1.4.1. Regulators, initial condition, and implementation of Wilson's RG approach

For the subsequent discussions, regarding the regulator and initial condition (IC) for the Wetterich equation, the following functional integral representation (2.39) for the EAA $\bar{\Gamma}_k[\chi]$ will be useful. Using Eq. (2.16) with the definitions (2.4) and (2.10) for Z_k and W_k respectively we arrive at

$$e^{-\bar{\Gamma}_k[\chi]} = \int \mathcal{D}[\tilde{\chi}] \exp \left(-S_\Lambda[\tilde{\chi}] + J^{\mathbf{m}}(\tilde{\chi}_{\mathbf{m}} - \chi_{\mathbf{m}}) - \frac{1}{2}R_k^{\mathbf{mn}}(\tilde{\chi}_{\mathbf{n}}\tilde{\chi}_{\mathbf{m}} - \chi_{\mathbf{n}}\chi_{\mathbf{m}}) \right) = \quad (2.38a)$$

$$= \int \mathcal{D}[\tilde{\chi}] \exp \left(-S_\Lambda[\chi + \tilde{\chi}] + J^{\mathbf{m}}\tilde{\chi}_{\mathbf{m}} - \frac{1}{2}R_k^{\mathbf{mn}}\tilde{\chi}_{\mathbf{n}}\tilde{\chi}_{\mathbf{m}} - R_k^{\mathbf{mn}}\tilde{\chi}_{\mathbf{n}}\chi_{\mathbf{m}} \right) = \quad (2.38b)$$

$$= \int \mathcal{D}[\tilde{\chi}] \exp \left(-S_\Lambda[\chi + \tilde{\chi}] + \bar{\Gamma}_k^{\mathbf{m}}[\chi]\tilde{\chi}_{\mathbf{m}} + \tilde{\chi}_{\mathbf{m}}\Delta S_k^{\mathbf{m}}[\chi] - \frac{1}{2}R_k^{\mathbf{mn}}\tilde{\chi}_{\mathbf{n}}\tilde{\chi}_{\mathbf{m}} - R_k^{\mathbf{mn}}\tilde{\chi}_{\mathbf{n}}\chi_{\mathbf{m}} \right) \quad (2.38c)$$

$$e^{-\bar{\Gamma}_k[\chi]} = \int \mathcal{D}[\tilde{\chi}] \exp \left(-S_\Lambda[\chi + \tilde{\chi}] - \Delta S_k[\tilde{\chi}] + \frac{\delta \bar{\Gamma}_k[\chi]}{\delta \chi_{\mathbf{m}}} \tilde{\chi}_{\mathbf{m}} \right) \quad (2.39)$$

where we shifted the integration variable according to $\tilde{\chi} \rightarrow \tilde{\chi} + \chi$ in Eq. (2.38a) and eliminated the source realizing the supremum J by means of the QEOM (2.20) in Eq. (2.38c).

In the following we will discuss the necessary properties of the regulator $R_k^{\varphi\varphi}(p^2)$,

$$R_k^{\hat{\varphi}p, \hat{\varphi}p'} = R_k^{\hat{\varphi}\hat{\varphi}}(p^2)(2\pi)^d \delta^{(d)}(p - p') \equiv p^2 r(p^2/k^2)(2\pi)^d \delta^{(d)}(p - p'), \quad (2.40)$$

related to the implementation of Wilson's RG approach for the bosonic FS components in d dimensions, cf. App. B.5 for related conventions. Regulators related to Grassmann-valued field components inherit similar properties modulo some modifications accounting for internal structure. In the end we will always use a unified regulator scheme for all fields completely specified by a regulator shape function $r(y)$ with the dimensionless ratio

$$y \equiv \frac{p^2}{k^2}, \quad (2.41)$$

of the momentum squared to the RG scale squared.

¹¹Note that through the propagator $\mathcal{F}_k[\chi]$ is a non-linear functional of $\bar{\Gamma}_k[\chi]$ – its matrix of second functional derivatives/two-point functions to be precise – and of the regulator, i.e., $\mathcal{F}_k[\chi] \equiv \mathcal{F}_k[\bar{\Gamma}_k, R_k; \chi]$. Symbolic integration of the Wetterich equation (2.37) over the FRG flux $\mathcal{F}_k[\chi]$ in RG time is to be understood as solving the functional differential equation in RG time.

Inserting regulator terms ΔS in the generating functionals of quantum field theories is not unique to the FRG. Similar or in certain limits even equivalent flow equations to the Wetterich equation in fact preceded it. Prominent examples are the Wegner-Houghton equation of the seminal paper [250] or the functional variant [251–253] of the well known Callan-Symanzik equation [254, 255]. The specific properties of the regulator insertion put forward with the Wetterich equation [211–216] distinguishes the FRG from earlier (functional) RG approaches. Certain constraints on R_k (or $r(y)$ respectively) are imperative to the correct and explicit implementation of Wilson’s non-perturbative continuum RG approach [233–235] outlined in the introduction of this section 2.1. Only a suitable regulator choice enables sensible computations in the FRG approach for a theory at hand.

The four major constraints on $R_k^{\hat{\varphi}\hat{\varphi}}(p^2)$ are:

1. Infrared finiteness:

$$\lim_{p^2/k^2 \rightarrow 0} R_k^{\hat{\varphi}\hat{\varphi}}(p^2) > 0 \quad (\text{typically } \sim k^2). \quad (2.42)$$

The quadratic ansatz (2.7) together with the requirement of Eq. (2.42) introduces a mass term (typically $\sim k^2$) for the low momentum modes, $p^2 < k^2$, of $\hat{\varphi}$. This additional mass term suppresses fluctuations of those low momentum components in the functional integral (2.4) and regularizes the theory in the IR.

2. Vanishing for high momentum modes: For fields with momenta larger than the current scale, $p^2 > k^2$ the regulator has to vanish in the limit

$$\lim_{p^2/k^2 \rightarrow \infty} R_k^{\hat{\varphi}\hat{\varphi}}(p^2) = 0 \quad (2.43)$$

in d dimensions at least with $(p^2)^{(d-1)/2} R_k(p^2) \rightarrow 0$ [226, 256]. This property implies for $k \rightarrow 0$ – in the physical limit – that all regulator-dependencies drop out and all generating functionals (Z_k , W_k and $\bar{\Gamma}_k$) include the full effect of all quantum fluctuations. In other words, the introduction of a suitable regulator does not spoil the physical IR observables extracted from these generating functionals at $k \rightarrow 0$. The requirement of Eq. (2.43) implies in the UV, $p^2/k^2 \gg 1$, the vanishing of the RG scale derivative $\partial_k R_k^{\hat{\varphi}\hat{\varphi}}(p^2)$, which ensures UV finiteness. Regulators fulfilling Eqs. (2.42) and (2.43) typically have a RG-scale derivative $\partial_k R_k^{\hat{\varphi}\hat{\varphi}}(p^2)$ which peaks around the momentum shell $p \sim k$ and thus the contributions from fields with momenta $\sim k$ dominate in the functional integral. This notion of momentum locality of RG steps implements Wilson’s non-perturbative RG approach [233–235] of integrating out fluctuations momentum shell by momentum shell.

3. Diverging in the ultraviolet: For $k \rightarrow \Lambda$, where Λ is an UV initial scale which should be larger than all relevant physical scales of the problem at hand, the regulator should diverge

$$\lim_{k \rightarrow \Lambda} R_k^{\hat{\varphi}\hat{\varphi}}(p^2) = \infty. \quad (2.44)$$

This can be discussed explicitly for the EAA $\bar{\Gamma}_k$ using its integral representation (2.39): the regulator insertion $\Delta S_k[\tilde{\chi}]$ in (2.4) diverges for $k \rightarrow \Lambda$ and thus dominates the functional integral on the r.h.s. In this limit $\Delta S_k[\tilde{\chi}]$ acts as a functional delta distribution [227, 229] and the functional integral on the r.h.s. of Eq. (2.39) can be evaluated to $\exp(-S_\Lambda[\chi])$. Subsequently the RG-scale-dependent EAA $\bar{\Gamma}_\Lambda[\chi]$ at the UV initial scale Λ reduces to the classical action $S_\Lambda[\chi]$.

Depending on the theory at hand, the explicit choice of regulator (shape function), and the chosen UV initial scale Λ , the simple identification of a plain classical action $S[\chi]$ as IC at $k = \Lambda$ for $\bar{\Gamma}_k[\chi]$ might be insufficient especially when working with a finite UV initial scale Λ . Subtleties related to the chosen normalization of generating functionals, renormalization procedure, and potentially gauge fixing might require the addition of suitable (counter) terms at $k = \Lambda$ and thus a modified IC $S_\Lambda[\chi]$, see, e.g., Refs. [222, 226, 257]. The concept of renormalization group consistency discussed in subsection 2.1.6 is closely related to the proper choice of $S_\Lambda[\chi]$. We will discuss problem/theory specific subtleties further when we introduce the ICs for the explicit FRG flows considered within this work. See, e.g., subsection 3.2.3.1, subsection 4.5.2, and section 5.2.

4. **Symmetry considerations:** The regulator should not break any symmetries of the theory, *i.e.*, its functional integral. Prime examples of such symmetries are chiral or $O(N)$ symmetries and for the relativistic theories considered here Poincaré invariance. If a regulator choice breaks such a symmetry computed observables might be spoiled by this artificial, explicit symmetry breaking. This situation might be remedied by introducing appropriate counter terms in $S_\Lambda[\chi]$, *cf.* subsection 5.2.1, or in case of the breaking of gauge symmetry by a more elaborate construction, *cf.* subsection 2.3.1.

The first three constraints related to the finiteness – proper regularization and IC for the FRG flow – in practice often compete with symmetry considerations like Poincaré invariance and related causality issues (unphysical poles in the complex frequency plane) arising during analytical continuation to real time quantities, for details, see, e.g., Sec. II of Ref. [258] and references therein. Furthermore, computational and numerical practicability considerations can conflict with especially symmetry considerations. A prime example of the latter is the use of purely spatial regulators in our computations of chapters 4 and 5 which introduces an explicit breaking of Poincaré invariance. The use of purely spatial regulators is mainly motivated by the facilitation or at least significant simplification of computations at non-zero temperature.

An explicit choice of regulator (shape function) is usually made weighing the different constraints and practicability/feasibility considerations. Common and in some cases even established regulator choices often strongly vary depending on the problem at hand, the employed truncation, *cf.* subsection 2.1.4.2, and scope of the investigation. Further details on the vast and important topic of adequate regulator choice in the FRG framework can be found in Refs. [152, 210, 222, 230, 256, 258–265] and references therein.

In this work we will employ regulators related to three explicit regulator shape functions (presented in the notation of Table 1 of Ref. [256]): the flat (LPA optimized Litim) regula-

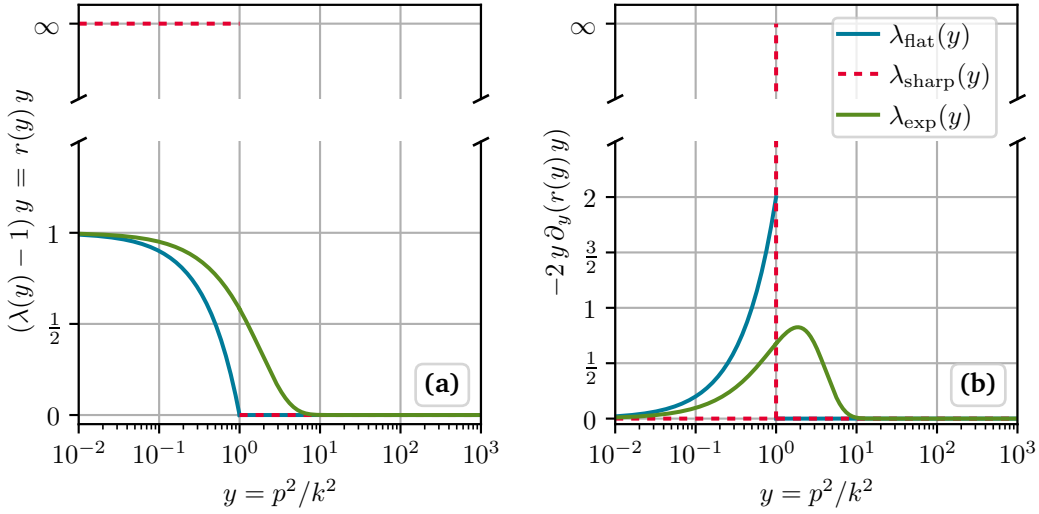


Figure 2.2.: Plots of selected – cf. Eqs. (2.45), (2.46), and (2.48) – regulator shape functions on the left (a) and their derivatives on the right (b). In terms of its properties the exponential regulator (shape function) $r_{\text{exp}}(y)$ may be considered as an archetypical FRG regulator implementing Wilson’s RG approach with a smooth focusing around $p = k$ and many sketches of FRG regulators, see, e.g., Fig. 1 of Ref. [227], resemble its plot here.

tor [259, 260]

$$r_{\text{flat}}(y) \equiv \left(\frac{1}{y} - 1\right) \Theta(1 - y), \quad (2.45)$$

the step-like sharp regulator

$$r_{\text{sharp}}(y) \equiv \frac{c}{y} \Theta(1 - y), \quad (2.46)$$

in the limit $c \rightarrow \infty$, and the exponential regulator

$$r_{\text{exp}}(y) \equiv (\exp(y) - 1)^{-1}. \quad (2.47)$$

When working with these shape functions it is convenient to define

$$\lambda(y) \equiv r(y) + 1 \quad (2.48)$$

as well as fermionic $r_{\text{f}}(y)$ and bosonic $r_{\text{b}}(y)$ shape functions related by

$$\lambda(y) \equiv r(y) + 1 \equiv r_{\text{b}}(y) + 1 \equiv (r_{\text{f}}(y) + 1)^2. \quad (2.49)$$

The three shape functions and their derivatives are visualized in figure 2.2. The particular choice of how the shape functions (2.45)–(2.47) and their derivatives are plotted in figure 2.2 is based on their appearance in explicit expressions, cf. Eq. (5.13). This visualization complements

the discussion of finiteness and the related first three constraints on $R_k^{\hat{\phi}\hat{\phi}}(p^2)$ which can be directly translated to constraints¹² for the shape functions, cf. Ref. [256],

$$\lim_{y \rightarrow 0} y r(y) > 0 \quad (\text{typically } 1), \quad (2.50a)$$

$$\lim_{y \rightarrow \infty, \epsilon > 0} y^{\frac{d}{2} + \epsilon} r(y) = 0, \quad (2.50b)$$

$$\lim_{y \rightarrow 0} r(y) = \infty. \quad (2.50c)$$

The flat regulator shape function is optimized [259, 260] for LPA computations, cf. subsection 2.1.4.2, in the sense that this regulator choice maximizes the gap in the inverse propagator which according to Ref. [259] provides the greatest stability of the flow. For additional details and a refined view of regulator optimization with a strong CFD perspective we refer the interested reader to Ref. [265]. Additionally the step function in Eq. (2.45) usually allows for a symbolic evaluation of momentum integrals and thus much simpler flow equations. We will employ the flat and the sharp regulator shape functions in chapter 4. The latter is particularly useful in MF computations since it also allows for a symbolic evaluation of momentum integrals and one usually recovers expressions known from conventional MF computations with a sharp cutoff, cf. section 4.4 and, e.g., Ref. [257]. The exponential regulator shape function $r_{\text{exp}}(y)$ is smooth and thus has certain advantages in explicit numerical computations, which we will leverage in chapter 5.

2.1.4.2. Truncation and projection strategies

With a suitable regulator choice according to the previous subsection 2.1.4.1 the Wetterich equation is exact, hence the synonym ERG for FRG. By construction the IR physics, *i.e.*, physical observables, are independent from the specific regulator choice as long as the regulator adheres to the previously established constraints. Exact in this context means solving the evolution equations (2.33) or (2.37) with a suitable IC and regulator choice from the UV down to the IR amounts to solving the underlying functional integral without any approximations. The blue lines in figure 2.3 represent two exact RG trajectories with different suitable regulators. Using the full/untruncated Wetterich equation, the IR physics encoded in $\bar{\Gamma}_0[\chi]$ is indeed regulator independent. The RG trajectories through theory space differ however for distinct regulators. Flowing from $\bar{\Gamma}_\Lambda[\chi]$ to $\bar{\Gamma}_0[\chi]$, one gains access to the full quantum effective action $\bar{\Gamma}_0[\chi] = \Gamma_{\text{1PI}}[\chi]$ and all related physical observables of the macroscopic theory prescribed by the microscopic action under consideration.

The issue a FRG practitioner faces however is one of *conservation of complexity*: solving the underlying functional integral for strongly interacting theories is at best an extremely involved task and often practically impossible. The functional flow equation for $\bar{\Gamma}_k[\chi]$ elegantly eliminates the need for the computation of the complicated functional integral at the cost of introducing a complicated functional differential equation to be solved. Solving such equations

¹²The constraints Eqs. (2.50a) and (2.50c) – *infrared finiteness* and *diverging in the ultraviolet* – are on the level of the regulator shape function $r(y)$ closely linked. Indeed considering $\lim_{y \rightarrow 0} y r(y) = 1$ entails $r(y) \rightarrow 1/y$ and thus guarantees Eq. (2.50c) in the limit $y \rightarrow 0$.

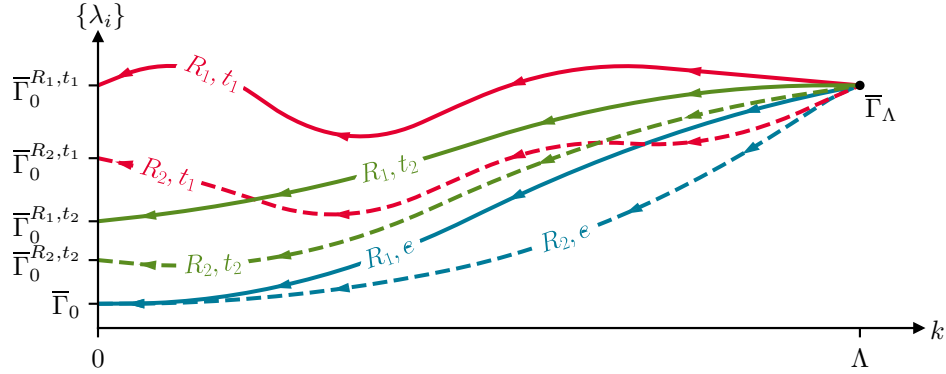


Figure 2.3.: Schematic FRG flow – RG-scale evolution of the EAA in the space of its couplings $\{\lambda_i\}$ for different regulators R_1 and R_2 (solid and dashed lines) and assuming an exact solution of the full Wetterich equation (blue lines) or solutions of the truncated Wetterich equation using two truncations t_1 and t_2 (red and green lines). Truncation t_2 is considered to be a systematic improvement of truncation t_1 .

without truncations or simplifying approximations is usually not possible for interacting QFTs, as there are no explicit numeric or symbolic methods to solve the arising non-linear functional differential equations. One notable exception are applications of the FRG to models in zero dimensions, which will be discussed at length in chapter 3. For theories in non-zero dimensions truncation schemes for the Wetterich equation are required to project from the full/exact functional differential equation onto a finite set of PDEs or even ODEs. For such differential equations numeric and in some cases even symbolic/analytic solution methods exist, which both facilitate practical computations in the FRG framework. However with a truncation to a finite set of non-functional differential equations the FRG is no longer exact due to the simplifying steps taken and furthermore results computed in a truncation may explicitly depend on the specific regulator choice even for completely valid regulators. This situation is visualized in figure 2.3 together with the untruncated/exact solution. The red and green curves in figure 2.3 represent the flow using two different truncations: the regulator-dependence and derivation from the exact result for $\bar{\Gamma}_0[\chi]$ are clearly visualized in the IR at $k = 0$. The truncation t_2 in figure 2.3 in green represent a systematic improvement over the truncation t_1 in red denoted by a weaker regulator-dependence and better error in the IR. Specifying errors related to truncation and regulator choice in the FRG can be extremely involved, especially when studying strongly interacting theories. The process usually involves improving the truncation in a systematic way and comparing results obtained at varying levels of improvement to check for an apparent convergence of the chosen truncation and improvement scheme.

In the following we will briefly discuss four common truncation schemes. For details we refer to literature [93, 95, 222, 226–231] and our applications in chapters 3–5.

Vertex expansion

Arguably the most natural truncation and expansion scheme for the Wetterich equation (2.37) is the so-called *vertex expansion*. The idea is to expand the RG-scale-dependent EAA $\bar{\Gamma}_k[\chi]$ in

its moments – in correlation functions – $\bar{\Gamma}_k^{(n)}(\chi_0)$ around the expansion point χ_0 with

$$\bar{\Gamma}_k[\chi] \equiv \lim_{N \rightarrow \infty} \bar{\Gamma}_k^N[\chi] \equiv \lim_{N \rightarrow \infty} \sum_{\{n\}=\{0\}}^{\{N\}} \bar{\Gamma}_k^{(n)}(\chi_0) \prod_{i \in \{n\}} (\chi_i - \chi_{0,i}), \quad (2.51)$$

where integration and summation over internal indices (position, flavor, . . .) is implied and all 1PI vertices of theory are summed up in $\bar{\Gamma}_k^N[\chi]$ up to order N . Inserting the ansatz (2.51) into the Wetterich equation (2.37) one can use functional derivatives in the spirit of subsection 2.1.5 to generate an infinite tower of coupled ODEs for all 1PI vertices

$$\partial_t \bar{\Gamma}_k^{\{0\}}(\chi_0) = \mathcal{F}_k^{\{0\}}(\bar{\Gamma}_k^{\{2\}}; \chi_0), \quad (2.52a)$$

$$\partial_t \bar{\Gamma}_k^{\{1\}}(\chi_0) = \mathcal{F}_k^{\{1\}}(\bar{\Gamma}_k^{\{2\}}, \bar{\Gamma}_k^{\{3\}}; \chi_0), \quad (2.52b)$$

$$\partial_t \bar{\Gamma}_k^{\{2\}}(\chi_0) = \mathcal{F}_k^{\{2\}}(\bar{\Gamma}_k^{\{2\}}, \bar{\Gamma}_k^{\{3\}}, \bar{\Gamma}_k^{\{4\}}; \chi_0), \quad (2.52c)$$

⋮

The r.h.s. of the flow equation for a 1PI vertex of order n contains only the propagator G_k (which non-linearly depends on the two-point functions), 1PI vertices up to order $n+2$, and the regulator insertion while maintaining one-loop structure. We may also note that the zero-point function $\bar{\Gamma}_k^{\{0\}}(\chi_0)$ does not couple back into the system.

One may expect good convergence of the tower of equations (2.52), if the higher-order n -point functions are suppressed. Such a suppression motivates a truncation of the infinite tower up to order N considering only $\bar{\Gamma}_k[\chi] = \bar{\Gamma}_k^N[\chi]$. The infinite tower gets truncated up to order N by either neglecting the flow of $\bar{\Gamma}_k^{\{N+1\}}(\chi_0)$ and $\bar{\Gamma}_k^{\{N+2\}}(\chi_0)$ or approximating the vertices, for the latter approach, see, *e.g.*, Ref. [266]. When properly tracking the momentum dependence of the involved 1PI vertices, *cf.* the works [267–269] of Jean-Paul Blaizot *et al.* and Refs. [228, 270, 271] of Peter Kopietz *et al.*, this approach provides excellent resolution in momentum space while having limited resolution in field space due to the expansion of the EAA in 1PI vertices. Due to the rapidly growing complexity of the flow equations when increasing N , practical computations are typically limited to a rather small order between $N = 4$ and $N = 6$. The high resolution in momentum space and proper resolution of the momentum-dependence of the involved 1PI vertices makes the vertex expansion a very attractive expansion scheme for quantum many-particle systems in condensed matter physics, see, *e.g.*, Refs. [270, 272–274], high-energy physics and especially for Yang-Mills theories and QCD, see, *e.g.*, Refs. [80, 97, 213, 237, 249, 275, 276], and quantum gravity, see, *e.g.*, Refs. [109, 277–280]. An overview and further relevant literature may be found in the Secs. 4, 5, and 6 of review [231]. When studying symmetry breaking – especially around phase transitions – the vertex expansion is of limited use since studies of such phenomena require a higher resolution in field space. Both symmetry breaking and also bound states can enhance higher-order n -point functions limiting or even destabilizing the vertex expansion, see also the discussion in the following paragraph [Taylor and other global expansions](#). In this work we are mainly interested in the study of

strongly coupled theories in field space and symmetry breaking in those systems. Thus we do not use the vertex expansion beyond the benchmark study of subsections 3.2.2.2 and 3.2.3.2 in zero dimensions.

Derivative expansion and the local potential approximation

The main FRG expansion scheme employed in this work is the *derivative expansion* (DE), which is a well established expansion and truncation scheme for the Wetterich equation in applications that require high resolution in field space, see, e.g., the review [231] and references therein. Prime examples are the zero-dimensional theories we study in chapter 3 and the LEFTs we discuss in chapters 4 and 5. The underlying idea behind the DE is to expand the RG-scale-dependent EAA $\bar{\Gamma}_k[\chi]$ in powers of momenta – i.e., derivatives in position space, hence the name DE. Such an expansion is justified when studying long range physics at small momentum scales p^2 satisfying

$$\frac{p^2}{s_k^2} \ll 1, \quad (2.53)$$

where s_k is a theory specific IR mass/momentum scale. Even in theories without a physical mass gap m_{gap} the regulators used in the FRG provide an IR regularization at finite k and the characteristic scale s_k is typically

$$s_k^2 \approx m_{\text{gap}}^2 + k^2. \quad (2.54)$$

Considering the regulator properties discussed in subsection 2.1.4.1 we may indeed note that the regulator insertion $\partial_t R_k$ in the Wetterich equation (2.37) suppresses momenta $p^2 \gtrsim k^2$ by focusing the integration over internal loop momenta around $p = k$, which is visualized in figure 2.2b. The aforementioned suppression of high momentum modes renders the condition $p^2/k^2 \lesssim 1$ valid in the loop of the Wetterich equation. This in turn implies that the condition (2.53) is indeed fulfilled – even for theories without a physical IR mass gap m_{gap} , cf. Eq. (2.54). A proper, i.e., for a given truncation optimized, regulator can greatly improve the stability and apparent convergence of the DE [222, 259, 260]. For the lowest-order DE – the so-called local potential approximation (LPA), which we will introduce in the following – the flat regulator that we introduced via its shape function in Eq. (2.45) is such an optimized regulator.

To illustrate the DE and related truncation strategies let us consider a theory of N interacting scalar fields $\vec{\phi}$ with $O(N)$ symmetry in d dimensions and corresponding mean-fields $\vec{\varphi}$. To lowest, zeroth-order DE – i.e., in LPA – the RG-scale-dependent EAA is simply given by

$$\bar{\Gamma}_k^{\text{DE}_0}[\vec{\varphi}] \equiv \bar{\Gamma}_k^{\text{LPA}}[\vec{\varphi}] \equiv \int_x \left(\frac{1}{2} \partial_\mu \varphi_i \partial_\mu \varphi_i + U_k(\varrho) \right), \quad (2.55)$$

with $\varrho \equiv \varphi_i \varphi_i / 2$ and the RG-scale-dependent, $O(N)$ -symmetric self-interaction potential $U_k(\varrho)$ as the only scale-dependent quantity. Quantum fluctuations at $\mathcal{O}(\partial^2)$ and above are neglected and only the classical kinetic – without a running wave-function renormalization – is included [281, 282].

The RG-scale-dependent local potential can be evolved from the UV at $k = \Lambda$ to the IR $k \rightarrow 0$ using the Wetterich Eq. (2.37). In the IR $U_{k=0}(\varrho)$ can be identified with (contributes to) the effective potential $\mathcal{V}[\mu, T; \chi]$, see App. C.1 and Eq. (C.15), when considering homogeneous (inhomogeneous) condensates. Thus $U_k(\varrho)$ and especially $U_{k=0}(\varrho)$ play a critical role in the study of symmetry breaking and thermodynamics. Further more the LPA can be used for mean-field and large- N computations, see, e.g., subsection 3.2.3 and sections 4.3, 4.4, and 5.2.

The explicit flow equations for the local potential $\partial_t U_k(\varrho)$ manifest in practice as PDEs, see, e.g., Eqs. (3.37), (3.63), (3.221), (4.21), and (5.13) in the main parts 3, 4, and 5 of this work. As alluded to in the introduction 1, various collocation methods, cf. Refs. [81, 87, 93, 100, 110–152] and also expansion schemes discussed in the next paragraph are common and established in the FRG community to solve LPA flow equations – the explicit PDEs for $U_k(\varrho)$. The FD and spline collocation methods used, are however based on the often tacit assumption, that $U_k(\varrho)$ is smooth. This is however, as we argue at length in chapter 3 and demonstrate also in chapter 4, *a priori* and also in prominent scenarios *a posteriori*, in general not a valid assumption. It has been established within the last few years by us and collaborators, cf. Refs. [1–4, 162, 210, 247, 283, 284] and subsection 2.1.7 as well as chapters 3 and 4, that the FRG flow equations – the LPA flow equation as a truncated one, most prominently included – are non-linear conservation/convection equations. Their non-linearity as well as explicit source/sink terms, cf. subsection 4.2.2, can lead to discontinuities in $\partial_\varrho U_k(\varrho)$ and thus kinks in $U_k(\varrho)$ which explains the poor (numerical) performance of the established “grid methods”. The adaptation of more suited numerical methods from the field of CFD, see section 2.2, is one major part of our research [1–4, 7] discussed in chapters 3 and 4.

The first systematic improvement DE_2 in the DE to LPA

$$\bar{\Gamma}_k^{\text{DE}_2}[\vec{\varphi}] = \int_x \left(\frac{1}{2} Z_k(\varrho) \partial_\mu \varphi_i \partial_\mu \varphi_i + \frac{1}{4} Y_k(\varrho) \partial_\mu \varrho \partial_\mu \varrho + U_k(\varrho) \right), \quad (2.56)$$

includes $\mathcal{O}(\partial^2)$ corrections in form of a field-dependent, running wave-function renormalization $Z_k(\varrho)$ and for $N > 1$ an additional term $Y_k(\varrho) \partial_\mu \varrho \partial_\mu \varrho$ due to the difference in transverse and longitudinal fluctuations of $\vec{\varphi}$ [106, 231]. A very common simplification to DE_2 is called local potential approximation prime (LPA') which entails omitting the $Y_k(\varrho)$ contribution and considering only a field-independent Z_k . Given an ansatz for the EAA in DE one can proceed to compute the propagators in the given truncation. The propagators and the ansatz for the EAA can then be inserted into the Wetterich equation (2.37) and/or corresponding flow equations for higher-order n -point functions to project out flow equations for the running couplings. Those flow equations manifest as PDEs or ODEs allowing for a numerical solution of the Wetterich equation. Further details will be discussed in this thesis in chapters 3–5 while additional details and references can be found in, e.g., Sec. 2.3 of the review [231].

FRG Taylor and other global expansions

The so-called *FRG Taylor expansion*, see, e.g., Refs. [80, 89–109], is closely related to the [vertex expansion](#) and the LPA of the [derivative expansion](#). In the context of the LPA the FRG Taylor

expansion is simply the expansion of the RG-scale-dependent local potential in a Taylor series

$$U_k(\varrho) = \sum_{n=0}^{N_\nu} \frac{\lambda_{n,k}}{n!} (\varrho - \kappa_k)^n, \quad (2.57)$$

around a potentially scale-dependent expansion point κ_k , with scale-dependent moments $\lambda_{n,k}$ and an expansion order N_ν , where we adopt the notation of Ref. [109]. Inserting the ansatz (2.57) into the LPA flow equation one can project onto the moments $\lambda_{n,k}$ and the expansion point κ_k by taking derivatives w.r.t. ϱ . The FRG Taylor expansion includes the zeroth-order contributions in momentum space to the vertex expansion. As such both FRG Taylor and vertex expansion are completely equivalent in zero-dimensional space-time, cf. subsections 3.2.2.2 and 3.2.3.2.

With a well chosen, potentially scale dependent expansion point and sometimes a rather low number of expansion coefficients, the FRG Taylor expansion is an established method within the FRG community, see, e.g., the certainly incomplete list of Refs. [80, 89–109]. However it is also acknowledged, that such a local expansion is rather limited in scenarios where global information about the potential is required, see, e.g., Refs. [96, 109, 226]. The study of symmetry breaking and phase transitions, especially first-order phase transitions, is one notable example. It should however be noted, that an expansion like Eq. (2.57) and the projection onto its scale-dependent moments $\lambda_{n,k}$ and expansion point κ_k , *a priori* assumes analyticity of $U_k(\varrho)$ around the expansion point κ_k . This is an incredibly restrictive assumption that is just not justified for certain applications. We will discuss this limitation further in subsections 3.2.2.2 and 3.2.3.2 in the context of our studies in zero dimensions.

The local nature of the FRG Taylor expansion (2.57) has, to an extent, motivated the adaptation of global pseudo-spectral collocation methods in the FRG community for an expansion of $U_k(\varrho)$ in Chebyshev polynomials, see, e.g., Refs. [109, 153–160]. While this certainly improves upon the FRG Taylor expansion by considering a global expansion of the potential $U_k(\varrho)$, such collocation methods are still severely limited when non-analyticities come into play. The application of plain global pseudo-spectral collocation methods to non-linear convection equations including complicated source terms – like the LPA flow equation – should be seriously reconsidered. This is not the personal opinion of my collaborators and me, but rather firmly established knowledge in the field of such pseudo-spectral collocation methods. It is interesting to note, that most of the aforementioned FRG Chebyshev literature references the excellent book “*Chebyshev and Fourier Spectral Methods*” [285] of John P. Boyd, which in no uncertain terms addresses the clear limitations of global-collocation methods when it comes to non-analyticities and shocks. The praised exponential and geometric convergence of global-collocation methods is lost in presence of shocks, corner singularities, or discontinuities [285]. Spectral filtering, sequence acceleration, spectral reconstruction, or outright discontinuous Galerkin methods (employing pseudo-spectral methods in control volumes, allowing for discontinuities) are mentioned as necessary improvements when applying pseudo-spectral collocation methods to problems involving non-analyticities [285]. In plain pseudo-spectral collocation methods such non-analyticities manifest in the frequency spectrum as Wilbraham-Gibbs-type oscillations [286–288] which without the aforementioned improvements completely destabilize the ODE system for the flow of the expansion coefficients.

Perturbative loop expansion

We will conclude the discussion on truncation strategies for the Wetterich equation with a short remark on the *perturbative loop expansion* following Refs. [226, 227, 238, 289, 290]. Conventional renormalized perturbation theory, see, *e.g.*, Refs. [177, 178, 239], in form of a loop expansion in terms of classical, tree-level propagators can be recovered from the FRG in an iterative procedure. The $(N + 1)$ -loop correction to the EA can be computed with the Wetterich equation (2.37) by inserting the N -loop expression for the propagator G_k into the r.h.s. of Eq. (2.37) and integrating the resulting equation from the UV $k = \Lambda$ to the IR $k = 0$.

For the sake of simplicity we will consider a quantum field theory of a single scalar field ϕ with the classical action S and corresponding mean-field φ in the following. Starting the iterative procedure with the zeroth-order tree-level propagator $G_k = (S^{(2)} + R_k)^{-1}$ and integrating over the RG scale, one obtains the EA to one-loop order

$$\Gamma_{1\text{-loop}}[\varphi] = S[\varphi] + \bar{\Gamma}_{\Lambda,1}[\varphi] + \frac{1}{2} \text{Tr} \ln S^{(2)}[\varphi] - \frac{1}{2} \text{Tr} \ln \left(S^{(2)}[\varphi] + R_\Lambda \right), \quad (2.58)$$

with the classical action $S[\varphi]$, a RG-scheme-/regulator-dependent one-loop counter term $\bar{\Gamma}_{\Lambda,1}[\varphi]$, the potentially divergent one-loop diagram $\frac{1}{2} \text{Tr} \ln S^{(2)}[\varphi]$, and the RG-scheme-/regulator-dependent diagram $\frac{1}{2} \text{Tr} \ln (S^{(2)}[\varphi] + R_\Lambda)$ to cancel the potential divergences in the aforementioned diagram. Thus the difference $\frac{1}{2} \text{Tr} \ln S^{(2)}[\varphi] - \frac{1}{2} \text{Tr} \ln (S^{(2)}[\varphi] + R_\Lambda)$ can be considered as a regularized, finite loop diagram. The counter term $\bar{\Gamma}_{\Lambda,1}[\varphi]$ can be determined by enforcing renormalization group consistency, see subsection 2.1.6 for details, which in this context simply entails the independence of the EA $\Gamma[\varphi]$ in the IR of Λ . The sum of the classical action and the counter term form the modified IC: $S_\Lambda[\varphi] = S[\varphi] + \bar{\Gamma}_{\Lambda,1}[\varphi]$.

The two-loop result can be obtained by computing the propagator from the one-loop result (2.58), inserting the result in the r.h.s. of the Wetterich equation (2.37) and again integrating over the RG scale, see, *e.g.*, Ref. [238].

Using the Wetterich equation as a master equation with the outlined iteration procedure is a simple and robust way to compute expressions for regularized and renormalized 1PI correlation functions to any desired perturbative loop-order. The generation and complete resummation of the perturbative loop expansion also serves as further proof – beyond the validity and exactness of its derivation – that the Wetterich equation (2.37) is indeed exact. A perturbative approach/loop expansion has only very limited applicability in the context of our work, since we are interested in strongly interacting systems which are notoriously elusive to tackle with such perturbative techniques. For discussions of perturbative results in the FRG context we refer the interested reader to, *e.g.*, Refs. [289, 291–294].

2.1.5. Higher-order flow equations and their combinatorics in field space

Since practical computations of observables with the full Wetterich Eq. (2.37) are for most theories impossible, truncations are employed to facilitate computations. As a result $\bar{\Gamma}_k[\chi]$ is usually not accessible in its full functional form. The study and practical computation of moments of $\bar{\Gamma}_k[\chi]$ – higher-order n -point functions – however is still possible within the FRG framework. To this end flow equations for higher-order n -point functions can be derived using the full Wetterich Eq. (2.37) as a master equation.

Flow equations for higher-order n -point functions can be obtained by taking functional derivatives of the Wetterich Eq. (2.37) w.r.t. external fields like $\chi_{\underline{x}}$ ¹³. Besides the vertices of the theory, the functional derivative of the propagator $G_{k;\underline{a}\underline{c}}^{\underline{x}}$ is required. An expression for $G_{k;\underline{a}\underline{c}}^{\underline{x}}$ is obtained by computing the functional derivative of Eq. (2.27) explicitly:

$$\frac{\delta}{\delta\chi_{\underline{x}}} \left(G_{k;\underline{a}\underline{m}}[\chi] \left(\bar{\Gamma}_k^{\underline{m}\underline{b}}[\chi] + R_k^{\underline{m}\underline{b}} \right) \right) = \frac{\delta}{\delta\chi_{\underline{x}}} \gamma_{\underline{a}}^{\underline{b}} = 0 \quad (2.59)$$

$$G_{k;\underline{a}\underline{m}}^{\underline{x}}[\chi] \left(\bar{\Gamma}_k^{\underline{m}\underline{b}}[\chi] + R_k^{\underline{m}\underline{b}} \right) = -(-1)^{\underline{x}\underline{a}}(-1)^{\underline{x}\underline{m}} G_{k;\underline{a}\underline{m}}[\chi] \bar{\Gamma}_k^{\underline{x}\underline{m}\underline{b}}[\chi] \quad (2.60)$$

$$G_{k;\underline{a}\underline{m}}^{\underline{x}}[\chi] \delta_{\underline{m}}^{\underline{c}} = -(-1)^{\underline{x}\underline{a}} G_{k;\underline{a}\underline{m}}[\chi] \bar{\Gamma}_k^{\underline{m}\underline{x}\underline{n}}[\chi] \left(\bar{\Gamma}_k[\chi] + \Delta S_k[\chi] \right)_{\underline{n}\underline{c}}^{-1} \quad (2.61)$$

$$G_{k;\underline{a}\underline{c}}^{\underline{x}}[\chi] = -(-1)^{\underline{x}\underline{a}} G_{k;\underline{a}\underline{m}}[\chi] \bar{\Gamma}_k^{\underline{m}\underline{x}\underline{n}}[\chi] \gamma_{\underline{n}}^{\underline{1}} G_{k;\underline{l}\underline{c}}[\chi] = \quad (2.62a)$$

$$= -(-1)^{\underline{x}\underline{a}}(-1)^{\underline{nn}} G_{k;\underline{a}\underline{m}}[\chi] \bar{\Gamma}_k^{\underline{m}\underline{x}\underline{n}}[\chi] G_{k;\underline{n}\underline{c}}[\chi]. \quad (2.62b)$$

Diagrammatically taking the functional derivative of a propagator amounts to inserting a three-point vertex while accounting for potential sign changes due to the possible Grassmann-nature of the involved field components. In a more compact form of our FS notation we summarize at this point

$$\frac{\delta}{\delta\chi_{\underline{x}}} R_k^{\underline{a}\underline{b}} = (R_k^{\underline{a}\underline{b}})^{\underline{x}} = 0, \quad (2.63)$$

$$\frac{\delta}{\delta\chi_{\underline{x}}} \bar{\Gamma}_k^{\underline{a}\dots} = \bar{\Gamma}_k^{\underline{x}\underline{a}\dots} = (-1)^{\underline{a}\underline{x}} \bar{\Gamma}_k^{\underline{a}\underline{x}\dots}, \quad (2.64)$$

$$\frac{\delta}{\delta\chi_{\underline{x}}} G_{k;\underline{a}\underline{b}} = (G_{k;\underline{a}\underline{b}})^{\underline{x}} = -(-1)^{\underline{x}\underline{a},\underline{nn}} G_{k;\underline{a}\underline{m}} \bar{\Gamma}_k^{\underline{m}\underline{x}\underline{n}} G_{k;\underline{n}\underline{b}}. \quad (2.65)$$

Within FS diagrams we use regular n -sided polygons with n legs/lines to represent FS vertices $\bar{\Gamma}_k^{\underline{x}_1 \dots \underline{x}_n}$. Diagrams can be translated into their corresponding explicit mathematical expressions by reading off the involved elements – regulator insertion, propagators, and vertices – following the loop and vertex legs counter-clockwise starting at the regulator insertion which always includes the first and last FS summation indices, see, *e.g.*, Eqs. (2.68a)–(2.68c) and Eqs. (2.68a')–(2.68c').

With Eqs. (2.63)–(2.65) we are equipped to compute functional derivatives of the full Wetterich Eq. (2.37)

$$2\partial_t \bar{\Gamma}_k = G_{k;\underline{a}\underline{b}} \partial_t R_k^{\underline{b}\underline{a}} = \text{Diagram: a circle with a cross inside, representing a regulator insertion}, \quad (2.66)$$

starting with a FS derivative w.r.t. the external (mean) field $\chi_{\underline{u}}$ we arrive at the flow equation for the one-point function

$$2\partial_t \bar{\Gamma}_k^{\underline{u}} = -(-1)^{\underline{u}\underline{a},\underline{cc}} G_{k;\underline{a}\underline{b}} \bar{\Gamma}_k^{\underline{b}\underline{u}\underline{c}} G_{k;\underline{c}\underline{d}} \partial_t R_k^{\underline{d}\underline{a}} = -(-1)^{\underline{u}\underline{a},\underline{cc}} \text{Diagram: a circle with a cross inside and an arrow pointing to the right labeled } \underline{u}. \quad (2.67)$$

¹³We highlight external, *i.e.*, non-contracted, FS-indices with an underscore, *e.g.*, \underline{x} , in the context of higher-order flow equations for a clear distinction between contracted and external indices.

An additional FS derivative w.r.t. the external (mean) field $\chi_{\underline{v}}$ of Eq. (2.67) leads to the flow equation of the two-point function

$$2\partial_t \bar{\Gamma}_k^{\underline{v}\underline{u}} = \langle\langle T_{2,2} \rangle\rangle + \langle\langle T_{2,1} \rangle\rangle = \langle\langle 2 \rangle\rangle + \langle\langle 1 \rangle\rangle \quad (2.68)$$

$$= (-1)^{\underline{u}\underline{a},\underline{v}\underline{a},\underline{c}\underline{c},\underline{e}\underline{e}} G_{k;\underline{a}\underline{b}} \bar{\Gamma}_k^{\underline{b}\underline{v}\underline{c}} G_{k;\underline{c}\underline{d}} \bar{\Gamma}_k^{\underline{d}\underline{u}\underline{e}} G_{k;\underline{e}\underline{f}} \partial_t R_k^{\underline{f}\underline{a}} + \quad (2.68a)$$

$$+ (-1)^{\underline{u}\underline{v},\underline{u}\underline{a},\underline{v}\underline{a},\underline{c}\underline{c},\underline{e}\underline{e}} G_{k;\underline{a}\underline{b}} \bar{\Gamma}_k^{\underline{b}\underline{u}\underline{c}} G_{k;\underline{c}\underline{d}} \bar{\Gamma}_k^{\underline{d}\underline{v}\underline{e}} G_{k;\underline{e}\underline{f}} \partial_t R_k^{\underline{f}\underline{a}} - \quad (2.68b)$$

$$- (-1)^{\underline{u}\underline{a},\underline{v}\underline{a},\underline{c}\underline{c}} G_{k;\underline{a}\underline{b}} \bar{\Gamma}_k^{\underline{b}\underline{v}\underline{u}\underline{c}} G_{k;\underline{c}\underline{d}} \partial_t R_k^{\underline{d}\underline{a}} \quad (2.68c)$$

$$= (-1)^{\underline{u}\underline{a},\underline{v}\underline{a},\underline{c}\underline{c},\underline{e}\underline{e}} \underline{u} \rightarrow \text{[Diagram: circle with two vertices, one crossed, one with arrow]} \leftarrow \underline{v} + \quad (2.68a')$$

$$+ (-1)^{\underline{u}\underline{v},\underline{u}\underline{a},\underline{v}\underline{a},\underline{c}\underline{c},\underline{e}\underline{e}} \underline{u} \rightarrow \text{[Diagram: circle with two vertices, one crossed, one with arrow]} \leftarrow \underline{v} - \quad (2.68b')$$

$$- (-1)^{\underline{u}\underline{a},\underline{v}\underline{a},\underline{c}\underline{c}} \text{[Diagram: circle with two vertices, one crossed, one with arrow]} \quad (2.68c')$$

Computing flow equations for higher-order n -point functions beyond $n = 2$ is in principle straight forward, but the number of involved diagrams grows rapidly making a computation by hand error prone and at some point simply unfeasible. Packages like *DoFun* [295, 296] or *QMeS-Derivation* [297, 298] can be used to automate this process using the computer algebra system MATHEMATICA [166]. We use our own MATHEMATICA code [299] for such and related diagrammatic computations. The expressions and diagrams in Eqs. (2.67)–(2.70) have been programmatically generated with our MATHEMATICA code [299] and exported to L^AT_EX using propose build export methods. The diagrams have been programmatically generated and rendered using *Axodraw Version 2* [53]. In the following Eqs. (2.69) and (2.70) we present the flow equations for the three- and four-point functions in a skeletonized form¹⁴ presenting mainly the classes of involved diagrams. The flow of the three-point function is governed by

$$2\partial_t \bar{\Gamma}_k^{\underline{w}\underline{v}\underline{u}} = \langle\langle T_{3,3} \rangle\rangle + \langle\langle T_{3,2} \rangle\rangle + \langle\langle T_{3,1} \rangle\rangle = \langle\langle 6 \rangle\rangle + \langle\langle 6 \rangle\rangle + \langle\langle 1 \rangle\rangle \quad (2.69)$$

$$= -(-1)^{\langle\langle 6 \rangle\rangle} G_{k;\underline{a}\underline{b}} \bar{\Gamma}_k^{\underline{b}\underline{w}\underline{c}} G_{k;\underline{c}\underline{d}} \bar{\Gamma}_k^{\underline{d}\underline{v}\underline{e}} G_{k;\underline{e}\underline{f}} \bar{\Gamma}_k^{\underline{f}\underline{u}\underline{g}} G_{k;\underline{g}\underline{h}} \partial_t R_k^{\underline{h}\underline{a}} + \langle\langle 5 \rangle\rangle + \quad (2.69a)$$

$$+ (-1)^{\langle\langle 5 \rangle\rangle} G_{k;\underline{a}\underline{b}} \bar{\Gamma}_k^{\underline{b}\underline{w}\underline{c}} G_{k;\underline{c}\underline{d}} \bar{\Gamma}_k^{\underline{d}\underline{v}\underline{u}\underline{e}} G_{k;\underline{e}\underline{f}} \partial_t R_k^{\underline{f}\underline{a}} + \langle\langle 5 \rangle\rangle - \quad (2.69b)$$

$$- (-1)^{\langle\langle 4 \rangle\rangle} G_{k;\underline{a}\underline{b}} \bar{\Gamma}_k^{\underline{b}\underline{w}\underline{v}\underline{u}\underline{c}} G_{k;\underline{c}\underline{d}} \partial_t R_k^{\underline{d}\underline{a}} \quad (2.69c)$$

¹⁴Following the convention introduced in App. B.1 we use $\langle\langle n \rangle\rangle$ to represent a sequence of n omitted elements. $(-1)^{\langle\langle n \rangle\rangle}$ are abbreviated FS sign factors, see Eqs. (B.33) and (B.34) and the related discussion in App. B.4. $\langle\langle T_{n,k} \rangle\rangle$ represents the number of diagrams of a specific type, see table 2.1 and the related discussion.

$$= -(-1)^{\ll 6 \gg} \begin{array}{c} \text{v} \\ \downarrow \\ \text{---} \circlearrowleft \text{---} \\ \uparrow \\ \text{u} \quad \otimes \quad \text{w} \end{array} + \ll 5 \gg + \quad (2.69a')$$

$$+ (-1)^{\ll 5 \gg} \begin{array}{c} \text{v} \\ \downarrow \\ \text{---} \circlearrowleft \text{---} \\ \uparrow \\ \text{u} \quad \otimes \quad \text{w} \end{array} + \ll 5 \gg - \quad (2.69b')$$

$$- (-1)^{\ll 4 \gg} \begin{array}{c} \text{u} \\ \downarrow \\ \text{---} \circlearrowleft \text{---} \\ \uparrow \\ \text{u} \quad \otimes \quad \text{w} \end{array}, \quad (2.69c')$$

and the flow of the four-point function follows as

$$2\partial_t \bar{\Gamma}_k^{\text{xwvu}} = \ll T_{4,4} \gg + \ll T_{4,3} \gg + (\ll T_{4,2} \gg) + \ll T_{4,1} \gg = \ll 24 \gg + \ll 36 \gg + (\ll 8 \gg + \ll 6 \gg) + \ll 1 \gg \quad (2.70)$$

$$= (-1)^{\ll 8 \gg} G_{k;ab} \bar{\Gamma}_k^{\text{bxc}} G_{k;cd} \bar{\Gamma}_k^{\text{dwe}} G_{k;ef} \bar{\Gamma}_k^{\text{fvg}} G_{k;gh} \bar{\Gamma}_k^{\text{hui}} G_{k;ij} \partial_t R_k^{\text{ja}} + \ll 23 \gg - \quad (2.70a)$$

$$- (-1)^{\ll 7 \gg} G_{k;ab} \bar{\Gamma}_k^{\text{bxc}} G_{k;cd} \bar{\Gamma}_k^{\text{dwe}} G_{k;ef} \bar{\Gamma}_k^{\text{fvug}} G_{k;gh} \partial_t R_k^{\text{ha}} + \ll 35 \gg + \quad (2.70b)$$

$$+ \left((-1)^{\ll 6 \gg} G_{k;ab} \bar{\Gamma}_k^{\text{bxc}} G_{k;cd} \bar{\Gamma}_k^{\text{dvwue}} G_{k;ef} \partial_t R_k^{\text{fa}} + \ll 7 \gg + \quad (2.70c)$$

$$+ (-1)^{\ll 6 \gg} G_{k;ab} \bar{\Gamma}_k^{\text{bxwuc}} G_{k;cd} \bar{\Gamma}_k^{\text{dvue}} G_{k;ef} \partial_t R_k^{\text{fa}} + \ll 5 \gg \right) - \quad (2.70d)$$

$$- (-1)^{\ll 5 \gg} G_{k;ab} \bar{\Gamma}_k^{\text{bxwvuc}} G_{k;cd} \partial_t R_k^{\text{da}} \quad (2.70e)$$

$$= (-1)^{\ll 8 \gg} \begin{array}{c} \text{v} \quad \text{w} \\ \downarrow \quad \downarrow \\ \text{---} \circlearrowleft \text{---} \\ \uparrow \quad \uparrow \\ \text{u} \quad \otimes \quad \text{x} \end{array} + \ll 23 \gg - \quad (2.70a')$$

$$- (-1)^{\ll 7 \gg} \begin{array}{c} \text{w} \\ \downarrow \\ \text{---} \circlearrowleft \text{---} \\ \uparrow \\ \text{u} \quad \otimes \quad \text{x} \end{array} + \ll 35 \gg + \quad (2.70b')$$

$$+ \left((-1)^{\ll 6 \gg} \begin{array}{c} \text{w} \\ \downarrow \\ \text{---} \circlearrowleft \text{---} \\ \uparrow \\ \text{u} \quad \otimes \quad \text{x} \end{array} + \ll 7 \gg + \quad (2.70c')$$

$$+ (-1)^{\ll 6 \gg} \begin{array}{c} \text{v} \quad \text{w} \\ \downarrow \quad \downarrow \\ \text{---} \circlearrowleft \text{---} \\ \uparrow \quad \uparrow \\ \text{u} \quad \otimes \quad \text{x} \end{array} + \ll 5 \gg \right) - \quad (2.70d')$$

$$-(-1)^{\ll 5 \gg} \text{diagram} \quad (2.70e')$$

A common way to reduce the number of diagrams, which only differ by the location of the regulator insertion in the loop, is to introduce the RG time/scale derivative $\tilde{\partial}_t$ ($\tilde{\partial}_k$) which only acts on the regulator, see, e.g., Ref. [296]. This allows for a unification of certain diagrams using

$$\tilde{\partial}_t G_{k;\mathbf{ab}}[\chi] = -(-1)^{\mathbf{bb}} G_{k;\mathbf{am}}[\chi] \partial_t R_k^{\mathbf{mn}} G_{k;\mathbf{nb}}[\chi], \quad (2.71)$$

which follows directly from the implicit definition (2.27) of the propagator. Using Eq. (2.71) to simplify, i.e., reduce the number of diagrams, in the flow Eqs. (2.68)–(2.70) requires some care w.r.t. the involved signs and sign factors $(-1)^{\dots}$. In the following we use $\tilde{\partial}_t$ ($\tilde{\partial}_k$) only for schematic discussions and to simplify final expressions after all traces in field and internal spaces have been performed.

We conclude this subsection with a remark on the involved combinatorics – diagrammatic complexity when computing flow equations for higher-order n -point functions in FS. The number of diagrams B_n involved on the r.h.s. of a FRG flow equation for the n -point function $\bar{\Gamma}_k^{\mathbf{x}_1 \dots \mathbf{x}_n}$ grows faster than $n!$. It is given by the n^{th} ordered Bell/Fubini number B_n [300]

$$B_n = \frac{1}{2} \Phi\left(\frac{1}{2}, -n, 0\right) = \sum_{k=1}^n T_{n,k} = \frac{1}{2 \ln^{n+1}(2)} n! + \mathcal{O}((n-1)!), \quad (2.72)$$

where the Triangle numbers $T_{n,k}$ [301] are given by

$$T_{n,k} = k! S_n^{(k)}, \quad (2.73)$$

with the Hurwitz-Lerch transcendent Φ and the Stirling number of the second kind $S_n^{(k)}$, see, e.g., Ref. [302] Secs. 25.14 and 26.8. In a combinatorics context B_n is the “number of preferential arrangements of n labeled elements; or number of weak orders on n labeled elements; or number of ordered partitions of $[n]$ ” [300]. For a given n and $k = n, \dots, 1$, $T_{n,k}$ represents the number of diagrams with k vertices, which always have $k+1$ propagators, cf. Eqs. (2.68)–(2.70). The asymptotic expansion in Eq. (2.72) can be found in Ref. [303]. The values of B_n and $T_{n,k}$ for $k = 1, \dots, n$ and $n = 1, \dots, 6$ are displayed in table 2.1. For further details regarding the underlying combinatorics/permutohedron, see, e.g., Ref. [304] p. 167ff and Ref. [305] p. 18ff. Computing the full flow equations in FS becomes extremely expensive/infeasible for larger n . In this work we mainly study the flow equation for $\bar{\Gamma}_k$ itself, with subsection 3.3.2 and section 4.4 as the most notable exceptions.

Table 2.1.: Number of field space diagrams B_n on the r.h.s. of the flow equation $\partial_t \bar{\Gamma}_k^{\mathbf{x}_1 \dots \mathbf{x}_n}$ for $n = 1, \dots, 6$. $T_{n,k}$ diagrams with $k + 1$ propagators for $k = 1, \dots, n$ contribute to B_n for a given n . B_n is given by Eq. (2.72) while $T_{n,k}$ is given by Eq. (2.73). The factors for $n = 2, \dots, 4$ appear in Eqs. (2.68)–(2.70) as $\ll T_{n,k} \gg$ and $\ll T_{n,k} - 1 \gg$ in respective subequations.

$T_{n,k}$	$k = 1$	$k = 2$	$k = 3$	$k = 4$	$k = 5$	$k = 6$	B_n
$n = 1$	1						1
$n = 2$	1	2					3
$n = 3$	1	6	6				13
$n = 4$	1	14	36	24			75
$n = 5$	1	30	150	240	120		541
$n = 6$	1	62	540	1560	1800	720	4683

2.1.6. Renormalization group consistency

In this subsection we discuss the concept of *renormalization group consistency* with focus on the FRG framework following the excellent discussion of Ref. [257]. Additional information can be found in Refs. [148, 306–309]. In the context of the FRG the question of RG consistency is closely related to the appropriate choice of UV initial scale Λ and corresponding initial action S_Λ , cf. subsection 2.1.4.1. For a given theory with classical action S the FRG provides both a renormalization and regularization scheme based on the EAA $\bar{\Gamma}_k$. The Wetterich equation can be used to study the RG scale evolution of the EAA $\bar{\Gamma}_k$ connecting the microscopic action S of the theory at hand to the full quantum EA $\Gamma_{1\text{PI}}$. This process however requires an initialization of the Wetterich equation at an UV initial scale Λ . The introduction of such a scale and corresponding regularization, which the regulator provides in the EAA $\bar{\Gamma}_k$, is a computational necessity. Physical observables encoded in $\bar{\Gamma}_0[\chi] = \Gamma_{1\text{PI}}[\chi] \equiv \Gamma[\chi]$ and its moments however should not depend on the scale Λ :

$$\Lambda \frac{d\Gamma[\chi]}{d\Lambda} \equiv \Lambda \frac{d\bar{\Gamma}_0[\chi]}{d\Lambda} \stackrel{!}{=} 0. \quad (2.74)$$

This seemingly simple requirement is the governing equation for a consistent regularization and renormalization of a given theory [257]. Eq. (2.74) is called *RG consistency condition* and a computation of $\Gamma[\chi]$ for a given theory is considered *RG-consistent* if and only if the condition (2.74) is met. In the FRG framework we can translate this requirement for the IR EAA $\bar{\Gamma}_0[\chi]$ to non-zero k by integrating the Wetterich equation (2.37) from the UV $k = \Lambda$ down to $k < \Lambda$ ¹⁵

$$\bar{\Gamma}_k[\chi] = \bar{\Gamma}_\Lambda[\chi] - \int_\Lambda^k \frac{dk'}{k'} \mathcal{F}_{k'}[\chi]. \quad (2.75)$$

¹⁵Due to our convention (2.12) for RG time, Eq. (2.75) and subsequent expressions differ from the corresponding ones in Ref. [257], see, e.g., Eq. (11a) of Ref. [257], involving the FRG flux $\mathcal{F}_k[\chi]$ by a sign.

By taking a derivative of Eq. (2.75) w.r.t. Λ and evaluating the subsequent expression at $k = 0$ and an arbitrary $k \neq \Lambda$ we obtain

$$\Lambda \frac{d\bar{\Gamma}_0[\chi]}{d\Lambda} = \Lambda \frac{d\bar{\Gamma}_\Lambda[\chi]}{d\Lambda} + \mathcal{F}_\Lambda[\chi], \quad (2.76a)$$

$$\Lambda \frac{d\bar{\Gamma}_k[\chi]}{d\Lambda} = \Lambda \frac{d\bar{\Gamma}_\Lambda[\chi]}{d\Lambda} + \mathcal{F}_\Lambda[\chi]. \quad (2.76b)$$

Using the RG consistency condition (2.74) with Eq. (2.76a) and equating it with Eq. (2.76b), we obtain a RG consistency condition for any $k \neq \Lambda$

$$0 \stackrel{!}{=} \Lambda \frac{d\bar{\Gamma}_0[\chi]}{d\Lambda} = \Lambda \frac{d\bar{\Gamma}_\Lambda[\chi]}{d\Lambda} + \mathcal{F}_\Lambda[\chi] = \Lambda \frac{d\bar{\Gamma}_k[\chi]}{d\Lambda}. \quad (2.77)$$

The included statement $0 = \Lambda \partial_\Lambda \bar{\Gamma}_\Lambda[\chi] + \mathcal{F}_\Lambda[\chi]$ in Eq. (2.77) dictates that RG consistency is realized in the FRG approach if the IC $\bar{\Gamma}_\Lambda[\chi]$ changes with Λ according to the FRG flux $\mathcal{F}_\Lambda[\chi]$ at the initial scale. The latter is an immensely powerful and practically useful statement and merits further elaboration.

2.1.6.1. Construction of RG consistent initial conditions

Lets first consider a scenario where Λ can be chosen asymptotically large in the sense that

$$\forall s_i \in s \quad \frac{s_i}{\Lambda} \ll 1, \quad (2.78)$$

with the set s which includes all mass scales of the theory at hand. This set consists of all intrinsic mass scales m_{phys} , *e.g.*, particle masses and decay widths, and external scales m_{ext} , *e.g.*, temperature T or chemical potential μ . If Λ is indeed asymptotically large compared to those scales, the initial action $\bar{\Gamma}_\Lambda[\chi] = S[\chi]$ can be considered classical in the sense that the FRG flux $\mathcal{F}_\Lambda[\chi]$ at the initial scale vanishes since all fluctuations are included in $\bar{\Gamma}_\Lambda[\chi]$. This entails initial-scale-independence of the IC $\Lambda \partial_\Lambda \bar{\Gamma}_\Lambda[\chi] = \Lambda \partial_\Lambda S[\chi] = 0$. Such situations with asymptotically large initial scale in the sense of Eq. (2.78) will be studied in chapters 3 and 4.

In certain applications – prominently when working with LEFTs of QCD, *cf.* section 2.3 and chapter 5 – choosing an asymptotically large Λ for a given classical action S is conceptually not feasible and in some cases even mathematically impossible. In those cases it is possible to use RG consistency as a construction principle for a RG-scale-dependent IC $\bar{\Gamma}_\Lambda[\chi] = S_\Lambda[\chi]$ in the following way.

Consider a LEFT for which we specify the action $\bar{\Gamma}_{\Lambda'}[\chi; m_{\text{ext}}^0] = S[\chi]$ at an intermediate scale Λ' with/at a corresponding set of physical parameters m_{phys}^0 / external scales m_{ext}^0 . Here m_{ext}^0 is typically (but not necessarily) the vacuum, *e.g.*, $T = \mu = 0$, and m_{phys}^0 a set of IR observables realized by properly chosen couplings in $\bar{\Gamma}_{\Lambda'}[\chi]$. In this scenario Λ' can not be considered as asymptotically large in the sense of Eq. (2.78) and thus $\bar{\Gamma}_{\Lambda'}[\chi]$ does not include all relevant fluctuations especially w.r.t. fluctuations related to external scales m_{ext} beyond m_{ext}^0 , *e.g.*, thermal and density fluctuations beyond the vacuum. $\bar{\Gamma}_{\Lambda'}[\chi; m_{\text{ext}}^0]$ is therefore not suited

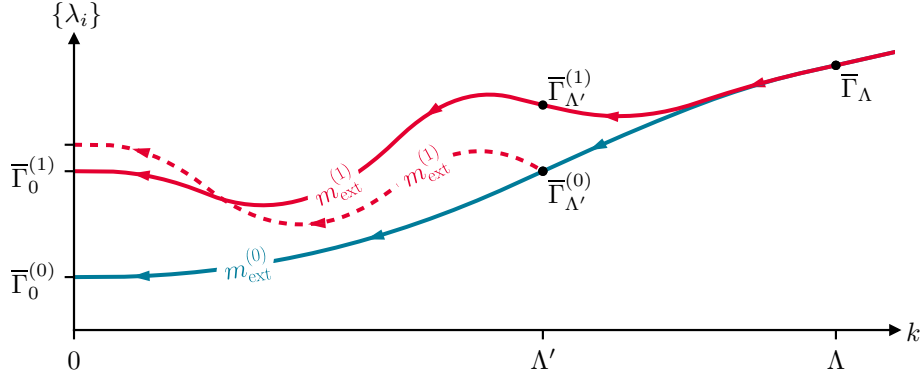


Figure 2.4.: Schematic FRG flow – RG-scale evolution of the EAA in the space of its couplings $\{\lambda_i\}$ – (in blue and red) from the UV initial condition $\bar{\Gamma}_\Lambda$ towards the IR at differing external parameter sets $m_{\text{ext}}^{(0)} \neq m_{\text{ext}}^{(1)}$. The red-dashed line represents a RG inconsistent flow at $m_{\text{ext}}^{(1)}$ starting from $\bar{\Gamma}_{\Lambda'}^{(0)}$ and not ending at the correct IR result $\bar{\Gamma}_\Lambda^{(1)}$. For readability in the figure we abbreviated $\bar{\Gamma}_k^{(0)} \equiv \bar{\Gamma}_k[\chi; m_{\text{ext}}^0]$ and $\bar{\Gamma}_k^{(1)} \equiv \bar{\Gamma}_k[\chi; m_{\text{ext}}^1]$.

for computations at $m_{\text{ext}}^1 \neq m_{\text{ext}}^0$. To remedy these situations and to enable RG-consistent computations at differing external scales $m_{\text{ext}}^1 \neq m_{\text{ext}}^0$ one can use the Wetterich equation (2.75) to reconstruct an UV initial action $\bar{\Gamma}_\Lambda[\chi; m_{\text{ext}}^0]$ at a higher, proper UV initial scale $\Lambda > \Lambda'$:

$$S_\Lambda[\chi] \equiv \bar{\Gamma}_\Lambda[\chi; m_{\text{ext}}^0] = \bar{\Gamma}_{\Lambda'}[\chi; m_{\text{ext}}^0] + \int_\Lambda^{\Lambda'} \frac{dk'}{k'} \mathcal{F}_{k'}[\chi; m_{\text{ext}}^0]. \quad (2.79)$$

$S_\Lambda[\chi]$ includes RG-scale-dependent counter terms – corrections to $S[\chi]$ – generated by the FRG flux $\mathcal{F}_k[\chi; m_{\text{ext}}^0]$ to ensure RG consistency $\Lambda \partial_\Lambda \bar{\Gamma}_0[\chi] = 0$ by guaranteeing $\Lambda \partial_\Lambda \bar{\Gamma}_\Lambda[\chi; m_{\text{ext}}^0] = -\mathcal{F}_\Lambda[\chi; m_{\text{ext}}^0]$ while maintaining $\bar{\Gamma}_{\Lambda'}[\chi; m_{\text{ext}}^0] = S[\chi]$. Therefore guaranteeing an unchanged $\bar{\Gamma}_k[\chi; m_{\text{ext}}^0]$ for $k < \Lambda'$ by construction, since Eq. (2.75) at m_{ext}^0 and Eq. (2.79) entail

$$\bar{\Gamma}_k[\chi; m_{\text{ext}}^0] = \bar{\Gamma}_{\Lambda'}[\chi; m_{\text{ext}}^0] - \int_{\Lambda'}^k \frac{dk'}{k'} \mathcal{F}_{k'}[\chi; m_{\text{ext}}^0] \quad (2.80a)$$

$$= \bar{\Gamma}_\Lambda[\chi; m_{\text{ext}}^0] - \int_\Lambda^k \frac{dk'}{k'} \mathcal{F}_{k'}[\chi; m_{\text{ext}}^0]. \quad (2.80b)$$

$S_\Lambda[\chi]$ represents an UV completion of the LEFT specified at Λ' with $\bar{\Gamma}_{\Lambda'}[\chi; m_{\text{ext}}^0] = S[\chi]$. This construction is visualized in figure 2.4 in blue.

By reconstructing $S_\Lambda[\chi] \equiv \bar{\Gamma}_\Lambda[\chi; m_{\text{ext}}^0]$ up to a scale Λ , which can be considered as asymptotically large in the sense of Eq. (2.78), we can ensure that a change in external parameters leaves the regularization and renormalization encoded in the running of $S_\Lambda[\chi]$ unchanged:

$$\frac{d}{dm_{\text{ext}}} \left[\Lambda \frac{dS_\Lambda[\chi]}{d\Lambda} \right] = 0. \quad (2.81)$$

In other words $S_\Lambda[\chi]$ is suited for computations at $m_{\text{ext}}^1 \neq m_{\text{ext}}^0$ since $\Lambda \gg m_{\text{ext}}$ and $\mathcal{F}_\Lambda[\chi; m_{\text{ext}}^0] = \mathcal{F}_\Lambda[\chi; m_{\text{ext}}^1]$. Integrating Eq. (2.81) from m_{ext}^0 to m_{ext}^1 we obtain

$$\Lambda \frac{dS_\Lambda[\chi]}{d\Lambda} \equiv \Lambda \frac{d\bar{\Gamma}_\Lambda[\chi; m_{\text{ext}}^0]}{d\Lambda} = \Lambda \frac{d\bar{\Gamma}_\Lambda[\chi; m_{\text{ext}}^1]}{d\Lambda}. \quad (2.82)$$

Note that $\bar{\Gamma}_\Lambda[\chi; m_{\text{ext}}^1] = \bar{\Gamma}_\Lambda[\chi; m_{\text{ext}}^0]$ is not necessary: an explicit dependence of $S_\Lambda[\chi]$ on m_{ext} is possible¹⁶ as long as Eq. (2.82) holds. In figure 2.4 and our applications in chapter 5 we consider $S_\Lambda[\chi]$ without an explicit dependence on m_{ext} . Using the Wetterich equation (2.75) at m_{ext}^1 with Eq. (2.79), we can construct a RG consistency condition at $m_{\text{ext}}^1 \neq m_{\text{ext}}^0$:

$$0 \stackrel{!}{=} \Lambda \frac{d\bar{\Gamma}_0[\chi; m_{\text{ext}}^1]}{d\Lambda} = \Lambda \frac{d\bar{\Gamma}_k[\chi; m_{\text{ext}}^1]}{d\Lambda} = \Lambda \frac{d\bar{\Gamma}_\Lambda[\chi; m_{\text{ext}}^1]}{d\Lambda} + \mathcal{F}_\Lambda[\chi; m_{\text{ext}}^1], \quad (2.83a)$$

$$0 \stackrel{!}{=} \Lambda \frac{d\bar{\Gamma}_0[\chi; m_{\text{ext}}^1]}{d\Lambda} = \mathcal{F}_\Lambda[\chi; m_{\text{ext}}^1] - \mathcal{F}_\Lambda[\chi; m_{\text{ext}}^0], \quad (2.83b)$$

where we used Eq. (2.82) in Eq. (2.83a) to obtain Eq. (2.83b). The latter can be used to conveniently define applicability ranges $\Lambda[m_{\text{ext}}^1]$, where $\Lambda[m_{\text{ext}}^1]$ is the range/scale for which Eq. (2.83b) holds to a given accuracy [257]. Using $S_\Lambda[\chi]$ as an IC for a large range of external parameters m_{ext} by guaranteeing Eq. (2.83b) (to a chosen accuracy), we note that at $k = \Lambda'$

$$\bar{\Gamma}_{\Lambda'}[\chi; m_{\text{ext}}^1] = \bar{\Gamma}_{\Lambda'}[\chi; m_{\text{ext}}^0] - \int_{\Lambda}^{\Lambda'} \frac{dk'}{k'} \left(\mathcal{F}_{k'}[\chi; m_{\text{ext}}^1] - \mathcal{F}_{k'}[\chi; m_{\text{ext}}^0] \right), \quad (2.84)$$

where we again used the Wetterich equation (2.75) with Eq. (2.79). $\bar{\Gamma}_{\Lambda'}[\chi; m_{\text{ext}}^1]$ differs from the specified action $\bar{\Gamma}_{\Lambda'}[\chi; m_{\text{ext}}^0] = S[\chi]$ by the fluctuations associated with m_{ext} . The latter are incorporated by integrating the difference of FRG fluxes $\mathcal{F}_{k'}[\chi; m_{\text{ext}}^1] - \mathcal{F}_{k'}[\chi; m_{\text{ext}}^0]$ from Λ to Λ' , cf. figure 2.4. It is imperative to include those fluctuations at $k = \Lambda'$ and $\bar{\Gamma}_{\Lambda'}[\chi; m_{\text{ext}}^0] = S[\chi]$ alone is not suited for a flow at m_{ext}^1 – a situation illustrated in figure 2.4 in red.

To conclude this section we want to comment on some practical limitations when leveraging the concept of RG consistency. Throughout this section we frequently used the symbolically integrated Wetterich equation (2.75) which is not a simple equation involving an ordinary integral. The integrals in Eq. (2.75) and subsequent derived expressions are meant as solutions of the Wetterich equation, which are obtained by solving the differential equations associated with the FRG flux $\mathcal{F}_k[\chi]$. Depending on the theory and truncation at hand this might be a rather involved process. Furthermore FRG time integration – evolving the Wetterich equation in RG scale from the UV to the IR – is for many theories and truncations irreversible. This irreversibility is formally mentioned in the next subsection 2.1.7 and discussed at length in chapter 3 and especially in subsection 3.2.4. Irreversibility makes the construction (2.79) of $S_\Lambda[\chi] \equiv \bar{\Gamma}_\Lambda[\chi; m_{\text{ext}}^0]$ in the context of LEFTs rather involved since a solution from the lower scale Λ' up to $\Lambda > \Lambda'$ is practically/computationally not possible and

$$\bar{\Gamma}_\Lambda[\chi; m_{\text{ext}}^0] - \int_{\Lambda}^{\Lambda'} \frac{dk'}{k'} \mathcal{F}_{k'}[\chi; m_{\text{ext}}^0] = \bar{\Gamma}_{\Lambda'}[\chi; m_{\text{ext}}^0] \quad (2.85)$$

¹⁶Certain LEFTs can require counter terms in $S_\Lambda[\chi]$, which depend on m_{ext} explicitly, see, e.g., Sec. III.B of Ref. [257] for an explicit example involving diquarks and chemical potential in the context of LEFTs for QCD.

would be the practical form of (2.79): $\bar{\Gamma}_\Lambda[\chi; m_{\text{ext}}^0]$ has to be tuned such that $\bar{\Gamma}_{\Lambda'}[\chi; m_{\text{ext}}^0]$ is recovered after flowing down from Λ to Λ' . This presents an extremely difficult optimization problem, which might not even have (depending on the theory, truncation, and regulator employed) a solution for some explicit choices of $\bar{\Gamma}_{\Lambda'}[\chi; m_{\text{ext}}^0] \equiv S[\chi]$.

That being said for some theories and truncations FRG time integration is reversible, cf. our large- N /mean-field studies in chapters 4 and 5, which simplifies the construction of suitable initial conditions $S_\Lambda[\chi] \equiv \bar{\Gamma}_\Lambda[\chi; m_{\text{ext}}^0]$ immensely since direct computation of appropriate counter terms from the Eq. (2.79) is possible and an optimization/tuning in the sense of Eq. (2.85) is not required.

2.1.7. Renormalization group equations as functional flow equations

Parts of this subsection are based on the Secs. II.B–C and IV.A of Ref. [1].

In the following we want to comment on the structure of the renormalization group equation for the RG-scale-dependent generating functionals $Z_k[\tilde{J}]$, $W_k[\tilde{J}]$, and $\bar{\Gamma}_k[\chi]$ for non-composite/non-scale-dependent fundamental fields $\hat{\chi}_a \equiv \tilde{\chi}_a \Leftrightarrow \partial_t \hat{\chi}_a = 0$ and corresponding sources $\hat{J}_a \equiv \tilde{J}_a$. The evolution equation (2.14) simplifies in this context to

$$\frac{dW_k[\tilde{J}]}{dt} = \frac{d}{dt} \ln Z_k[\tilde{J}] = \frac{1}{Z_k[\tilde{J}]} \frac{dZ_k[\tilde{J}]}{dt} = -\frac{1}{2} \partial_t R_k^{\text{mn}} \langle \tilde{\chi}_n \tilde{\chi}_m \rangle_{k; \tilde{J}}, \quad (2.86)$$

from which we can deduce the following evolution equations

$$\frac{dZ_k[\tilde{J}]}{dt} = -\frac{1}{2} (\partial_t R_k^{\text{mn}}) \frac{\delta}{\delta J^n} \frac{\delta}{\delta J^m} Z_k[\tilde{J}] = -\frac{1}{2} (\partial_t R_k^{\text{mn}}) Z_{k, \text{nm}}[\tilde{J}], \quad (2.87)$$

$$\begin{aligned} \frac{dW_k[\tilde{J}]}{dt} &= -\frac{1}{2} (\partial_t R_k^{\text{mn}}) \left(\frac{\delta}{\delta J^n} \frac{\delta}{\delta J^m} W_k[\tilde{J}] + \frac{\delta W_k[\tilde{J}]}{\delta J^n} \frac{\delta W_k[\tilde{J}]}{\delta J^m} \right) = \\ &= -\frac{1}{2} (\partial_t R_k^{\text{mn}}) \left(W_{k, \text{nm}}[\tilde{J}] + W_{k, n}[\tilde{J}] W_{k, m}[\tilde{J}] \right), \end{aligned} \quad (2.88)$$

by rewriting the expectation value using the generating functionals. The structure of Eq. (2.87) is that of a linear functional diffusion equation (*heat equation*) [230, 310–314], where t corresponds to an effective temporal direction, while \tilde{J} corresponds to an effective spatial direction. Sometimes Eq. (2.87) is even explicitly denoted as a (non-linear) heat equation, cf. subsection 2.2.4. The regulator insertion $-\frac{1}{2} \partial_t R_k^{\text{mn}}$ acts as a diffusion coefficient contracted with the Hessian $Z_{k, \text{nm}}[\tilde{J}]$. The RG time evolution of the generating functional $Z_k[\tilde{J}]$ is governed by the change – functional derivative $\delta/\delta \tilde{J}_n$ – of the functional gradient $Z_{k, m}[\tilde{J}]$ weighted by the diffusion coefficient $-\frac{1}{2} \partial_t R_k^{\text{mn}}$. The closely related evolution equation (2.88) for $W_k[\tilde{J}]$ has a similar structure, but the Hessian $W_{k, \text{nm}}[\tilde{J}]$ gets modified by the product of two functional gradient terms $W_{k, n}[\tilde{J}] W_{k, m}[\tilde{J}]$. The evolution equations for $Z_k[\tilde{J}]$ and $W_k[\tilde{J}]$ are due to their nature as functional diffusion equations *flow equations*.

The Wetterich equation (2.37)

$$\partial_t \bar{\Gamma}_k[\chi] = \frac{1}{2} G_{k; \text{mn}}[\chi] \partial_t R_k^{\text{nm}} \equiv \mathcal{F}_k [\bar{\Gamma}_k^{\text{mn}}[\chi], \chi], \quad (2.89)$$

does not manifest itself as a diffusion or flow equation at first glance. The r.h.s. of Eq. (2.89) depends non-linearly on the Hessian $\bar{\Gamma}_k^{\text{mn}}[\chi]$ through the propagator, cf. Eq. (2.27), which prevents a direct interpretation as a linear functional diffusion equation. Noting however that the r.h.s. of Eq. (2.89) does not depend on $\bar{\Gamma}_k[\chi]$ itself, we may consider the functional gradient $\bar{\Gamma}_k^{\text{a}}[\chi]$ as the fundamental variable and by taking a corresponding functional derivative reformulate Eq. (2.89) as

$$\partial_t \bar{\Gamma}_k^{\text{a}}[\chi] = \frac{\delta}{\delta \chi_{\mathbf{a}}} \mathcal{F}_k [\bar{\Gamma}_k^{\text{mn}}[\chi], \chi] \equiv \mathcal{F}_k^{\text{a}} [\bar{\Gamma}_k^{\text{mn}}[\chi], \chi], \quad (2.90)$$

which has the form of a functional convection¹⁷ equation [1, 247]. The RG time evolution of the one-point function $\bar{\Gamma}_k^{\text{a}}[\chi]$ is governed by the change – functional derivative $\delta/\delta \chi_{\mathbf{a}}$ – of the convection flux $\mathcal{F}_k [\bar{\Gamma}_k^{\text{mn}}[\chi], \chi]$, which due to the non-linear dependence on $\bar{\Gamma}_k^{\text{mn}}[\chi]$ can include both advective and diffusive contributions [1, 247], cf. subsection 3.2.2.1.

The fact that the non-perturbative RG evolution equations manifest as flow equations in the form of functional convection equations has many interesting and relevant consequences. We will not go into detail at this point and reserve an in-depth discussion for the main part of this thesis. The only aspect we want to mention at this point is the fact, that the manifestation as functional convection equations is closely linked to the semigroup property – the irreversibility of non-perturbative RG steps – of the (F)RG. The related loss of micro-physical information in the (F)RG due to the successive integration over high-momentum modes, cf. subsection 2.1.4.1, manifests on the level of the evolution Eqs. (2.87), (2.88), and (2.90) in their nature as convection equations. Especially the diffusive nature of the equations seems rather intuitive and natural in the context of non-perturbative implementations of the RG.

On the level of the RG-scale-dependent generating functionals $Z_k[\tilde{J}]$, $W_k[\tilde{J}]$, and $\bar{\Gamma}_k[\chi]$, without specifying an explicit theory and truncation, it is difficult to discuss the implications of this formulation and the understanding of RG evolution equations as flow equations explicitly. We will do so in the main part of this thesis using zero-dimensional theories in chapter 3 and the GN model in chapter 4. To facilitate this, we discuss flow equations/conservation laws with advective, diffusive, and source terms in the following section 2.2.

2.2. Conservation laws, hydrodynamics, and the finite volume method

Parts of this section are based on Secs. IV.B–C of Ref. [1] and on the Apps. B–E of Ref. [3].

In this section we discuss systems of PDEs in one effective temporal direction (t) and one effective spatial direction (x) of the following generic form

$$\begin{aligned} d_t u_i(t, x) + d_x F_i[t, x, \{u_i(t, x)\}] = d_x Q_i[t, x, \{u_i(t, x)\}, \{\partial_x u_i(t, x)\}] + \\ + S_i[t, x, \{u_i(t, x)\}], \end{aligned} \quad (2.91)$$

¹⁷In the following we use the term *convection* in the fluid-dynamical sense as a phenomenon including both *advection* and *diffusion*. For more details on those terms we refer to section 2.2.

$$d_t u_i(t, x) + d_x C_i[t, x, \{u_i(t, x)\}, \{\partial_x u_i(t, x)\}] = S_i[t, x, \{u_i(t, x)\}], \quad (2.92)$$

where we distinguish between advective contributions $d_x F_i[\dots]$, diffusive contributions $d_x Q_i[\dots]$, and source/sink contributions $S_i[\dots]$. Whether S_i acts as a source or sink in the dynamics of $\{u_i(t, x)\}$ depends on its explicit form. Nevertheless we will usually refer to S_i as a source term. We also introduced the convective contribution $d_x C_i[\dots] \equiv d_x F_i[\dots] - d_x Q_i[\dots]$, which incorporates both advective and diffusive contributions for the sake of discussion. In this section we will explicitly distinguish between partial ($\partial_x \equiv \partial/\partial x$) and total ($d_x \equiv d/dx$) derivatives. In the following, we occasionally suppress the t - and x -dependencies of u_i , C_i , F_i , Q_i , and S_i for the sake of simplicity. Equation (2.91) is a system of PDEs describing the evolution of m conserved quantities $\{u_i(t, x)\} \equiv \{u_i\} \equiv \{u_1, \dots, u_m\}$ in t and x . Depending on the problem at hand these two directions are not necessarily identical with physical spatial and temporal dimensions, but for the following discussion we denote them as such. The functions

- $F_i[\{u_i\}] \equiv F_i[t, x, \{u_i(t, x)\}]$ are components of a non-linear advection flux,
- $Q_i[\{u_i\}, \{\partial_x u_i\}] \equiv Q_i[t, x, \{u_i(t, x)\}, \{\partial_x u_i(t, x)\}]$ are components of a non-linear diffusion(dissipation) flux, and
- $S_i[\{u_i\}] \equiv S_i[t, x, \{u_i(t, x)\}]$ are components of a source term.

The aforementioned fluxes are discussed in detail in subsections 2.2.3–2.2.5 respectively. The concepts discussed in the following can be generalized beyond one spatial dimension to ($d = s + 1$)-dimensional space-time: $(x, t) \rightarrow (\vec{x}, t) = (x_1, \dots, x_d, t)$. Equation systems similar or even identical to Eq. (2.91) are often referred to as conservation laws and appear in many areas of the natural sciences, engineering, and economics. They are extensively studied in the field of computational fluid dynamics (CFD).

A complete and self-contained introduction to conservation laws in the context of CFD is beyond the scope of this thesis. We rather focus on introducing the computational methods we employ, establishing relevant nomenclature, and discussing selected properties of the system (2.91). We will discuss the different contributions to Eq. (2.91) in subsections 2.2.3–2.2.6 using explicit educational examples. The methodological introduction of subsections 2.2.1 and 2.2.2 is meant to facilitate the computations and discussions in the main part of this thesis, *i.e.*, chapters 3 and 4. For more details we refer the interested reader to the vast literature discussing conservation laws, *cf.* Refs. [315–324].

This section has a corresponding digital auxiliary file [325], which includes our latest MATHEMATICA-implementation of the KT/KNP scheme discussed in subsection 2.2.2 and the code to produce all the explicit (numerical) examples discussed in subsections 2.2.3–2.2.6.

2.2.1. The finite volume method

This subsection follows the discussion in Sec. IV.B of Ref. [1] with slight modifications due to the fact that we want to discuss a system of conservation laws for $\{u_i(t, x)\}$ instead of a single conservation law for $u(t, x)$.

In this section we discuss a numerical solution scheme for convection/advection-diffusion equations¹⁸ with source terms of the generic type (2.92). Considering the convection equation (2.92) with specified terms F_i , Q_i , and S_i in a finite computational domain $\Omega = \mathcal{V} \times [t_0, t_N]$, where $\mathcal{V} \subset \mathbb{R}^1$ denotes the spatial volume, with an IC $u_i(t_0, x)$ and Dirichlet (Neumann) boundary conditions (BCs) specifying $(\partial_x)u_i(t, x)|_{x \in \partial\mathcal{V}}$, the natural question arises how to evolve the IC in time from t_0 to $t_N > t_0$ to acquire a solution $u(t_N, x)$ respecting the specified BCs – i.e., how to explicitly solve the posed initial-value problem. For most problems of the type (2.92) an analytic/symbolic explicit solution is not known or even considered to be non-existent. Strategies for finding numerical (weak) solutions are required. Numerical schemes in the broad class of so-called finite volume (FV) methods are very popular for the numerical solution of PDEs describing the conservation or balance of quantities. For additional details regarding especially the FV method we refer the interested reader to the textbooks [317, 322]. Alternative high-resolution shock-capturing (HRSC) schemes in modern computational fluid dynamics are among others: finite-difference schemes including flux limiters/numerical viscosity or finite-element methods.

The concept that all numerical FV methods share is a discretization of the computational domain into space-time control volumes $\mathcal{V}_j \times [t^l, t^{l+1}]$, where the set of spatial control volumes \mathcal{V}_j covers the spatial computational domain \mathcal{V} . Integrating Eq. (2.92) over such a control volume centered at x , using the divergence theorem (Gauss-Ostrogradsky theorem) on the convection flux, and introducing the sliding cell average

$$\bar{u}_i(t, x) \equiv \frac{1}{|\mathcal{V}_j|} \int_{\mathcal{V}_j} d\xi u_i(\xi, t) \quad (2.93)$$

$$\Rightarrow \bar{u}_{i,j}(t) \equiv \bar{u}_i(t, x_j) \equiv \frac{1}{\Delta x_j} \int_{x_{j-\frac{1}{2}}}^{x_{j+\frac{1}{2}}} d\xi u_i(\xi, t), \quad (2.94)$$

where $\mathcal{V}_j = \{\xi : |\xi - x_j| \leq \Delta x_j/2\}$, we arrive at an equivalent integral form of Eq. (2.92),

$$\bar{u}_i(t^{l+1}, x) = \bar{u}_i(t^l, x) - \bar{C}_i[t^{l+1}, t^l, x, \{u_i\}] + \bar{S}_i[t^{l+1}, t^l, x, \{u_i\}], \quad (2.95)$$

with the integral over the convection flux

$$\begin{aligned} \bar{C}_i[t^{l+1}, t^l, x, \{u_i\}] &\equiv \frac{1}{\Delta x_j} \int_{t^l}^{t^{l+1}} d\tau C_i\left[\tau, x + \frac{\Delta x_j}{2}, u_i\left\{\left(\tau, x + \frac{\Delta x_j}{2}\right)\right\}\right] - \\ &- \frac{1}{\Delta x_j} \int_{t^l}^{t^{l+1}} d\tau C_i\left[\tau, x - \frac{\Delta x_j}{2}, u_i\left\{\left(\tau, x - \frac{\Delta x_j}{2}\right)\right\}\right], \end{aligned} \quad (2.96)$$

¹⁸Oftentimes, such equations are also referred to as “convection-diffusion equations”. The semantically correct term is nevertheless “advection-diffusion equation” because “convection” also includes diffusive processes besides the transport by bulk motion (advection), see also Ref. [315].

and the integral over the source term

$$\bar{S}_i[t^{l+1}, t^l, x, \{u_i\}] \equiv \frac{1}{\Delta x_j} \int_{t^l}^{t^{l+1}} d\tau \int_{x_{j-\frac{1}{2}}}^{x_{j+\frac{1}{2}}} d\xi S_i[\tau, \xi, \{u_i(\tau, \xi)\}], \quad (2.97)$$

with $x \in \mathcal{V}_j$. Considering a system without explicit source terms ($S_i = 0$), Eq. (2.95) with Eq. (2.96) implies that the change in the cell average $\bar{u}_i(t^{l+1}, x) - \bar{u}_i(t^l, x)$ is given by the time-integral over the convection flux (2.96) – *i.e.*, the time-integral over the in- and out-flux at the cell interfaces $x \pm \frac{\Delta x_j}{2}$. Assuming appropriate closed BCs on the compact spatial volume \mathcal{V} , the spatial integral over the cell averages $\bar{u}_i(t, x)$ is conserved since change in the individual control volumes is only possible due to in- or out-flux through the cell interfaces into the neighboring control volumes – hence the name conservation laws. In a system with closed BCs changes in the sum/integral over the cell averages $\bar{u}_i(t, x)$ are only possible due to source/sink terms S_i , which modify the conservation law according to Eq. (2.95) with Eq. (2.97). The reformulation of Eq. (2.92) in terms of cell averages has several advantages which we will discuss in the following. Arguably the most important one, which we want to mention right away, is the fact, that the integral/weak formulation of Eq. (2.95) in terms of cell averages allows for a proper treatment of discontinuous solutions $u_i(t, x)$, which are notorious in the context of conservation laws.

The solution of Eq. (2.95) – *i.e.*, the explicit computation of Eqs. (2.96) and (2.97) – presents the central challenge for an explicit FV scheme. Details regarding the explicit resolution and computation of Eqs. (2.96) and (2.97) are discussed in subsection 2.2.2 and specifically in subsections 2.2.3–2.2.5 respectively.

A central aspect of each practical FV scheme is an appropriate and informed choice of the space-time control volumes, which, depending on the scheme and problem at hand, might change during the time evolution. Given a set of control volumes and a corresponding set of cell averages $\bar{u}_i(t^l, x_j) \equiv \bar{u}_{i,j}^l$ the time evolution to $t^{l+1} \equiv t^l + \Delta t$ requires the solution of the Riemann problems at each cell interface. A Riemann problem in this CFD context is the initial value problem (IVP) related to the time evolution of two initially spatially constant states left and right of an initial interface, see, *e.g.*, Refs. [315, 317–319, 322, 326–328] for details. Part of these problems are the fluxes through the cell boundaries. The computation of those fluxes requires a reconstruction of the values of u_i on the cell interfaces located at $x_{j+\frac{1}{2}}$, which we denote as $u_{i,j+\frac{1}{2}}^l$, from the given set of cell averages $\bar{u}_{i,j}^l$. This is usually done by means of a carefully constructed polynomial approximation respecting the given cell averages of the neighboring cells. The order of the chosen approximation is one of the factors contributing to the overall spatial order (of the error) of the scheme at hand.

Given the cell averages $\bar{u}_{i,j}^l$ and fluxes through the cell interfaces at $t = t^l$ it remains to solve the Riemann problems at each cell interface. The solution of the Riemann problem amounts to the exact evaluation of the flux integrals on the r.h.s. of Eq. (2.95). Depending on the complexity of the underlying conservation equation an exact solution of the Riemann problems at the cell boundaries might be either impossible or simply not feasible. Most explicit FV schemes, especially those for general advection-diffusion equations, either use approximate

Riemann solvers (e.g., the Roe [329] or the HLLC [330, 331] solver) or do not require Riemann solvers at all (e.g., the KT [167] scheme). For a pedagogic introduction into the broad field of FV methods and HRSC schemes in general we refer the interested reader to Refs. [315, 317–319, 322, 328] and references therein.

In the following subsection 2.2.2 we will introduce the particular FV scheme, which we have chosen for its flexibility, efficiency, and relative simplicity.

2.2.2. The KT/KNP scheme and the MUSCL reconstruction

This subsection follows the discussion in Sec. IV.C of Ref. [1] and App. E.1 of Ref. [3] with slight modifications due to the fact that we want to discuss a system of conservation laws for $\{u_i(t, x)\}$ instead of a single conservation law for $u(t, x)$.

In this subsection we will summarize the central scheme presented in Ref. [167] by A. Kurganov and E. Tadmor, which we will refer to in the following as *Kurganov-Tadmor* (KT) scheme, and a variant of it introduced in Ref. [168] by A. Kurganov, S. Noelle, and G. Petrova, which we will refer to in the following as *Kurganov-Noelle-Petrova* (KNP) scheme. The KT and KNP scheme differ only in their implementation of the advection flux and we will use the term KNP scheme in the following only when discussing specifics of this variant. The KT scheme can be implemented and applied as a black-box solver for systems of the type of Eq. (2.91). Apart from the PDEs with their initial and boundary conditions the only additional information about the system required for its solution using the KT scheme are selected eigenvalues of the Jacobian of the advection term, see Eq. (2.103) and the related discussion. The scheme does not require a Riemann solver of any kind and as such does not rely on a characteristic decomposition of the advection flux.

The KT scheme provides a direct method for evaluating the flux integrals on the r.h.s. of Eq. (2.95). The main focus lies on the treatment and implementation of the flux integrals for the advection flux $F_i[\dots]$ – specific applications will be discussed in subsection 2.2.3. A careful treatment of the advection flux $F_i[\dots]$ is imperative when dealing with (non-linear) advection terms. The diffusion and source terms are treated separately and will be discussed at the end of this subsection with specific applications in subsections 2.2.4 and 2.2.5.

The KT scheme admits a meaningful $t^{l+1} - t^l \equiv \Delta t \rightarrow 0$ limit in the context of Eq. (2.95) and is thus an improvement on its predecessor: the *Nessyahu-Tadmor* (NT) scheme [332], with which it shares its piecewise-linear *Monotonic Upstream-centered Scheme for Conservation Laws* (MUSCL) reconstruction [333]. We will focus on the KT scheme in its so-called semi-discrete form – i.e., in the limit $\Delta t \rightarrow 0$ – which involves only an explicit spatial discretization. The KT scheme is formally second-order accurate in the spatial direction and as such an improved version of the first-order accurate *Lax-Friedrichs* (LxF) scheme [334, 335]. A semi-discrete form reduces the PDEs (2.92) or equivalently (2.95) to a set of coupled ODEs, which can be solved by a large class of general-purpose ODE solvers. This is especially useful when working on stiff problems or PDE systems coupled to additional ODEs. We will proceed with the introduction of quantities involved in the semi-discrete form (2.113) of the KT scheme. The following quantities are especially relevant for the numerical advection flux (2.108).

Consider a set of volume averages $\bar{u}_{i,j}^l$ at t^l based on an equidistant¹⁹ grid of volume cells $\mathcal{V}_j \equiv [x_{j-\frac{1}{2}}, x_{j+\frac{1}{2}}]$, with $\forall j, x_{j+\frac{1}{2}} - x_{j-\frac{1}{2}} = \Delta x$. At the initial time t_0 an IC – i.e., the corresponding set of volume averages $\bar{u}_{i,j}^0$ – has to be provided to initialize the flow. If the IC is provided in functional form $u_i(t_0, x)$, the corresponding cell averages $\bar{u}_{i,j}^0$ should be computed according to Eq. (2.94). Approximating the averages at t_0 , e.g., using the midpoint values $\bar{u}_{i,j}^0 \approx u_i(t_0, x_j)$, can introduce significant errors – especially when the volume grid is coarse (Δx is large) or when the IC $u_i(t_0, x)$ contains significant discontinuities. To prevent such errors we use the proper cell averages according to Eq. (2.94) either by integrating/averaging the IC $u_i(t_0, x)$ symbolically or numerically. The implementation of BCs in the KT scheme will be discussed at the end of this section after the introduction of some useful nomenclature.

The time evolution of the averages $\bar{u}_{i,j}^l$ at t^l to averages at $\bar{u}_{i,j}^{l+1}$ at $t^{l+1} = t^l + \Delta t$ on the same volume grid is a three-step process:

1. **The Reconstruction** (piecewise-linear MUSCL) is computed from the cell averages:

$$\tilde{u}_i(t^l, x) = \sum_{j=0}^{n-1} \left\{ \bar{u}_{i,j}^l + (\partial_x u)_{i,j}^l (x - x_j) \right\} \mathbb{1}_{[x_{j-\frac{1}{2}}, x_{j+\frac{1}{2}}]}, \quad (2.98)$$

where the sum runs over all n volume cells and with the projection operator $\mathbb{1}_{[x_{j-\frac{1}{2}}, x_{j+\frac{1}{2}}]}$, which is one if $x_{j-\frac{1}{2}} \leq x \leq x_{j+\frac{1}{2}}$ and zero otherwise. The reconstruction step is needed to gain access to the function values $\tilde{u}_i(t^l, x)$ and it uses approximations to the exact derivatives $(\partial_x u)_{i,j}^l$ by employing a scalar total variation non-increasing (TVNI)²⁰ reconstruction [315, 317, 339],

$$(\partial_x u)_{i,j}^l = \frac{\bar{u}_{i,j+1}^l - \bar{u}_{i,j}^l}{\Delta x} \phi \left(\frac{\bar{u}_{i,j}^l - \bar{u}_{i,j-1}^l}{\bar{u}_{i,j+1}^l - \bar{u}_{i,j}^l} \right), \quad (2.99)$$

with a TVNI limiter $\phi(r)$. An overview of TVNI flux limiters can be found, e.g., on the web page [340], in Refs. [315, 317], or in Sec. 9.3.1 of Ref. [319]. Here, we follow Ref. [167] and use the so-called *minmod* limiter [341]²¹,

$$\phi(r) = \max[0, \min(1, r)]. \quad (2.100)$$

The limiter ϕ is used in Eq. (2.99) to limit the slopes during the reconstruction process. This is crucial to prevent spurious oscillations around discontinuities, e.g., shocks, in

¹⁹The generalization of the KT scheme to non-uniform grids is on a conceptual level straightforward and especially useful for higher-dimensional extensions and for adaptive or moving mesh variants, see, e.g., Ref. [336]. Such generalizations require a more involved implementation and are not needed in this work. However, in the context of FRG flow equations this might be relevant for models with multiple condensate directions, see, e.g., Refs. [99, 127, 145, 147, 337, 338].

²⁰In literature *total variation-diminishing* (TVD) is often used as a less precise synonym for *total variation non-increasing* (TVNI), cf. Sec. 9.2.2 of Ref. [319]. Throughout this work we will adopt the more precise term *total variation non-increasing* (TVNI).

²¹We also implemented and tested other flux limiters, which however did not influence our numerical results in a significant manner – thus we restrict our discussions to results obtained with the *minmod* limiter (2.100). A problem specific optimization of the choice of flux limiters with regard to numerical performance could be part of future work.

high-resolution schemes like the KT scheme. The KT scheme can also be used with higher-order reconstruction schemes²² to increase the spatial accuracy of the scheme.

When using a piecewise-constant or -linear reconstruction the cell averages $\bar{u}_{i,j}^l$ coincide with the midpoint values $u_{i,j}^l$. While we employ a piecewise-linear reconstruction, we still maintain the distinction between averages and midpoint values for the sake of clarity.

2. **The time step** from t^n to t^{l+1} is performed by computing the flux integrals on the r.h.s. of Eq. (2.95) using the reconstruction $\tilde{u}_i(t^l, x)$ from Eq. (2.98) and carefully chosen control volumes discussed below. In the limit $t^{l+1} - t^l \equiv \Delta t \rightarrow 0$ only the expressions for $a_{j+\frac{1}{2}}^{l,-}$, $a_{j+\frac{1}{2}}^{l,+}$, $u_{i,j+\frac{1}{2}}^{l,-}$, and $u_{i,j+\frac{1}{2}}^{l,+}$ from Eqs. (2.101) and (2.102) respectively are relevant for the semi-discrete KT scheme. The other quantities discussed for this second step of the KT scheme are however necessary to understand the underlying algorithm.

At each cell interface $x_{j+\frac{1}{2}}$ the respective left- and right-sided local speed of propagation $a_{j+\frac{1}{2}}^{l,\mp}$ is estimated in the KNP scheme using

$$a_{j+\frac{1}{2}}^{l,-} \equiv \max \left\{ \lambda_m \left[\left\{ u_{i,j+\frac{1}{2}}^{l,-} \right\} \right], \lambda_m \left[\left\{ u_{i,j+\frac{1}{2}}^{l,+} \right\} \right], 0 \right\} \quad (2.101a)$$

$$a_{j+\frac{1}{2}}^{l,+} \equiv \min \left\{ \lambda_1 \left[\left\{ u_{i,j+\frac{1}{2}}^{l,-} \right\} \right], \lambda_1 \left[\left\{ u_{i,j+\frac{1}{2}}^{l,+} \right\} \right], 0 \right\} \quad (2.101b)$$

with the left- and right-sided intermediate values $u_{i,j+\frac{1}{2}}^{l,\mp}$ of $\tilde{u}_i(t^l, x)$ at the cell interface $x_{j+\frac{1}{2}}$:

$$u_{i,j+\frac{1}{2}}^{l,-} = \bar{u}_{i,j}^l + \frac{\Delta x}{2} (\partial_x u)_{i,j}^l, \quad (2.102a)$$

$$u_{i,j+\frac{1}{2}}^{l,+} = \bar{u}_{i,j+1}^l - \frac{\Delta x}{2} (\partial_x u)_{i,j+1}^l. \quad (2.102b)$$

The original KT variant uses a simplified/balanced estimate for left- and right-sided local speed of propagation:

$$a_{j+\frac{1}{2}}^l \equiv -a_{j+\frac{1}{2}}^{l,-,\text{KT}} \equiv +a_{j+\frac{1}{2}}^{l,+,\text{KT}} \equiv \quad (2.103a)$$

$$\equiv \max \left\{ \rho \left(\frac{\partial F}{\partial u} \left[\left\{ u_{i,j+\frac{1}{2}}^{l,+} \right\} \right] \right), \rho \left(\frac{\partial F}{\partial u} \left[\left\{ u_{i,j+\frac{1}{2}}^{l,-} \right\} \right] \right) \right\}, \quad (2.103b)$$

with the spectral radius $\rho(M) \equiv \max_i |\lambda_i(M)|$. Eqs. (2.101) and (2.103) include information from the eigenvalue spectrum $\lambda_1 < \dots < \lambda_m$ of the Jacobian $\frac{\partial F}{\partial u}$. The KT and KNP scheme are limited to systems with *strictly hyperbolic* advection fluxes signaled by a non-degenerate eigenvalue spectrum $\lambda_1 < \dots < \lambda_m$ of the Jacobian $\frac{\partial F}{\partial u}$ for all x, t , and

²²Examples for such improvements are the use of the third-order central weighted essentially non-oscillatory (C-WENO) reconstruction [342–344] outlined in Ref. [345], the fifth-order WENO scheme (WENO5) [346, 347] employed in Ref. [348], or the fifth-order monotonicity-preserving (MP5) reconstruction [349] used in Ref. [350].

u [167, 168]²³. For the numerical applications in this thesis, the simple balanced estimate (2.103) – the KT scheme – has proven to be sufficient for most computations. The slightly more involved KNP scheme with its more refined estimates (2.101a) and (2.101b) is primarily used in subsection 3.2.5.3. For single-valued conserved quantities $u \equiv \{u_1\}$ the expressions (2.101) and (2.103) for local speed of propagation simplify significantly. Details regarding advection phenomena and (hyperbolicity) constraints on advection fluxes are discussed in subsection 2.2.3.

Using the estimated local speed of propagation, a space-time control volume

$$[x_{j+\frac{1}{2},L}^l, x_{j+\frac{1}{2},R}^l] \times [t^l, t^l + \Delta t] \quad (2.104)$$

around each cell interface $x_{j+\frac{1}{2}}$ is chosen. The spatial extent corresponds to the domain which is causally affected by information propagating with the local velocities away from the cell interface at $x_{j+\frac{1}{2}}$. The flux integrals of Eq. (2.95) are performed on these space-time control volumes separately using the midpoint rule to approximate the flux integrals and leading to averages $\bar{\omega}_{i,j}^{l+1}$ and $\bar{\omega}_{i,j+\frac{1}{2}}^{l+1}$ based on the new intermediate spatial grid spanned by the points

$$x_{j+\frac{1}{2},L}^l = x_{j+\frac{1}{2}} + a_{j+\frac{1}{2}}^{l,-} \Delta t, \quad (2.105a)$$

$$x_{j+\frac{1}{2},R}^l = x_{j+\frac{1}{2}} + a_{j+\frac{1}{2}}^{l,+} \Delta t. \quad (2.105b)$$

In the regions $[x_{j-\frac{1}{2},R}^l, x_{j+\frac{1}{2},L}^l]$ the solutions underlying the computed averages $\bar{\omega}_{i,j}^{l+1}$ are smooth. The solutions underlying the computed averages $\bar{\omega}_{i,j+\frac{1}{2}}^{l+1}$ based on the regions $[x_{j+\frac{1}{2},L}^l, x_{j+\frac{1}{2},R}^l]$ are non-smooth. Details of this step can be found in Refs. [167, 168].

3. **The projection:** A MUSCL-type piecewise-linear reconstruction based on $\bar{\omega}_{i,j+\frac{1}{2}}^{l+1}$ and $\bar{\omega}_{i,j}^{l+1}$ is used to project these averages back onto the original uniform grid spanned by $x_{j+\frac{1}{2}}$. This results in a fully discrete second-order central scheme, see Eq. (3.9) of Ref. [167] and Eq. (3.7) of Ref. [168], which gives an algebraic expression for $\bar{u}_{i,j}^{l+1}$ in terms of the averages

$$\{\{\bar{u}_{i,j-2}^l\}, \{\bar{u}_{i,j-1}^l\}, \{\bar{u}_{i,j}^l\}, \{\bar{u}_{i,j+1}^l\}, \{u_{i,j+2}^l\}\} \quad (2.106)$$

and $\{a_{j\pm\frac{1}{2}}^{l,\pm}\}$. A pictographic representation of the multi-step evolution procedure with the involved quantities and grids can be found in Fig. 3.2 of Ref. [167] and the corresponding Fig. 3.1 of Ref. [168]. The numerical viscosity of this second-order scheme is $\mathcal{O}(\Delta x^3)$ and does not depend on Δt , which represents the mentioned an improvement when compared to the Δt -dependent numerical viscosities $\mathcal{O}(\Delta x^2/\Delta t)$ and $\mathcal{O}(\Delta x^4/\Delta t)$ of the LxF and NT schemes, respectively [167, 168].

²³A further improvement in terms of estimates of local speeds of propagation engineered for non-convex hyperbolic (systems of) conservation laws is presented in Ref. [348] using further information about the eigensystem of the Jacobian $\frac{\partial F}{\partial u}$. When an explicit evaluation of the Jacobian is impossible or unfeasible numerical approximations can be employed [167, 351, 352]. Throughout this work, however, we employ the exact or symbolic expressions for the Jacobian.

The Δt -independent numerical viscosity allows for a controlled limit $\Delta t \rightarrow 0$, in Eq. (2.95), resulting in a reduction to a practical semi-discrete scheme in conservative form [167], which can be implemented straightforwardly:

$$\partial_t \bar{u}_{i,j} = -\frac{H_{i,j+\frac{1}{2}} - H_{i,j-\frac{1}{2}}}{\Delta x} + \ll 2 \gg, \quad (2.107)$$

where $\ll 2 \gg$ denotes the sum of the diffusion and source fluxes. The numerical advection flux $H_{i,j+\frac{1}{2}}$ is given by

$$H_{i,j+\frac{1}{2}}^{\text{KT}} \equiv \frac{F_i \left[t, x_{j+\frac{1}{2}}, \{u_{i,j+\frac{1}{2}}^+\} \right] + F_i \left[t, x_{j+\frac{1}{2}}, \{u_{i,j+\frac{1}{2}}^-\} \right]}{2} - a_{j+\frac{1}{2}} \frac{u_{i,j+\frac{1}{2}}^+ - u_{i,j+\frac{1}{2}}^-}{2}, \quad (2.108)$$

for the KT variant and by

$$H_{i,j+\frac{1}{2}}^{\text{KNP}} \equiv \frac{a_{j+\frac{1}{2}}^+ F_i \left[t, x_{j+\frac{1}{2}}, \{u_{i,j+\frac{1}{2}}^-\} \right] - a_{j+\frac{1}{2}}^- F_i \left[t, x_{j+\frac{1}{2}}, \{u_{i,j+\frac{1}{2}}^+\} \right]}{a_{j+\frac{1}{2}}^+ - a_{j+\frac{1}{2}}^-} + \frac{a_{j+\frac{1}{2}}^+ a_{j+\frac{1}{2}}^+}{a_{j+\frac{1}{2}}^+ - a_{j+\frac{1}{2}}^-} \left(u_{i,j+\frac{1}{2}}^+ - u_{i,j+\frac{1}{2}}^- \right), \quad (2.109)$$

for the KNP variant. Note that Eq. (2.108) presents as a simplification of Eq. (2.109) when using the balanced approximation (2.103a) for the left- and right-sided local speed of propagation. This semi-discrete scheme is formally second-order accurate in Δx and can be used in conjunction with various ODE time-step algorithms. In this work, we use MATHEMATICA's *NDSolve* [166, 353] and *solve_ivp* with the *LSODA* option using an Adams/BDF method with automatic stiffness detection and switching from the *SciPy 1.0* library [354], cf. chapters 3 and 4. Time-stepping has not been a focus of our work and we refer the interested reader to the excellent Ref. [355] discussing the issue in the context of FRG in detail.

The KT/KNP scheme for a position-independent advection flux is conservative, meaning that detailed balance at the cell interfaces is maintained. It is also TVNI [315, 317, 339] when used with appropriate flux limiters like the minmod limiter (2.100). The total variation (TV) [339] – which is simply the arc length – of the solution $u(t, x)$ is given by

$$\text{TV}_i[\partial_x u_i(t, x)] \equiv \int_{x_{-\frac{1}{2}}}^{x_{n-\frac{1}{2}}} dx |\partial_x u_i(t, x)|, \quad (2.110)$$

on the (computational) interval $[x_{-\frac{1}{2}}, x_{n-\frac{1}{2}}]$. On a FV grid, a typical discretized version of Eq. (2.110) is given by, cf. Refs. [315, 317, 319, 339],

$$\text{TV}_i[\{\bar{u}_{i,j}(t)\}] \equiv \sum_{j=0}^{n-1} |\bar{u}_{i,j+1}(t) - \bar{u}_{i,j}(t)|, \quad (2.111)$$

where a first-order forward stencil is used to discretize the first derivative²⁴. (Weak) solutions of broad classes of hyperbolic and parabolic conservation laws – without source terms – are TVNI during time evolution when considered on a finite interval, see, *e.g.*, Refs. [315, 326, 339] and especially Ref. [356]: meaning their arc length only decreases. The differences $\text{TV}[\{\bar{u}_i(t^m)\}] - \text{TV}[\{\bar{u}_i(t^{m+1})\}]$ on a discrete trajectory $\bar{u}_i(t)$ of an admissible solution at different times separated by one time step Δt , where $t^{m+1} = t^m + \Delta t$, is greater or equal to zero for all t^m , *i.e.*, TV is non-increasing. This TVNI property of discrete weak solutions is an important guiding principle in the construction of numerical schemes in CFD meant to resolve shocks and discontinuities, since TVNI schemes do not produce spurious oscillations around discontinuities. Such spurious oscillations would violate the TVNI property since they would increase arc-length. The TV will be important for our discussion of numerical entropy and irreversibility of RG-flows in subsection 3.2.4 and we will also comment on it in subsection 2.2.3 in the context of backward time integration.

Diffusion and source/sink terms

So far we only considered the advection term $d_x F[\dots]$ in the discussion of the KT scheme. We will now turn our attention to diffusion fluxes $d_x Q[\dots]$ completing our discussion of convective contributions. When considering a non-linear diffusion flux $d_x Q_i[t, x, \{u_i(t, x)\}, \{\partial_x u_i(t, x)\}]$ Eq. (2.91) can manifest as a strongly degenerate parabolic equation system admitting potentially non-smooth solutions. In the KT scheme the hyperbolic and parabolic parts of the PDE (2.91) are treated simultaneously based on the strict splitting between F and Q . Kurganov and Tadmor [167] presented a discretization of the diffusion flux based on a central-difference approximation,

$$P_{i,j+\frac{1}{2}} = \frac{1}{2} Q_i \left[t, x_j, \{\bar{u}_{i,j}\}, \left\{ \frac{\bar{u}_{i,j+1} - \bar{u}_{i,j}}{\Delta x} \right\} \right] + \frac{1}{2} Q_i \left[t, x_{j+1}, \{\bar{u}_{i,j+1}\}, \left\{ \frac{\bar{u}_{i,j+1} - \bar{u}_{i,j}}{\Delta x} \right\} \right]. \quad (2.112)$$

An alternative second-order discretization, like the one put forward in App. B of Ref. [357], can also be successfully employed with the KT scheme, *cf.* Eq. (124) and (125) of Ref. [1] and the corresponding discussion. We will limit our discussion to results obtained with the diffusion flux (2.112). Improved KT-type schemes employing higher-order reconstructions (like, *e.g.*, C-WENO/WENO5 or MP5 [345, 348, 350]) also use higher-order discretizations for the diffusion flux like the fourth-order one put forward in Eqs. (4.9) and (4.10) of Ref. [345].

The inclusion of source-/sink-terms in the semi-discrete KT scheme is rather simple, but again relying on a strict separation from the convective terms, *cf.* Example 9 of Ref. [167]. In the following we use $S_{i,j}$ as the source/sink contribution to the flow $\partial_t \bar{u}_{i,j}$ of the i^{th} component in the j^{th} volume cell. The implementation of $S_{i,j}$ is rather problem specific depending on the explicit structure of the source term $S_i[t, x, \{u_i(t, x)\}]$. For simple u -independent source terms $S_i[t, x]$ symbolically evaluating Eq. (2.97) can be a good choice. For more complicated u -dependent source terms an approximation based on the midpoint value $S_{i,j} = S_i[t, x_j, \{\bar{u}_{i,j}\}]$ can be beneficial. We reserve further discussion of source terms for our explicit application involving sources/sinks in subsections 2.2.5 and 2.2.6 and especially in subsection 4.2.2.

²⁴Please note that $\{\bar{u}_{i,j}(t)\}$ in the definition Eq. (2.111) of TV_i refers to the set of all the i^{th} component cell averages and not the set of all components in the j^{th} volume cell.

Semi-discrete form and boundary conditions

To summarize: in full semi-discrete KT scheme the time evolution equation for the i^{th} component of the j^{th} cell average is given by

$$\partial_t \bar{u}_{i,j} = - \frac{H_{i,j+\frac{1}{2}} - H_{i,j-\frac{1}{2}}}{\Delta x} + \frac{P_{i,j+\frac{1}{2}} - P_{i,j-\frac{1}{2}}}{\Delta x} + S_{i,j}, \quad (2.113)$$

which includes advection, diffusion, and source fluxes. Eq. (2.113) is second-order accurate in Δx and presents as a FV method-of-lines discretization of the original PDE system (2.91). The initial cell averages $\bar{u}_{i,j}^0$ provide the IC for the ODE system (2.113).

The adept reader might immediately point out that this system is underdetermined: at the j^{th} cell the convection flux depends on the five-point stencil (2.106), which in the first cell ($j = 0$) includes $\{\bar{u}_{i,-2}\}$ and $\{\bar{u}_{i,-1}\}$, while in the last cell $j = n - 1$ it involves $\{\bar{u}_{i,n}\}$ and $\{\bar{u}_{i,n+1}\}$. Those so-called *ghost cells* formally lie outside the computational spatial domain $\mathcal{V} : x_{-\frac{1}{2}} \leq x \leq x_{n-\frac{1}{2}}$ and are centered around x_{-2} , x_{-1} , x_n , and x_{n+1} , respectively. Specific spatial BCs $(\partial_x)u_i(t, x)|_{x \in \partial\mathcal{V}}$ can be implemented in the KT scheme by an appropriate choice for the volume averages of those ghost cells. The implementation of BCs using ghost cells is not unique to the KT scheme and in fact quite common in FV methods, see, e.g., Refs. [315, 317, 322] for a detailed discussion. Using ghost cells is a very flexible and programmatically simple way to practically implement BCs.

Specific BCs for FRG flow equations are discussed at length in subsection 3.2.2.4 in the main part of this thesis. Additionally we will discuss BCs for canonical examples in subsections 2.2.3, 2.2.4, and 2.2.6 to conceptualize and facilitate the discussion of BCs for the FRG flow equations.

Total variation and explicit position- and time-dependent fluxes

At this point we have to remark that the original KT numerical scheme presented in Ref. [167] was constructed for position- and time-independent convection fluxes. Since we employ the KT scheme in its semi-discrete form a resolution of potentially highly complicated and non-linear dynamics in t is possible and ultimately outsourced to the ODE solver. Thus an explicit t -dependence in $H_{i,j+\frac{1}{2}}$ and $P_{i,j+\frac{1}{2}}$ is expected to be unproblematic when using Eq. (2.113).

Explicitly position-dependent advection and diffusion terms on the other hand are more worrisome, since they spoil the proper split between advective, diffusive, and source contributions. By performing the total derivatives in (2.91) to study the equation in its primitive form, cf. subsections 2.2.3 and 2.2.4, we note that explicit x -dependencies in $F_i[\dots]$ and $Q_i[\dots]$ manifest as internal source-/sink-like contributions, see explicitly Eqs. (2.116) and (2.137). Those internal and also explicit source terms spoil the TVNI property, which will be especially relevant for subsection 3.2.4.3. Defining or constructing an explicit numerical entropy functional for general non-linear conservation laws is a difficult task, especially when source terms are involved, see, e.g., Refs. [358–361] and references therein. Similarly explicit u -dependencies $Q_i[\dots]$ lead to advective contributions in primitive form which are not treated on the same level as the ones stemming from $F_i[\dots]$, cf. again subsection 2.2.4 and Eq. (2.137).

In the scope of this work we could not trace any practical problems back to the explicit position- and time-dependence of the advection and diffusion fluxes. The comparisons in

chapter 3 between results obtained from a direct computation of correlation functions using the generating functional and the results computed using FRG flow equations via the KT scheme (with t and x -dependent fluxes) can be seen as hard tests for both – the FRG methodology as well as the (slightly modified) KT scheme – depending on the respective perspective. In total, the precision of our results for the non-trivial test cases gives us some confidence, that our approach is generically justified and the KT scheme is suitable for our application throughout the main part of this thesis.

First-order reduction

An in Δx first-order accurate reduction of the semi-discrete KT/KNP scheme of Eq. (2.113) can be obtained by switching from the piece-wise linear MUSCL reconstruction (2.98) to a piecewise constant reconstruction with $(\partial_x u)_{i,j}^l = 0$ in the numerical advection fluxes $H_{i,j+\frac{1}{2}}$. For explicit expressions we refer to Remark 3 in Sec. 3.1 of Ref. [168], Eq. (4.8) of Ref. [167], and our explicit implementation in Ref. [325]. To have a consistent order in Δx for the convective contributions, the numerical diffusion flux $P_{i,j+\frac{1}{2}}$ has to be changed to a first-order accurate one, *i.e.*, for our purposes to the first-order upwind flux

$$P_{i,j+\frac{1}{2}}^{\mathcal{O}(1)} = Q_i \left[t, x_j, \{ \bar{u}_{i,j} \}, \left\{ \frac{\bar{u}_{i,j+1} - \bar{u}_{i,j}}{\Delta x} \right\} \right]. \quad (2.114)$$

Implementation

The semi-discrete, method-of-lines FV discretization (2.113) of the KT scheme and the KNP variant can be implemented in only a few lines of code in most modern programming languages using list or vector based operations. Its relative simplicity however should not unsettle the uninitiated: the scheme is almost shockingly powerful as a black-box solver even for complicated, non-linear systems (2.91) when paired with a robust ODE time-stepper. Such time-steppers are available in libraries for most modern programming languages, *i.e.*, *NDSolve* for MATHEMATICA [353], *solve_ivp* from *SciPy 1.0* for PYTHON [354], or *SUNDIALS* [362, 363] for C++. With the auxiliary file [325] we provide the MATHEMATICA notebook “*Computational fluid dynamic*” which includes my latest MATHEMATICA-implementation of the KT/KNP scheme. It includes a completely modular black box solver using *compiled* functions for performance²⁵. The auxiliary file [325] includes the numerical computations of the following subsections 2.2.3–2.2.6. The numerical results in chapter 3 and selected results of chapter 4 were obtained with older versions of this code [364–366].

2.2.3. Advection and shocks

In this subsection we will discuss the advective contributions to Eq. (2.91), *viz.* the ones governed by the advection term $d_x F_i[t, x, \{u_i(t, x)\}]$. Focusing on the latter, let us consider the non-linear system of advection equations

$$d_t u_i(t, x) + d_x F_i[t, x, \{u_i(t, x)\}] = 0, \quad (2.115)$$

²⁵The performance of a MATHEMATICA implementation with proper low-level *compiled* functions is on a par with implementations in C++ and PYTHON using *SUNDIALS* [362, 363] and *solve_ivp* [354] respectively.

which can be brought into *primitive form*²⁶

$$\partial_t u_i(t, x) + \frac{\partial F_i[t, x, \{u_i(t, x)\}]}{\partial u_i(t, x)} \partial_x u_i(t, x) = -\partial_x F_i[t, x, \{u_i(t, x)\}]. \quad (2.116)$$

Eq. (2.116) includes the Jacobian $\frac{\partial F}{\partial u}$ – the matrix of advection speeds – in the actual advection term $\frac{\partial F_i}{\partial u_i} \partial_x u_i$ and on the r.h.s. an internal source term $-\partial_x F_i[\dots]$ related to the explicit position dependency of the advection flux F . In this sense position-dependence of the advection flux can be understood in terms of additional/internal source terms. Eq. (2.116) or in our context the flux F itself is understood to be *hyperbolic*, if the Jacobian/the matrix of advection speeds $\frac{\partial F}{\partial u}$ is diagonalizable with a set of real eigenvalues $\lambda_1 \leq \dots \leq \lambda_m$ for all t, x , and $u_i(t, x)$ under consideration. The application of the KT/KNP numerical advection fluxes $H_{i,j+\frac{1}{2}}$ (2.108)/(2.109) requires *strictly hyperbolic* systems with a non-degenerate eigenvalue spectrum $\lambda_1 < \dots < \lambda_m$. When studying only one conserved quantity – not a system of m conserved quantities $\{u_1(t, x), \dots, u_m(t, x)\}$ – its conservation equation is hyperbolic if the advection speed $\frac{\partial F}{\partial u}$ is real and finite for all t, x , and $u(t, x)$ under consideration. For hyperbolic systems IVPs are well posed [317, 319, 322]. Hyperbolic systems typically describe processes where information or disturbance are propagated through space-time in a wave-like manner with a finite advection speed [315, 317, 318, 322, 323], cf. subsection 2.2.3.2 for instructive and canonical examples.

For the remainder of this subsection we will limit our discussion to the single conservation law

$$\partial_t u(t, x) + d_x F[t, x, u(t, x)] = 0, \quad (2.117)$$

$$\partial_t u(t, x) + \frac{\partial F[t, x, u(t, x)]}{\partial u(t, x)} \partial_x u(t, x) = -\partial_x F[t, x, u(t, x)], \quad (2.118)$$

for $u(t, x)$, which is the relevant scenario for our numerical computations in chapters 3 and 4. An application to a canonical system of conservation laws, *i.e.*, the Euler equations of ideal fluid dynamic, will be presented in subsection 2.2.6.

2.2.3.1. Method of characteristics and Rankine–Hugoniot (jump) condition

This subsection is based on the first parts of Apps. C and D of Ref. [3].

An important computational tool for *quasilinear* – *i.e.*, linear in the derivatives $\partial_t u$ and $\partial_x u$ but not necessarily linear in u – hyperbolic PDEs of the form (2.118) is the *method of characteristics*, cf. Ref. [367] and Refs. [317, 323] for a general overview.

The method of characteristics states that a quasilinear hyperbolic PDE

$$a(t, x, u) \partial_t u(t, x) + b(t, x, u) \partial_x u(t, x) = c(t, x, u) \quad (2.119)$$

²⁶In the FV context the following equation should be understood in integral form (2.95) to avoid any conceptual and mathematical problems especially when dealing with discontinuities [317, 319, 322].

presents as a set of ODEs along so-called characteristic curves, which are given by the Lagrange–Charpit equations [367] (also called characteristic equations):

$$\frac{\partial t(\tau)}{\partial \tau} = a(t(\tau), x(\tau), u(\tau)), \quad (2.120a)$$

$$\frac{\partial x(\tau)}{\partial \tau} = b(t(\tau), x(\tau), u(\tau)), \quad (2.120b)$$

$$\frac{\partial u(\tau)}{\partial \tau} = c(t(\tau), x(\tau), u(\tau)), \quad (2.120c)$$

with the curve-parameter τ and ICs

$$t(\tau = 0) = t_0, \quad (2.121a)$$

$$x(\tau = 0) = x_0, \quad (2.121b)$$

$$u(\tau = 0) = u_0(t_0, x_0), \quad (2.121c)$$

related to the original PDE (2.119). Solving this ODE system yields the functions $t(\tau)$, $x(\tau)$ and $u(\tau)$, which can be used to extract information about the actual solution of the PDE (2.119) including, in some cases, the full solution itself. More details can be found in the textbooks [315, 317, 318, 322, 323, 328] and explicit applications follow in subsection 2.2.3.2 and subsection 3.2.5 as well as in subsection 3.2.5.4 and App. D.1.3.3.

Using $t(\tau)$, $x(\tau)$ and $u(\tau)$ one can reconstruct the solution $u(t, x)$ as an implicit solution in terms of τ . Such a reconstruction however is only valid as long as the characteristic curves $t(\tau)$ and $x(\tau)$ do not intersect. If they do, the implicit solution $u(t, x)$ becomes multivalued and the PDE no longer has a solution in the classical sense [317, 319, 322]. The physical/weak-solution develops a *shock* – a discontinuity in $u(t, x)$ – which can only be treated properly using a weak formulation, e.g., a FV discretization like Eq. (2.95). The speed $\partial_t \xi_s(t)$ of such a shock can be determined with the *Rankine-Hugoniot condition* [368, 369]

$$F_R(t) - F_L(t) = \partial_t \xi_s(t)(u_R - u_L), \quad (2.122)$$

where the subscripts R and L denote the state to the right and left of the shock $\xi_s(t)$, see, e.g., Refs. [317, 318, 326, 328] for further details. The characteristic curves on both sides of the shock run into the shock wave with $\lambda(u_L) > \partial_t \xi_s(t) > \lambda(u_R)$.

An instructive example of shock formation is part of subsection 2.2.3.2 with our discussion of the *Bateman-Burgers equation* (2.130) and the phenomenon is further discussed in subsection 2.2.6 and chapters 3 and 4.

2.2.3.2. Linear and non-linear advection equations

The part of this subsection discussing the Bateman-Burgers equation (2.130) includes material from Sec. III.A and App. A of Ref. [9].

Up to this point our discussion of CFD has been extremely technical with the goal to introduce relevant nomenclature and the explicit FV method we use for numerical computation, viz. the

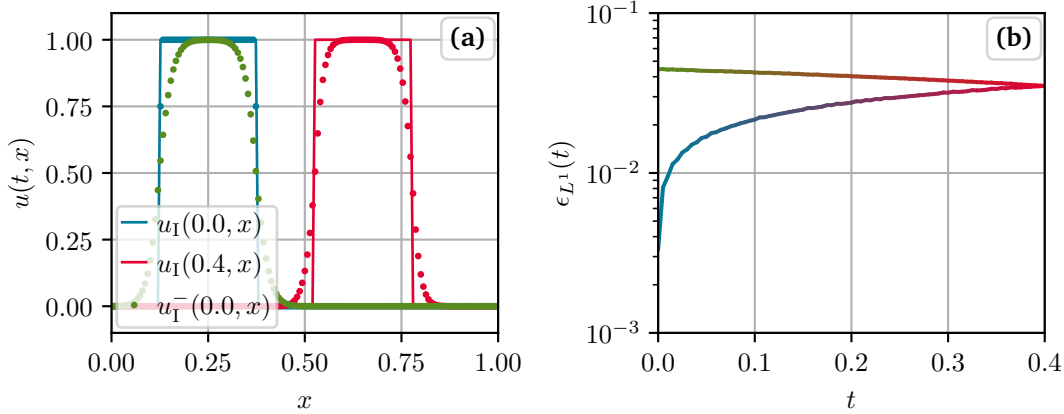


Figure 2.5.: Analytical (solid lines) and numerical solution (dots) to the LAE (2.123) with IC (2.125a) and open BC (2.126) at different times on the left (a) and relative error (2.127) between the analytical and numerical solution on the right (b). The solution $u_I^-(0.0, x)$ has been computed by numerically evolving $\{\bar{u}_{I,j}(t = 0.4)\}$ back in time to $t = 0$. The numerical solution has been computed with the KT scheme using $n = 151$ volume cells equidistantly spaced in the interval $x_0 = 0$ and $x_{150} = 1$, cf. subsection 2.1.1 of the auxiliary notebook [325].

KT scheme. It is high time to “show some pictures” – discuss and present some applications of the framework to explicit problems. We will do so using two explicit examples: the linear advection equation and the non-linear Bateman-Burgers equation.

The linear advection equation

We begin this discussion with an archetypical advection equation, *viz.* the *linear advection equation* (LAE)

$$\partial_t u(t, x) + \partial_x u(t, x) = 0, \quad (2.123)$$

$$u(t, x) = u(t = 0, x - t), \quad (2.124)$$

$$u_I(t = 0, x) = \Theta(x - \frac{1}{8}) - \Theta(x - \frac{3}{8}), \quad (2.125a)$$

$$u_{II}(t = 0, x) = \frac{1}{2} + \frac{1}{2} \sin(2\pi x), \quad (2.125b)$$

with the linear hyperbolic PDE (2.123), its analytic solution (2.124), and two explicit initial conditions (2.125a) and (2.125b), which we will use in the following. With $F = u(t, x)$ in the LAE (2.123), the characteristic speed is constant: $\partial F / \partial u = 1$. The LAE with an IC very similar to Eq. (2.125a) is also discussed in Sec. 6.1 of Ref. [167] as a standard benchmark problem. The analytic solution (2.124) follows directly from the method of characteristics, where the Lagrange–Charpit Eqs. (2.120) can be integrated trivially for the LAE with $a = b = 1$ and $c = 0$, cf. subsubsection 2.2.3.1. According to Eq. (2.124) the LAE simply transports/advects the IC through the computational domain from left to right with a constant speed of 1 without changing its initial shape.

The analytical and numerical solution of the LAE (2.123) with the non-analytic IC (2.125a) are visualized in figure 2.5a with open BCs implemented in the KT scheme by linear extrapolation for the ghost cells [315, 317, 322], *i.e.*,

$$\bar{u}_{-2} = 3\bar{u}_0 - 2\bar{u}_1, \quad \bar{u}_{-1} = 2\bar{u}_0 - \bar{u}_1, \quad (2.126a)$$

$$\bar{u}_n = 2\bar{u}_{n-1} - \bar{u}_{n-2}, \quad \bar{u}_{n+1} = 3\bar{u}_{n-1} - 2\bar{u}_{n-2}. \quad (2.126b)$$

From a numerical standpoint, discretizing and evolving the LAE (2.123), especially when allowing for discontinuous IC like Eq. (2.125a), is quite challenging. Naive discretization schemes, like FDs, and even more involved global collocation methods are notoriously ill-suited to tackle this problem [315, 317, 318, 322, 323, 370]. The relative error in L^1 -norm, *i.e.*, the sum of all errors divided by the number of volume cells n :

$$\epsilon_{L^1}(t) = \frac{1}{n} \sum_{j=0}^{n-1} |\bar{u}_j(t) - u(t, x_j)| \quad (2.127)$$

using Eq. (2.124) as reference, is plotted in figure 2.5b. After the uncertainty due to the initial discretization of the discontinuous IC (2.125a), the error starts to plateau, allowing for a stable numerical evolution of the discretized initial condition.

The LAE is in theory time-reversible: switching the sign of the advection speed one can evolve a solution $u(t, x)$ backwards in time without any conceptual difficulties. The simple linear advection of the IC prescribed by the LAE in an ideal case is free of numerical entropy production. In practice time-reversal is studied in figure 2.5 by evolving the computed solution $\{\bar{u}_{I,j}(t = 0.4)\}$ back in time to $t = 0$ by flowing with a reversed advection speed $\partial F/\partial u = -1$ arriving at a numerical solution $\{\bar{u}_{I,j}^-(t = 0)\}$ visualized in green in figure 2.5. We notice that the relative L^1 error grows slowly as we try to reconstruct the IC at $t = 0$. This is due to inevitable inaccuracies in time integration and spatial discretion errors. Nevertheless we recover a solution $\{\bar{u}_{I,j}^-(t = 0)\}$ very close to the discretized version of the IC $u_I(t = 0, x)$.

The analytical and numerical solution of the LAE (2.123) with the analytic IC (2.125b) are visualized in figure 2.6a with periodic BCs implemented in the KT scheme by mirroring the opposite end of the computational interval in the ghost cells²⁷ [315, 317, 322], *i.e.*,

$$\bar{u}_{-2} = \bar{u}_{n-3}, \quad \bar{u}_{-1} = \bar{u}_{n-2}, \quad \bar{u}_0 = \bar{u}_{n-1}, \quad \bar{u}_n = \bar{u}_1, \quad \bar{u}_{n+1} = \bar{u}_2. \quad (2.128)$$

Discretizing the smooth IC (2.125b) even with slightly less volume cells ($n = 101$ instead of $n = 150$ in figure 2.5) the overall error is around an order of magnitude lower when comparing figures 2.5b and 2.6b. Forward and backward time integration with the KT scheme is possible, but due to numerical errors we note a visible difference (most notable at $x = 0.25$ and $x = 0.75$ in figure 2.6a) between the initial set of volume averages $\{\bar{u}_{II,j}(t = 0)\}$ and the one computed with backward time integration from $t = 0.4$ to $\{\bar{u}_{II,j}^-(t = 0)\}$.

²⁷Whether or not to enforce $\bar{u}_0 = \bar{u}_{n-1}$ depends on the explicit choice of the location of the first and last volume cell x_0 and x_{n-1} . We chose to center both on the respective boundaries of the computational domain and thus enforce $\bar{u}_0 = \bar{u}_{n-1}$.

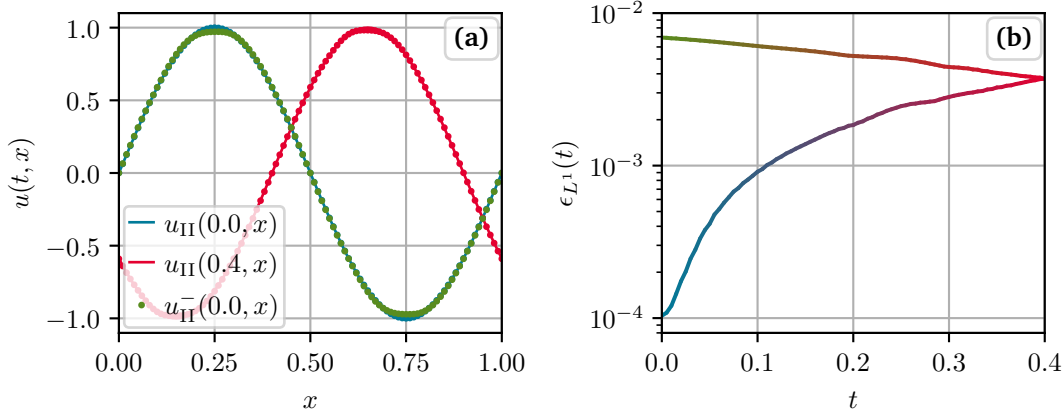


Figure 2.6.: Analytical (solid lines) and numerical solution (dots) to the LAE (2.123) with IC (2.125b) and periodic BC (2.128) at different times on the left (a) and relative error (2.127) between the analytical and numerical solution on the right (b). The numerical solution has been computed with the KT scheme using $n = 101$ volume cells equidistantly spaced in the interval $x_0 = 0$ and $x_{100} = 1$, cf. subsection 2.1.2 of the auxiliary notebook [325].

The relative errors in L^1 norm, the rate of convergence in the scheme S

$$r_S \equiv \ln \left(\frac{\epsilon_{S,i}}{\epsilon_{S,i-1}} \right) / \ln \left(\frac{n_{i-1}}{n_i} \right), \quad (2.129)$$

and the wall time in seconds for different number of volume cells $n = \{32, \dots, 1024\}$ for the first- and second-order KT scheme, cf. subsection 2.2.2, are shown in table 2.2 for the smooth IC (2.125b). We observe a rather consistent rate of convergence of ~ 0.97 for the formally first-order accurate scheme and ~ 1.89 for the formally second-order accurate scheme. For this rather simple example we can numerically integrate up to $t = 0.4$ in under two seconds using $n = 1024$ cells and a notebook CPU from 2018.

A non-linear advection equation

So far we discussed the arguably rather simple LAE (2.123). In the following we want to focus on one particular non-linear but still quasilinear advection equation, viz. the *Bateman-Burgers equation* (BBE) [371, 372]

$$\partial_t u(t, x) + \partial_x \left(\frac{1}{2} u(t, x)^2 \right) = \partial_t u(t, x) + u(t, x) \partial_x u(t, x) = 0, \quad (2.130)$$

$$x(\tau) = u(t = 0, \tau) t + \tau, \quad (2.131)$$

$$u(t, x) = u(t = 0, \tau) = u(t = 0, x - u(t, x) t), \quad (2.132)$$

$$u(t = 0, x) = \sin(2\pi x), \quad (2.133)$$

with the BBE (2.130) and an explicit IC (2.133), which we will use in the following. The BBE with this IC (2.133) is also discussed in Sec. 6.2 of Ref. [167] as a standard benchmark problem. Using the method of characteristics with the Eqs. (2.120) and (2.121) yields the non-trivial characteristic curve (2.131) and in consequence the implicit symbolic solution (2.132) in terms

Table 2.2.: Relative errors in L^1 -norm ϵ using Eqs. (2.124) and (2.125b) as reference in Eq. (2.127), convergence rate r from Eq. (2.129), and wall time t_w in seconds for first- and second-order KT scheme numerical solutions at $t = 0.4$ of the LAE (2.123) with IC (2.125b) and periodic BC (2.128) in the interval $x_0 = 0$ and $x_n = 1$ with varying number n of equidistantly spaced volume cells, cf. subsection 2.1.3 of the auxiliary notebook [325]. The wall time refers to a single run on an Intel[®] Core™ i7-8750H processor running up to 6 threads simultaneously using the auxiliary notebook [325] with MATHEMATICA 13.0.1.0 [166].

n	KT $\mathcal{O}(\Delta x^1)$			KT $\mathcal{O}(\Delta x^2)$		
	ϵ_{KTO1}	r_{KTO1}	t_w (s)	ϵ_{KTO2}	r_{KTO2}	t_w (s)
32	$1.43 \cdot 10^{-1}$	-	$3.96 \cdot 10^{-3}$	$3.12 \cdot 10^{-2}$	-	$7.70 \cdot 10^{-2}$
64	$7.51 \cdot 10^{-2}$	0.93	$4.96 \cdot 10^{-3}$	$8.67 \cdot 10^{-3}$	1.85	$1.48 \cdot 10^{-1}$
128	$3.84 \cdot 10^{-2}$	0.97	$1.50 \cdot 10^{-2}$	$2.38 \cdot 10^{-3}$	1.87	$1.79 \cdot 10^{-1}$
256	$1.94 \cdot 10^{-2}$	0.98	$4.00 \cdot 10^{-2}$	$6.36 \cdot 10^{-4}$	1.90	$1.77 \cdot 10^{-1}$
512	$9.76 \cdot 10^{-3}$	0.99	$1.60 \cdot 10^{-1}$	$1.69 \cdot 10^{-4}$	1.91	$3.81 \cdot 10^{-1}$
1024	$4.90 \cdot 10^{-3}$	1.00	$4.43 \cdot 10^{-1}$	$4.44 \cdot 10^{-5}$	1.93	$1.32 \cdot 10^{+0}$

of the initial condition $u(t = 0, x)$. The analytical and numerical solution of the BBE with the IC (2.133) are visualized in figure 2.7 including the corresponding characteristic curves. We observe that the first characteristic curves intersect at $x = 1/2 \equiv \xi_s$ and $t = 1/(2\pi) \equiv t_s$, thus, according to subsection 2.2.3.1, a shock forms. Specifically, by means of the Rankine-Hugoniot condition (2.122), we find a standing shock at $\xi_s(t) = 1/2$ for $t \geq 1/(2\pi)$. Since the flow is exactly mirrored around $x = 1/2$, we observe that the opposing waves annihilate since they travel at opposite velocity according to $\partial F/\partial u = u$. For times $t > t_s$ – after the shock formation – the implicit solution (2.132) becomes multi-valued, but due to the symmetry of the problem and the fact that the shock is standing, it is not difficult to reconstruct the solution for $t > t_s$, cf. section 2.2 of the auxiliary notebook [325]. For $0 \leq t \leq t_s$ we use the implicit solution (2.132) and for $t > t_s$ we use the reconstructed solution as reference. Intuitively (imaging the situation in terms of waves) and for the CFD initiated this example of shock formation might seem rather natural, but let us make one important mathematical observation: non-linear advection equations can develop shocks – even if the initial condition is smooth and even if the advection flux is simple, i.e., for the BBE (2.130) $F[u] = \frac{1}{2}u^2$. In turn, any numerical scheme deployed in practice for non-linear advection equations or equations involving such non-linear hyperbolic contributions should be able to handle discontinuities in $u(t, x)$. This simple statement outright disqualifies large classes of methods for PDEs for this application. Such methods are for example naive finite differences (the large gradients induced by the shock will destabilize the method-of-lines ODE system) and global collocation methods, which in principle rely on analyticity or at least smoothness (the shock discontinuity will again destabilize the ODE system in spectral space due to the Wilbraham-Gibbs phenomenon [286–288], see, e.g., the textbook [285]). Recall the related discussion of such issues in the context of truncated flow equations in subsection 2.1.4.2.

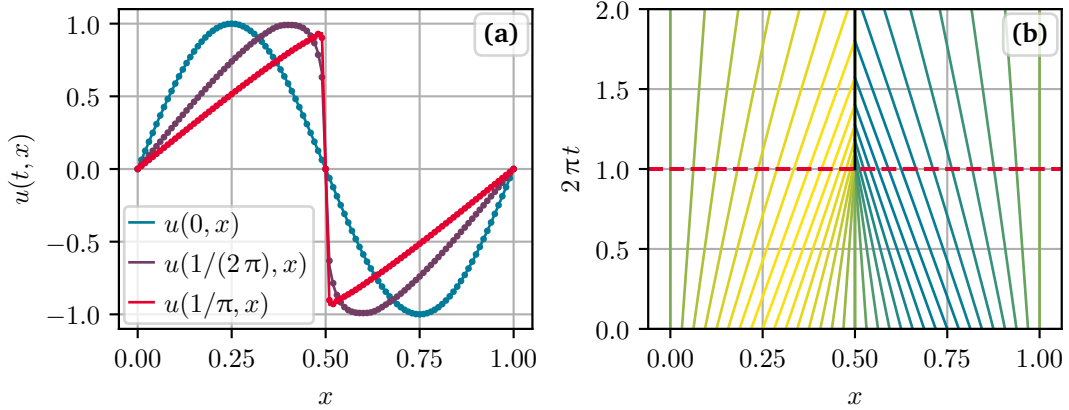


Figure 2.7.: Analytical/reconstructed (solid lines) and numerical solution (dots) to the BBE with IC (2.133) and periodic BC (2.128) at different times on the left (a) and corresponding characteristic curves on the right (b). The shock position at $\xi_s(t) = 1/2$ for $t \geq 1/(2\pi)$ is marked as a black line, the shock formation time is marked as a red-dashed line, and the constant function value on the characteristics are color coded (yellow for +1, green for 0 and blue for -1) on the right (b). The numerical solution has been computed with the KT scheme using $n = 101$ volume cells equidistantly spaced in the interval $x_0 = 0$ and $x_{100} = 1$, cf. section 2.2 of the auxiliary notebook [325].

The shock formation in this example also has implications for the reversibility of non-linear advection equations. It is well known from the study of non-linear advection equations, see, e.g., the textbooks [315, 317–319, 326–328], that there is a meaningful notion of numerical entropy and that its increase is linked to the appearance and/or interaction of discontinuities like shocks. An increase in numerical entropy signals the irreversibility of the underlying flow, see, e.g., Refs. [317, 319] for this in the context of non-linear (especially hyperbolic) conservation laws. It turns out that the TV – arc-length – from Eq. (2.111) can, due to the TVNI property, be used to define a numeric entropy functional

$$\mathcal{C}_{\text{TV}}[\{\bar{u}_j(t)\}] \equiv \text{TV}[\{\bar{u}_j(0)\}] - \text{TV}[\{\bar{u}_j(t)\}], \quad (2.134)$$

which is due to the chosen sign convention only increasing: $\partial_t \mathcal{C}_{\text{TV}}[\{\bar{u}_j(t)\}] \geq 0$ during time evolution. The notion of numerical entropy (and TV as a possible candidate for it) is very important in the study, construction and numerical computation of physical weak solutions of conservative equations, see, e.g., the textbooks [315, 317–319, 326–328] for further details. We plot \mathcal{C}_{TV} for the current example in figure 2.8a and observe an increase of numerical entropy in general as expected. However, after shock formation – if only delayed at $t \sim 1.5$ – a massive increase in numerical entropy can be observed, which we identify with a delayed signal of the shock formation in \mathcal{C}_{TV} . Figure 2.8b includes the corresponding relative L^1 errors, including three attempts at backwards time integration. The first one starting exactly at $t = 1/(2\pi)$ – the point where the shock forms – and integrating back to $t = 0$ is comparable to the ones in figures 2.5b and 2.6b and is successful in reproducing the IC up to an observed accuracy. The two attempts of starting from $t = 1.25/(2\pi)$ and $t = 2/(2\pi)$ fail: the numerical error is

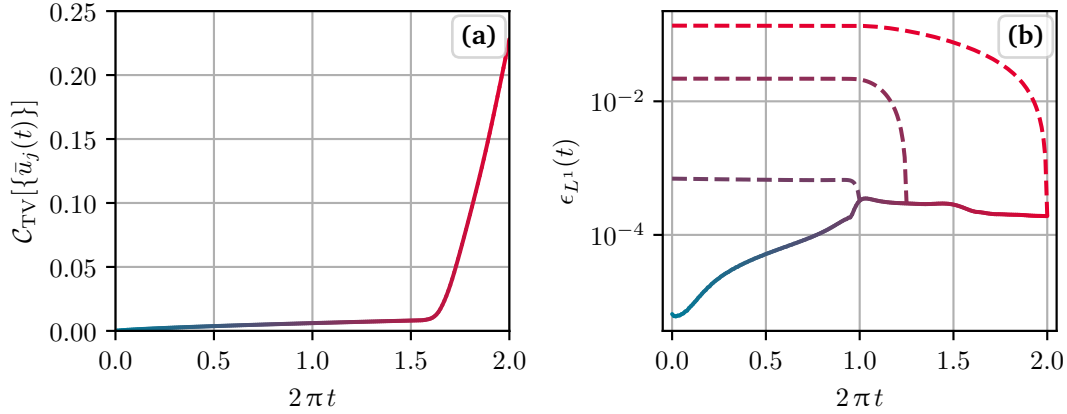


Figure 2.8.: Numerical entropy \mathcal{C}_{TV} for the BBE with IC (2.133) and periodic BC (2.128) at different times on the left (a) and related relative errors on the right (b). The solid line corresponds to forward time integration and the three dashed lines in the right figure (b) are errors of three attempts of backwards time integration starting from $t = 1/(2\pi)$, $t = 1.25/(2\pi)$, and $t = 2/(2\pi)$ respectively. The numerical solution has been computed with the KT scheme using $n = 101$ volume cells equidistantly spaced in the interval $x_0 = 0$ and $x_{100} = 1$, cf. section 2.1 of the auxiliary notebook [325].

significantly increased and even more severe since the qualitative features of the IC at $t = 0$ are not reproduced correctly.

We conclude the discussion of the BBE with remarks on the rate of convergence and errors, cf. table 2.3. The wall time for the $n = 1024$ computation in table 2.3 is still below two seconds, cf. table 2.2, even for this non-linear advection equation. Before the shock at $t = 0.5/(2\pi)$ we observe a rate of convergence of ~ 1.9 for ϵ_{L^1} and ~ 1.3 for ϵ_{L^∞} , which quantifies the largest deviation in the FV grid from the reference solution:

$$\epsilon_{L^\infty}(t) = \sup_j |\bar{u}_j(t) - u(t, x_j)|. \quad (2.135)$$

After the shock at $t = 1.5/(2\pi)$ we observe a reduced rate of convergence of ~ 1.1 for ϵ_{L^1} and no convergence in ϵ_{L^∞} , since there are always some outliers directly at the shock front. For a more refined discussion of errors and scaling post-shock-formation in this scenario we refer the interested reader to Refs. [167, 373].

2.2.4. Diffusion and the heat equation

Parts of this subsection include material from Sec. III.B and App. B of Ref. [9].

In this subsection we will discuss the diffusive contributions to Eq. (2.91), viz. the ones governed by the diffusive term $d_x Q_i[t, x, \{u_i(t, x)\}, \{\partial_x u_i(t, x)\}]$. Focusing on the latter, let us consider the non-linear system of equations

$$d_t u_i(t, x) = d_x Q_i[t, x, \{u_i(t, x)\}, \{\partial_x u_i(t, x)\}], \quad (2.136)$$

Table 2.3.: Relative errors in L^1 -norm ϵ_{L^1} using Eq. (2.127) and errors in L^∞ -norm ϵ_{L^∞} using Eq. (2.135) and corresponding convergence rates at $t = 0.5/(2\pi) < t_s$ and $t = 1.5/(2\pi) > t_s$ – before and after shock formation – between the constructed reference solution and the numerical solutions obtained with the KT scheme for the BBE (2.130) with IC (2.133) and periodic BC (2.128) in the interval $x_0 = 0$ and $x_n = 1$ with varying number n of equidistantly spaced volume cells, cf. subsection 2.2.3 of the auxiliary notebook [325].

n	$t = 0.5/(2\pi) < t_s$				$t = 2.0/(2\pi) > t_s$			
	ϵ_{L^1}	r	ϵ_{L^∞}	r	ϵ_{L^1}	r	ϵ_{L^∞}	r
32	$6.50 \cdot 10^{-3}$	-	$2.42 \cdot 10^{-2}$	-	$2.01 \cdot 10^{-2}$	-	$2.68 \cdot 10^{-1}$	-
64	$1.75 \cdot 10^{-3}$	1.89	$1.04 \cdot 10^{-2}$	1.22	$9.02 \cdot 10^{-3}$	1.16	$2.64 \cdot 10^{-1}$	+0.02
128	$4.59 \cdot 10^{-4}$	1.93	$4.21 \cdot 10^{-3}$	1.30	$4.32 \cdot 10^{-3}$	1.06	$2.68 \cdot 10^{-1}$	-0.02
256	$1.20 \cdot 10^{-4}$	1.93	$1.70 \cdot 10^{-3}$	1.31	$2.16 \cdot 10^{-3}$	1.00	$2.68 \cdot 10^{-1}$	-0.00
512	$3.23 \cdot 10^{-5}$	1.90	$6.88 \cdot 10^{-4}$	1.30	$1.07 \cdot 10^{-3}$	1.01	$2.68 \cdot 10^{-1}$	+0.00
1024	$8.46 \cdot 10^{-6}$	1.93	$2.79 \cdot 10^{-4}$	1.30	$3.91 \cdot 10^{-4}$	1.45	$1.96 \cdot 10^{-1}$	+0.46

which can be brought into primitive form

$$\partial_t u_i(t, x) - \frac{\partial Q_i[\dots]}{\partial(\partial_x u_l)} \partial_x^2 u_l(t, x) = \frac{\partial Q_i[\dots]}{\partial u_l} \partial_x u_l(t, x) + \partial_x Q_i[\dots]. \quad (2.137)$$

Eq. (2.137) includes the matrix of diffusion coefficients $\frac{\partial Q_i}{\partial(\partial_x u_l)}$ on the left-hand side (l.h.s.) in the actual diffusion term $\frac{\partial Q_i}{\partial(\partial_x u_l)} \partial_x^2 u_l$ and on the r.h.s. an advection term $\frac{\partial Q_i}{\partial u_l} \partial_x u_l$ and an internal source term $\partial_x Q_i$ related to the explicit u - and x -dependency of the diffusion flux Q . In this sense position dependency of the diffusion flux can be understood in terms of additional/internal source terms and dependency on the velocities u manifest as additional advective contributions. Depending on the application it might be advantageous to separate those out to integrate them properly in the (numerical) advection flux $F(H_{i,j+\frac{1}{2}})$. Eq. (2.137), or in our context the flux Q itself, is understood to be *parabolic*, if the matrix of diffusion coefficients satisfies the (weak) *parabolicity condition* $\frac{\partial Q_i}{\partial(\partial_x u_l)} \geq 0$ for all t, x , and $u_i(t, x)$ under consideration [167]. In the following we will usually refer to this constraint using the more descriptive term: *positivity of diffusion coefficient(s)*. The numerical KT diffusion flux (2.112) $P_{i,j+\frac{1}{2}}$ is applicable to such diffusion fluxes. Diffusive systems fulfilling the (weak) parabolicity condition typically have well posed IVPs, if suitable boundary conditions are supplied [167, 320, 374, 375]. Parabolic systems typically describe diffusive/dissipative processes which involve a smoothing of information through space-time with formally infinite propagation speeds²⁸ [319, 320, 324].

²⁸This infinite speed of information propagation can be studied with the fundamental solution (heat kernel) of the heat Eq. (2.138): a point-like heat source spreads out like a Gaussian function. This implies that, even after an infinitesimal time-step, the effect of the heat source is felt in the entire computational domain. Albeit only exponentially suppressed at large distances, this still formally constitutes a propagation of information at infinite speed. For details, see, e.g., Chap. 5 of Ref. [320] and Sec. 6.5 of Ref. [319] for a comment on this in the context of relativistic hydrodynamics.

Parabolic PDEs describe inherently irreversible processes from a CFD point of view: time reversal for a parabolic PDE amounts to forward time integration with a negative diffusion coefficient. Such a process of *reverse diffusion* – transport towards regions of higher concentration – amplifies existing gradients in $u(t, x)$ without any limit. In a practical numerical computation any discretization errors (to an extent present in all discretization schemes with a finite number of cells) get amplified throughout the computational domain and introduce rapidly growing spurious oscillations making time reversal practically impossible. This is again linked to the aforementioned concept of numerical entropy, which in parabolic systems grows as the arc length of solutions decreases. The latter can be intuitively linked to the dissipative nature of parabolic systems: gradients get smoothed out resulting in a reduction of arc length.

The heat equation

In the following we will limit our discussion to one archetypical parabolic diffusion equation, *viz.* the *heat equation* (HE) [376]

$$\partial_t u(t, x) = \partial_x^2 u(t, x) \quad (2.138)$$

in its mathematical form, see, *e.g.*, the textbooks [314, 315, 317] for additional details. In physics this equation can be used to study heat diffusion and goes back to Joseph J. B. Fourier's seminal work [376]: *Théorie analytique de la chaleur* on the topic from 1822. When using it in this context $u(t, x)$ would be a temperature distribution $T(t, x)$ and the r.h.s. of Eq. (2.138) would include a dimensionful, positive diffusion coefficient α , called the *thermal diffusivity* of the medium, *i.e.*, $\alpha = 111 \text{ mm}^2/\text{s}$ for copper at 25°C [377]. In order to define a well-posed IVP for the HE (2.138) it is imperative to specify BCs. In the following we will study the HE (2.138) with two different boundary conditions (2.139b) and (2.140b) while using the identical ICs (2.139a) and (2.140a).

Setting *Dirichlet* BCs by fixing the values of $u(t, x)$ on the boundaries of the computational domain ($x_{-1/2}$ and $x_{n-1/2}$) amounts to connecting the HE with a heath bath:

$$u_I(t = 0, x) = 1 + \frac{1}{2} \cos(\pi x), \quad (2.139a)$$

$$u_I(t, x_{-1/2}) = \frac{3}{2}, \quad u_I(t, x_{n-1/2}) = \frac{1}{2}, \quad (2.139b)$$

$$u_I(t, x) = \frac{3}{2} - x + \sum_{n=1}^{\infty} \frac{2 \sin(2n\pi x)}{(2n\pi) ((2n)^2 + 1)} e^{-(2n\pi)^2 t}, \quad (2.139c)$$

$$\Rightarrow u_{I,e}(x) \equiv \lim_{t \rightarrow \infty} u_I(t, x) = \frac{3}{2} - x. \quad (2.139c')$$

Choosing *Neumann* BCs by fixing the derivatives $\partial_x u(t, x)$ to zero on the boundaries of the computational domain amounts to isolating BC – preventing any in- or out-flow of heat into or out of the computational domain:

$$u_{II}(t = 0, x) \equiv u_I(t = 0, x) = 1 + \frac{1}{2} \cos(\pi x) \quad (2.140a)$$

$$\partial_x u_{II}(t, x)|_{x=x_{-1/2}} = \partial_x u_{II}(t, x)|_{x=x_{n-1/2}} = 0 \quad (2.140b)$$

$$u_{II}(t, x) = 1 + \frac{1}{2} \cos(\pi x) e^{-\pi^2 t} \quad (2.140c)$$

$$\Rightarrow u_{II,e}(x) \equiv \lim_{t \rightarrow \infty} u_{II}(t, x) = 1. \quad (2.140c')$$

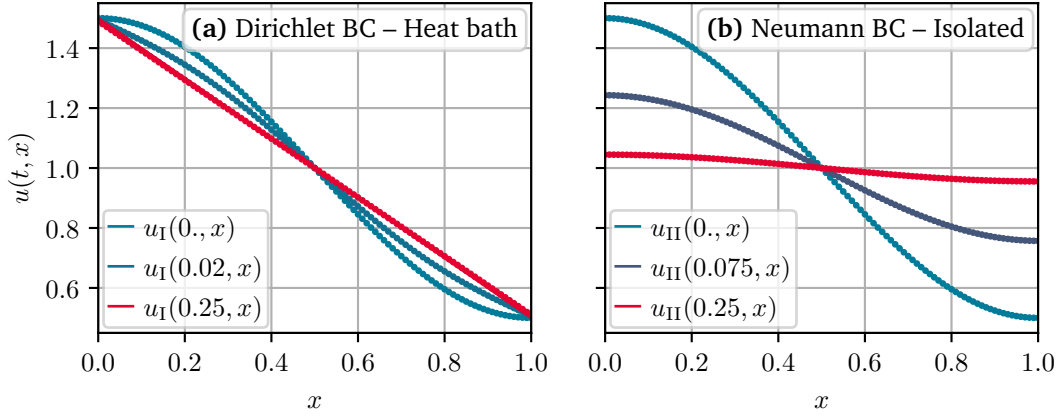


Figure 2.9.: Semi-analytical (solid lines) and numerical solution (dots) to the HE (2.138) with identical ICs (2.139a)/(2.140a), Dirichlet BC (2.139b) on the left (a), and Neumann BC (2.140b) on the right (b) at different times. The numerical solution has been computed with the KT scheme using $n = 101$ volume cells equidistantly spaced in the interval $x_0 = 0$ and $x_{100} = 1$, cf. section 2.3 of the auxiliary notebook [325].

The specific *Dirichlet* BCs (2.139b) are readily implemented in our FV scheme by choosing

$$\bar{u}_{-2} = \frac{3}{2}, \quad \bar{u}_{-1} = \frac{3}{2}, \quad \bar{u}_n = \frac{1}{2}, \quad \bar{u}_{n+1} = \frac{1}{2}, \quad (2.141)$$

for the ghost cells. While the *Neumann* BCs (2.140b) are realized by choosing

$$\bar{u}_{-2} = \bar{u}_0, \quad \bar{u}_{-1} = \bar{u}_0, \quad \bar{u}_n = \bar{u}_{n-1}, \quad \bar{u}_{n+1} = \bar{u}_{n-1}. \quad (2.142)$$

The semi-analytical/symbolic solutions (2.139c) and (2.140c) can be computed using a separation ansatz and employing a Fourier/heat kernel expansion [9, 376], see, e.g., Sec. 8.3 of Ref. [324]. Resulting flows for both problems are visualized in figure 2.9. Using the numerical diffusion flux (2.112) from subsection 2.2.2 we are able to reproduce the semi-analytical reference solutions (2.139c) and (2.140c). We can observe how the flows approach their respective equilibrium solutions (2.139c') and (2.140c'). Eq. (2.139c') describes a constant temperature gradient between the two heat baths left and right of the computation domain, while Eq. (2.140c') describes a constant temperature distribution which is solely determined by the heat/energy of the IC. Even though we study the same PDE with identical ICs $u_I(t = 0, x) = u_{II}(t = 0, x)$, we observe completely different behavior based on the two distinct BCs. This highlights the imperative importance of BC for convection and especially parabolic equations.

We conclude the discussion of the HE with remarks on the rate of convergence and errors, cf. table 2.4. The wall time for the $n = 1024$ computation in table 2.4 is almost six seconds, cf. table 2.2. Somewhat curiously we observe a convergence rate of basically 1, even though we are technically using a four-point stencil based on Eq. (2.112), cf. subsection 2.2.2, for which one would expect second-order accuracy. This highlights the fact that the practical rate of convergence is rather problem specific in numerical applications of the KT scheme.

Table 2.4.: Relative errors in L^1 -norm ϵ_{L^1} using Eq. (2.127) and errors in L^∞ -norm ϵ_{L^∞} using Eq. (2.135) and corresponding convergence rates at $t = 0.25$ between the semi-analytical solutions and the numerical solutions obtained with the KT scheme for the HE (2.138) with BCs (2.139b) and (2.140b) in the interval $x_0 = 0$ and $x_n = 1$ with varying number n of equidistantly spaced volume cells, cf. subsection 2.3.3 of the auxiliary notebook [325].

n	Dirichlet BC (2.139b) – Heat bath				Neumann BC (2.140b) – Isolating			
	ϵ_{L^1}	r	ϵ_{L^∞}	r	ϵ_{L^1}	r	ϵ_{L^∞}	r
32	$1.56 \cdot 10^{-2}$	-	$3.03 \cdot 10^{-2}$	-	$4.48 \cdot 10^{-3}$	-	$7.73 \cdot 10^{-3}$	-
64	$7.81 \cdot 10^{-3}$	1.00	$1.54 \cdot 10^{-2}$	0.98	$2.14 \cdot 10^{-3}$	1.06	$3.73 \cdot 10^{-3}$	1.05
128	$3.90 \cdot 10^{-3}$	1.00	$7.75 \cdot 10^{-3}$	0.99	$1.05 \cdot 10^{-3}$	1.03	$1.83 \cdot 10^{-3}$	1.03
256	$1.95 \cdot 10^{-3}$	1.00	$3.89 \cdot 10^{-3}$	0.99	$5.19 \cdot 10^{-4}$	1.02	$9.08 \cdot 10^{-4}$	1.01
512	$9.76 \cdot 10^{-4}$	1.00	$1.95 \cdot 10^{-3}$	1.00	$2.58 \cdot 10^{-4}$	1.01	$4.52 \cdot 10^{-4}$	1.01
1024	$4.88 \cdot 10^{-4}$	1.00	$9.76 \cdot 10^{-4}$	1.00	$1.29 \cdot 10^{-4}$	1.00	$2.26 \cdot 10^{-4}$	1.00

2.2.5. Sources and the heat equation

At this point we only want to comment briefly on the inclusion of explicit source terms. We will do so by including the explicit source term

$$S(x) = \sin(\pi x) \quad (2.143)$$

on the r.h.s. of the HE (2.138) and by studying the two examples introduced in the previous subsection 2.2.4. In the case of Dirichlet BC (2.139b) it is possible to construct a semi-analytic solution

$$u_{\text{IS}}(t, x) = \frac{3}{2} - x + \frac{1 - e^{-\pi^2 t}}{\pi^2} \sin(\pi x) + \sum_{n=1}^{\infty} \frac{2 \sin(2n\pi x)}{(n\pi) ((2n)^2 - 1)} e^{-(2n\pi)^2 t}, \quad (2.144a)$$

$$\Rightarrow u_{\text{IS,e}}(t, x) \equiv \lim_{t \rightarrow \infty} u_{\text{I}}(t, x) = \frac{3}{2} - x + \frac{1}{\pi^2} \sin(\pi x), \quad (2.144b)$$

by first computing an equilibrium solution $u_{\text{IS,e}}(t, x) \equiv \lim_{t \rightarrow \infty} u_{\text{IS}}(t, x)$ and then solving the homogeneous system with the established Fourier methods by considering perturbations around $u_{\text{IS,e}}(t, x)$, cf. section 2.4 of the auxiliary notebook [325]. For the isolating Neumann BC (2.140b) such a construction is not possible, since there is no equilibrium solution – the continuous heating in the isolated computational interval leads to a steady increase in $u(x, t)$. Results from the KT scheme with the source term (2.143) naively discretized in the volume cells by its midpoint value, cf. subsection 2.2.2, are shown in figure 2.10. Figure 2.10a also includes the semi-analytical solution (2.144a), which we are able to reproduce with our numerical scheme. For large times the equilibrium solution (2.144b) is approached in figure 2.10a, while figure 2.10b displays a continuously rising but flattening temperature distribution.

A detailed discussion of sinks and sources in the context of our research can be found in subsection 4.2.2.

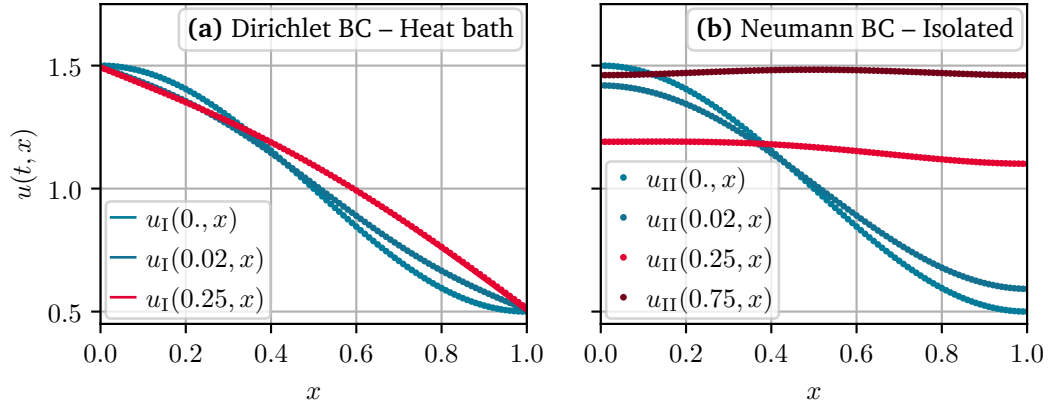


Figure 2.10.: Solutions to the HE (2.138) with ICs (2.139a),(2.140a), Dirichlet BC (2.139b) on the left (a), and Neumann BC (2.140b) on the right (b) at different times including the source (2.143). The numerical solution has been computed with the KT scheme using $n = 101$ volume cells equidistantly spaced in the interval $x_0 = 0$ and $x_{100} = 1$, cf. section 2.4 of the auxiliary notebook [325].

2.2.6. Euler equations – the KT scheme showing its MUSCLes

To conclude our discussion of CFD and the KT scheme we want to present one more involved example of advection equations, viz. the system of *Euler equations* [378]

$$\partial_t \begin{pmatrix} \rho(t, x) \\ \mu(t, x) \\ \epsilon(t, x) \end{pmatrix} + \partial_x \begin{pmatrix} \mu(t, x) \\ p(t, x) + \rho(t, x)v(t, x)^2 \\ v(t, x)(p(t, x) + \epsilon(t, x)) \end{pmatrix} = \begin{pmatrix} 0 \\ 0 \\ 0 \end{pmatrix}, \quad (2.145)$$

including the derived quantities pressure $p = (\gamma - 1)(\epsilon - \frac{\rho}{2}v^2) = \rho R_s T$ and velocity $v = \mu/\rho$. The vector of conserved quantities $\vec{u} = (\rho, \mu, \epsilon)^\top$ includes the mass density ρ , the momentum density μ , and the energy density ϵ . The Euler Eqs. (2.145) describe the advective evolution of an inviscid, compressible, adiabatic, i.e., ideal, fluid in one spatial x and one temporal t dimension. They are based on the conservation of mass, momentum, and energy and are frequently used in CFD to construct challenging benchmark problems for numerical schemes.

One established problem is the so-called *Sod shock tube problem* [380] which is a specific Riemann problem for the Euler Eqs. (2.145): an as one-dimensional idealized tube is considered with two constant states \vec{u}_L and \vec{u}_R , separated at initial time $t_0 = 0$ by an diaphragm/burst-disc. At the begin of the computation at $t = 0_+$ this diaphragm is considered to be instantaneously removed and a pure Riemann problem is simulated. The computational domain (time) typically under consideration is large (short) enough such that explicit boundary conditions are not required, since the dynamics do not reach the spatial computational boundary. Following EXAMPLE 5 of Sec. 6.3 of Ref. [167], we will consider a computational domain stretching from

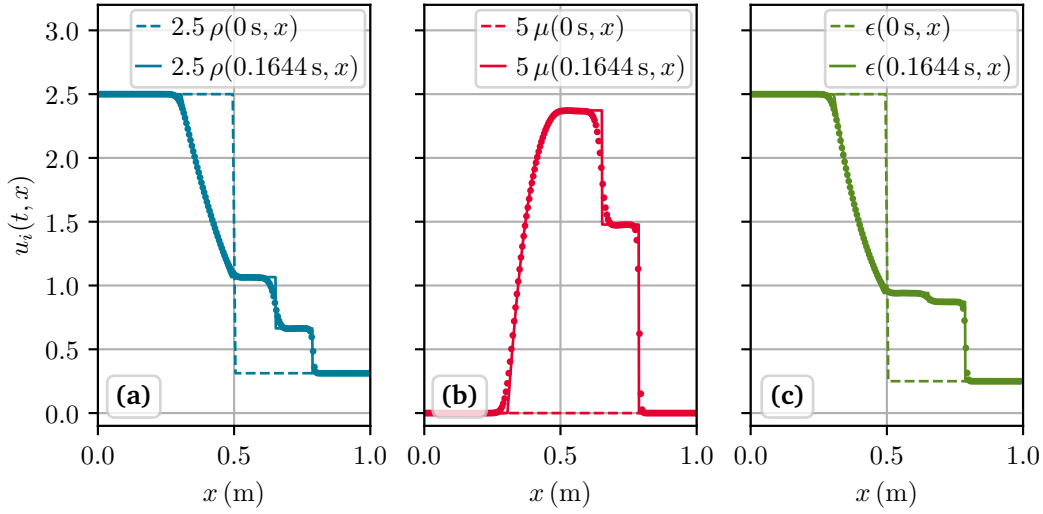


Figure 2.11.: Semi-analytical (solid lines) and numerical solutions (dots) of the Sod shock tube problem (2.146) for the Euler Eqs. (2.145), with density on the left (a), momentum density in the middle (b), and energy density on the right (c) at $t = 0.1644$ s with the initial condition at $t = 0$ as reference (dashed lines). The semi-analytical solution has been obtained using an exact Riemann-Solver [326, 379]. The numerical solution has been computed with the KT scheme using $n = 201$ volume cells equidistantly spaced in the interval $x_0 = 0$ and $x_{200} = 1$ m, cf. subsection 2.5.2 of the auxiliary notebook [325].

$x_0 = 0$ to $x_{n-1} = 1$ m up to a time of $t = 0.1644$ s with the two constant initial states

$$\vec{u}_L = \begin{pmatrix} 1.0 \text{ kgm}^{-3} \\ 0 \text{ kgms}^{-1} \\ 2.5 \text{ Jm}^{-3} \end{pmatrix}, \quad \vec{u}_R = \begin{pmatrix} 0.125 \text{ kgm}^{-3} \\ 0 \text{ kgms}^{-1} \\ 0.25 \text{ Jm}^{-3} \end{pmatrix}, \quad (2.146)$$

separated at $x = 0.5$ m and assuming an adiabatic index of $\gamma = 1.4$. A numerical solution obtained with the KT scheme and the semi-analytical solution obtained using an exact Riemann-Solver [326, 379] is shown in figure 2.11. We observe a shock wave traveling into the dilute right half of the tube, which is followed by a contact discontinuity. A rarefaction fan is spreading into the denser left half of the tube. We observe that the KT scheme is able to reproduce this complicated dynamic with several extreme discontinuities perfectly (to given accuracy based on the employed spatial discretization, *i.e.*, number of volume cells) without any spurious oscillations or under/over shooting around the discontinuities.

To illustrate the dynamic inside such a shock tube further we adapt a Sod shock tube problem, in parts motivated by Ref. [381], to study a more realistic scenario. We consider a tube of 20 meters, filled with dry air (adiabatic index $\gamma = 1.4$ and specific gas constant

$R_s = 0.287 \cdot 10^3 \text{ Jkg}^{-1}\text{K}^{-1}$ [382]), and the two constant states

$$\vec{u}_L = \begin{pmatrix} 1.177 \text{ kgm}^{-3} \\ 0 \text{ kgms}^{-1} \\ 2.533 \cdot 10^5 \text{ Jm}^{-3} \end{pmatrix}, \quad \vec{u}_R = 0.1\vec{u}_L = \begin{pmatrix} 1.177 \cdot 10^{-1} \text{ kgm}^{-3} \\ 0 \text{ kgms}^{-1} \\ 2.533 \cdot 10^4 \text{ Jm}^{-3} \end{pmatrix}, \quad (2.147)$$

separated at $x = 10 \text{ m}$. The IC (2.147) is constructed to have a pressure of one standard atmosphere $p_L = 101,325 \text{ Pa} = 1 \text{ atm}$ at room temperature of $T_L = 299.852 \text{ K}$ in the left half of the tube. The pressure in the right half of the tube is decreased by 90% to $p_R = 0.1p_L = 0.1 \text{ atm}$ while the temperature is still $T_R = T_L = 299.852 \text{ K}$. This amounts to an adiabatic speed of sound of $c_s \simeq 347 \text{ ms}^{-1}$ in both halves. Overall we are considering a system which has units and magnitudes which we are accustomed to in our day-to-day life – far away from the extremes of high-energy physics with temperatures in excess of 10^{10} K and densities well above 10^{17} kgm^{-3} . We now want to study the time evolution with this IC from $t = 0$ up to $t = 60 \text{ ms}$ assuming reflective boundary conditions at the edges of the computational interval $x_{-\frac{1}{2}} = -0.025 \text{ m}$ and $x_{n-\frac{1}{2}} = 20.025 \text{ m}$, which for the Euler Eqs. (2.145) can be implemented by choosing

$$\bar{u}_{i,-2} = c_i \bar{u}_{i,1}, \quad \bar{u}_{i,-1} = c_i \bar{u}_{i,0}, \quad \bar{u}_{i,n} = c_i \bar{u}_{i,n-1}, \quad \bar{u}_{i,n+1} = c_i \bar{u}_{i,n-2}, \quad (2.148)$$

for the ghost cells with $c_i = 1$ for $i = 1$ and $i = 3$ (ρ and ϵ) and $c_i = -1$ for $i = 2$ (μ) [383].

We visualize the solution of this *physical shock tube problem* in figure 2.12 as a set of six density plots (including contour lines). We plot only two primitive, conserved quantities: ρ and ϵ in figures 2.12a and 2.12f and four derived quantities. Note that the momentum density – the missing primitive, conserved quantity – is simply given by the product of density and velocity $\mu = \rho v$, the latter is plotted in figure 2.12c. Pressure and temperature in figures 2.12b and 2.12d follow from the ideal gas law $p = (\gamma - 1)(\epsilon - \frac{\rho}{2}v^2) = \rho R_s T$, while the (adiabatic) speed of sound in figure 2.12e follows from $c_s^2 = (\partial p / \partial \rho)_s = \gamma p / \rho = \gamma R_s T$. At the beginning of time evolution we recognize the dynamics of the Sod shock tube problem: a rarefaction fan travels to the left while a contact discontinuity and a shock wave travel to the right. Here the left edge of the rarefaction fan travels into the denser left half with a velocity of $v_{rl} \simeq -347 \text{ ms}^{-1}$ at the speed of sound. The right edge of the rarefaction fan travels at only $v_{rr} \simeq -5 \text{ ms}^{-1}$. The contact discontinuity is driven into the dilute right half with a substantial subsonic velocity of $v_{cd} \simeq 285 \text{ ms}^{-1}$ while velocity and pressure stay constant across it. The shock travels at a supersonic velocity of $v_s \simeq 558 \text{ ms}^{-1}$ towards the right wall. The dilution, i.e., adiabatic expansion of the gas, due to the rarefaction fan, cools the left half. The gas in the region between the contact discontinuity and the shock front gets compressed and heated by the shock. The latter hits the right wall at $t \simeq 17.9 \text{ ms}$ and the rarefaction fan hits the left wall at $t \simeq 28.8 \text{ ms}$. They both get reflected leading to a complicated interaction between the shock and the contact discontinuity at $t \simeq 25.9 \text{ ms}$ and an interaction within the rarefaction fan at $t \gtrsim 28.8 \text{ ms}$. The computation with the KT scheme using $n = 401$ volume cells, hence solving a method-of-lines ODE system of $401 \times 3 = 1203$ equations, takes 24 seconds on a single thread of an Intel® Core™ i7-8750H processor using our latest MATHEMATICA code [325].

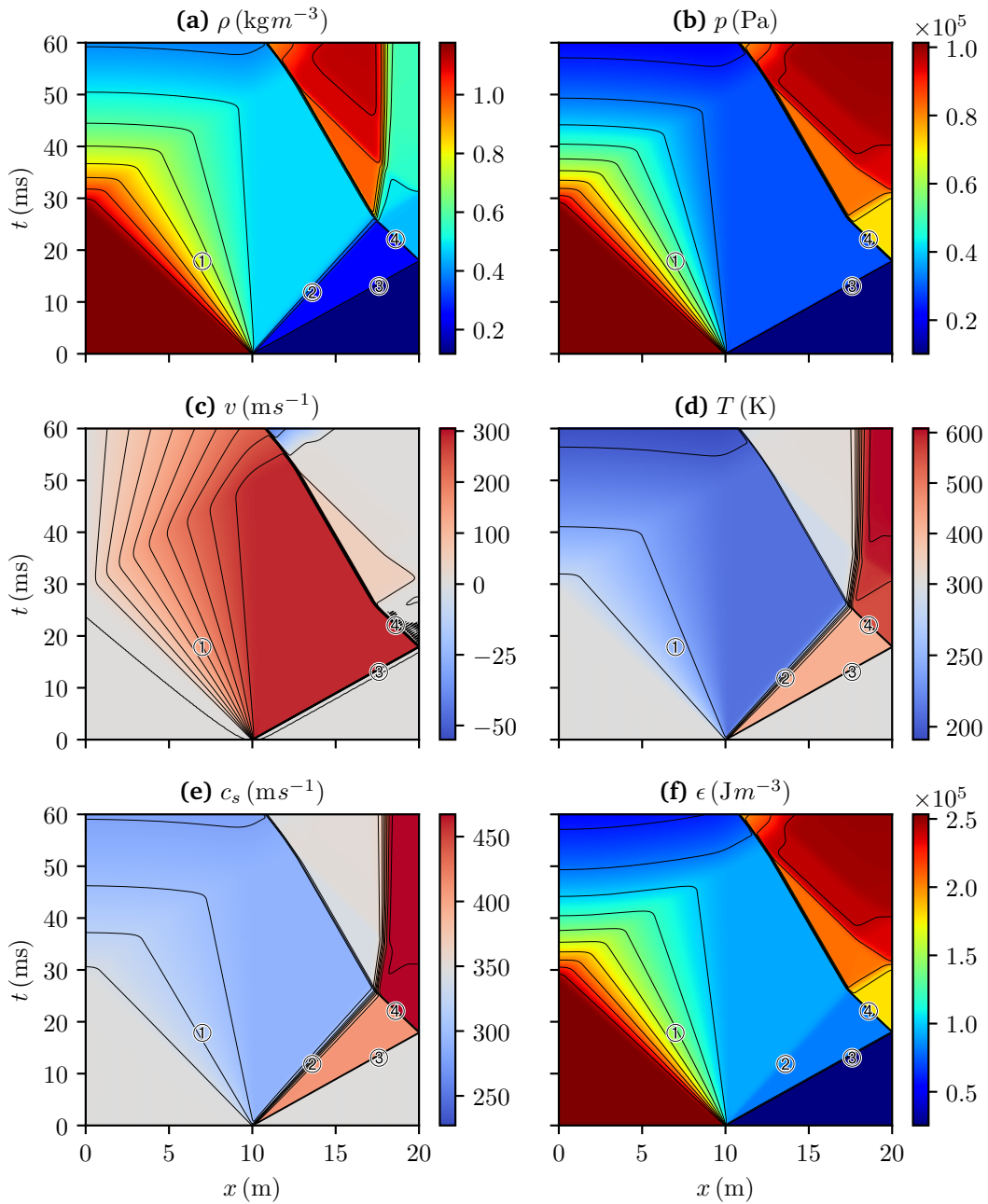


Figure 2.12.: Numerical solution of the physical shock tube problem (2.147) for the Euler Eqs. (2.145) with reflective BCs (2.148) from $t = 0$ to $t = 60$ ms. For plotting the density ρ in (a), the pressure p in (b), and the energy density ϵ in (f) we use the canonical 'jet' color map [56]. For plotting the velocity v in (c), the temperature T in (d), and the speed of sound c_s in (e) we use the 'coolwarm' color map [56] diverging non-linearly around the respective initial values. The rarefaction fan is marked with ①, the contact discontinuity with ②, the shock wave with ③, and the reflected shock wave with ④. The numerical solution has been computed with the KT scheme using $n = 401$ volume cells equidistantly spaced in the interval $x_0 = 0$ and $x_{400} = 20$ m, cf. subsection 2.5.3 of the auxiliary notebook [325].

Navier-Stokes equations and gravity

The Euler Eqs. (2.145) can be extended to include the effects of gravity by adding a simple source term, see, e.g., Refs. [384–387]. A further extension to include viscous effects by means of a diffusion term incorporating the effects of thermal conductivity and bulk viscosity²⁹ leads to a generalization of the Euler Eqs. (2.145) to the one-dimensional *Navier-Stokes equations*, see, e.g., Refs. [388–390], which in a constant gravitational field read

$$\partial_t \begin{pmatrix} \rho \\ \mu \\ \epsilon \end{pmatrix} + \partial_x \begin{pmatrix} \mu \\ p + \rho v^2 \\ v(p + \epsilon) \end{pmatrix} = \partial_x \begin{pmatrix} 0 \\ \lambda \partial_x v \\ \lambda v \partial_x v + \kappa \partial_x T \end{pmatrix} + \begin{pmatrix} 0 \\ -g\rho \\ -g\mu \end{pmatrix}, \quad (2.149)$$

including the gravitational acceleration g , bulk viscosity coefficient λ , and thermal conductivity coefficient κ . Eq. (2.149) is a system of non-linear advection-diffusion-source equations and in this sense similar to the differential equations discussed in the main part of this thesis, cf. chapters 3 and 4. While the Navier-Stokes equations (of course including the practically relevant applications in three dimension) are numerically well under control in the field of CFD, there are still open mathematical questions regarding their structure and solutions – notably the unsolved *Navier–Stokes existence and smoothness problem* [391] stated as one of the seven *Millennium Prize Problems*. This is the second, cf. chapter 1, time we reference one of these problems. Explicit additional numerical computations with the KT scheme and Euler/Navier-Stokes equations with and without gravitational sources can be found at the end of the auxiliary notebook [325]. We will not discuss these here, apart from the note, that the shock tube problems of this subsection are completely advection dominated: the relatively low bulk viscosity $\lambda = 1.846 \cdot 10^{-5} \text{kgm}^{-1} \text{s}^{-1}$ and thermal conductivity $\kappa = 2.624 \cdot 10^{-2} \text{Jm}^{-1} \text{s}^{-1} \text{K}^{-1}$ of air [382] lead to diffusive contributions which are several orders of magnitude smaller than the advective ones.

2.3. Quantum chromodynamics and low-energy effective theories

At his point we want to give a brief overview and introduction into quantum chromodynamics (QCD) as the established fundamental, microscopic theory of the strong interaction. The purpose of this introduction is to facilitate the introduction of the quark-meson (QM) model as a natural LEFT of QCD, in subsection 2.3.3. In this work we are mainly focused on chiral symmetry and its spontaneous breaking and subsequent restoration at non-zero temperature and quark chemical potential by quantum and thermodynamic fluctuations.

A complete and self-contained introduction to QCD in general and in the context of FRG is far beyond the scope of this work. For a more detailed discussion, we refer to, e.g., the textbooks [177, 392–395] and Refs. [80, 97, 109, 209, 222, 226, 227, 230, 231, 237, 308, 396–398] in the context of FRG.

This section has a corresponding digital auxiliary file [399], which includes some computations and plots for the PCAC relation (2.168) and the running coupling in Eq. (2.160) of

²⁹In this context also referred to as *dynamic* or *absolute* viscosity.

Table 2.5.: Properties and quantum numbers of the quarks and gluons of QCD, see, *e.g.*, Chap. 15. *Quark Model* of Ref. [36] for additional details. The values for the masses M with their experimental uncertainties are from Ref. [36]. Details regarding the definition and potential renormalization (mass-independent subtraction scheme, *viz.* $\overline{\text{MS}}$) of the different masses are included in Ref. [36]. The listed quantum numbers are spin S , baryon number B , electric charge Q in units of the elementary charge e , the third-/ z -component of the isospin I_3 , and $I(J^P)$ – isospin I , total angular momentum J (here for elementary particles equal to their spin: $J = S$), and conventional, intrinsic parity P . The quarks have corresponding anti-quarks with identical masses and spins but otherwise quantum numbers of opposite sign and they carry anti-colors in $\bar{\mathbf{3}}$. The gluons are considered to be massless in QCD but experimentally “A mass as large as a few MeV may not be precluded” [36, 400].

Name	Symbol	M (MeV/ c^2)	S	B	Q (e)	I_3	$I(J^P)$	colors in
up	u	$2.16^{+0.49}_{-0.26}$	$\frac{1}{2}$	$\frac{1}{3}$	$+\frac{2}{3}$	$+\frac{1}{2}$	$\frac{1}{2}(\frac{1}{2}^+)$	3
down	d	$4.67^{+0.48}_{-0.17}$	$\frac{1}{2}$	$\frac{1}{3}$	$-\frac{1}{3}$	$-\frac{1}{2}$	$\frac{1}{2}(\frac{1}{2}^+)$	3
strange	s	$93.4^{+8.6}_{-3.4}$	$\frac{1}{2}$	$\frac{1}{3}$	$-\frac{1}{3}$	0	$0(\frac{1}{2}^+)$	3
charm	c	1270^{+20}_{-20}	$\frac{1}{2}$	$\frac{1}{3}$	$+\frac{2}{3}$	0	$0(\frac{1}{2}^+)$	3
bottom	b	4180^{+30}_{-20}	$\frac{1}{2}$	$\frac{1}{3}$	$-\frac{1}{3}$	0	$0(\frac{1}{2}^+)$	3
top	t	$172,690^{+300}_{-300}$	$\frac{1}{2}$	$\frac{1}{3}$	$+\frac{2}{3}$	0	$0(\frac{1}{2}^+)$	3
gluon	g	0	1	0	0	0	$0(1^-)$	8

subsection 2.3.2. Furthermore it includes the diagrammatic expressions (2.172'), (2.174), and (2.178) of subsection 2.3.3, making use of the functionalities of our MATHEMATICA code [299].

2.3.1. Quantum chromodynamics

QCD is a non-Abelian gauge theory of massive, spin- $\frac{1}{2}$ fermions called quarks, which exist in $N_f = 6$ distinct flavors – up, down, strange, charm, bottom, and top – and each flavor can come in one of $N_c = 3$ colors – referred to as red, green, and blue in loose analogy to the colors perceived by humans. In QCD, the gauge group $SU(N_c) = SU(3)$ is obtained by promoting the color charge to a local symmetry. The massless, spin-1 gauge bosons of QCD are called gluons and mediate the strong interaction of quarks as color charged quanta of the gauge field. A major difference between QCD, as a non-Abelian $SU(3)$ gauge theory, and an Abelian gauge theory, like quantum electrodynamics (QED), which has an $U(1)$ gauge symmetry, is that gluons in QCD carry color charge. This allows them to interact not only with quarks but also among themselves, in stark contrast to photons in QED, which carry no electric charge and hence cannot self-interact. Masses and quantum numbers for quarks and gluons can be found in table 2.5 and will be explained further in the following.

Quarks, gluons, six flavors, and three colors

Historically quarks as elementary particles were first introduced as part of the *quark model* devised by Murray Gell-Mann [12] and George Zweig [13, 14], see, e.g., Chap. 15. *Quark Model* of Ref. [36] for additional details, to explain the large number of diverse hadrons being discovered in maturing collider experiments in the 1950s and continuing through the 1960s. The preceding organization scheme – the “*Eightfold Way*” – to classify hadrons by Murray Gell-Mann [10] and Yuval Ne’eman [11] follows naturally from the quark model. The original quark model introduces a $SU(3)$ flavor symmetry by postulating that hadrons are composed of three types – flavors – of quarks: up, down, and strange. Mesons are understood as quark-anti-quark bound states by coupling quarks in the fundamental representation $\mathbf{3}$ of flavor $SU(3)$ with anti-quarks in the complex conjugate representation $\bar{\mathbf{3}}$ to form a nonet of meson. The latter can be decomposed into a singlet in trivial representation $\mathbf{1}$ and an octet in adjoint representation $\mathbf{8}$, i.e., $\mathbf{3} \otimes \bar{\mathbf{3}} = \mathbf{8} \oplus \mathbf{1}$. Baryons are understood as bound states of three quarks.

In the early days of the quark model it was soon realized, first by Oscar W. Greenberg [18], that the construction of the antisymmetric wave function required by the Pauli exclusion principle/spin-statistic theorem [401–403] was problematic for certain baryons, like the spin $S = \frac{3}{2}$ baryon Δ^{++} . Nine months later, Moo-Young Han and Yoichiro Nambu suggested the existence of a hidden degree of freedom [19], which they originally called $SU(3)'$ – from a modern point of view the concept of three colors was born. It took a few years until 1972 when William Bardeen, Harald Fritzsch, and Murray Gell-Mann [20] established color as the charge of the strong force, which completely commutes with all other charges. At this point it was possible to understand and construct the antisymmetric wave function of baryons as fully antisymmetric in color and symmetric in the combination of flavor, spin, and space, allowing for a decomposition in flavor as $\mathbf{3} \otimes \mathbf{3} \otimes \mathbf{3} = \mathbf{10}_S \oplus \mathbf{8}_M \oplus \mathbf{8}_M \oplus \mathbf{1}_A$. This allows for a classification of spin- $\frac{3}{2}$ baryons (like, e.g., Delta resonances $\Delta^{++}, \dots, \Delta^-$) in the flavor symmetric decuplet $\mathbf{10}_S$. Light spin- $\frac{1}{2}$ baryons (most notably protons and neutrons) and heavy spin- $\frac{1}{2}$ baryons (excited states or resonances, like, e.g., the Roper resonance $N(1440)1/2^+$) are mixtures of both octets $\mathbf{8}_M$ with mixed flavour symmetry.

Those developments were driven and in some cases verified by a multitude of high-energy particle physics experiments, see, e.g., Ref. [35] for a review of deep inelastic scattering experiments and Refs. [30–34] for information on three-jet events, which in conjunction with aforementioned theoretical advances established the up, down, and strange quark as fundamental particles and the gluon as mediator of the strong force. Recent experimental data [36] put the masses of the three “light” flavors up, down, and strange at $m_u \approx 2$ MeV, $m_d \approx 5$ MeV, and $m_s \approx 93$ MeV, cf. table 2.5.

Today the quark model and QCD also include the three heavy quark flavors. The charm quark ($m_c \approx 1.27$ GeV [36]) was theorized by James Bjorken and Sheldon Glashow [15] (1964) and Sheldon Glashow, John Iliopoulos, and Luciano Maiani [16] (1970) and experimentally discovered with the J/ψ meson by Samuel Ting *et al.* [25] (1974) at BNL and Burton Richter *et al.* [26] (1974) at SLAC. The third generation of bottom ($m_b \approx 4.18$ GeV [36]) and top ($m_t \approx 172.69$ GeV [36]) heavy quark flavors was theorized by Makoto Kobayashi and Toshihide Maskawa [17] (1973). The bottom quark was experimentally discovered by Leon M. Lederman

et al. [27] (1977) at Fermilab and the top quark was experimentally discovered by the CDF [28] and DØ [29] collaborations (1995). Quantum numbers for the heavy quarks are listed in table 2.5.

The classical action of QCD

QCD as a QFT, as we would recognize it today, was developed by Harald Fritzsch, Heinrich Leutwyler, and Murray Gell-Mann [21] in 1973 using the gauge theory developed by Chen Ning Yang and Robert Mills [47] (1954) – the special case of a $SU(3)$ Yang–Mills (YM) theory, see also Ref. [404]. In the following we want to give a brief overview of QCD as a QFT.

The classical action of QCD in Euclidean space-time is given by

$$S_{\text{QCD}}^0[\tilde{A}, \tilde{\psi}, \tilde{\bar{\psi}}] \equiv \int_x \left(\frac{1}{4} F_{\mu\nu}^a F_{\mu\nu}^a + \tilde{\bar{\psi}}(\gamma_\mu D_\mu + \hat{m} - \gamma_4 \hat{\mu}) \tilde{\psi} \right), \quad (2.150)$$

using the conventions and compact notations of App. B. In the following we will use $\tilde{\psi}(x) \equiv q(x)$ and $\tilde{\bar{\psi}}(x) \equiv \bar{q}(x)$ to denote the fundamental quark fields and $\tilde{A}(x)$ for the gauge fields. Equation (2.150) includes the mass matrix \hat{m} and the matrix of $\hat{\mu}$, which allow for different quark masses m_f and chemical potentials μ_f for each flavor. By construction the action (2.150) is invariant under local $SU(N_c) = SU(3)$ gauge transformations $\mathcal{U}(x) \in SU(N_c)$ with

$$\mathcal{U}(x) = \exp(i\theta_a(x)T^a), \quad (2.151)$$

with the $N_c^2 - 1 = 8$ generators of the Lie group $SU(N_c) = SU(3)$ in fundamental representation, cf. App. B.3.

Quark (anti-quark) fields are in the (conjugate) fundamental representation of the gauge group and thus transform as

$$\tilde{\psi}(x) \mapsto \mathcal{U}(x)\tilde{\psi}(x), \quad (2.152a)$$

$$\tilde{\bar{\psi}}(x) \mapsto \tilde{\bar{\psi}}(x)\mathcal{U}^\dagger(x). \quad (2.152b)$$

The quarks are minimally coupled to the gluons, which are elements of the Lie algebra $\mathfrak{su}(N_c)$ of $SU(N_c)$, by introducing the covariant derivative

$$D_\mu(x) = \partial_\mu - ig\tilde{A}_\mu(x), \quad (2.153)$$

with the dimensionless gauge coupling g .

Gluons $\tilde{A}_\mu(x) \equiv \tilde{A}_\mu^a(x)\tilde{T}^a$ are in the adjoint representation of the gauge group and thus transform as

$$\tilde{A}_\mu(x) \mapsto \mathcal{U}(x)\tilde{A}_\mu(x)\mathcal{U}^\dagger(x) + \frac{i}{g}\mathcal{U}(x)(\partial_\mu\mathcal{U}^\dagger(x)), \quad (2.154)$$

where the last term is crucial to maintain gauge invariance of the kinetic term of the quarks.

The field strength tensor $F_{\mu\nu}^a$ of Eq. (2.150) is given by and transforms as

$$F_{\mu\nu}^a(x) = \partial_\mu\tilde{A}_\nu^a(x) - \partial_\nu\tilde{A}_\mu^a(x) + gf^{abc}\tilde{A}_\mu^b(x)\tilde{A}_\nu^c(x), \quad (2.155a)$$

$$F_{\mu\nu}^a(x) \mapsto \mathcal{U}(x)F_{\mu\nu}^a(x)\mathcal{U}^\dagger(x). \quad (2.155b)$$

Quantization, gauge fixing, and gauge invariance

In the spirit of section 2.1 we would now like to quantize the classical action (2.150) using the functional integral, *i.e.*, the partition function (2.4). Naively one would be tempted to make use of the FS formalism and treat gauge fields as ordinary scalar fields. This leads to two problems. The first one is that the regulators employed in the FRG break gauge invariance by construction, since they enter as momentum-dependent mass terms, *cf.* Eq. (2.7) and subsection 2.1.4.1. This issue is not inherent to the FRG: the underlying idea of Wilson’s RG approach is not gauge invariant. Naively integrating out fluctuations momentum shell by momentum shell breaks gauge invariance. The second, arguably even more pressing issue is, that it is impossible to compute the propagator, *cf.* Eq. (2.27), for the gauge field $G_{k;AA}$, because the inversion of the Γ_k^{AA} – on a classical level/in the UV of $S_{\text{QCD}}^{0,AA}$ – is not possible due to the transverse nature of the gluon two-point function. This again is not inherent to the FRG: this problem is a general problem in the quantization of gauge theories using a functional integral.

The underlying technical issue is, that the functional integral includes contributions from an infinite number of degenerate configurations due to the gauge invariance. It is necessary to remove those redundant gauge configurations – called gauge orbits – to ensure a well-defined integration over the gauge field space. This is usually realized by fixing a gauge to limit the functional integral to physically differing gauge field configuration by means of the *Faddeev-Popov* method, developed by Ludvig Faddeev and Victor Popov [405] (1967) in their study of YM theories. Details regarding this procedure can be found in textbooks, *e.g.*, Refs. [177, 392–395], and in the context of FRG in, *e.g.*, Refs. [97, 222, 226, 227, 230, 231, 237, 396, 398] and we do not want to go into further detail here, but rather present a resulting gauge-fixed action for QCD. In covariant Lorenz gauge $\partial_\mu \tilde{A}_\mu = 0$ the gauge fixed action for QCD, including scalar, Grassmann-valued Faddeev–Popov ghosts \tilde{c} and $\tilde{\bar{c}}$, is given by

$$S_{\text{QCD}}[\tilde{A}, \tilde{c}, \tilde{\bar{c}}, \tilde{\psi}, \tilde{\bar{\psi}}] \equiv \int_x \left(\frac{1}{4} F_{\mu\nu}^a F_{\mu\nu}^a + \tilde{\bar{\psi}} (\gamma_\mu D_\mu + \hat{m} - \gamma_4 \hat{\mu}) \tilde{\psi} + \tilde{\bar{c}}^a (\partial_\mu D_\mu^{ab}) \tilde{c}^b + \frac{1}{2\xi} (\partial_\mu \tilde{A}_\mu^a) (\partial_\mu \tilde{A}_\mu^a) \right), \quad (2.156)$$

with

$$\partial_\mu D_\mu^{ab} = \partial_\mu \partial_\mu \delta^{ab} - ig f^{abc} \partial_\mu \tilde{A}_\mu^c, \quad (2.157)$$

and where the gauge fixing term $\frac{1}{2\xi} (\partial_\mu \tilde{A}_\mu^a)^2$ can be used to realize different variants of covariant Lorenz gauge, *e.g.*, Landau gauge ($\xi = 0$) or Feynman gauge ($\xi = 1$). The ghost (anti-ghost) fields are introduced during gauge fixing and are transforming under the adjoint representation of $SU(3)$ as

$$\tilde{c}^a(x) \mapsto \mathcal{U}^{ab}(x) \tilde{c}^b(x), \quad (2.158a)$$

$$\tilde{\bar{c}}^a(x) \mapsto \tilde{\bar{c}}^b(x) (\mathcal{U}^\dagger)^{ba}(x), \quad (2.158b)$$

under gauge transformations $\mathcal{U}^{ab}(x) = (\exp(i\theta_c(x) \tilde{T}^c))^{ab}$. The gauge fixed action (2.156) and its field content is suited for studies using the perturbative RG and the non-perturbative FRG.

We will discuss results and application of both in the following subsections 2.3.2 and 2.3.3, but before that we have to comment on the issue of gauge invariance.

Ensuring gauge invariance, at the very least in the IR, is crucial in order to obtain meaningful results for observables in QCD. In the context of the FRG, the topic is exceptionally complicated, yet equally important. Since we will not perform computations within QCD itself, a detailed discussion of the topic is beyond the scope of this work. We will only introduce the relevant jargon and provide some exemplary references suited as sources for further relevant material.

The Becchi-Rouet-Stora-Tyutin (BRST) formalism can be used to extend the classical notion of gauge invariance to the quantum level. BRST symmetry transformations combine gauge transformations with transformations involving ghost fields leading to the notion of BRST invariance as a quantum analog to classical gauge invariance. Slavnov-Taylor identities (STIs) carry the information of BRST symmetry transformations on an infinitesimal level. They can be seen as generalization of Ward-Takahashi identities, *e.g.*, known from QED, and they are crucial for ensuring the consistency/gauge invariance after renormalization. In the FRG approach, the Slavnov-Taylor identities are modified (mSTI) to account for the scale-dependent terms introduced by the FRG procedure. For details we refer to Sec. VII.B of Ref. [222] and Sec. 5.2.1 of the review [231]. Alternative approaches to ensure gauge invariance with gauge-invariant flows in the background field formalism or using geometrical effective actions are discussed in Secs. VII.C.1 and 2 of Ref. [222] and Sec. 5.2.3 of the review [231].

2.3.2. Asymptotic freedom, confinement, and chiral symmetry (breaking)

The gauge fixed action S_{QCD} of Eq. (2.156) is suitable for direct computations and the first theoretical result we want to discuss the now seminal perturbative computation [66, 67] of the running coupling of QCD for which David J. Gross, H. David Politzer and Frank Wilczek were awarded the *Nobel Prize in Physics* in 2004.

Asymptotic freedom

Using the Callan-Symanzik equations [252, 254, 255] and perturbation theory to one-loop order, Gross, Politzer, and Wilczek computed the running coupling of QCD – *i.e.*, the change of the strong coupling g with RG scale μ and momentum transfer Q for massless quarks:

$$\frac{\partial g}{\partial \ln(Q/\mu)} \equiv \beta(g) = -\frac{g^3}{(4\pi)^2} \left(\frac{11}{3} N_c - \frac{2}{3} N_f \right). \quad (2.159)$$

Details regarding this computation can be found in the original publications [66, 67], the textbooks [177, 392–395] and the review [406]. The first term in Eq. (2.159) proportional to N_c is due to gluons, while the second term is associated with the quarks. Neglecting the first term for a moment, the beta function turns positive and we encounter a situation reminiscent of QED – $\beta(e) = e^3/(12\pi^2)$, where the coupling strength increases for larger momentum transfers and conversely the coupling strength decreases for larger distances. This can be understood by a screening of electric charges due to the polarization of the vacuum by virtual electron-positron pairs. The situation in QCD however is different: at the physical point ($N_c = 3$ and $N_f = 6$)

the QCD beta function (2.159) is negative (for $N_c = 3$ this would be the case for $N_f < 17$). This implies, that the coupling strength decreases for larger momentum transfers – conversely the coupling strength increases for larger distances. The self-interacting gluons of QCD, as a non-Abelian gauge theory, have an anti-screening effect: virtual gluons in vacuum augment color charges at larger distances. For large momentum transfers g approaches zero and QCD becomes a free/non-interacting theory, *i.e.*, it is *asymptotically free*. Asymptotic freedom has been identified as a prominent property of non-Abelian gauge theories in general [68].

Gross, Politzer, and Wilczek received their Nobel prize for “*the discovery of asymptotic freedom in the theory of the strong interaction*”, which in the context of the running coupling of QCD, is the very notion that its coupling strength decreases with increasing momentum transfer as

$$\alpha_s(Q) \equiv \frac{g(Q)^2}{4\pi} = \frac{2\pi}{\left(\frac{11}{3}N_c - \frac{2}{3}N_f\right) \ln(Q/\Lambda_{\text{QCD}})}, \quad (2.160)$$

where we integrated Eq. (2.159) with $g(\mu) = g$ and introduced the characteristic scale Λ_{QCD} , which manifests in Eq. (2.160) as the position of the *Landau pole* of the running coupling. The characteristic scale Λ_{QCD} is RG-scheme-dependent, but a typical value is $\Lambda_{\text{QCD}}^{\overline{\text{MS}}} \approx 340 \text{ MeV}$ for $N_f = 3$ [406]. Perturbative computations (today available to much higher-order in perturbation theory, *e.g.*, N³LO) are paired with experimental measurements to measure the running coupling of QCD, see, *e.g.*, Sec. 9.4 and Fig. 9.3 of Ref. [36] for an overview of recent results. The latest *final world average value* for the strong coupling at $Q = M_Z \approx 91 \text{ GeV}$ is $\alpha_s(M_Z) = 0.1179(9)$ according to Eq. (9.25) of Ref. [36].

The running of the strong coupling in Eq. (2.160) predicts a weakly coupled (asymptotically free) regime for large momentum transfers/energies – the aforementioned QGP – but also a strongly coupled, non-perturbative regime with $\alpha_s(Q) > 1$ for $Q \lesssim 680 \text{ MeV}$ from the running coupling (2.160) with $\Lambda_{\text{QCD}}^{\overline{\text{MS}}} = 340 \text{ MeV}$ for $N_f = 3$. The latter regime is not accessible with perturbative methods.

Color confinement

The effect of confinement – the absence of color charged particles in vacuum and at low temperatures and densities – has been mentioned a few times already. In its ground state QCD only contains color neutral composites like mesons, baryons, or more exotic composites like tetraquarks or glueballs. In this paragraph we want to briefly comment on order parameters and measures for confinement.

In pure YM theory at non-zero temperature the Polyakov loop [407] can serve as an order parameter for confinement. It is defined as the Wilson loop that winds around the compactified Euclidean temporal extent

$$P(\vec{x}) \equiv \frac{1}{N_c} \text{Tr}_c \mathcal{P} \exp \left(\int_0^\beta d\tau \tilde{A}_4(\vec{x}, \tau) \right), \quad (2.161)$$

with the path-ordering operator \mathcal{P} in terms of τ and the fluctuating quantum field $\tilde{A}_4(\vec{x}, \tau)$. The expectation value $L(\vec{x})$ of the Polyakov loop $P(\vec{x})$ is commonly used as an order parameter

for confinement with

$$L(\vec{x}) \equiv \langle P(\vec{x}) \rangle \begin{cases} = 0, & \text{in the confined phase,} \\ > 0, & \text{in the deconfined phase} \end{cases} . \quad (2.162)$$

A non-zero expectation value $L(\vec{x})$ signals a spontaneous breaking of the center group Z_3 of the gauge group $SU(3)$, implying confinement in the pure YM gauge theory. The expectation value $\langle P(\vec{x})P^\dagger(\vec{y}) \rangle$ is proportional to $\exp(-\beta V_{q\bar{q}}(|\vec{x} - \vec{y}|))$, with the static quark-anti-quark potential $V_{q\bar{q}}(r)$, up to thermally suppressed corrections due to excited states. The expectation values in Eq. (2.162) can be linked to the expectation values of the gauge field $A_4 = \langle \tilde{A}_4 \rangle$ in a non-trivial manner: $L[A_4]$. As a consequence of confinement the transversal gluon propagator develops a physical mass gap, explaining the name *Yang-Mills & The Mass Gap* problem [69], and the ghost propagator gets enhanced [408–410]. Additional details can be found in Refs. [97, 98, 411–416] and in references therein.

The confinement of dynamical quarks in the FRG and model computations is usually modeled by a statistical confinement in terms of a Polyakov loop potential, see, e.g., Refs. [80, 99, 109, 396, 417–421] and references therein. We will elaborate on this a bit further in the next subsection 2.3.3.

Chiral symmetry (breaking)

In our discussion of QCD so far we focused on the field content and $SU(N_c)$ gauge symmetry. Assuming vanishing quark masses and zero temperature the Euclidean action of QCD, cf. Eq. (2.156), has a multitude of additional symmetries:

- (Euclidean) Poincaré symmetry including rotations and translations,
- conformal symmetry, since the action S_{QCD} of Eq. (2.156) is free of any scales,
- discrete symmetries – like charge conjugation C , parity P , (Euclidean) time reversal T and the usual combined symmetries CP and CPT , and
- chiral symmetry.

Non-zero temperature breaks Euclidean Poincaré invariance down to spatial rotations and translations and discrete translations in Euclidean time, due to the compactification of the Euclidean time direction and the accompanying (anti-)periodic boundary conditions. Further details, especially regarding the discrete symmetries in Euclidean space-time, can be found in Ref. [422]. Quantum and thermodynamic fluctuations break conformal symmetry as scales like μ , T , Λ_{QCD} , and physical mass gaps enter the problem or dynamically emerge. We will devote the rest of this paragraph to the chiral symmetry of QCD.

For massless quarks, i.e., in the chiral limit, the action/Lagrangian of QCD, cf. Eq. (2.156), is invariant under global

$$U(N_f)_L \otimes U(N_f)_R \simeq U(N_f)_V \otimes U(N_f)_A \quad (2.163)$$

transformations, where L and R refer to left- and right-handed quark components $\tilde{\psi}_{L/R}$ (Weyl spinors) which are defined as

$$\tilde{\psi}_L \equiv \tilde{\psi}_- = \gamma_- \tilde{\psi} = \frac{1}{2}(\mathbb{1} - \gamma^{\text{ch}})\tilde{\psi}, \quad (2.164a)$$

$$\tilde{\psi}_R \equiv \tilde{\psi}_+ = \gamma_+ \tilde{\psi} = \frac{1}{2}(\mathbb{1} + \gamma^{\text{ch}})\tilde{\psi}, \quad (2.164b)$$

cf. Eqs. (B.80) and (B.81) and the accompanying brief discussion of chirality in App. B.6. The $U(N_f)_V$ transformation in Eq. (2.163) does not distinguish between quarks of differing chirality ($\theta_V = \theta_L = \theta_R$), while $U(N_f)_A$ acts oppositely ($\theta_A = \theta_L = -\theta_R$) on left- and right-handed quarks. Here $\theta_{L/R/A/V}$ refers to the parameters of the corresponding transformations

$$U(N_f)_L : \tilde{\psi}_L \mapsto e^{i\theta_L^i t_i} \tilde{\psi}_L, \quad \tilde{\psi}_R \mapsto \tilde{\psi}_R, \quad \tilde{\psi}_L \mapsto \tilde{\psi}_L e^{-i\theta_L^i t_i}, \quad \tilde{\psi}_R \mapsto \tilde{\psi}_R, \quad (2.165a)$$

$$U(N_f)_R : \tilde{\psi}_L \mapsto \tilde{\psi}_L, \quad \tilde{\psi}_R \mapsto e^{i\theta_R^i t_i} \tilde{\psi}_R, \quad \tilde{\psi}_L \mapsto \tilde{\psi}_L, \quad \tilde{\psi}_R \mapsto \tilde{\psi}_R e^{-i\theta_R^i t_i}, \quad (2.165b)$$

$$U(N_f)_V : \tilde{\psi}_L \mapsto e^{i\theta_V^i t_i} \tilde{\psi}_L, \quad \tilde{\psi}_R \mapsto e^{i\theta_V^i t_i} \tilde{\psi}_R, \quad \tilde{\psi}_L \mapsto \tilde{\psi}_L e^{-i\theta_V^i t_i}, \quad \tilde{\psi}_R \mapsto \tilde{\psi}_R e^{-i\theta_V^i t_i}, \quad (2.165c)$$

$$U(N_f)_A : \tilde{\psi}_L \mapsto e^{-i\theta_A^i t_i} \tilde{\psi}_L, \quad \tilde{\psi}_R \mapsto e^{i\theta_A^i t_i} \tilde{\psi}_R, \quad \tilde{\psi}_L \mapsto \tilde{\psi}_L e^{i\theta_A^i t_i}, \quad \tilde{\psi}_R \mapsto \tilde{\psi}_R e^{-i\theta_A^i t_i}, \quad (2.165d)$$

with $i \in \{0, 1, 2, 3\}$. The transformations in Eq. (2.165) can be formulated on the level of the Dirac spinors $\tilde{\psi}$ and $\tilde{\bar{\psi}}$ using the projection operators γ_{\pm} and γ^{ch} in the exponents. Note that $U(N_f)_A$ lacks closure and is thus not a group by itself, but the combination $U(N_f)_V \otimes U(N_f)_A$ constitutes a group in the sense of Eq. (2.163).

In nature, *i.e.*, at the physical point, the chiral symmetry (2.163) is only an approximate symmetry for the light quark flavors and we will limit our discussion in the following to the two light flavors up and down. Up to irrelevant Z_2 phase factors the groups $U(N_f = 2)_{A/V}$ may be decomposed further leading to

$$U(2)_L \otimes U(2)_R \simeq U(2)_V \otimes U(2)_A \simeq SU(2)_V \otimes SU(2)_A \otimes U(1)_V \otimes U(1)_A. \quad (2.166)$$

The $U(1)_V$ symmetry is, according to Noether's theorem [423, 424], associated to the conservation of baryon number

$$Q_V = \int_{V_3} d^3x \left(\tilde{\psi}_L \gamma_4 \tilde{\psi}_R + \tilde{\bar{\psi}}_R \gamma_4 \tilde{\psi}_L \right), \quad (2.167)$$

with the associated density $n = Q_V/V_3$, cf. App. C.1. The quark chemical potential μ is introduced as a Lagrange multiplier to study the physically relevant systems with quark-anti-quark-asymmetry, *i.e.*, non-zero quark number density n .

The $U(1)_A$ symmetry is anomalously broken on quantum level [425–428] by topologically non-trivial gauge configurations, *viz.* instantons [429, 430]. On a technical level this anomalous symmetry breaking is related to the fact, that the measure of the functional integral used for quantization is not invariant under $U(1)_A$ transformations. For a discussion of this phenomenon in the FRG context, see, *e.g.*, Ref. [431]. The anomalous breaking of $U(1)_A$ in QCD has important phenomenological implications: it explains the $\eta - \eta'$ mixing [432–436] and is involved in the

resolution of the partially conserved axial current (PCAC) puzzle of the electromagnetic decay $\pi^0 \rightarrow \gamma\gamma$ [427], see, e.g., Secs. 8.3.6.2 and 9.3.4 of Ref. [393] for additional details.

The $SU(2)_V$ symmetry, i.e., the isospin symmetry, remains unbroken as long as one assumes equal masses for the quarks. Since the difference in the masses of the up and down quark is rather small with $m_d - m_u \approx 2.5 \text{ MeV}$ when compared to typical scales of QCD, e.g., $\Lambda_{\text{QCD}}^{\overline{\text{MS}}} \approx 340 \text{ MeV}$, $SU(2)_V$ isospin symmetry is an approximate symmetry at the physical point.

The $SU(2)_A$ symmetry, i.e., “the” chiral symmetry, is the part of chiral symmetry (2.166) we are primarily focused on. When discussing chiral symmetry breaking (χ SB) in the following we are referring to the spontaneous breaking of the $SU(2)_A$ symmetry. The symmetry is explicitly broken at the physical point by the non-vanishing masses of the up and down quark, but since they are rather small, again when compared with other characteristic scales of QCD, $SU(2)_A$ chiral symmetry is an approximate symmetry of QCD in the UV – on the classical level. The slight, explicit breaking of $SU(2)_A$ chiral symmetry together with observations in the electroweak sector of the standard model inform the PCAC hypothesis:

$$\langle 0 | \partial^\mu J_{\text{ch};\mu}^a(x) | \pi^b(q) \rangle = -f_\pi m_\pi^2 \delta^{ab} e^{-iq \cdot x}, \quad (2.168)$$

with the axial current $J_{\text{ch};\mu}^a = \tilde{\psi} \gamma_\mu \gamma^{\text{ch}t^a} \tilde{\psi}$, the pion mass m_π and the pion decay constant $f_\pi \approx 93 \text{ MeV}$ [36], see, e.g., Refs. [393, 437] for further details. These observations are confronted with the experimental hadron spectrum of strongly interacting matter, which does not reflect axial symmetry. The $1^-(0^-)$ isovector, pseudoscalar pions are significantly lighter than their chiral partner the $0^+(0^+)$ ³⁰ isoscalar, scalar σ -meson $f_0(500)$ ³¹ – 135 MeV compared to 400 – 550 MeV [36]. The same holds for other chiral partners, e.g., for the $1^-(1^+)$ isovector, axialvector mesons $a_1(1260)$ and the $1^+(1^-)$ isovector, vector mesons $\rho(700)$ – 1230 MeV compared to 775 MeV [36].

The resolution of this potentially rather serious tension in the standard model comes in the form of spontaneous $SU(2)_A$ chiral symmetry breaking (χ SB). This phenomenon is analogous to magnetization and superconductivity in condensed matter physics and in the context of QCD, or more precisely the nucleon model, it was introduced in 1961 by Yoichiro Nambu and Giovanni Jona-Lasinio with their seminal works [64, 65] using their now famous Nambu-Jona-Lasinio (NJL) model. Yoichiro Nambu was awarded the *Nobel Prize in Physics* in 2008 for “the discovery of the mechanism of spontaneous broken symmetry in subatomic physics”³². While the action of QCD and the NJL model exhibit $SU(2)_A$ chiral symmetry (in the chiral limit $m_u = m_d = 0$), their respective ground states do not. Quantum fluctuations lead to the dynamical formation

³⁰In the following we will use the $I^G(J^P)$ -notation for mesons with isospin I , G -parity, total angular momentum J , and parity P , see, e.g., Ref. [36].

³¹The experimentally observed $f_0(500) 0^+(0^+)$ resonance is likely a superposition of multiple components, including possible contribution from exotic states like tetraquarks and glueballs. However, recent research suggests, that $f_0(500)$ is indeed primarily the scalar σ meson, see, e.g., the review [438].

³²The 2008 Nobel prize committee denied Giovanni Jona-Lasinio the same recognition due to the limitation that a maximum of three individuals can share a prize for not more than two discoveries or achievements [439]. The other two recipients were Makoto Kobayashi and Toshihide Maskawa for their work on the CKM matrix, with Nicola Cabibbo suffering the same fate as Giovanni Jona-Lasinio. Giovanni Jona-Lasinio gave the Nobel lecture in Yoichiro Nambu place upon Nambu’s request as a recognition of Jona-Lasinio’s contribution [440].

of a chiral condensate $\langle \bar{q}q \rangle \propto \langle \sigma \rangle \neq 0$ signaling a breaking of $SU(2)_A$ chiral symmetry with the pions as corresponding Nambu-Goldstone bosons [441, 442] and σ as the massive radial mode. Pions gain their small mass – become pseudo Nambu-Goldstone bosons – due to the small explicit $SU(2)_A$ chiral symmetry breaking caused by the small light quark mass. This allows for small pion masses and PCAC in accordance to Eq. (2.168), while providing an explanation for the hadron spectrum of strongly interacting matter: the non-zero chiral condensate and the related substantial spontaneous χ SB is responsible for the higher masses of the σ meson, $a_1(1260)$, and the nucleons for that matter.

We will discuss the mechanism of χ SB and its restoration at higher temperatures due to thermodynamic fluctuations further in chapter 5 and its analog in the (1+1)-dimensional GN model in chapter 4.

2.3.3. χ SB and the emergence of LEFTs from QCD

In this subsection we want to give a concise introduction of the emergence of low-energy effective theories, *viz.* the QM model, from QCD within the framework of FRG, see, *e.g.*, Refs. [80, 97, 109, 162, 209, 237, 249, 396, 397, 443] for further details. For the following discussion we closely follow and summarize Refs. [80, 109] with small modifications to adapt our notation and limitation to $N_f = 2$ in the chiral limit $m_u = m_d = 0$.

In this subsection we will discuss the following EAA for gauge fixed QCD

$$\begin{aligned} \bar{\Gamma}_k^{\text{QCD}}[\chi] \equiv \int_x \left(\mathcal{L}_A[A, c, \bar{c}] + \mathcal{L}_{\Delta A}[A] + \mathcal{L}_{\bar{\psi}\psi}[A, \psi, \bar{\psi}] + \right. \\ \left. + \mathcal{L}_{(\bar{\psi}\psi)^2}[\psi, \bar{\psi}] + \mathcal{L}_{\bar{\psi}\psi\varphi}[\varphi, \psi, \bar{\psi}] + \mathcal{L}_\varphi[\varphi] + \mathcal{L}_V[A, \varphi] \right), \end{aligned} \quad (2.169)$$

$$\mathcal{L}_A[A, c, \bar{c}] \equiv \frac{1}{4} F_{\mu\nu}^a F_{\mu\nu}^a + Z_{c;k} \bar{c}^a (\partial_\mu D_\mu^{ab}) c^b + \frac{1}{2\xi} (\partial_\mu A_\mu^a)^2, \quad (2.170a)$$

$$\mathcal{L}_{\bar{\psi}\psi}[A, \psi, \bar{\psi}] \equiv Z_{\psi;k} \bar{\psi} (\gamma_\mu D_\mu - \gamma_4 \mu) \psi, \quad (2.170b)$$

$$\mathcal{L}_{(\bar{\psi}\psi)^2}[\psi, \bar{\psi}] \equiv -\lambda_{\psi;k} \left((\bar{\psi} t^0 \psi)^2 + (\bar{\psi} i \gamma^{\text{ch}} \vec{t} \psi)^2 \right), \quad (2.170c)$$

$$\mathcal{L}_{\bar{\psi}\psi\varphi}[\varphi, \psi, \bar{\psi}] \equiv h_k \bar{\psi} (t^0 \varphi_0 + i \gamma^{\text{ch}} t^a \varphi_a) \psi \equiv h_k \bar{\psi} (\varphi_i \tau^i) \psi, \quad (2.170d)$$

$$\mathcal{L}_\varphi[\varphi] \equiv \frac{1}{2} Z_{\varphi;k} (\partial_\mu \varphi)^2, \quad (2.170e)$$

$$\mathcal{L}_V[A, \varphi] \equiv V_k(\varrho, A_4) \equiv V_{\text{glue};k}(A_4) + V_{\text{mat};k}(\varrho, A_4), \quad (2.170f)$$

with the running wave-function renormalizations $Z_{c;k}$, $Z_{\psi;k}$, and $Z_{\varphi;k}$, the running four-fermi coupling $\lambda_{\psi;k}$, the running Yukawa coupling h_k , the effective self-interaction potential $V_k(\varrho, A_4)$, and the RG-scale-dependent, non-classical contributions $\mathcal{L}_{\Delta A}[A]$ to the gauge sector, *viz.* the gluon two-point function, *cf.* Eq. (39) and Eq. (48) of Ref. [80] and Ref. [109] respectively for $N_f = 2$ in the chiral limit. In Eq. (2.170c) we introduced the triple of $SU(N_f = 2)$ generators $\vec{t} \equiv (t_1, t_2, t_3)$ and further the four-component array $\tau \equiv (\mathbb{1}, t_0, i \gamma^{\text{ch}} \vec{t})$ in Eq. (2.170d).

The multi component composite mean-field χ contains the fundamental mean-fields χ_f : $A = \langle \tilde{A} \rangle$, $c = \langle \tilde{c} \rangle$, $\bar{c} = \langle \tilde{\bar{c}} \rangle$, $\psi = \langle \tilde{\psi} \rangle$, $\bar{\psi} = \langle \tilde{\bar{\psi}} \rangle$ and the anti-quark-quark composite mean-field $\varphi = \langle \hat{\phi}_k[\tilde{\chi}_f] \rangle \equiv (\varphi_0, \pi_1, \pi_2, \pi_3)$. The related $O(4)$ invariant is $\varrho \equiv \frac{1}{2}\varphi^2$. As composite mean-fields the components of φ are generated via dynamical hadronization, as we will elaborate later in this subsection.

$\mathcal{L}_A[A, c, \bar{c}]$ and $\mathcal{L}_{\bar{\psi}\psi}[A, \psi, \bar{\psi}]$ include the classical contributions from the gauge-fixed action S_{QCD} of Eq. (2.156), while $\mathcal{L}_{\Delta A}[A]$ incorporates non-classical contributions. For details regarding the gauge sector we refer the interested reader to especially Secs. III.B, III.C, and IV.B of Ref. [80], which includes the here omitted definitions in Eqs. (54)-(60) for the gauge sector and the involved scale-dependent couplings.

$\mathcal{L}_V[A, \varphi]$ includes the effective self-interaction potential $V_k(\varrho, A_4)$, which depends on the $O(4)$ invariant ϱ and the expectation value of the Euclidean temporal gauge field $A_4 = \langle \tilde{A}_4 \rangle$, which is closely related to the expectation value of the Polyakov loop $L[A_4]$, cf. subsection 2.3.2. The expectation values $\varrho = \frac{1}{2}\varphi_0^2$ and A_4 ($L[A_4]$) serve as order parameters for χ SB and the confinement-deconfinement phase transition respectively, cf. subsection 2.3.2 and Secs. III.F, V.A., and V.D of Ref. [80].

Inserting the ansatz (2.169) into the Wetterich Eq. (2.33) for general scale-dependent mean-fields yields

$$\frac{d}{dt} \bar{\Gamma}_k[\chi] = \partial_t|_{\chi} \bar{\Gamma}_k[\chi] + \bar{\Gamma}_k^{\prime\varphi}[\chi] \partial_t \varphi = \frac{1}{2} (\partial_t R_k^{\text{mn}}) G_{k;\text{nm}}[\chi] + R_k^{\prime\varphi\varphi} G_{k;\varphi\varphi}[\chi] \frac{\delta \partial_t \varphi}{\delta \chi_1}. \quad (2.171)$$

The flow of the EAA of QCD includes contributions

$$\begin{aligned} \frac{1}{2} G_{k;\text{nm}}[\chi] \partial_t R_k^{\text{mn}} &= \frac{1}{2} G_{k;\varphi\varphi}[\chi] \partial_t R_k^{\prime\varphi\varphi} + \frac{1}{2} G_{k;AA}[\chi] \partial_t R_k^{\prime AA} - \\ &\quad - G_{k;c\bar{c}}[\chi] \partial_t R_k^{\prime c\bar{c}} - G_{k;\psi\bar{\psi}}[\chi] \partial_t R_k^{\prime\psi\bar{\psi}}, \end{aligned} \quad (2.172)$$

$$= \frac{1}{2} \text{[purple loop]} + \frac{1}{2} \text{[orange loop]} - \text{[red dashed loop]} - \text{[green loop]}, \quad (2.172')$$

from fluctuating composites, gluons, ghosts, and quarks. Using various projections and evaluating Eq. (2.171) on the QEOM, it is possible to derive flow equations for all RG-scale-dependent couplings of the ansatz (2.169), see Refs. [80, 109] for details and the corresponding flow equations. Solutions to the QEOM

$$\chi_{\text{EoM}} = \underline{\chi} \equiv (\varphi, \underline{A}, c, \bar{c}, \psi, \bar{\psi}) \quad (2.173a)$$

$$= ((\sigma, 0, 0, 0), (0, 0, 0, \underline{A}_4), 0, 0, 0, 0), \quad (2.173b)$$

with \underline{A}_4 and $\varphi_0 \equiv \sigma$ as the only, homogeneous, non-vanishing expectation values are considered. This allows a study of both the confinement-deconfinement and the chiral phase transition. The flow is initialized at an UV initial scale of $\Lambda = 20 \text{ GeV}$ with the only input being the strong coupling constant $\alpha_{s,\Lambda}$ and parameters for the explicit chiral symmetry breaking due to quark masses, see Tab. I of Ref. [80] for details.

Four-fermi couplings, dynamical hadronization, and χ SB

During the RG-scale evolution from the UV to the IR, the four-fermi interactions of $\mathcal{L}_{(\bar{\psi}\psi)^2}[\psi, \bar{\psi}]$ in Eq. (2.170c) get generated by quark-gluon interactions $\lambda_{\psi,k} \propto \alpha_{s,k}^2$ and get enhanced once generated by mixed terms $\lambda_{\psi,k} \propto \lambda_{\psi,k} \alpha_{s,k}$ and $\lambda_{\psi,k} \propto \lambda_{\psi,k}^2$:

$$\partial_t \lambda_{\psi,k} = \partial_t \text{[diagram]} = \tilde{\partial}_t \left(\frac{1}{2} \text{[diagram 1]} + \dots + \frac{1}{2} \text{[diagram 2]} + \dots + \frac{1}{2} \text{[diagram 3]} + \dots \right), \quad (2.174)$$

where we used the RG time derivative $\tilde{\partial}_t$ which acts only on regulators, cf. Eq. (2.71) and the corresponding discussion.

In principle all four-fermi interaction channels with $SU(N_c = 3) \otimes SU(2)_R \otimes SU(2)_L \otimes U(1)_V$ symmetry are generated, which for $N_f = 2$ corresponds to a Fierz-complete set of ten four-fermi channels, see, e.g., Refs. [209, 249, 262, 444–446] and Sec. III.A and App. B of Ref. [109]. In this work we will focus solely on the $\sigma - \pi$ ($0^+(0^+)$ isoscalar, scalar – $1^-(0^-)$ isovector, pseudoscalar) channel, which is crucial for the dynamics of χ SB. Studies including the Fierz-complete set of four-fermi couplings have shown, that the $\sigma - \pi$ channel dominates the dynamics, especially in the chiral limit for $N_f = 2$ and $\mu_B/T \lesssim 6$ [80, 209, 446]. It should be noted at this point, that especially at high chemical potentials and low temperatures ($\mu_B/T \gtrsim 6$) diquark and vector-meson channels gain importance [80, 209, 262, 445, 446]. Diquark condensation and color superconductivity, see, e.g., Refs. [59, 61] for details, become very relevant for the phase structure of strongly interacting matter at high chemical potentials, cf. figure 1.1. The interplay between inhomogeneous phases and color superconductivity might play an important role for χ SB, see, e.g., Refs. [337, 447–451]. That being said, we will focus solely on $\sigma - \pi$ channel in this work.

As the strong coupling increases towards lower RG-/momentum-scales, cf. Eq. (2.160), four-fermi interactions become the dominant mode of interaction. Mainly diagrams $\lambda_{\psi,k} \propto \alpha_{s,k}^2$, cf. the first diagram in Eq. (2.174), lead to a shift of the dynamics from quark-gluon interactions towards quark-anti-quark scatterings. This will be discussed further in the [next paragraph](#).

The $\sigma - \pi$ channel eventually becomes resonant at $k_\chi \approx 500$ MeV, signaling condensation and χ SB in the $\sigma - \pi$ channel. When considering a momentum-independent four-fermi coupling $\lambda_{\psi,k}$, this condensation is signaled by a diverging $\lambda_{\psi,k}$ as $k \rightarrow k_\chi$. The formation of a chiral condensate and χ SB can be studied either by considering momentum-dependent four-fermi couplings, see, e.g., Sec. III.A of Ref. [109] for an overview, or by bosonizing the channel.

In the latter approach the four-fermi channel gets bosonized by means of a Hubbard-Stratonovich (HS) transformation [452, 453], replacing the four-fermi interaction on a technical level by a Yukawa-type [454] interaction of the form (2.170d), cf. Eq. (4.3) ff. for an explicit bosonization of the GN model. The complicated momentum-dependence of the resonant higher-order quark-anti-quark scatterings gets resolved elegantly in terms of meson exchanges.

In the FRG such a bosonization can be implemented neatly and RG-scale-dependently by means of *dynamical hadronization* [80, 237, 249]: dynamical meson fields $\hat{\phi}_k$ are introduced as quark-anti-quark composites in the generating functional (2.4) with corresponding source

terms $\hat{J}^\phi \hat{\phi}_k$. As such they are pure auxiliary fields and their introduction does not spoil any IR observables: when evaluating the EAA in the IR on the QEOM, *i.e.*, $\hat{J}^\phi = 0$, one in fact recovers the original EA of gauge fixed QCD

$$\Gamma_{\text{QCD}}[\chi_f] = \Gamma_{k=0}[\varphi_{\text{EoM}}[\chi_f], \chi_f]. \quad (2.175)$$

The composites are however extremely useful to study χSB and to elegantly extract related correlation functions. The RG-scale-dependent hadronization relation, *cf.* Eq. (2.32), employed for $\hat{\phi}_k$:

$$\langle \partial_t \hat{\phi}_k \rangle_{k;J} = \partial_t \varphi_k \equiv \dot{A}_k \bar{\psi} \tau \psi + \dot{B}_k \varphi, \quad (2.176)$$

can be considered as a successive bosonization of the quark-anti-quark channel, see Sec. II.A of Ref. [80] for further details including subtleties regarding explicit chiral symmetry breaking. The so-called hadronization function \dot{A}_k controls the overlap between the composites and the quark-anti quark channel. The hadronization function \dot{B}_k affects the wave-function renormalization Z_φ . Both \dot{A}_k and \dot{B}_k can be chosen freely to implement specific hadronization prescriptions. In Ref. [80] $\dot{B}_k = 0$ is chosen and the renormalized and rescaled hadronization function $\tilde{A}_k \equiv \dot{A}_k k^2 Z_{\varphi;k}^{1/2} / Z_{\psi;k}$ is fixed by completely bosonizing the four-fermi interaction at all scales by enforcing

$$\forall k \quad \bar{\lambda}_{\psi;k} \equiv \frac{k^2}{Z_{\psi;k}^2} \lambda_{\psi;k} \stackrel{!}{=} 0. \quad (2.177)$$

Diagrammatically this choice entails for the flow of the four-fermi coupling

$$\partial_t \text{[diagram]} = \tilde{\partial}_t \left(\frac{1}{2} \text{[diagram 1]} + \dots + \frac{1}{2} \text{[diagram 2]} + \dots + \frac{1}{2} \text{[diagram 3]} + \dots \right), \quad (2.178)$$

where the diagrams $\propto \lambda_{\psi,k}^2$ and $\propto \lambda_{\psi,k} \alpha_{s,k}$ from Eq. (2.178) vanish due to the hadronization constraint (2.177). Further details and explicit flow equations can be found in Sec. III.E and the corresponding App. L of Ref. [80].

This complete bosonization of the four-fermi coupling entails, that the complete dynamics of the $\sigma - \pi$ channel is encoded using the effective hadronic composites. The emergent four-fermi coupling is on a computational level completely replaced by the Yukawa-type interaction of $\mathcal{L}_{\bar{\psi}\psi\varphi}[\varphi, \psi, \bar{\psi}]$ from Eq. (2.170d), with multi scatterings of the resonant channel encoded in the effective potential $V_k(\varrho, A_4)$ of Eq. (2.170f). $V_k(\varrho, A_4)$ is directly related to the equilibrium thermodynamic grand potential density Ω , see Eq. (C.8) of App. C.1 and Sec. III.F of Ref. [80] for specifics. $V_k(\varrho, A_4)$ is the central quantity used to study χSB and the confinement-deconfinement transition.

At this point we want to comment and present one of the central results of Ref. [80], the phase diagram of $N_f = 2 + 1$ and $N_f = 2$ flavor QCD in figure 2.13 with realistic quark/pion masses and decay constants f_π and f_K . These phase diagrams must be considered seminal

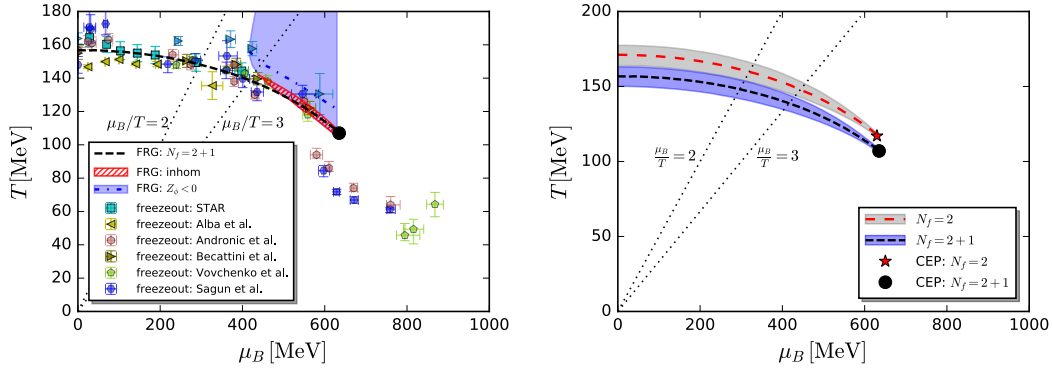


Figure 2.13.: Phase diagram of $N_f = 2 + 1$ flavor QCD including experimental freeze-out data [70–75] on the left (a) and $N_f = 2$ and $2 + 1$ flavor QCD phase diagram on the right (b). Information about the resulting and underlying (physical) parameters can be found in Tab. I of Ref. [80]. The red and blue regions on the left (a) are related to the possible emergence of inhomogeneous phases and are discussed in detail in subsection 2.4.2. The bands and dotted lines on the right (b) mark the crossover region on temperature for the chiral condensate. An augmented version of the left figure (a) can be found in Fig. 13 of Ref. [397], including lattice data [455, 456], DSEs results [457, 458], and of course the results of Ref. [397] itself. Taken from the arXiv source for Fig. 21 and 20 of Ref. [80]. Publication under CC BY-SA 4.0 license with the permission of W.-j. Fu.

results and represent the culmination of a massive research effort by large parts of the FRG community towards such first principle results for QCD.

The phase diagrams are computed up to $\mu_B/T \approx 6$ and include the chiral crossover transition between a homogeneously broken phase (HBP) at low temperatures and an approximately symmetric phase (SP) at high temperatures. The chiral crossover transition ends in a critical endpoint (CEP). Note that due to non-vanishing quark masses chiral symmetry only gets approximately restored and the transition is a smooth crossover instead of a second-order phase transition, which is found in the chiral limit. The crossover temperatures at vanishing μ_B are found to be

$$T_{c,N_f=2} = 171 \text{ MeV}, \quad T_{c,N_f=2+1} = 156 \text{ MeV}, \quad (2.179)$$

with a curvature κ of the phase boundary $T_c(\mu_B)$ of

$$\kappa_{N_f=2} = 0.0176(1), \quad \kappa_{N_f=2+1} = 0.0142(2), \quad (2.180)$$

as the quadratic expansion coefficient of $T_c(\mu_B)$ around $\mu_B = 0$:

$$\frac{T_c(\mu_B)}{T_c} = 1 - \kappa \left(\frac{\mu_B}{T_c} \right)^2 + \dots \quad (2.181)$$

The CEPs are located at

$$(T, \mu_B)_{\text{CEP}, N_f=2} = (117, 630) \text{ MeV}, \quad (2.182a)$$

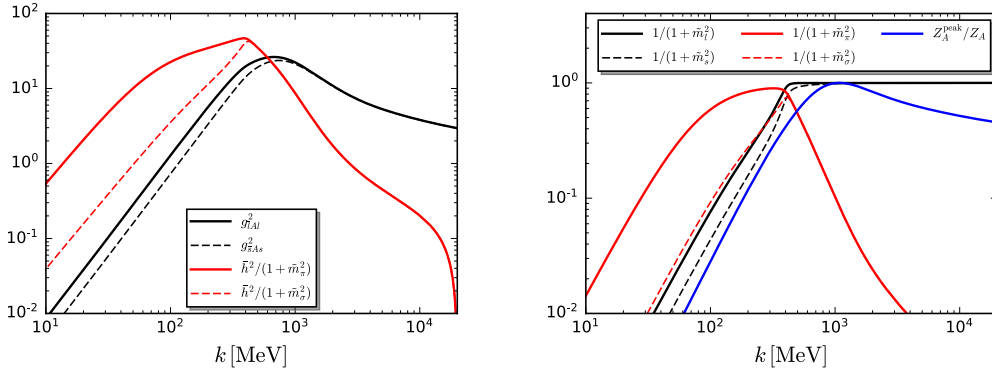


Figure 2.14.: Dimensionless four-quark single gluon couplings (in black) and dimensionless four-quark single meson exchange couplings (red) on the left (a) and dimensionless propagator gaps for quarks (in black), mesons (in red), and a gluon dressing function for comparison (in blue) on the right (b). Taken from the arXiv source for Fig. 18 and 19 of Ref. [80]. Publication under CC BY-SA 4.0 license with the permission of W.-j. Fu.

$$(T, \mu_B)_{\text{CEP}, N_f=2+1} = (107, 635) \text{ MeV}, \quad (2.182b)$$

which entails

$$(T/\mu_B)_{\text{CEP}, N_f=2} = 5.38, \quad (2.183a)$$

$$(T/\mu_B)_{\text{CEP}, N_f=2+1} = 5.93. \quad (2.183b)$$

A discussion of these results (and the values themselves) can be found in Sec. V.D – Eqs. (121)–(127) – of Ref. [80]. Since we are primarily working with quark chemical potential μ : note that $\mu_B = 3\mu$ and thus $\kappa \rightarrow 9\kappa \equiv \kappa'$, *i.e.*, $\kappa'_{N_f=2} = 0.1584(9)$ in terms of μ instead of μ_B in Eq. (2.180).

The indication for inhomogeneous phases in figure 2.13a will be discussed in subsection 2.4.2. The limitation of the results in Ref. [80] to $\mu_B/T \lesssim 6$ has several reasons. One is the inclusion of only the scalar-pseudoscalar $\sigma - \pi$ channel – a discussion with qualitative and quantitative predictive power at $\mu_B/T \gtrsim 6$ should include at least the dominant diquark and vector-meson channels. Another technical limitation of Ref. [80] is the application of a FRG Taylor expansion, *cf.* subsection 2.1.4.2, for the effective potential $V_k(\varrho, A_4)$. A study of non-smooth, potentially first-order, chiral phase transitions requires – as we will argue throughout this work – proper shock capturing schemes for the underlying PDEs, *cf.* Refs. [1–4, 162, 210, 247, 283, 284] and subsection 2.1.7 as well as chapters 3 and 4. In the context of Ref. [80] especially the recent work [210] represents significant progress in terms of an application of the recently developed CFD perspective for FRG flow equations.

Sequential decoupling and the emergence of NJL-/QMM-type LEFTs from QCD

One extremely interesting and for our work relevant observation in Ref. [80] is the observed *sequential decoupling of dynamic, relevant degrees of freedom* during RG scale-evolution from

the UV towards the IR. The phenomenon is visualized in figure 2.14 and described at length in Sec. V.D of Ref. [80]. We will give a concise summary here using figure 2.14.

Figure 2.14a includes dimensionless quark-gluon couplings and dimensionless quark-meson couplings and we can observe, that the quark-gluon coupling dominates in the UV for scales $k \gtrsim 1$ GeV. In turn, for scales $k \lesssim 1$ GeV, the quark-meson couplings gain importance and become dominant at $k \approx 0.6$ GeV, while the quark-gluon couplings decay rapidly – note the logarithmic scale on the vertical axis of figure 2.14a. This observation is further supported by considering the propagator gappings in figure 2.14b: the gluons decouple first only followed by the quarks and mesons. First the gluonic dynamics decouples from the matter sector, followed by the quark- and σ -modes and ultimately the pion decouples last. Note the dominance of pions for the dynamics at low RG scales $k \approx 0.2$ GeV. The connection and emergence of chiral perturbation theory in vacuum in this context is discussed in Refs. [105–107]. We will discuss the dynamics of such pionic modes in comparison to radial σ -modes at length in our study of zero-dimensional $O(N)$ models in subsection 3.2.3. The discussion of the interplay of bosonic and fermionic fluctuations is at the heart of our study of the GN model at finite N in subsection 4.5.3 and we observe a similar decoupling hierarchy between fermionic and bosonic modes in this low-dimensional model.

This sequential decoupling of dynamic/relevant degrees of freedom gives rise to an intriguing and for the FRG practitioners extremely attractive point of view: first principle FRG QCD computations [80] show, that the highly complicated and involved gauge-dynamics of QCD decouples for low RG scales $k \approx 1$ GeV. Furthermore, by employing dynamic hadronization, we observe the emergence of Polyakov loop enhanced LEFTs, see, e.g., Refs. [309, 417, 419]. With the currently discussed hadronization prescription, viz. the Polyakov loop enhanced quark-meson model (PQM model) emerges. The relevant dynamic degrees of freedom, viz. quarks and mesons (as quark-anti-quark composites), and their interactions at $k \lesssim 1$ GeV are properly captured by LEFTs like the PQM model. Studies like Ref. [80] allow for *QCD-assisted* LEFTs: using full fledged, first principle FRG computations for QCD to initialize LEFTs like the PQM model at scales $k \lesssim 1$ GeV. Typically such theories have been used as low-energy effective models by fitting vacuum observables to determine model parameters, cf. section 5.2 and, e.g., Ref. [417]. The maturing FRG computations for QCD can be used to eliminate the need for such parameter fits by providing input for the model parameters from first principle QCD flows. Thus promoting them from “*mere effective models*” to *QCD-assisted* LEFTs. First steps of such improvements can be found in Refs. [148, 307, 309] and the more recent works [210, 459].

2.3.3.1. The quark-meson model

We want to conclude our introduction into QCD and LEFTs by actually introducing the LEFT we will be using in chapter 5: the *quark-meson* (QM) model, sometimes also referred to as linear- σ model. The QM model and variants/extensions of it – including the PQM model – are incredibly popular in the field of theoretical high-energy physics. An extensive review of the vast literature regarding the model is beyond the scope of the current work. At this point we only want to reference the very incomplete list of QM model FRG literature [81, 87, 99, 105–107, 162, 210, 237, 421, 460]. For a review of primarily mean-field/large- N_c results we

refer to Ref. [461] and for a review of FRG studies with the QM model we refer to Sec. III.B of Ref. [109]. Additional/complementary references to the ones provided in Ref. [109] may be found in the last line of the fourth-to-last paragraph of Sec. V.C of Ref. [80].

In this work we consider the $N_f = 2$ flavor QM model, which in the present context, emerges as the part of Eq. (2.169) relevant for the dynamics at low RG scales $k \lesssim 1$ GeV. The QM model is formed by $\mathcal{L}_{\bar{\psi}\psi}[\chi, \psi, \bar{\psi}]$, $\mathcal{L}_{\bar{\psi}\psi\varphi}[\varphi, \psi, \bar{\psi}]$, $\mathcal{L}_\varphi[\varphi]$, and $\mathcal{L}_V[\chi, \varphi]$ from Eqs. (2.170b)–(2.170f). We will consider it primarily in LPA, cf. subsection 2.1.4.2, and without considering the statistical confinement provided by the Polyakov loop potential. To get specific, we study the following EAA,

$$\bar{\Gamma}_k^{\text{QMM}}[\chi] \equiv \int_x \left(\bar{\psi}(\gamma_\mu \partial_\mu - \gamma_4 \mu + h \varphi_i \tau^i) \psi + \frac{1}{2} (\partial_\mu \varphi)^2 + U_k(\varrho) \right), \quad (2.184)$$

with the field-independent, constant Yukawa coupling h and the scale-dependent mesonic self-interaction potential $U_k(\varrho)$ as a function of the $O(4)$ invariant $\varrho \equiv \frac{1}{2} \varphi^2$. In $\chi \equiv (\varphi, \psi, \bar{\psi})$ we consider four dynamic, on this level fundamental, mesons $\varphi = \langle \phi \rangle \equiv (\varphi_0, \pi_1, \pi_2, \pi_3)$ and $N_c = 3$ dynamic quarks $\psi = \langle \tilde{\psi} \rangle$ and $\bar{\psi} = \langle \tilde{\bar{\psi}} \rangle$ with $N_f = 2$ flavors.

The QM model – its EAA (2.184) in LPA – shares the chiral symmetry

$$SU(2)_L \otimes SU(2)_R \otimes U(1)_V \simeq SU(2)_V \otimes SU(2)_A \otimes U(1)_V \quad (2.185)$$

with QCD, see subsection 2.3.2. The model, especially in the context of a QCD-assisted LEFT, is ideally suited to study the dynamics of χ SB. For the mesons chiral symmetry manifests through the equivalence $SU(2)_L \otimes SU(2)_R \simeq SO(4)$ as an $SO(4)$ symmetry, which motivates the $O(4)$ vector

$$\varphi \equiv (\varphi_0, \pi_1, \pi_2, \pi_3), \quad (2.186)$$

with the $1^-(0^-)$ isovector, pseudoscalar pions³³ and the $0^+(0^+)$ isoscalar, scalar φ_0/σ ³⁴. The pions are in the isospin triplet $SU(2)_V \simeq SO(3)$ and are the Nambu-Goldstone bosons of the $SU(2)_A$ chiral symmetry breaking, which manifests in the mesonic sector as a breakdown of $SO(4)$ to $SO(3)$ with the radial φ_0 as massive σ -mode.

We will reserve further discussions for the applications in chapter 5 apart from one last remark at this point regarding $U(1)_A$ symmetry in the $N_f = 2$ QM model. For $N_f = 2 + 1$ flavors the anomalous $U(1)_A$ symmetry breaking, mentioned in subsection 2.3.2, is usually included in the three flavor QM model by means of a t'Hooft determinant [429], see, e.g., Refs. [99, 104, 445, 461, 462]. It is a determinant in flavor space resulting in a six-point interaction and it is crucial to properly reproduce the aforementioned $\eta - \eta'$ mixing [432–436].

³³Note that we are referring here to flavor eigenstates with (π_1, π_2, π_3) . The charge eigenstates π_\pm and π_0 can be obtained in the usual manner $\pi_\pm = (\pi_1 \mp i\pi_2)/\sqrt{2}$ and $\pi_0 = \pi_3$.

³⁴We reserve the symbol σ in equations and expressions for the value we evaluate φ_0 on, i.e., the possible solution of $\varphi_{0;\text{EoM}} \equiv \sigma$ we probe for. This distinction will become clearer with the applications in the main part of this thesis in chapters 3–5. In the text we will usually refer to the zeroth component of φ as radial, massive, or σ -mode depending on the context.

In the $N_f = 2$ case such a determinant manifests, in terms of quark-anti-quark bilinears, as an ordinary four-fermi coupling

$$\mathcal{O}_{ijlm}^{(S+P)-} \bar{\psi}_i \psi_j \bar{\psi}_l \psi_m = (\bar{\psi} t^0 \psi)^2 + (\bar{\psi} \gamma^{\text{ch}} t^0 \psi)^2 - (\bar{\psi} t^a \psi)^2 - (\bar{\psi} \gamma^{\text{ch}} t^a \psi)^2, \quad (2.187)$$

where we adapted the notation of App. B of Ref. [109]. The $N_f = 2$ QM model is constructed (in terms of Fierz-complete couplings) by the linear combination (sum) of Eq. (2.187) with the $U(1)_A$ -symmetric channel

$$\mathcal{O}_{ijlm}^{(S-P)+} \bar{\psi}_i \psi_j \bar{\psi}_l \psi_m = (\bar{\psi} t^0 \psi)^2 - (\bar{\psi} \gamma^{\text{ch}} t^0 \psi)^2 + (\bar{\psi} t^a \psi)^2 - (\bar{\psi} \gamma^{\text{ch}} t^a \psi)^2. \quad (2.188)$$

Such a linear combination completely eliminates/decouples the three $1^-(0^+)$ isovector, scalars $\bar{\psi} t^a \psi$ and the $0^+(0^-)$ isoscalar, pseudoscalar $\bar{\psi} \gamma^{\text{ch}} t^0 \psi$ as the chiral partners of the pions and σ . In that sense $U(1)_A$ is “maximally broken” in the $N_f = 2$ flavor QM model [104]. Phenomenologically these chiral partners correspond to the heavy a_0 and η_N mesons – with $m_{a_0} \approx 980 \text{ MeV}$ [36] and η_N not really observable (only as a mixture/part of η/η'). For the dynamics of $N_f = 2$ χ SB those heavy partners are not relevant and are thus usually not considered in the $N_f = 2$ QM model.

2.4. Inhomogeneous (chiral) condensates

With this section we will conclude the methodological introductions of this chapter, by providing a concise introduction to inhomogeneous chiral condensates $\langle \bar{q}q \rangle(\vec{x})$. We will mainly focus on computational challenges, employed methods, and selected literature results of particular relevance for this work, *i.e.*, for chapters 4 and 5. This section is compiled from various Refs. [4, 5, 63, 208, 463–465], which informed our discussion here and have served as sources for most of the referenced publications.

A lot of studies in the field of theoretical high-energy physics of the phase structure of strongly interacting systems are based on the tacit assumption that the involved condensates – *i.e.*, mean-fields, expectation values, solutions for the QEOM/gap equation – do not vary in space \vec{x} and (Euclidean) time $(\tau) t$.

Before continuing with our discussion of inhomogeneous condensates, *viz.* condensates that vary only in space \vec{x} and not in (Euclidean) time $(\tau) t$, we want to comment on the explicit assumption of (Euclidean) time-independent condensates. The possibility of time-dependent condensates in the context of high-energy physics has been brought forward by Frank Wilczek and Alfred Shapere with their proposition of quantum and classical *time crystals* [466, 467] in 2012. The proposition of such time-dependent ground states for time-independent systems has sparked intensive research and scientific discourse, see, *e.g.*, the review [468] for an overview. Both real and imaginary time crystals have been considered and their relation and connection at non-zero temperature has been explored. Through the years a consensus has been reached, especially with important contributions in Refs. [469, 470], that such time crystals do not appear as energetically favored ground states of time-independent systems, *i.e.*, there is no spontaneous breaking of (Euclidean) time-translation invariance [468]. There is however still

quite intensive research, see, *e.g.*, Refs. [471–474], into such states in excited and especially externally driven systems. For our work however those scenarios are not relevant and we will limit our discussion to only spatially varying inhomogeneous condensates.

The general phenomenon of inhomogeneous phases/condensates in dense and strongly interacting systems is certainly not a new one. Especially in the field of solid-state physics inhomogeneous condensates – charge density waves – in superconductors related to the Peierls instability [475] are well known, with pioneering works by Peter Fulde and Richard A. Ferrell [476] (1964) as well as by Anatoly Larkin and Yuri Ovchinnikov [477] (1965), see, *e.g.*, the reviews [478–480] for further details on charge density waves. The idea of density waves in nuclear matter and pion condensation was already discussed in the 1960s and 1970s by Albert Overhauser, Arkadi B. Migdal, Francois Dautry, Ebbe M. Nyman, and others [481–484].

In the 1990s these concepts were first applied to quark matter by Wojciech Broniowski, Andrzej Kotlorz, Marek Kutschera, and others [83, 84, 485, 486] in their studies of chiral quark models. In the early 2000s there has been a lot of research of color superconducting (CSC) phases, see, *e.g.*, the reviews [59, 61], also including studies [487–492] of crystalline CSC phases. These findings triggered a renewed interest, see, *e.g.*, Refs. [193, 493–495], in inhomogeneous chiral condensates [63]. Also the interplay between CSC and chiral phases has been explored, see, *e.g.*, Refs. [337, 447–451].

Parallel studies [180–182, 197, 201, 496–508] in $(1+1)$ -dimensional chiral models, especially in the GN model [169], have firmly established inhomogeneous chiral condensates in such low-dimensional models in the mean-field/infinite- N limit. Inhomogeneous phases have also been shown to appear in imbalanced Fermi gases [509–513].

The aforementioned research efforts lead to the realization, see, *e.g.*, the review [63], that inhomogeneous chiral condensates $\langle \bar{q}q \rangle(\vec{x})$ are an important and rather robust feature in chiral models like the Nambu-Jona-Lasinio (NJL) model and quark-meson (QM) model. The predominantly mean-field and large- N_c computations and their findings in these models are in parts supported by some (in this context exploratory) FRG, DSEs, and weak-coupling studies of QCD and its LEFTs [80, 87, 485, 486, 514]. The phase structure of QCD – including the question of inhomogeneous chiral condensation – is still not fully understood at intermediate temperatures and densities, see chapter 1 and the previous section 2.3. We will present and discuss some of the relevant literature results for inhomogeneous chiral condensates in subsection 2.4.2.

In general it can however be noted, that it is an open question whether inhomogeneous chiral condensates exist beyond mean-field. It remains unclear whether, bosonic thermal and quantum fluctuations – which are neglected in mean-field and large- N_c computations – could destabilize inhomogeneous chiral condensates. These condensates are formed, in the first place, by thermodynamic fermionic fluctuations, *cf.* chapters 4 and 5.

Another question that arose with Refs. [202, 206, 515, 516] and related earlier works [517, 518], is whether and to what extent the appearance of inhomogeneous chiral condensates depends on regularization. In certain studies with a finite cutoff, the emergence of inhomogeneous chiral condensates has to be regarded as a cutoff artifact, rather than a physical phenomenon [202, 206, 515, 516]. This is why we choose to investigate inhomogeneous

phases in renormalizable models – GN model and QM model – in $d = 1+1$ and $d = 3+1$ in chapters 4 and 5. Especially in our MF studies of the QM model we elaborate on the role of cut-offs/UV initial scales and the importance of RG consistency in this context, *cf.* subsection 2.1.6 and section 5.2. Ultimately, the goal is to move away from model studies and instead focus on *QCD-assisted* LEFTs [80, 210, 308], as discussed in subsection 2.3.3.

2.4.1. Technical challenges and methods

The main technical challenge arising when studying inhomogeneous chiral condensates $\langle \bar{q}q \rangle(\vec{x})$, is the fact that the involved two-point functions manifest with explicit position-dependencies. In momentum space this translates to a non-diagonal, complicated coupling of different spatial momenta. One such explicit situation is discussed in chapter 5 for the CDW condensate (5.3) and the corresponding fermionic and bosonic two-point functions in Eqs. (5.7) and (5.8). Computations within QFT (especially functional and related approaches) usually involve the inversion of such two-point functions to compute propagators. This is simply not possible with standard techniques when inhomogeneous phases are involved due to the complicated coupling of different spatial momenta.

In the following we will list some of the methods that have been adapted or developed to study inhomogeneous phases. We distinguish between direct methods, which involve explicit computations with inhomogeneous condensates and indirect methods, which do not include such explicit computations. Examples of direct methods are:

- **Specialized analytic and semi-analytic methods** exist for certain models, truncations (usually large- N), and condensate shapes, allowing for direct computations. In the field of high-energy physics the most prominent examples of such methods are the studies [180–182, 197, 201, 496–508] in $1+1$ dimensions and computations using the CDW, like, *e.g.*, Refs. [83–86, 88, 193, 484–486, 514].
- **Lattice simulations** use a discretization of space-time in position space to tackle the problem by discretization, see, *e.g.*, Refs. [519–524] for recent results of this developing field.
- **Lattice field theory** uses the same discretization in position space but does not consider fluctuations beyond a saddle-point expansion, see, *e.g.*, Refs. [182, 204, 205, 525] for applications and details.
- **Mode expansions** are basically the momentum-space analog to lattice field theory, see, *e.g.*, Refs. [194, 463, 506] for applications and details.

Examples for indirect methods are:

- **A stability analysis** of the homogeneous ground state against inhomogeneous fluctuations is by far the most common indirect way to study inhomogeneous phases, see, *e.g.*, Refs. [5, 80, 87, 180, 182, 193–208].
- **Generalized Ginzburg-Landau/Gradient expansions** are closely related to the former but usually employ a simpler expansion approach, see, *e.g.*, Refs. [197, 493, 495, 526, 527].

We will comment and elaborate on these methods further especially in chapters 4 and 5. For a comprehensive overview we again refer to literature: Refs. [193, 495, 497, 505, 528] and the reviews [63, 88].

2.4.2. Literature results

In this subsection we want to present a very limited subset of the aforementioned results in form of relevant figures for this thesis.

First we present the original version [180] of the inhomogeneous phase diagram of the GN model in figure 2.15a. This result will be discussed at length in section 4.4 and has to be considered one of the most influential direct results.

We continue with a series of phase diagrams for the QM model with CDW condensates at infinite N_c . Figure 2.15b is the pioneering study [83] of Broniowski *et al.* and figures 2.16a and 2.16b from [86] are basically the current reference values for the standard mean-field diagram (disregarding vacuum fermionic vacuum fluctuation) and the completely renormalized QM model phase diagram including fermionic fluctuations completely. Figures 2.16a and 2.16b can at this point be considered conclusive results in the respective scenarios.

The last two sets of figures are the FRG results mentioned earlier which influenced the discussion in this thesis immensely. The negative values for the bosonic wave-function renormalization of figure 2.17, found in the phase diagram of QCD figure 2.13, signal the possibility for an instability of the homogeneous ground state against inhomogeneous condensation. The role of $Z < 0$ as an indicator for inhomogeneous phases is discussed in detail in subsection 4.4.2.

Figure 2.18 displays related results from a FRG based stability analysis of the QM model in LPA, with figure 2.18a showing clear indications for an instability towards inhomogeneous condensation during the FRG flow. Figure 2.18b marks a large region in the phase diagram where the pion two-point function develops such instability towards inhomogeneous condensation during the FRG flow. Whether or to what extent the instability at non-zero k persists or manifests in the IR limit ($k \rightarrow 0$) is not fully settled yet.

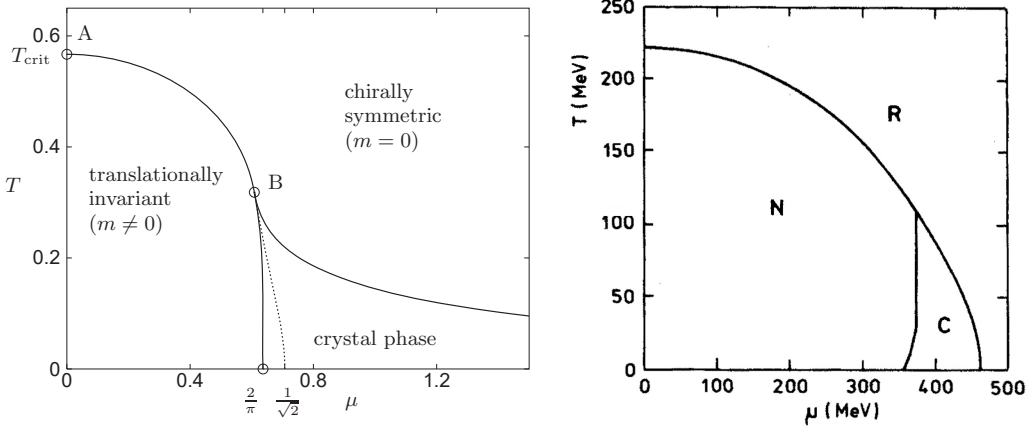


Figure 2.15.: Exact/semi-analytic result [180] for the inhomogeneous phase diagram of the GN model at infinite N in 1+1 dimensions on the left (a). Pioneering mean-field study [83] of the QM model allowing for CDW-type condensates, considering only fermionic vacuum fluctuations at large N_c on the right (b). The difference between this and the revised version in figure 2.16a, is that in the original work no in amplitude and wave vector-independent minimization was performed. Hence the correct inhomogeneous ground state is not found. Nevertheless, the impact of Ref. [83] in the study of inhomogeneous phases with the CDW is immense. Taken from the arXiv source for Fig. 8 of Ref. [180] and from the upper panel of Fig 8 of Ref. [83] but for the presentation here we flipped the axes in the latter using Photoshop CS6 [57]. Publication under CC BY-SA 4.0 license with the permission of M. Thies and W. Broniowski.

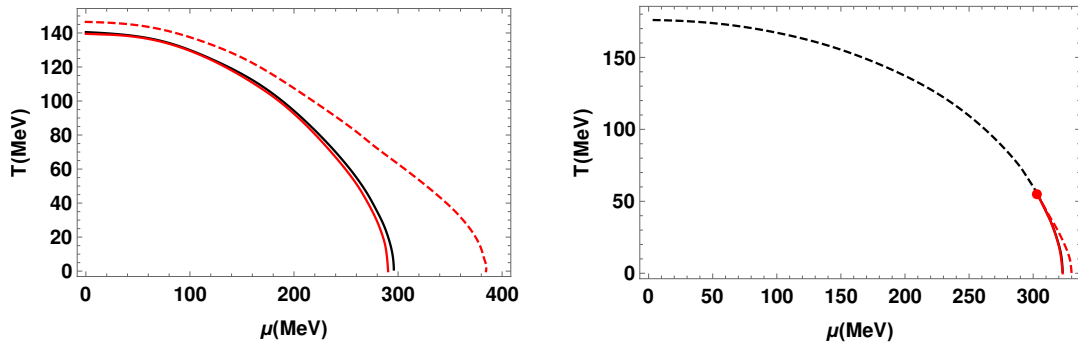


Figure 2.16.: Improved version [86] of figure 2.15b on the left (a): standard mean-field results for the QM model disregarding vacuum fluctuations. Renormalized mean-field result for the QM model on the right (b) including all fermionic fluctuations completely. The black lines are the homogeneous reference results, the red lines are the inhomogeneous computations, and the solid (dashed) lines mark first-(second-)order phase transitions. Taken from the arXiv source for Figs. 2 and 3 of Ref. [86]. Publication under CC BY-SA 4.0 license with the permission of J. O. Andersen.

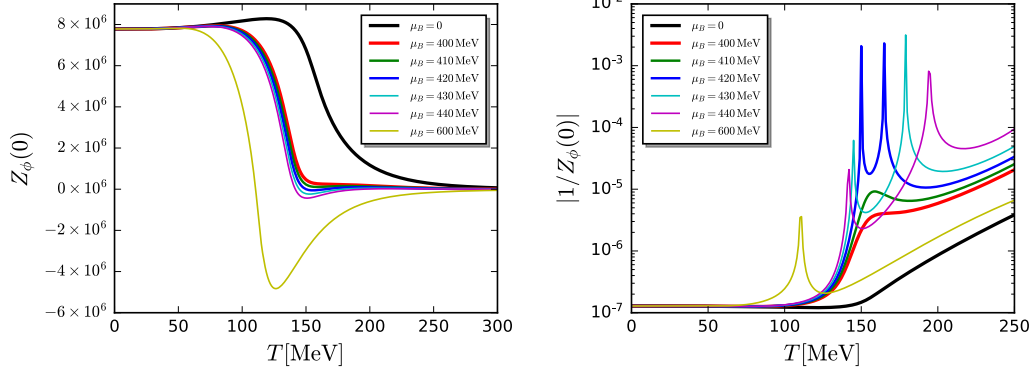


Figure 2.17.: Mesonic wave-function renormalization for the FRG QCD results discussed in the previous section, cf. figure 2.13a. Regions with $Z_\phi < 0$ signal the possibility for an instability of the homogeneous ground state against inhomogeneous condensation. The peaks around the roots of Z_ϕ clearly signal the boundaries of the corresponding (blue) region plotted in the phase diagram in figure 2.13a. The red hatched area in the latter is the region where “the inhomogeneous regime overlaps with a sizable homogeneous chiral condensate” Ref. [80]. Taken from the arXiv source for Fig. 12 of Ref. [80]. Publication under CC BY-SA 4.0 license with the permission of W.-j. Fu.

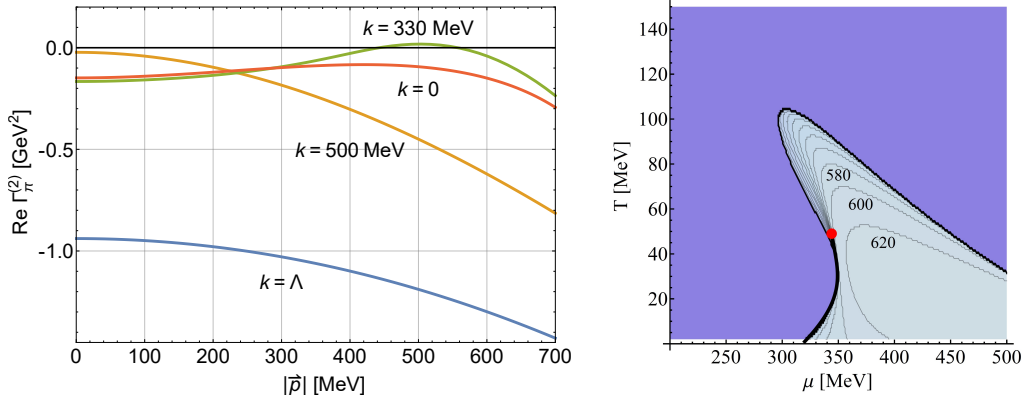


Figure 2.18.: Results [87] from an FRG stability analysis in LPA for the QM model. On the left (a) the static pion two-point function is shown for $\mu = 400$ MeV and $T = 15$ MeV at various RG scales k . The zero crossings at $k = 330$ MeV are attributed to an instability of the homogeneous phase. On the right (b) the region in the μ - T -plane is marked where and when during the FRG flow such an instability occurs. Taken from the arXiv sources for Fig. 5 and 6 of Ref. [87] but for the presentation here we changed the location of the axes labels in the latter using Photoshop CS6 [57]. Publication under CC BY-SA 4.0 license with the permission of R.-A. Tripolt.

3. Models in zero dimensions

Large parts of this chapter are based on Refs. [1–3, 7, 8]. The individual sections include more detailed disclaimers. The involved collaborators are A. Koenigstein, N. Wink, E. Grossi, J. Braun, M. Buballa, and D. H. Rischke.

Refs. [1–3] are published manuscripts and parts of a series discussing zero-dimensional $O(N)$ models in the context of the FRG. The discussed research is also part of the dissertation [165] of A. Koenigstein. Most symbolic calculations, all numerical computations, and the majority of these manuscripts have been prepared by A. Koenigstein and me in equal shares. The other co-authors have been primarily involved in the conceptualization, discussion, and the finishing of the manuscripts.

Ref. [7] is an unpublished manuscript draft, which has been planed as a continuation and supplement to the series on FRG in zero dimensions. Ref. [8] are unpublished notes on fixed-point solutions in the context of Ref. [2].

The following introduction of this chapter has been compiled from the introductions and abstracts of Refs. [1–3, 7].

We begin the main part of this thesis with the detailed discussion of our research regarding theories in zero space-time dimensions. As demonstrated beautifully by Jan Keitel and Lorenz Bartosch with their work [163] and by numerous other authors, see, e.g., Refs. [312, 529–549], zero-dimensional theories are by no means trivial. While it is true that they are easily solvable by just computing simple, ordinary integrals, their treatment within perturbative and non-perturbative methods employed in QFT is non-trivial. Applying the FRG, DSEs, nPI techniques, $\frac{1}{N}$ -expansion schemes, and/or perturbative methods to zero-dimensional theories can be very illuminating. Not only academic and didactic insights can be gained, but also deep conceptual and methodological developments are indeed possible with such studies.

As outlined in the introduction 1, the main purpose of the following discussions of this chapter is twofold.

1. Using zero-dimensional theories, we want to gain academic, didactic, and conceptual insight into the FRG framework.
2. Making use of the unique properties of QFTs in zero dimensions, we want to adapt and benchmark numerically stable methods for the solution of FRG flow equations.

To achieve these goals we will apply and adapt methods from the field of CFD, which we introduced in section 2.2, to the FRG, which we introduced in section 2.1.

Zero-dimensional QFTs are uniquely well suited for such discussions, since the functional flow equations encountered in the FRG manifest directly as PDEs in zero dimensions. It is possible to study the Wetterich Eq. (2.37) and the related flow Eqs. (2.87) and (2.88) for $W_k[\tilde{J}]$ and $Z_k[\tilde{J}]$ directly, *i.e.*, without the need of any truncations or approximations. The flow equations can be readily expressed as conservation laws, allowing for a direct adaptation of concepts and methods from the field of CFD to FRG. Applications in zero dimensions make the somewhat vague notion of functional flow equations explicit as flow equations for functions. This supports and extends on the findings [162] of Eduardo Grossi and Nicolas Wink and firmly establishes the very explicit notion of FRG flow equations as flow equations in a fluid-dynamical sense. The exact flow equations encountered in zero dimensions share many crucial qualitative and, to an extent, even quantitative features with flow equations encountered in non-zero dimensions. As such, our research and development in zero dimensions is far more than just an academic exercise, since it is very relevant and to a significant extent directly applicable in non-zero dimensions.

We begin this chapter with a detailed discussion of zero-dimensional QFT using the $O(1)$ model of a single scalar as an instructive example in section 3.1. We discuss general peculiarities of such QFTs in a single space-time point, but then shift focus especially on the manifestation of FRG in zero dimensions. The FRG can be understood very intuitively as an integral deformation – making the underlying idea of Wilson’s RG approach and the governing equations very tangible. We retrace the general derivation of the Wetterich Eq. (2.37) of section 2.1 in zero-dimensions commenting in detail on the involved subtleties. The fact that this discussion is based on functions and integrals instead of functionals and functional integrals allows for a simpler, but at the same time in many regards more concise discussion.

In section 3.2 we extend our discussion to zero-dimensional $O(N)$ models, where we allow for condensation in one radial direction leading to one massive σ -mode and $(N - 1)$ π -modes. We use this model to study $O(N)$ symmetry restoration, by studying the FRG flow for various initial conditions/actions. Basic symmetries of the underlying integrals prevent symmetry breaking in the IR in zero dimensions. This can be seen as an extreme limiting case of the Coleman-Mermin-Wagner-Hohenberg (CMWH) theorem [550–552], *cf.* App. B of Ref. [1].

We will discuss the FRG flow evolution equation for the zero-dimensional $O(N)$ model at length. Starting by casting it in conservative form, we continue to discuss initial conditions, boundary conditions, RG consistency, and irreversibility at length. The conservative formulation allows for an identification of the σ -mode as diffusive contribution and of the π -modes as advective contributions.

In subsection 3.2.3 we construct a series of test cases (initial conditions/actions) in the zero-dimensional $O(N)$ model at finite N . For our explicit numerical computations with the FRG flow equation, we adopt the KT scheme of subsection 2.2.2 as our finite volume method of choice. We discuss the advective and diffusive nature of FRG flows in detail using explicit numerical computations. The impact of initial scales in the context of RG consistency, boundary conditions, and discretization in field space is discussed at length. We also discuss the, as it turns out rather limited, applicability of the FRG Taylor expansion as a possible truncation scheme in zero dimensions.

After our discussions of various finite N results, we focus on the limiting cases $N = 1$ and $N \rightarrow \infty$ in subsection 3.2.4 and subsection 3.2.5 respectively. The focus of our discussion of the purely diffusive system at $N = 1$ is the irreversibility of (F)RG flows from a CFD perspective and the associated concept of (numerical) entropy. A connection between the later and the concept of \mathcal{C}/\mathcal{A} -functions is also discussed. At large N and ultimately in the limit $N \rightarrow \infty$ we study advection dominated and in the limit ultimately purely advective systems. The focus here are limitations of the large- N saddle-point approximation and related FRG/CFD concepts. For our discussion we construct yet another test case, which we study using both numeric and analytic methods. Shocks and rarefaction waves and their implications for the large- N limit are discussed, including again comments on the irreversibility of (F)RG flows in such scenarios.

In the penultimate section 3.3 of this chapter we discuss Grassmann numbers as zero-dimensional analogs to fermions. We present a $SU(2)$ model including two pairs of associated Grassmann numbers and three scalars, which we constructed as a zero-dimensional analog to the QM model. We discuss the model and the involved flow equations and comment at length on our plans for further research with such theories. Compared to our, for the most parts, complete discussion of scalars in zero-dimensions, this work on Grassmann numbers is in a very early state.

In section 3.4 we summarize our key research results of our extensive studies in zero dimensions and give an outlook for even further research with zero-dimensional QFTs. Especially zero-dimensional models involving Grassmann numbers are identified as a very interesting and relevant area for further research.

3.1. Quantum ~~field~~ theory in zero dimensions

This section follows the discussion presented in Sec. II of Ref. [1].

This section provides an introduction to zero-dimensional QFT using the theory of a single scalar as an instructive example. We will focus on details and structure of the flow equations and the technical subtleties in their solution in zero dimensions thus without any direct reference to regularization and renormalization. In addition we use this introduction to establish some notation and special features of zero-dimensional field theory.

As already mentioned in the introduction to this chapter, the efficient and sufficiently precise calculation of correlation functions is key to understanding the properties of a particular model or theory. Usually this is done by introducing a partition function or functional integral that provides a probability distribution for the microstates of the model and serves as a generating functional for the n -point (correlation) functions [177, 178, 240, 553]. The partition function is based on an energy function that can be a discrete or continuous Hamilton function or an action, which determines the microscopic properties of the model, cf. Eq. (2.4). The FRG provides an alternative to a direct computation using the functional integral. For generic QFTs we introduced this approach in section 2.1 but in this section we want to focus on the special

case of a zero-dimensional QFT of a single scalar. We will discuss the direct computation of observables using the generating functional and the alternative approach using the FRG flow equation.

3.1.1. The partition function

Consider a zero-dimensional QFT with a single real bosonic scalar field ϕ ³⁵. In zero dimensions the “field” ϕ is due to the complete absence of a notion of space-time in zero dimensions mathematically not a field but just a single scalar degree of freedom, *i.e.*, a plain real number – hence the typographic pun with striking out the word *field* in the title of this section. In our following discussion we will however maintain the term field even though mathematically we are just discussing numbers. Due to the absence of space-time in zero dimensions derivatives and space-time integrals simply do not exist. This implies that the action $\mathcal{S}[\phi]$ of the model is identical to the Lagrangian $\mathcal{L}[\phi]$. The action, the Lagrangian, and also the Hamiltonian $\mathcal{H}[\phi]$ are simply functions of ϕ instead of functionals³⁶. The complete absence of space-time derivatives/integrals, fields, and functionals makes the following discussion mathematically rather simple in stark contrast to the situation encountered by QFT practitioners in $d > 0$: where dealing with potentially divergent space-time integrals and complicated functional integrals is the norm. This simplicity is the beauty of zero-dimensional QFTs which are by no means trivial: a lot can be learned from their study. Because of the absence of a space-time derivative and thus of kinetic terms, $\mathcal{S}[\phi] = \mathcal{L}[\phi] = \mathcal{H}[\phi] = U(\phi)$, where $U(\phi)$ is the (effective) potential. Therefore, the only requirement for these functions is that they must be bounded from below, in order to exclude “negative-energy states”³⁷ and to obtain positive normalizable probability distributions. Apart from this requirement, for the moment we do not demand any additional properties, like symmetries (*e.g.*, \mathbb{Z}_2 , $\phi \rightarrow -\phi$) or analyticity.

If we choose a specific model with action $\mathcal{S}[\phi]$ all expectation values of arbitrary functions $f(\phi)$ that do not grow exponentially in ϕ are defined and can be calculated via the following expression

$$\langle f(\phi) \rangle \equiv \frac{\int_{-\infty}^{+\infty} d\phi f(\phi) e^{-\mathcal{S}[\phi]}}{\int_{-\infty}^{+\infty} d\phi e^{-\mathcal{S}[\phi]}}, \quad (3.1)$$

where $e^{-\mathcal{S}[\phi]}$ provides the partition of probabilities among the microstates. Note that due to the zero-dimensional nature all expectation values for such a model reduce to indefinite one-dimensional integrals over ϕ . Such integrals can be computed to extremely high precision

³⁵Throughout this chapter we will use ϕ denote a fluctuating scalar (not $\tilde{\phi}$) since we will use φ for the expectation value $\langle \phi \rangle = \varphi$. Later in section 3.3, we will also introduce θ and $\bar{\theta}$ as fluctuating Grassmann numbers with the corresponding expectation values $\langle \theta \rangle = \vartheta$ and $\langle \bar{\theta} \rangle = \bar{\vartheta}$. Sadly variant versions are not available for all Greek characters, which led us to introduce the tilde-overline in our general discussion of section 2.1.

³⁶Nevertheless, we will stick to the notation of functionals using square brackets, to maintain a degree of consistency with the corresponding expressions in non-zero space-time dimensions, as long as we do not focus on particular zero-dimensional examples.

³⁷We put “negative-energy states” in quotation marks, because all quantities in zero-dimensional field theory are dimensionless, *viz.* bare numbers without physical dimensions. For convenience, we will still use the well-established notions from higher-dimensional QFTs in our discussion.

using standard techniques of numerical integration [554, 555]. It is worth emphasizing that the current discussion holds also for non-analytic $\mathcal{S}[\phi]$ and/or $f(\phi)$. Some specific choices of $\mathcal{S}[\phi]$ and $f(\phi)$ even allow for an analytic evaluation of Eq. (3.1), see, e.g., Ref. [163]. The possibility to compute expectation values to high precision makes zero-dimensional field theory of great interest as a testing ground for approximations and/or numerical methods.

Some explicit examples of zero-dimensional field theories used as a testing ground for methods in statistical mechanics and QFT can be found in Refs. [163, 312, 529–549]. In Ref. [538], for example, the asymptotic convergence and the vanishing convergence radius of perturbation theory of ϕ^4 -theory is discussed. Approximation schemes such as the large- N , the FRG vertex expansion, or the FRG Taylor expansion were analyzed in Ref. [163]. Zero-dimensional field theory was also used to study density-functional theory in Refs. [537, 540, 542] and applied to fermionic fields in Ref. [312]. Recently, it was used to study and visualize 2PI effective actions [544] – also in the FRG framework [545, 546, 549].

The calculation of expectation values is facilitated by a suitably defined generating functional

$$\mathcal{Z}[J] \equiv \mathcal{N} \int_{-\infty}^{+\infty} d\phi e^{-\mathcal{S}[\phi]+J\phi}, \quad (3.2)$$

from which one can derive all correlation functions by taking the corresponding number of derivatives w.r.t. the external source J ,

$$\langle f(\phi) \rangle = \left. \frac{f\left(\frac{\delta}{\delta J}\right) \mathcal{Z}[J]}{\mathcal{Z}[J]} \right|_{J=0}. \quad (3.3)$$

One should note that if $f(\phi)$ is non-analytic, then Eq. (3.3) is to be understood symbolically. Otherwise, it is defined through a Taylor series in $\frac{\delta}{\delta J}$. Irrespective of that, Eq. (3.1) and (3.2) are always well defined and Eq. (3.2) can be always calculated for arbitrary J . One can even show in zero dimensions that $\mathcal{Z}[J] \in C^\infty$, hence, $\mathcal{Z}[J]$ is a smooth function, see Ref. [536] and App. B of Ref. [1].

The normalization \mathcal{N} is not an observable quantity and for our discussion here, it is convenient to choose

$$\mathcal{Z}[0] \stackrel{!}{=} 1 \quad \longleftrightarrow \quad \mathcal{N}^{-1} = \int_{-\infty}^{+\infty} d\phi e^{-\mathcal{S}[\phi]}. \quad (3.4)$$

As already mentioned above, calculating expectation values in a zero-dimensional QFT via Eq. (3.1) is (at the very least numerically) rather straightforward. In contrast, for higher-dimensional models or theories with non-trivial field content, calculating functional integrals similar to Eq. (3.1), cf. Eq. (2.5), with sufficient precision is usually extremely challenging or might even be impossible with limited computational resources. Therefore, alternative methods like the FRG or approximation schemes apart from “direct numerical integration”, like in lattice simulations, are of great interest.

In the following, we will again focus on the FRG as a specific method for calculating n -point functions in zero-dimensional QFTs. In contrast to the usual motivation of the FRG, cf. the introduction of section 2.1, we will use a different but as it turns out closely related approach

to motivate and ultimately arrive at the FRG flow equation (3.36) in zero-dimensions. To this end, we will follow and extend the discussion in Refs. [163, 312, 535, 536, 539] and discuss its technical properties as an alternative way of solving the integrals in Eq. (3.1) and (3.2).

3.1.2. Solving integrals with flow equations

The starting point of our following discussion, is the observation that there is one well-known non-trivial class of actions $\mathcal{S}[\phi]$ for which the calculation of integrals like Eq. (3.1) is straightforward, even in higher dimensions and even for more complicated field content. These actions are QFTs for “(massive) free particles” and correspond to Gaussian-type integrals. In the present case the Gaussian-type action takes the following simple form,

$$\mathcal{S}[\phi] = \frac{m^2}{2} \phi^2. \quad (3.5)$$

where m is called a “mass” for convenience, although it is actually a dimensionless quantity in zero space-time dimensions.

For non-trivial actions $\mathcal{S}[\phi]$, Eq. (3.1) can still be approximated by a Gaussian integral, as long as $\mathcal{S}[\phi]$ contains a mass term (3.5) with a coefficient m^2 that is much larger than all other scales contained in $\mathcal{S}[\phi]$. If this is the case, the Gaussian part of the integrand $e^{-\mathcal{S}[\phi]}$ completely dominates the integrals in Eq. (3.1) and (3.2). The reason is that the mass term $\sim \phi^2$ is dominant for small and moderate ϕ , and most of the area under the curve $e^{-\mathcal{S}[\phi]}$ lies in the region of small ϕ , similar to a pure Gaussian integral. For very large values of ϕ other terms in the action $\mathcal{S}[\phi]$ may become more important. Nevertheless, if m^2 is large enough, the corresponding area under the curve $e^{-\mathcal{S}[\phi]}$ is completely negligible in regions where ϕ is large, because $\mathcal{S}[\phi]$ is bounded from below such that $e^{-\mathcal{S}[\phi]}$ tends to zero exponentially fast for $\phi \rightarrow \infty$. In summary, the Gaussian part with the huge mass term dominates the integral and even integrals involving non-trivial actions can be approximated. This is illustrated in figure 3.1.

3.1.2.1. The scale-dependent partition function

Based on the above observation, let us now (re)introduce the following quantity:

$$\mathcal{Z}_t[J] \equiv \mathcal{N} \int_{-\infty}^{+\infty} d\phi e^{-\mathcal{S}[\phi] - \Delta\mathcal{S}_t[\phi] + J\phi}, \quad (3.6)$$

which is called the *scale-dependent generating functional* or *scale-dependent partition function*. It differs from the usual partition function (3.2) only by a scale-dependent mass term

$$\Delta\mathcal{S}_t[\phi] \equiv \frac{1}{2} r(t) \phi^2. \quad (3.7)$$

We directly adopt the common notation from the FRG community and call $r(t)$ the *regulator (shape) function*, which depends on the RG scale (“time”) $t \in [0, \infty)$, see, e.g., Refs. [256, 259]. We have now constructed the zero-dimensional analog to the RG-scale-dependent generating functional (2.4) purely based on the notion of an integral deformation. For now, we only

demand that the function $r(t)$ has such properties that $\mathcal{Z}_t[J]$ interpolates between an almost Gaussian-type partition function³⁸ with extremely massive free fields at $t = 0$ and the actual partition function $\mathcal{Z}[J]$ of interest at $t \rightarrow \infty$. In order to achieve this behavior, $r(t)$ has to have the following properties:

1. In the limit of $t \rightarrow 0$, $r(t)$ ($\Delta\mathcal{S}_t[\phi]$) should behave like a mass (term), similar to what we discussed at the beginning of this section, and be much larger than all other scales in $\mathcal{S}[\phi]$. We will discuss this further in subsection 3.1.3.
2. For $t \rightarrow \infty$, $r(t)$ is supposed to vanish, such that $\lim_{t \rightarrow \infty} \mathcal{Z}_t[J] = \mathcal{Z}[J]$. The same applies to expectation values calculated from $\mathcal{Z}_t[J]$, which become expectation values of $\mathcal{Z}[J]$. For practical calculations it is sufficient to assume that, for $t \rightarrow \infty$, $r(t)$ becomes much smaller than all scales in $\mathcal{S}[\phi]$, because then the contribution $\Delta\mathcal{S}_t[\phi]$ to the whole integrand $e^{-\mathcal{S}[\phi] - \Delta\mathcal{S}_t[\phi]}$ is negligible and the integrand is almost identical to $e^{-\mathcal{S}[\phi]}$. The value $\lim_{t \rightarrow \infty} r(t) = r_{\text{IR}} \gtrsim 0$ is usually referred to as (*numerical*) *IR cutoff*.
3. The interpretation of $r(t)$ ($\Delta\mathcal{S}_t[\phi]$) as a mass (term) is guaranteed by further demanding monotonicity, $\forall t, \partial_t r(t) \leq 0$. We will provide additional arguments for monotonicity in subsubsection 3.1.2.2.
4. In order to be able to smoothly deform the integral in Eq. (3.2) and for the following derivation of evolution equations, we further require $r(t) \in C^1$.

Apart from these four properties there are no further requirements on $r(t)$ in zero dimensions and ultimately the regulator choice in zero-dimensions manifests as simple reparametrizations in the flow time t . The first (UV) property is the zero-dimensional realization of general regulator property 3. *Diverging in the Ultraviolet* of subsubsection 2.1.4.1. The second (IR) property is the zero-dimensional realization of general regulator property 2. *Vanishing for high momentum modes* of subsubsection 2.1.4.1. Note that for higher-dimensional field theories the fourth requirement turns into $\Delta\mathcal{S}_t[\phi] \in C^1$. A specific choice which is used in large parts of our work is the zero-dimensional exponential regulator (shape) function

$$r(t) = \Lambda e^{-t}, \quad (3.8)$$

with an UV cutoff/scale Λ , which must be chosen much larger than all scales in $\mathcal{S}[\phi]$.

In order to get a better intuition of the effect of $r(t)$ on the integral (3.6), we show the integrand at $J = 0$, $e^{-\mathcal{S}[\phi] - \Delta\mathcal{S}_t[\phi]}$, and the respective exponent for different values of t for the analytic action

$$\mathcal{S}(\phi) = -\frac{1}{2}\phi^2 + \frac{1}{4!}\phi^4, \quad (3.9)$$

in figure 3.1a and in figure 3.1b the same quantities for the non-analytic action

$$\mathcal{S}(\phi) = \begin{cases} -\phi^2, & \text{if } |\phi| \leq \frac{5}{4}, \\ -\left(\frac{5}{4}\right)^2, & \text{if } \frac{5}{4} < |\phi| \leq 2, \\ \frac{1}{48}, (\phi^4 - 91) & \text{if } |\phi| > 2. \end{cases} \quad (3.10)$$

³⁸This is also why the UV fixed point of (F)RG flows is denoted as the *trivial* or *Gaussian fixed point*.

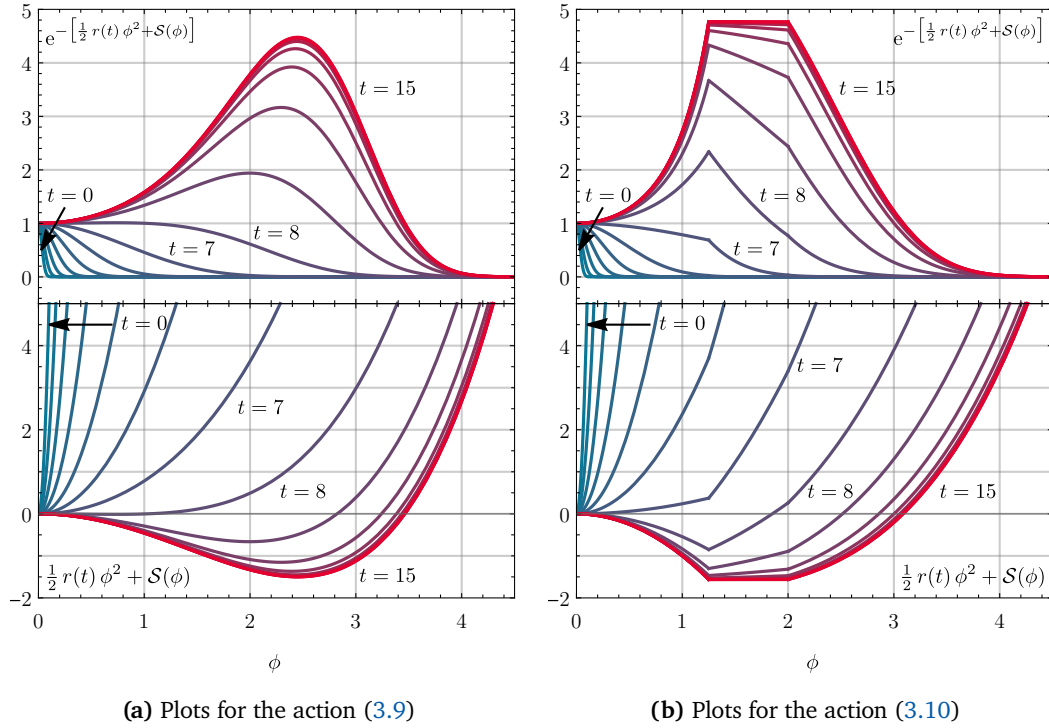


Figure 3.1.: The integrand (upper panel) and exponent (lower panel) from Eq. (3.6) (at $J = 0$) as a function of the field variable ϕ for various RG times $t = 0, 1, 2, \dots, 15$ and for different actions on the left (a) and on the right (b). We choose the exponential regulator (3.8) with UV scale $\Lambda = 10^3$. The IR cutoff scale is chosen at $r_{\text{IR}} \simeq 3.06 \cdot 10^{-4}$ which corresponds to $t = 15$. The numerical value of r_{IR} is significantly smaller than all scales in $\mathcal{S}[\phi]$. From Figs. 1 and 2 of Ref. [1].

The figures show how the integrands are deformed from Gaussian-shaped integrands to the integrands $e^{-\mathcal{S}[\phi]}$. One observes that, as long as $r(t)$ is much larger than all other parameters in $\mathcal{S}[\phi]$, the Gaussian-like mass term dominates, while for increasing t the regulator $r(t)$ becomes negligible. The most interesting part, where the integrands change their shapes significantly, is where $r(t)$ is of the same order as the scales in $\mathcal{S}(\phi)$.

3.1.2.2. A flow equation for the scale-dependent partition function

The change of the integrals with t between the two limiting cases at $t = 0$ and $t \rightarrow \infty$ is the in section 2.1 established *FRG flow* from the UV to the IR. By knowing/mathematically prescribing the integral deformation, we can obtain the function $\mathcal{Z}(J) \equiv \lim_{t \rightarrow \infty} \mathcal{Z}_t[J] = \mathcal{Z}[J]$ right from the Gaussian-like partition function $\mathcal{Z}_{t=0}[J]$ without the need to calculate the ϕ -integral in the partition function (3.2) directly. In zero dimensions this might arguably be one of the most complicated ways to compute the partition function (3.2), because the integrals in field space are (at least numerically) simple to compute. For higher dimensions, however, circumventing

the corresponding challenging functional integration is a tremendous benefit.

The FRG flow of $\mathcal{Z}_t[J]$, *i.e.*, its deformation, is prescribed by a differential equation which can be obtained by taking the derivative w.r.t. the RG time t of Eq. (3.6):

$$\partial_t \mathcal{Z}_t[J] = - \left[\frac{1}{2} \partial_t r(t) \right] \mathcal{N} \int_{-\infty}^{+\infty} d\phi \phi^2 e^{-\mathcal{S}[\phi] - \Delta \mathcal{S}[\phi] + J\phi} = \quad (3.11a)$$

$$= - \left[\frac{1}{2} \partial_t r(t) \right] \frac{\delta^2 \mathcal{Z}_t[J]}{\delta J \delta J} \equiv - \left[\frac{1}{2} \partial_t r(t) \right] \mathcal{Z}_{t,JJ}^{(2)}[J], \quad (3.11b)$$

which directly manifests as a simple PDE for the function $\mathcal{Z}(t, J)$ in the t - J -plane,

$$\partial_t \mathcal{Z}(t, J) = - \left[\frac{1}{2} \partial_t r(t) \right] \partial_J^2 \mathcal{Z}(t, J). \quad (3.12)$$

Solving this equation with appropriate initial and boundary conditions results in a function $\mathcal{Z}(J)$ from which one can calculate expectation values by taking ordinary (numerical) derivatives w.r.t. J at $J = 0$, *cf.* Eq. (3.3).

The higher-dimensional analog to Eq. (3.12) is Eq. (2.87) and thus we again recognize Eq. (3.12) as a linear one-dimensional diffusion equation (*heat equation*) [230, 312–314], where t corresponds to the temporal direction, while J corresponds to the spatial direction. We discussed this type of conservation equation in detail in subsection 2.2.4. The term $-\frac{1}{2} \partial_t r(t)$ corresponds to a time-dependent (positive definite) diffusion coefficient³⁹. This further supports the notion of RG “time” for the parameter t . We will come back to the concept of RG “time” in the true sense of the word and the diffusive, irreversible character of FRG flows in subsection 3.2.2.3.

For the remainder of this subsection we will discuss properties and practical issues considering the exact PDE (3.12). We will neither discuss any kind of expansions in J nor its application in higher dimensions here. However, some of the issues and questions raised in the following are also relevant for higher-dimensional theories.

Finding the correct initial and boundary conditions for numerical solutions of Eq. (3.12) as an exact PDE is challenging. By construction $\mathcal{Z}_{t=0}[J]$ approaches a Gaussian integral,

$$\mathcal{Z}_{t=0}[J] = \mathcal{N} \int_{-\infty}^{+\infty} d\phi e^{-\frac{1}{2}r(0)\phi^2 + J\phi} e^{-\mathcal{S}(\phi)} = \quad (3.13a)$$

$$= \mathcal{N} \int_{-\infty}^{+\infty} \frac{d\tilde{\phi}}{\sqrt{r(0)}} e^{-\frac{1}{2}\tilde{\phi}^2 + J\frac{\tilde{\phi}}{\sqrt{r(0)}}} \left[1 - \mathcal{O}(\mathcal{S}(r(0)^{-\frac{1}{2}})) \right] = \quad (3.13b)$$

$$= \mathcal{N} \sqrt{\frac{2\pi}{r(0)}} e^{\frac{J^2}{2r(0)}} \left[1 - \mathcal{O}(\mathcal{S}(r(0)^{-\frac{1}{2}})) \right], \quad (3.14)$$

³⁹Note that in zero dimensions one can get rid of $\partial_t r(t)$ by an appropriate reparametrization of the time coordinate t , which nevertheless keeps the structure of the equation unchanged. In higher dimensions this elimination of $r(t)$ is in general not possible. The positivity of the diffusion coefficient is directly related to the stability of solutions of the heat equation [315, 317] and positivity – here guaranteed by the regulator properties – is necessary for a stable solution [230, 261].

with $\tilde{\phi} \equiv \sqrt{r(0)} \phi$ and independent of the explicit shape of $\mathcal{S}[\phi]$. Considering different actions $\mathcal{S}[\phi]$ with couplings of the same order of magnitude we can choose the same regulator with an $r(0)$ larger than all internal scales involved in the different actions. The IC $\mathcal{Z}(0, J)$ is then independent of the explicit action under consideration.

According to the integral formulation (3.6), $\mathcal{Z}(t, J)$ changes for different actions when $t > 0$. In the differential formulation of the Eq. (3.12) those changes are generated by the diffusion term on the r.h.s. However, we argued that it is permissible to use identical ICs $\mathcal{Z}(0, J)$ for different actions involving similar scales (as long as these are much smaller than $r(0)$). This then results in an identical diffusion on the r.h.s. of Eq. (3.12) when the latter is computed by means of a second derivative of $\mathcal{Z}(0, J)$. If one uses identical large- J BCs for the solution of the PDE (3.12) for different actions, this would imply that, despite different $\mathcal{S}[\phi]$, the RG time evolution leads to identical $\mathcal{Z}(J)$ for $t \rightarrow \infty$, which in general cannot be correct.

In order to resolve this problem, particular action-dependent spatial BCs seem to be necessary for a direct numerical solution starting at $t = 0$ with a Gaussian for $\mathcal{Z}(0, J)$. It is not obvious how to derive or formulate such BCs from the asymptotics of Eq. (3.12) alone. In light of this, a numerical solution of Eq. (3.12) in the t - J -plane by means of a spatial discretization in J -direction and an integration in t -direction in the spirit of subsection 2.2.4 appears to be conceptually questionable.

However, this invalidates by no means the flow equation for $\mathcal{Z}(t, J)$ in general. Augmenting it (at $t = 0$) with information from the integral formulation (3.6) or, equivalently, other additional information, could enable practical computations using the PDE (3.12). But it is at this point (at least to us) not obvious how one would implement a numerical solution strategy for the PDE (3.12) avoiding integrals of the action.

There is another well-known drawback in using the partition function $\mathcal{Z}[J]$ for calculating n -point functions (or expectation values) $\langle \phi^n \rangle$. The latter are rather inefficient in storing information, because they contain redundant information in the form of disconnected and reducible terms, see Refs. [177, 178, 239, 240] or the mathematical theory of moment- and cumulant-generating functionals in statistics for details [556]. This is also discussed in Sec. II.E of Ref. [1]. However, the redundant information in $\langle \phi^n \rangle$ is not necessarily a strong argument against the use of the flow equation (3.12) in practical computations, since the irreducible information can be extracted from the correlation functions $\langle \phi^n \rangle$.

3.1.3. The functional renormalization group equation

To resolve both the problem of initial and BCs for $\mathcal{Z}(t, J)$ as well as the issue of redundant information in $\langle \phi^n \rangle$, we now consider two different generating functionals the *scale-dependent Schwinger functional* in subsection 3.1.3.1 and the *scale-dependent effective action* in subsection 3.1.3.2. Especially the latter will turn out to be much better suited for practical calculations of correlation functions/expectation values. In this subsection we will derive and discuss the FRG flow Eq. (3.36) for our zero-dimensional toy model QFT by subsequently (re)discovering the zero-dimensional analogs to the general expressions of section 2.1.

3.1.3.1. The scale-dependent Schwinger functional

We begin our journey towards the FRG flow Eq. (3.36) by introducing the *scale-dependent Schwinger functional* starting from definition (3.6),

$$\mathcal{W}_t[J] \equiv \ln \mathcal{Z}_t[J], \quad (3.15)$$

in direct analogy to Eq. (2.10). It follows from our previous discussion that for $t \rightarrow \infty$ the Schwinger functional $\mathcal{W}[J] \equiv \ln \mathcal{Z}[J]$ with $\mathcal{W}[0] = 0$ is recovered,

$$\lim_{t \rightarrow \infty} \mathcal{W}_t[J] = \mathcal{W}[J], \quad (3.16)$$

while $\mathcal{W}_{t=0}[J]$ is given by the logarithm of Eq. (3.14).

In general $\mathcal{W}[J]$ is convex with a positive definite Hessian $\mathcal{W}_{JJ}^{(2)}[J]$. In the present case the convexity of $\mathcal{W}[J] = \mathcal{W}(J)$ becomes apparent considering its second derivative,

$$\partial_J^2 \mathcal{W}(J) = \langle \phi^2 \rangle_J - \langle \phi \rangle_J \langle \phi \rangle_J = \langle (\phi - \langle \phi \rangle_J)^2 \rangle_J, \quad (3.17)$$

which, as the expectation value of a positive quantity, is always positive. Note that also $\mathcal{Z}[J]$ is convex, which can be seen by investigating its second derivative. In zero dimensions, also smoothness, *i.e.*, $\mathcal{Z}[J] \in C^\infty$, directly translates to $\mathcal{W}[J] \in C^\infty$, because all moments of $\mathcal{W}[J]$ can be entirely expressed in terms of derivatives of $\mathcal{Z}[J]$, see Sec. II.E of Ref. [1] for explicit expressions. The insertion of the regulator (3.7) into $\mathcal{Z}_t[J]$ does not spoil the convexity and smoothness (in zero dimensions) of the Schwinger functional: $\mathcal{W}_t[J]$ and $\mathcal{Z}_t[J]$ are convex and smooth for all t .

Completely analogous to Eq. (3.11) one can derive a PDE for $\mathcal{W}_t[J] = \mathcal{W}(t, J)$ in the t - J -plane,

$$\partial_t \mathcal{W}(t, J) = -\left[\frac{1}{2} \partial_t r(t)\right] \left(\partial_J^2 \mathcal{W}(t, J) + [\partial_J \mathcal{W}(t, J)]^2\right). \quad (3.18)$$

which describes the flow of $\mathcal{W}(t, J)$ from $t = 0$ to $t \rightarrow \infty$. We have recovered the zero-dimensional analog to Eq. (2.88).

We could now repeat the discussion about the issues of initial and boundary conditions for the solution of this PDE. However, the problems are almost identical to those of Eq. (3.12), because on the level of the PDE, we only substituted the function $\mathcal{Z}(t, J)$ by $\mathcal{W}(t, J)$ via the logarithm, which does not change the structure of the problem fundamentally. Formulating appropriate initial and boundary conditions in the spatial J -direction therefore remains as complicated as before. Note that the PDE (3.18) is even more complicated when compared to Eq. (3.12) due to the non-linear term on the right-hand side. In summary, the scale-dependent Schwinger functional is, from a practical point of view, as badly suited as $\mathcal{Z}(t, J)$ to perform the (numeric) calculation of the functional integral via a flow equation starting from a Gaussian-type integral.

3.1.3.2. The scale-dependent effective action

In the following we will focus on the scale-dependent effective (average) action and its respective flow equation. We define the *scale-dependent effective action* $\Gamma_t[\varphi]$ via the Legendre transform

of Eq. (3.15) w.r.t. the sources J at a RG time t ,

$$\Gamma_t[\varphi] \equiv \sup_J (J\varphi - \mathcal{W}_t[J]), \quad (3.19a)$$

$$\equiv J_t(\varphi)\varphi - \mathcal{W}_t[J_t(\varphi)], \quad (3.19b)$$

where we introduced the source $J_t(\varphi)$ which realizes the supremum. Note that, analogous to $\mathcal{Z}_t[J]$ and $\mathcal{W}_t[J]$, the convexity and smoothness (in zero dimensions) of $\Gamma_t[\varphi]$ is not spoiled by the t -dependence, because the properties of the Legendre transformation still ensure both, since the Legendre transform of the convex function $\mathcal{W}_t[J]$ is convex by definition, see, *e.g.*, Refs. [557, 558] for details.

To obtain an explicit relation for the scale-dependent source $J_t(\varphi)$, which realizes the supremum in Eq. (3.19a), we consider the functional derivative of Eq. (3.19a) at the supremum to find the important relation

$$\mathcal{W}_{t,J}^{(1)}[J_t(\varphi)] \equiv \left. \frac{\delta \mathcal{W}_t[J]}{\delta J} \right|_{J=J_t(\varphi)} = \varphi, \quad (3.20)$$

which will be used frequently in the following. Taking the functional derivative of Eq. (3.19b) w.r.t. φ and using Eq. (3.20) we ultimately rediscover the *quantum equation of motion* in zero-dimensions:

$$\Gamma_{t,\varphi}^{(1)}[\varphi] \equiv \frac{\delta \Gamma_t[\varphi]}{\delta \varphi} = J_t(\varphi), \quad (3.21)$$

as a special simplification of the general analog (2.20). Due to the strict convexity of $\Gamma_t[\varphi]$ the function $J_t(\varphi)$ is bijective and as such can be inverted, which can be achieved by considering Eq. (3.20) at fixed value J for J_t :

$$\varphi_t(J) \equiv \frac{\delta \mathcal{W}_t[J]}{\delta J}, \quad (3.22)$$

where $\varphi_t(J)$ is the so-called *scale-dependent classical field* (sometimes also referred to as *scale-dependent mean-field*), *cf.* Eq. (2.18).

The subtle relations between, and scale-dependencies of, $\varphi_t(J)$ and $J_t(\varphi)$ on this formal level are rarely discussed in literature and usually suppressed in the notation. The relation between φ_t and J_t is of particular importance for discussion and relations between of n -point correlation functions, see, *e.g.*, Sec. II.E of Ref. [1]. The scale-dependence of $\varphi_t(J)$ from Eq. (3.22) is not related to a rescaling (RG transformation) using, *e.g.*, a wave-function renormalization for φ , *cf.* Eq. (2.34) and the corresponding discussion.

IC and the UV limit $t \rightarrow 0$

Before we reintroduce the Wetterich equation, which is the flow equation for $\Gamma_t[\varphi]$ and a PDE for the function $\Gamma(t, \varphi)$ in the t - φ -plane, we check whether we will run into the same issues (related to initial and boundary conditions) as before. Hence, first of all, we must derive

the IC for the PDE for $\Gamma(t, \varphi)$. To this end, we study the limit $t \rightarrow 0$ of $\Gamma_t[\varphi]$. We use the definitions (3.6), (3.15), (3.19a), and (3.19b) to obtain

$$e^{-\Gamma_t[\varphi]} = e^{-\sup_J (J\varphi - \mathcal{W}_t[J])} = e^{\ln \mathcal{Z}_t[J_t(\varphi)] - J_t(\varphi)\varphi} = \quad (3.23a)$$

$$= \mathcal{N} \int_{-\infty}^{+\infty} d\phi e^{-S[\phi] - \Delta \mathcal{S}_t[\phi] + J_t(\varphi)(\phi - \varphi)}. \quad (3.23b)$$

We now shift the integration variable⁴⁰ $\phi \mapsto \phi' = \phi - \varphi$. Using Eq. (3.7), we find

$$e^{-\Gamma_t[\varphi] + \Delta \mathcal{S}_t[\varphi]} = \mathcal{N} \int_{-\infty}^{+\infty} d\phi' e^{-S[\phi' + \varphi] - \Delta \mathcal{S}_t[\phi'] - r(t)\phi'\varphi + \Gamma_{t,\varphi}^{(1)}[\varphi]\phi'}. \quad (3.24)$$

In the next step, we reintroduce the *scale-dependent effective average action*,

$$\bar{\Gamma}_t[\varphi] \equiv \Gamma_t[\varphi] - \Delta \mathcal{S}_t[\varphi], \quad (3.25)$$

which also tends to the effective action $\Gamma[\varphi]$ for $t \rightarrow \infty$, because the second term vanishes in this limit, cf. Eq. (3.8).

At any finite value of t (including $t = 0$), $\bar{\Gamma}_t[\varphi]$ differs from $\Gamma_t[\varphi]$ and is no longer guaranteed to be convex, which can be seen directly from the second term in Eq. (3.25). Convexity is only recovered for $t \rightarrow \infty$. However, the second term in Eq. (3.25) does not violate the smoothness of $\bar{\Gamma}_t[\varphi]$ in zero dimensions for all t , because $\Delta \mathcal{S}_t[\varphi] \equiv \mathcal{S}_t(\varphi) \in C^\infty$ in φ .

We express Eq. (3.24) in terms of the scale-dependent effective average action (3.25) and, for the sake of convenience, revert the notation $\phi' \rightarrow \phi$,

$$e^{-\bar{\Gamma}_t[\varphi]} = \mathcal{N} \int_{-\infty}^{+\infty} d\phi e^{-S[\phi + \varphi] - \Delta \mathcal{S}_t[\phi] + \bar{\Gamma}_{t,\varphi}^{(1)}[\varphi]\phi}. \quad (3.26)$$

We have arrived at the zero-dimensional analog of Eq. (2.39) which has already facilitated our discussion in subsection 2.1.4.1 of ICs for general FRG flow equations. In the next step one formally introduces the normalization of a Gaussian integral with mass $r(t)$ and takes the logarithm, which results in

$$\bar{\Gamma}_t[\varphi] = -\ln \int_{-\infty}^{+\infty} d\phi \sqrt{\frac{r(t)}{2\pi}} e^{-S[\phi + \varphi] - \frac{1}{2}r(t)\phi^2 + \bar{\Gamma}_{t,\varphi}^{(1)}[\varphi]\phi} - \ln \left[\mathcal{N} \sqrt{\frac{2\pi}{r(t)}} \right]. \quad (3.27)$$

We are now ready to study the limit $t \rightarrow 0$, which corresponds to the IC for a possible flow equation for $\Gamma_t[\varphi]$ or $\bar{\Gamma}_t[\varphi]$, respectively. Focusing on the ϕ integral in the first term on the r.h.s. of Eq. (3.27), we leverage the fact that the regulator terms act like a Gaussian representation of the Dirac delta distribution,

$$\lim_{t \rightarrow 0} \sqrt{\frac{r(t)}{2\pi}} e^{-\frac{1}{2}r(t)\phi^2} \approx \delta(\phi), \quad (3.28)$$

⁴⁰It is the same shift that is used in the background field formalism [559, 560], where the full fluctuating quantum field ϕ is split into a background field configuration φ and additional fluctuations ϕ' about the background field. This is why φ in this context is referred to as the *classical* or *mean* field.

as long as $r(t)$ is much larger than all scales in $\mathcal{S}[\phi]$. Thus, denoting

$$c(t) \equiv -\ln \left[\mathcal{N} \sqrt{\frac{2\pi}{r(t)}} \right], \quad (3.29)$$

we find as

$$\lim_{t \rightarrow 0} \bar{\Gamma}_t[\varphi] = -\ln \int_{-\infty}^{+\infty} d\phi \delta(\phi) e^{-\mathcal{S}[\phi+\varphi] + \bar{\Gamma}_{t,\varphi}^{(1)}[\varphi] \phi} + c(t) = \mathcal{S}[\varphi] + c(t). \quad (3.30)$$

This means that the IC for a flow of $\bar{\Gamma}_t[\varphi]$ is given by the classical action \mathcal{S} evaluated for the classical field φ and some additional t -dependent, but φ -independent term $c(t)$. This choice for an IC of a PDE for $\bar{\Gamma}_t[\varphi]$ has subtle consequences:

Although $c(t)$ does not depend on φ , it is large, $c(t) \sim \frac{1}{2} \ln r(t)$. Consequently, as far as the IC for the PDE for $\Gamma_t[\varphi]$ or $\bar{\Gamma}_t[\varphi]$ is concerned, it seems as if we run into the same problem as before: The IC is dominated by the artificial mass of the regulator $r(t)$, independent of the specific action $\mathcal{S}[\phi]$, and differences in the specific choice for $\mathcal{S}[\phi]$ enter the IC only as small deviations from the large term $c(t)$. Furthermore, $c(t)$ contains the normalization constant \mathcal{N} , which was fixed according to Eq. (3.4).

However, precisely because $c(t)$ appears like the normalization \mathcal{N} , it should be irrelevant for all physical observables. Indeed this is the case, because all φ -independent terms in $\Gamma_t[\varphi]$ do not enter the n -point functions, since the latter are calculated as derivatives of $\Gamma[\varphi]$ w.r.t. φ at $t \rightarrow \infty$, see, e.g., Sec. II E of Ref. [1] for explicit expressions. This implies that an additive, φ -independent term in the three effective actions $\Gamma[\varphi]$, $\Gamma_t[\varphi]$, and $\bar{\Gamma}_t[\varphi]$ is irrelevant and only relative differences in the effective actions are observable. Therefore, we can simply omit $c(t)$ and take $\mathcal{S}[\varphi]$ as IC for the PDE for $\bar{\Gamma}_t[\varphi]$. This is however only valid if the PDE for $\bar{\Gamma}_t[\varphi]$ is independent of its zeroth moment – viz. only derivatives $\delta_\varphi^n \bar{\Gamma}_t[\varphi]$ contribute to the flow equation – otherwise $c(t)$ would influence the flow in a time-dependent manner. Fortunately, we know from our general discussion in subsection 2.1.4 that this is the case for the Wetterich Eq. (2.37) and by extension its zero-dimensional analog (3.36).

We want to conclude this discussion regarding the IC $\bar{\Gamma}_t[\varphi] = \mathcal{S}[\varphi]$ with a discussion of convexity, smoothness and RG consistency.

After Eq. (3.25) we argued that $\bar{\Gamma}_t[\varphi]$ does not need to be convex, but must still be smooth for all t . Let us for example consider the non-analytic action (3.10) as an IC, $\bar{\Gamma}_{t=0}[\varphi] = \mathcal{S}[\varphi]$, which does not cause any problems for the convexity and the smoothness of $\mathcal{Z}_t[J]$ and $\mathcal{W}_t[J]$ at arbitrary t , as discussed in App. B and especially with Fig. 36 of Ref. [1]. The non-convexity of $\mathcal{S}[\varphi]$ is also not a problem for $\bar{\Gamma}_t[\varphi]$, which does not necessarily need to be convex at finite t . Nevertheless, the smoothness of $\bar{\Gamma}_t[\varphi]$ is violated by this choice of $\mathcal{S}[\varphi]$ at $t = 0$. This issue originates from relation (3.28), which is exactly fulfilled only in the limit $\Lambda \rightarrow \infty$ for the UV scale. This, however, leads to a trivial theory of infinitely massive particles at $t = 0$, cf. Eq. (3.6).

If one chooses a reasonably large but finite Λ and does not use Eq. (3.28), one would ensure that $\bar{\Gamma}_t[\varphi]$ is also smooth at $t = 0$. However, then the IC is not exactly $\mathcal{S}[\varphi]$. In consequence, if we use the approximation (3.28) even for finite Λ , one has to pay the price of introducing errors into the IC as well as violating the smoothness of $\bar{\Gamma}_t[\varphi]$ at $t = 0$. But in return one has a

well-defined IC $\mathcal{S}[\varphi]$ for the PDE for $\bar{\Gamma}_t[\varphi]$. However, if Λ is chosen to be much larger than all scales in $\mathcal{S}[\phi]$, the errors from the IC are minor and expected to be of magnitude

$$\text{error} \approx \frac{\text{largest scale in } \mathcal{S}}{\Lambda}, \quad (3.31)$$

We will come back to this issue in subsection 3.2.3.1 in the context of RG consistency, see also subsection 2.1.6.

Additionally, we will find that also the smoothness of $\bar{\Gamma}_t[\varphi]$ is recovered automatically for all $t > 0$ by the structure of the PDE for $\bar{\Gamma}_t[\varphi]$, because it always contains diffusive contributions which immediately smear out kinks in the IC right in the first time step. We will also come back to this issue later on, after we have derived the flow equation (3.36) in zero dimensions and discussed its diffusive, irreversible character.

3.1.3.3. The exact renormalization group equation in zero dimensions

In analogy to the previous flow equations in zero dimensions, the flow equation for $\bar{\Gamma}_t[\varphi]$ is obtained by taking the derivative of $\bar{\Gamma}_t[\varphi]$ w.r.t. t and using the definitions (3.19a) and (3.25) to express the derivative of $\bar{\Gamma}_t[\varphi]$ by the scale-dependent Schwinger functional,

$$\partial_t \bar{\Gamma}_t[\varphi] = \partial_t (\Gamma_t[\varphi] - \Delta \mathcal{S}_t[\varphi]) = \partial_t (J_t(\varphi) \varphi - \mathcal{W}_t[J_t(\varphi)] - \Delta \mathcal{S}_t[\varphi]) = \quad (3.32a)$$

$$= [\partial_t J_t(\varphi)] \varphi - \partial_t \mathcal{W}_t[J_t(\varphi)] - [\partial_t J_t(\varphi)] \mathcal{W}_{t,J_t}^{(1)}[J_t] - \left[\frac{1}{2} \partial_t r(t)\right] \varphi^2 = \quad (3.32b)$$

$$= -\partial_t \mathcal{W}_t[J_t(\varphi)] - \left[\frac{1}{2} \partial_t r(t)\right] \varphi^2, \quad (3.33)$$

where we used the chain rule and Eq. (3.20). Using the flow equation for the Schwinger functional (3.18) to substitute the first term on the r.h.s. of Eq. (3.33) and again employing the identity (3.20), we arrive at

$$\partial_t \bar{\Gamma}_t[\varphi] = \left[\frac{1}{2} \partial_t r(t)\right] \mathcal{W}_{t,J_t}^{(2)}[J_t(\varphi)]. \quad (3.34)$$

It remains to replace the second derivative of the scale-dependent Schwinger functional by a corresponding derivative of $\bar{\Gamma}_t[\varphi]$. This is done via the identity

$$1 = \frac{\delta J_t(\varphi)}{\delta \varphi} \frac{\delta \varphi}{\delta J_t(\varphi)} = \Gamma_{t,\varphi\varphi}^{(2)}[\varphi] \mathcal{W}_{t,J_t}^{(2)}[J_t(\varphi)], \quad (3.35)$$

which follows from Eq. (3.20) and (3.21). Plugging this into Eq. (3.34) and using Eq. (3.25) with Eq. (3.7) we rediscover the *Exact Renormalization Group equation* or *Wetterich equation* [212, 214, 216]

$$\partial_t \bar{\Gamma}_t[\varphi] = \left[\frac{1}{2} \partial_t r(t)\right] [\bar{\Gamma}_{t,\varphi\varphi}^{(2)}[\varphi] + r(t)]^{-1}, \quad (3.36)$$

as the application of the general Wetterich Eq. (2.37) to the zero-dimensional theory of a single scalar ϕ with expectation value φ .

Eq. (3.36) manifests as a PDE for the scale-dependent EAA $\bar{\Gamma}(t, \varphi)$ in the t - φ -plane,

$$\partial_t \bar{\Gamma}(t, \varphi) = \frac{1}{2} \frac{1}{\partial_\varphi^2 \bar{\Gamma}(t, \varphi) + r(t)} \partial_t r(t), \quad (3.37)$$

with the IC $\bar{\Gamma}(t = 0, \varphi) = \mathcal{S}[\varphi]$. Some remarks are in order:

1. In contrast to the PDEs for $\mathcal{Z}(t, J)$ and $\mathcal{W}(t, J)$ the Wetterich equation can be initialized with a suitable IC at $t = 0$ that produces distinct flows for different actions $\mathcal{S}[\phi]$, as was discussed in the previous subsection 3.1.3.2.
2. The spatial BCs, *i.e.*, for $\varphi \rightarrow \pm\infty$ are provided by the asymptotics of the Wetterich equation (3.37) itself and by the requirement that $\mathcal{S}[\varphi]$ must be bounded from below: The action $\mathcal{S}[\varphi]$ of an (interacting) field theory must at least grow like φ^2 for large $|\varphi|$ and the dominant contribution for large $|\varphi|$ must be even in φ . For actions $\mathcal{S}[\varphi]$ that grow asymptotically faster than φ^2 the denominator on the r.h.s. of the PDE (3.37) already diverges at $t \approx 0$, such that

$$\lim_{|\varphi| \rightarrow \infty} \partial_t \bar{\Gamma}(t, \varphi) \approx 0. \quad (3.38)$$

It follows that for $|\varphi| \rightarrow \infty$ the function $\bar{\Gamma}(t, \varphi)$ does not change at all, but keeps its initial value $\mathcal{S}[\varphi]$. These are perfectly valid BCs for a PDE. The scenario for ICs with $\lim_{|\varphi| \rightarrow \infty} \mathcal{S}[\varphi] \sim \varphi^2$ is more delicate. We will return to this issue and a detailed discussion of BCs, when we discuss the numerical implementation and solution of Eq. (3.37) in subsection 3.2.2.4 in the context of numerical fluid dynamics.

3. The PDE (3.37) can be recast into a non-linear diffusion equation in the spirit of subsection 2.1.7, *viz.* Eq. (2.90) by considering the flow equation for $\partial_t(\partial_\varphi \bar{\Gamma}(t, \varphi))$:

$$\partial_t (\partial_\varphi \bar{\Gamma}(t, \varphi)) = \partial_\varphi \frac{\frac{1}{2} \partial_t r(t)}{\partial_\varphi (\partial_\varphi \bar{\Gamma}(t, \varphi)) + r(t)} = - \frac{\partial_t r(t)}{(\partial_\varphi (\partial_\varphi \bar{\Gamma}(t, \varphi)) + r(t))^2} \partial_\varphi^2 (\partial_\varphi \bar{\Gamma}(t, \varphi)). \quad (3.39)$$

In contrast to the PDEs (3.12) and (3.18) it is non-linear in the second-order spatial derivatives of $\bar{\Gamma}(t, \varphi)$. Using the flow equation for $\bar{\Gamma}(t, \varphi)$ and its IC, a worthwhile subject of future work could be a study of the resulting flows for $\mathcal{Z}(t, J)$ and $\mathcal{W}(t, J)$. By applying the same formalism to models with different field content, the FRG flow equations can also acquire convective/advective terms and source terms, see subsection 3.2.2.3 and subsection 3.3.2 for a detailed discussion.

4. In zero dimensions, similar to the flow equations for $\mathcal{Z}(t, J)$ and $\mathcal{W}(t, J)$, one can reparameterize the flow time t in terms of r in Eq. (3.37) and get rid of the prefactor $\partial_t r(t)$. Additionally, one could eliminate $r(t)$ in the denominator in Eq. (3.37) by shifting $\bar{\Gamma}(t, \varphi) \rightarrow \bar{\Gamma}(r, \varphi) - \frac{1}{2} r \varphi^2$ and switching from t to r as flow parameter, which corresponds to the zero-dimensional analogue of the rescaled “dimensionless” flow equation in fixed-point form, but is not suited for most practical calculations in this work. The exception is our discussion in subsection 3.2.4.3.

This reparameterization effectively corresponds to different choices of regulator (shape) functions in zero dimensions. However, for higher-dimensional problems, different choices of regulators do not need to be related to each other via simple reparameterization of the RG time. In any case, the effective dynamics in the PDE during the FRG flow strongly depends on the parametrization of the RG scale as well as the explicit choice of regulator, which has two direct consequences: First, although the dynamics and t -evolution of observables (the n -point functions) during the FRG flow might be highly interesting and must also be studied to ensure that the UV and IR cutoff scales are chosen appropriately, one must clearly state that only the IR value of $\Gamma[\varphi]$ is physically meaningful. This is demonstrated and discussed again in the context of numerical precision tests of the $O(N)$ model in subsection 3.2.3. Second, from a numerical point of view, some parametrizations or choices of regulators might be more challenging for the numerical integrators than others and must be adopted to the specific problems at hand. On the level of the PDE this corresponds to the time-dependent strength of the diffusion, cf. subsection 3.2.2.3.

Using a zero-dimensional field theory with one degree of freedom, we have therefore demonstrated that it is possible to transform the problem of solving functional integrals like Eq. (3.1) and (3.2) for a model with action $\mathcal{S}[\phi]$ into solving the PDE (3.37) in t and φ with the IC $\mathcal{S}[\varphi]$. The Wetterich Eq. (3.36) thus directly implements the idea of transforming Gaussian-type functional integrals into arbitrary functional integrals, but on the level of the effective action $\Gamma[\varphi]$ rather than the partition function $\mathcal{Z}[J]$. Both formulations of the problem of calculating n -point correlation functions – the functional-integral formulation and the FRG formulation – are mathematically equivalent. This, however, is, as we have seen, a highly non-trivial statement and demands for numerical precision tests, which are part of this work.

For our following discussions in section 3.2 we want to extend the current scope by including additional scalars in our theory, respecting $O(N)$ symmetry. On a conceptual level this is a straight forward extension and its is of course possible to derive the generalization, cf. (3.63), of the flow equation (3.37) to N scalars under $O(N)$ symmetry by repeating the derivation of this section. After having derived the Wetterich equation twice already, first resulting the general Eq. (2.37) and then in this subsection resulting in Eq. (3.39), we will refrain from a third derivation and make use the general expression (2.37) in subsection 3.2.2.1 instead.

3.2. The $O(N)$ model – strongly interacting scalars

The introduction of this section follows the discussion presented in Sec. III.A of Ref. [1].

Zero-dimensional $O(N)$ models – i.e., models of N scalars interacting in a point with $O(N)$ symmetry – are predominantly studied for pedagogical and conceptual purposes [163, 312, 529–539, 541, 543, 544, 546, 549]. The zero-dimensional $O(N)$ model is also referred to as $O(N)$ -vector model and can be seen as the high-temperature limit of a quantum mechanical system [536]. It was also considered as a statistical model for the formation of polymers [531]. In Ref. [163] the model was used to compare the quality of perturbation theory, the large- N expansion, and the FRG vertex/Taylor expansion with the exact result. The primary focus of

the present work is to push this analysis even further and to study the limits of untruncated FRG flow equations as well as the FRG Taylor expansion.

$O(N)$ models in higher dimensions play an important role in understanding spin systems, like the Ising model [95, 561, 562], and magnetization phenomena. Furthermore, they are often used as toy models and are of utmost importance for understanding the Anderson-Brout-Englert-Guralnik-Hagen-Higgs-Kibble mechanism and the formation of a chiral condensate in strong-interaction matter. In the context of numerical methods for the FRG the $O(N)$ model in three dimensions and in the large- N limit is discussed in detail in Ref. [247].

In the following we introduce the zero-dimensional $O(N)$ model on the level of the classical action and the functional integral and comment on the calculation of expectation values and 1PI vertex functions, which are our observables of interest.

Consider a zero-dimensional theory of N bosonic scalars ϕ_a , which transform according to

$$\phi_a \mapsto \phi'_a = O_{ab} \phi_b, \quad (3.40)$$

where $O \in O(N)$ and $a, b \in \{1, \dots, N\}$. In vector notation, this reads

$$\vec{\phi} \mapsto \vec{\phi}' = O \vec{\phi}, \quad (3.41)$$

where $\vec{\phi} \equiv (\phi_1, \phi_2, \dots, \phi_N)$. If the action $\mathcal{S}[\vec{\phi}]$ of the model possesses an $O(N)$ symmetry, it can contain all possible terms that are functions of the $O(N)$ invariant

$$\rho \equiv \frac{1}{2} \phi_a \phi_a \equiv \frac{1}{2} \vec{\phi}^2 \quad (3.42)$$

This implies that the most general action obeying this symmetry is given by

$$\mathcal{S}[\vec{\phi}] = U(\vec{\phi}) = U(\rho), \quad (3.43)$$

where $U(\rho)$ is the effective potential, in analogy to models from higher-dimensional space-times. This effective potential might for example include a bosonic “mass term” $m^2\rho$ as well as other interaction terms containing arbitrary powers of ρ . Although one may now be tempted to assume that the effective potential $U(\rho)$ must be a power series or an analytic function of ρ , as long as it fulfills all symmetries it can be any continuous function of ρ which is bounded from below, cf. the discussion in section 3.1 for the special case of the $O(1)$ model.

In the remainder of this section we will summarize relevant relations for the $O(N)$ model. For a more detailed discussion, we refer the interested reader to Ref. [163] and references therein. All generating functionals of the theory retain the $O(N)$ symmetry of the action, which makes them functionals of the invariants $\frac{1}{2} \vec{J}^2$ for \mathcal{Z} and \mathcal{W} and $\varrho \equiv \frac{1}{2} \vec{\varphi}^2$ for Γ . This entails that all n -point functions for odd n vanish by symmetry and all correlation functions of a given order of even n are proportional to each other, e.g., for the four-point function we find

$$\langle \phi_i \phi_i \phi_j \phi_j \rangle = \frac{1}{3} \langle \phi_i \phi_i \phi_i \phi_i \rangle, \quad (3.44)$$

for $i \neq j$ and $i, j \in \{1, \dots, N\}$ (no summation over repeated indices implied here). For the proof, use that $\frac{\delta}{\delta J_i} \mathcal{Z}(\frac{1}{2} \vec{J}^2) = J_i \mathcal{Z}'(\frac{1}{2} \vec{J}^2)$ and set the source $\vec{J} = 0$ at the end of the calculation. Using the $O(N)$ symmetry on the r.h.s. of

$$\langle \phi_{i_1} \cdots \phi_{i_n} \rangle = \frac{1}{\mathcal{Z}[0]} \int_{-\infty}^{+\infty} d^N \phi \phi_{i_1} \cdots \phi_{i_n} e^{-U(\vec{\phi}^2/2)}, \quad (3.45)$$

one can relate correlation functions of even order $2n$ to the expectation value $\langle (\vec{\phi}^2)^n \rangle$. For the two-, four-, and six-point functions, which are studied in this work, we find

$$\langle \phi_i \phi_j \rangle = \frac{1}{N} \delta_{i,j} \langle \vec{\phi}^2 \rangle, \quad (3.46)$$

$$\langle \phi_i \phi_j \phi_k \phi_l \rangle = \frac{1}{N(N+2)} (\delta_{i,j} \delta_{k,l} + \delta_{i,k} \delta_{j,l} + \delta_{i,l} \delta_{j,k}) \langle (\vec{\phi}^2)^2 \rangle, \quad (3.47)$$

$$\langle \phi_i \phi_j \phi_k \phi_l \phi_m \phi_n \rangle = \frac{1}{N(N+2)(N+4)} (\delta_{i,j} \delta_{k,l} \delta_{m,n} + \ll 14 \gg) \langle (\vec{\phi}^2)^3 \rangle. \quad (3.48)$$

Connected correlation functions and 1PI vertex functions are related to correlation functions in the usual manner, cf. Sec. II.E of Ref. [1] or Ref. [163]. Using the fact that, for odd n , all n -point correlation functions and all n -point 1PI vertex functions vanish by symmetry, the following relations hold for the two-, four-, and six-point functions (no summation over repeated indices):

$$\langle \phi_i \phi_i \rangle^c = \langle \phi_i \phi_i \rangle = (\Gamma_{\varphi_i \varphi_i}^{(2)})^{-1}, \quad (3.49)$$

$$\langle \phi_i \phi_i \phi_i \phi_i \rangle^c = \langle \phi_i \phi_i \phi_i \phi_i \rangle - 3 \langle \phi_i \phi_i \rangle^2 = -\langle \phi_i \phi_i \rangle^4 \Gamma_{\varphi_i \varphi_i \varphi_i \varphi_i}^{(4)}, \quad (3.50)$$

$$\begin{aligned} \langle \phi_i \phi_i \phi_i \phi_i \phi_i \phi_i \rangle^c &= \langle \phi_i \phi_i \phi_i \phi_i \phi_i \phi_i \rangle - 15 \langle \phi_i \phi_i \phi_i \phi_i \rangle \langle \phi_i \phi_i \rangle + 30 \langle \phi_i \phi_i \rangle^3 = \\ &= -\langle \phi_i \phi_i \rangle^6 \Gamma_{\varphi_i \varphi_i \varphi_i \varphi_i \varphi_i \varphi_i}^{(6)} + 10 \langle \phi_i \phi_i \rangle^{-1} (\langle \phi_i \phi_i \phi_i \phi_i \rangle^c)^2. \end{aligned} \quad (3.51)$$

Inserting Eq. (3.46) – (3.48) into Eq. (3.49) – (3.51) and solving for the 1PI vertex functions yields

$$\Gamma^{(2)} \equiv \Gamma_{\varphi_i \varphi_i}^{(2)} = N \frac{1}{\langle \vec{\phi}^2 \rangle}, \quad (3.52)$$

$$\Gamma^{(4)} \equiv \Gamma_{\varphi_i \varphi_i \varphi_i \varphi_i}^{(4)} = 3 N^2 \frac{1}{\langle \vec{\phi}^2 \rangle^2} \left[1 - \frac{N}{N+2} \frac{\langle (\vec{\phi}^2)^2 \rangle}{\langle \vec{\phi}^2 \rangle^2} \right], \quad (3.53)$$

$$\begin{aligned} \Gamma^{(6)} \equiv \Gamma_{\varphi_i \dots \varphi_i}^{(6)} &= 60 N^3 \frac{1}{\langle \vec{\phi}^2 \rangle^3} \left[1 - \frac{9N}{4(N+2)} \frac{\langle (\vec{\phi}^2)^2 \rangle}{\langle \vec{\phi}^2 \rangle^2} + \frac{3N^2}{2(N+2)^2} \frac{\langle (\vec{\phi}^2)^2 \rangle^2}{\langle \vec{\phi}^2 \rangle^4} - \right. \\ &\quad \left. - \frac{N^2}{4(N+2)(N+4)} \frac{\langle (\vec{\phi}^2)^3 \rangle}{\langle \vec{\phi}^2 \rangle^3} \right]. \end{aligned} \quad (3.54)$$

In summary, computing arbitrary correlation functions (or 1PI vertex functions) of the zero-dimensional $O(N)$ model boils down to computing expectation values $\langle (\vec{\phi}^2)^n \rangle$. The latter can be computed using Eq. (3.45). Because of the $O(N)$ symmetry of the integrand, this is most

easily done in spherical coordinates. Performing the integration over spherical coordinates, we have

$$\int_{-\infty}^{+\infty} d\phi_1 \cdots \int_{-\infty}^{+\infty} d\phi_N = \frac{2\pi^{\frac{N}{2}}}{\Gamma(\frac{N}{2})} \int_0^\infty d\rho (2\rho)^{\frac{N}{2}-1}, \quad (3.55)$$

Then the expectation value is a simple one-dimensional integral,

$$\langle (\vec{\phi}^2)^n \rangle = \frac{2^n \int_0^\infty d\rho \rho^{\frac{N}{2}-1} \rho^n e^{-U(\rho)}}{\int_0^\infty d\rho \rho^{\frac{N}{2}-1} e^{-U(\rho)}}. \quad (3.56)$$

For certain potentials $U(\rho)$, the integral (3.56) can even be computed symbolically in terms of known functions [3, 163, 537], whereas for general $U(\rho)$ a numerical evaluation to high precision is straightforward using standard methods [554, 555]. Thus, the zero-dimensional $O(N)$ model is an ideal testing ground for alternative methods to calculate correlation functions, such as, *e.g.*, the FRG.

3.2.1. Symmetry restoration during the FRG flow

This subsection follows the discussion presented in Sec. III.B of Ref. [1].

Besides being invariant under $O(N)$ transformations the classical action (potential) $\mathcal{S}[\vec{\phi}] = U(\vec{\phi})$ is also invariant under the discrete \mathbb{Z}_2 transformation

$$\phi_a \rightarrow -\phi_a, \quad (3.57)$$

which, as already mentioned, implies that all n -point functions with odd n vanish, *e.g.*, the one-point function $\varphi_a = \langle \phi_a \rangle = 0$.

However, it is possible to consider actions (potentials) $\mathcal{S}[\rho] = U(\rho)$ which possess non-trivial minima $\rho_0 \neq 0$. This means that the FRG flow of $\bar{\Gamma}_t[\vec{\varphi}]$ of such models is initialized in a symmetry-broken regime in the UV, where the $O(N)$ symmetry is broken to its $O(N-1)$ subgroup for $N > 1$ and for $N = 1$ this reduces just to the breaking of the \mathbb{Z}_2 symmetry. Following the discussion in App. B of Ref. [1], this property of the classical action neither translates to the full quantum effective action $\Gamma[\vec{\varphi}]$ in the IR nor to the n -point functions, due to a limiting case of the CMWH theorem [550–552]. The theorem states that there is no long-range order in $d \leq 2$ dimensions if the interactions between the constituents are sufficiently short of range. Therefore, there is no breaking of a (continuous) symmetry in such systems in the IR, *i.e.*, after integrating out all quantum fluctuations, even when starting with a classical action in the UV that has non-trivial minima. This is the equivalent of the statement that $\varphi_a = \langle \phi_a \rangle = 0$, which follows directly from the integral (3.45) in zero dimensions. The “Nambu-Goldstone modes” [441, 442, 563]⁴¹, which we will also call pions⁴² $\vec{\pi}$ in the zero-

⁴¹We put the term “Nambu-Goldstone modes” in quotation marks, because in zero dimensions the concept of “massless modes” can only refer to the curvature masses in the corresponding bosonic field direction, which are obtained from the effective potential $U(\rho)$. But the actual particle masses in a higher-dimensional QFT are derived from the poles of the real-time propagators, which simply do not exist in zero dimensions.

⁴²We adopt the high-energy terminology. Condensed-matter physicists associate the pions with quasiparticles – the Anderson-Bogoliubov modes.

dimensional $O(N)$ model, and the radial σ -mode “vaporize” any condensate and smear out all cusps in $\bar{\Gamma}_t[\vec{\varphi}]$ during the FRG flow. In the IR all modes are then “massive” again.

There are two reasons, why this feature of symmetry restoration on the level of $\bar{\Gamma}_t[\vec{\varphi}]$ is desirable for our numerical tests:

1. Symmetry breaking/restoration associated with condensation/“vaporization” is an essential property of all kinds of QFTs [177, 178, 240] and we have to show that it is correctly captured by our numerical tools. This is especially important, because it was shown in Refs. [162, 247] that non-analytic behavior in the effective potential $U(t, \vec{\varphi})$, cf. Refs. [564, 565], which is directly associated with dynamical symmetry breaking/restoration, is realized as shock and rarefaction waves in field space during the FRG flow.
2. The possibility of dynamical symmetry restoration on the level of $\bar{\Gamma}_t[\vec{\varphi}]$ is also a desired feature in order to demonstrate that it is of utmost importance to choose the UV scale Λ and the IR cutoff r_{IR} as well as initial and BCs in numerical FRG flow calculations carefully. For our example it is expected that if the IR cutoff time t_{IR} is chosen too small, such that the regulator $r(t)$ is still too large, the system might still be in the symmetry-broken phase (indicated by a non-trivial minimum). This means that the scale-dependent effective average action $\bar{\Gamma}_{t_{\text{IR}}}[\vec{\varphi}]$ at this RG scale cannot be interpreted as the full quantum effective action $\Gamma[\vec{\varphi}]$, because the CMWH theorem is still violated. The same applies to a problematic implementation BCs, especially at $\varrho = 0$, which can lead to a violation of the CMWH theorem such that the system is not in the restored phase in the IR.

We will discuss subtleties in the dynamical symmetry restoration on the level of $\bar{\Gamma}_t[\vec{\varphi}]$ further especially in subsection 3.2.5 and section 3.3 and chapter 4.

3.2.2. Exact FRG flow equation of the zero-dimensional $O(N)$ model

This subsection follows the discussion presented in Sec. III.C of Ref. [1].

This subsection is dedicated to the FRG formulation of the $O(N)$ model introduced in this section 3.2. To this end, we explicitly demonstrate how to arrive at the exact, untruncated FRG flow equation of the $O(N)$ model. Furthermore, we will comment on the FRG Taylor expansion, introduced in subsection 2.1.4.2 in this context, as a truncation scheme for the exact flow equation in zero dimensions.

In general zero-dimensional QFTs take up a very special place in the discussion of truncation schemes, cf. subsection 2.1.4.2. Due to the absence of space-time and momentum-dependencies of the fields, the EAA $\bar{\Gamma}_t[\chi] = \bar{\Gamma}_t(\chi)$ is merely a function (not a functional). As such it can be parameterized by a finite set of χ - and of the t -dependent coupling functions. In the general FRG context this simply means that the derivative expansion of subsection 2.1.4.2 is exact already at zeroth-order and the EAA is just given by (a set of) local potential(s). In consequence, truncating the system is superfluous and the PDEs, which are derived via projections from the Wetterich equation, constitute an exact and complete system. Solving this system must therefore lead to the exact effective action $\Gamma[\chi]$ in the IR and is therefore formally equivalent to solving the functional integral. In other words, calculating n -point functions via

the (functional) integral or via the Wetterich equation (if done properly) must yield identical results without systematic truncation errors.

This feature makes zero-dimensional QFT particularly interesting for several reasons:

1. It can be used to test the quality of numerical schemes which are used to solve the flow equations.
2. It can be used to estimate the errors resulting from the choices of various parameters entering the FRG flow equations like UV and IR cutoff scales, *etc.*
3. It can be used to test commonly used truncation schemes by artificially truncating the exact system of PDEs to a truncated set of ODEs.

All these tests can be performed on a quantitative level, by studying the relative errors of the FRG results for n -point functions compared to the exact results from the functional integral. We provide results for various precision tests in subsection 3.2.3.

For the remainder of this section, we will proceed as follows: First, we will derive the untruncated exact FRG flow equation for the zero-dimensional $O(N)$ model. Afterwards, we introduce FRG Taylor expansion as a truncation of this system.

3.2.2.1. The exact FRG flow equation of the $O(N)$ model in $d = 0$

For the special case of the zero-dimensional $O(N)$ model, the most general ansatz for the EAA is given by a scale-dependent effective potential

$$\bar{\Gamma}_t[\vec{\varphi}] = U(t, \vec{\varphi}) = U(t, \varrho). \quad (3.58)$$

This ansatz can describe arbitrary $O(N)$ invariant effective actions and can include terms at all orders of $\varrho = \frac{1}{2} \vec{\varphi}^2$. However, it is in principle not restricted to analytic (Taylor-expandable) functions. Truncations of $\bar{\Gamma}_t[\vec{\varphi}]$ are not required to facilitate practical computations.

In order to arrive at the exact flow equation for $U(t, \vec{\varphi})$ one has to perform the following steps:

1. Insert the function (3.58) into the Wetterich equation (2.37).
2. Invert the full field-dependent two-point function in field space

$$(\bar{\Gamma}_{t,\varphi\varphi}^{(2)}[\vec{\varphi}] + R_t)_{ij}, \quad (3.59)$$

to obtain the propagator $G_{t,\varphi\varphi}[\vec{\varphi}]_{i,j}$.

3. Take the trace in field space.
4. Remove the redundant $N - 1$ field space directions in $\vec{\varphi}$.

For the last step, the FRG flow equation can be evaluated on a constant background field configuration⁴³ $\varphi_1 = \dots = \varphi_{N-1} = 0$ and $\varphi_N = \underline{\varphi}_N = \sigma \equiv \sqrt{2\varrho}$. Without loss of generality

⁴³Here we adopt terminology from higher-dimensional FRG: The word ‘‘constant’’ is therefore somewhat misleading in a QFT which cannot vary in space-time, but it is used anyhow.

(w.l.o.g.) the φ_N -direction is singled out as the direction of the radial σ -mode and the constant background field.

The inversion of the full field-dependent two-point function (3.59) can be performed analytically [95, 211, 226, 566] by introducing the complete, orthogonal, and idempotent field space projection operators

$$\mathcal{P}_{ij}^\perp(\vec{\varphi}) \equiv \delta_{i,j} - \frac{\varphi_i \varphi_j}{\vec{\varphi}^2}, \quad \mathcal{P}_{ij}^\parallel(\vec{\varphi}) \equiv \frac{\varphi_i \varphi_j}{\vec{\varphi}^2}. \quad (3.60)$$

The projection operators are used to decompose the full field-dependent two-point function (3.59) into components perpendicular (\perp) and parallel (\parallel) to $\vec{\varphi}$, which can be inverted separately. The regulator R_t is matrix-valued but diagonal in field space,

$$(R_t)_{i,j} = \delta_{i,j} r(t), \quad (3.61)$$

where $r(t)$ again is denoted as *regulator shape function*, cf. Eq. (3.7) and (3.8). One finds that

$$\begin{aligned} G_{t,\varphi_i\varphi_j}[\vec{\varphi}] &= (\bar{\Gamma}_{t,\varphi\varphi}^{(2)}[\vec{\varphi}] + R_t)_{ij}^{-1} = \\ &= \mathcal{P}_{ij}^\parallel(\vec{\varphi}) \frac{1}{r(t) + \partial_\rho U(t, \rho) + 2\rho \partial_\rho^2 U(t, \rho)} + \mathcal{P}_{ij}^\perp(\vec{\varphi}) \frac{1}{r(t) + \partial_\rho U(t, \rho)}, \end{aligned} \quad (3.62)$$

which can be inserted directly into the Wetterich equation (2.37). A summary of these results, ‘‘Feynman’’ rules to translate the following diagrams, and expressions for additional vertices can be found in App. D.1.1.

After taking the field space trace in Eq. (2.37) and evaluating the resulting equation on the constant background field configuration, we arrive at the FRG flow equation for the effective potential

$$\partial_t U(t, \sigma) = \frac{1}{2} \frac{N-1}{r(t) + \frac{1}{\sigma} \partial_\sigma U(t, \sigma)} \partial_t r(t) + \frac{1}{2} \frac{1}{r(t) + \partial_\sigma^2 U(t, \sigma)} \partial_t r(t) \quad (3.63)$$

$$= \frac{1}{2} \text{[red dashed circle with } \otimes \text{]} + \frac{1}{2} \text{[blue dashed circle with } \otimes \text{]}. \quad (3.63')$$

This FRG flow equation is an exact non-linear PDE for the effective potential $U(t, \sigma)$, which is of first-order in RG time t and of first- and second-order in the field space direction σ . It also includes an explicit σ -dependence. A detailed analysis of the structure of this PDE, including its relation to the CFD systems, discussed in section 2.2, is provided in subsection 3.2.2.3.

For the special case $N = 1$, the $O(N)$ model reduces to the $O(1)$ model. Such a theory of a single scalar field in zero dimensions, was used in the introductory section 3.1. In this limit, the pion contributions to the flow equation vanish. As already hinted in subsection 3.1.3.3, we find that for non-zero pion contributions ($N > 1$) the flow equation for $U(t, \sigma)$ acquires a term that is of first-order in the spatial derivative, $\partial_\sigma U(t, \sigma)$, which no longer has diffusive character, but corresponds to advection in field space.

3.2.2.2. FRG Taylor (vertex) expansion

The FRG Taylor expansion is based on the assumption that the effective (average) action $\bar{\Gamma}_t[\vec{\varphi}]$ can be expanded in a series in field space with RG-time-dependent expansion coefficients [93]. Due to the absence of momenta in zero dimensions the [FRG Taylor expansion](#) and the [Vertex expansion](#) of subsection 2.1.4.2 are identical and we will use both terms or the combined term *FRG Taylor (vertex) expansion* for our discussion.

This expansion in zero dimensions effectively reduces to an expansion of the effective potential $U(t, \varrho)$, cf. Eq. (3.58). The RG-scale-dependent expansion coefficients $\bar{\Gamma}^{(2n)}(t)$ correspond directly to the scale-dependent vertex functions $\bar{\Gamma}_{t, \varphi_i \dots \varphi_i}^{(2n)}$ of the QFT. For $d > 0$, these expansion coefficients are usually momentum-dependent in the vertex expansion, whereas in $d = 0$ the coefficients depend only on the RG time t .

The assumption of expandability and thus differentiability significantly restricts the form of the effective action $\bar{\Gamma}_t[\vec{\varphi}] = U(t, \vec{\varphi})$, cf. Refs. [567, 568]. In fact, it neither allows for the formation of any non-analytic behavior throughout the FRG flow nor for any non-analytic ICs. However, non-analytic ICs are by no means forbidden, as we will see in subsection 3.2.3. Furthermore, it is well known that non-analyticities can (and in some models have to) form in the effective potential during the FRG flow [155, 162, 247, 565] – especially in the context of dynamic symmetry breaking. Considering these caveats, an expansion in vertices of a given theory must *a priori* be approached with caution. Still, this expansion scheme is widely used in certain applications, cf. subsection 2.1.4.2.

In our work, we restrict our analysis of the precision of this truncation scheme to FRG flows with rather specific properties: We study ICs that are analytic. Furthermore, we know, cf. App. B of Ref. [1], that the IR effective action is smooth for the special case of zero dimensions, which is a necessary condition for the convergence of a (Taylor) series. It should, however, be noted that smoothness is only a necessary but not a sufficient condition for the convergence of a Taylor series⁴⁴. Only analyticity would formally imply the convergence of a Taylor series at all $\vec{\varphi}$. Additionally, we argue that for sufficiently small N , the diffusive contributions to the FRG flow are important, which smear out any possible cusps. In summary, we expect that for these extremely special scenarios it is unlikely that non-analyticities will form and disappear again during the FRG flow. Nevertheless, we do not know if a limited number of expansion coefficients is always enough to reach a reliable approximation of $\bar{\Gamma}_t[\vec{\varphi}]$ during the FRG flow or if it is always necessary to flow the effective potential as a PDE without additional assumptions. This (rather limited) applicability of the FRG Taylor expansion to analytic ICs will be tested by calculating the relative errors of 1PI n -point functions in the FRG Taylor expansion in comparison with the exact results and the results from the flows of a full field-dependent $U(t, \sigma)$ in subsection 3.2.3.

The FRG Taylor expansion of the zero-dimensional $O(N)$ model is given by the following

⁴⁴A textbook example for a smooth function which has a non-converging Taylor series around $x = 0$ is

$$f(x) = \begin{cases} e^{-1/x} & \text{if } x > 0, \\ 0 & \text{else.} \end{cases}$$

ansatz [163, 536, 537, 539],

$$\bar{\Gamma}_t[\vec{\varphi}] = \sum_{n=0}^m \frac{\bar{\Gamma}^{(2n)}(t)}{(2n-1)!!} \frac{1}{n!} \left(\frac{\vec{\varphi}^2}{2} \right)^n = \bar{\Gamma}^{(0)}(t) + \bar{\Gamma}^{(2)}(t) \frac{\vec{\varphi}^2}{2} + \frac{\bar{\Gamma}^{(4)}(t)}{3} \frac{1}{2} \left(\frac{\vec{\varphi}^2}{2} \right)^2 + \dots, \quad (3.64)$$

where $\bar{\Gamma}^{(2n)}(t)$ are t -dependent expansion coefficients and m is the truncation order. The factors of $(2n-1)!!$ and $n!$ were introduced in order to have $\bar{\Gamma}^{(2n)}(t_{\text{IR}}) = \Gamma_{\varphi_i \dots \varphi_i}^{(2n)}$ in the IR, where $\Gamma_{\varphi_i \dots \varphi_i}^{(2n)}$ are the 1PI $2n$ -point vertex functions in the IR, with all indices being identical (no summation over i here), see also Eq. (3.52) – (3.54). In order to arrive at the corresponding flow equations, we proceed in a similar manner as before in subsection 3.2.2.1: We insert our ansatz (3.64) into the full field-dependent two-point function (3.59) and use the field space projection operators (3.60) to invert the latter. We obtain

$$\left(\bar{\Gamma}_{t, \varphi\varphi}^{(2)}[\vec{\varphi}] + R_t \right)_{ij}^{-1} = \mathcal{P}_{ij}^{\perp}(\vec{\varphi}) G_t^{\pi\pi}(\vec{\varphi}) + \mathcal{P}_{ij}^{\parallel}(\vec{\varphi}) G_t^{\sigma\sigma}(\vec{\varphi}), \quad (3.65)$$

where

$$G_t^{\pi\pi}(\vec{\varphi}) \equiv \left[r(t) + \sum_{n=1}^{m+1} \frac{\bar{\Gamma}^{(2n)}(t)}{(2n-1)!!} \frac{1}{(n-1)!} \left(\frac{\vec{\varphi}^2}{2} \right)^{n-1} \right]^{-1}, \quad (3.66a)$$

$$G_t^{\sigma\sigma}(\vec{\varphi}) \equiv \left[r(t) + \sum_{n=1}^{m+1} \frac{\bar{\Gamma}^{(2n)}(t)}{(2n-3)!!} \frac{1}{(n-1)!} \left(\frac{\vec{\varphi}^2}{2} \right)^{n-1} \right]^{-1}, \quad (3.66b)$$

are the field-dependent propagators of the pion and sigma field in the Taylor expansion.

This result can be inserted into the Wetterich equation (2.37), where the trace in field space is evaluated to

$$\partial_t \bar{\Gamma}_t[\vec{\varphi}] = \frac{1}{2} [\partial_t r(t)] [(N-1) G_t^{\pi\pi}(\vec{\varphi}) + G_t^{\sigma\sigma}(\vec{\varphi})]. \quad (3.67)$$

Finally, we insert the ansatz (3.64) for the EAA into the l.h.s. of this equation and expand the propagators $G_t^{\circ\circ}(\vec{\varphi})$ up to order $n = m$ in the expansion coefficients $\bar{\Gamma}^{(2n)}(t)$. This can also be achieved by successively taking derivatives w.r.t. the fields and setting $\vec{\varphi} = 0$ afterwards. By comparing the expansion coefficients on the left- and right-hand sides of the equation, one arrives at a coupled set of ordinary differential equations for the $\bar{\Gamma}^{(2n)}(t)$ with $0 \leq n \leq m$. The flow equation for $\bar{\Gamma}^{(2m)}(t)$ contains $\bar{\Gamma}^{(2m+2)}(t)$ on the right-hand side. We truncate the system by neglecting the flow of $\bar{\Gamma}^{(2m+2)}(t)$, i.e., assuming $\partial_t \bar{\Gamma}^{(2m+2)}(t) = 0$.

For an automatization of the derivation of the flow equations (the system of ODEs) via computer algebra routines such as MATHEMATICA [166], it is advisable to formulate the FRG Taylor expansion in the invariant $\varrho = \frac{1}{2} \vec{\varphi}^2$,

$$\bar{\Gamma}_t[\varrho] = \sum_{n=0}^m \frac{\bar{\Gamma}^{(2n)}(t)}{(2n-1)!!} \frac{\varrho^n}{n!}, \quad (3.68)$$

for which Eq. (3.67) manifests as

$$\partial_t \bar{\Gamma}_t[\varrho] = \frac{1}{2} [\partial_t r(t)] [(N-1) G_t^{\pi\pi}(\varrho) + G_t^{\sigma\sigma}(\varrho)], \quad (3.69)$$

while

$$G_t^{\pi\pi}(\varrho) \equiv \left[r(t) + \sum_{n=1}^{m+1} \frac{\bar{\Gamma}^{(2n)}(t)}{(2n-1)!!} \frac{\varrho^{n-1}}{(n-1)!} \right]^{-1}, \quad (3.70a)$$

$$G_t^{\sigma\sigma}(\varrho) \equiv \left[r(t) + \sum_{n=1}^{m+1} \frac{\bar{\Gamma}^{(2n)}(t)}{(2n-3)!!} \frac{\varrho^{n-1}}{(n-1)!} \right]^{-1}. \quad (3.70b)$$

The coupled set of ODEs for the expansion coefficients $\bar{\Gamma}^{(2n)}(t)$ is given by [163, 536],

$$\partial_t \bar{\Gamma}^{(0)}(t) = \frac{N}{2} \frac{\partial_t r(t)}{r(t) + \bar{\Gamma}^{(2)}(t)}, \quad (3.71a)$$

$$\partial_t \bar{\Gamma}^{(2)}(t) = -\frac{N+2}{6} \frac{\partial_t r(t)}{[r(t) + \bar{\Gamma}^{(2)}(t)]^2} \bar{\Gamma}^{(4)}(t), \quad (3.71b)$$

$$\partial_t \bar{\Gamma}^{(4)}(t) = \frac{N+8}{3} \frac{\partial_t r(t)}{[r(t) + \bar{\Gamma}^{(2)}(t)]^3} [\bar{\Gamma}^{(4)}(t)]^2 - \frac{N+4}{10} \frac{\partial_t r(t)}{[r(t) + \bar{\Gamma}^{(2)}(t)]^2} \bar{\Gamma}^{(6)}(t), \quad (3.71c)$$

⋮

with

$$\forall n \geq 2m+2 \quad \partial_t \bar{\Gamma}^{(n)}(t) = 0 \quad (3.72)$$

in this approximation. The system (3.71) is an explicit example for the tower of equations (2.52) discussed in subsection 2.1.4.2. An alternative derivation to the explicit expansion discussed here can be obtained by using the *higher-order flow equations* of subsection 2.1.5 for the the expansion coefficients $\bar{\Gamma}^{(2n)}(t)$.

3.2.2.3. Conservative form

This subsection follows the discussion presented in Sec. IV.A of Ref. [1].

In this subsection, we discuss the formulation of the FRG flow equation (3.63) as an advection-diffusion equation, as well as its interpretation in the context of CFD, cf. section 2.2. The fluid-dynamical formulation of the FRG flow equation for the effective potential $U(t, \varrho)$ of models of $O(N)$ -type (in the large- N limit [566]) is also presented in recent publications [162, 247] by some of our collaborators. It was shown that the FRG flow equation can be recast in the form of a pure advection equation (a hyperbolic conservation law) for the derivative of the effective potential $u(t, \varrho) = \partial_\varrho U(t, \varrho)$, where $u(t, \varrho)$ serves as the conserved quantity (the fluid), the RG time t as a temporal coordinate and ϱ as a spatial coordinate. In this subsection, we generalize this result and discuss various consequences for the numerical implementation and interpretation of FRG flow equations. Generalizations of the fluid-dynamical picture of FRG flow equations from the large- N results of Ref. [247] to systems with finite N as well as the inclusion of fermions were initially presented in various talks, see, e.g., Refs. [569, 570]. Further early

developments in this context are discussed in the master thesis [283] of Friederike Ihssen, the PhD thesis [398] of Nicolas Wink, and also in Ref. [162]. Furthermore, Ref. [565] includes a formulation of the flow equation as a conservation law and a discussion of shock waves based on the characteristics is presented, however, without really elaborating on a fluid-dynamical interpretation and its consequences.

The formulation of FRG flow equations in terms of a fluid-dynamical language has two major advantages:

1. It provides an intuitive explanation for different kinds of phenomena observed in FRG flow equations, *e.g.*, the flattening of the effective potential for small σ in the IR, which occurs in conjunction with a non-differentiable point of the effective potential at the ground state. Such non-analytic behavior cannot be handled and systematically analyzed by commonly used numerical schemes such as the Taylor expansion or related discretization schemes for the effective potential, since the latter strongly rely on differentiability. However, these phenomena have a direct impact on the physics, for instance on the occurrence of phase transitions [162, 247, 558, 564, 565, 567, 568, 571], and therefore must be resolved and analyzed accurately also on a numerical level.
2. The formulation of the FRG flow equations in terms of fluid-dynamical concepts provides access to the highly developed and extremely powerful toolbox of CFD, *cf.* section 2.2, which finds applications in a wide area of fields, ranging from the natural sciences and engineering all the way to economics. Recasting FRG flow equations as conservation laws allows a direct application of the numerical methods, *viz.* the KT scheme, and the related CFD concepts established in section 2.2.

Interestingly, the idea of interpreting RG flow equations as “flow” equations in the true sense of the word is not new and explains the term “RG flow equations”: A discussion of analogies between “RG flow” and hydro-dynamical flow can be found in widely used textbooks [177, 572] and is discussed via the example of field-independent coupling constants in the context of perturbative renormalization. Furthermore, the RG flow was already associated with gradient flow and dissipative processes in Refs. [230, 311, 573–576], even though a stringent fluid-dynamical interpretation and formulation was not presented.

It is therefore also not accidental that the (F)RG community has chosen the term “RG time” for the logarithm of the RG scale k over the UV scale Λ , $\tilde{t} = \ln\left(\frac{k}{\Lambda}\right)$. In contrast, we find that $t = -\tilde{t} \in [0, \infty)$ can be naturally identified as a temporal coordinate in the fluid-dynamical picture of (F)RG flow equations, see below. Hence we outright adopted the latter convention for this thesis, *cf.* Eq. (2.12). An interpretation of the scale-dependent generation functionals $\mathcal{Z}_t[J]$ or $\mathcal{W}_t[J]$ as functional flow equations in subsection 2.1.7 was part of our methodological introduction in chapter 2. We now want to discuss this explicitly in zero dimensions unburdened by the functional nature of the general expressions.

Considering the obvious analogies between flow equations arising in the FRG framework and fluid-dynamical equations, it is remarkable that the Wetterich Eq. (2.37) has not been more systematically investigated and compared to well-known fluid-dynamic equations. For the related RG flow equations the situation is slightly different and the mathematical analysis

on the level of PDEs was more systematic, see, *e.g.*, Refs. [230, 311, 576–578]. Furthermore, certain phenomena well-known in fluid dynamics, such as discontinuities (shock waves), rarefaction waves, or cusps, occur in the solution of such PDEs. These require a careful numerical treatment to resolve them, but their occurrence was very often ignored by numerical approaches to solve the Wetterich equation by erroneously assuming that the solution $U(t, \sigma)$ is continuous, smooth, and differentiable. Still, there are some publications which use numerical schemes to systematically capture non-analytic behavior or discuss the limitations of numerical methods in the presence of these effects, see, *e.g.*, Refs. [155, 565].

In order to make the fluid-dynamical analogy apparent, we present a formulation of the FRG flow equation (3.63) for the effective potential $U(t, \sigma)$ in terms of a conservation law. Furthermore, we discuss its fluid-dynamical interpretation on a qualitative level and classify the various contributions to the PDE – the (F)RG flow – in the fluid-dynamical picture. This sets the stage for an adequate qualitative interpretation of the FRG flow equation and a direct application of the KT scheme established in subsection 2.2.2.

The conservative form of Eq. (3.63)

Starting from the FRG flow equation (3.63) of the effective potential $U(t, \sigma)$, we have several options to recast the flow equation in a conservative form, two of which are:

1. Following Refs. [162, 247, 283, 398, 565, 569], we can take an overall derivative of Eq. (3.63) w.r.t. the $O(N)$ invariant $\varrho = \frac{1}{2} \sigma^2$ and express the resulting equation in terms of ϱ and $u(t, \varrho) \equiv \partial_\varrho U(t, \varrho)$,

$$\partial_t u(t, \varrho) = \frac{d}{d\varrho} \left(\frac{1}{2} \frac{N-1}{r(t) + u(t, \varrho)} \partial_t r(t) + \frac{1}{2} \frac{1}{r(t) + u(t, \varrho) + 2\varrho \partial_\varrho u(t, \varrho)} \partial_t r(t) \right). \quad (3.73)$$

2. Another option is to formulate the problem on the level of the background field σ itself [570] and by alternatively defining $u(t, \sigma) \equiv \partial_\sigma U(t, \sigma)$. Taking an overall derivative of Eq. (3.63) w.r.t. σ yields,

$$\partial_t u(t, \sigma) = \frac{d}{d\sigma} \left(\frac{1}{2} \frac{N-1}{r(t) + \frac{1}{\sigma} u(t, \sigma)} \partial_t r(t) + \frac{1}{2} \frac{1}{r(t) + \partial_\sigma u(t, \sigma)} \partial_t r(t) \right). \quad (3.74)$$

In both cases one ends up with a one-dimensional conservation law, where u plays the role of the conserved quantity (the fluid), t can be identified with the time variable and ϱ or σ are identified as the spatial variable.

The conservative form of the FRG flow equation (3.63) for the effective potential U on the level of its derivative u is not restricted to zero space-time dimensions or models with purely bosonic field content, see also Refs. [162, 247, 283, 398, 565, 569, 570] and chapters 4 and 5. As a matter of fact, this formulation generalizes to arbitrary dimensions and also to models which include fermionic degrees of freedom on the level of the LPA. In particular, the flow equation for the effective potential for models of strong-interaction matter, such as the quark-meson, the Nambu-Jona-Lasinio, and the Gross-Neveu(-Yukawa) model can be formulated in this fashion [4, 162, 210, 283, 284].

In this context, it is also worthwhile to note that Eq. (3.74) can be derived not only by taking a derivative of the FRG flow equation for the effective potential $U(t, \sigma)$ w.r.t. the background field σ . It is also possible to use the flow equation for the one-point function (2.67) directly and hence deriving the flow equation for $u(t, \sigma)$ via a projection on the one-point function $\bar{\Gamma}_t^{(1)}(\sigma)$,

$$\partial_t u(t, \sigma) = \left(\partial_t \bar{\Gamma}_t^{(1)}[\bar{\varphi}] \right)_{\varphi_1=\dots=\varphi_{N-1}=0, \varphi_N=\sigma} \equiv \partial_t \bar{\Gamma}_k^{\sigma} \quad (3.75)$$

$$= -\frac{1}{2} \text{diagram} - \frac{1}{2} \text{diagram} \quad (3.76)$$

$$= -\frac{1}{2} \frac{N-1}{\left[r(t) + \frac{1}{\sigma} u(t, \sigma) \right]^2} \partial_\sigma \left[\frac{1}{\sigma} u(t, \sigma) \right] \partial_t r(t) - \frac{1}{2} \frac{1}{\left[r(t) + \partial_\sigma u(t, \sigma) \right]^2} \partial_\sigma^2 u(t, \sigma) \partial_t r(t) \quad (3.77)$$

$$= \frac{d}{d\sigma} \left(\frac{1}{2} \text{diagram} + \frac{1}{2} \text{diagram} \right). \quad (3.78)$$

This corresponds to an interchange in the order of operations (evaluating the Wetterich equation on the background field configuration and taking derivatives w.r.t. the background field versus taking functional derivatives of the FRG equation and afterwards evaluating on the background field) and it is non-trivial (especially for flow equations for more complex models in higher dimensions and with truncation beyond LPA) that the resulting equations are identical, cf. App. B.3.1.

Before we turn to the fluid-dynamical interpretation of the conservation laws (3.73) and (3.74), we comment on the question whether one of the two formulations (3.73) and (3.74) is preferable or if even others should be considered. The answer to this question is not yet settled. From our present understanding, a formulation of the conservation equation in terms of σ is preferable, for reasons of numerical implementability in the FV scheme we use. This is discussed at length in the context of the PDE BCs for the FRG flow equation in subsection 3.2.2.4. Therefore, our discussion in the next sections is based on Eq. (3.74), and hence we identify σ with the spatial coordinate x and $u(t, \sigma) \equiv \partial_\sigma U(t, \sigma)$ as the conserved quantity.

The rest of this subsection is dedicated to the fluid-dynamical interpretation of the FRG flow equation (3.74). To this end, we split the flux (current) on the r.h.s. of the conservation law (3.74) and rewrite the whole equation in terms of an advection-diffusion equation, cf. Eq. (2.91) and subsections 2.2.3 and 2.2.4, in one spatial dimension $x = \sigma$ and one temporal dimension t ,

$$\partial_t u(t, x) + \frac{d}{dx} F[t, x, u(t, x)] = \frac{d}{dx} Q[t, \partial_x u(t, x)]. \quad (3.79)$$

The pionic contributions to the FRG flow,

$$F[t, x, u(t, x)] = -\frac{1}{2} \frac{N-1}{r(t) + \frac{1}{x} u(t, x)} \partial_t r(t) = -\frac{1}{2} \text{diagram}, \quad (3.80)$$

are identified with a non-linear, position-dependent advection flux, while the contribution of the radial σ -mode,

$$Q[t, \partial_x u(t, x)] = + \frac{1}{2} \frac{1}{r(t) + \partial_x u(t, x)} \partial_t r(t) = \frac{1}{2} \text{⊗}, \quad (3.81)$$

corresponds to a non-linear diffusion flux. We discussed conservation equations like Eq. (3.79) in a CFD context at length in our methodological introduction 2.2. In the following paragraphs we want to comment on the nature of the pionic/advective and radial σ /diffusive contributions using the established CFD terminology.

Advection

If we ignore the contribution of the σ -mode for a moment (which – after rescaling – corresponds to the large- N limit of the $O(N)$ model [3, 162, 247, 566]), we can rewrite the l.h.s. of Eq. (3.79) as follows,

$$\partial_t u(t, x) + \frac{d}{dx} F[t, x, u(t, x)] = 0 \quad (3.82)$$

$$\partial_t u(t, x) + \partial_u F[t, x, u(t, x)] \partial_x u(t, x) + \partial_x F[t, x, u(t, x)] = 0 \quad (3.83)$$

This is a hyperbolic, non-linear advection equation for $u(t, x)$, cf. Eq. (2.115), and its accompanying *primitive form*, cf. Eq. (2.116), including an internal source term. $\partial_u F[t, x, u(t, x)]$ is identified with the velocity of the characteristics (the local u -dependent flow velocity of the quantity u) and $\partial_x F[t, x, u(t, x)]$ acts like an x - and u -dependent internal source term. Hence $F[t, x, u(t, x)]$ is not purely advective nevertheless we will continue to refer to it as advection term.

The form of Eq. (3.82) motivated our discussion of linear and non-linear advection equations in subsection 2.2.3.2 with the LAE (2.123) and BBE (2.130) as instructive examples. When compared to the BBE (2.130) we notice that in our pionic FRG flow the local flow velocity is highly non-linear in t , x and u and explicitly reads

$$\partial_u F[t, x, u(t, x)] = \frac{1}{2} \frac{N - 1}{x \left[r(t) + \frac{1}{x} u(t, x) \right]^2} \partial_t r(t). \quad (3.84)$$

Considering for example the exponential regulator shape function (3.8), one finds that the advection velocity $\partial_u F[t, x, u(t, x)]$ is always negative (positive) for $x > 0$ ($x < 0$). In a fluid-dynamical picture, this means that the conserved quantity $u(t, x)$ is always propagated from larger values of $|x|$ towards the point $x = 0$ by advection. Furthermore, the closer the fluid $u(t, x)$ is to $x = 0$, the faster the fluid moves, due to the factor $\frac{1}{x}$. Since $u(t, x)$ is antisymmetric in x , because of the $O(N)$ symmetry of $U(t, \vec{\varphi})$, this implies that “waves” of positive and negative $u(t, x)$ collide with huge velocity at $x = 0$ and annihilate. At large $|x|$, the fluid velocity tends to zero.

We also observe that the advection velocity (3.84) is proportional to the number of pions, $N - 1$. Hence, in the large- N limit the system, discussed at length in subsection 3.2.5, is

completely advection driven, while for small N the diffusive contributions (3.81) gain in importance. In the case $N = 1$, discussed at length in subsection 3.2.4, there is no advection at all and the dynamics of the fluid $u(t, x)$ is purely diffusive.

At this point we want to remind the reader of the general properties and features of non-linear advection equations – like shock formation, (numerical) entropy production, and irreversibility – discussed in general in subsection 2.2.3. Naturally those properties also play an important role in the dynamics of FRG flows, which we will discuss in the following conceptually and also using explicit examples.

Diffusion

Next, we turn to the contribution of the radial σ -mode to the FRG flow. We find that it enters the conservation law (3.79) as a non-linear diffusion flux (3.81), because it is overall of second-order in spatial derivatives of $u(t, x)$. The characteristic property of diffusive processes is that they transport a quantity, in this case $u(t, x)$, from regions where its density or concentration is high to regions where it is low [315, 317, 319, 328], cf. subsection 2.2.4. Diffusive processes are therefore usually important in regions of high gradients and smear out cusps, shocks *etc.*, which might form via advection. Besides this, diffusive processes are generically undirected, which is also the case for the diffusion flux (3.81) which propagates the quantity $u(t, x)$ in both directions, depending on the local gradients of $u(t, x)$, which is especially relevant for models in their symmetry-broken phase with rather weak advection (small N). The effective transport velocities via diffusion are usually much slower than those via advection, which is, due to the non-linearity, not necessarily true for FRG flow equations. We discussed the HE (2.138) as an archetypal linear diffusion equation at length in subsection 2.2.4. The diffusion flux (3.79) can be formulated as a non-linear time-dependent realization of the heat equation. By performing the spatial derivative in the advection-diffusion equation (3.79) for the purely diffusive ($N = 1$) case, one finds

$$\partial_t u(t, x) = \alpha[t, \partial_x u(t, x)] \partial_x^2 u(t, x), \quad (3.85)$$

where

$$\alpha[t, \partial_x u(t, x)] \equiv - \frac{\frac{1}{2} \partial_t r(t)}{[r(t) + \partial_x u(t, x)]^2}, \quad (3.86)$$

plays the role of a non-linear time-dependent, strictly positive – parabolic – diffusion coefficient. The positivity of the diffusion coefficients ensures that $u(t, x)$ is only dispersed and never accumulates locally, *i.e.*, that $u(t, x)$ tends to equilibrate towards a linear function in space. A positive diffusion coefficient also ensures stability and uniqueness of (numerical) weak solutions, as discussed in the beginning of subsection 2.2.4.

Directly comparing these findings with the HE, we can already qualitatively predict the behavior of the diffusion transport for the FRG flow of $u(t, x)$, as long as N is small and the system is diffusion-dominated. At a constant RG time t , we find that the diffusion coefficient is much larger in regions where the gradient $\partial_x u(t, x)$ is negative with a large absolute value, compared to regions where it is positive, because in the first case the denominator of Eq. (3.86)

is smaller than in the second case. This plays a crucial role for systems that involve symmetry breaking, where $\partial_x u(t, x)$ is negative for at least some small $|x|$, while asymptotically for $|x| \rightarrow \infty$ the sign of $\partial_x u(t, x)$ is always positive. Hence, for diffusion-dominated problems in FRG flow equations (small number N of pions), the symmetry restoration is driven by the negative gradients $\partial_x u(t, x)$ at small $|x|$. Furthermore, we find that for $t \rightarrow \infty$, the numerator of the diffusion coefficient (3.86) tends to zero such that the diffusion stops, the system equilibrates and the dynamics freezes, even though there are still gradients in $u(t, x)$. This would not happen for the linear HE with its constant diffusion coefficient. The same is true for $t = 0$, where the diffusion coefficient is suppressed by $1/\Lambda$.

Irreversibility and entropy production

In a fluid-dynamical setting, it is very easy to understand the role of the radial σ -mode: Due to its diffusive character, it is directly responsible for the irreversibility of the (F)RG flow and RG transformations in general. Diffusion is a particular example of a dissipative process, which is irreversible and increases the entropy of the system⁴⁵. The dissipative and irreversible character can be seen as a “thermodynamic” version of the irreversible Kadanoff block-spin transformations [95, 235, 236]. Hence, the dissipation clearly singles out the RG time t as a temporal direction, because it introduces a “thermodynamic arrow of time” and “thermodynamic time asymmetry” via entropy production [579]. This also explains why our definition (2.12):

$$t \equiv -\ln\left(\frac{k}{\Lambda}\right) = \ln\left(\frac{\Lambda}{k}\right), \quad t \in [0, \infty). \quad (3.87)$$

is a natural choice for a temporal coordinate also in higher dimensions, see also Refs. [247, 311, 576, 578, 580].

Interestingly, the irreversibility and the dissipative character of the system is lost if one does not include the full field-dependence of the effective potential in the flow equation, but instead uses a truncated system like the Taylor expansion (3.71). Then, the system (3.71) of coupled ODEs for the vertices can theoretically be integrated in either direction in RG time, as long as it consists of a finite number of couplings⁴⁶. The most extreme examples are the RG flows of one single t -dependent coupling, *e.g.*, the quartic coupling of ϕ^4 theory or the QCD beta function [66, 67, 581, 582], see also the textbooks [177, 178]. Here the integration to both higher and smaller RG scales is possible, which is the well-known result for the universal one-loop beta function and is an artifact of the restriction (truncation) to a finite number of couplings [235]. However, this reversibility of RG transformations is not possible for the field-dependent effective potential, which is obvious from the advection-diffusion equation (3.79),

⁴⁵Interestingly, Ref. [575] comes to the same conclusion arguing in reverse order: “Some of the information on the ultraviolet behavior of the field theory is lost under renormalization transformations with $t > 0$, since in the field theory it is not legitimate to examine correlations at scales smaller than the cutoff. We would therefore expect that a motion of the space Q [a change of the set of all couplings] under the influence of the renormalization group would become an ‘irreversible’ process, similar to the time evolution of dissipative systems.” We remark that also Ref. [576] stated that a term of second-order in field space derivatives in related RG flow equations “[...] corresponds to a dissipation in the flow and is responsible for the semi-group property of the RG”.

⁴⁶In momentum space this enables an integration to higher energy scales, which corresponds to a reversion of the coarse-graining in position space. More generally speaking, this implies that it is possible to resolve the microphysics from the macrophysics. Both are physically not possible and solely an artifact of the truncation.

where entropy increases and the information about the IC in the UV cannot be recovered from the IR anymore.

This point of view was already shared, presented, and discussed by K. G. Wilson: In Ref. [235] he pointed out the differences between his “coarse-graining” version of the RG, which is also applicable in highly non-perturbative regimes, and the RG flow equations used by C. Callan, K. Symanzik, M. Gell-Mann, F. Low, G. t’Hooft, S. Weinberg, H. Georgi, D. Politzer and others to calculate the running of a single (or small number of) coupling constants, which solely describes a system correctly in a perturbative regime.

The irreversibility of the FRG flow and entropy production is also directly related to the presence of discontinuities in the solution, which can arise from the advective contributions to the flow. As shown in Refs. [3, 162, 247, 565] for the large- N limit, a shock wave arises when the weak solution of the PDE is multi-valued. The correct solution is usually constructed by means of the Rankine-Hugoniot condition [315, 317, 319, 328, 368, 369]. This would lead to ambiguities when one tries to invert the flow (integrating backwards in time) in the presence of a shock. Hence, shock formation is an irreversible process and produces entropy. In summary, these are further strong arguments why the assumption of expandability of the effective average action in terms of vertices as well as the truncation of the system should in general be considered with care.

Therefore, it would be extremely interesting to explicitly construct an entropy function for the flow equation, *i.e.*, a quantity that is either non-decreasing or non-increasing under the RG transformations during the FRG flow (depending on the sign convention), and that is a functional of the quantity $u(t, x)$. The entropy for the flow equation will be a helpful instrument to design a stable numerical scheme for generic truncations [315, 317, 319] and will also highlight general properties of the (F)RG flow. In this context we also have to mention the recent publication [245] by J. Cotler and S. Rezhikov who were able to interpret the Polchinski equation as an “optimal transport gradient flow of a field-theoretic relative entropy” thus establishing a firm and explicit connection between an information-theoretic entropy and (F)RG flows.

Additionally, a numeric entropy (function) might provide a direct link to \mathcal{C} -/ \mathcal{A} -theorems [230, 575, 583–588], which state that in certain QFTs there exists some positive real function $\mathcal{C}(\{g_i\}, t)$, which depends on all coupling constants of the QFT and which is monotonically increasing⁴⁷ during RG flows (transformations), while it stays constant at (critical) fixed points,

$$\frac{d}{dt} \mathcal{C}(\{g_i\}, t) \geq 0. \quad (3.88)$$

Here, $\{g_i\}$ denotes the set of all (possibly infinitely many) dimensionless coupling constants. In contrast to previous formulations [589–595], a non-local version, which is directly linked to the numerical entropy function (similar to versions presented in Refs. [230, 576, 580] for related field-dependent flow equations), would not rely on expandability in the couplings or vertices and could naturally display the dissipative character of RG transformations, which was already

⁴⁷It can also be defined as a monotonically decreasing function. This flip of sign corresponds to the difference of the mathematicians’ and physicists’ definition of entropy. We chose to the “thermodynamic convention” of increasing entropy for this and subsequent publications.

described by Refs. [575, 576]. Fixed-point solutions of the FRG flow would directly correspond to steady-state or thermal-equilibrium solutions [315] in the fluid-dynamical picture⁴⁸. A caveat at this point is that a \mathcal{C} function is based on the rescaled dimensionless RG flow equations. Hence, also a numerical entropy should be formulated in this framework, if one seeks a direct link to a \mathcal{C} function. The dimensionless flow equations in the LPA can be recast in terms of conservation laws, which might be a good starting point.

An explicit discussion of (numerical) entropy for the zero-dimensional $O(1)$ model as well as possible links to \mathcal{C} functions is discussed in great detail in subsection 3.2.4. The situation for the $O(N)$ model in the limit $N \rightarrow \infty$ is discussed in subsection 3.2.5. The construction of an explicit (numerical) entropy has proven to be elusive in the case of finite $N > 1$ for the $O(N)$ model [2, 3] due to the explicit position-dependencies in Eq. (3.74) and (3.73) and the related internal source terms, cf. Eq. (3.82).

Generalizations

At this point we want to briefly comment on the generalization of the fluid-dynamical picture to FRG flow equations in higher-dimensional QFTs, systems with more (field-dependent) couplings, and FRG flow equations that involve fermions.

In higher-dimensional QFTs, the fluid-dynamical interpretation of the FRG flow of the effective potential survives, see for example Refs. [4, 162, 210, 247, 284, 570] and especially chapter 4. In zero dimensions, t merely parametrizes some dimensionless (mass-like) scale $r(t)$, see Eq. (3.8). In contrast, in higher dimensions, the RG time is defined as the negative logarithm of the ratio between the RG momentum scale k and the UV reference scale Λ , see Eq. (3.87). The fluxes gain further t -dependent prefactors via the momentum integrals of the trace in the Wetterich equation. This leads to a different time scaling but does not affect the overall discussion. The inclusion of further field-independent but scale-dependent couplings (such as a scale-dependent Yukawa coupling) adds ODEs to the advection-diffusion equation for the effective potential, which does not spoil its conservative fluid-dynamical character. It is currently investigated by us and collaborators [162, 210, 248, 283, 284] whether the inclusion as well as the conservative formulation of further field-dependent couplings (such as a field- and scale-dependent wave-function renormalization $Z(t, \vec{\varphi})$ in higher-dimensional models) is possible. In any case, simply adding fermions in the LPA does not destroy the fluid-dynamical character of the FRG flow equation at all: On the level of the LPA for the FRG flow equation of the effective potential, the contributions from fermion loops can be interpreted as a source/sink term, which only depends on σ , *i.e.*, the spatial position x . We discuss such fermionic source/sink terms in zero dimensions in section 3.3 and in non-zero, *i.e.*, $1+1 = 2$ dimensions, at zero and non-zero temperature and especially quark chemical potential in chapter 4. Another possible generalization concerns models with more than one invariant of the underlying symmetry group of the model and respective condensation directions in field space, see, *e.g.*, Refs. [99, 127, 145, 147, 337, 338]. Here, the fluid-dynamical framework should still be applicable. However,

⁴⁸This actually brings up the interesting question whether previous studies about global fixed-point solutions for field-dependent flow equations, which seemed to deliver interesting results, *e.g.*, Refs. [154, 243, 576], should be reanalyzed from the fluid-dynamical steady-flow perspective, especially regarding their interpretation and the spatial discretization methods [315].

a suitable identification of a complete basis of field space directions with “spatial directions” of the fluid-dynamical problem and a clear separation of the single contributions into advection, diffusion, and source terms might be challenging and calls for future investigations – especially when it comes to an actual numerical implementation. For first attempts of generalizing our findings to a quark-meson-diquark model, we refer to Ref. [596].

Summarizing we find that the fluid-dynamical interpretation of flow equations has tremendous benefits, because it allows for a rather intuitive understanding of the dynamics of the system. Furthermore, it allows for a novel, physically intuitive interpretation of the FRG flow and provides an understanding of its irreversibility. Finally, it opens up the opportunity to employ extremely powerful numerical tools from CFD.

3.2.2.4. Boundary conditions and computational domain

This subsection follows the discussion presented in Sec. IV.D of Ref. [1].

In the form of the conservation laws (3.73) or (3.74), the FRG flow equation (3.63) is a non-linear PDE which has contributions of parabolic (diffusion terms) as well as hyperbolic (advection terms) nature. In this subsection, we specify the BCs for Eqs. (3.73) or (3.74) in field space (the effective spatial x -direction).

For (non-linear) PDEs of hyperbolic and parabolic type, the spatial BCs are needed (in addition to the IC) to make finding a (weak) solution a well-defined problem, cf. subsections 2.2.3 and 2.2.4. We are dealing with a *Cauchy* or to be even more specific an *initial-boundary-value* problem. Thus, without explicitly specifying the BCs, e.g., of Neumann- or Dirichlet-type, as well as the ICs, the problem of finding a unique (weak) solution is actually ill-posed and therefore impossible to solve – a well-known mathematical fact with particular and severe implications in, e.g., classical electrodynamics [597], fluid dynamics [598], soliton and instanton solutions of classical field equations [599, 600], general relativity [601–603], and other fields of research. This – unsurprisingly – also holds true for the FRG. However, explicit BCs and especially their numerical implementation are rarely discussed in FRG literature, with, e.g., Refs. [567, 568, 592, 604] as notable exceptions before the advent of CFD methods for the FRG [1–4, 162, 210, 247, 248, 283, 284].

For the derivative of the effective potential $u(t, \sigma)$, we find that the spatial BCs must be imposed at $\sigma = \pm\infty$, because the field space domain of $u(t, \sigma)$ is given by \mathbb{R} . Thus, when considering the flow equation on the non-compact domain $(-\infty, \infty)$ the problem represents a *pure initial-value/Cauchy problem* [315, 317, 328] and, given the asymptotics of the flow equation and the IC, explicit BCs at $\sigma \rightarrow \pm\infty$ are not required. However, spanning a non-compact computational interval from $-\infty$ to $+\infty$ is practically impossible on a finite computational grid. A possible solution is a compactification [155] of \mathbb{R} to the interval $[-1, +1]$, via a suitable mapping $\sigma \mapsto x(\sigma)$ usually supplemented with a mapping $u \mapsto v(u)$ rendering v finite on $[-1, +1]$. Another popular solution is a truncation of the computation interval at a large value $\sigma_{\max} \sim x_{\max}$ with a suitable BC [154, 155, 567, 604]. We will return to this issue below.

In any case, one of the boundaries at spatial infinity can already be replaced by a finite value by making use of the $O(N)$ symmetry of the potential $U(t, \vec{\varphi})$ and the flow equations, which

implies a \mathbb{Z}_2 antisymmetry of $u(t, \sigma) = \partial_\sigma U(t, \sigma)$,

$$U(t, \sigma) = U(t, -\sigma) \quad \iff \quad u(t, \sigma) = -u(t, -\sigma). \quad (3.89)$$

This reduces the spatial domain to the half-open interval $\sigma \in [0, +\infty)$, but now we need an additional artificial BC at $\sigma = 0$, see, e.g., Ref. [567]. In previous studies, the use of the $O(N)$ symmetry was usually implemented right from the beginning by replacing the variable $\vec{\varphi}$ by the $O(N)$ invariant $\varrho = \frac{1}{2} \vec{\varphi}^2$, whose domain is already by definition $[0, \infty)$.⁴⁹ In this case one has to define

$$u(t, \varrho) \equiv \partial_\varrho U(t, \rho) = \frac{1}{\sigma} \partial_\sigma U(t, \sigma) = \frac{1}{\sigma} u(t, \sigma), \quad (3.90)$$

to obtain a flow equation for $u(t, \varrho)$ in a manifestly conservative form, see Eqs. (3.73) and (3.74). Before returning to the remaining BC at $+\infty$, we first consider the newly introduced artificial BC at $x = \sigma = 0$ or, correspondingly, at $\varrho = 0$.

The boundary condition at $\sigma = 0$

At first sight it might be appealing to formulate the whole problem – the conservation equation and the BC at $\sigma = 0$ – in the variable ϱ . However, we believe that a formulation in σ is more suitable and easier to implement in our numerical FV setup.⁵⁰ A key feature of (non-linear) hyperbolic/parabolic conservation equations is that their weak solutions may exhibit non-analyticities in the form of shock and rarefaction waves *etc.*, which manifest themselves in the solution in cusps or discontinuities in spatial direction during the time evolution, *cf.* subsection 2.2.6. These effects can develop during the time evolution even if the IC is smooth/analytic, see, e.g., Refs. [155, 167, 315, 317, 371, 372, 609] and our discussion of the BBE (2.130) in subsection 2.2.3.2. As demonstrated in Refs. [4, 162, 210, 247, 283, 284, 398, 565, 569] this also holds for FRG flow equations, where non-analyticities are inherent properties of the effective IR potential $U(t_{\text{IR}}, \sigma)$. These statements are also true for the point $\sigma = 0$, where $U(t, \sigma)$ and $u(t, \sigma)$ do not need to be analytic, see subsection 3.2.3.4. Hence, there might be a scenario where the potential $U(t, \sigma)$, although it is symmetric in σ , has a cusp at $\sigma = 0$, which would correspond to a jump in a weak solution for $u(t, \sigma) = \partial_\sigma U(t, \sigma)$ at $\sigma = 0$. If formulated in ϱ , any scenario (analytic or non-analytic at $\sigma = 0$) merely corresponds to

⁴⁹In any case, independent of the implementation of the BC itself, one should make use of symmetries of the flow equations in numerical implementations. First of all, this leads to a reduction of the number of computational grid points in spatial direction, while keeping the spatial resolution fixed, which significantly speeds up the calculations (independently of the specific numerical method for spatial discretization). An additional consequence is the reduction of numerical errors: It is highly unlikely that the numerical errors are symmetric in x , if a symmetric interval around $x = \sigma = 0$ is used. This might lead to an artificial breaking of the \mathbb{Z}_2 antisymmetry by unbalanced numerical errors. Although these errors might be tiny and almost negligible they can be easily circumvented by exploiting the symmetries. Using the symmetries of a problem is a standard procedure in practical computations and of particular importance in, e.g., numerical fluid dynamics and numerical (general) relativity, see Refs. [605–608].

⁵⁰We do not claim that it is impossible to formulate well-defined discrete BCs in ϱ at $\varrho = 0$, as can be seen for example in Refs. [3, 162, 247] for the specific case of the large- N limit of the $O(N)$ model and generalizations to finite N [210, 284]. However, we were not able to provide a suitable discretization of the BC at $\varrho = 0$ in the implementation of the FV method for flow equations that include diffusion via the radial σ -mode.

some arbitrary value for $u(t, \varrho) = \partial_\varrho U(t, \varrho)$ at $\varrho = 0$, which seems to be of great advantage, because one does not have to deal with possible discontinuities in the conserved quantity u . Furthermore, the problematic factors of $\frac{1}{\sigma}$ in the pion propagator and the advection flux (3.80), which are diverging at $\sigma = 0$, can be avoided when formulating the flow equations in ϱ .

Nevertheless, a problem with the variable ϱ becomes apparent when turning to the discretized form of u within the FV scheme introduced in section 2.2 and specifically subsection 2.2.2: FV methods (and also other discretization schemes) usually require ghost cells at the boundaries of the computational domain, since the in- and out-flows for the i^{th} cell are calculated from the cell averages \bar{u} of its neighboring cells, cf. Eq. (2.106). However, initially these values are not specified for the cells at the boundaries of the computational domain. Thus, artificial ghost cells must be introduced and the numerical values for \bar{u} in these ghost cells have to be implemented by hand or reconstructed from the cells within the computational domain in accordance with the BCs [315, 317], cf. subsections 2.2.3 and 2.2.4 and Eqs. (2.126), (2.128), (2.141), (2.142), and (2.148). In the second-order formulation of the one-dimensional KT scheme one needs two ghost cells at each of the two spatial boundaries, cf. Eq. (2.106).

However, implementing ghost cells for $u(t, \varrho)$ at $\varrho = 0$ is conceptually difficult, because these ghost cells must be centered at negative values for ϱ outside the computational domain $[0, \infty)$, which by definition do not exist due to the positivity of $\varrho = \frac{1}{2} \sigma^2$. *A priori*, it is therefore not clear how numerical values $\bar{u}(t, \varrho_i)$ should be assigned to ghost cells at negative ϱ_i , because symmetry arguments cannot be applied anymore.

Furthermore, it is also not a feasible option to move the ghost cells to positive values of ϱ_i , such that the point $\varrho = 0$ is no longer part of the computational domain. Namely, having ghost cells centered at small but positive ϱ_i implies that one has to extrapolate the numerical values $\bar{u}(t, \varrho_i)$ to these ghost cells and to the point $\varrho = 0$ from the other ordinary cells of the computational domain. However, the functional behavior of $u(t, \varrho)$ is unknown for small ϱ and is actually exactly what we want to calculate in the first place by solving the PDE. Thus, any extrapolation at small ϱ can only be considered an educated guess. It is especially dangerous, because the physical point will be part of the extrapolated ghost cells if it is located at $\varrho = 0$, which is the case for all models in their symmetric phase [4], irrespective of the dimensionality of space-time. Consequently, extrapolation errors at the physical point have the potential to spoil the numerical values of all n -point functions, which are calculated at the physical point via derivatives of u and contain the physics of the model. Even if the physical point is at finite non-zero ϱ far away from the ghost cells and the boundary at $\varrho = 0$, any kind of extrapolation at small ϱ leads to numerical errors, because the diffusive contributions of the radial σ -mode will propagate this information from smaller to larger ϱ and hence to the physical point. Similar problems in formulating appropriate BCs at $\varrho = 0$ also exist in other discretization schemes like finite-difference or finite-element methods.

There is one exception to this conclusion: In the large- N limit of the $O(N)$ model the flow equation for u reduces to a pure advection equation. Studying the characteristic velocities, which are given by $\partial F / \partial u$, respectively, see Eq. (3.84), we find that these cannot change their sign, and information (or the conserved quantity u) is always propagated via advection in the direction of smaller ϱ or $|\sigma|$. In this scenario, ghost cells can be positioned at negative ϱ_i and the corresponding cell averages \bar{u}_i in the ghost cells can take any numerical value since

information from the ghost cells is never propagated back into the computational domain and cannot cause any errors, cf. Refs. [3, 162, 247] and especially subsection 3.2.5. Shifting the ghost cells into regions of positive ϱ is still not suitable for the reasons already discussed above.

In order to avoid all these difficulties when formulating the problem in the variable ϱ , we suggest a formulation in σ and an implementation of the BC at $\sigma = 0$. The key argument for using σ instead of ϱ is that positioning ghost cells at negative σ poses no problem at all, since negative σ exist in the first place. Furthermore, it is clear how the cell averages $\bar{u}(t, \sigma_i)$ in the ghost cells have to be chosen: Using the antisymmetry (3.89), one merely has to mirror the last physical cells of the computational domain at $\sigma = 0$ to the ghost cells (including a flip in sign). The only issue that requires careful consideration is the choice of the position of the first physical cell x_0 next to $\sigma = 0$: The flux term of our PDE contains factors $\frac{1}{\sigma}$ via the pion propagators, which diverge if evaluated at $\sigma = 0$. Therefore, we must avoid evaluating the fluxes $F[t, x, u(t, x)]$ at $x = \sigma = 0$. However, inspecting the KT scheme, we find that the fluxes as well as the Jacobian $\frac{\partial F[u]}{\partial u}$ must only be evaluated at the cell boundaries $x_{j \pm \frac{1}{2}}$, cf. Eq. (2.103) and (2.108). Consequently, the natural choice for the position of the cell center x_0 of the first physical cell in the computational domain is at $x = \sigma = 0$, such that the in- and out-fluxes of this cell are evaluated at $x_{\pm \frac{1}{2}}$, which is not problematic. Incidentally, this automatically cures the problem of the possibility of non-analyticities in $u(t, \sigma)$ at $\sigma = 0$: Even if $u(t, \sigma)$ is discontinuous at $\sigma = 0$ we do not run into problems, because all numerical calculations are performed on the level of cell averages $\bar{u}(t, \sigma_i)$. The cell average of an antisymmetric function in a cell that is centered at $\sigma = 0$ must always vanish identically, independent of all other properties of the function, see also Refs. [567, 568].

In summary, we switch from the open computational interval $(-\infty, +\infty)$ to the half-open computational interval $[0, +\infty)$ by means of the \mathbb{Z}_2 (anti-)symmetry using

$$\bar{u}_{-2}(t) = -\bar{u}_2(t), \quad \bar{u}_{-1}(t) = -\bar{u}_1(t), \quad \bar{u}_0(t) = 0, \quad (3.91)$$

for the cell averages in the ghost cells left of $x_0 = 0$ and in the cell at x_0 itself. This construction is visualized in figure 3.2 for exemplary continuous and discontinuous initial conditions. It effectively corresponds to reflective BCs frequently imposed in CFD [315, 317, 383], see, e.g., Eq. (2.148).

The boundary condition at $\sigma \rightarrow \infty$

Now we return to the BC at $\sigma \rightarrow +\infty$. W.l.o.g. we discuss the interval $\sigma \in [0, +\infty)$ since the situation in $\sigma \in (-\infty, 0]$ follows from \mathbb{Z}_2 antisymmetry of $u(t, \sigma)$.

We have already argued that there are no real BCs at spatial infinity on a non-compact domain. The behavior of u at $\sigma \rightarrow \infty$ is rather given by the asymptotics of the Wetterich equation, which makes the PDE an pure initial-value problem. The BC at spatial infinity is actually fixed implicitly: As long as the initial potential $U(t = 0, \sigma)$ is bounded from below and grows faster than σ^2 for $\sigma \rightarrow \infty$ both pion and sigma propagator tend to zero for sufficiently large σ , such that the r.h.s. of the PDE (3.74) vanishes during the entire FRG flow. In the fluid-dynamical picture this corresponds to vanishing advection (3.80) and diffusion fluxes (3.81)

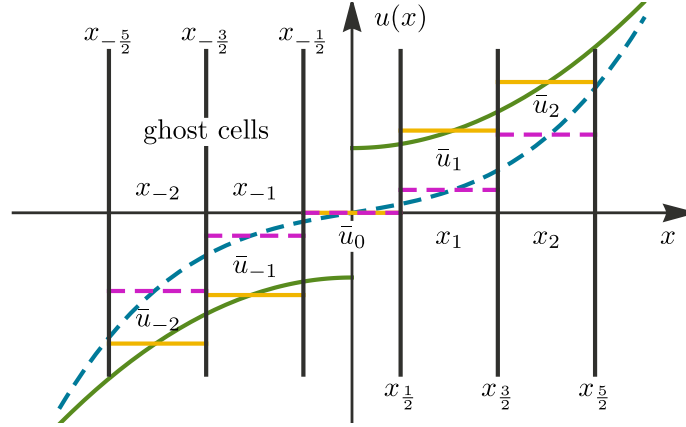


Figure 3.2.: Second-order accurate FV implementation of the spatial BC for $u(t, x)$ or $\bar{u}_i(t)$, respectively, at $x = 0$ using Eq. (3.91). We use the fact that $u(t, x)$ is an odd function in x by positioning the first computational cell x_0 at $x = 0$, such that the cell average is exactly zero, $\bar{u}_0 = 0$, which is true for $u(t, x)$ which are continuous (blue-dashed) as well as discontinuous (green-solid) at $x = 0$. Corresponding cell averages \bar{u}_i are depicted as horizontal bars (magenta-dashed and yellow-solid). This BC can be generalized to lower- and higher-order accurate FV schemes as well as finite-difference or finite-element schemes. From Fig. 3 of Ref. [1].

at $\sigma \rightarrow \infty$, which is a zero-influx BC for $u(t, \sigma)$. The derivative of the effective potential $u(t, \sigma)$ is therefore fixed to its initial value $u(t = 0, \sigma)$ at $\sigma \rightarrow \infty$.

The limiting case, when the asymptotic behavior of the UV initial potential is quadratic,

$$\lim_{\sigma \rightarrow \infty} U(t = 0, \sigma) \sim \sigma^2 \quad \iff \quad \lim_{\sigma \rightarrow \infty} u(t = 0, \sigma) \sim \sigma, \quad (3.92)$$

is more delicate. In this case, the advection and diffusion fluxes (3.80) and (3.81) do not vanish for $\sigma \rightarrow \infty$ for all RG times. However, for small RG times $t \approx 0$, the fluxes are actually independent of σ at large σ due to the constant asymptotic slope of the IC $u(t = 0, \sigma)$. This in turn implies that the in- and out-flux for all volume cells at large σ only depend on t and must cancel exactly, such that the net flux of these cells vanishes. Therefore, also in this scenario $u(t, \sigma)$ is fixed to its IC at $\sigma \rightarrow \infty$ not only for small t , but rather for all RG times t . For late RG times $t \rightarrow \infty$, the advection and diffusion fluxes (3.80) and (3.81) vanish anyhow, due to the derivatives of the regulator shape functions in the numerators, i.e., $\partial_t r(t) = -\Lambda e^{-t}$. In the language of fluid dynamics, ICs with quadratic asymptotics can therefore be interpreted as BCs with time-dependent but spatially constant influx, cf. EXAMPLES 7 and 9 in Ref. [167].

However, both cases cannot be implemented directly on a finite computational domain and we basically have two options:

1. We could map the interval $[0, \infty)$ to a compact interval $[0, 1]$ via a suitable map $\sigma \mapsto x(\sigma)$. This also includes a suitable mapping of $u \mapsto v(u)$ to keep the values for the conserved quantity finite on $[0, 1]$. This option has the advantage that the correct asymptotic behavior $u(t, \sigma)$ can be implemented as BCs for $v(t, x)$ at $x = 1$. However, the same question then

arises as before in the discussion of an appropriate choice of ghost cells for negative values of ϱ : It is highly non-trivial how the cell averages \bar{v}_i should be fixed for ghost cells which no longer belong to the physical values of x within the interval $[0, 1]$. Additionally, the two mappings would introduce at least two new numerical functional-mapping parameters. A suitable choice of these parameters is not obvious. Still, these mappings would have to ensure dense grids and high resolution around the physical point and low resolution at large field values. All this is extremely hard to achieve. Therefore, we propose and favor another option.

2. The second option, which is our preferred choice, is to split the physical domain $[0, \infty)$ into a compact domain $[0, \sigma_{\max}]$ and a non-compact domain $[\sigma_{\max}, \infty)$. Here, σ_{\max} should be chosen much larger than the physical scales of the problem and the position of the physical point, see, *e.g.*, Refs. [4, 154, 210, 247, 283, 284, 567, 604]. We will provide explicit tests for an appropriate choice of σ_{\max} later on in subsection 3.2.3. For the compact domain $[0, \sigma_{\max}]$, we keep a direct identification of the field σ and the computational spatial variable x , thus $x = \sigma$. For higher-dimensional models this might be replaced by a linear map of σ to a dimensionless spatial variable x via appropriate rescaling with some characteristic dimensionful quantity, *e.g.*, the UV scale Λ or a non-vanishing condensate.

In the compact domain $[0, \sigma_{\max}]$, we have to ensure a high spatial resolution via a sufficiently large number of cells, in order to capture all aspects of the dynamics around the physical point. Explicit tests to find an appropriate spatial resolution are also presented in subsection 3.2.3.

For the non-compact domain $[\sigma_{\max}, \infty)$, instead of using a discretization scheme like the FV method, we suggest an expansion or approximation of $u(t, \sigma)$ via polynomials or complete sets of functions with t -dependent expansion coefficients, which account for the asymptotic behavior of the IC $u(t = 0, \sigma)$ for large σ . As discussed before, it is expected that for large σ the deviations of $u(t, \sigma)$ from the IC $u(t = 0, \sigma)$ are small during the FRG flow, such that a finite amount of expansion coefficients should be satisfactory to capture this minimal dynamics.

At the point σ_{\max} , the ghost cells for the FV method in $[0, \sigma_{\max}]$ can therefore be fixed via the values $u(t, \sigma)$ from the asymptotic expansion in the non-compact interval $[\sigma_{\max}, \infty)$.

Interestingly, our numerical tests showed that, as long as σ_{\max} is chosen sufficiently large, the fluxes at σ_{\max} are already negligibly small. As a consequence, the deviation of $u(t, \sigma)$ from the IC in the non-compact interval $[\sigma_{\max}, \infty)$ is extremely small and can be ignored. In this case, the computational BCs for the ghost cells at σ_{\max} can be fixed via an extrapolation using the asymptotics of the IC. For extremely high spatial resolution, hence rather small Δx , even a simple linear extrapolation might be sufficient:

$$\bar{u}_n(t) = 2\bar{u}_{n-1}(t) - \bar{u}_{n-2}(t), \quad \bar{u}_{n+1}(t) = 3\bar{u}_{n-1}(t) - 2\bar{u}_{n-2}(t), \quad (3.93)$$

cf. Eq. (2.126). On the other hand, choosing σ_{\max} rather large while keeping a high spatial resolution in the compact computational domain $[0, \sigma_{\max}]$ requires a large number of cells. However, this slows down the computations drastically. For problems where this issue becomes

relevant, we suggest to further divide the compact domain $[0, \sigma_{\max}]$ into several smaller subdomains. In each of these subdomains one can implement the FV method with different spatial resolution Δx for each domain. This ensures high resolution at small σ next to the physical point and also allows to truncate the spatial interval at large σ_{\max} , while keeping a decent and manageable total number of cells [162, 210, 247, 284]. An alternative approach would be switching from equally sized volume cells on a uniform grid to a non-uniform (potentially even moving/time-dependent) grid, see, e.g., Ref. [336]. Such numerical improvements over our approach using just one uniform FV grid might become especially relevant in the context of FRG flow equations for models with multiple condensate directions, see, e.g., Refs. [99, 145, 147, 337]. For our computations within this work a further subdivision of the compact interval $[0, \sigma_{\max}]$ or a formulation on non-uniform grids was, however, not necessary. Our specific choice and implementation (3.93) might not be the best option at hand for arbitrary (higher-dimensional) models and arbitrary ICs within the FRG framework. In the current context of the zero-dimensional $O(N)$ model ICs without a proper large- $|\vec{\phi}|$ asymptotics, e.g., $[2 - \sin(\vec{\phi}^2)] \vec{\phi}^2$ or even worse $[2 - |\sin(\vec{\phi}^2)|] \vec{\phi}^2$, and/or periodic potentials could be a very interesting topics for further research.

3.2.3. The $O(N)$ model at finite N

In this subsection we follow the discussion of results presented in Sec. V of Ref. [1]. The plots of Ref. [1] and the underlying numerical data were produced by A. Koenigstein and numerically cross-checked by my own computations with the KT scheme.

Selected numerical results and accompanying symbolic computations are included in the digital auxiliary file [364]. The single thread wall time on various consumer processors for the numeric results of this subsection is of the order of several days.

After our general discussion of the theoretical basis for the solution of FRG flow equations, it is again high time to “show some pictures”: we will discuss concrete applications of the zero-dimensional $O(N)$ at finite N in the following subsections. To this end, we study the FRG flow of various zero-dimensional field theories – *test cases* – which differ by distinct initial conditions. Our choices for the initial conditions range from smooth potentials to extreme choices featuring non-analyticities. Note that such extreme choices are not only relevant to demonstrate the numerical performance and stability of our implementation but also for phenomenological reasons. In fact, in higher dimensions we expect non-analytic behavior to build up, e.g., in the IR limit, as a consequence of spontaneous symmetry breaking and the emergence of convexity of the effective action.

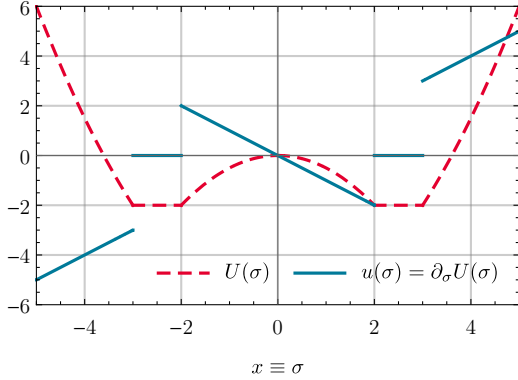


Figure 3.3.: The plot shows the UV potential $U(\sigma)$ (red-dashed) and its first derivative $u(\sigma) = \partial_\sigma U(\sigma)$ (blue, solid) of test case I from Eq. (3.94). From Fig. 4 of Ref. [1].

Table 3.1.: Exact results for $\Gamma^{(2n)}$ of the $O(N)$ model with the UV initial potential (3.94) for selected N . They are obtained by a high-precision one-dimensional numerical integration of the expectation values $\langle (\overline{\phi}^2)^n \rangle$ from Eq. (3.56) using *NIntegrate* in MATHEMATICA [353]. Here, we present the first six digits only. From Tab. I of Ref. [1].

N	$\Gamma^{(2)}$	$\Gamma^{(4)}$	$\Gamma^{(6)}$
1	0.176813	0.052055	0.086573
3	0.397354	0.140864	0.224996
10	0.845144	0.151933	-0.069134

3.2.3.1. Test case I: Non-analytic initial condition

Consider the following UV initial potential,

$$U(\vec{\varphi}) = \begin{cases} -\frac{1}{2} \vec{\varphi}^2, & \text{if } |\vec{\varphi}| \leq 2, \\ -2, & \text{if } 2 < |\vec{\varphi}| \leq 3, \\ +\frac{1}{2} (\vec{\varphi}^2 - 13), & \text{if } |\vec{\varphi}| > 3, \end{cases} \quad (3.94)$$

which is plotted in figure 3.3. This initial condition for the zero-dimensional $O(N)$ model – in the following sometimes just referred to as *test case I* – is designed this way for the following reasons:

1. All parameters of the potential $U(\vec{\varphi})$ are by default dimensionless and chosen to be approximately of order one, such that scales can easily be compared with each other.
2. The UV potential evaluated on the mean-field σ , $U(\sigma)$, has non-analytical points at $\sigma = 2$ and $\sigma = 3$, which correspond to discontinuities in its derivative $u(\sigma)$. In the fluid-dynamical context such discontinuities present a Riemann problem and result in rarefaction waves, cf. subsection 2.2.6. In QFT and thermodynamics such discontinuities can be associated with phase transitions, see App. B of Ref. [1]. The non-analytical behavior of this potential makes commonly used techniques like the FRG Taylor expansion inapplicable. Furthermore, naive discretizations that rely on smoothness are doomed to fail. One has to choose numerical schemes that can handle this numerically challenging dynamics.
3. The potential is initialized in the symmetry-broken phase, with infinitely many degenerate minima at $\sigma \in (2, 3]$. Furthermore, the UV potential is neither convex nor smooth. However, in the IR the $O(N)$ symmetry has to be restored and there must only be one minimum at $\sigma = 0$, due to the CMWH theorem, i.e., in zero-dimensions $\varphi_a = \langle \phi_a \rangle = 0$,

which follows directly from the integral (3.45). Furthermore, for $t \rightarrow \infty$ the potential has to be convex and smooth, see App. B of Ref. [1]. This non-trivial transition and complicated dynamics from the UV to the IR is a numerically challenging test.

4. Furthermore, we choose a potential which is asymptotically quadratic in σ . This is to ensure that the large- σ BC for $u(t, \sigma)$ is fully under control and errors can be excluded, see subsection 3.2.2.4. This allows for a high-precision analysis of all other sources of numerical errors.

The reference values for the exact IR 1PI vertex functions $\Gamma^{(2n)}$ of the $O(N)$ model are calculated numerically from the UV potential (3.94) via the integral (3.56) using Eq. (3.52)–(3.54). They are listed in table 3.1 for selected N which are relevant for the following discussions.

In the remainder of this subsection we will use test case I (3.94) to discuss

- Advection and diffusion in FRG flows,
- Tests of the spatial resolution,
- Tests of the size of the computational domain,
- Tests of the UV and IR scales,

in the corresponding paragraphs which are based on Secs. V. A.1–4 of Ref. [1].

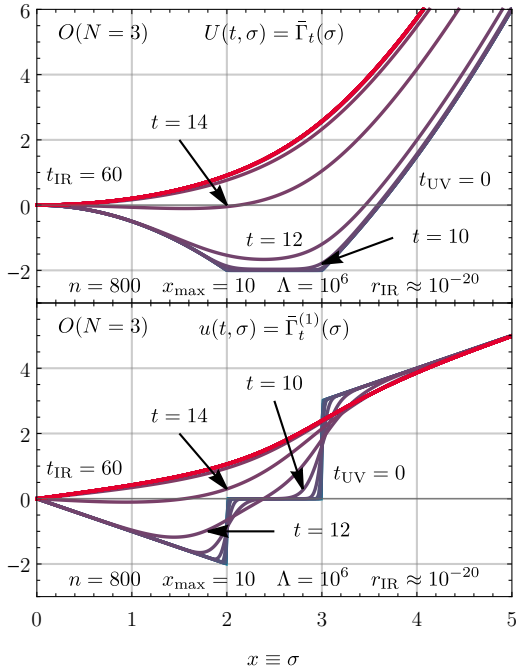
Advection and diffusion in FRG flows

We start our analysis with a general discussion of the FRG flow with IC (3.94). To this end, we fix $O(N = 3)$ to include both diffusive and advective contributions via the radial σ -mode and two pions. For $N = 3$ the number of pions is reasonably small and the (diffusive) effects of the σ -mode remain visible. Furthermore, we choose $[0, x_{\max} = 10]$ as the spatial computational domain with $n = 800$ volume cells and use the KT scheme from subsection 2.2.2 for spatial discretization. The initial cell averages $\bar{u}_i(t = 0)$ are computed by exact averaging⁵¹

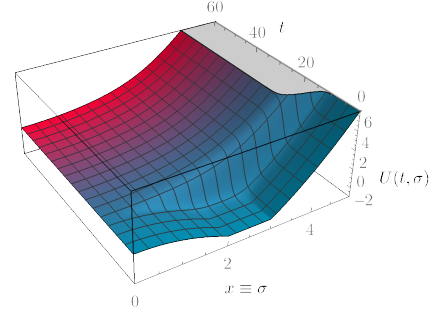
$$\bar{u}_i(t = 0) = \frac{1}{\Delta\sigma} [U(\sigma_{i+\frac{1}{2}}) - U(\sigma_{i-\frac{1}{2}})], \quad (3.95)$$

using the UV IC (3.94). We use linear extrapolation (2.126) as spatial BC at x_{\max} as discussed in subsection 3.2.2.4. The UV scale is set to $\Lambda = 10^6$ at $t = 0$. Time evolution of the semi-discrete KT ODE system is performed with *NDSolve* of MATHEMATICA [353] with a *PrecisionGoal* and *AccuracyGoal* of 10 and stopped in the IR at $r(t_{\text{IR}} = 60) \approx 10^{-20}$ using the exponential regulator shape function (3.8). Time-stepping has not been a focus of our work and we refer the interested reader to the excellent Ref. [355] discussing the issue in the context of FRG in detail. We find that this choice of parameters suffices to produce decent results, as discussed in the following. There, we quantitatively analyze sources and severity of possible errors related to those (numerical) parameters.

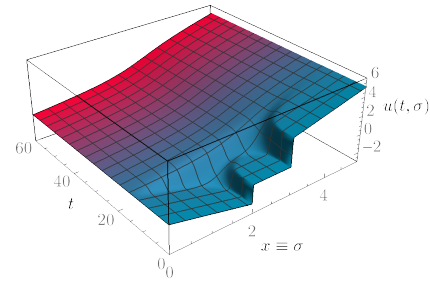
⁵¹Using the exact averages for $\bar{u}_i(t = 0)$ has proven advantageous in terms of achievable numerical precision in the IR compared to taking the mid-point values of the exact derivative of $\bar{u}_i(t = 0) = \partial_\sigma U(\sigma)|_{\sigma=\sigma_i}$ when considering non-analytic ICs like Eq. (3.94) or (3.104).



(a) Snapshots of the FRG flow at different times $t = 0, 2, 4, \dots, 60$ (integer values for t were chosen for convenience and readability).



(b) Three-dimensional rendering of the flow $U(t, \sigma)$ displayed on the left – Figure 3.4a (upper panel).



(c) Three-dimensional rendering of the flow $u(t, \sigma)$ displayed on the left – Figure 3.4a (lower panel).

Figure 3.4.: The FRG flow of the effective potential $U(t, \sigma)$ – upper panel/figure on the left (a) and on the right (b) – and its derivative $u(t, \sigma) = \partial_\sigma U(t, \sigma)$ – lower panel/figure on the left (a) and on the right (c) – for the zero-dimensional $O(3)$ model with initial condition (3.94). The blue curves correspond to the UV and the red curves to the IR. We used the exponential regulator (3.8) with UV scale $\Lambda = 10^6$. For the sake of readability, the plots do not show the region $x \in [5, 10]$, because the tiny differences between $u(t, \sigma)$ and $u(0, \sigma)$ are not visible in this region and vanish for large $x = \sigma$ anyhow. From Figs. 5, 6, and 7 of Ref. [1].

We first provide qualitative results of our numerical methods in figure 3.4, where we show the FRG flow of the effective potential $U(t, \sigma)$ and its derivative $u(t, \sigma) = \partial_\sigma U(t, \sigma)$ from the UV (blue) to the IR (red). In the beginning, *i.e.*, in the UV, the system is in the broken phase. This changes only marginally until $t \approx 7$, which indicates that the UV scale is chosen sufficiently large with $\Lambda = 10^6$. When $r(t)$ reaches the scales of the model at $t \gtrsim 11$ most of the dynamics takes place (symmetry restoration) and $u(t, \sigma)$ changes rapidly and drastically until it freezes out in the IR. In the IR the system is in the restored phase as expected *a priori*. After $t \approx 26$ the potential does not change anymore, which indicates that one has reached a sufficiently small IR scale to stop the integration. We render this statement more precise in the following subsection 3.2.3.1. Note that the evolution in t is logarithmic and corresponds to a change in scale over 25 orders of magnitude. At first glance this range sounds excessive, but its necessity is explained in detail in subsection 3.2.3.1.

During the FRG evolution one observes that diffusive processes smear out the discontinuities

at the non-analytic points at $\sigma = 2$ and $\sigma = 3$. We also find that the diffusion acts in both directions – towards larger and smaller values of σ – as expected from our discussion in subsection 3.2.2.3. Nevertheless, the diffusive effects do not reach the computational boundary, which is outside the plot range at $\sigma_{\max} = 10$. This suggests that $\sigma_{\max} = 10$ is sufficiently large. Additionally, we observe a propagation of the conserved quantity u towards smaller values of σ via advection. Close to the initial discontinuities these advective processes can be interpreted as rarefaction waves. In a more pictorial language, the advection and diffusion “fill up the pit” in $u(t, \sigma)$ at small values of σ by moving more and more of the quantity u from larger values of σ to smaller σ (via advection and diffusion) as well as from small negative σ to small positive σ (via diffusion). Eventually the symmetry is restored and $u(t, \sigma)$ is smoothed towards the IR by diffusion. Furthermore, the conserved quantity u does not “pile up” at $\sigma = 0$ after symmetry restoration, because at negative σ exactly the opposite dynamics happens, due to the \mathbb{Z}_2 antisymmetry of $u(t, \sigma)$, which is encoded in the BC at $\sigma = 0$, see subsection 3.2.2.4. The differences between advective and diffusive contributions become apparent when comparing the same system for different N , cf. figure 3.5 and the surrounding discussion.

From a numerical perspective, the KT scheme is able to handle the highly non-linear dynamics, including the non-analyticities in $u(t, \sigma)$, without any spurious oscillatory behavior (under-/over-shooting) and allows for a stable t integration to extremely small IR scales.

For the sake of completeness and illustrative purposes, we also provide the FRG flow of the integral of $u(t, \sigma)$, i.e., the effective potential $U(t, \sigma)$, in figure 3.4a (upper panel) and figure 3.4b. Here, the integration constant was set to zero⁵² and the integration was performed via Riemann summation⁵³ of the discrete cell averages,

$$U(t, x_i) = \Delta x \sum_{j=0}^i \frac{\bar{u}(t, x_j)}{(1 + \delta_{j,0} + \delta_{j,i})}. \quad (3.96)$$

Figure 3.4b perfectly illustrates the restoration of the $O(3)$ symmetry of the potential $U(t, \sigma)$ during the FRG flow via “vaporization” of the infinitely many minima. Nevertheless, we find that it is hardly possible to intuitively understand the contributions of the radial σ -mode and the pions to the FRG flow on the level of $U(t, \sigma)$ only. This complements the discussion in subsection 3.2.2.3 and lends support to our claim that the fluid-dynamical interpretation of the FRG flow in terms of $u(t, \sigma)$ is superior to the canonical formulation in terms of $U(t, \sigma)$ commonly used in the FRG literature.

Before discussing quantitative results and sources of (numerical) errors in FRG flows, we briefly return to the interpretation of the radial σ -mode as diffusion and the interpretation of the pions as advection in the FRG flow along the field space direction. To this end, we discuss FRG flows for the same UV initial potential (3.94) as before, but for different N . This corresponds to a different number of pions in the flow and different advection velocities (3.84).

⁵² $U(t, 0) = 0$ is dictated by our choice of normalization for the zero-point function(s), see Eq. (3.4).

⁵³At this point we should mention that numerical results for $U(t, \sigma)$ via Riemann summation should be treated with great caution: Numerical errors in the cell averages $\bar{u}(t, x_j)$ which arise from the numerical FRG flow can accumulate during integration (here summation) along $\sigma = x$. More precise quadrature methods should be used if precise, quantitative values for $U(t, \sigma)$ are needed.

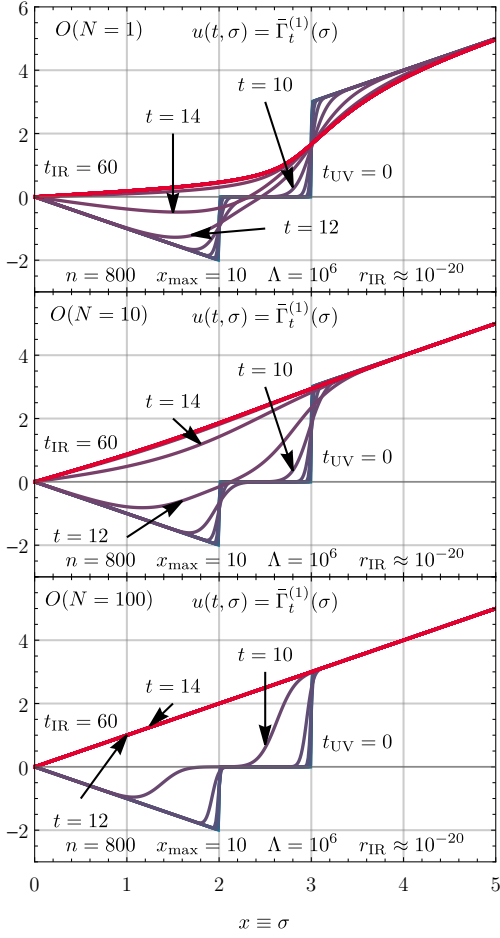


Figure 3.5.: The FRG flow of the derivative of the effective potential $u(t, \sigma) = \partial_\sigma U(t, \sigma)$ for the zero-dimensional $O(N)$ model for $N = 1, 10, 100$ with IC (3.94). All other parameters are identical to those in figure 3.4. From Fig. 8 of Ref. [1].

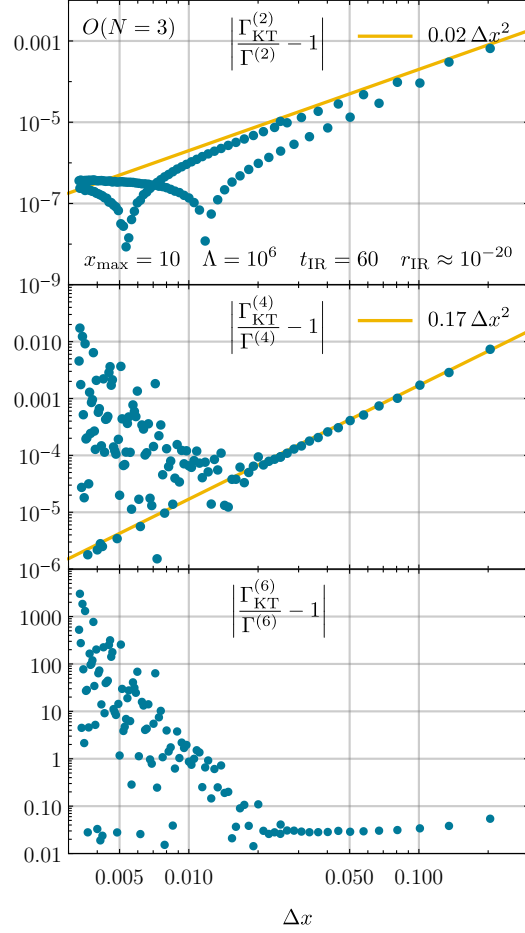


Figure 3.6.: The relative error of the numerical results (blue dots) from the KT scheme for the 1PI n -point functions $\Gamma^{(2n)}$ for $n = 1, 2, 3$ as a function of Δx with IC (3.94). The numerical derivatives at $\sigma = 0$ of $u(t_{\text{IR}} = 60, \sigma)$ were calculated via the second-order accurate central schemes (D.6), (D.9), and (D.12). The plot was produced with $x_{\text{max}} = 10$, but could have been calculated for any sufficiently large x_{max} . We used the exponential regulator (3.8) with UV scale $\Lambda = 10^6$. The yellow straight lines $\propto \Delta x^2$ are for optical guidance. From Fig. 9 of Ref. [1].

All other parameters remain unchanged. In addition to the $N = 3$ case in figure 3.4, we provide the FRG flows of $u(t, \sigma)$ for $N = 1, 10, 100$ in figure 3.5. The figure again demonstrates on a qualitative level that the σ -mode enters the FRG as diffusion, while pions enter as advection: Increasing the number of pions the problem becomes more advection-driven exhibiting more pronounced waves and faster propagation. This can be seen by comparing the plots at equal RG times. For $N = 1$, the problem reduces to the pure diffusion equation (3.37), where the dynamics is slowest and the diffusion propagates the fluid from negative σ to small positive σ close to $\sigma = 0$. Furthermore, one observes stronger smearing of the discontinuities at $\sigma = 2$ and $\sigma = 3$. The $N = 100$ case is extremely advection-dominated. In the fluid-dynamical language, this corresponds to a complete suppression of diffusion, which is clearly observed from the fast propagation of the rarefaction waves and almost negligible smoothing of the discontinuities at $\sigma = 2$ and $\sigma = 3$. We will discuss the qualitative and quantitative differences between FRG flows at small N with flows large and even infinite N in subsection 3.2.5.

Tests of the spatial resolution

This paragraph is dedicated to quantifying numerical errors in the FRG flow arising from the finite spatial resolution $\Delta x \equiv \Delta \sigma$ of the cells in the KT scheme. Any spatial discretization comes with a discretization error. The KT scheme, which is used throughout this thesis, is formally of second-order accuracy in Δx when employing the numerical fluxes of Eq. (2.113) with the five-point stencil (2.106). Therefore, the numerical errors arising from the spatial discretization should scale with Δx^2 when Δx is decreased.

As test values (observables) we use the modulus of the relative errors of the 1PI n -point functions $\Gamma^{(2n)}$ for $n = 1, 2, 3$,

$$\left| \frac{\Gamma_{\text{KT}}^{(2n)}}{\Gamma^{(2n)}} - 1 \right|, \quad (3.97)$$

where $\Gamma_{\text{KT}}^{(2n)}$ is calculated from the FRG (via the KT scheme) and $\Gamma^{(2n)}$ from the integral, see table 3.1. In order to determine how much of the relative numerical error (3.97) is directly related to the spatial discretization, we have to optimize all other parameters of the computation in order to reduce other sources of errors. We basically choose the same parameter set – viz. $\Lambda = 10^6$, $x_{\text{max}} = 10$ and $t_{\text{IR}} = 60$ – and UV IC (3.94) which was also used for the qualitative analysis in the previous paragraph and only vary the number of cells n to change the resolution Δx . W.l.o.g. we keep $N = 3$.

Before we embark on our discussion, we remark that the spatial-discretization error enters the relative errors (3.97) in a twofold way:

1. There is the discretization error which comes from the KT scheme during the FRG time integration. This error shows up directly in the IR values $u(t_{\text{IR}}, x_i)$ and should scale according to Δx^2 for the chosen second-order KT scheme.
2. There is a discretization error which is related to the extraction of the 1PI n -point functions from the discrete $\bar{u}(t_{\text{IR}}, x_i)$. They have to be calculated at the physical point (the minimum at $x = \sigma = 0$) via numerical differentiation, which also comes with a discretization error.

The latter is also related to the spatial resolution Δx . In general (especially in higher-dimensional models) it is not clear whether these numerical derivatives at the physical point are always well-defined. We argued before that $u(t, \sigma)$ might exhibit non-analytical behavior also at the physical point in the IR, *cf.* Refs. [4, 155, 162, 247], such that a naive numerical differentiation is not allowed in general. In the special case of zero-dimensional QFTs, we proved in App. B of Ref. [1] that the IR effective action and the IR potential $U(t \rightarrow \infty, \vec{\varphi})$ are smooth, which also translates to $u(t \rightarrow \infty, \sigma)$, such that numerical differentiation (*e.g.*, via finite-difference approximations) is well-defined.

However, even though finite-difference formulas are reliable approximations for derivatives of a smooth function and have a well-defined truncation-error scaling in powers of Δx , there remains a well-known subtlety: While decreasing the resolution Δx , one eventually will reach a point where the error starts increasing again contrary to the formal truncation-error scaling. This is related to the ill-conditioned nature of finite-difference formulas and to explicit rounding errors in floating-point arithmetic, which increase the error of the numerical derivative below a certain Δx , see, *e.g.*, Chap. 5.7 of Ref. [555]. Related spurious cancellations occur if the discrete data of a smooth function include some sort of noise. In our case this “noise” is directly related to the spatial-discretization errors from the KT scheme and the errors from RG time integration using numerical ODE solvers. These errors might be tiny, but can easily inflate the errors of the numerical derivatives, especially for higher-order derivatives.

In conclusion, while decreasing Δx , we expect that long before the relative errors from the KT scheme start increasing again (because the KT scheme begins operating close to machine precision or because the error of the time stepping becomes relevant) the relative errors (3.97) start increasing due to the numerical differentiation of slightly “noisy data”. This phenomenon is expected to set in at larger Δx for approximations for higher-order derivatives and long before the formal error scaling of the KT scheme is no longer valid.

Our explicit results for the scaling of the relative errors with decreasing spatial resolution are presented in figure 3.6, where we show the relative errors (3.97) for the two-, four-, and six-point functions in a double-logarithmic plot over Δx . For $\Gamma^{(2)}$ and $\Gamma^{(4)}$ we find that the corresponding relative errors scale with Δx^2 (or even slightly better) as expected from the error scaling of the KT scheme as well as the error scaling of the finite-difference stencils (D.6) and (D.9). We observe two groups of points for $\Gamma^{(2)}$ (upper panel of figure 3.6), which are related to discretization errors of the discontinuous IC (3.94) at $x = 2$ and $x = 3$. The error scaling of $0.02 \Delta x^2$ for $\Gamma^{(2)}$ is a conservative estimate for the observed errors, which are actually lower for $\Delta x \gtrsim 0.005$. For $\Delta x \lesssim 0.005$ we observe deviations from the conservative estimate for the error scaling of $\Gamma^{(2)}$ related to other error sources. In the middle panel of figure 3.6, we clearly see that there is an optimal minimal $\Delta x \approx 0.02$ where the correct formal scaling of the numerical derivative breaks down and the relative error of $\Gamma^{(4)}$ increases again for smaller Δx . We can be sure that this breakdown of the error scaling is related to the numerical differentiation and not the KT scheme because we observe scaling with at least Δx^2 for $\Gamma^{(2)}$ in the upper panel of figure 3.6 well below $\Delta x \approx 0.02$. This is expected for lower-order numerical derivatives. Furthermore, we find that for $\Gamma^{(6)}$ (lower panel of figure 3.6) the order of the numerical derivative is already too large, such that the theoretical error scaling of the KT scheme cannot be seen at all and is completely obscured by the errors from the numerical

differentiation of $\bar{u}(t_{\text{IR}}, x_i)$.

We conclude that the KT scheme is perfectly suited for the spatial discretization of the FRG flow equation for $u(t, \sigma)$ and shows correct scaling with decreasing spatial resolution Δx . This is also confirmed by tests with different ICs, see, e.g., figure 3.14.

In addition, we actually found that a more severe problem is the correct extraction of physical observables from the IR values $\bar{u}(t_{\text{IR}}, x_i)$, which are usually related to derivatives of $u(t_{\text{IR}}, \sigma)$. We predict that this problem might even become more severe in higher dimensions, were the IR potential is no longer guaranteed to be smooth. We therefore suggest to search for better ways of calculating those derivatives as well as for careful analysis tools for numerically calculated 1PI n -point functions in the vicinity of non-analyticities in general. However, this is beyond the scope of the present work.

We remark that our numerical findings indicate that – independent of the specific numerical discretization scheme – the number of grid points or expansion coefficients might have been chosen too small in previous FRG studies in literature to obtain a decent resolution. However, other works, cf. Refs. [154, 155, 567, 568, 604, 610], which also discuss the limitations of their numerical schemes in detail, have used a rather large number of discretization points – in some cases to compensate the demand for continuity of the specific schemes.

In the following we will mostly use a spatial resolution of

$$\Delta x = \frac{x_{\text{max}}}{n-1} \simeq 0.025, \quad (3.98)$$

where we can trust the results for the two- and four-point functions. The relative errors for the six-point function will only be plotted for the sake of completeness, but cannot be included in any reasonable quantitative analysis of other sources of (numerical) errors in FRG flow equations although they are still at a reasonably small level of $\sim 5\%$ at $\Delta x \simeq 0.025$.

Tests of the size of the computational domain

In this paragraph, we discuss the influence of the size of the computational domain $[0, \sigma_{\text{max}}]$ on the relative errors of the IR observables (3.97). As discussed in subsection 3.2.2.4, we expect that, if the spatial BCs are not implemented with great caution and the computational domain is too small, one cannot trust the results from the numerical integration of the FRG flow. If the computational domain is too small, we expect large errors, because the BCs at σ_{max} are no longer valid due to wrong extrapolation to the ghost cells and consequently wrongly estimated influx.

In the case with UV IC (3.94), the BC at σ_{max} is implemented as a linear extrapolation (2.126) of $u(t, \sigma)$ to the two ghost cells of the KT scheme to mimic the asymptotic behavior of $u(t, \sigma)$. As long as σ_{max} is sufficiently large, we expect only tiny deviations of $u(t, \sigma)$ from its initial UV value $u(t_{\text{UV}} = 0, \sigma)$ around σ_{max} . However, if σ_{max} is too small and approaches the model scales, we expect the diffusive effects to reach the boundary of the computational domain, such that a linear extrapolation is no longer a good approximation in order to determine the spatial BC.

To this end, we test the scaling of the relative errors (3.97) with decreasing computational domain size $x_{\text{max}} = \sigma_{\text{max}}$ for $N = 1$ (purely diffusive) and $N = 3$. The results and (numerical)

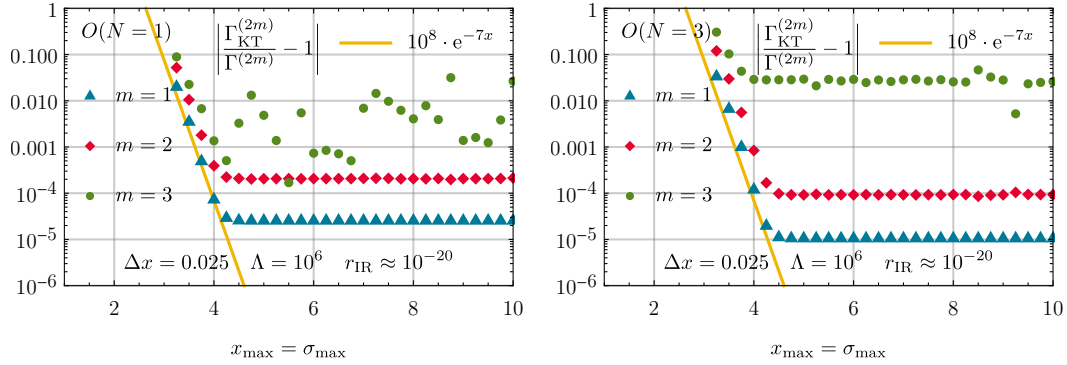


Figure 3.7.: The relative error for $\Gamma^{(2m)}$ for $m = 1, 2, 3$ for the UV potential (3.94) of the $O(1)$ model on the left (a) and of the $O(3)$ model on the right (b) as a function of x_{\max} , while keeping the cell size constant, $\Delta x = 0.025$. $\Gamma^{(2m)}$ are computed from the discrete values of the derivative of the IR potential $u(t_{\text{IR}} = 60, \sigma)$ via the second-order accurate central finite-difference stencils (D.6), (D.9), and (D.12) at $\sigma = 0$. We use the exponential regulator (3.8) with UV scale $\Lambda = 10^6$. The yellow straight line $\propto \exp -7x_{\max}$ is for optical guidance. From Figs. 10 and 11 of Ref. [1].

parameters are shown in figure 3.7. In both cases ($N = 1$ and $N = 3$ in figures 3.7a and 3.7b respectively) we find that the relative errors are independent of σ_{\max} for sufficiently large σ_{\max} . However, if the spatial cutoff σ_{\max} is approaching the model scales (here the discontinuity in $u(t_{\text{UV}} = 0, \sigma)$ at $\sigma = 3$, see figure 3.3) the relative errors for $\Gamma^{(2)}$ and $\Gamma^{(4)}$ start rising exponentially.

Contrary to our expectations, the results for $N = 1$ and $N = 3$ are very similar and the exponential rise of the relative errors sets in at a similar $\sigma_{\max} \approx 4.2$. *A priori* we expected that for the purely diffusive scenario with $N = 1$, the diffusive effects arising from the large gradients at $\sigma = 3$ might have more time to reach and influence the shape of $u(t, \sigma)$ at larger values of σ , which does not seem to be the case. Our employed monitors for numerical errors – the 1PI n -point functions in the IR computed at $\sigma = 0$ and $t = 0$ – are rather intensive to such changes. A possible explanation is the fact that observable errors from the boundary at σ_{\max} propagate into the computational domain at a finite speed⁵⁴, which is rather low in the purely diffusive case and in general small at large σ , and thus do not influence the physical point at $t = 0$ and $\sigma = 0$.

Nevertheless, we conclude from figures 3.7a and 3.7b that it is extremely important to use sufficiently large computational domains to minimize numerical errors in field-dependent FRG flows. This implies that σ_{\max} should be chosen much larger than all relevant scales of the model.

From our findings, it is therefore expected that choosing a large σ_{\max} might even gain in

⁵⁴In the context of “infinite propagation speeds” in parabolic PDEs, cf. the discussion and corresponding footnote 28 in subsection 2.2.4, we refer here to the fact that observable changes on the relevant scales of the problem travel with apparently finite speed independent from some formal instantaneous, infinitesimal (exponentially decaying) changes.

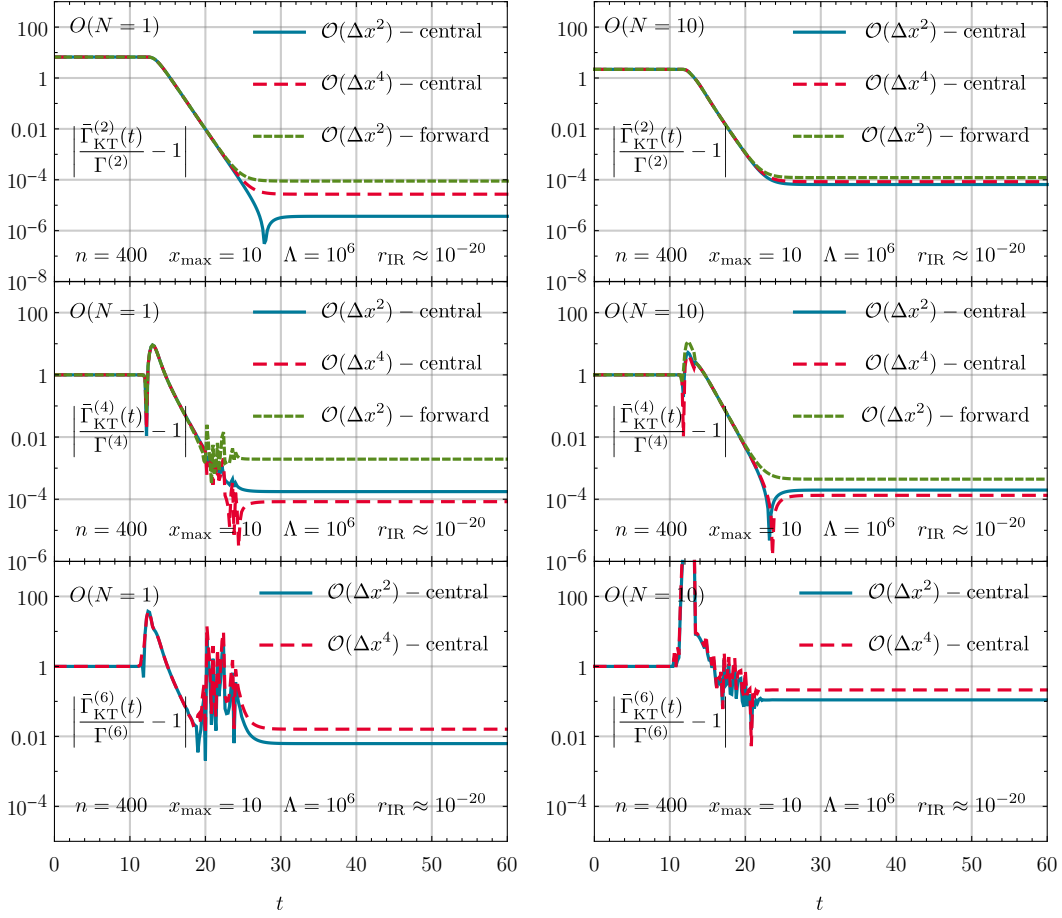


Figure 3.8.: The relative error for $\Gamma^{(2m)}$, for $m = 1, 2, 3$, calculated with the KT scheme as a function of the RG time t for the $O(1)$ model on the left (a) and of the $O(10)$ model on the right (b). The UV initial potential is given by Eq. (3.94). We use the exponential regulator (3.8) with UV scale $\Lambda = 10^6$. The computational grid has $n = 400$ cells and $\sigma_{\max} = x_{\max} = 10$. $\Gamma^{(2m)}$ are extracted from $u(t_{\text{IR}} = 60, \sigma)$ via the finite-difference stencils (D.6)–(D.13). From Figs. 13 and 15 of Ref. [1].

importance in higher-dimensional models, where the physical point may be located at a non-trivial minimum in the IR, like in the QM and GN(Y) model of chapters 4 and 5. If the physical point is closer to the boundary of the computational domain the relative errors for observables might even be larger than for our zero-dimensional model where the physical point moves towards $\sigma = 0$ during the FRG flow. In terms of errors originating from the boundary at σ_{\max} , the physical point at $\sigma = 0$ is ideal since it has the largest spatial and – in a sense causal, due to the finite speed of propagation – distance to σ_{\max} .

Lastly, we have to warn that there is no panacea for the construction of a sufficiently large computational domain and the choice of σ_{\max} has to be adjusted to the specific model and specific IC under consideration. For some problems even more involved approaches (like using

several computational grids of different resolution Δx) might be needed or are at least highly advantageous [162, 210, 247, 284]. In any case one has to check that the IR results do not depend on the size of the computational domain (even if exact reference values for observables are unknown), *cf.* Refs. [4, 567, 604]. This can be done by fixing appropriate values for the spatial resolution Δx as well as for all other (numerical) parameters and successively increasing σ_{\max} until the IR observables do not change anymore.

Tests of the UV and IR scales

We now turn to a long-standing discussion in the FRG community, namely the question: How do we have to choose the initial UV and numerical IR cutoff scale for the calculation of the FRG flow for a specific model?

A common argument is based on the energy scales of a given model. The UV IC is fixed at UV scales Λ that are close to the largest energy scale of the model. Higher Λ are excluded by arguing that at higher energy scales other physical degrees of freedom (*e.g.*, other interaction channels or new particles) are relevant and the model at hand is only valid within a certain energy regime. On the other hand, the IR cutoff k_{IR} scale is oftentimes fixed by arguing that if it decreases below the lowest energy scale of the model, the FRG flow is effectively “frozen in” and the effective potential no longer changes anyway. A relatively low UV initial scale and a high IR cutoff lead to rather short flow times of only $t_{\text{UV}} - t_{\text{IR}} \approx 3 - 4$.

Another approach, which is sometimes employed in conjunction with the first strategy, is guided by the principle of “numerical stability” of the FRG flow, where cutoffs are chosen in a certain way to “improve performance and stability” during the numerical RG time integration. In turn, in Refs. [155, 567, 568, 604, 610] relatively small IR cutoff scales are reached due to the use of numerical stable schemes or the control of stability. Careful extrapolations into the deep IR like the ones discussed in, *e.g.*, Refs. [162, 247, 610] are another possibility to achieve low IR cutoffs. Note that, for theories in $d > 0$ dimensions, numerical integration into the (deep) IR becomes very demanding due to multiple reasons, see also Refs. [4, 162, 247, 610] and especially Ref. [355]. This is probably the main reason why often large numerical IR cutoffs are used.

In general, however, there is a well-defined strategy for the choice of the UV scale scale: the notion of *renormalization group consistency* introduced in subsection 2.1.6. Recalling the central statement of Eq. (2.74):

$$\Lambda \frac{d\Gamma[\vec{\varphi}]}{d\Lambda} \equiv \Lambda \frac{d\bar{\Gamma}_0[\vec{\varphi}]}{d\Lambda} \stackrel{!}{=} 0, \quad (3.99)$$

i.e., the full effective action $\Gamma[\vec{\varphi}]$ in the IR must be independent of the UV initial scale [257]. In the context of FRG as an integral deformation in zero dimensions, see subsection 3.1.2, the UV scale scale Λ has to be much larger than all scales in the model. Hence our zero-dimensional models fall in the scenario discussed with Eq. (2.78) in the first paragraph of subsection 2.1.6.1. In this sense, a high UV initial scale is necessary to include all fluctuations – to guarantee Eq. (2.78). It was already demonstrated in Ref. [257] that if the UV initial scale Λ is chosen too small and too close to the model scales or external scales, physical results are spoiled drastically by slightly varying Λ and Eq. (3.99) is not fulfilled anymore,

cf. Refs. [148, 306, 307, 309] for related discussions in the context of LEFTs of QCD and also chapters 4 and 5 for further discussions of RG consistency in the context of this thesis.

A hard lower limit for Λ arises from the fact that for a given IC $U(t=0, \sigma)$

$$\Lambda + \frac{1}{\sigma} \partial_\sigma U(t=0, \sigma) > 0, \quad (3.100a)$$

$$\Lambda + \partial_\sigma^2 U(t=0, \sigma) > 0, \quad (3.100b)$$

must hold $\forall \sigma$ to have a non-singular flow equation (3.74). This is discussed, *e.g.*, in Refs. [124, 610] and represents a minimal requirement for Λ when considering a given IC $U(t=0, \sigma)$. However, guaranteeing the inequalities (3.100) does by itself *a priori* not guarantee RG consistency in the sense of Eq. (3.99).

For higher-dimensional QFTs it is actually complicated to quantify the relative error of observables from violations of Eq. (3.99), because “exact” reference values, *e.g.*, by numerical calculation of expectation values from the functional integral, are rarely known, especially for LEFTs. In zero-dimensional QFT this is different, because we can directly calculate the relative errors for observables like 1PI n -point functions, *cf.* Eq. (3.97), for different values of Λ .

Similar arguments apply to the IR cutoff, where the numerical integration of the FRG flow is stopped. Here, one must clearly state that the full effective average action $\Gamma[\chi]$ in the IR is unambiguously defined via the limit $t \rightarrow \infty \leftrightarrow r(t) \rightarrow 0$ of $\bar{\Gamma}_t[\chi]$, *cf.* Eq. (3.25). In practice, a direct integration to $t \rightarrow \infty$ is numerically impossible, which implies that one has at least to make sure that the numerical RG time integration is stopped no earlier than when all observables of interest do not change anymore, or one has to systematically extrapolate to $t \rightarrow \infty$, see, *e.g.*, Refs. [162, 247]. It is worth mentioning that, depending on the specific observable, these “freeze-out scales” can be extremely different, see figure 3.9.

In the following, we will therefore explicitly explore the influence of UV and IR cutoff scales on the relative errors (3.97) for the $\Gamma^{(2n)}$. We start our discussion by providing results for the relative errors (3.97) depending on the RG time t for different N of $O(N)$ and UV IC (3.94). In figure 3.8 we plot the relative errors of $\Gamma^{(2n)}$ for $n \in \{1, 2, 3\}$ for $N \in \{1, 10\}$, which are all extracted via various finite-difference stencils from $u(t, \sigma)$ at the physical point $\sigma = 0$ and different t during the FRG flow. A corresponding plot for $N = 3$ can be found in Fig. 14 of Ref. [1]. All (numerical) parameters are mentioned in the figures or the respective captions.

In figure 3.8 (*i.e.*, for $N = 1$ and 10) and independent of the choice of discretization of the numerical derivatives, we observe plateaus for the relative errors for $\Gamma^{(2n)}$ at the beginning and the end of the FRG time evolution. The plateau at small t corresponds to the UV regime and indicates that the UV scale is chosen sufficiently large because no fluctuations are present at the IR physical point until $r(t)$ reaches the scales of the model. RG consistency (3.99), hence UV-scale-independence should therefore be fulfilled, as long as we initialize our FRG flow at some RG scale which is at the far left of this plateau. Such a plateau at small t is a sufficient condition for RG consistency but not a necessary one, because quantum fluctuations could already work at positions in field space away from the IR physical point and only influence higher-order correlation functions. We will quantify this in the following. In the plots various finite-difference stencils with distinct error scaling in Δx are used to demonstrate that the

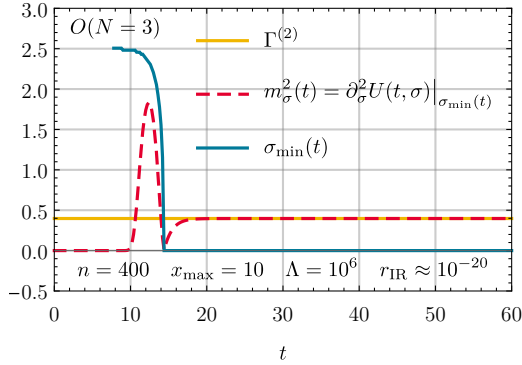


Figure 3.9.: The FRG flow of the minimum $\sigma_{\min}(t)$ (blue) of the effective potential $U(t, \sigma)$ and of the curvature mass $m_\sigma^2(t)$ of the σ -mode (red-dashed) evaluated on the equations of motion (3.21), *i.e.*, at the flowing minimum. The blue curve sets in after a unique minimum at $\pm\sigma_{\min}(t)$ has formed. As UV IC we use Eq. (3.94). We used the exponential regulator (3.8) with UV scale $\Lambda = 10^6$. The curvature mass $m_\sigma^2(t)$ was extracted from $u(t, \sigma)$ via Eq. (D.8) at the moving $\sigma_{\min}(t)$. The horizontal (yellow) line denotes the exact IR result $\Gamma^{(2)} \simeq 0.397$ at $\sigma = 0$, which must agree with m_σ^2 in the IR, where $\sigma_{\min}(t) = 0$. From Fig. 12 of Ref. [1].

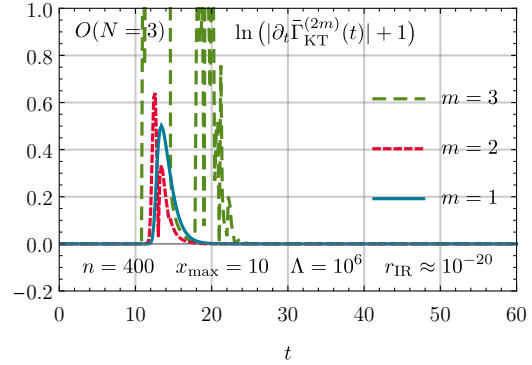


Figure 3.10.: The rate of change in t of $\bar{\Gamma}^{(2m)}(t)$ at the IR minimum $\sigma = 0$ for $n = 1, 2, 3$ during the FRG flow. This rate of change is defined as the numerical RG time derivative $\partial_t \bar{\Gamma}^{(2m)}(t)$ over the RG time. $\partial_t \bar{\Gamma}^{(2m)}(t)$ are calculated via a finite-difference approximation $[\bar{\Gamma}^{(2m)}(t) - \bar{\Gamma}^{(2m)}(t - \Delta t)]/\Delta t$, where $\Delta t = 0.2$. $\bar{\Gamma}^{(2m)}(t)$ are obtained via numerical derivatives (D.6), (D.9), and (D.12) of $u(t, \sigma)$ at $x = \sigma = 0$. For convenience, we added 1 and took the logarithm to highlight the regions with high rates of change of the observables $\bar{\Gamma}^{(2m)}(t)$ and to identify the freeze-out plateau, where these rates vanish. We used the exponential regulator (3.8) with UV scale $\Lambda = 10^6$. From Fig. 17 of Ref. [1].

plateaus are independent of other sources of errors, like spatial discretization errors⁵⁵.

For intermediate t , we observe strong dynamics and rapid changes in the relative errors for the $\Gamma^{(2n)}$. The actual values of the relative errors for intermediate t are irrelevant for the current discussion on UV and IR scales.

The plateau at late RG times t corresponds to the IR scale of the theory and indicates that the physical observables are frozen and do not change anymore, such that the numerical time integration can be stopped. As expected, we find that the explicit IR scale strongly depends on the choice of N , thus the number of pions and the related strength of advection. The smaller N and the more diffusive the system, the longer it takes to reach the IR⁵⁶: For $N = 10$ the freeze-out already sets in at $t \approx 26$, while for $N = 1$ one has to wait until $t \approx 30$ to find that the dynamics ends. This is a difference of two orders of magnitude in the RG scale. In general, our toy model tests indicate that rather small IR scales are needed to actually reach the regime

⁵⁵Incidentally, figure 3.8 also underlines our statement that the spatial discretization errors stemming from the numerical differentiation of $u(t, \sigma)$ are much more severe than the discretization errors of the KT scheme. Otherwise, the curves for the various finite-difference stencils would coincide in the IR.

⁵⁶This is a well-known observation from all kinds of fluid-dynamical systems. It typically takes much longer to reach thermal equilibrium via diffusion alone than when including advective processes.

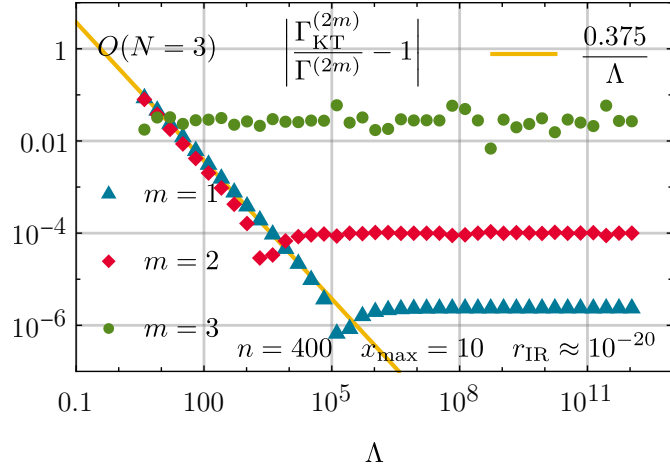


Figure 3.11.: The relative error for $\Gamma^{(2m)}$ for $m = 1, 2, 3$ from the KT scheme as a function of the UV scale Λ for the initial potential (3.94). We use the exponential regulator (3.8) and keep the IR cutoff scale constant at $r(t_{\text{IR}}) = 10^{-20}$. Furthermore, for all data points the computational grid size is fixed at $\sigma_{\text{max}} = x_{\text{max}} = 10$ and the number of volume cells is set to $n = 400$. $\Gamma^{(2m)}$ are calculated from $u(t_{\text{IR}} = 60, \sigma)$ via the approximations (D.6), (D.9), and (D.12) for the numerical derivatives. The yellow straight line $\propto \Lambda^{-1}$ is for optical guidance. From Fig. 16 of Ref. [1].

where the observables are frozen. Still, for $N = 10$, $r(t \approx 26) \approx 5 \cdot 10^{-6}$, *i.e.*, the IR regime begins six orders of magnitude below the model scales.

This observation might also partially translate to higher-dimensional models, meaning that commonly used IR cutoffs might be systematically chosen too large, such that predictive power is lost. Nevertheless, we expect this problem to be the less severe the higher the space-time dimensionality of a model under consideration, because of the larger phase-space (momentum suppression). The smaller the space-time dimension of a model, the more important are long-range interactions – quantum fluctuations at small RG scales k – for the macroscopic observables, which is of course most extreme for $d = 0$.

Furthermore, we observe from figure 3.9 as well as figure 3.8 that the freeze-out scale is slightly different for different observables, because higher 1PI n -point functions seem to be more sensitive to tiny changes in $u(t, \sigma)$. In particular, we observe from figure 3.9 that the minimum σ_{min} is already frozen at $t \approx 14$, while the curvature mass m_σ^2 still changes drastically after $t \approx 14$ over several orders of magnitude in RG scale. This is especially interesting for higher-dimensional models: Oftentimes the freeze-out of the minimum is considered a suitable IR scale to stop the FRG flow, which is definitely not justified, since the derivatives of the potential – the curvature mass – at the physical point are usually still changing. Using the changing rates of the curvature mass instead of the position of the minimum as a monitor for the dynamic range – viable numerical IR cutoffs – has proven crucial in the FRG study [4] of the GNY model in section 4.5.

Next, we explicitly quantify the relative errors of $\Gamma^{(2n)}$, which stem from too small UV scales

Λ and the violation of RG consistency (3.99). To this end, we plot the relative errors (3.97) as a function of the UV scale Λ , while keeping the IR cutoff scale fixed at extremely small $r(t_{\text{IR}}) = 10^{-20}$. In figure 3.11 we observe that the IR observables become independent of Λ at rather large $\Lambda \approx 10^6$. This is several orders of magnitude above the model scales, contrary to what is often used in FRG studies in higher dimensions. If the UV scale is chosen too small, we find that the relative errors of $\Gamma^{(2n)}$ grow proportional to $\frac{1}{\Lambda}$, as estimated in Eq. (3.31). Surprisingly, it turns out that the RG consistency condition (3.99) is already violated at rather large UV scale scales $\Lambda \approx 10^5$ and is only fulfilled for $\Lambda \gtrsim 10^5$. We conclude that great care is required when specifying the UV scale in a FRG calculation.

Before we close this discussion, we provide a natural measure to estimate the correct UV and IR scales of a model or theory, even if there are no exact reference values for observables that can be used for comparison with the FRG results. To this end, we plot in figure 3.10 the shifted logarithm of the changing rates of the $\bar{\Gamma}^{(2n)}(t)$ at the IR minimum $\sigma = 0$ over RG time t . These quantities have to vanish in the UV and the IR, when the relative errors (3.97) are not changing.

A similar investigation can be done for any other model or theory and can be used as an indication to ensure sufficiently large UV and sufficiently small IR cutoffs: A first estimate may be obtained by choosing Λ and t_{IR} in a way that the plateaus (or scaling regimes) in figures similar to figure 3.10 are of approximately equal RG time duration than the time interval in which the actual dynamics takes place. In the absence of an explicit and accessible error estimate, rates of change are a cheap and simple tool to study the UV and IR limits of RG time evolution, cf. subsection 4.5.3.

3.2.3.2. Test case II: ϕ^4 theory

The *test case II* is a zero-dimensional version of ϕ^4 theory with the UV initial potential

$$U(\vec{\varphi}) = \mp \frac{1}{2} \vec{\varphi}^2 + \frac{1}{4!} (\vec{\varphi}^2)^2, \quad (3.101)$$

where a theory with negative mass term $-\frac{1}{2} \vec{\varphi}^2$ has a “*sombrero*”-type (symmetric double-well) potential well-known from standard textbook discussions of spontaneous symmetry breaking [442, 563]. The corresponding IC with negative mass term for the FRG flow is illustrated in figure 3.12. When not explicitly stated otherwise we will consider the IC (3.101) with negative mass term. The reference values for the exact IR 1PI vertex functions $\Gamma^{(2n)}$ of the $O(N)$ model (3.52)–(3.54) are calculated numerically from the UV potential (3.101) and are listed for selected values of N in table 3.2 both for positive and negative mass terms.

In the remainder of this subsection we will use test case II to discuss

- Results obtained using the KT scheme,
- FRG Taylor expansion: Flow of the n -point functions,
- FRG Taylor expansion: Truncation error,
- FRG Taylor expansion: ϕ^4 potential with positive mass term,
- FRG Taylor expansion: Numerical irreversibility,

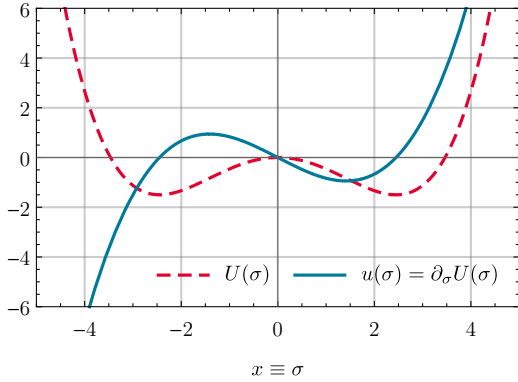


Figure 3.12.: UV potential $U(\sigma)$ (red-dashed) and its first derivative $u(\sigma) = \partial_\sigma U(\sigma)$ (blue, solid) of test case II from Eq. (3.103) with negative mass term. From Fig. 18 of Ref. [1].

Table 3.2.: Exact results for $\Gamma^{(2n)}$ of the $O(N)$ model with the UV initial potential (3.101) for selected N with negative and positive* mass term. They are obtained by a high-precision one-dimensional numerical integration of the expectation values $\langle(\vec{\phi}^2)^n\rangle$ from Eq. (3.56) using *NIntegrate* in MATHEMATICA [353]. Here, we present the first six digits only. In parts from Tab. II of Ref. [1] and Tab. I of Ref. [2].

N	$\Gamma^{(2)}$	$\Gamma^{(4)}$	$\Gamma^{(6)}$
1	0.199510	0.062258	0.107744
4	0.506444	0.182415	0.280288
1*	1.332430	0.607899	0.771451
4*	1.580920	0.611848	0.568631

in the corresponding paragraphs which are based on Secs. V.B.1–2 of Ref. [1].

Results obtained using the KT scheme

In this paragraph we will discuss selected numerical results of the application of the KT scheme for the analytic IC (3.101). We have performed the full set of numerical tests discussed in subsection 3.2.3.1 for this IC and found results supporting the general statements made there. For brevity, we will not repeat the complete discussion of that subsection. We will limit our discussion to UV/IR scales, the computational domains size (x_{\max}), and its resolution (Δx).

UV and IR scales: In figure 3.13 we present the FRG flow of the derivative of the effective potential $u(t, \sigma)$ from the UV (blue) to the IR (red). For the smooth IC – in the absence of large gradients – the highly non-linear advection and diffusion contribute almost an equal amount to the dynamics. Between $t \approx 25$ and $t \approx 30$ we observe significant changes in the shape of the potential: the non-trivial minimum moves towards $\sigma = 0$ and vanishes at $t \approx 28$ resulting in a convex potential with a trivial minimum at $\sigma = 0$ as expected and required. At small and large t outside the apparent dynamic range between $t \approx 25$ and $t \approx 30$ we observe only very marginal changes in figure 3.13.

A close inspection of the relative errors for the first three non-vanishing n -point functions in figure 3.15 reveals that actually the relevant dynamics sets in much earlier at $t \approx 10$ for the six-point function. The values for the n -point functions freeze out at late times around $t \approx 40$, which is due to the diffusion close to $\sigma = 0$. On the level of $u(t, \sigma)$ these subtle changes in the n -point functions cannot be observed by a simple visual inspection of figure 3.13.

The plateaus in the UV (at small t) and the IR (at large t) support the choice of $\Lambda = 10^{12}$ and $t_{\text{IR}} = 60$ to be valid initial UV and IR cutoff scales in terms of RG consistency. The present UV initial scale is larger when compared to $\Lambda = 10^6$, which corresponds to $t \approx 14$ in the

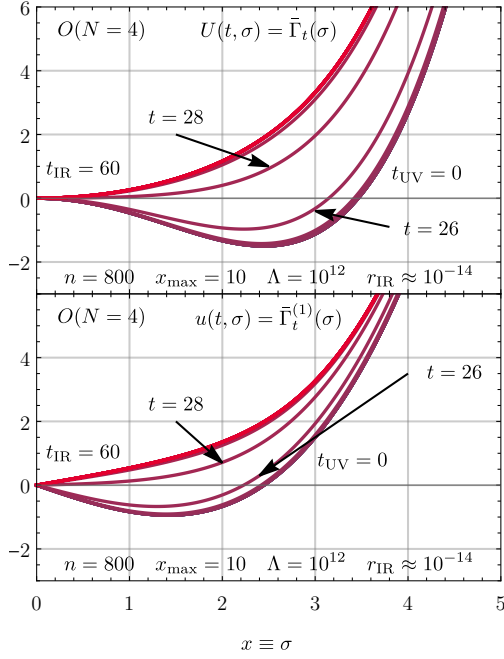


Figure 3.13.: The FRG flow of the effective potential $U(t, \sigma)$ (upper panel) and its derivative $u(t, \sigma) = \partial_\sigma U(t, \sigma)$ (lower panel) for the zero-dimensional $O(4)$ model with IC (3.101), evaluated at $t = 0, 2, 4, \dots, 60$ (integer values for t were chosen for convenience and readability). The (overlapping) blue and violet curves correspond to the UV and the red curves to the IR. We used the exponential regulator (3.8) with UV scale $\Lambda = 10^{12}$. The plot does not show the region $x \in [5, 10]$, because the tiny differences between $u(t, \sigma)$ and $u(t_{UV}, \sigma)$ are not visible in this region and vanish for large $x = \sigma$ anyhow. From Fig. 19 of Ref. [1].

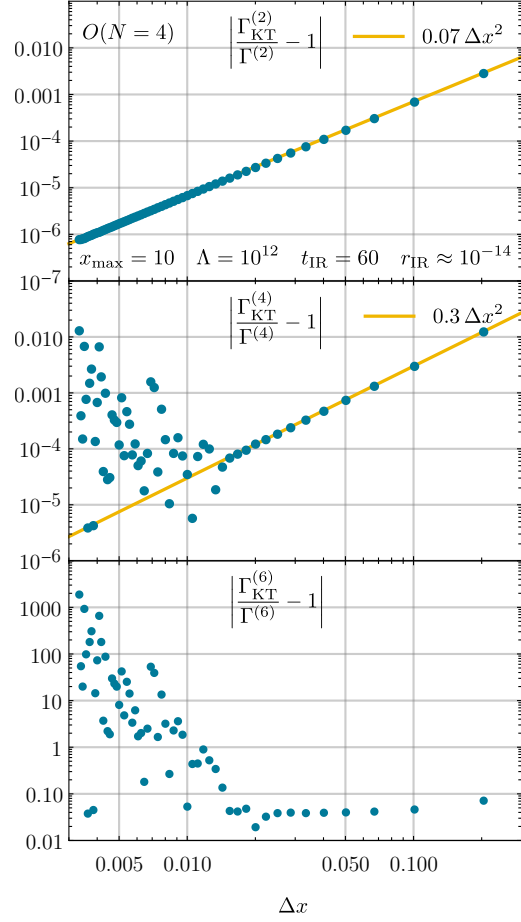


Figure 3.14.: The relative error as a function of the cell size Δx for the numerical results (blue dots) from the KT scheme for the coefficients $\Gamma^{(2n)}$ for $n = 1, 2, 3$ with initial potential (3.101). The numerical derivatives at $\sigma = 0$ of $u(t_{IR} = 60, \sigma)$ were calculated via the second-order accurate central schemes (D.6), (D.9), and (D.12). Here, $x_{\max} = 10$, but we could have used any sufficiently large x_{\max} . We used the exponential regulator (3.8) with UV scale $\Lambda = 10^{12}$. The yellow straight lines $\propto \Delta x^2$ are for optical guidance. From Fig. 21 of Ref. [1].

dynamic region in figure 3.15, used for most computations involving the non-analytic potential considered in the previous subsection 3.2.3.1.

Hence, the inclusion of a quartic interaction term in Eq. (3.101) seems to require higher UV initial scales to ensure RG consistency. This supports the statements made in subsection

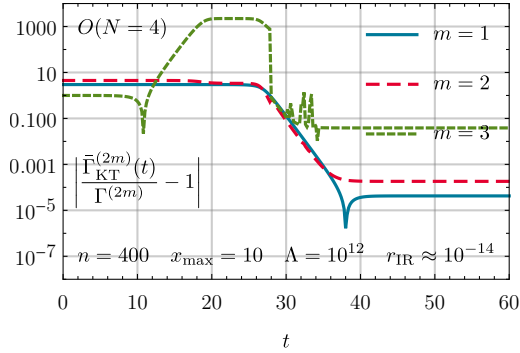


Figure 3.15.: The relative error for $\Gamma^{(2m)}$, for $m = 1, 2, 3$, calculated with the KT scheme as a function of the RG time t for the $O(4)$ model. The UV initial potential is given by Eq. (3.101). We use the exponential regulator (3.8) with UV scale $\Lambda = 10^{12}$. The computational grid has $n = 400$ cells and $\sigma_{\max} = x_{\max} = 10$. $\Gamma^{(2m)}$ are extracted from $u(t_{\text{IR}} = 60, \sigma)$ via the finite-difference stencils (D.6), (D.9), and (D.12). From Fig. 20 of Ref. [1].

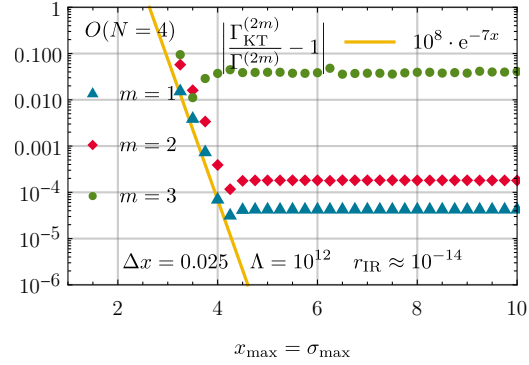


Figure 3.16.: The relative error for $\Gamma^{(2m)}$ for $m = 1, 2, 3$ for the UV potential (3.101) of the $O(4)$ model as a function of x_{\max} , keeping the cell size $\Delta x = 0.025$ constant. $\Gamma^{(2m)}$ are computed from the discrete values of the derivative of the IR potential $u(t_{\text{IR}} = 60, \sigma)$ via the second-order accurate central finite-difference stencils (D.6), (D.9), and (D.12) at $\sigma = 0$. We used the exponential regulator (3.8) with UV scale $\Lambda = 10^{12}$. The yellow straight line $\propto \exp(-7 x_{\max})$ is for optical guidance. From Fig. 22 of Ref. [1].

tion 3.2.3.1: RG consistency and UV/IR scales have to be re-evaluated when changing the IC in the UV, *i.e.*, the model under consideration, since characteristic internal scales then also change.

Size and resolution of the computational domain: We conclude this paragraph on the KT scheme with a brief discussion regarding the computational domain. The relative error for the first three non-vanishing n -point functions is shown as a function of the cell size Δx in figure 3.14. For the two-point function we recover a perfect error scaling with Δx^2 down to extremely small Δx . The last data point in figure 3.14 is at $\Delta x \approx 3.3 \cdot 10^{-3}$ corresponding to $n = 3000$ cells. For the two-point function the rounding errors of the employed finite-difference extraction (D.6) for $\Gamma^{(2)}$ and the finite precision of the ODE integrator (*NDSolve* from MATHEMATICA [353] with a *PrecisionGoal* and *AccuracyGoal* of 10) seem to be small for all depicted Δx in this scenario. A comparison with the present perfect error scaling for $\Gamma^{(2)}$ supports the comments made about discretization errors for the discontinuous IC (3.94) in figure 3.6. For the higher-order n -point functions $\Gamma^{(4)}$ and $\Gamma^{(6)}$, however, we find that rounding errors related to the finite-difference extractions (D.9) and (D.12) limit the achievable precision. Again, we identify $\Delta x \approx 0.025$ as an optimal cell size for the extraction of $\Gamma^{(4)}$ and $\Gamma^{(6)}$ but note that typical relative errors for $\Gamma^{(6)}$ are at $\approx 4\%$ around $\Delta x \approx 0.025$.

In figure 3.16, we study the effect of the size of the computational domain x_{\max} on the achievable relative errors for $\Gamma^{(2)}$, $\Gamma^{(4)}$, and $\Gamma^{(6)}$ at a constant $\Delta x = 0.025$. One major difference between the ϕ^4 potential (3.101) studied in this subsection and the non-analytic poten-

tial (3.94) of the previous subsection 3.2.3.1 is their asymptotic behavior for large σ . For large σ the leading-order term of the ϕ^4 potential is – as the name suggests – quartic while the non-analytic potential of test case I grows only quadratic. In terms of the conserved quantity $u = \partial_\sigma U$ one might expect problems when using a linear extrapolation for the ghost cells at large σ as discussed in subsection 3.2.2.4 with a potential where u grows $\sim \sigma^3$ for large σ . For the non-analytic IC (3.101) we avoided this possible source of error by construction. However, considering the results plotted in figure 3.16 together with the perfect error scaling displayed in the previous figure 3.14, we conclude that a linear extrapolation is not problematic even in the case of cubic asymptotics for u . This might be again in part related to the large spatial distance between the physical minimum in the IR and the upper boundary of the grid. For $x_{\max} \gtrsim 5$ we find a complete insensitivity of the relative errors on the interval size.

FRG Taylor expansion: Flow of the n -point vertex functions

In this paragraph we confront the theoretical results and concerns stated in subsection 2.1.4.2 and especially in subsection 3.2.2.2 for the zero-dimensional $O(N)$ model w.r.t. the Taylor expansion around the fixed expansion point $\bar{\varphi} = 0$ with the exact results for the zero-dimensional $O(N)$ model. The ϕ^4 potential of Eq. (3.101) with negative mass term is the, in terms of ICs, simplest UV potential with a non-trivial minimum. At the end of this subsection we will briefly discuss the Taylor expansion for the ϕ^4 potential with positive mass term and therefore a scenario without a non-trivial minimum, which has to be considered the simplest non-trivial, *i.e.*, interacting, UV IC in the context of the Taylor expansion for the zero-dimensional $O(N)$ model.

In the following we integrate the ODE system (3.71) truncated at $m = 2n_{\text{trunc}}$ with the IC

$$\bar{\Gamma}^{(2)}(0) = -1, \quad \bar{\Gamma}^{(4)}(0) = +1, \quad \forall n > 2 \quad \bar{\Gamma}^{(2n)}(0) = 0, \quad (3.102)$$

corresponding to the potential (3.101) numerically up to $t_{\text{IR}} = 60$ employing the exponential regulator (3.8) with $\Lambda = 10^{12}$ and using the same ODE solver *NDSolve* from *MATHEMATICA* [353] with a *PrecisionGoal* and *AccuracyGoal* of 10 as before. Using the n -point functions at the physical minimum as the flow variables makes an additional extraction procedure (like finite differences) obviously obsolete. The n -point functions in the IR can be directly obtained from the values $\bar{\Gamma}^{(2n)}(t_{\text{IR}}) = \Gamma^{(2n)}$.

In figure 3.17 we show the flow of the relative deviations for the first six non-vanishing n -point functions towards the IR using $m = 2n_{\text{trunc}} = 20$ vertices in the expansion for the $O(4)$ model. We can identify a dynamic range between $t \approx 24$ and $t \approx 38$ in which the vertices vary significantly and change their signs before they reach their respective IR values. This range is substantially smaller than the dynamic range observed when solving the full PDE (3.74) using the KT scheme, *cf.* figure 3.15. In the IR, the errors range from $2.3 \cdot 10^{-3}$ for $\Gamma^{(2)}$ to $1.1 \cdot 10^1$ for $\Gamma^{(12)}$. However, the strict hierarchy observed in figure 3.17 for $n = 1, \dots, 6$ is not a general feature of the Taylor expansion for this model. Using different n_{trunc} or including higher-order vertices changes this hierarchy.

FRG Taylor expansion: Truncation error

The truncation error for the $O(4)$ model is discussed using figure 3.19a, where we show the

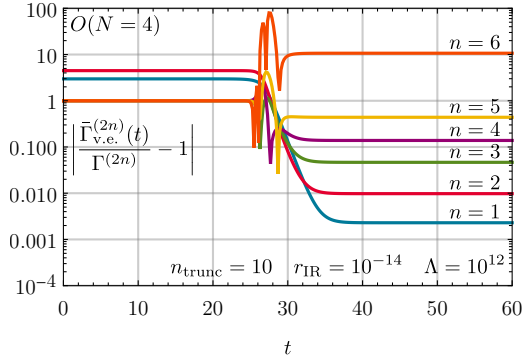


Figure 3.17.: The relative errors for $\Gamma^{(2n)}$ as a function of the RG time t for $n \in \{1, \dots, 6\}$ for the $O(4)$ model. $\Gamma^{(2n)}$ were calculated via the FRG flow of the FRG Taylor expansion with truncation order $m = 2n_{\text{trunc}} = 20$ using the exponential regulator (3.8). As initial condition we use the UV potential (3.101). From Fig. 23 of Ref. [1].

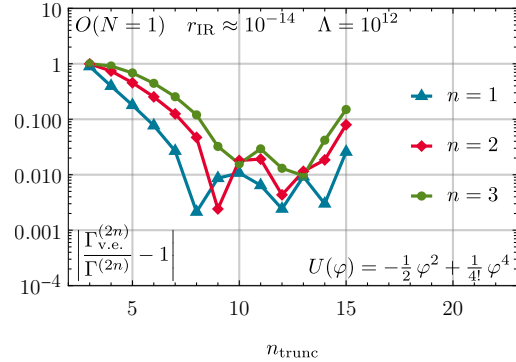


Figure 3.18.: The relative errors for $\Gamma^{(2n)}$ in the IR for $n = 1, 2, 3$ for the $O(1)$ model, calculated via the FRG flow of the FRG Taylor expansion to order $m = 2n_{\text{trunc}}$ with $n_{\text{trunc}} \in \{3, \dots, 15\}$ using the exponential regulator (3.8). As initial condition we use the UV potential (3.101). The discrete results for integer n_{trunc} are connected by straight lines to improve readability and for a better trend analysis. From Fig. 25 of Ref. [1].

relative errors for $\Gamma^{(2)}$, $\Gamma^{(4)}$, and $\Gamma^{(6)}$ for the Taylor expansion using different truncation orders $m = 2n_{\text{trunc}}$ between $n_{\text{trunc}} = 3$ and $n_{\text{trunc}} = 14$. Beyond $n_{\text{trunc}} = 10$ the relative errors for the n -point functions no longer decrease and we observe rather strong oscillations for different n_{trunc} . The errors for the two and four-point function are with $2.3 \cdot 10^{-3}$ and $9.8 \cdot 10^{-3}$ larger than the errors ($4.2 \cdot 10^{-5}$ and $1.8 \cdot 10^{-4}$ respectively) obtained in the KT scheme, see, e.g., figure 3.16. The relative error for the six-point function is with $4.7 \cdot 10^{-2}$ comparable to the $3.7 \cdot 10^{-2}$ error obtained in the KT scheme. While the extraction of higher-order n -point functions beyond $n = 6$ is in general possible in the Taylor expansion, their relative errors grow overall rapidly with increasing n .

For the IC (3.101) we do not observe any meaningful error scaling in orders of n_{trunc} . Furthermore a numerical solution at and beyond $n_{\text{trunc}} = 15$ has proven impossible with the current set-up. At $n_{\text{trunc}} = 15$ an ODE integration to the IR at $r(t_{\text{IR}} = 60) \approx 10^{-14}$ is impossible due to an instability of the ODE system occurring at $t \approx 30$ where all coefficients $\Gamma^{(2n)}(t)$ with $n > 1$ start diverging. This divergence seems to be driven by $\Gamma^{(30)}(t)$ for $n_{\text{trunc}} = 15$. The ODE system is in general poorly conditioned since the $\Gamma^{(2n)}(t)$ for different n vary vastly over multiple orders of magnitude. The instability at $t \approx 30$ cannot be overcome by increasing the numerical precision of the employed ODE integrator (*NDSolve* from *MATHEMATICA* [353]) and seems to be an inherent problem of the ODE systems with $n_{\text{trunc}} \geq 15$.

The Taylor expansion for $\Gamma^{(2n)}(t)$, with a fixed expansion point at $\vec{\varphi} = 0$, for the zero-dimensional $O(4)$ model and the simple IC (3.101) with its non-trivial global minimum in the UV is severely limited in its performance. The absence of a proper error scaling in orders of n_{trunc} and the instability of the ODE system beyond $n_{\text{trunc}} = 14$ support the conceptual

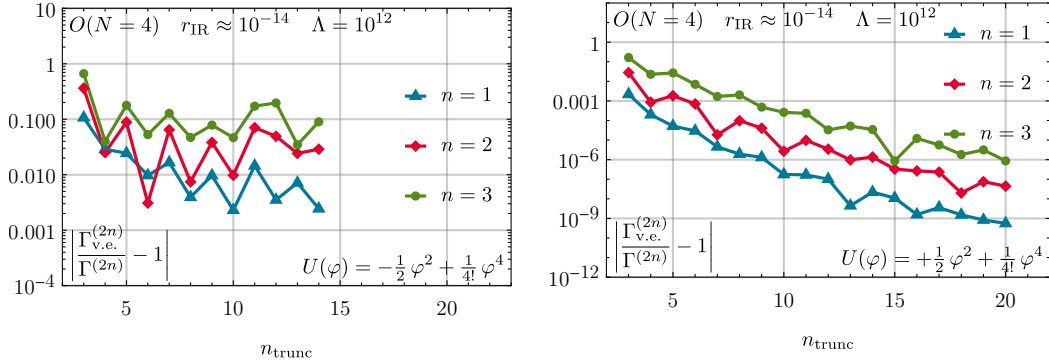


Figure 3.19.: The relative errors for $\Gamma^{(2n)}$ in the IR for $n = 1, 2, 3$ for the $O(4)$ model, calculated via the FRG flow of the Taylor (vertex) expansion to order $m = 2n_{\text{trunc}}$ with $n_{\text{trunc}} \in \{3, \dots, 14\}$ using the exponential regulator (3.8). As initial condition we use the UV potential (3.101) with negative mass term on the left (a) and positive mass term on the right (b). The discrete results for integer n_{trunc} are connected by straight lines to improve readability and for a better trend analysis. From Figs. 24 and 26 of Ref. [1].

reservations of subsection 2.1.4.2 and subsection 3.2.2.2. It seems that the expansion around $\vec{\varphi} = 0$ is either incapable of capturing the dynamics driven by the non-trivial minima located at $|\vec{\varphi}| = \sqrt{6}$ in the UV or the desired solution might be non-analytic in $\vec{\varphi} = 0$.

The situation does not improve when considering the same IC in the purely diffusive $O(1)$ model. In figure 3.18 we display relative errors for the first three non-vanishing $\Gamma^{(2n)}$ as a function of n_{trunc} for the IC (3.101) in the $O(1)$ model. The overall errors are even worse when compared to the $O(4)$ results discussed previously. The ODE integration becomes impossible at $n_{\text{trunc}} = 16$ where we encounter an instability at $t \approx 31$.

FRG Taylor expansion: ϕ^4 potential with positive mass term

We continue our discussion of the FRG Taylor expansion by considering the IC (3.101) with a positive mass term $+\frac{1}{2}\vec{\varphi}^2$ and therefore without a non-trivial minimum. In the context of zero-dimensional $O(N)$ models this IC is in the family of UV potentials discussed qualitatively at length and to some extent even quantitatively in Refs. [163, 536, 541].

In figure 3.19b we show relative errors for the first three non-vanishing $\Gamma^{(2n)}$ as a function of n_{trunc} for this IC for the $O(4)$ model. These results were obtained using *NDSolve* of MATHEMATICA [353] with an increased *PrecisionGoal* and *AccuracyGoal* of 12, which became necessary for a proper truncation-error scaling beyond $n_{\text{trunc}} = 15$ for the two-point function. In figure 3.19b we observe a truncation-error scaling following power laws in n_{trunc} with approximately $n_{\text{trunc}}^{-8.2}$, $n_{\text{trunc}}^{-7.6}$, and $n_{\text{trunc}}^{-7.3}$ for the two-point, four-point, and six-point function respectively. For this IC the expansion point $\vec{\varphi} = 0$ is located at the global minimum of the potential and the potential is also convex for all t . The dynamics of the FRG flow is rather unspectacular for this potential, see Fig. 13 of Ref. [163] or figure 3.27a for a visualization. For the two- and four-point functions, the numerical results at $n_{\text{trunc}} = 3$ ($\Leftrightarrow m = 6$) have already acceptable relative errors of $\approx 2.2 \cdot 10^{-3}$ and $\approx 2.8 \cdot 10^{-2}$, respectively, which was observed and discussed in Ref. [163],

where results for the Taylor expansions were presented only up to $n_{\text{trunc}} = 3$.

The Taylor expansion outperforms the KT scheme in this setting in terms of relative errors. The performance and practical applicability of the Taylor expansion seem to depend strongly on the IC under consideration. We will discuss another analytic IC for the Taylor expansion briefly in the next subsection [3.2.3.3](#).

FRG Taylor expansion: Numerical irreversibility

Before we conclude this subsection we will briefly comment on the irreversibility of (F)RG flows when employing the FRG Taylor expansion. We discussed in subsection [3.2.2.3](#) that the projection onto a finite set of couplings underlying the FRG Taylor expansion theoretically allows for an unphysical reversibility of the (F)RG flow. The ODE systems for the running couplings of the FRG Taylor expansion in principle allow for an integration both in positive and negative RG time-direction. Thus an unphysical resolution of microphysics from macrophysics – an inversion of the underlying RG transformations connecting them – is possible when considering a finite set of couplings $\{\bar{\Gamma}^{(2n)}(t)\}$.

We performed practical test with the ϕ^4 theory discussed in this subsection. For the ϕ^4 theory with positive mass term discussed in the previous paragraph a complete inversion of the FRG flow (from $t = 60$ back to $t = 0$ using $\Lambda = 10^{12}$) is numerically possible for systems with $n_{\text{trunc}} < 7$ for $N = 1$. For larger systems the strong oscillations of the higher-order couplings prevent a numerical integration from the IR back to the UV. The ODE system becomes numerically unstable when approaching $t \approx 24$ from above. The recovery of the exact UV IC is very good for small n_{trunc} but deteriorates when approaching $n_{\text{trunc}} = 7$. For the ϕ^4 theory with positive mass term this situations remains qualitatively unchanged for higher $N > 1$.

For the ϕ^4 theory with negative mass term an inversion of the FRG flow from the IR to the UV is numerically impossible. We were not able to find a n_{trunc} and N in heuristic tests which allowed for a numerical inversion of the FRG flow from $t = 60$ back to $t = 0$ using $\Lambda = 10^{12}$. The dynamics related to the vaporization of the non-trivial minimum seems to prevent a numerical inversion. In our heuristic tests it has proven impossible to form back the non-trivial minimum when approaching the UV from the IR. This is a rather interesting observation which might warrant a detailed investigation of the ODE systems involved in the FRG Taylor expansion. Further investigations in higher-dimensional models might be interesting in this context.

We will conclude our discussion of the FRG Taylor expansion in the next subsection with the paragraph [FRG Taylor expansion: Concluding remarks](#).

3.2.3.3. Test case III: ϕ^6 potential

For the third test case we consider the potential

$$U(\vec{\varphi}) = \frac{1}{2} \vec{\varphi}^2 - \frac{1}{20} (\vec{\varphi}^2)^2 + \frac{1}{6!} (\vec{\varphi}^2)^3. \quad (3.103)$$

This potential includes terms up to $(\vec{\varphi}^2)^3$ and has two local minima and one local maximum and is therefore not convex. The global minimum is located at $\vec{\varphi} = 0$ and the potential and its derivative (evaluated on the constant field configuration σ) are depicted in figure [3.20](#).

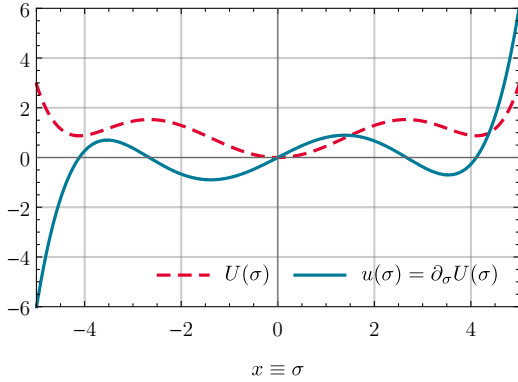


Figure 3.20.: UV potential $U(\sigma)$ (red-dashed) and its first derivative $u(\sigma) = \partial_\sigma U(\sigma)$ (blue, solid) of test case III from Eq. (3.103). From Fig. 27 of Ref. [1].

Table 3.3.: Exact results for $\Gamma^{(2n)}$ of the $O(N)$ model with the UV initial potential (3.103) for selected N . They are obtained by a high-precision one-dimensional numerical integration of the expectation values $\langle (\bar{\phi}^2)^n \rangle$ from Eq. (3.56) using *NIntegrate* in MATHEMATICA [353]. Here, we present the first six digits only. In parts from Tab. III of Ref. [1] and Tab. I of Ref. [2].

N	$\Gamma^{(2)}$	$\Gamma^{(4)}$	$\Gamma^{(6)}$
1	0.174051	0.015618	0.013440
4	0.250333	0.048131	0.043282

Selected reference values for the first three non-vanishing n -point functions can be found in table 3.3.

We have again performed the full set of numerical tests of subsection 3.2.3.1 and found results supporting the general statements made in that subsection. For brevity, we will not repeat the complete discussion of that subsection but instead focus again on selected results.

Figure 3.21 shows the FRG flow with the initial condition (3.103) for the $O(4)$ model computed with the KT scheme again using *NDSolve* of MATHEMATICA [353] with *PrecisionGoal* and *AccuracyGoal* of 10 for the FRG time evolution. Both non-trivial local extrema fade away during FRG time evolution towards the IR. At $t \approx 28$ the potential $U(t, \sigma)$ becomes convex as $u(t, \sigma)$ turns strictly positive for $\sigma > 0$. We again observe that the linear extrapolation used at the right boundary x_{\max} of the computational domain seems surprisingly efficient even for an initial condition with quintic asymptotics. Studying figure 3.22 we observe that the relative errors in the IR become independent of the size of the computational domain for $x_{\max} \gtrsim 6$.

FRG Taylor expansion: Concluding remarks

We were not able to evolve the ODE system of the Taylor expansion with the current initial condition to the IR for any setup at all⁵⁷. Independent of n_{trunc} and ODE integrator (*NDSolve* of MATHEMATICA [353]) settings we encounter a numerical instability of the ODE systems at around $t \approx 28$ preventing a complete integration to the IR. The expansion coefficients $\bar{\Gamma}^{(2n)}(t)$ simply diverge at $t \approx 28$. From figure 3.21 we deduce that this is approximately the RG time point at which the non-trivial extrema vanish and the potential turns convex. The precise underlying dynamics generated by the full PDE and resolved by the KT scheme cannot be captured by the Taylor expansion (at least not in our set-up). However, also switching to a set-up

⁵⁷We thank J. Eser for discussions on this issue and a cross-check using his FRG Taylor expansion code [105–108], which reproduced our findings.

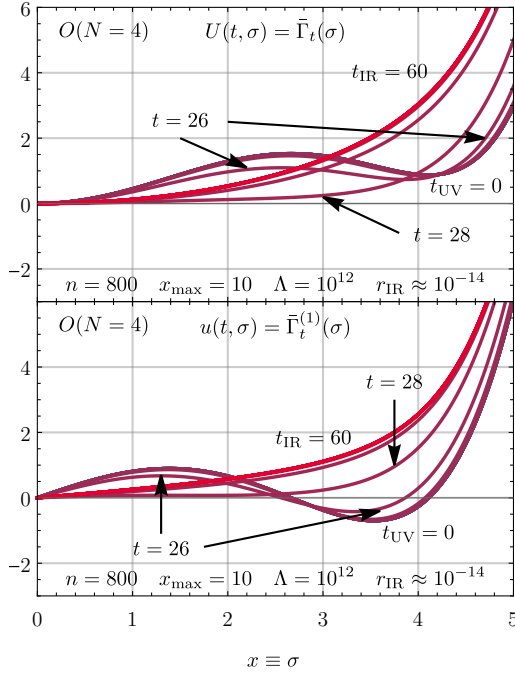


Figure 3.21.: The FRG flow of the effective potential $U(t, \sigma)$ (upper panel) and its derivative $u(t, \sigma) = \partial_\sigma U(t, \sigma)$ (lower panel) for the zero-dimensional $O(4)$ model with initial condition Eq. (3.103), evaluated at $t = 0, 2, 4, \dots, 60$ (integer values for t were chosen for convenience and readability). The (overlapping) blue and violet curves correspond to the UV and the red curves to the IR. We used the exponential regulator (3.8) with UV scale $\Lambda = 10^{12}$. The plot does not show the region $x \in [5, 10]$, because the tiny differences between $u(t, \sigma)$ and $u(t_{UV}, \sigma)$ are not visible in this region and vanish for large $x = \sigma$ anyhow. From Fig. 28 of Ref. [1].

with a t -dependent expansion point will not cure this problem, because the expansion point (the global minimum) does not move for this initial potential – a conscious design decision for test case III. The instability of the solution of the coupled system of ODEs might be explained *a posteriori* by the formation of a non-analyticity at or around the RG time $t \approx 28$ of the collapse of the expansion. Inevitably, due to the non-analyticity of the potential, Wilbraham-Gibbs-type [286–288] oscillations arise in the Taylor expansion, making the expansion scheme unstable [285]. This phenomenon is also observed and discussed in detail in the context of Fourier expansions of periodic potentials in the FRG in Sec. 2.2.2 of Ref. [568].

However, a vertex expansion for a convex sextic potential including only positive coefficients

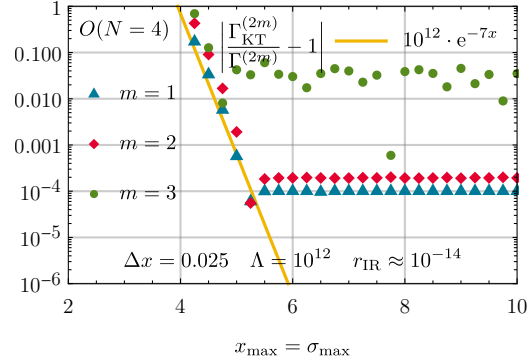


Figure 3.22.: The relative error for $\Gamma^{(2m)}$ for $m = 1, 2, 3$, for the $O(4)$ model using the UV potential (3.103), as a function of the size of the computational interval x_{\max} . The cell size is $\Delta x = 0.025$. $\Gamma^{(2m)}$ are computed from the discrete values of the derivative of the IR potential $u(t_{IR} = 60, \sigma)$ via the second-order accurate central finite-difference stencils (D.6), (D.9), and (D.12) at $\sigma = 0$. We used the exponential regulator (3.8) with UV scale $\Lambda = 10^{12}$. The yellow straight line $\propto \exp(-7 x_{\max})$ is for optical guidance. From Fig. 29 of Ref. [1].

in the UV is possible, similar to ϕ^4 theory with a positive mass term discussed at the end of the previous subsection 3.2.3.2. A numerical inversion of the FRG flow is again possible for systems with a small number of couplings.

At this point we have discussed numerical results for the FRG Taylor expansion for quartic and sextic potentials. The numerical performance in terms of achievable relative errors for the n -point functions in the IR is rather poor for the quartic potential (3.101) with the negative mass term and very good for the potential with the positive mass term. A numerical solution of ODE system of the Taylor expansion with the non-convex sextic potential (3.103) has proven impossible

The zero-dimensional $O(N)$ model has proven very challenging for the Taylor expansion. It seems that only convex, analytic UV initial conditions and the resulting rather simple FRG flows can be treated with a vertex expansion in $\bar{\Gamma}^{(2n)}(t)$ around $\vec{\varphi} = 0$ in the zero-dimensional $O(N)$ model.

At this point we also want to reference our comments in subsection 2.2.3.2: the treatment of non-linear advection-diffusion equations requires *a priori* shock capturing schemes, capable of handling non-analyticities and even discontinuities. An application of expansion schemes relying on analyticity like the Taylor expansion is only possible in very special situations and require an *a posteriori* case-by-case evaluation of the method. In scenarios where the FRG flows are driven by an interplay of advection and diffusion around non-trivial minima and/or large gradients of the conserved quantity u , the Taylor expansion is inevitably doomed to fail. It is not possible to capture the dynamics of such equations reliably with the simple Taylor expansion discussed here. A numerical inversion of the (F)RG flow is also impossible in those scenarios. The appearance of a non-analytic behavior is also understood via a rise of entropy, cf. subsections 3.2.4.2 and 3.2.5.4.

It should be noted that in this work we discussed the simplest possible Taylor/vertex-expansion scheme. Other versions of the FRG Taylor (vertex) expansion including a moving expansion point or a rescaling of the expansion coefficients might improve the performance of the expansion scheme in certain cases, cf. Refs. [104, 124, 611]. Implementing and testing different approaches to the Taylor expansion for zero-dimensional $O(N)$ models would certainly be an interesting topic for further studies.

3.2.3.4. Test case IV: The $\sigma = 0$ boundary

The last test case is again a non-analytic and discontinuous potential,

$$U(\vec{\varphi}) = \begin{cases} -(\vec{\varphi}^2)^{\frac{1}{3}}, & \text{if } |\vec{\varphi}| \leq \sqrt{8}, \\ \frac{1}{2}\vec{\varphi}^2 - 6, & \text{if } |\vec{\varphi}| > \sqrt{8}. \end{cases} \quad (3.104)$$

The numerically challenging features are the cusp at $\varphi = 0$ as well as a non-trivial minimum at the kink at $\varphi = \sqrt{8}$. As displayed in figure 3.23 (evaluated on the constant field configuration), the cusp⁵⁸ at $\sigma = 0$ in $U(\sigma)$ translates to a pole in $\partial_\sigma U(\sigma) \equiv u(\sigma)$. This scenario was

⁵⁸Potentials with cusps in field space are not just academic thought experiments. They are encountered in, e.g., theories in $2 + 1$ space-time dimensions, such as the Gross-Neveu model [612].

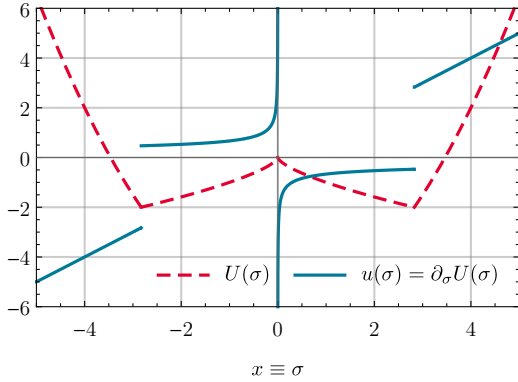


Figure 3.23.: UV potential $U(\sigma)$ (red-dashed) and its first derivative $u(\sigma) = \partial_\sigma U(\sigma)$ (blue, solid) of test case IV from Eq. (3.104). From Fig. 30 of Ref. [1].

Table 3.4.: Exact results for $\Gamma^{(2n)}$ of the $O(N)$ model with the UV initial potential (3.104) for selected N . They are obtained by a high-precision one-dimensional numerical integration of the expectation values $\langle (\overline{\phi}^2)^n \rangle$ from Eq. (3.56) using *NIntegrate* in MATHEMATICA [353]. Here, we present the first six digits only. In parts from Tab. IV of Ref. [1] and Tab. I of Ref. [2].

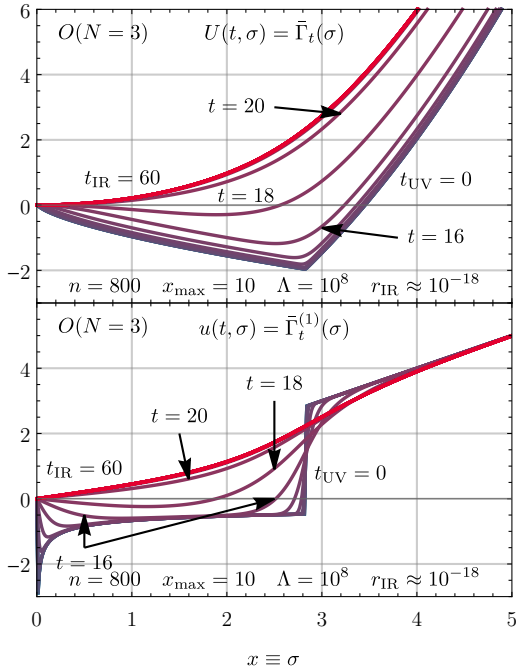
N	$\Gamma^{(2)}$	$\Gamma^{(4)}$	$\Gamma^{(6)}$
1	0.204698	0.064682	0.112849
3	0.421674	0.153559	0.249252

engineered as an extreme test case for the boundary condition at $\sigma = 0$ discussed at length in subsection 3.2.2.4.

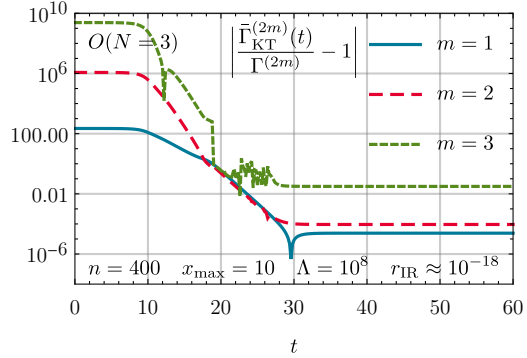
We have again performed the full set of numerical tests of subsection 3.2.3.1 and found results supporting the general statements made in subsection 3.2.3.1. For brevity, we will not repeat the complete discussion of that subsection but instead focus again on selected results.

Figure 3.24a depicts the FRG flow for the $O(3)$ model computed with the KT scheme for the UV initial condition (3.104). Figure 3.24b displays the corresponding flow of the first three non-vanishing n -point functions. With our implementation of the KT scheme using *NDSolve* of MATHEMATICA [353] with a *PrecisionGoal* and *AccuracyGoal* of 10 we are able to compute precise solutions, where the achievable precision for $\Gamma^{(4)}$ and $\Gamma^{(6)}$ is, as discussed in the previous subsections, limited by the finite-difference rounding errors. The discretization-error scaling shows the same peculiarities as the test case I of subsection 3.2.3.1 due to the discontinuities in the initial conditions. The corresponding reference values for the $O(3)$ model are listed in table 3.4. The dynamics during the FRG flow is dominated by the pole at $\sigma = 0$ and the discontinuity at $\sigma = \sqrt{8}$ in $u(\sigma)$. The diffusion smears out the discontinuity and advection transports it towards $\sigma = 0$ “filling up the well” at $\sigma = 0$. Considering the corresponding values for $u(\sigma)$ for $\sigma < 0$ using the antisymmetry of $u(\sigma)$, the boundary at $\sigma = 0$ can be seen as a point where waves of opposite amplitude annihilate – a situation very reminiscent of our discussion of the BBE (2.130) in subsection 2.2.3.2.

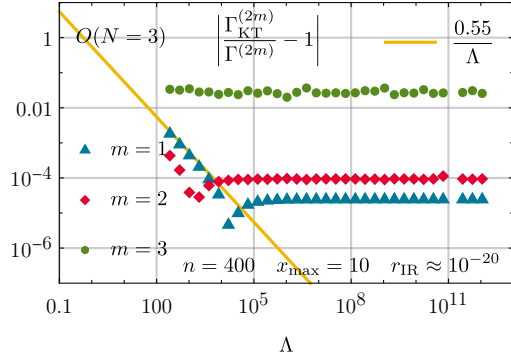
Only the carefully engineered boundary condition at $\sigma = 0$ together with corresponding ghost cells allows for practical computations with the present initial condition. The pole at $\sigma = 0$ presents no problem in practical computations because the boundary condition at $\sigma = 0$ makes use of the antisymmetry of $u(t, \sigma)$. The first cell containing the pole is centered at $\sigma = 0$ and due to the antisymmetry, the corresponding cell average $\bar{u}_0(t)$ vanishes by construction. Enforcing $\bar{u}_0(t) = 0$ and for the two ghost cells $\bar{u}_{-2}(t) = -\bar{u}_2(t)$ and $\bar{u}_{-1}(t) = -\bar{u}_1(t)$ at each



(a) The FRG flow of the effective potential $U(t, \sigma)$ (upper panel) and its derivative $u(t, \sigma) = \partial_\sigma U(t, \sigma)$ (lower panel) evaluated at $t = 0, 2, 4, \dots, 60$ (integer values for t were chosen for convenience and readability). The (overlapping) blue and violet curves correspond to the UV and the red curves to the IR. We used the exponential regulator (3.8) with UV scale $\Lambda = 10^8$ and $n = 800$ volume cells. The plot does not show the region $x \in [5, 10]$, because the tiny differences between $u(t, \sigma)$ and $u(t_{UV}, \sigma)$ are not visible in this region and vanish for large $x = \sigma$ anyhow.



(b) The relative error for $\Gamma^{(2m)}(t)$, for $m = 1, 2$, calculated with the KT scheme as a function of the RG time t for the $O(3)$ model. We used the exponential regulator (3.8) with UV scale $\Lambda = 10^8$ and $n = 400$ volume cells.



(c) The relative error for $\Gamma^{(2m)}(t_{IR})$ for $m = 1, 2, 3$ from the KT scheme as a function of the UV scale Λ . We use the exponential regulator (3.8) and keep the IR cutoff scale constant at $r(t_{IR}) = 10^{-15}$ for all runs. The number of volume cells is $n = 400$. The straight yellow line $\propto \Lambda^{-1}$ is for optical guidance.

Figure 3.24.: FRG flow on the left (a), relative errors over RG time on the top right (b), and relative errors in the IR as function of the UV cutoff Λ on the bottom right (c) for the zero-dimensional $O(3)$ model with initial condition Eq. (3.104). The computational grid size is $\sigma_{\max} = x_{\max} = 10$ and $\Gamma^{(2m)}(t)$ are calculated from $u(t, \sigma)$ via the approximations (D.6), (D.9), and (D.12) for the numerical derivatives. From Figs. 31, 32, and 33 of Ref. [1].

time step allows for a stable and accurate FRG time evolution even for such extreme initial conditions like the one of Eq. (3.104).

Treating this initial condition using a formulation in the invariant $\varrho = \frac{1}{2} \sigma^2$ with some naive boundary conditions without strict mathematical justification is hazardous, because $u(t, \varrho) = \partial_\varrho U(t, \varrho)$ diverges as $\varrho^{-2/3}$ as $\varrho \rightarrow 0$. As mentioned in subsection 3.2.2.4, it is

unclear to us how to deal with the $\varrho = 0$ boundary especially in a case like the one discussed in this subsection.

We conclude this subsection with a short discussion of RG consistency. The plateaus in figure 3.24b in the UV (at small t) and the IR (at large t) are again a strong indication for appropriately chosen UV and IR scales. From figure 3.24c, showing the Λ -dependence of $\Gamma^{(2)}$, $\Gamma^{(4)}$, and $\Gamma^{(6)}$, one observes that, even in the presence of the pole at $\sigma = 0$ in $u(t = 0, \sigma)$, an initial UV scale of $\Lambda = 10^8$ is sufficient to realize RG consistency. Arguably even $\Lambda = 10^6$ – the scale used in subsection 3.2.3.1 – would suffice, suggesting that in the current case the scale is primarily set by the discontinuity and linear asymptotics at and beyond $\sigma = \sqrt{8}$, which both are also present (with very similar values) in the initial condition (3.94) of subsection 3.2.3.1.

However, decreasing Δx would lead to larger numerical gradients for the initial condition at $\sigma = 0$ due to the discretization of the pole in $u(\sigma)$, which in turn implies that Λ has to be simultaneously increased in order to keep the propagators (3.80) and (3.81) dominated by Λ in the UV.

Also, if the cusp at $\sigma = 0$ in the UV initial potential $U(t = 0, \sigma)$ in figure 3.23 pointed downwards and $u(0, x)$ had negative gradients on both sides of the corresponding pole, it would formally be extremely hard to guarantee the inequalities (3.100) and to have a non-singular flow equation in the UV, because the giant negative gradients would not be restricted to the cell at $\sigma = 0$. In a discretized version with non-zero Δx a calculation is still possible, as long as Λ is chosen extremely large, much larger than the huge, but finite negative gradient of $u(\sigma)$. Hence, RG consistency is not only a physical requirement, but also sets strict limits on the choice of numerical parameters, respectively. We observe similar effects in subsection 4.2.2, where the chemical potential enters as a shock wave in field space with (at $T = 0$) infinite negative slope in $u(t, \sigma)$ at positive σ .

3.2.4. The $O(1)$ model – entropy production and irreversibility of RG flows

This subsection is based on Ref. [2] and contains parts of the unpublished notes [8]. The plots of Ref. [2] and the underlying numerical data were produced by A. Koenigstein and numerically cross-checked by my own computations with the KT scheme.

Selected numerical results and accompanying symbolic computations are included in the digital auxiliary file [365]. The single thread wall time on an Intel® Core™ i7-8750H processor for the numeric results of this subsection is only around eight minutes, since we only discuss five FRG trajectories.

The introduction of this subsection follows Secs. I and II of Ref. [2].

In this subsection we will focus on $O(N = 1)$ models, i.e., a zero-dimensional \mathbb{Z}_2 -symmetric model of a single scalar, as discussed especially at the beginning of this chapter in section 3.1. In the spirit of subsection 3.2.2.3, the limitation to $N = 1$ entails, that the flow equation gets purely diffusive as the advective contributions $\propto (N - 1)$ vanish. We are left with the

scalar parabolic conservation law,

$$\partial_t U(t, \sigma) = \frac{1}{2} \frac{1}{r(t) + \partial_\sigma^2 U(t, \sigma)} \partial_t r(t) = \frac{1}{2} \text{⊗}, \quad (3.105)$$

which in primitive form reads

$$\partial_t u(t, x) = \alpha[t, \partial_x u(t, x)] \partial_x^2 u(t, x), \quad (3.106)$$

with the non-linear, strictly positive diffusion coefficient

$$\alpha[t, \partial_x u(t, x)] \equiv - \frac{\frac{1}{2} \partial_t r(t)}{[r(t) + \partial_x u(t, x)]^2}, \quad (3.107)$$

cf. Eqs. (3.85) and (3.86). We can identify Eq. (3.106) as a heat equation with non-linear diffusion coefficient (3.107), cf. subsection 2.2.4. The present discussion makes our general remarks about functional flow/heat equations in subsection 2.1.7 explicit. The conservative formulation (3.105) and interpretation in terms of (numerical) fluid dynamics has tremendous benefits and consequences for understanding and solving this FRG flow equation:

1. The explicit identification of the FRG flow Eq. (3.105) as a heat equation allows us to directly apply the CFD methods of section 2.2 and especially subsection 2.2.4.
2. An interpretation of FRG flow equations as flow equations in the narrow sense of the word makes the dynamics during the flow intuitively understandable. The non-linear diffusive contribution (the radial σ -mode) smears out cusps and jumps in $u(t, x)$ and corresponds to undirected movement of $u(t, x)$, depending on the local “concentration differences”, the gradient $\partial_x u(t, x)$, via the highly non-linear diffusion coefficient (3.107).
3. The described dissipative dynamics goes hand in hand with entropy production and irreversibility as discussed in the CFD context in subsection 2.2.4. We can therefore conclude that the irreversibility of the RG transformations during the FRG flow is hard coded in the diffusive character of the flow Eq. (3.105), not only in zero space-time dimensions, but for any dimension and any QFT, cf. Refs. [311, 576, 580]. Hence, the rise of entropy during the FRG flow might therefore be directly linked to \mathcal{C} -/ \mathcal{A} -theorems. This is explained in detail in this subsection in the context of our minimalistic toy model QFT.

To be specific, we shall show that the numerical entropy, which is of utmost importance in the theoretical treatment of PDEs, as outlined in section 2.2 and especially subsection 2.2.2, has a very close connection to an entropy in the (F)RG flow⁵⁹ and further possible connections to the so-called \mathcal{C} -/ \mathcal{A} -functions, cf. Refs. [230, 575, 583–595] and subsection 3.2.4.3 for more details on \mathcal{C} -/ \mathcal{A} -functions.

⁵⁹In this context we also have to mention the publication [245] by J. Cotler and S. Rezchikov, who were able to interpret the Polchinski equation as an “optimal transport gradient flow of a field-theoretic relative entropy”, thus establishing a firm and explicit connection between an information-theoretic entropy and (F)RG flows.

One of the most important direct consequences of this is, that the same “(thermodynamic) arrow of time” or “thermodynamic time asymmetry” [579] identified by the entropy of a PDE, is also present from a FRG perspective.

In nature as well as in the PDEs that describe our physical world, entropy is produced by diffusion (dissipation) as well as discontinuities of different kinds. Consequently the evolution of such systems and also their numerical solutions are irreversible and usually only weak solutions are accessible numerically [315, 317–319, 326–328]. As we will demonstrate in this subsection, the *total variation non-increasing* (TVNI) property and related numerical entropy, cf. Eq. (2.110) and the subsequent discussions of section 2.2, used to guarantee the stability of numeric solution schemes, can be promoted to a “physical” entropy function. This entropy function shares characteristics with a \mathcal{C} -function and its properties transfer from the PDE to the QFT and vice versa. Therefore, (F)RG flows are also not reversible.⁶⁰ This makes the semi-group character of the RG, see, e.g., Ref. [613], explicit. This semi-group character manifests very explicitly in Kadanoff’s block-spin picture [233–236] – it is intuitively obvious that the averaging over a set of spins is an irreversible process. The irreversibility of (F)RG flows is not just an abstract concept, but is present on a practical level in rather simple truncations of the Wetterich equation.

These statements may have no severe practical implications for studies of, e.g., QCD and condensed-matter systems, where the (F)RG flow is in general followed from small (UV limit) to large length scales (IR limit). In these cases, the dynamics in the long-range limit is predicted from a given known UV action by integrating out high momentum modes along the “natural” RG time-direction. However, in situations where (F)RG flows are followed from large to small length scales, such as studies of the asymptotic safety scenario in QFTs (see Refs. [230, 614–617] in general, Refs. [618, 619] for a recent review in the context of (quantum) gravity, and Refs. [612, 620] for applications in condensed-matter physics), the question of irreversibility of (F)RG flows and the associated production of entropy may indeed be very relevant.

Whereas FRG flows are indeed reversible for certain classes of truncations (of the underlying effective action), we shall demonstrate in the present work – with the aid of simple models – that it becomes formally impossible to reverse FRG flows in cases where no truncations of the effective action are made. Even more, already for often employed truncation schemes (e.g., LPA), we shall see that irreversibility associated with numerical entropy production can already be a manifest feature of FRG flows. Of course, irreversibility of FRG flows does not imply, that it is not possible to construct theories, which are valid on all scales. It only implies, that the search for such theories may in general be more complicated. We already mentioned in our discussion of RG consistency of subsection 2.1.6, that irreversibility of (F)RG flows might complicate RG-consistent reconstructions significantly, cf. Eq. (2.85) and the corresponding discussion. In any case, generalizations of the arguments presented in our present work may help to provide a fresh view on these aspects (and/or revive some already existing discussions [230, 311, 575–578, 580]).

As we shall discuss below, fixed points still play an important role within the fluid-dynamic

⁶⁰Note that similar arguments, which link the dissipative character of RG flow equations to the irreversibility of the RG flow, were already brought up in Refs. [575, 576] already before or parallel to the development of the functional RG framework pioneered in Ref. [212].

interpretation of FRG flows. In fact, fixed points can be identified with steady-flow solutions and/or (thermal) equilibrium situations on the level of the rescaled dimensionless flow equations, which have advective and diffusive character.

One major benefit of the connection revealed in this work is that a measure for the irreversibility of the FRG flow is explicitly provided via the identification with numerical entropy and especially total variation [167, 315, 317, 319, 339]. Hence, the construction and analysis of such a measure, at least in certain truncations, might be greatly simplified. In the future, this might also help to single out adequate truncation schemes for FRG flow equations as those truncations, which maintain the inherently irreversible character of the flow. We note that observations similar to ours have already been pointed out in Refs. [230, 311, 576, 580] for related (partially linearized) flow equations.

The rest of this subsection is organized as follows: Numerical entropy and the TVNI property are discussed in detail in subsection 3.2.4.1. Explicit computations and a detailed analysis of numerical entropy production for our test cases are presented in subsection 3.2.4.2. In subsection 3.2.4.3, we discuss the manifestation of a \mathcal{C} -theorem for the zero-dimensional $O(1)$ model, challenges for the generalization to finite $N > 1$ in zero dimensions, and we briefly comment on possible generalizations of our findings to higher-dimensional theories.

3.2.4.1. (Numerical) entropy and the total variation

This subsection is based on Sec. III of Ref. [2].

The [first part](#) of this subsection deals with the explicit construction of a (numerical) entropy for the conservation law (3.105). This entropy has to be a functional of the conserved quantity $u(t, x)$ and/or its derivatives⁶¹ that is monotonically rising during the FRG flow. Monotonicity is explicitly proven for valid initial conditions $U(t = 0, x)$. Since $u(t, x)$ is by definition a function of all couplings of the theory, the (numerical) entropy function might therefore be linked to a zero-dimensional version of \mathcal{C} -/ \mathcal{A} -function. In fact it might have some practical advantages compared to other approaches toward \mathcal{C} -/ \mathcal{A} -functions studied in literature, since $u(t, x)$ does not even need to be expandable in explicit couplings at all, but still contains all degrees of freedom.

In the [second part](#) of this subsection, we derive a discrete formulation of this entropy functional and demonstrate that it can be directly related to the *total variation* (TV), *i.e.*, the arc-length, of $u(t, x)$. Thus providing a link between the total TVD/TVNI property – commonly used in numeric schemes for conservation laws [167, 327, 339] – and our field theoretical notion of entropy here.

Construction of the (numerical) entropy

The construction of our (numerical) entropy function is directly inspired by the construction

⁶¹The purely diffusive character of Eq. (3.105) is expected to smoothen $u(t, x)$ during the FRG flow which renders $u(t, x)$ differentiable (but not necessarily analytic) at least for $0 < t < \infty$. This does not need to be the case for hyperbolic conservation laws where taking derivatives of $u(t, x)$ has to be handled with great care, *e.g.*, around shocks, *i.e.*, in a proper weak formulation, see section 2.2.

of entropy/energy functionals for the BBE (2.130) [371, 372] or the HE (2.138) [314] of subsection 2.2.3.2 and subsection 2.2.4.

Let $y \in \mathbb{R}$ and

$$s : \mathbb{R} \rightarrow \mathbb{R}, \quad y \mapsto s(y), \quad (3.108)$$

be a continuously twice differentiable convex function on \mathbb{R} , hence

$$s(y) \in C^2(\mathbb{R}), \quad s''(y) \geq 0, \quad (3.109)$$

for all $y \in \mathbb{R}$. Furthermore, we require that $s(y)$ shall not grow faster than y^2 for $|y| \rightarrow \infty$, which is explained below. Using $s(y)$ we define the functional

$$S[f(x)] \equiv - \int_{-\infty}^{+\infty} dx s(f(x)), \quad (3.110)$$

which we shall refer to as *entropy functional*. In general, the bounds of integration are chosen according to the domain of our problem at hand. Next, we prove that, choosing $f(x) = \partial_x u(t, x)$, Eq. (3.110) indeed plays the role of an (numerical) entropy for the PDE (3.105). Hence, it measures, similarly to \mathcal{C} -/ \mathcal{A} -functions for RG flows, the degrees of freedom and irreversibility. To this end, we explicitly demonstrate that $S[\partial_x u(t, x)]$ is monotonically increasing during the FRG flow, thus being a monotonic function on $t \in [0, \infty)$:

$$\frac{d}{dt} S[\partial_x u(t, x)] \geq 0. \quad (3.111)$$

The only further ingredient, which is needed for the proof is the spatial derivative of the flow-equation (3.105):

$$\partial_t [\partial_x u(t, x)] = - \frac{d}{dx} \left(\frac{1}{2} \frac{\partial_x^2 u(t, x)}{[r(t) + \partial_x u(t, x)]^2} \partial_t r(t) \right). \quad (3.112)$$

Taking spatial derivatives of $u(t, \sigma)$ should be allowed at any $t \in (0, \infty)$ because of the smoothening character of the diffusion – at least in zero space-time dimensions⁶². Only for $t = 0$ the initial condition may violate smoothness, see subsection 3.1.3.2 for details. In the following, we normalize the entropy and subtract the entropy of the initial condition $S[\partial_x u(t = 0, x)]$, such that this should not spoil any of our subsequent arguments.

⁶²The generalization of this argument to higher-dimensional $O(N)$ -type models might be delicate, because the non-linear diffusion can also cause non-analyticities in potentials in the IR if these end up in the symmetry broken phase. In that case it might be unavoidable to base and repeat the entire discussion using a rigorous weak/integral formulation of the PDEs under consideration.

Let us now prove Eq. (3.111):

$$\frac{d}{dt} S[\partial_x u(t, x)] = - \frac{d}{dt} \int_{-\infty}^{+\infty} dx s(\partial_x u(t, x)) = \quad (3.113a)$$

$$= - \int_{-\infty}^{+\infty} dx (\partial_t [\partial_x u(t, x)]) s'(\partial_x u(t, x)) = \quad (3.113b)$$

$$= \int_{-\infty}^{+\infty} dx \left[\frac{d}{dx} \left(\frac{1}{2} \frac{\partial_x^2 u(t, x)}{[r(t) + \partial_x u(t, x)]^2} \partial_t r(t) \right) \right] s'(\partial_x u(t, x)) = \quad (3.113c)$$

$$= \int_{-\infty}^{+\infty} dx \left[-\frac{1}{2} \partial_t r(t) \frac{[\partial_x^2 u(t, x)]^2}{[r(t) + \partial_x u(t, x)]^2} s''(\partial_x u(t, x)) + \right. \\ \left. + \left[\frac{1}{2} \frac{\partial_x^2 u(t, x)}{[r(t) + \partial_x u(t, x)]^2} \partial_t r(t) s'(\partial_x u(t, x)) \right]_{-\infty}^{+\infty} \right] \quad (3.113d)$$

$$= \int_{-\infty}^{+\infty} dx \left[-\frac{1}{2} \partial_t r(t) \frac{[\partial_x^2 u(t, x)]^2}{[r(t) + \partial_x u(t, x)]^2} s''(\partial_x u(t, x)) \right] \geq 0 \quad \square. \quad (3.113e)$$

where the sought after inequality in Eq. (3.113e) follows from the facts, that the first term in Eq. (3.113d) is positive and the surface term in Eq. (3.113d) vanishes. This can be reasoned by analyzing both terms in Eq. (3.113d) separately.

1. We note that all factors in the integrand of the first term are greater or equal to zero: For the regulator insertion, we have

$$-\frac{1}{2} \partial_t r(t) \geq 0, \quad (3.114)$$

because $r(t)$ is a monotonically decreasing function. The numerator and the denominator are obviously positive. In fact, for the denominator of the fraction

$$r(t) > \partial_x u(t, x), \quad (3.115)$$

for all t anyhow, as long as the initial condition $u(t=0, x)$ and the UV scale Λ are chosen accordingly, cf. Eq. (3.100b) of subsection 3.2.3.1. Finally,

$$s''(\partial_x u(t, x)) \geq 0, \quad (3.116)$$

holds by construction according to Eq. (3.109).

In total, we find that the integrand of the first term is always greater or equal to zero, which directly transfers to the integral itself.

2. For the second term, we first use that, for large $|x|$, the potential $U(t, x)$ and all its derivatives do not change during the FRG flow, as we have elaborated and demonstrated at length in the previous subsection 3.2.3. Furthermore, we use that $s(y)$ maximally grows like y^2 for $|y| \rightarrow \infty$ by definition. This implies that its derivative $s'(y)$ increases asymptotically as y^1 at most. Additionally, we use that $U(t, x)$ is at least proportional to

x^2 for $|x| \rightarrow \infty$ in order to have well-defined expectation values (3.56). Consequently, we have to distinguish two scenarios.

If $U(t, x) \sim x^2$ for large $|x|$, the second term vanishes identically, due to the third spatial derivative of $U(t, x)$, namely $\partial_x^2 u(t, x)$, in the numerator.

Otherwise, if $U(t, x)$ grows faster than x^2 for large $|x|$, the denominator $[r(t) + \partial_x u(t, x)]^2$ will always grow faster than the product $[\partial_x^2 u(t, x)] s'(\partial_x u(t, x))$ for $|x| \rightarrow \infty$.

Hence we ultimately conclude that the second term always vanishes, provided that the initial conditions come with the assumed large- $|x|$ -asymptotic behavior.

In summary, we have shown that the statement of Eq. (3.111) holds on account of the proof (3.113), which promotes S to an entropy (functional) of our system that can only increase.

For what follows, we choose the twice differentiable convex function $s(y) = y^2$. This implies

$$S[\partial_x u(t, x)] = - \int_{-\infty}^{+\infty} dx [\partial_x u(t, x)]^2. \quad (3.117)$$

S can be viewed as measure for the richness of structure of the potential – the information encoded in the potential – by integrating the square of the gradient of $u(t, x)$ over all positions x in field space.

With the definition (3.117) the following practical problem arises: For practical purposes $S[\partial_x u(t, x)]$ formally diverges at any time t because $\partial_x u(t, x)$ is at least constant for $|x| \rightarrow \infty$. This problem can be cured, by subtracting the entropy $S[\partial_x u(t = 0, x)]$ of the initial condition. Since $u(t, x)$ does not change for large $|x|$ during the entire FRG flow, the infinite but constant contributions cancel and we can observe the relative rise in entropy. This should be a valid approach, since we are only interested in these relative changes anyhow. We therefore define and consider the normalized entropy

$$\mathcal{C}[\partial_x u(t, x)] = S[\partial_x u(t, x)] - S[\partial_x u(t = 0, x)], \quad (3.118)$$

which is finite. Potential subtleties regarding the finiteness of S and \mathcal{C} will be discussed in subsection 3.2.4.2. The alphabetic character “ \mathcal{C} ” is chosen because this function quantifies irreversibility similarly to \mathcal{C} -/ \mathcal{A} -functions. We are aware of the fact that a real \mathcal{C} -/ \mathcal{A} -function should be based on the dimensionless rescaled flow equation. This issue is discussed in subsection 3.2.4.3.

Eq. (3.118) for the \mathcal{C} -function makes the loss of information/richness of structure of the effective potential $u(t, x)$ during FRG time evolution explicit. \mathcal{C} monotonically increases with FRG time t because the richness of structure/information decreases with t . A loss of information about a system (effective potential $u(t, x)$) during RG time evolution goes hand in hand with the impossibility to reconstruct/recover earlier states of the system (which had more information) and thus the RG time evolution is irreversible. In the present setup the purely diffusive flow equation of the zero-dimensional $O(1)$ model is responsible for this loss of information as large gradients are smeared out by diffusion during RG time evolution, *cf.* subsection 3.2.4.2 for explicit numerical examples.

Discrete formulation and relation to the TVNI property

In this paragraph we discuss a discretized version of Eq. (3.118), which is suited for practical computations. In the following and w.l.o.g. we consider a FV discretization of $u(t, x)$ in x with n volume cells of constant width Δx , centered at x_i , $i \in \{0, 1, \dots, n-1\}$, see subsection 2.2.1 for details. Recall that the FRG flow in this setup is described by the temporal evolution of the n volume averages $\bar{u}_i(t)$, which are formally defined as the spatial averages of $u(t, x)$ over $[x_{i-\frac{1}{2}}, x_{i+\frac{1}{2}}]$, where $x_{i\pm\frac{1}{2}} \equiv x_i \pm \frac{\Delta x}{2}$. For the purpose of calculating $\mathcal{C}[\partial_x u(t, x)]$, we reconstruct the first derivatives from the set of volume averages $\{\bar{u}_i(t)\}$ by a first-order FD forward stencil,

$$\partial_x u(t, x_i) = \frac{\bar{u}_{i+1}(t) - \bar{u}_i(t)}{\Delta x} + \mathcal{O}(\Delta x). \quad (3.119)$$

For the scope of this work this has proven sufficient since the purely diffusive character of the PDE smoothens $u(t, x)$. However, for non-smooth/non-differentiable initial conditions at $t = 0$, such as Eq. (3.94) and (3.104) of our numeric examples, a naive FD stencil is of course generically ill-conditioned at the discontinuities⁶³. As a direct consequence, the absolute value of $S[\partial_x u(t = 0, x)]$ strongly depends on the explicit discretization points and the ‘‘capturing of the discontinuity’’ in the respective volume cells. For $t \rightarrow \infty$ (as a direct consequence of the CMWH theorem [550–552], cf. App. B of Ref. [1]), $u(t, x)$ is smooth and the FD approximation is well-behaved as long as Δx is not too small. We conclude that the absolute values of our entropy function (3.118) will strongly depend on Δx for non-differentiable initial conditions in the IR because we use $S[\partial_x u(t = 0, x)]$ as normalization, while the qualitative behavior (monotonic rise) is independent of the discretization, which is also true for the discrete total variation (2.111). For the smooth initial conditions (3.101) and (3.103), we observed little dependence of the absolute values of the $\mathcal{C}[\partial_x u(t, x)]$ on Δx , as expected.

We use a grid with the first volume cell of the computational domain centered at zero, $x_0 = 0$, and the last centered at a finite x_{\max} , hence $x_{n-1} = x_{\max}$. x_{\max} is chosen large enough, such that $u(t, x_{\max}) = u(t = 0, x_{\max})$ holds to a sufficient level for all t , cf. our discussion in subsection 3.2.3 as well as Refs. [154, 247, 567, 604]. This enables a computation of $\mathcal{C}[\partial_x u(t, x)]$ considering only $x \in [-x_{\max}, +x_{\max}]$ since the difference

$$S[\partial_x u(t, x)] - S[\partial_x u(t = 0, x)] \quad (3.120)$$

practically vanishes for $|x| \geq x_{\max}$. We therefore study the following quantity:

$$\mathcal{C}[\partial_x u(t, x)] = -2 \int_0^{x_{\max}} dx [\partial_x u(t, x)]^2 + 2 \int_0^{x_{\max}} dx [\partial_x u(t = 0, x)]^2, \quad (3.121)$$

leveraging the \mathbb{Z}_2 symmetry of the problem at hand. Inserting Eq. (3.119) and performing the integrals over the constant segments in the volume cells leads to our semi-discrete formulation

$$\mathcal{C}[\{\bar{u}_j(t)\}] = -\frac{2}{\Delta x} \left(\sum_{j=0}^{n-1} \frac{[\bar{u}_{j+1}(t) - \bar{u}_j(t)]^2}{(1 + \delta_{j,0} + \delta_{j,n-1})} - \sum_{j=0}^{n-1} \frac{[\bar{u}_{j+1}(0) - \bar{u}_j(0)]^2}{(1 + \delta_{j,0} + \delta_{j,n-1})} \right), \quad (3.122)$$

⁶³Similar discussions will arise in higher space-time dimensions, e.g., in models where the FRG flows ends in a symmetry broken phase with a non-analytic IR-potential. Coming back to a related comment made in an earlier footnote 62: such generalizations might require a retracing of the current discussion using a proper weak formulation and in context of Eq. (3.119) probably a limiting procedure like the MUSCL reconstruction (2.99).

where the factor $(1 + \delta_{j,0} + \delta_{j,n-1})$ accounts for the fact that we only integrate over the right half of the first and the left half of the last volume cell.

Recall that practical computations of solutions to the PDE (3.105) on the compact interval $x \in [0, x_{\max}]$ require carefully chosen boundary conditions [1, 3] to be consistent with solutions of the pure initial value problem posed by Eq. (3.105) on the interval $x \in (-\infty, +\infty)$ [154, 155]. In the present FV setup we implement boundary conditions with ghost cells, see Eqs. (3.91) and (3.93) of subsection 3.2.2.4 for details. For the computation of $\mathcal{C}[\{\bar{u}_i(t)\}]$ we require only the ghost-cell average $\bar{u}_n(t) = 2\bar{u}_{n-1}(t) - \bar{u}_{n-2}(t)$ as well as the cell averages at x_i for $i \in \{0, 1, \dots, n-1\}$.

The entropy functional $S[\partial_x u(t, x)]$ of Eq. (3.117) discussed in this subsection is closely related to the *total variation* (TV) [339] – the arc length – of the solution $u(t, x)$, which we introduced in the context of FV methods and CFD in subsection 2.2.2, viz. in Eqs. (2.110) and (2.111). For a single component system on the (computational) interval $[0, x_{\max}]$ Eq. (2.110) reads

$$\text{TV}[\partial_x u(t, x)] \equiv \int_0^{x_{\max}} dx |\partial_x u(t, x)|. \quad (3.123)$$

The TV qualitatively differs only by a global sign from the entropy functional S , where the sign used for the TV is compatible with the mathematical convention for (numerical) entropy. The use of the absolute value $|\partial_x u(t, x)|$ in Eq. (3.123) instead of the square $[\partial_x u(t, x)]^2$ used for S presents only as quantitative difference, which is not of any practical relevance in this work. On a FV grid, a discretized version of Eq. (3.123) is given by

$$\text{TV}[\{\bar{u}_j(t)\}] \equiv \sum_{j=0}^{n-1} |\bar{u}_{j+1}(t) - \bar{u}_j(t)|, \quad (3.124)$$

where a first-order forward FD stencil is used to discretize the first derivative, cf. Eq. (2.111).

We discussed the TV and the TVNI property of conservation laws in subsections 2.2.2–2.2.4 and discussed \mathcal{C}_{TV} of Eq. (2.134) as a numerical entropy and measure linked to the irreversibility of non-linear convection equations. The flow Eq. (3.105) under consideration in this subsection is a non-linear, parabolic pure diffusion equation and the construction of the normalized entropy functional \mathcal{C} of Eq. (3.118) can be adapted to prove directly that solutions of the flow Eq. (3.105) are in fact TVNI.

Table 3.5.: The table lists the “exact” results for $\Gamma^{(2)}$ of the $O(1)$ model (second column) for the various UV initial potentials of our test cases (first column), which are calculated by a brute-force, high-precision one-dimensional numerical integration of the expectation value $\langle \vec{\phi}^2 \rangle$ from Eq. (3.56) using *NIntegrate* in MATHEMATICA [353] with a *PrecisionGoal* and *AccuracyGoal* of 10, cf. tables 3.1–3.4. Here, we shall present the first ten digits. The last column lists the relative errors of the numerical solution of the purely diffusive FRG flow equation obtained with the second-order accurate KT scheme using the parameters listed in the corresponding figures 3.25a, 3.26a, 3.27a, 3.28a, and 3.29a, see also subsection 3.2.3 for a detailed discussion of such errors.

UV potential	$\Gamma^{(2)}$	$ \Gamma_{\text{FRG}}^{(2)}/\Gamma^{(2)} - 1 $
Eq. (3.94)	0.1768130358	$6.0 \cdot 10^{-6}$
Eq. (3.101) (negative mass)	0.1995098930	$1.1 \cdot 10^{-5}$
Eq. (3.101) (positive mass)	1.3324252475	$1.4 \cdot 10^{-5}$
Eq. (3.103)	0.1740508127	$2.5 \cdot 10^{-5}$
Eq. (3.104)	0.2046977422	$5.8 \cdot 10^{-6}$

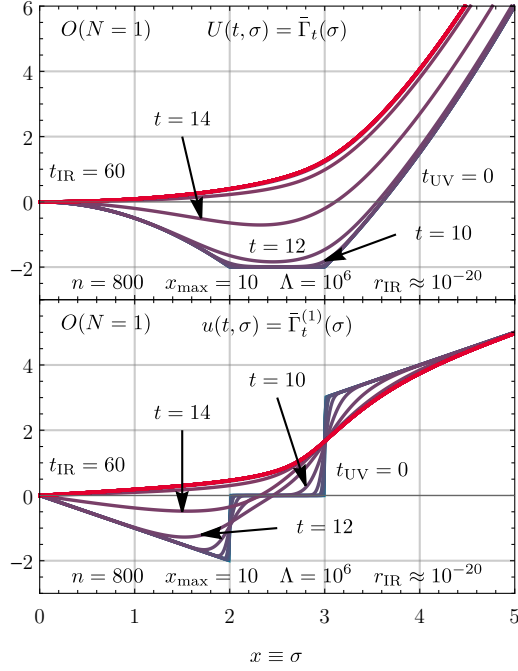
3.2.4.2. Numerical entropy production in zero-dimensional models

This subsection is based on Sec. IV of Ref. [2].

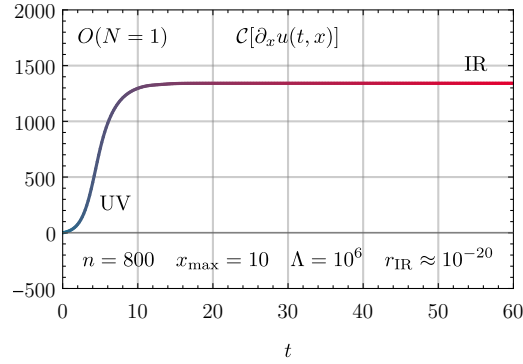
In this subsection we present explicit numerical results for the FRG flows of the (numerical) entropy function (3.118) for some selected zero-dimensional $O(1)$ models differing by their action – UV initial condition for the FRG flow. As explicit examples, we choose the test cases from subsection 3.2.3 with their established numerical and model parameters. The following paragraphs

- Test case I: Non-analytic initial condition,
- Test case II: ϕ^4 potential,
- Test case III: ϕ^6 potential,
- Test case IV: The $\sigma = 0$ boundary,

contain discussions for the zero-dimensional $O(1)$ model with the respective ICs (3.94), (3.101), (3.103), and (3.104) and are based on Secs. IV. A–D of Ref. [2]. For the sake of completeness and as proof of reliability of our numerical scheme and the choice of our numerical parameters, we provide a comparison in table 3.1 between numerical results for the 1PI two-point-function $\Gamma^{(2)}$ calculated via the solution of the flow equation (3.105) with the KT scheme and “exact” results calculated via expectation values (3.56) from the partition function. Note that all plots of the entropy in this subsection are based on a direct implementation of Eq. (3.122).



(a) FRG flow of the effective potential $U(t, \sigma)$ (upper panel) and its derivative $u(t, \sigma) = \partial_\sigma U(t, \sigma)$ (lower panel)



(b) FRG flow of the numerical entropy $\mathcal{C}[\partial_x u(t, x)]$

Figure 3.25.: FRG flow of the effective potential and its derivative on the top (a) and corresponding flow of the numerical entropy below (b) for the zero-dimensional $O(1)$ model with initial condition Eq. (3.94). Blue color is associated to the UV and red color to the IR. We used the exponential regulator Eq. (3.8) with UV scale $\Lambda = 10^6$. The lower panel in (a) is identical to the upper panel in figure 3.5. From Figs. 1 and 2 of Ref. [2].

Test case I: Non-analytic initial condition

We begin our discussion of $O(1)$ models with test case I (3.94), recall figure 3.3 for a visualization of this IC. The FRG flow of $u(t, x)$ for $N = 1$ is presented in figure 3.25a.

The diffusive character of the σ -mode is clearly visible from the fact that it smoothens the discontinuities at $x = 2$ and $x = 3$, without any directed propagation (advection) of the conserved quantity $u(t, x)$. Recall that the system has to restore the \mathbb{Z}_2 symmetry in the ground state as dictated the CMWH theorem [550–552]. In particular, the potential has to become convex [557, 558]. This can be directly observed in the plot of the FRG flow and read off from table 3.5 – the two-point function is positive at $\sigma = 0$.

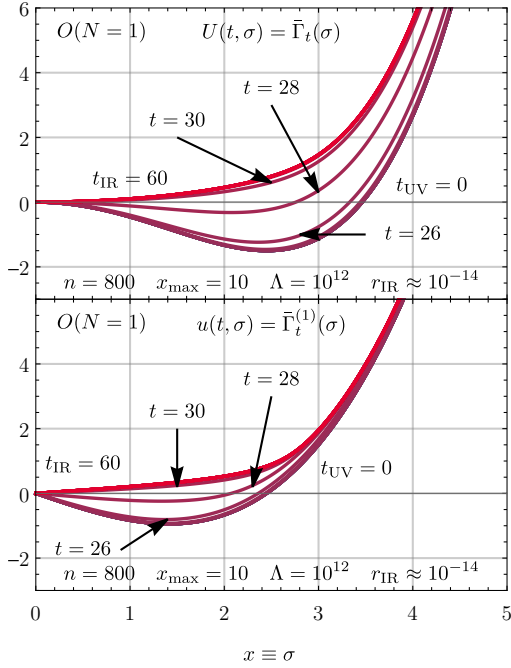
In figure 3.25b we present the FRG flow of the (discretized numerical) entropy function for our first test case.

As expected from our discussion in subsection 3.2.4.1, the entropy grows monotonically. It increases by two orders of magnitude starting at zero in the UV until it reaches (again) a plateau in the IR. We find that the entropy grows most when the regulator (3.8) reaches the model scales. Loosely speaking, this is where most of the dynamics takes place, see figure 3.25a (approximately between $t \approx 4$ and $t \approx 8$). This is the RG time frame in which the diffusion smears out the discontinuities. From a fluid- and thermodynamic perspective and directly on the level of the PDE, the whole process is intuitively understandable: Diffusion goes hand in hand with strong dissipation and a loss of information about the initial state of the system – the UV, cf. Refs. [575, 576]. This is directly comparable to heat conduction, where the information about the initial temperature distribution gets lost during the flow toward “thermal” equilibrium [314, 315, 579] as discussed in our introduction of the linear HE (2.138) in subsection 2.2.4.

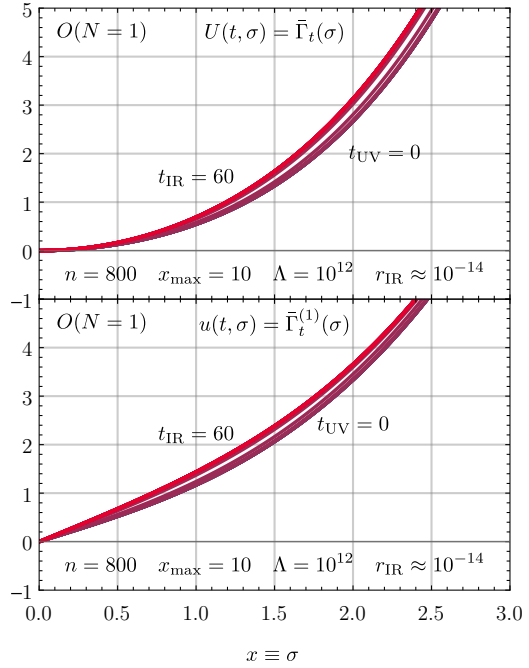
In the FRG framework, this translates to integrating out degrees of freedom from the UV to the IR and a growth in the number of coupling constants in $U(t, \sigma)$, which is directly related to the growth of entropy. The entropy plateau in the IR is identified with the interacting IR regime and an “thermal” equilibrium on the level of the diffusive PDE, whereas a plateau in the UV is associated with a Gaussian UV fixed point [178, 621]. As expected the entropy stops changing at these points. IR solutions therefore correspond either to steady-flow solutions (in advection dominated systems for a large number of “Goldstone” modes [441, 442, 563]) or to (thermal) equilibrium solutions (in diffusion dominated $O(1)$ -symmetric systems) in the fluid-dynamical picture [1].

Note that $t \in [0, 60]$ corresponds to an integration over 26 orders of magnitude in $r(t)$, starting 6 orders of magnitude above the model scales (which are of order one) and ending up 20 orders of magnitude below the model scales. Interestingly, we find that the almost total absence of a plateau in the entropy in the UV for our first test case implies that we almost violated RG consistency. The absence of the zero-entropy plateau can also be seen by closer inspection of figure 3.11, where $\Lambda = 10^6$ is barely on the plateau of RG-consistent UV scales.

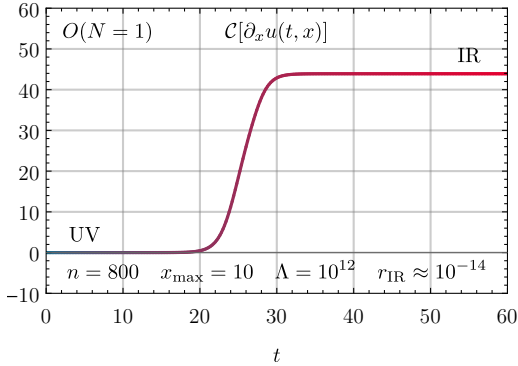
Before we continue with our next test case, we again note that the absolute value of $\mathcal{C}[\partial_x u(t, x)]$ in the IR in figure 3.25b has no quantitative meaning, due to the ill-conditioned behavior when applied to the discontinuous initial condition (3.94) of the numerical derivative (3.119). However, this does not spoil our qualitative arguments at all.



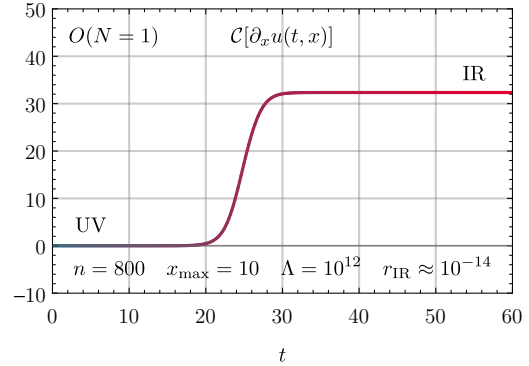
(a) FRG flow of the effective potential $U(t, \sigma)$ (upper panel) and its derivative $u(t, \sigma) = \partial_\sigma U(t, \sigma)$ (lower panel)



(a) FRG flow of the effective potential $U(t, \sigma)$ (upper panel) and its derivative $u(t, \sigma) = \partial_\sigma U(t, \sigma)$ (lower panel).



(b) FRG flow of the numerical entropy $\mathcal{C}[\partial_x u(t, x)]$



(b) FRG flow of the numerical entropy $\mathcal{C}[\partial_x u(t, x)]$

Figure 3.26.: FRG flow of the effective potential and its derivative on the top (a) and corresponding flow of the numerical entropy below (b) for the zero-dimensional $O(1)$ model with initial condition (3.101) with negative mass term. Blue color is associated to the UV and red color to the IR. We used the exponential regulator Eq. (3.8) with UV scale $\Lambda = 10^{12}$. From Figs. 3 and 5 of Ref. [2].

Figure 3.27.: FRG flow of the effective potential and its derivative on the top (a) and corresponding flow of the numerical entropy below (b) for the zero-dimensional $O(1)$ model with initial condition (3.101) with positive mass term. Blue color is associated to the UV and red color to the IR. We used the exponential regulator Eq. (3.8) with UV scale $\Lambda = 10^{12}$. From Figs. 4 and 6 of Ref. [2].

Test case II: ϕ^4 potential

We continue our discussion of $O(1)$ models with test case II (3.101) with positive and negative mass term, recall figure 3.12 for a visualization of this IC with a negative mass term. Depending on the sign of the mass term, we either start the FRG flow with a broken or restored \mathbb{Z}_2 symmetry.

When considering Eq. (3.101) with negative mass term, we argued in subsection 3.2.3.2 that during the FRG flow, while the physical point moves from $\sigma = \pm\sqrt{6}$ to $\sigma = 0$, presumably an excessively large or even infinitely many new couplings are generated in $U(t, \sigma)$. This renders FRG Taylor expansion discussed in subsection 3.2.3.2 at a finite order a potentially problematic approximation scheme for the evolution of non-convex potentials, see also subsection 3.2.3.3. In this paragraph, we reinforce our findings about the non-convergence of (Taylor) expansions of the potential during the FRG flow by studying the (numerical) entropy production during the FRG flows.

The FRG flows of $u(t, x)$ for the IC (3.101) with negative mass term is depicted in figure 3.26a and figure 3.27a shows the corresponding FRG flow⁶⁴ for positive mass term. Both FRG flows are by visual inspection not really spectacular: For the “negative mass”-case, we find that, according to the CMWH theorem [550–552], the diffusion via the σ -mode again restores the \mathbb{Z}_2 symmetry and drives the potential convex during the RG flow before the system equilibrates in the IR. For the FRG flow of the “positive mass”-case we only find minimal changes in the shape of $u(t, x)$ also originating from the non-linear diffusion during the FRG flow. Hence, the equilibrated solution in the IR is relatively close to the UV initial potential.

The plots of the corresponding entropies in figure 3.26b (for negative mass term) and figure 3.27b (for positive mass term) are more instructive. In both cases we find a clear monotonic rise of the (numerical) entropy exactly in the FRG time period, in which most of the dynamics takes place. Furthermore, we clearly find plateaus in the UV and the IR, which correspond to the trivial UV regime and the non-trivial interacting IR regime. This plateau-like behavior signals RG consistency. In comparison with our first test case (3.94), where we used exactly the same discretization points (volume cells), the monotonic growth of entropy is less drastic and significantly smaller. This is expected because the jumps in $u(t = 0, x)$ at $x = 2$ and $x = 3$ in the first test case (3.94) lead to greater changes in the discrete total variation – the arc length in x of $u(t, x)$ – than the rather small changes of the profiles of $u(t, x)$ for the ϕ^4 -models, cf. subsection 3.2.4.1. Also from a fluid-dynamic perspective, this is intuitively understandable because the smoothening of huge gradients is a substantial source of entropy and obviously an irreversible process, whereas only a small transport of a fluid is not a source of excessive but rather small entropy production, even though it is diffusion driven. Still, also for both ϕ^4 -cases the entropy increases during the FRG flow, which first signals an increasing number of coupling constants generated during the FRG flow, and second also renders the flows irreversible.

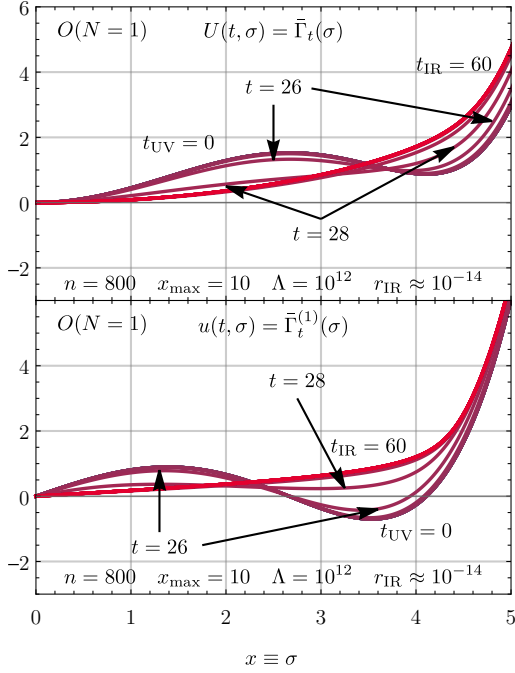
The second observation has severe consequences: Any FRG flow in a FRG Taylor expansion

⁶⁴Note that the plot range $x \in [0, 3]$ for the “positive mass”-case differs from the one ($x \in [0, 5]$) used in all other plots of FRG flows of $u(t, x)$ in this subsection. This is necessary to make the tiny changes during the FRG flow at least somewhat visible.

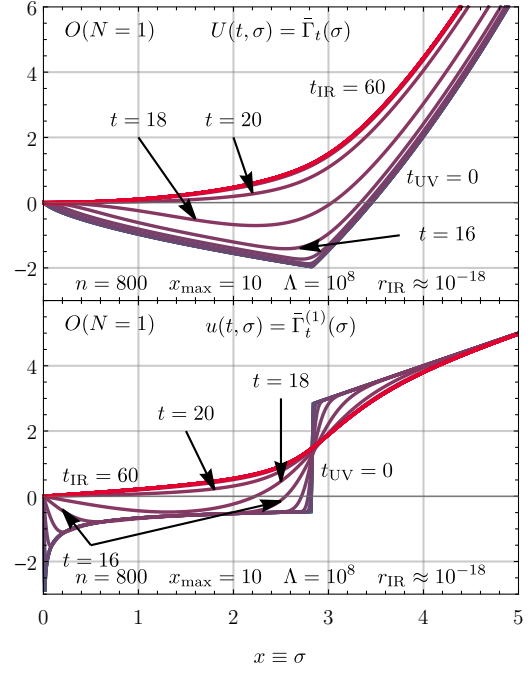
employs a finite set of coupled ODEs for the couplings (vertices). Since the system is finite, it seems to be theoretically possible integrate in either RG time-direction. In higher dimensions, one can formally integrate to larger scales when considering the perturbative beta functions of QCD, QED, *etc.* [66, 67, 581, 582], *cf.* subsection 2.3.2. However, this is in principle not compatible with the irreversibility of (F)RG flows as shown in our present work (as, *e.g.*, signaled by the rise of entropy) and may only be reliable within small subspaces of the theory space associated with a given theory. In fact, the computation of fundamental couplings at small scales (high energies) from effective couplings at large scales (low energies) is in general not possible, *cf.* Ref. [235]. We conclude that the increase of entropy, which we also observe during the FRG flow of our analytic initial conditions (3.101) reveals potential limitations of Taylor expansion of effective actions because most likely an extremely large (or even infinite) number of couplings is generated in the FRG flow and would be required to correctly describe the FRG flow ⁶⁵.

When considering an expansion in vertices (especially in higher/non-zero dimensions), it might be possible that higher-order couplings/vertices are strongly suppressed (especially when considering higher-dimensional QFTs), such that an expansion of the Wetterich equation (2.37) in vertices is applicable and meaningful in practice, see, *e.g.*, Refs. [105–108]. This should go hand in hand with only a small growth of an entropy for the exact FRG flow. Exactly this seems to be the case for our “positive mass” case (3.101), which shows almost no dynamics at all and yields the smallest increase in entropy of all our test cases. A reason, why here a rather small number of couplings might be sufficient to describe the entire FRG flow is that the potential is convex during the entire flow and has a single unique non-moving minimum. Hence, the UV regime of this model and the IR regime do not differ much and, as long as the quartic coupling is extremely small, also perturbation theory [538] leads to results which are consistent with the exact values for the lowest 1PI n -point functions [163].

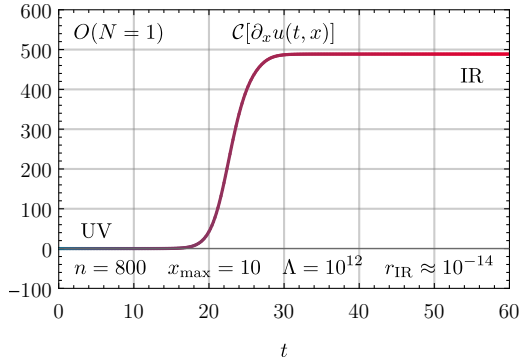
⁶⁵At this point, one might be tempted to apply our definition of the normalized (numerical) entropy directly to some $\partial_x u(t, x)$ that is reconstructed from the flow of the coefficients of a Taylor expansion of the potential to study the validity of the expansion. However, this is not possible, because the FRG Taylor expansion in general provides only an adequate local description of the potential, while our (numerical) entropy or the TV requires knowledge about the global shape of the potential or its derivatives.



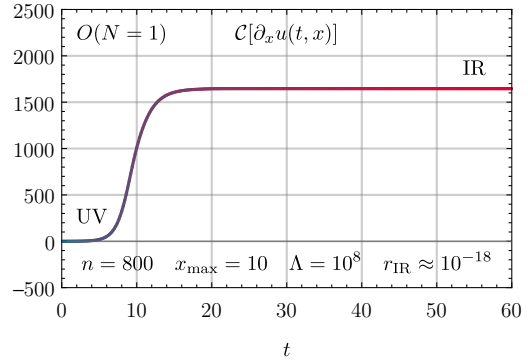
(a) FRG flow of the effective potential $U(t, \sigma)$ (upper panel) and its derivative $u(t, \sigma) = \partial_\sigma U(t, \sigma)$ (lower panel).



(a) FRG flow of the effective potential $U(t, \sigma)$ (upper panel) and its derivative $u(t, \sigma) = \partial_\sigma U(t, \sigma)$ (lower panel).



(b) FRG flow of the numerical entropy $\mathcal{C}[\partial_x u(t, x)]$



(b) FRG flow of the numerical entropy $\mathcal{C}[\partial_x u(t, x)]$

Figure 3.28.: FRG flow of the effective potential and its derivative on the top (a) and corresponding flow of the numerical entropy below (b) for the zero-dimensional $O(1)$ model with initial condition (3.103). Blue color is associated to the UV and red color to the IR. We used the exponential regulator Eq. (3.8) with UV scale $\Lambda = 10^{12}$. From Figs. 7 and 8 of Ref. [2].

Figure 3.29.: FRG flow of the effective potential and its derivative on the top (a) and corresponding flow of the numerical entropy below (b) for the zero-dimensional $O(1)$ model with initial condition (3.104). Blue color is associated to the UV and red color to the IR. We used the exponential regulator Eq. (3.8) with UV scale $\Lambda = 10^8$. From Figs. 9 and 10 of Ref. [2].

Test case III: ϕ^6 potential

We continue our discussion of $O(1)$ models with test case III (3.103), recall figure 3.20 for a visualization of this IC. In subsection 3.2.3.3, we came to the conclusion that there has to be a time interval during the FRG flow, where $u(t, x)$ exhibits highly non-local dynamics – preventing the applicability of a Taylor expansion, even though the expansion point is unique and does not move. The FRG flows of $u(t, x)$ for (3.103) with negative mass term is depicted in figure 3.28a.

At $t \approx 27$ the local minimum (the second non-trivial zero-crossing) vaporizes via the diffusion and merges with the local maximum. It is this dynamics which triggers the breakdown of the Taylor expansion manifesting as strongly oscillating and ultimately diverging couplings at $t \approx 27$.

Interestingly, also the (numerical) entropy function signals exactly the discussed non-local behavior at $t \approx 27$. At that point in time, when the local minimum vaporizes, we observe the strongest increase of entropy, see figure 3.28b. We also find that by absolute measures, the entropy production for the ϕ^6 -initial potential (3.103) is greater than the entropy production observed for both quartic initial conditions (3.101). Nevertheless, the entropy production for the non-analytic initial condition (3.94) is still greater than the one in the ϕ^6 -case. This can be understood from the relation of the numerical entropy to the TV, *i.e.*, the arc length of $u(t, x)$ which even formally diverges for Eq. (3.94) in the UV, keeping in mind that a comparison of absolute values of the numerical entropy should be considered with some care, *cf.* subsection 3.2.4.1.

We conclude this paragraph noting that that the (numerical) entropy might be a useful measure for deciding whether a system at a given RG scale/time is in a perturbative or non-perturbative regime. In other words, it is a tool to discuss whether the FRG flow is governed by strong (non-perturbative) dynamics or by weak (perturbative) dynamics. The CFD analogy to this situation would be the difference between a fluid evolving through an out-of-equilibrium state, before finally equilibrating or showing steady-flow behavior, in contrast to a fluid that is already close to its equilibrium state.

Test case IV: The $\sigma = 0$ boundary

We conclude our discussion of explicit numerical results for the $O(1)$ model with test case IV (3.104), recall figure 3.23 for a visualization of this IC. The test case (3.104) turns out to be a highly interesting almost pathological example in this context. The FRG flow of $u(t, x)$ is shown in figure 3.29a.

Of specific interest regarding the (numeric) entropy is of course the pole of $u(t = 0, x)$ at $x = 0$. Formally, the arc length of $u(t, x)$, which is directly related to our entropy function, diverges due to the pole at $x = 0$ for all $t > 0$. This divergence is of different nature than the divergence caused by integrating from $x = -\infty$ to $x = +\infty$ in Eq. (3.117). Whereas the latter can be cured by normalizing the entropy w.r.t. the entropy of $u(t = 0, x)$, the present divergence also occurs on the level of the “normalized” entropy function (3.118) similar to the other non-analytic jumps in the UV. The reason for the infinite entropy production while going from $t = 0$ to $t > 0$ is exactly that the total variation between $-x_{\max}$ and $+x_{\max}$ turns finite for

$u(t, x)$ during the flow because the potential turns convex and smooth. Moreover, symmetry restoration in the ground state sets in for $t \rightarrow \infty$. However, it is still normalized against the infinite total variation of $u(t = 0, x)$. Interestingly, this problem can be traced back to the initialization of the FRG flow equations at $t = 0$ with the classical UV action $\Gamma_{t=0}(\varphi) = \mathcal{S}(\varphi)$, which is actually not totally exact but rather an almost perfect approximation for sufficiently large Λ , see also our discussion in subsection 3.1.3.2. However both the inherent diffusive nature of the FRG flow equation and the employed finite-volume discretization render the pole at $\sigma = 0$ a huge but already finite jump captured in three volume cells on the level of the cell averages $\bar{u}_i(t)$ at $t = 0$. Therefore, we can use $u(t = 0, x)$ as our reference entropy for the normalization of Eq. (3.118) as it is numerically finite right from the beginning of the flow.

The explicit result for the FRG flow of our (numerical) entropy is shown in figure 3.29b. Irrespective of the subtleties of the preceding discussion, we find a rather large entropy production at exactly those times when the pole vanishes and the jumps at $x = \pm\sqrt{8}$ are smeared out via the diffusion.

Additionally, we find that the total entropy production is much larger for this test case than for the previous ones. Again, this is of course directly related to the huge gradients in the initial condition, which are tremendous sources of entropy via dissipation, directly analogous to the HE discussed in subsection 2.2.4.

In this subsection, we confronted our theoretical findings of subsection 3.2.4.1 with direct numerical computations using the KT scheme. We verified the behavior of the function $\mathcal{C}[\partial_x u(t, x)]$ from Eq. (3.118) by means of its discretized version in Eq. (3.122) as a valid numerical entropy measure in four test cases. Using the numerical entropy and the Wetterich equation in the form (3.105), we made several, at this point almost intuitive, connections between phenomena known in fluid- and thermodynamic processes and directly related processes and aspects of (F)RG flows. Most notable, the diffusive character of the flow equation (3.105) results directly in irreversible FRG flows. This also establishes a connection between steady-state/(thermal) equilibrium solutions and the UV and IR regime. Moreover, the application of the numerical entropy and total variation appears to be an attractive monitor for RG consistency and the origin of an “thermodynamic” time asymmetry.

3.2.4.3. Irreversibility of the RG flow, entropy, and the \mathcal{C} -theorem

This subsection summarizes and references the findings of Sec. V of Ref. [2]. The first paragraph of this subsection includes material for the Virasoro algebra and fixed-point solutions for the zero-dimensional $O(1)$ from the unpublished notes [8].

The (re)discoveries within this work unravel the connection between the (numerical) entropy and total variation, employed in applied mathematics, and the irreversibility inherent to (F)RG flows. Furthermore, they might even provide some connections to \mathcal{C} -/ \mathcal{A} -theorems within the framework of truncated FRG flow equations.

The original formulation of Zamolodchikov’s \mathcal{C} -theorem [575] states that for a two-dimensional field theory the following properties hold:

1. There exists a positive function

$$\mathcal{C}(\{g_i\}, t) \geq 0, \quad (3.125)$$

of all (possibly infinitely many) dimensionless couplings $\{g_i\}$ of the theory and RG time t , with the additional property

$$+ \frac{d}{dt} \mathcal{C}(\{g_i\}, t) \geq 0, \quad (3.126)$$

where the choice of sign in front of the derivative is convention.

2. The \mathcal{C} -function takes a fixed value at (critical) fixed points g_i^* of the theory:

$$\mathcal{C}(\{g_i^*\}, t) = c_i, \quad (3.127)$$

where the fixed value c_i can be identified with the central charge c (giving the \mathcal{C} -theorem its name) of a *Virasoro algebra* [622]

$$[L_m, L_n] = L_m L_n - L_n L_m = (m - n) L_{m+n} + \frac{c}{12} (m^3 - m) \delta_{m+n,0}, \quad (3.128)$$

with the generators L_n of the infinite conformal group. The central charge is different for different fixed points.

\mathcal{C} -theorems and their generalizations especially from two to four dimensions \mathcal{A} -theorems [584] are still under active research, see, e.g., Refs. [230, 575, 583–595]. \mathcal{A} -theorems get their name from anomaly coefficients which are proposed to take the role of the central charge in four dimensions. A general overview of this field is beyond the scope of the current work and we will focus in the following paragraphs on specific aspects relevant to this work and the FRG.

One other interesting aspect, related to the introduction of a numeric entropy for FRG flows, was pointed out by the referee of Ref. [2]: the present formulation based on the effective potential shares some similarities with the macroscopic description of systems in statistical mechanics. Instead of working with an infinite set of couplings (microstates in statistical mechanics) we switch to a description in terms of an effective potential (a macroscopic formulation in statistical mechanics). The inability (of a macroscopic observer) to track the dynamics of an infinite set of couplings (microstates in statistical mechanics) leads to a macroscopic entropy production/information loss and irreversible processes. An approach to formalize this notion in statistical mechanics was made by Ludwig Boltzmann [623] and later Josiah W. Gibbs [624] with the introduction of H -theorems, see, e.g., Chap. VI and XII of the textbook [625] for further details. Exploring this connection and possible relations between \mathcal{C} -/ \mathcal{A} - and H -theorems further could be a very interesting prospect for further research.

The \mathcal{C} -theorem of the zero-dimensional $O(1)$ model

In this paragraph we will argue that our numerical entropy (3.118) for the zero-dimensional $O(1)$ model is in fact a direct analogon to Zamolodchikov's \mathcal{C} -function in zero dimensions. Our numerical entropy (3.118) fulfills the first two defining properties (3.125) and (3.126) by construction. $\mathcal{C}[\partial_x u(t, x)]$ and its FV equivalent $\mathcal{C}[\{\bar{u}_j(t)\}]$ are also functions of all (infinitely many)

coupling constants which are dimensionless in $d = 0$ and encoded via $u(t, x)$ or equivalently in FV discretization in the set of volume averages $\{\bar{u}_j(t)\}$.

The only open question regarding the interpretation of our numerical entropy (3.118) as a \mathcal{C} -theorem is related to the question of fixed points and the central charge. *A priori* it is difficult to just imagine a meaningful zero-dimensional analog of central charge and conformal symmetry. *A posteriori* – after an extensive review of the literature of zero-dimensional QFTs and specifically zero-dimensional $O(N)$ models – there might be a meaningful analogon for the central charge, *i.e.*, the absence of such charges, in zero dimension. S. Nishigaki and T. Yoneya in Ref. [531] and P. Di Vecchia, M. Kato, and N. Ohta in Ref. [532] observe, that it is possible to derive DSEs for the zero-dimensional $O(N)$ model which can be recast into a Virasoro algebra. Following Ref. [531] we consider the partition function \mathcal{Z} as a function of all, infinitely many couplings $\{\lambda_j\}$ of a zero-dimensional $O(N)$ model

$$\mathcal{Z}(\{\lambda_j\}) \equiv \int d^N \phi \exp \left[- \sum_{j=1}^{\infty} \lambda_j (\vec{\phi}^2)^j \right]. \quad (3.129)$$

From the divergence theorem, we find for $n \in \mathbb{N}_0$

$$0 = \int d^N \phi \frac{\partial}{\partial \phi^i} \left(\phi^i (\vec{\phi}^2)^n \exp \left[- \sum_{j=1}^{\infty} \lambda_j (\vec{\phi}^2)^j \right] \right), \quad (3.130)$$

which when evaluated for $n = 0$ and $n \geq 1$ allow for the definition of

$$L_n \equiv - \left(\frac{N}{2} + n \right) \frac{\partial}{\partial \lambda_n} + \sum_{j=1}^{\infty} j \lambda_j \frac{\partial}{\partial \lambda_{j+n}} \quad (3.131)$$

such that

$$0 = L_n \mathcal{Z}(\{\lambda_j\}). \quad (3.132)$$

These operators L_n form an algebra

$$[L_m, L_n] = (m - n) \left[- \left(\frac{N}{2} + m \right) \frac{\partial}{\partial \lambda_{m+n}} + \sum_{i=1}^{\infty} i \lambda_i \frac{\partial}{\partial \lambda_{i+m+n}} \right] = (m - n) L_{m+n}, \quad (3.133)$$

which is a Virasoro algebra (3.128) with vanishing central charge c , *i.e.*, a so-called *Witt algebra* [626]. The DSEs (3.132) for $\mathcal{Z}(\{\lambda_j\})$ inform and establish the Witt algebra (3.133), *i.e.*, a Virasoro algebra with vanishing central charge, for the zero-dimensional $O(N)$ model. Following Zamolodchikov and assuming that the operators for the DSEs L_n from Eq. (3.131) are a meaningful zero-dimensional analogon to the generators L_n of the infinite conformal group in two dimensions, one would assume that Eq. (3.133) implies an absence of fixed-point solutions in zero-dimensional $O(N)$ models.

We will prove the latter for the zero-dimensional $O(1)$ model explicitly. We start from the FRG flow equation (3.105) by reformulating the equation at finite RG time in terms of the regulator itself

$$\partial_r u(r, x) = \frac{1}{2} \frac{d}{dx} \frac{1}{r + \partial_x u(r, x)}, \quad (3.134)$$

which in turn may be rewritten using the substitution $u(r, x) \equiv w(r, x) - r x$:

$$\partial_r w(r, x) - x = \frac{1}{2} \frac{d}{dx} \frac{1}{\partial_x w(r, x)}. \quad (3.135)$$

Hence, the global fixed-point equation (with $\partial_r w(r, x) = 0$) reads

$$-x = \frac{1}{2} \frac{d}{dx} \frac{1}{\partial_x w(r, x)}, \quad (3.136)$$

which can be integrated to

$$x_0^2 - x^2 = \frac{1}{\partial_x w(r, x)} - \frac{1}{\partial_{x_0} w(r, x_0)} \quad (3.137)$$

The potential $U(r, x)$ has to be \mathbb{Z}_2 -symmetric and convex for all r , if it is supposed to be an admissible global fixed-point solution. Thus, $\partial_x w(r, x)$ has to be positive for all $x_0 \neq 0$. As long as we choose $x_0 \in (0, \pm\infty)$, explicitly excluding $x_0 = 0$ and $x_0 = \pm\infty$, we can absorb both integration constants in a non-zero, positive integration constant, which we set w.l.o.g. to unity in the following, and derive

$$\partial_x w(r, x) = \frac{1}{1 - x^2}. \quad (3.138)$$

This equation can be integrated to obtain

$$w(r, x) = \begin{cases} \operatorname{artanh}(x), & |x| < 1, \\ \operatorname{arcoth}(x), & |x| > 1, \end{cases} \quad (3.139)$$

which however implies, that there is only a convex solution to the fixed-point equation for $x \in (-1, +1)$. In conclusion, a global convex fixed-point solution does not exist. We may also note that the partition function (3.2) for the potential $U(r, x) = W(r, x) - \frac{1}{2} r x^2$ with the integral of Eq. (3.139) does not converge since $\lim_{x \rightarrow \pm\infty} W(r, x) = 1 + \frac{1}{2} \ln(x^2) + \mathcal{O}(x^{-2})$.

In summary we note that our numerical entropy (3.118) for the zero-dimensional $O(1)$ model is a proper analogon to Zamolodchikov's \mathcal{C} -function. The following \mathcal{C} -theorem holds for the zero-dimensional $O(1)$ model: $\mathcal{C}[\partial_x u(t, x)]$ from Eq. (3.118) and its discrete FV equivalent $\mathcal{C}[\{\bar{u}_j(t)\}]$ from Eq. (3.122) are positive and monotonically increasing during FRG flow and there are no global, convex fixed-point solutions with the Witt algebra (3.133) for the DSEs (3.132) as analogon to the Virasoro algebra (3.128).

The challenges of a generalization to finite $N > 1$ in zero dimensions

To discuss the construction of a \mathcal{C} -function for $N > 1$ we recall the FRG flow Eq. (3.79)

$$\partial_t u + \frac{d}{dx} F[t, x, u] = \frac{d}{dx} Q[t, \partial_x u], \quad (3.140)$$

and its primitive form

$$\partial_t u + \frac{\partial F[t, x, u]}{\partial u} \partial_x u - \frac{\partial Q[t, \partial_x u]}{\partial(\partial_x u)} \partial_x^2 u(t, x) = -\partial_x F[t, x, u]. \quad (3.141)$$

Eq. (3.141) includes convective contributions on the l.h.s. but also an internal source term, stemming from the position-dependence of the advection flux, on the r.h.s. We discussed such a situation in the general CFD context in subsection 2.2.3 and implications for the TV in subsection 2.2.2: (internal) source terms lead to a loss of the TVNI property – they change and crucially increase TV/arc length during time evolution. Hence TV is no longer a valid candidate for a numerical entropy functional, which in presence of sources is notoriously difficult to construct in a CFD context, see, *e.g.*, Refs. [358–361] and references therein.

The explicit position-dependence of the advection flux prevented us from formulating a numerical entropy for the zero-dimensional $O(N)$ model for finite $N > 1$. The corresponding contribution to the entropy function (3.118) allows for $\frac{d}{dt} \mathcal{C}[\partial_x u(t, x)] < 0$ during FRG flow for certain initial conditions and N in the case of $N > 1$. For the zero-dimensional cases (3.101) and (3.103) discussed, we find $\frac{d}{dt} \mathcal{C}[\partial_x u(t, x)] < 0$ during the RG evolutions for $N \geq 8$. For the cases (3.94) and (3.104) with their σ^2 asymptotics for large σ the inequality $\frac{d}{dt} \mathcal{C}[\partial_x u(t, x)] \geq 0$ seems to hold for all N and t .

Reformulating the FRG flow Eq. (3.74) in the invariant $y \equiv \frac{1}{2} x^2$, *cf.* Eq. (3.73), does not solve the issue of internal source terms at finite N . While the advection flux in Eq. (3.73) loses its explicit position-dependence the diffusion flux gains both a dependence on $u(t, y)$ and y which does not improve our situation at finite N . In the infinite- N limit however diffusive contributions vanish after rescaling with $N - 1$ and a formulation in y with a y -independent advection flux allows for an identification of the TV as an entropy functional. We will discuss this in subsection 3.2.5.4.

Comments on a generalization to (higher-dimensional) $O(N)$ models

A direct generalization of our findings regarding numerical entropy measures for the FRG flow from zero to non-zero dimensions is hindered by two new conceptual issues:

1. The LPA as part of the leading-order of a DE is in general only a truncation in $d > 0$, *cf.* subsection 2.1.4.2. This makes very general statements for the QFT under consideration *a priori* impossible when just discussing the FRG flow of the potential. That being said the established concept of numerical entropy might still be of some use in higher-dimensional $O(1)$ models.
2. In contrast to the zero-dimensional model, the couplings in $d > 0$ can have non-zero energy dimensions. Thus, our numerical entropy (3.118) cannot adequately describe the second property of the \mathcal{C} -theorem (3.127) – namely capturing the properties of fixed points, which are defined via the zeroes of the beta functions of all dimensionless couplings and additionally a constant \mathcal{C} -/ \mathcal{A} -function. To resolve the fixed-point structure, one has to consider the flow equation for rescaled quantities which gains additional internal source terms due to the rescaling, *cf.* Eq. (37) of Ref. [2]. Such source terms make TV-like entropy measures unviable.

Further details can be found in Sec. V of Ref. [2].

3.2.5. The $O(N)$ model in the large- N limit

This subsection is based on Ref. [3]. The plots of Ref. [3] and the underlying numerical data were produced by myself and numerically cross-checked by A. Koenigstein.

The plots, numerical results, and accompanying symbolic computations are included in the digital auxiliary file [366]. The single thread wall time on an Intel® Core™ i7-8750H processor for the numeric results of Ref. [3] is around three days.

The introduction of this subsection follows Sec. I of Ref. [3].

After focusing on the limiting case of $O(N = 1)$ models in the previous subsection 3.2.4, we now want to focus on the other extreme: large and even infinite N . In this subsection we set out to study zero-dimensional $O(N)$ models at large and infinite N with three computational approaches: direct computation of the underlying integrals (3.56), $\frac{1}{N}$ -expansion, and the FRG in our newly developed CFD perspective.

The $\frac{1}{N}$ -expansion is an established “non-perturbative” approach to compute observables in QFT. Depending on the context, author, and explicit implementation it is also referred to as large- N expansion, the ’t Hooft limit, or just mean-field approximation. This method relies on a systematic expansion of characteristic quantities of the theory, like expectation values, correlation functions, and observables, in powers of $\frac{1}{N}$. Here, N is the number of different kinds of interacting degrees of freedom of the theory (particle or field types, spins, molecules, color charges *etc.*), which is considered to be large in this context ($1 \lll N$). Hence, extensive quantities need to be rescaled by appropriate powers of N in advance to allow for a meaningful $\frac{1}{N}$ -expansion. Although involving an expansion in a small, dimensionless parameter, namely $\frac{1}{N}$, the method is considered to be non-perturbative, because it is also applicable to systems with strong interactions, where an expansion in couplings is doomed to fail. In consequence, various great successes and precise predictions trace back to this method, see, *e.g.*, Refs. [163, 169, 247, 627–632] or the review [633] – in some cases maintaining predictive power even for systems, where N is surprisingly small. However, the large- N expansion and especially retaining only its zeroth-order contribution – the infinite- N limit – also comes with some limitations and certain fundamental characteristics of a (quantum) field theoretical or statistical models, like the convexity of the $\frac{1}{N}$ -rescaled effective action may be altered.

In order to elucidate some of these aspects and interesting consequences, we study the large- N expansion and the infinite- N limit within two totally different setups. On the one hand, we perform a conventional saddle-point expansion of the functional integral (partition function) by assuming that N is large (or even infinite) [163, 634]. On the other hand, we study the same problem within the FRG approach, also considering large and/or (in)finite N , see, *e.g.*, Refs. [162, 243, 247, 566, 611, 632, 635–639] for material regarding the infinite- N limit in the FRG framework.

To keep our discussion as simple as possible we limit our discussion to the sober and exactly solvable zero-dimensional $O(N)$ model – the gift that keeps on giving. A lot of aspects of the large-/infinite- N limit have been discussed already within this setup, *cf.* Refs. [163, 529–534] – especially for quartic actions (potentials).

Within this work we use the zero-dimensional $O(N)$ model at large N to highlight the following aspects:

1. Considering a rather simple – but non-analytic – one-parameter family of classical actions (potentials) as a new purpose-built test case, we demonstrate that there is a narrow line between a straightforward applicability of the large- N saddle-point expansion and a total failure of this method. In our zero-dimensional pedagogical and tailor made example, this point of failure is easy to detect. However, it may serve as a warning for applications of the large- N limit and the corresponding saddle-point expansion of the functional integral in higher-dimensional scenarios, where it is not necessarily easy to judge, if all requirements for a meaningful $\frac{1}{N}$ -expansion are fulfilled. Note that in our large- N applications of chapters 4 and 5 we use this limit – the mean-field – approximation as a technical simplification to study fermionic fluctuations. We do not assess or discuss whether or when such a limit is justified when describing physical systems, since we are not interested in describing physical systems in this limit.
2. Switching perspectives to the FRG formalism, we make use of the fact that the corresponding FRG flow equation is exact for the zero-dimensional $O(N)$ model. Being “exact” in this context means, that truncating the flow equation is not necessary (for finite and infinite N), since the involved PDEs, can be solved numerically, with our at this point firmly established methods of subsections 3.2.2 and 3.2.3. Within our fluid-dynamic framework, we show that the FRG flow in the infinite- N limit is purely advection driven, while diffusive contributions enter only at finite N . This also generalizes to higher space-time dimensions.

As a direct consequence, depending on the classical action (potential) – UV IC, the infinite- N FRG flows tend to form or sustain non-analyticities of different kinds, *e.g.*, shock and rarefaction waves or jump discontinuities, *cf.* subsections 2.2.3 and 2.2.6 and Refs. [162, 247].

We find that for our toy model with non-analytic classical action, shock and rarefaction waves are present and the problem encountered at the UV initial scale involves two Riemann problems. But we do not stop by turning the calculation of ordinary N -dimensional integrals with spherical symmetry for expectation values into a fluid-dynamical problem. We also demonstrate that the (non-)applicability of the large- N saddle-point expansion translates into the (collision) freezing of interacting shock waves in these fluid-dynamic FRG flows.

3. Still working in the FRG fluid-dynamic framework, we also demonstrate that the inclusion of the radial σ -mode, thus switching from infinite- N to arbitrary but finite N , totally changes the physics of the system. In the infinite- N limit, we explicitly show by numerical calculations that convexity and smoothness are not necessarily realized for $\frac{1}{N}$ -rescaled IR potentials, which effectively violates the CMWH theorem [550–552], *i.e.*, a special zero-dimensional version of the theorem [1, 536]. Interestingly, as soon as N is finite, the highly non-linear diffusive contribution of the radial σ -mode unavoidably restores convexity and smoothness of the $\frac{1}{N}$ -rescaled IR potentials. Hence, the large- N expansion

with finite N and the infinite- N limit (only retaining the zeroth-order of the $\frac{1}{N}$ -expansion) may lead to two fundamentally different results. We will encounter a qualitatively similar situation in subsection 4.5.3.3 for the GNY model.

4. As a last aspect, we also highlight further direct consequences of our fluid-dynamic interpretation of FRG flows. Utilizing the method of characteristics [317, 323, 367] and the Rankine-Hugoniot condition [368, 369], see also subsection 2.2.3.1, we directly track the locations of shock and rarefaction waves in the field space derivative of the scale-dependent potential during the RG flows. Applications of the aforementioned methods in (F)RG studies can be found in, e.g., Refs. [247, 565, 566, 635, 640].

Interacting shock and rarefaction waves, but also diffusive processes – as discussed at length in the previous subsection 3.2.4 – go hand in hand with the rise of entropy in fluid-dynamic problems, cf. subsection 2.2.3. Using the CFD framework and the TVNI property, we are able to provide an entropy function in the $N \rightarrow \infty$ limit.

At this point, we remark that our research in this subsection was partially influenced by the excellent publication [247] on the infinite- N limit of the FRG flow equations of the $O(N)$ model in three Euclidean space-time dimensions and the interpretation of these FRG flows as advection equations, which can develop different kinds of discontinuities [247]. The application of the method of characteristics in the large- N limit of FRG flow equation predates the explicit identification and detailed understanding of infinite- N FRG flow equations as advection equations and goes back (to the best of our knowledge) to Refs. [566, 635]. The authors of Ref. [247], E. Grossi and N. Wink, were involved in the first two parts of our series of publications [1, 2] and also worked together with F. Ihssen and J. M. Pawłowski on calculations in the QM model in the infinite- N limit [162, 210, 283], which was also based on a fluid dynamic interpretation of FRG flows.

In addition, we thank the referee of Ref. [3] for pointing out that there are recent works, which also deal with the shortcomings of the standard infinite- N limit in the context of FRG and link this to non-analytic structures in the fixed-point potential [243, 639]. An interesting future prospect is certainly to draw a connection between our works in the fluid-dynamic framework and these results.

The remainder of this subsection is structured as follows. In subsection 3.2.5.1 we discuss the zero-dimensional $O(N)$ model at large N and in the paragraph [An instructive toy model](#) we introduce the test case/action we will consider thereafter. In subsection 3.2.5.2 we discuss the $\frac{1}{N}$ -saddle-point-expansion for this test case and in subsection 3.2.5.3 we discuss the corresponding FRG flows.

3.2.5.1. The zero-dimensional $O(N)$ model at large N

This subsection follows Sec. II of Ref. [3].

Free theory

For later reference, we recapitulate some results for the massive non-interacting free theory. The action of the corresponding $O(N)$ model is given by

$$U_{\text{free}}(\rho) \equiv m^2 \rho, \quad (3.142)$$

with the positive non-zero “mass” m . The expectation values (3.56) can be computed analytically in terms of Gamma functions resulting in

$$\langle (\vec{\phi}^2)^0 \rangle = \langle 1 \rangle = 1, \quad (3.143)$$

$$\langle (\vec{\phi}^2)^n \rangle = \frac{N + 2n - 2}{m^2} \langle (\vec{\phi}^2)^{n-1} \rangle, \quad \text{for } n > 1. \quad (3.144)$$

For the 1PI correlation functions this result implies

$$\Gamma^{(2)} = m^2, \quad \text{and} \quad \forall n \neq 2 \quad \Gamma^{(n)} = 0, \quad (3.145)$$

where we used the short-hand notation $\Gamma^{(n)} \equiv \Gamma_{\varphi_i \dots \varphi_i}^{(n)}$ from section 3.2. In their interpretation as interaction vertices these results for $\Gamma^{(n)}$ are rather intuitive for a “massive non-interacting” theory, which has only a non-vanishing 1PI two-point function, because the underlying probability distribution is Gaussian.

Reformulation for large- N

For computations at large N and in the limit $N \rightarrow \infty$ the rescaling

$$\rho \mapsto y = \frac{1}{N} \rho, \quad U(\rho) \mapsto V(y) = \frac{1}{N} U(\rho), \quad (3.146)$$

has proven particularly useful, see, e.g., Refs. [163, 247], because both y and $V(y)$ are of $\mathcal{O}(N^0)$. The expression (3.56) for $\langle (\vec{\phi}^2)^n \rangle$ reads

$$\langle (\vec{\phi}^2)^n \rangle = \frac{2^n N^n \int_0^\infty dy y^{\frac{(N-2)}{2}} y^n e^{-NV(y)}}{\int_0^\infty dy y^{\frac{(N-2)}{2}} e^{-NV(y)}} = \frac{2^n N^n \int_0^\infty dy y^{n-1} e^{-N[V(y) - \frac{1}{2} \ln(y)]}}{\int_0^\infty dy y^{-1} e^{-N[V(y) - \frac{1}{2} \ln(y)]}}, \quad (3.147)$$

in terms of y and $V(y)$ and we note $\langle (\vec{\phi}^2)^n \rangle = \mathcal{O}(N^n)$. For certain potentials $V(y)$ the involved integrals

$$I_n^N[V] \equiv \int_0^\infty dy y^{n-1} e^{-N[V(y) - \frac{1}{2} \ln(y)]} \quad (3.148)$$

can be solved in terms of known functions, see, e.g., Refs. [1, 163] as well as subsection 3.2.5.1, and/or they can be computed in the limit $N \rightarrow \infty$ by means of a saddle-point expansion, see subsection 3.2.5.2 and App. D.1.3.2.

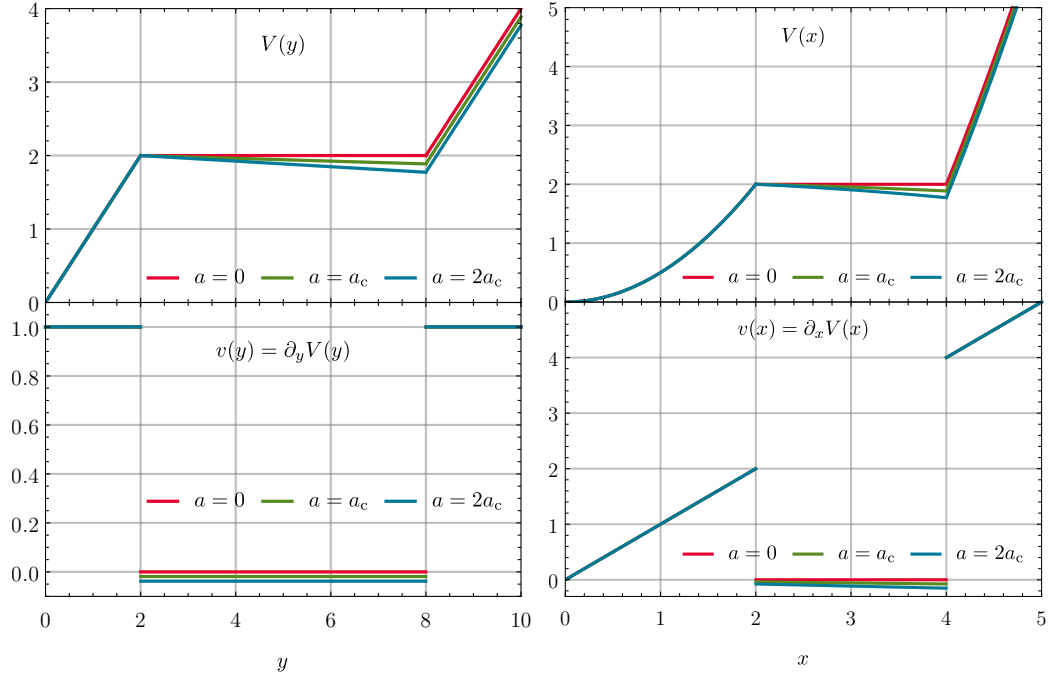


Figure 3.30.: The potential $V(y)$ from Eq. (3.149) in the upper, left panel (a) and its y -derivative $v(y) = \partial_y V(y)$ from Eq. (3.150) in the lower, left panel (b) as well as the corresponding potential $V(x)$ from Eq. (3.177) in the upper, right panel (c) and its x -derivative $v(x) = \partial_x V(x)$ from Eq. (3.178) in the lower, right panel (d) for selected values of the parameter a – with $a_c \simeq 0.018951$ from Eq. (3.151). From Figs. 1 and 3 of Ref. [3].

An instructive toy model

In this paragraph we present an explicit $O(N)$ model, respectively its $\frac{1}{N}$ -rescaled self-interaction potential $V(y)$, which turns out to be a rather instructive toy model when studied at large and infinite N . We consider a family of piecewise linear potentials

$$V(y) = \begin{cases} y & \text{for } 0 \leq y \leq 2, \\ -ay + 2(a+1) & \text{for } 2 < y \leq 8, \\ y - 6(a+1) & \text{for } y > 8, \end{cases} \quad (3.149)$$

with a parameter $a \geq 0$. The first derivative of $V(y)$ presents as a simple piecewise constant function in the $\frac{1}{N}$ -rescaled invariant y

$$v(y) = \partial_y V(y) = \begin{cases} 1 & \text{for } 0 \leq y \leq 2, \\ -a & \text{for } 2 < y \leq 8, \\ 1 & \text{for } y > 8, \end{cases} \quad (3.150)$$

which is very similar to the IC (32) studied in Ref. [247]. The potential (3.149) and its y -derivative (3.150) are plotted in figures 3.30a and 3.30b for illustrative purposes. In fig-

ures 3.30c and 3.30d, we also plot the potential and its derivative as functions of the rescaled field x , where $\frac{1}{2}x^2 \equiv y \equiv \frac{1}{2N}\vec{\phi}^2$, which might be more familiar after the preceding discussions of section 3.2. We recognize such an initial value problem with piecewise constant ICs involving a set of contact discontinuities as a series of Riemann problem in the context of conservation equations and CFD, *cf.* section 2.2. When considering Eq. (3.150) as the IC of a conservation equation in y , *cf.* subsection 3.2.5.4, we are faced with two Riemann problems (one at $y = 2$ and one at $y = 8$) at the UV initial scale.

This model has several interesting properties:

1. The expectation values of Eq. (3.147) can be evaluated in terms of known functions. In the limit $N \rightarrow \infty$ the 1PI correlation functions can be computed analytically for all $a \geq 0$. We will discover within this subsection that there are two distinct parameter regimes, which are particularly interesting when studying this problem within the saddle-point and FRG frameworks.
2. For certain parameters a , which are smaller than some critical value a_c , the 1PI correlation functions $\Gamma^{(n)}$ – the underlying expectation values (3.147) – can be computed by means of a saddle-point expansion. For $a \geq a_c$ the saddle-point expansion is not applicable. This is discussed in detail in the following subsection 3.2.5.2.
3. The model under consideration presents initially as two Riemann problems in the FRG (fluid-dynamic) framework. The distinct parameter regimes, $0 \leq a \leq a_c$ and $a > a_c$, present with qualitatively different FRG flows. The interpretation involving Riemann problems, its numerical solution, and its consequences are discussed in detail in subsection 3.2.5.3. At this point we also want to remind the reader of the methodological introduction of subsections 2.2.3 and 2.2.6 which will be of great relevance for this subsection – the discussion of FRG flows at large and infinite N .

For now, we turn to the computation of the correlation functions of the model under consideration. Solutions in terms of known functions for the necessary integrals (3.148) for the potential (3.149) are presented in App. D.1.3.1. In the limit $N \rightarrow \infty$ the direct computations of App. D.1.3.1 revealed two distinct regimes in parameter space separated by

$$a_c = \frac{1}{4} - \frac{1}{3} \ln(2) \simeq 0.018951. \quad (3.151)$$

For the infinite- N limit of the expectation values (3.56) we find,

$$\lim_{N \rightarrow \infty} \frac{1}{N^n} \langle (\vec{\phi}^2)^n \rangle = \begin{cases} 1, & \text{for } 0 \leq a \leq a_c, \\ 16^n, & \text{for } a > a_c, \end{cases} \quad (3.152)$$

For the corresponding 1PI correlation functions this implies in the limit $N \rightarrow \infty$

$$\Gamma^{(2)} = \begin{cases} 1, & \text{for } 0 \leq a \leq a_c, \\ \frac{1}{16}, & \text{for } a > a_c, \end{cases} \quad (3.153)$$

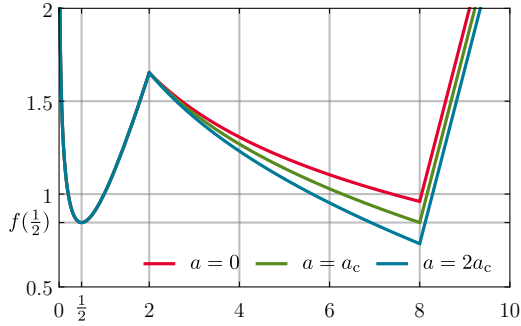


Figure 3.31.: Plot of $f(y) = V(y) - \frac{1}{2} \ln(y)$ for the potential (3.149) for selected values of the parameter a – with $a_c \simeq 0.018951$ from Eq. (3.151). The local minima of $f(y)$ are located at $y_0 = \frac{1}{2}$ and $y_{0,2} = 8$, where y_0 ($y_{0,2}$) presents as the unique global minimum for $0 \leq a < a_c$ ($a > a_c$). At $a = a_c$ both minima coincide and present both as global minima of $f(y)$. The non-analyticity of $f(y)$ in $y_{0,2} = 8$ inherited from the piecewise definition of $V(y)$ is clearly visible in the plot. From Fig. 2 of Ref. [3].

Table 3.6.: Reference values for selected N and a of $\Gamma^{(2)} = N(\langle \vec{\phi}^2 \rangle)^{-1}$ computed with the expressions (D.14) and (D.15) as well as their large N asymptotics. The exact analytical results are in some cases rather lengthy and therefore we present in those cases only six decimal digits for readability. From Tab. I of Ref. [3].

N	$a = 0$	$a = a_c$	$a = 2a_c$
2	0.356907	0.327332	0.299162
32	0.962306	0.475285	0.087158
∞	1	1	0.0625

as well as for all $a \geq 0$

$$\forall n \neq 2 \quad \Gamma^{(n)} = 0. \quad (3.154)$$

Thus, in the limit $N \rightarrow \infty$ and in terms of 1PI vertices the current model under consideration presents as a massive non-interacting theory for all $a \geq 0$, cf. Eq. (3.145). The situation for $0 \leq a < a_c$ and the corresponding “mass” as well as the origin of the critical value a_c can be understood intuitively in the context of the saddle-point expansion discussed in subsection 3.2.5.2. The situations for $a = a_c$ and $a > a_c$ are more involved and not accessible with a saddle-point expansion. However, a study in the FRG framework is possible and rather instructive as we will demonstrate in subsection 3.2.5.3. In terms of correlation functions the theory undergoes a first-order phase transition at a_c when varying the external parameter a , cf. Sec. III.C of Ref. [247] and references therein.

For finite N higher-order n -point functions do not vanish and the theory is of “interactive type”, but in the scope of this subsection we nevertheless mainly focus on $\Gamma^{(2)}$ – especially when it comes to numerical computations. In table 3.6 we summarize several (exact) reference values for $\Gamma^{(2)}$ for later use.

3.2.5.2. The saddle-point expansion at large N

This subsection follows Sec. III of Ref. [3].

In this subsection we will analyze the instructive toy model of subsection 3.2.5.1 within a saddle-point approximation for large N . In App. D.1.3.2 we discuss the large- N saddle-point expansion of integrals like (3.148) concluding in the asymptotic series (D.24) for $\langle(\vec{\phi}^2)^n\rangle$. To apply the series (D.24) to the interaction potential (3.149) of the model under consideration, we first have to compute the global minimum y_0 of the exponents of the integrands in Eq. (3.147),

$$f(y) = V(y) - \frac{1}{2} \ln(y), \quad (3.155)$$

and check for analyticity of $f(y)$ and $g(y) = y^{n-1}$ around y_0 . The function $f(y)$ for the model under consideration is plotted in figure 3.31 for different parameters a .

There is always a minimum on the first section ($0 \leq y \leq 2$) of the piecewise linear potential

$$0 \stackrel{!}{=} \partial_y f(y)|_{y=y_0} = \left[\partial_y V(y) - \frac{1}{2y} \right]_{y=y_0} = 1 - \frac{1}{2y_0}. \quad (3.156)$$

It follows that

$$y_0 = \frac{1}{2}, \quad V(y_0) = \frac{1}{2}, \quad f(y_0) = \frac{1}{2} \left[1 - \ln\left(\frac{1}{2}\right) \right], \quad (3.157)$$

and for the second and third derivatives, we find

$$\partial_y^2 V(y)|_{y=y_0} = 0, \quad \partial_y^2 f(y)|_{y=y_0} = 2, \quad (3.158)$$

$$\partial_y^3 V(y)|_{y=y_0} = 0, \quad \partial_y^3 f(y)|_{y=y_0} = -8. \quad (3.159)$$

We note that $V(y)$ and therefore also $f(y)$ are smooth, thus C^∞ , and analytic around $y_0 = \frac{1}{2}$. Also $g(y) = y^{n-1}$ is analytic and C^∞ around $y_0 = \frac{1}{2}$. We can therefore use the asymptotic series (D.24) to compute the non-vanishing expectation values,

$$\frac{1}{N} \langle \vec{\phi}^2 \rangle = 1, \quad (3.160a)$$

$$\frac{1}{N^2} \langle (\vec{\phi}^2)^2 \rangle = 1 + \frac{2}{N}, \quad (3.160b)$$

$$\frac{1}{N^3} \langle (\vec{\phi}^2)^3 \rangle = 1 + \frac{6}{N} + \frac{8}{N^2}, \quad (3.160c)$$

⋮

and the corresponding 1PI correlation functions

$$\Gamma^{(2)} = 1, \quad \forall n \neq 2 \quad \Gamma^{(n)} = 0. \quad (3.161)$$

Both are exact results (without taking any limits) and we find that $\frac{1}{N^n} \langle (\vec{\phi}^2)^n \rangle = 1 + \mathcal{O}(N^{-1})$, while the maximal correction to 1 is always of $\mathcal{O}(N^{-(n-1)})$. Considering the corresponding $\Gamma^{(2n)}$ we recover the 1PI correlation functions of a free massive theory, see Eq. (3.145) with $m^2 = 1$, which – as an exact and N -independent result – also holds trivially in leading order in the limit $N \rightarrow \infty$. This is a rather unsurprising result since the $\frac{1}{N}$ -rescaled potential $V(y)$

manifests as a linear potential with slope 1 – corresponding to a non-interacting theory with $m^2 = 1$ – for $0 \leq y \leq 2$.

The previous large- N saddle-point approximation is however limited to potentials (3.149) with $0 \leq a < a_c$. For $a \geq a_c$ the function $f(y) = V(y) - \frac{1}{2} \ln(y)$ develops a global minimum at $y_{0,2} = 8$, which becomes the unique global minimum for $a > a_c$ while at $a = a_c$ both y_0 and $y_{0,2}$ are global minima, see figure 3.31. For $a \geq a_c$ the saddle-point expansion breaks down since at $a = a_c$ the function $f(y)$ has no unique minimum and for $a > a_c$ the function $f(y)$ is non-analytic in its global minimum (the “expansion point”) $y_{0,2} = 8$. The value of a_c and the related qualitatively distinct scenarios were established in subsection 3.2.5.1. In the corresponding exact computations of App. D.1.3.1 the threshold $a_c = \frac{1}{4} - \frac{1}{3} \ln(2) \simeq 0.018951$ appears when considering the limit $N \rightarrow \infty$ of rather complicated symbolic expressions. On the other hand, within the framework of the saddle-point expansion the value of a_c can be derived and understood in a very instructive way as the breakdown point of the saddle-point expansion,

$$f(y_0 = \frac{1}{2}) \stackrel{!}{=} f(y_{0,2} = 8) \quad (3.162a)$$

$$\frac{1}{2} - \frac{1}{2} \ln\left(\frac{1}{2}\right) = 8 - 6(a_c + 1) - \frac{1}{2} \ln(8), \quad (3.162b)$$

which is solved again by

$$a_c = \frac{1}{4} - \frac{1}{3} \ln(2) \simeq 0.018951. \quad (3.163)$$

For $a < a_c$ the model presents as a free massive theory in its saddle-point and the analytical results in the limit $N \rightarrow \infty$ of subsection 3.2.5.1 make perfect sense.

In this subsection we are not interested in a quantitative review of the large- N saddle-point expansion beyond the limit $N \rightarrow \infty$. For such a discussion in the context of zero-dimensional $O(N)$ models we refer the interested reader to the excellent and pedagogical Ref. [163].

At and beyond the critical value a_c – at and beyond the corresponding first-order phase transition – the saddle-point expansion is no longer applicable and alternative methods are required for the computation of correlation functions. Apart from the direct symbolic computations of subsection 3.2.5.1 the FRG has proven to be a potent tool for computations in zero dimensions at finite N , cf. subsections 3.2.3 and 3.2.4, and as we will demonstrate in subsection 3.2.5.3 it loses none of its potency in the infinite- N limit when employing proper numerical schemes, like the KT and KNP scheme.

3.2.5.3. FRG flow equations at large and infinite N

This subsection follows Sec. IV and App. E of Ref. [3].

We proceed with our FRG studies at large and infinite N using our established CFD methods and concepts.

The $\frac{1}{N}$ -rescaled FRG flow equation

To facilitate the studies at large N and in the limit $N \rightarrow \infty$, we have to rescale the flow Eqs. (3.73) and (3.74) according to subsection 3.2.5.1.

To this end, we make use of the rescalings (3.146) of extensive quantities,

$$\sigma \mapsto x = \frac{1}{\sqrt{N}} \sigma, \quad U(t, \sigma) \mapsto V(t, x) = \frac{1}{N} U(t, \sigma). \quad (3.164)$$

and additionally introduce $v(t, x) \equiv \partial_x V(t, x)$,

$$u(t, \sigma) \mapsto v(t, x) = \frac{1}{\sqrt{N}} u(t, \sigma). \quad (3.165)$$

On the level of the FRG flow equation, this results in a slight modification of the prefactors of the fluxes (3.80) and (3.81). The rescaled flow equation in x follows as

$$\partial_t v(t, x) = \frac{d}{dx} \left[\frac{N-1}{N} \frac{\frac{1}{2} \partial_t r(t)}{r(t) + \frac{1}{x} v(t, x)} + \frac{1}{N} \frac{\frac{1}{2} \partial_t r(t)}{r(t) + \partial_x v(t, x)} \right], \quad (3.166)$$

which makes it easily possible to take the infinite- N limit and to compare FRG flows for infinite and finite values of N . Already at this point we find that increasing N makes the problem more and more advection driven. In the limit $N \rightarrow \infty$ the diffusion flux vanishes completely and we are left over with the infinite- N flow equation,

$$\partial_t v(t, x) = \frac{d}{dx} \left[\frac{\frac{1}{2} \partial_t r(t)}{r(t) + \frac{1}{x} v(t, x)} \right]. \quad (3.167)$$

This PDE presents as an advective hyperbolic conservation law, cf. subsection 2.2.3, and is very similar to its higher-dimensional counterpart [247, 566, 635].

Of course, we can also formulate the FRG flow equation (3.166) as a fluid-dynamic problem in the $\frac{1}{N}$ -rescaled invariant $y = \frac{1}{2} x^2$,

$$\partial_t v(t, y) = \frac{d}{dy} \left[\frac{N-1}{N} \frac{\frac{1}{2} \partial_t r(t)}{r(t) + v(t, y)} + \frac{1}{N} \frac{\frac{1}{2} \partial_t r(t)}{r(t) + v(t, y) + 2y \partial_y v(t, y)} \right], \quad (3.168)$$

as is done in Refs. [162, 247]. Overall the structure of the equation keeps its conservative form in terms of an advection-diffusion equation⁶⁶.

The main difference is that the advective contribution lost its unpleasant position-dependence, which is now found in the second (formerly purely diffusive) contribution. The diffusive term has changed drastically and can no longer be exclusively interpreted as a non-linear diffusion flux, cf. the related discussion in subsection 2.2.4.

In subsections 3.2.2.3 and 3.2.2.4 we argued at length, that, due to several reasons, we currently believe that a formulation in x instead of y is favorable as soon as we allow for diffusive contributions to the FRG flow – hence at finite N . In subsection 3.2.2.4 we discuss

⁶⁶This generalizes in x and y to arbitrary dimensions and also to the fixed-point form of the FRG flow equation [1, 2, 4]. Regarding fixed points in the infinite- N limit for the $O(N)$ model in the FRG context we refer the interested reader to Refs. [244, 637] for a detailed discussion of the situation in $d = 3$ dimensions.

the difficulties arising when attempting to formulate the inevitable spatial boundary condition at $y = 0$, when using the (rescaled) invariant y . An oversimplified argument is that there is no physical meaning of negative values of y , which makes a correct formulation of a boundary condition, that correctly captures possible influx due to diffusion, extremely challenging – if not impossible. In a formulation in x , this is not a problem at all, since negative x formally exist and antisymmetric boundary conditions can be used for $u(t, x)$ at $x = 0$. Additionally, it is understandable that a sober split of advection and diffusion fluxes is no longer possible in y , by simply executing the total y -derivative on the r.h.s. of Eq. (3.168) for the last term. Hence, as long as N is finite, one has to live with the challenging x -dependence in the advection flux of the PDE (3.166), which can however be handled by suitable discretizations, as demonstrated at length in subsections 3.2.2 and 3.2.3.

However, in the infinite- N limit the second term of the PDE (3.168) vanishes and the problem again reduces to a hyperbolic non-linear advection equation – without any explicit position-dependencies,

$$\partial_t v(t, y) = \frac{d}{dy} \left[\frac{\frac{1}{2} \partial_t r(t)}{r(t) + v(t, y)} \right] \equiv - \frac{d}{dy} G[t, v] = -(\partial_v G[t, v]) \partial_y v(t, y). \quad (3.169)$$

Because the newly defined advection flux $\partial_v G[t, v]$ has manifestly negative sign – cf. Eq. (3.170), there can not be any influx at $y = 0$ into the spatial domain $y \in [0, \infty)$ of the problem resolving the conceptual issues with the $y = 0$ boundary and allowing practical computations in the rescaled invariant y . Note that the computations of Refs. [162, 210, 247] use this zero influx argument for their computations with discontinuous Galerkin methods in the invariant q/y .

The KNP scheme can be used to solve the flow equation in the invariant y in the infinite N -limit. For the problematic left boundary we consider the primitive form in Eq. (3.169) using

$$\frac{\partial G}{\partial v} = - \frac{1}{2} \frac{\Lambda e^{-t}}{(\Lambda e^{-t} + v)^2}. \quad (3.170)$$

For all $y \in \mathbb{R}^+$ and $t \in \mathbb{R}^+$ $\partial_v G[t, v] < 0$, holds for all well-defined initial conditions, which realize $r(t) + v(t, y) > 0$ at $t = 0$.

Eq. (3.170) is manifest negative and finite for all $y \in \mathbb{R}^+$ and $t \in \mathbb{R}^+$ for all valid initial conditions/UV initial scales realizing $\Lambda e^{-t} + v > 0$ in the UV. The latter inequality is guaranteed dynamically at $t > 0$ by the flow equation as long as it is realized in the UV at the initial scale $t = 0$, cf. Eq. (3.100) and the related discussion of RG consistency subsection 3.2.3.1. This however implies in Eq. (2.101b) a vanishing right-sided local speed $a_{j+\frac{1}{2}}^+ = 0$. Physically this means that the fluid is only propagated to the left which simplifies the expression (2.109) for the numerical flux of the KNP scheme immensely

$$H_{j+\frac{1}{2}}^{\text{KNP}} \Big|_{a_{j+\frac{1}{2}}^+ = 0} = G[t, v_{j+\frac{1}{2}}^+] \quad (3.171)$$

resulting in the numerical upwind advection flux for the KNP scheme

$$\partial_t \bar{v}_j = \frac{1}{\Delta y} \left(G[t, v_{j-\frac{1}{2}}^+] - G[t, v_{j+\frac{1}{2}}^+] \right). \quad (3.172)$$

It is this reduction to an upwind scheme in regions with directed local speeds equivalent to monotonic advection fluxes with either $a_{j+\frac{1}{2}}^+ = 0$ or $a_{j+\frac{1}{2}}^- = 0$, which has led the authors of Ref. [168] to call their scheme a central-upwind scheme. Note that Eq. (3.172) does no longer include the left-sided local speed $a_{j+\frac{1}{2}}^-$ and only contains advection terms evaluated at $v_{j\pm\frac{1}{2}}^+$ involving the reconstructions from the cells to the right, *cf.* Eq. (2.102b) and (2.99). As a result the numerical flux of Eq. (3.172) is based on a right-leaning four-point stencil $\{\bar{v}_{j-1}, \bar{v}_j, \bar{v}_{j+1}, \bar{v}_{j+2}\}$, where \bar{v}_{j-1} is required together with \bar{v}_j and \bar{v}_{j+1} to compute $(\partial_y v)_j$. For the numerical flux of the first volume cell $j = 0$ which we choose to span over $y_{-\frac{1}{2}} = 0$ to $y_{\frac{1}{2}} = \Delta y$ we require $\{\bar{v}_{-1}, \bar{v}_0, \bar{v}_1, \bar{v}_2\}$, where only \bar{v}_{-1} is a ghost cell. Since it only appears in the flux limiting procedure, see (2.99), it is arguably not a ghost point related to physical boundary conditions but rather a computational one necessary to ensure formal second-order accuracy of the MUSCL reconstruction while preventing spurious oscillations around discontinuities – TVD time steps.

Two naive strategies for a practical choice of \bar{v}_{-1} come to mind. The first one would be switching from a central reconstruction to a right-sided reconstruction. Constructing a right-sided TVD reconstruction or searching for one in literature seemed unappealing for our limited discussion of this subsection. The second option is much simpler and related to the fact, that the KNP scheme with the position-independent advection flux G of Eq. (3.169) has a meaningful first-order reduction. Switching from a piecewise linear to a piecewise constant reconstruction in Eq. (2.102):

$$v_{j+\frac{1}{2}}^- = \bar{v}_j + \mathcal{O}(\Delta y), \quad (3.173a)$$

$$v_{j+\frac{1}{2}}^+ = \bar{v}_{j+1} + \mathcal{O}(\Delta y), \quad (3.173b)$$

results in a first-order accurate (in Δy) semi-discrete upwind scheme [168, 330, 331]

$$\partial_t \bar{v}_j = \frac{1}{\Delta y} (G[t, \bar{v}_j] - G[t, \bar{v}_{j+1}]), \quad (3.174)$$

valid for monotone advection fluxes with $\partial_u G < 0$. The first-order accurate KNP scheme is in this context equivalent to the so-called Godunov upwind scheme [330, 331]. Application of such first-order upwind-schemes within the FRG framework are discussed and presented in Refs. [398, 569]. To avoid the ghost cell \bar{v}_{-1} altogether we always use the first-order accurate KNP scheme (3.174) for the explicit results discussed in the following. Selected results with the second-order accurate KNP scheme can be found in App. F of Ref. [3].

We conclude this paragraph with a brief remark on the KT scheme. Using the conservative, equal sided estimate $a_{j+\frac{1}{2}}^+ = -a_{j+\frac{1}{2}}^- = a_{j+\frac{1}{2}}$ for the right- and left-sided local speeds $a_{j+\frac{1}{2}}^\pm$, the numerical advection flux (2.109) of the KNP scheme reduces to the advection flux the KT scheme

$$H_{j+\frac{1}{2}}^{\text{KT}} \equiv \frac{G[t, v_{j+\frac{1}{2}}^+] + G[t, v_{j+\frac{1}{2}}^-]}{2} - a_{j+\frac{1}{2}} \frac{v_{j+\frac{1}{2}}^+ - v_{j+\frac{1}{2}}^-}{2}, \quad (3.175)$$

with

$$a_{j+\frac{1}{2}} \equiv \max \left\{ \left| \frac{\partial G}{\partial v} [t, v_{j+\frac{1}{2}}^+] \right|, \left| \frac{\partial G}{\partial v} [t, v_{j+\frac{1}{2}}^-] \right| \right\}. \quad (3.176)$$

In the first volume cell \bar{v}_{-1} appears outside of the flux limiting procedure and is also present in the first-order accurate reduction of the KT scheme (3.175) using Eqs. (3.173a) and (3.173b) since the latter is based on a central scheme based on the stencil $\{\bar{v}_{j-1}, \bar{v}_j, \bar{v}_{j+1}\}$. Lacking the more refined estimates for the right- and left-sided local speeds $a_{j+\frac{1}{2}}^\pm$ of the KNP scheme it is not obvious how to deal with the ghost cell at \bar{v}_{-1} . This is, why we chose the KNP scheme for our numerical computations in y . The advection flux of the KNP scheme is also suited for the position depended advection flux F of the flow equation (3.167) in x . We have performed some heuristic tests with the KNP scheme and the flow equation (3.167) in x and we come to the preliminary conclusion that it is in terms of accuracy and performance on par with the KT scheme in this scenario. Nevertheless, further detailed tests might be of interest for upcoming challenges in the context of FRG problems in $d > 0$ with more sophisticated truncations.

The UV initial condition for the flows in $v(y)$ and $v(x)$ are visualized in figures 3.30b and 3.30d. For the FRG flow equations (3.166) and (3.167) the initial conditions (3.149) and (3.150) have to be transformed to the variable x . For the one parameter family of UV potentials, this reads

$$V(x) = \begin{cases} \frac{1}{2} x^2 & \text{for } |x| \leq 2, \\ -a \frac{1}{2} x^2 + 2(a+1) & \text{for } 2 < |x| \leq 4, \\ \frac{1}{2} x^2 - 6(a+1) & \text{for } |x| > 4. \end{cases} \quad (3.177)$$

Hence, our UV potential is actually a piecewise quadratic function of $x = \frac{1}{\sqrt{N}} \sigma$, while its x -derivative is given by the piecewise linear function

$$v(x) = \partial_x V(x) = \begin{cases} x & \text{for } |x| \leq 2, \\ -a x & \text{for } 2 < |x| \leq 4, \\ x & \text{for } |x| > 4. \end{cases} \quad (3.178)$$

3.2.5.4. FRG flows at infinite N – shocks and rarefaction waves in advective flows

This subsection follows Sec. IV.E and App. E of Ref. [3].

Next, we turn to the results for the FRG flows for Eq. (3.178) in the limit $N \rightarrow \infty$. Before presenting the numerical results, which are obtained by a numerical solution of the PDE (3.167) with the KT/KNP scheme [167, 168], we use the method of characteristics to discuss analytic results for solutions of the purely hyperbolic conservation law (3.167). This helps to better understand the underlying processes in the fluid-dynamical framework and the results of our numeric calculations.

In the FRG framework the method of characteristics was used by N. Tetradis and D. Litim in Refs. [566, 635] to obtain analytical solutions to FRG flow equations of the $O(N)$ model in dimensions $d > 0$ in the infinite- N limit. K.-I. Aoki, S.-I. Kumamoto, D. Sato, and M. Yamada also used the method of characteristics and the Rankine-Hugoniot condition in their

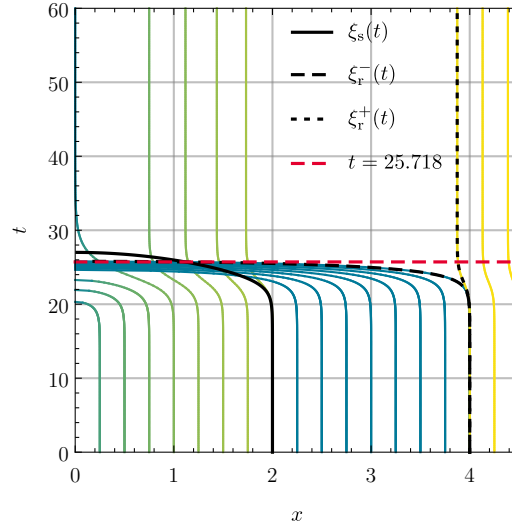


Figure 3.32.: Selected characteristic curves $(t, x(t))$, see Eq. (D.30), for $a = 0$ and $\Lambda = 10^{10}$ in blue, green and yellow, shock position $\xi_s(t)$, see Eq. (D.41), as solid black line, and the tips of the rarefaction fan $\xi_r^\mp(t)$, see Eq. (3.179) and (3.181) originating at $(t = 0, \xi_r^\mp(0) = 4)$ as dashed black lines. The changing color on the characteristic curves indicates the change of $v(t, x(t))$ along them, see Eq. (D.31), where blue corresponds to $v(t, x(t)) = 0$ and yellow corresponds to $v(t, x(t)) = 4.5$. The shock wave and the rarefaction fan collide at $(t, x) \approx (25.718, 1.115)$ (the time is marked with the red-dashed line) rendering the expressions $\xi_r^\pm(t)$ and $\xi_s(t)$ as well as the characteristics that intersect with the shock and rarefaction wave invalid for later times. From Fig. 4 of Ref. [3].

studies [565, 640] of weak solutions and dynamical symmetry breaking. Unfortunately (or luckily for my collaborators and me and our works [1, 2, 4, 7, 162, 247]), their otherwise remarkable work lacks the fluid-dynamical interpretation and with it an instructive way to understand characteristic curves in this context. The latter was put forward in the context of the FRG for the first time in Ref. [247].

Characteristic curves

The characteristic curves of the fluid are visualized in figure 3.32. These are defined as those (parametric) curves $(t, x(t))$ in the domain $[0, \infty) \times (-\infty, +\infty)$ of the problem, where the ratio $\frac{v(t, x(t))}{x(t)}$ stays constant⁶⁷. In App. D.1.3.3 we derive these implicit analytic solutions for the PDE (3.167) with initial condition (3.178) in great detail and the explicit solutions for $x(t)$ and $v(t, x(t))$ are given by Eq. (D.30) and (D.31). If needed, $x(t)$ and $v(t, x(t))$ can be used to reconstruct the full solution of the PDE, $v(t, x)$, for $t \in [0, \infty)$ and $x \in (-\infty, +\infty)$, which usually needs to be done numerically since the involved expressions can usually not

⁶⁷If formulated in terms of the $\frac{1}{N}$ -rescaled invariant y , these are the (parametric) curves $(t, y(t))$ on $[0, \infty) \times [0, \infty)$, where $v(t, y(t))$ is constant, see, e.g., Ref. [247]. Both formulations can be transformed into each other by simple coordinate transformations, see App. D.1.3.3.

be inverted analytically. Though, this method only works as long as the solution $v(t, x)$ is not multi-valued, which means that it is valid until any characteristics intersect at some point x in position space (here field space). Once the analytical solution becomes multi-valued, the physical solution exists only in a weak sense, see, *e.g.*, Refs. [315, 317–319, 328] or section 2.2 for details. Intersecting characteristics correspond to the formation of a shock wave, since several fluid elements are approaching the same point in the spatial domain at different velocities [315, 317–319, 328]. The movement of this shock wave, its (parametric) curve $(t, \xi_s(t))$, is described by the Rankine-Hugoniot shock condition [368, 369]. A derivation is presented in App. D.1.3.4. On the other hand, there might also be positions in field space that “separate” the characteristic curves into distinct regimes and that are the origin of infinitely many characteristic curves. These are so-called *rarefaction waves*, which each cause a *rarefaction fan* of infinitely many characteristic curves. As their name suggests, they are associated to points x (in field space), where fluid elements are moving apart from each other and cause a rarefaction of the fluid (in physical fluids corresponding to a reduction of density as a direct opposite of a compression wave), *cf.* subsection 2.2.6. A rarefaction fan can be described by the spatially closest characteristic curves $(t, \xi_r^\pm(t))$ that are moving to the left (–) and right (+) apart from each other.

Now we are equipped with the vocabulary to efficiently interpret and analyze figure 3.32. W.l.o.g. we choose the initial condition (3.178) with $a = 0$ – the plots and the discussion for different choices of a are qualitatively very similar. Furthermore, we only restrict our plot of the characteristics and parts of the discussion to positive x . For negative x the dynamics is perfectly mirrored about the t axis in figure 3.32.

The initial condition $v(t = 0, x) = v(x)$ corresponds to the initial values of $v(t, x(t))$ on the characteristic curves at $t = 0$ along the x -axis. The color-coding indicates the value of $v(t, x(t))$ according to Eq. (D.31) along the curves $(t, x(t))$, where blue corresponds to $v(t, x(t)) = 0$ and yellow corresponds to $v(t, x(t)) = 4.5$.

Firstly and in general, we observe that all characteristic curves only move towards smaller $|x|$, while $v(t, x(t))$ only decreases (increases) along each characteristic curve at positive (negative) x . This implies that the fluid $v(t, x)$ only moves towards $x = 0$. This can already be seen from the manifestly (positive) negative sign of the local fluid velocity $\partial_v F[t, x, v]$ for (negative) positive x , *cf.* Eq. (3.80) and Eq. (3.169). Hence, we find that right-moving waves of the fluid from negative x and left-moving waves of the fluid from positive x annihilate in $x = 0$, which is also manifestly encoded in the antisymmetry $v(t, x) = -v(t, -x)$.

Secondly we observe that the fluid elements, which start off in the interval $2 < |x| < 4$, move faster towards $x = 0$ than the fluid elements, that start at $|x| < 2$. As soon as the former try to overtake the latter, the solution gets multi-valued and a shock forms. Actually, this happens already at $t = 0$, but we can also see how more and more characteristics “join” and “accelerate” the shock wave. The movement of the shock wave, $(t, \xi_s(t))$ is described analytically by Eq. (D.41) and depicted as a black solid line in figure 3.32.

Thirdly, there is another important phenomenon going on around $|x| = 4$. We find that fluid elements at $|x| < 4$ are traveling fast towards $x = 0$, while the characteristic curves that start at $|x| > 4$ move slower towards $x = 0$ and that only for a very short period of (RG) time, before the characteristic curve closest to $|x| = 4$ freezes at $|x| \simeq \sqrt{15} \simeq 3.873$. This effectively causes

a rarefaction wave in $v(t, x)$, which is described analytically by

$$\xi_r^-(t) = \pm \sqrt{16 - \frac{1}{\Lambda e^{-t} - a} + \frac{1}{\Lambda - a}}, \quad (3.179)$$

$$v_r^-(t) = -a \xi_r^-(t), \quad (3.180)$$

$$\xi_r^+(t) = \pm \sqrt{16 - \frac{1}{\Lambda e^{-t} + 1} + \frac{1}{\Lambda + 1}}, \quad (3.181)$$

$$v_r^+(t) = \xi_r^+(t), \quad (3.182)$$

where $v_r^\mp(t)$ are the values of the fluid at the edges of the rarefaction fan. The rarefaction fan is marked in figure 3.32 by black-dashed lines that are analytically described by Eq. (3.179) and (3.181). The rarefaction wave also forms already at $t = 0$.

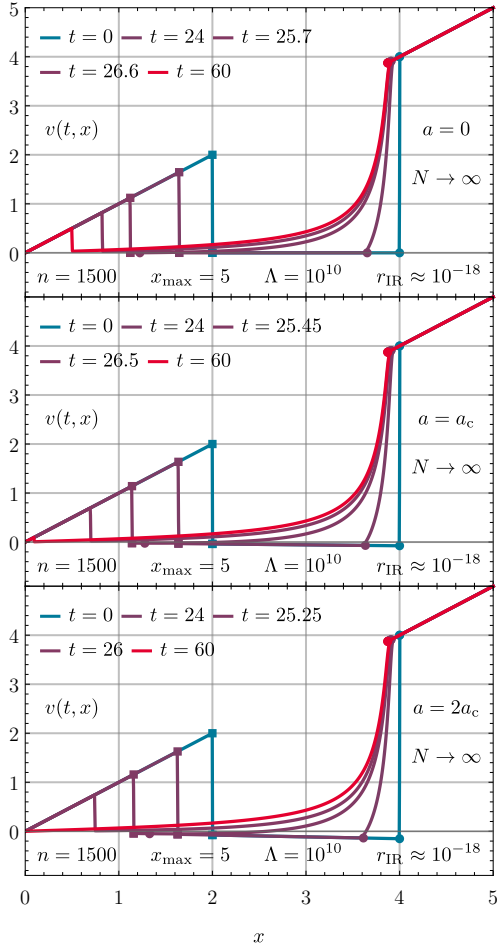
Interestingly, there is a (RG) time and field space position $(t, x) \simeq (25.718, 1.115)$, where the rarefaction fan catches up the shock wave (indicated by the red-dashed horizontal line). Up to this point, our analytical solutions for the shock $\xi_s(t)$ and the left tip of the rarefaction wave $\xi_r^-(t)$ are valid and we could in principle even integrate backwards in (RG) time and reconstruct the UV potential. However, when the shock and the rarefaction wave meet and interact, some highly non-linear dynamics is going on and we can no longer trust our analytical solutions. At later (RG) times, we have to rely on adequate numerical solutions.

Interestingly, it is exactly this complicated non-analytic dynamics, which makes the FRG flow manifestly irreversible and produces some abstract form of entropy, see subsection 3.2.5.4 and especially figure 3.35 as well as Refs. [1, 2], because information about the UV initial potential is unavoidably lost. Actually, this is the dynamics that fundamentally encodes the irreversibility of RG transformations on the level of the PDE, cf. also Refs. [235, 575, 576] for similar discussions.

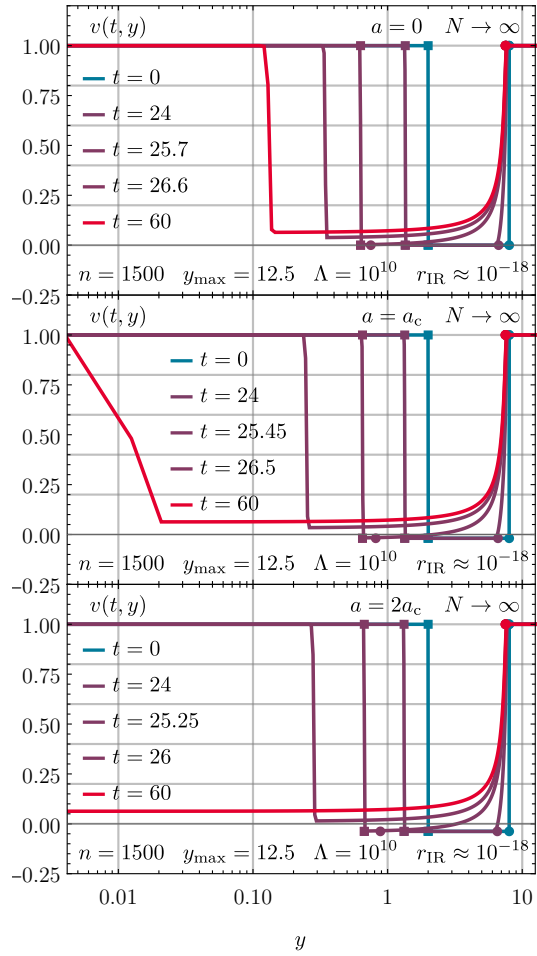
However, most remarkably in the context of the infinite- N limit: We find numerically that it is the complicated interplay between the shock and rarefaction waves (at positive and negative x), which either causes the shock waves to freeze at some non-zero $|x|$ or to crash into each other and annihilate in $x = 0$, depending on the choice of a – smaller, equal, or greater than a_c . This means that the (non-)applicability of the large- N saddle-point expansion of subsection 3.2.5.2, which was caused by a (non-)analytic “expansion point” – the underlying first-order phase transition, translates into the freezing or the annihilation of shock waves in field space in FRG flow equations. For further details on the relation between first-order phase transitions and the interaction/freezing of shock and rarefaction waves we refer the interested reader to Sec. III.C of Ref. [247]. However, to proceed with this discussion and to understand this interrelation, we have to leave the sure ground of analytical solutions and turn to high precision numerical computations of this challenging dynamics.

Numerical results at infinite N in x

Next, we apply the KT scheme [167] from numerical fluid dynamics to the problem posed by the PDE (3.167) with initial condition (3.178). The corresponding (numerical) parameters are either incorporated in the figures or their corresponding captions. Additionally, we discuss



(a) FRG flow of the derivative of the rescaled effective potential $v(t, x)$



(b) FRG flow of the derivative of the rescaled effective potential $v(t, y)$. We choose a logarithmic scale for the y -axis for better visibility around $y = 0$ which is particularly useful for the visualization of the freezing shocks in the IR for $a = 0$ and $a = a_c$.

Figure 3.33.: FRG flows for the zero-dimensional $O(N)$ model in x on the left (a) and in the $\frac{1}{N}$ -rescaled invariant $y \equiv \frac{1}{2} x^2$ on the right (b) in the limit $N \rightarrow \infty$ for the IC (3.178) with $a = 0$, $a = a_c$, and $a = 2a_c$ in the upper, middle, and lower panel respectively. Blue curves represent the UV initial conditions at $t = 0$, red curves correspond to the IR potentials at $t = 60$ and the violet curves are at intermediate, selected RG times t chosen around the respective collision of the shock $\xi_s(t)$ with the left tip of the rarefaction fan $\xi_r^-(t)$. The squares mark the shock $(\xi_s(t), v(t, \xi_s(t)^\pm))$, while the disks mark the tips of the rarefaction fan $(\xi_r^\pm(t), v(t, \xi_r^\pm(t)))$. The left tip of the rarefaction fan and the shock are only marked up to the RG time when they meet since the underlying analysis based on the method of characteristics and Rankine-Hugoniot condition breaks down after their collision. From Figs. 5 and 10 of Ref. [3].

the choice of some of our (numeric) parameters and some aspects of the implementation in App. F of Ref. [3].

We obtain the following numeric results for the FRG flows of $v(t, x)$: In figure 3.33a we plot the FRG flow of $v(t, x)$ from the UV initial condition (3.178) (see figure 3.30c) at $t = 0$ to the IR at $t \rightarrow \infty$. Of course, for practical (numerical) calculations one has to stop the integration at some finite t in the IR. Here we chose $t = 60$, which corresponds to an IR cutoff $r_{\text{IR}} \approx 10^{-18}$, which is 18 orders of magnitude below model scales (which are considered to be of order one in $\frac{1}{N}$ -rescaled quantities). Our UV scale Λ was chosen to be ten orders of magnitude above model scales to guarantee RG consistency [1, 257] to a sufficient level. In total, we are integrating over 28 orders of magnitude in the regulator scale and corresponding tests for UV-scale-independence are presented in App. F of Ref. [3].

Figure 3.33a shows FRG flows for $v(t, x)$ for different values of a . In the upper panel $a = 0$ and therefore clearly below a_c , such that this FRG flow corresponds to the situation, where the $\frac{1}{N}$ -expansion is applicable. The middle panel shows the FRG flow exactly at the threshold $a = a_c$, where the exponent (3.155) has two degenerate minima (3.162), with one being a non-analytic point, preventing a saddle-point expansion. The bottom panel in figure 3.33 corresponds to a situation, where $a > a_c$ and the saddle-point expansion again fails as it is not applicable to this initial condition.

As already mentioned at the end of the previous subsection, we find that the different situations within the saddle-point expansion are realized by freezing or colliding and annihilating shock waves, caused by the interplay with the rarefaction fan. This is clearly seen in figure 3.33a, where the position $\xi_s(t)$ of the shock wave is marked with squares and the positions $\xi_r^-(t)$ and $\xi_r^+(t)$ of the tips of the rarefaction fan are marked with disks – up to the RG time, where they meet and interact rendering the analytic expressions invalid.

Explicitly, we find that for $a = 0$ (upper panel figure 3.33a) the opposing shock waves ultimately freeze at $|x| = |\xi_s(t = 60)| \approx 0.496$. We obtained this value using computations at different numerical spatial resolutions Δx by varying the number of volume cells n while keeping the computational extent fixed to $x \in [0, 5]$. The explicit value of $|x| \approx 0.496$ has been extracted from the fit

$$|\xi_s(t \rightarrow \infty)| \approx |\xi_s(t = 60)| = 0.496 + 0.788 \Delta x^{0.869}. \quad (3.183)$$

obtained from 41 data points with n varying between 64 and 2048. The non-vanishing value of $|\xi_s(t \rightarrow \infty)| \approx 0.496$ has the effect that the x -derivatives of $v(t, x)$ at $x = 0$ never change during the FRG flow and $\partial_x v(t, x)|_{x=0} = 1$ for all times t , while all higher x -derivatives vanish. Yet, these derivatives are in direct correspondence to the 1PI correlation functions $\Gamma^{(n)}$, which are extracted from $v(t, x)$ in the IR at the physical point $x = 0$ by differentiation w.r.t. x ,

$$N^{\frac{n-1}{2}} \Gamma^{(n+1)} = \partial_x^n v(t, x)|_{t \rightarrow \infty, x=0}. \quad (3.184)$$

Hence, although having highly non-linear dynamics involving the interaction shocks and rarefaction waves for $|x| \gtrsim 0.496$, the function $v(t, x)$ never changed its shape for $-0.496 \lesssim x \lesssim 0.496$ and always resembles a massive free QFT in this part of field space. Metaphorically speaking and to stay in the fluid-dynamic picture: It is as if the physical point $x = 0$ in field space is “sitting in the eye of a cyclone”.

Increasing a towards the critical threshold a_c one observes that the shock waves freeze closer and closer to $x = 0$. Considering the metaphor of the previous paragraph, as a approaches a_c from below the radius of the eye of the cyclone vanishes. At $a = a_c$ (middle panel figure 3.33a) one still observes a freezing of the shock wave in the IR at $|x| \approx 0.095$, which however is an artifact of the finite spatial resolution Δx of the numerical scheme. This effect can be removed by successively decreasing the FV computational cells Δx . We find that for $a = a_c$ the shock freezes at $x = 0$, because the shock position in the IR scales as follows with Δx for this situation,

$$|\xi_s(t \rightarrow \infty)| \approx |\xi_s(t = 60)| = 0.983 \Delta x^{0.413}, \quad (3.185)$$

again obtained from a fit to 41 data points with the number of volume cells n varying between 64 and 2048 while keeping x_{\max} fixed.

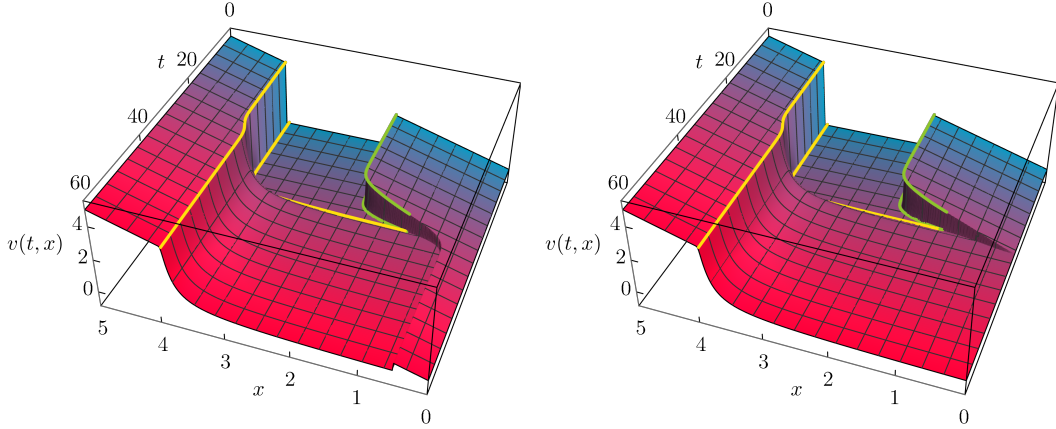
However, as soon as $a > a_c$ (middle panel figure 3.33a) the interplay of the rarefaction waves and the shock waves no longer hinders the shock waves to collide and annihilate at $x = 0$. In turn, this has two direct consequences: Firstly, in the hydrodynamic language, the additional interaction of two discontinuities (the annihilation of the shock waves) again unavoidably leads to a loss of information and an abstract production of entropy on the level of the PDE. This is discussed in more detail in the [next paragraph](#). Secondly, in the quantum field theoretical picture the annihilation of the shock waves caused a change in the slope of $v(t, x)$ at the physical point $x = 0$. This directly affects the 1PI correlation functions, which are again extracted in the IR via Eq. (3.184). Indeed, we find that our numeric calculations reproduce the exact results (3.153) and (3.154).

In summary and again metaphorically speaking, the slight change in the slope a of the initial condition (3.178) at $t = 0$ on the interval $x \in [2, 4]$ causes a tremendous change of the non-linear dynamics of the fluid $v(t, x)$, also at other positions in field space and later RG times, which can be seen as a “butterfly effect” in a QFT. The small deviations in the initial condition in the UV – in the metaphor the minor perturbations caused by a distant butterfly flapping its wings – have tremendous impact on the solution in the IR at the physical point – whether or not the formed cyclone has an eye or not. This further supports the notion of a first-order phase transition at a_c and the corresponding mechanism discussed in Ref. [247].

For a better/alternative visualization of this dynamics, we present two supplemental 3D-plots for the FRG flows of the upper and bottom panel of figure 3.33a. The curves from figure 3.33a are slices of constant intermediate times of the 3D-plots in figure 3.34. The color coding of all figures is identical. The attentive reader might recognize figure 3.34a (without its axes) as the cover picture of this thesis.

In addition to this rather qualitative discussion, we also provide explicit numerical errors, which can be used to judge to quality of the KT scheme [167] and our implementation in the context of FRG flows. In table 3.7 we list the relative errors of the 1PI two-point function $\Gamma^{(2)}$ extracted from the numerical FRG flows of $v(t, x)$ using Eq. (D.6) and the exact results (3.153) with (3.154) as reference values.

We close our discussion on the analysis of the infinite- N FRG flows by noting that, in contrast to the $\frac{1}{N}$ -saddle point expansion or perturbative methods, the FRG in its fluid-dynamic framework is applicable and also produces reliable results in a highly non-perturbative regime.



(a) FRG flow of $v(t, x)$ for $a = 0$ as 3D-plot corresponding to the flow displayed in the upper panel of figure 3.33 (b) FRG flow of $v(t, x)$ for $a = 2a_c$ as 3D-plot corresponding to the flow displayed in the lower panel of figure 3.33

Figure 3.34.: FRG flows of $v(t, x)$ for $a = 0$ on the left (a) and $a = 2a_c$ on the right (b). The left and right tips ($\xi_r^\mp(t), t, v(t, \xi_r^\mp(t))$) of the rarefaction fan are plotted as yellow lines while the shock ($\xi_s(t), t, v(t, \xi_s(t)^\pm)$) is marked with green lines. The left tip of the rarefaction fan and the shock are only marked up to $(t, x) \approx (25.718, 1.115)$ and $(t, x) \approx (25.270, 1.146)$ in (a) and (b) respectively, where they meet and the analysis based on the method of characteristics and Rankine-Hugoniot condition breaks down. From Figs. 6 and 7 of Ref. [3].

Furthermore, the FRG-fluid-dynamic framework, naturally copes with different kinds of non-analyticities, while all kind of “expansion-type” methods tend to collapse in the vicinity of relevant non-analytical physics that is only correctly described by fully fledged non-perturbative setups, cf. subsections 3.2.3.2 and 3.2.3.3.

Numerical results at infinite N in y

In figure 3.33b we present numerical results for the FRG flow in the rescaled invariant y using the flow equation (3.169) with the piecewise constant initial condition of Eq. (3.150) obtained with the KNP $\mathcal{O}(\Delta y^1)$ scheme discussed in the previous paragraph. The flow equation (3.169) with the piecewise constant initial condition of Eq. (3.150) constitutes two Riemann problems as outlined in subsection 3.2.5.1. The FRG flows in y displayed in figure 3.33b are equivalent to the ones in x presented in figure 3.33a hence we will not repeat the preceding qualitative discussion. In the following we will instead focus on certain aspects and problems inherent to the formulation and solution in the rescaled invariant y .

For small RG times $t \lesssim 25$ the FRG flows present as typical Riemann problems with a moving shock wave and a rarefaction fan, cf. our discussion of Euler equations in subsection 2.2.6. In figure 3.33b the evolution for $t \lesssim 25$ is for all a under consideration similar to the dynamics studied in Fig. 2 (a) of Ref. [247], which originally motivated the chosen initial condition in this work. Beyond $t \approx 25$ the shock wave and the left tip of the rarefaction fan start interacting leading to a freeze-out of the shock wave for $a = 0$ with $v(t = 0, y = 0) = 1 = \partial_x v(t = 0, x)|_{x=0}$.

For $a = 2a_c$ the shock moves out of the computational domain at $y = 0$ and we recover $v(t = 0, y = 0) = \frac{1}{16} = \partial_x v(t = 0, x)|_{x=0}$. So far in complete agreement with the corresponding results in x of subsection 3.2.5.4.

For $a = a_c$ we observe the remnant of the shock wave in the computational interval but the shock is strongly deformed by numerical(!) diffusion/the finite resolution of the computation. The situation at $a = a_c$ can be understood quite easily. The presented numerical computations use $n = 1500$ volume cells equidistantly distributed in the interval $y \in [0, 12.5]$ resulting in $\Delta y = \frac{1}{120} \simeq 8.33 \cdot 10^{-3}$. Consequently the first two volume cells are centered at $y_0 = \frac{1}{240} \simeq 4.17 \cdot 10^{-3}$ and $y_1 = \frac{1}{80} = 1.25 \cdot 10^{-2}$. Those two volume cells are clearly visible in the middle panel of figure 3.33b and contain the frozen shock for $a = a_c$. From our computation in x we found with the fit (3.185) that the shock for $a = a_c$ approaches $x = 0$ with $0.983 \Delta x^{0.413}$. For $n = 1500$ volume cell this amounts to a numerical shock position of $|x| \approx 0.095$ and consequently $y \approx 4.513 \cdot 10^{-3}$, which is for a computation in y with $n = 1500$ retaining $x_{\max} = 5 \Leftrightarrow y_{\max} = 12.5$ approximately at the center of the first volume cell. Having no volume cell to the right of the shock makes it numerically impossible to resolve $v(t = 0, y = 0) = 1 = \partial_x v(t = 0, x)|_{x=0}$ accurately. Using the fit (3.185) we can extrapolate that having the shock centered in the second or third cell would already require an extensive amount of volume cells namely $n = 3.7 \cdot 10^5$ or $n = 6.4 \cdot 10^6$ respectively while maintaining $y_{\max} = 12.5$. Computations with 10^5 and more volume cells overtax our current implementation and computational capacities, see App. F of Ref. [3] for details. Resolving dynamics at small x with an equidistant grid of volume cells in $y = \frac{1}{2}x^2$ is in general difficult because equidistant cells in y have a poor resolution around $x = \sqrt{2y} = 0$. A drastic example is the freezing shock for $a = a_c$ at $x = 0$, where the scaling $\propto \Delta x^{0.413}$ is already challenging. A situation with a scaling $\propto \Delta x^p$ with $p \geq \frac{1}{2}$ is also conceivable. Such a scenario would be impossible to resolve with an equidistant grid in the rescaled invariant $y = \frac{1}{2}x^2$. To improve or in some cases even facilitate computations at all around $x = 0$ in the rescaled invariant y a non-uniform mesh in y seems necessary. The generalization of the KT and KNP scheme to non-uniform grids is straightforward in one spatial dimension, see, e.g., Ref. [641], but will not be discussed in this work.

Entropy and irreversibility at infinite N

We now turn to the discussion of the (numerical) entropy associated with the purely advective FRG flows in the rescaled invariant y at infinite N . In subsection 3.2.4 we discussed the concept of (numerical) entropy of FRG flows and its relation to the inherent irreversibility of (F)RG flows in detail. We further argued for a connection between the (numerical) entropy of FRG flows and Zamolodchikov's [575] or more recent [592, 593] formulations of the \mathcal{C} -function.

In subsection 3.2.4 we focused on the limiting case $N = 1$ of the purely diffusive zero-dimensional $O(1)$ model. The focus of this paragraph is the opposite limit of $N \rightarrow \infty$ yielding purely advective flow equations. While a (numerical) entropy production is almost intuitively understood for diffusive problems the present situation might seem less obvious for a non-expert reader. In our introduction of non-linear advection equations in subsection 2.2.3.2 we discussed, that the appearance and/or interaction of discontinuities like shocks and rarefaction waves can be linked to an increase in numerical entropy. Which in turn signals the irreversibility

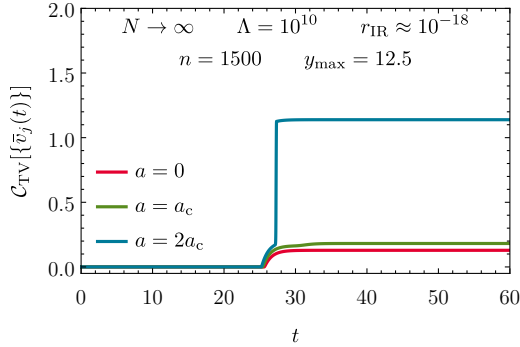


Figure 3.35.: The FRG flow of the \mathcal{C} -function, see Eq. (2.134), for the zero-dimensional $O(N)$ model in the limit $N \rightarrow \infty$ for the Riemann problem of Eq. (3.150) with $a = 0$, $a = a_c$, and $a = 2a_c$ obtained with the KNP scheme of $\mathcal{O}(\Delta y^1)$. We observe plateaus in the UV and IR. The IR plateaus end for the individual values of $a = 0$, $a = a_c$, and $a = 2a_c$ at the RG times when the shock wave and rarefaction fan intersect namely at $t \approx 25.718$, 25.469 , and 25.270 respectively. The second jump in the curves for $a \geq a_c$ is due to the collision of the shock waves at $x = 0$. From Fig. 11 of Ref. [3].

Table 3.7.: Relative numerical errors for the 1PI two-point function $\Gamma^{(2)}$, see Eq. (D.6), for the results plotted in figures 3.33a, 3.36a, and 3.36b, with corresponding exact reference values from the last row of table 3.6. The scaling of these errors with the number of volume cells can be found in Tabs. V, VIII, and IX of Ref. [3] for $N \rightarrow \infty$, $N = 2$, and $N = 32$ for $a = 2a_c$. From Tabs. II and III of Ref. [3].

N	$a = 0$	$a = a_c$	$a = 2a_c$
∞	$8.0 \cdot 10^{-15}$	$1.2 \cdot 10^{-14}$	$3.3 \cdot 10^{-3}$
2	$6.4 \cdot 10^{-5}$	$5.5 \cdot 10^{-5}$	$4.5 \cdot 10^{-5}$
32	$4.2 \cdot 10^{-3}$	$6.4 \cdot 10^{-4}$	$8.5 \cdot 10^{-3}$

of the underlying flow. Defining or constructing an explicit numerical entropy functional for general non-linear conservation laws is a difficult task especially when source terms are involved, cf. Refs. [358–361] and references therein.

When considering the flow equations (3.166) and (3.168) in x or y respectively, we note that the formulation in x (y) involves a position-dependent advection term (diffusion term). When executing the x -derivative in Eq. (3.166) we can differentiate between three contributions in the resulting flow equation in primitive form: a parabolic diffusion term $\propto \partial_x^2 v(t, x)$ with a non-linear diffusion coefficient, a hyperbolic advection term $\propto \partial_x v(t, x)$ with a non-linear, position-dependent advection velocity $\partial_v F$ and a non-linear, position-dependent internal source term $\propto v(t, x)$ stemming from the product rule. As a consequence of the latter term the r.h.s. of the flow Eq. (3.166) and hence $\partial_t v(t, x)$ is non-vanishing for $v(t, x)$ constant in x . Similarly the flow Eq. (3.168) in y contains such a non-linear, position-dependent internal source term $\propto v(t, y)$ arising from the derivative of the explicitly y -dependent second term in Eq. (3.168). Those internal source terms, explicit x - or y -dependencies before executing the derivatives, in the flow equations in primitive form make the construction of explicit numerical entropy functionals at finite $N > 1$ challenging.

In subsection 3.2.4 we discussed (numerical) entropy functions at length for the purely diffusive system at $N = 1$. The TV had been identified as one suitable entropy functional.

Incidentally in the opposite limit $N \rightarrow \infty$ but using the flow Eq. (3.169) in the rescaled invariant y the TV/arc-length is again a viable entropy functional. This goes back to general properties of (weak) solutions of purely hyperbolic non-linear advection equations – like our $N \rightarrow \infty$ flow Eq. (3.169). Among other general qualitative statements about monotonicity and convexity (weak) solutions of hyperbolic non-linear advection equations like Eq. (3.169) have a decreasing arc length – they are total variation non-increasing (TVNI) as discussed in subsection 2.2.2. Since solutions of the underlying flow Eq. (3.169) are TVNI ($\partial_t \text{TV}[v(t, y)] \leq 0$) the entropy functional \mathcal{C} is non-decreasing ($\partial_t \mathcal{C} \geq 0$).

Solutions of the flow Eq. (3.166) in x at $N > 1$ are in general not TVNI. A fact we tested in numerical experiments with several initial conditions at various $N > 1$ [1, 2, 365, 366]. The loss of the TVNI property is directly linked to the explicit position-dependencies in the flow equation manifesting as source terms when executing the x -derivatives of the r.h.s. of Eq. (3.166). Formal results supporting this can be found in Ref. [356]: non-linear parabolic differential equations of the type $0 = \partial_t v - f(t, z, v, \partial_z v, \partial_z^2 v)$ have TVNI solutions if (among some other restrictions) the flux f vanishes, i.e., $0 = f(t, z, v, 0, 0)$ on constant solutions $0 = \partial_z v = \partial_z^2 v$. The latter is not the case for flow equations in x at $N > 1$ and in y for finite N as discussed earlier in this subsection. It is intuitively obvious that source terms can increase the arc length of a (weak) solution and implications in the context of TVNI schemes are discussed in, e.g., Refs. [358–361].

For $N \rightarrow \infty$ solutions in x are still not TVNI but a reformulation in y eliminates the explicit position-dependence in the advection flux and the resulting source term. The solutions of the flow Eq. (3.169) in y are TVNI. A fact we tested numerically, see figure 3.35, for the Riemann problems posed by the initial condition (3.150) with the flow Eq. (3.169) and which is theoretically well established cf. Refs. [327, 339].

We conclude this subsection with a qualitative discussion of the numerical entropy for the Riemann problems posed by the initial condition (3.150) with the flow Eq. (3.169) for different a . The numerical entropies associated to the flows presented in figure 3.33b are plotted in figure 3.35.

The numerical entropy stays constant in the UV up until the point where the shock wave and rarefaction fan intersect namely at $t \approx 25.718$, 25.469 , and 25.270 for $a = 0$, $a = a_c$, and $a = 2a_c$ respectively. Since both shock and rarefaction wave are already present in the initial condition $v(t = 0, y)$ their simple advection does not increase the numerical entropy of Eq. (2.134). The flow in the UV is therefore arguable reversible, which can be seen from the analytic solutions via the method of characteristics, but practical computations involving a finite resolution Δy and finite precision during time evolution prevent an accurate reversion by numerically integrating up in time t .

Between $t \approx 25$ and $t \approx 35$ we observe an increase in numerical entropy related to the interaction of the shock and the rarefaction fan. For $a \leq a_c$ the rise in entropy is rather small related to only marginal changes in arc length/TV during the flow, see upper and middle panel of figure 3.33b. For $a > a_c$ namely $a = 2a_c$ we observe a steep rise in entropy at $t \approx 27.275$, which is the RG time at which the shock leaves the computational domain for $a = 2a_c$. Without the shock the arc length/TV decreases dramatically leading to the observed rise in numerical

entropy.

In the IR for $t \gtrsim 35$ we again observe a plateau in the numerical entropy, related to the fact, that $k(t)$ for $t \gtrsim 35$ is sufficiently below the internal model scales of the problem under consideration meaning that all relevant fluctuations are already included. The plateaus in the numerical entropy in the UV and IR are indicators of RG consistency and sufficiently small numerical IR cutoffs respectively.

3.2.5.5. FRG flows at finite N – diffusion as a game changer

This subsection follows Sec. IV.F of Ref. [3].

Next, we turn to the FRG flows of our initial potential (3.149) at finite N . To this end, we use the fluid-dynamic FRG flow equation (3.166) including advective and diffusive contributions by the pions and the σ -mode. As explained above, we cannot use Eq. (3.168) in the presence of diffusion, because the problem of diffusive influx at the ($y = 0$)-boundary, if formulated in y , is not settled yet to our satisfaction, cf. again subsection 3.2.2.4. For the following discussions at finite N we hence use Eq. (3.166) in x and the robust KT scheme.

The main scope of this subsection is to demonstrate the astonishing role of the radial σ -mode in terms of highly non-linear and unconventional diffusion in FRG flows of scale-dependent effective potentials $V(t, x)$ or rather their derivatives $v(t, x) = \partial_x V(t, x)$. To this end, let us again focus solely on the purely diffusive contribution of the FRG flow equation (3.166) and rewrite it in terms of a non-linear heat equation by executing the σ -derivative on the r.h.s.,

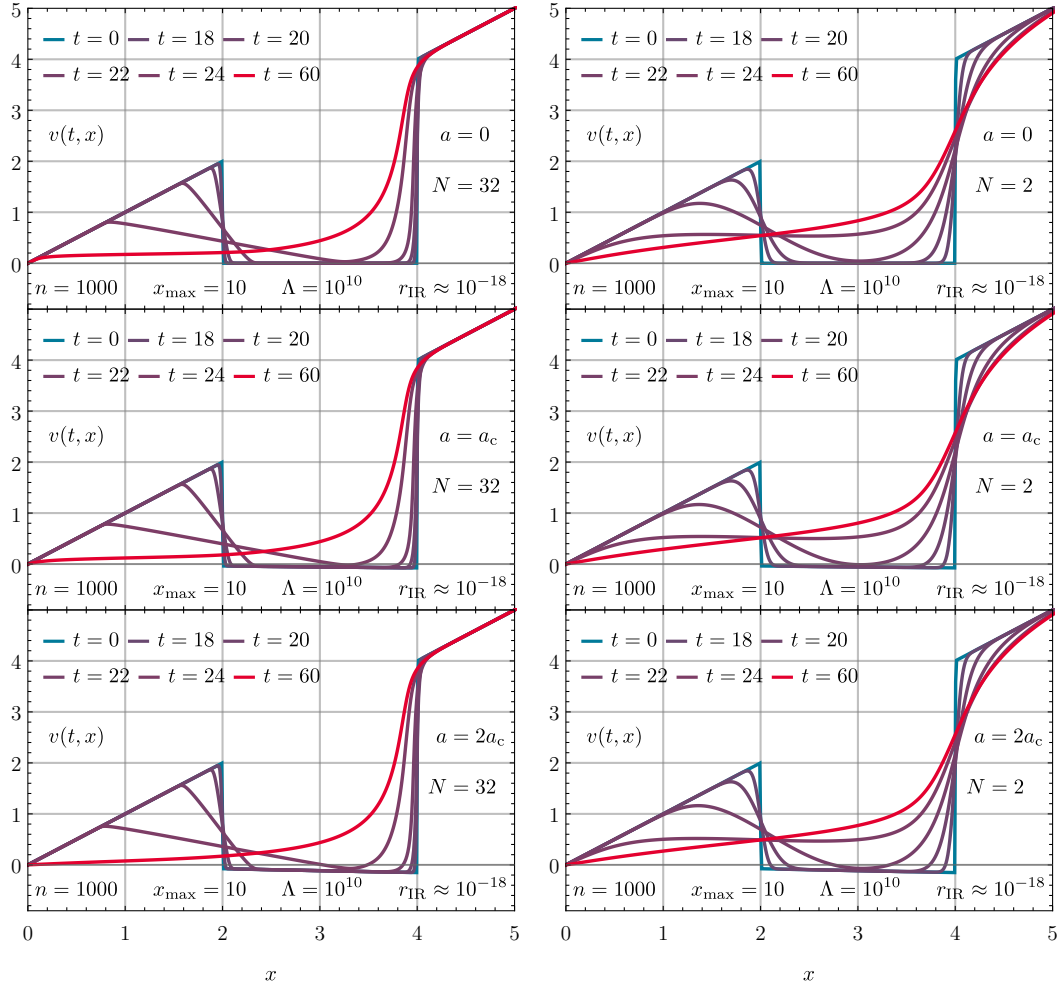
$$\partial_t v(t, x) = \frac{d}{dx} \left[\dots + \frac{1}{N} \frac{\frac{1}{2} \partial_t r(t)}{r(t) + \partial_x v(t, x)} \right] = \dots + \alpha[t, \partial_x v] \partial_x^2 v(t, x),$$

where we again recovered the manifestly positive diffusion coefficient (note the definition (3.8) of the regulator $r(t)$ and the rescalings),

$$\alpha[t, \partial_x v] \equiv -\frac{1}{N} \frac{\frac{1}{2} \partial_t r(t)}{[r(t) + \partial_x v(t, x)]^2}, \quad (3.186)$$

cf. Eq. (3.86) for the unrescaled/original diffusion coefficient. The identification of the sigma loop as a parabolic, diffusive contribution has severe conceptual implications. The diffusive contribution to the flow of $v(t, x)$ clearly introduces a dissipative process into the FRG flow and renders it manifestly irreversible, see again subsection 3.2.4 for further details.

In the context of this work, however, we are mainly interested in the influence of the non-linear diffusion on the explicit shape of $v(t, x)$ and its drastic consequences for the reliability of $\frac{1}{N}$ -expansions and the infinite- N limit. To this end, we present our numerical solutions of Eq. (3.166) with initial condition (3.178) (see figure 3.30c) for two choices of N . W.l.o.g. we choose $N = 2$ and $N = 32$ and present respective FRG flows for $a = 0$, $a = a_c$, and $a = 2a_c$ in figure 3.36. The figures 3.36a and 3.36b are structured analogously to figure 3.33a (for infinite N). For our numerical computations we used the same UV and IR cutoffs as for the infinite- N case. Nevertheless, we had to change the size of the computational interval from $[0, 5]$ to $[0, 10]$



(a) FRG flow with $N = 32$ for the IC (3.178) with $a = 0$, $a = a_c$, and $a = 2a_c$ in the upper, middle, and lower panel respectively. (b) FRG flow with $N = 2$ for the IC (3.178) with $a = 0$, $a = a_c$, and $a = 2a_c$ in the upper, middle, and lower panel respectively.

Figure 3.36.: The FRG flow of the derivative of the rescaled effective potential $v(t, x)$ for the zero-dimensional $O(N)$ model for $N = 32$ on the left (a) and $N = 2$ on the right (b). Blue curves represent the UV initial conditions at $t = 0$, red curves correspond to the IR potentials at $t = 60$ and the violet curves are at intermediate, selected RG times t . From Figs. 8 and 9 of Ref. [3].

in order to exclude boundary effects due to the diffusion. Furthermore, it suffices to use $n = 1000$ volume cells on this interval, because it is no longer necessary to resolve the sharp shock fronts at extremely high resolution to obtain small numerical errors. For details on these two aspects, we refer to our detailed discussion of subsection 3.2.3.

Qualitatively, we observe the following: Even though $N = 32$ seems to be rather large⁶⁸ the FRG flow of the $\frac{1}{N}$ -rescaled $v(t, x)$ entirely changes, if one compares corresponding panels of figures 3.33a and 3.36a directly. Although the underlying shock, stemming from the still rather strong advective π -modes, dominates the overall shape of $v(t, x)$ in figure 3.36a for all three choices of a , the diffusive character sets in rather early during the beginning of the FRG flow and smears out the infinite negative slope of $v(t, x)$ at the shock front. Inspecting the non-linear diffusion coefficient (3.186) this is expected for all finite N . Huge negative gradients $\partial_x v(t, x)$ lower the difference $r(t) + \partial_x v(t, x)$, which in turn drastically increases the diffusion coefficient leading, in combination with large $\partial_x^2 v(t, x)$, to strong diffusion in regions where $v(t, x)$ has large negative slopes, *e.g.*, next to the shock front. On the other hand, if $\partial_x v(t, x)$ has large positive slope, as is the case close to the rarefaction fan, the diffusion coefficient is drastically suppressed, even if $\partial_x^2 v(t, x)$ is large, such that the advection still dominates close to the rarefaction wave. For large $x \gg 5$ both, $\alpha[t, \partial_x v]$ and $\partial_x^2 v(t, x)$ tend to zero (as is the case for $\frac{1}{x} v(t, x)$ for the advection). For all other regions in x we find complicated variations of these conceptual behaviors.

Concerning the freezing or colliding of the shock wave, which was observed for infinite- N in figure 3.33, we find that remnants of the freezing shocks are still visible in Figs. 3.36a (upper and middle panel). However, the gradient $\partial_x v(t, x)$ no longer changes its sign at the right of the remnants of the freezing shock waves, such that overall the potential $V(t, x)$ turns convex in the IR.

Turning to figure 3.36b for the $N = 2$ scenario, where only one π - and one σ -mode are included in the calculation, we find that the overall the dynamics is very similar to the $N = 32$, but even more dominated by the diffusive contribution to the FRG flow. The freezing shock waves are no longer visible in the IR for $a = 0$ and $a = a_c$ and the rarefaction wave is totally washed out. The latter effect is the reason, why the computational interval had to be increased.

Before we turn to the overall interpretation of these findings, we remark that we also compared our numerical results for the 1PI two-point functions for all three choices of a and $N = 2$ and $N = 32$ against exact results. In table 3.7 we present the corresponding relative errors which are discussed further in App. F of Ref. [3].

In summary, we find that the radial σ -mode and the corresponding diffusion is a game changer in a QFT when switching from infinite to finite N . By directly comparing the infinite- N and finite- N results of the FRG flows, we observe that for infinite- N the $\frac{1}{N}$ -rescaled potential $V(t, x)$ does not turn convex in the IR and may still involve non-analyticities in terms of cusps. This is in direct opposition to the zero-dimensional version of the CMWH theorem [550–552], which states that the zero-dimensional IR potential has to be convex and smooth. On the other hand, we find that independent of the specific choice of N – as long as N is finite – the highly non-linear diffusion of the σ -mode restores convexity and smoothness of the IR potential. Depending on the specific choice of N this may however happen at later times in the FRG flow, respectively at lower RG scales, thus deeper in the IR. This situation is very similar to the

⁶⁸Especially in the context of the large- $N_{\text{color}}/N_{\text{flavor}}$ discussions in the context of QCD, QCD-inspired models, or holographic methods, where N is typically between 1 and 6.

one we encounter in our studies in the GNY model at finite N , see subsection 4.5.3.3 for details. We conclude from these non-perturbative FRG studies, that calculations at infinite- N and large- N , may lead to totally different results for certain aspects of a QFT. This can by no means be considered a novel insight – however the FRG CFD aspects in this context are.

3.3. A $SU(2)$ model – strongly interacting Grassmann numbers

This section is based on the draft [7] and related ongoing work. So far the main contributions to this work have come from Adrian Koenigstein and Jens Braun. The complete set of flow equations for the field-dependent couplings is original to this thesis.

The automated symbolic computations, full expressions, and the code for diagram generation and export are included in the digital auxiliary file [642] which relies heavily on our MATHEMATICA code [299] for flow equations. These symbolic computations, including the export of diagrams and L^AT_EX expressions, take a few minutes on an Intel[®] Core™ i7-8750H processor running multi-threaded on up to six cores.

So far in our studies of theories in zero dimensions we have only considered scalar degrees of freedom. Fermionic and Fermion-Boson models and theories, like the QM model and GN model, including Grassmann-valued fields are at the core of our research in chapters 4 and 5. This is why the wish to study fermions in zero dimensions, *i.e.*, just Grassmann numbers, arose very early in our research project in zero dimensions.

Early on in our work on the manuscript for Ref. [1], we considered an extension of the $O(N = 3)$ model by coupling it with four Grassmann numbers – an associated pair of Grassmann numbers with two flavors. The idea was to construct a simple $SU(2)$ -symmetric model as a zero-dimensional analog to a Yukawa theory/QM-like model. We will present the construction of such a theory in subsection 3.3.1. The corresponding FRG flow equations will be discussed in subsection 3.3.2. The hope is, that such a more involved zero-dimensional theory would be suited to study more interesting symmetry breaking and restoration patterns than the one realized in the zero-dimensional $O(N)$ model. In the zero-dimensional $O(N)$ model one can only study symmetry restoration by specifying an initial condition for the FRG flow which has a non-trivial minimum and study its evaporation during the FRG flow, see, *e.g.*, subsection 3.2.3. The Grassmann-numbers of our $SU(2)$ model manifest as a source/sink-term in the flow equation for the RG-scale-dependent potential, as we will demonstrate in subsection 3.3.2. This is a feature they share with fermionic contributions in higher dimensions, which also manifest as source/sink-like contributions in LPA flow equations, *cf.* subsection 4.2.2. The hope is that such a source term would allow for a dynamically generated breaking of $SU(2)$ invariance in form of a precondensation effect, see also subsection 4.5.3. While we still ultimately expect $SU(2)$ symmetry restoration in the IR in zero-dimensions – due to the limiting case of the CMWH theorem [550–552], *i.e.*, basic symmetry-properties of the involved integrals – dynamic symmetry breaking and subsequent restoration during the FRG flow might be possible with a carefully constructed test cases.

The work on this zero-dimensional $SU(2)$ model is still ongoing and we will only present

some symbolic results, conceptual ideas and challenges in the following. We have made only limited progress on this part of our research in zero dimensions from its conception in the early days of the manuscript for Ref. [1] (in the fall of 2020) until now (fall of 2023) for various reasons:

- We decided to work and publish our results for the $O(N)$ model as a “first step”. During our work on the $O(N)$ model in $d = 0$ it turned out that this scalar theory alone is incredibly rich and the “first step” turned into a series of three publications [1–3] covered in around 100 pages in this thesis, with still some open questions left.
- Applications of our results from this series [1–3] to $d > 0$, cf. chapter 4 and the corresponding preprint [4], took precedence over further work in $d = 0$.
- The constructed $SU(2)$ model in its non-bosonized, completely field-dependent form turned out to be diagrammatically rather complex. This complexity also manifests at the level of the flow equations, which presents an ambivalence. On the one hand, a conservative formulation (and related robust numerical implementation) of the involved flow equation has proven challenging and is still a work in progress. But on the other hand, this challenge in zero dimensions might be able to provide important insight into the conservative formulation of the FRG flow equation in general. The latter is very relevant for studies in higher dimensions, e.g., in with the QM model, where a conservative formulation for the field-dependent Yukawa coupling is also still elusive [162, 210].

We spent a lot of time developing code [299, 642] to derive, manipulate, and visualize diagrammatic flow equations. We hope to use these tools in the future to gain further insight into the zero-dimensional $SU(2)$ model, or a simplified version of it. We firmly believe that developing a better (or, in the best case, complete) understanding of zero-dimensional theories involving Grassmann numbers within the FRG-CFD framework is a very promising research direction, with possibly significant implications beyond zero dimensions. A part of the outlook 3.4 for this chapter will be dedicated to discussing our plans and hopes for this research.

3.3.1. Construction of the $SU(2)$ Grassmann-scalar theory

This subsection is based on Sec. II.A of the draft [7]. The main conceptual work in the explicit construction of the discussed model, based on symmetry considerations, has been done by Adrian Koenigstein.

The aim of this subsection is to construct a preferably simple toy model for a consistent QFT in zero space-time dimensions, that contains bosonic and fermionic degrees of freedom, i.e., scalars and Grassmann-numbers. We are interested in a theory, that has more than one scalar and more than one Grassmann-valued degree of freedom, to generate different types of contributions to the FRG flow equations. We want a theory with convection-, diffusion-, and source/sink-like contributions in its FRG flow equations to mimic the situation found in the LPA/DE of higher-dimensional theories, like the GN model and QM model, discussed in chapters 4 and 5.

In addition, the model should allow for the possibility of the breakdown/restoration of a continuous symmetry and the formation of a condensate on the level of the EAA $\bar{\Gamma}_t[\chi]$. Such a dynamic symmetry breaking could be induced by attractive Grassmann-valued interactions during the FRG flow from $t = 0$ to $t \rightarrow \infty$. The bosonic scalar degrees of freedom are however expected to restore the full symmetry and vaporize the condensate for the full quantum effective theory $\Gamma[\chi]$ in the deep infrared at $t \rightarrow \infty$, due to a limiting case of the CMWH theorem [550–552], cf. App. B of Ref. [1]. To allow for all these phenomena and to use them as testing tools, the action S of the theory, to be constructed, has to be invariant under transformations of a continuous symmetry-group. To have a non-trivial field theory, we include (self-)interaction terms in the action. To enable interactions between scalar and Grassmann-valued degrees of freedom, we include a Yukawa-like coupling. This inclusion also allows for the possibility of condensate formation and symmetry-breaking in $\bar{\Gamma}_t[\chi]$ during the RG-flow. All fermion self-interactions beyond a specific order must vanish due to the limited amount of distinct Grassmann numbers.

Grassmann numbers – the fermions in $d = 0$

We consider two anticommuting Grassmann numbers $\theta = (\theta^1, \theta^2)$ and two associated anticommuting Grassmann numbers $\bar{\theta} = (\bar{\theta}_1, \bar{\theta}_2)$. These tuples shall transform under the fundamental representation of a global $SU(N = 2)$ symmetry group,

$$\theta \mapsto \theta' = \mathcal{U} \theta, \quad \bar{\theta} \mapsto \bar{\theta}' = \bar{\theta} \mathcal{U}^\dagger, \quad (3.187)$$

where

$$\mathcal{U} = e^{+i\omega_a t^a}, \quad \mathcal{U}^\dagger = e^{-i\omega_a t^a}, \quad (3.188)$$

with $a = 1, 2, 3$, the generators t^a of the group $SU(2)$ in fundamental representation forming the $\mathfrak{su}(2)$ -algebra

$$[t_a, t_b] = i \varepsilon^{abc} t_c, \quad (3.189)$$

cf. App. B.3.1 for further details and explicit expressions. Using these Grassmann numbers, we can construct all contributions formed by θ and $\bar{\theta}$ to the action S , which are invariant under $SU(2)$ symmetry. From the transformation laws (3.187) we directly read off that there can not be any $SU(2)$ -invariant terms involving only odd powers fermion flavors. Furthermore, we find that there can only be a single term of fourth-order in fermion fields $\sim \bar{\theta}_1 \bar{\theta}_2 \theta^1 \theta^2$, because there are simply just four distinct Grassmann numbers available. All higher-order terms vanish. Conventionally, we write the fourth-order term as

$$\frac{1}{2} g (\bar{\theta} \frac{1}{2} \mathbb{1}_2 \theta)^2 = \frac{1}{8} g (\bar{\theta} \theta)^2 = \frac{1}{4} g \bar{\theta}_1 \theta^1 \bar{\theta}_2 \theta^2, \quad (3.190)$$

with a four-Grassmann coupling constant g .

It remains to study the quadratic order terms: All possible terms are of the following form,

$$\bar{\theta} M \theta, \quad (3.191)$$

where M is a 2×2 complex matrix. If this term is supposed to be invariant under the $SU(2)$ symmetry transformations (3.187), assuming that M does not transform itself under these symmetry transformations, then M has to commute with all fundamental generators (B.17). This implies that M must be proportional to the only Casimir-operator of $SU(2)$, which is in turn proportional to the identity matrix:

$$M = \frac{1}{2} m \mathbb{1}_2 \quad (3.192)$$

with the coupling constant m , which we will typically refer to as “mass function“ even though there is no notion of physical mass in $d = 0$. Of course there is also the option that M does not transform trivially under $SU(2)$, which we will discuss in the [next-to-next paragraph](#) after discussing scalars first.

Scalars – the bosons in $d = 0$

We consider three scalars which are supposed to transform under the adjoint representation of $SU(2)$, thus forming a $SU(2)$ -triplet. We consider the components $(\phi_a) = (\phi_1, \phi_2, \phi_3)$ of a vector $\phi = \tilde{t}^a \phi_a$, that transforms according to

$$\phi_a \mapsto \phi'_a = \mathcal{U}^{ab} \phi_b, \quad (3.193)$$

where

$$\mathcal{U}^{ab} \equiv (\exp(i\omega_c \tilde{t}^c))^{ab}, \quad (3.194)$$

with $a = 1, 2, 3$ and ω_a being the same group parameters as in Eq. (3.188). The generators of $SU(2)$ in the adjoint representation \tilde{t}^c , cf. Eq. (B.25), are given by the structure constant, $(\tilde{t}^a)^{bc} = -i\varepsilon^{abc}$, which also form a basis of the Lie-algebra (3.189). However, due to the double cover of $SU(2) \rightarrow SO(3)$, the adjoint representation maps elements of $SU(2)$ to the real vector representation of $SO(3)$. Thus Eq. (3.193) can also be written as the transformation of the components ϕ_a of an Euclidean vector ϕ under $SO(3)$ -rotations

$$\phi_a \mapsto \phi'_a = O_{ab} \phi_b, \quad (3.195)$$

with

$$O = e^{i\omega_a L_a} \in SO(3), \quad (3.196)$$

where $(L_b)_{ac} = -i\varepsilon_{abc}$ are the generators of three-dimensional rotations that coincide with \tilde{t}^c .

From this, we can start to construct all scalar contributions to the action S , which are invariant under $SU(2)$ transformations, or the corresponding $SO(3)$ rotations respectively. Naturally, all terms that are functions of the $SO(3)$ invariant

$$\rho \equiv \frac{1}{2} \phi_a \phi^a \quad (3.197)$$

must be included in the action of the theory. This implies that for the purely scalar part of the action S , the only term that contributes and can be included in S , is the effective self-interaction potential $U(\rho)$, which we are familiar with from section 3.2.

It remains to study all $SU(2)$ -invariant mixed interaction terms.

Grassmann-scalar interaction – the Yukawa coupling in $d = 0$

To construct all possible $SU(2)$ -invariant Grassmann-scalar interaction terms, we come back to the crucial observation, that all terms that are functions of ρ are invariant under the $SO(3)$ symmetry transformations of the model. This implies that the first step is, to promote the two couplings m and g to field-dependent couplings $m(\rho)$ and $g(\rho)$, which maximally generalizes both terms, while keeping their symmetry untouched.

In the last step, it is sufficient to go back to the quadratic fermion interaction (3.191). This time, however, we allow for a non-trivial transformation behavior of M under $SU(2)$,

$$\bar{\theta} M \theta \mapsto \bar{\theta}' M' \theta' = \bar{\theta} \mathcal{U}^\dagger M' \mathcal{U} \theta. \quad (3.198)$$

If we demand that the whole term should be invariant under $SU(2)$ transformations it follows that M has to transform as ,

$$M \mapsto M' = \mathcal{U} M \mathcal{U}^\dagger. \quad (3.199)$$

This can of course be fulfilled trivially by a field-dependent mass-term $M \sim m(\rho) \bar{\theta} \frac{1}{2} \mathbb{1}_2 \theta$, which we already included in the action S . Additionally, Eq. (3.199) is exactly the transformation law that defines the adjoint representation. We can therefore include another $SU(2)$ -invariant term in the action S that is quadratic in the fermion flavors,

$$i h(\rho) \bar{\theta} T_a^{(f)} \phi_a \theta, \quad (3.200)$$

where $h(\rho)$ is a field-dependent Yukawa-coupling. The complex factor i is introduced for later convenience.

In total, the most general action of the zero-dimensional $SU(2)$ model reads

$$S[\vec{\phi}, \theta, \bar{\theta}] = U(\rho) + \bar{\theta} \left(\frac{m(\rho)}{2} \mathbb{1}_2 + i h(\rho) t_a \phi_a \right) \theta + \frac{g(\rho)}{2} \left(\bar{\theta} \frac{1}{2} \mathbb{1}_2 \theta \right)^2. \quad (3.201)$$

At this point, we remark, that in addition to the $SU(2)$ symmetry, the model exhibits a completely independent $U(1)$ symmetry, which manifests itself as pure phase-transformations of the fermion-fields, while the bosonic degrees of freedom stay unchanged,

$$\bar{\theta} \mapsto \bar{\theta}' = \bar{\theta} e^{+i\omega}, \quad \theta \mapsto \theta' = e^{-i\omega} \theta, \quad \phi_a \mapsto \phi'_a = \phi_a. \quad (3.202)$$

This is the zero-dimensional analog to the conservation of baryon number, cf. subsection 2.3.2.

Regarding the action (3.202) two issues remain to be discussed: Firstly, we have to discuss the symmetry breaking/restoration pattern, which can emerge dynamically during the FRG flow in $\bar{\Gamma}_t[\chi]$. Secondly, we have to discuss the restrictions on the functions $m(\rho)$, $h(\rho)$, $g(\rho)$, and $U(\rho)$ and if they have to be chosen real or complex valued. The action S of our model should be real-valued, to allow for an interpretation as a probability distribution.

Symmetry breaking/restoration pattern

The possible symmetry breaking/restoration pattern at finite RG time t comprises: The $SU(2)$ symmetry can only break down to one of its $U(1)$ subgroups, if we want to end up in a continuous subgroup with “Goldstone-modes”, cf. subsection 3.2.1, because there are no other continuous subgroups of $SU(2)$. In the bosonic sector, this $SU(2)$ symmetry breaking corresponds to a symmetry breaking of $SO(3)$ to one of its continuous $SO(2)$ subgroups, thus in total, the breaking pattern is given by

$$U(1) \otimes SU(2) \rightarrow U(1) \otimes U(1), \quad (3.203)$$

$$SO(3) \rightarrow SO(2). \quad (3.204)$$

On the level of the EAA $\bar{\Gamma}_t[\chi]$ this is realized as follows: During the dynamical symmetry breaking, a condensate σ and two “Goldstone-modes” π_1 and π_2 are formed. The number of “Goldstone-modes” is given by the number of broken generators of the symmetry group $SO(3)$, which is two, if we end up with a $SO(2)$ symmetry, that has only one remaining generator. Because there is no external parameter that distinguishes a single field space direction in ϕ from the other directions (because we do not consider explicit symmetry breaking), we can choose any of the field directions as the direction of the condensate σ . Without loss of generality, we choose ϕ_3 as the direction of condensation and ϕ_1 and ϕ_2 as the pion directions π_1 and π_2 . This implies that the remainder $SO(2)$ symmetry corresponds to rotations in the ϕ_1 - ϕ_2 -plane in field space, which leaves the condensate $\phi_3 = \sigma$ invariant. This is obtained by setting $\omega_1 = \omega_2 = 0$ in Eq. (3.196),

$$\phi_a \mapsto \phi'_a = O_{ab} \phi_b, \quad O = e^{i\omega_3 L_3}, \quad (3.205)$$

and explicitly reads

$$\begin{pmatrix} \phi_1 \\ \phi_2 \\ \phi_3 \end{pmatrix} \mapsto \begin{pmatrix} \phi'_1 \\ \phi'_2 \\ \phi'_3 \end{pmatrix} = \begin{pmatrix} \cos(\omega_3) & \sin(\omega_3) & 0 \\ -\sin(\omega_3) & \cos(\omega_3) & 0 \\ 0 & 0 & 1 \end{pmatrix} \begin{pmatrix} \phi_1 \\ \phi_2 \\ \phi_3 \end{pmatrix}.$$

Thus, we find that the $SO(3) \rightarrow SO(2)$ symmetry breaking is realized as a non-vanishing condensate σ in one of the field space directions, which corresponds to a non-trivial minimum $\rho = \underline{\rho} = \frac{1}{2}\sigma^2 > 0$ in at least one of the field-dependent couplings $m(\rho)$, $g(\rho)$, $h(\rho)$ or the effective potential $U(\rho)$.

In the fermionic sector, the condensate σ can be interpreted as a condensation of associated Grassmann pairs in one of the channels, here, w.l.o.g. it is the channel $\bar{\theta} t_3 \theta$, because we chose ϕ_3 as the direction of the condensate σ in the bosonic field space. This implies that the elements of the remainder $U(1)$ -subgroup of $SU(2)$ must be generated by t_3 , such that the condensation channel $\bar{\theta} t_3 \theta$ stays invariant under the remaining $U(1)$ symmetry. Formally this is again achieved by setting $\omega_1 = \omega_2 = 0$ in Eq. (3.188), such that the $U(1)$ transformations of the subgroup are given by

$$\theta \mapsto \theta' = \mathcal{U}_3 \theta, \quad \bar{\theta} \mapsto \bar{\theta}' = \bar{\theta} \mathcal{U}_3^\dagger, \quad (3.206)$$

with

$$\mathcal{U}_3 = e^{i\omega_3 t_3}, \quad \mathcal{U}_3^\dagger = e^{i\omega_3 t_3}. \quad (3.207)$$

3.3.1.1. The scale-depended generating functional $Z_t[\tilde{J}]$ and the EAA $\bar{\Gamma}_t[\chi]$

In analogy to subsection 2.1.1 and subsection 3.1.1 we may now use the action Eq. (3.201) to define a scale-dependent generating functional. To this end we want to make use of the FS formalism of App. B.4 and introduce the fundamental multi-field

$$\tilde{\chi} = (\vec{\phi}, \theta, \bar{\theta}) \quad (3.208)$$

with the associated mean-field

$$\chi = (\vec{\varphi}, \vartheta, \bar{\vartheta}), \quad (3.209)$$

where $\langle \vec{\phi} \rangle \equiv \vec{\varphi}$, $\langle \theta \rangle \equiv \vartheta$, and $\langle \bar{\theta} \rangle \equiv \bar{\vartheta}$. The FRG regulator term, cf. Eqs. (2.7) and (3.7), reads

$$\Delta S_t[\tilde{\chi}] = \frac{1}{2} R_t^{:\phi_i \phi_i} \phi_i \phi_i + \frac{1}{2} R_t^{:\theta^\alpha \bar{\theta}_\beta} \bar{\theta}_\beta \theta^\alpha + \frac{1}{2} R_t^{:\bar{\theta}_\alpha \theta^\beta} \theta^\beta \bar{\theta}_\alpha \quad (3.210a)$$

$$= \frac{1}{2} R_t^{:\phi_i \phi_i} \phi_i \phi_i + R_t^{:\theta^\alpha \bar{\theta}_\beta} \bar{\theta}_\beta \theta^\alpha \quad (3.210b)$$

$$= \frac{1}{2} r_b(t) \phi_i \phi_i + r_f(t) (\mathbf{1})^\alpha_\beta \bar{\theta}_\alpha \theta^\beta \quad (3.210c)$$

and may be used to define the RG-scale-dependent generating functional

$$Z_t[\tilde{J}] = \exp \left(-\Delta S_t \left[\frac{\delta}{\delta \tilde{J}} \right] \right) Z[\tilde{J}] = \int d[\tilde{\chi}] \exp \left(-S[\tilde{\chi}] - \Delta S_t[\tilde{\chi}] + \tilde{J}^m \tilde{\chi}_m \right), \quad (3.211)$$

cf. Eqs. (2.4) and (3.6). Note that for the $SU(2)$ model in $d = 0$, we truly have a regulator choice since we can introduce different regulator terms for Grassmann numbers and scalars. The regulator is no longer just a parametrization of RG time, like it is in the $O(N)$ model of the previous section 3.2. A natural choice, following Eq. (3.8), seems

$$r_b(t) = \Lambda e^{-t}, \quad (3.212a)$$

$$r_f(t) = \Lambda_f e^{-\gamma_f t}, \quad (3.212b)$$

where the scale Λ_f and scaling factor γ_f for the fermionic shape function are not necessarily equal to the ones implied for $r_b(t)$. It might be very interesting to study how such shifts in RG scales between Grassmann numbers and scalars manifest in FRG flows in zero dimensions, especially since similar shifts have recently gained some attention in the context of the QM model as LEFT [210].

The measure $d[\tilde{\chi}]$ in Eq. (3.211) is given by

$$d[\tilde{\chi}] \equiv d\phi_1 d\phi_2 d\phi_3 d\bar{\theta}_1 d\theta^1 d\bar{\theta}_2 d\theta^2, \quad (3.213)$$

assuming the usual conventions, see, e.g., the textbooks [177, 643, 644], for Berezin integration [643] over Grassmann-variables, e.g.:

$$\int d\theta^1 1 = 0, \quad \int d\theta^1 \theta_1 = +1, \quad \dots \quad \int d\bar{\theta}_1 \int d\theta^1 \int d\bar{\theta}_2 \int d\theta^2 \theta^2 \bar{\theta}_2 \theta^1 \bar{\theta}_1 = +1. \quad (3.214)$$

For the computation of the Berezin integrals, the exponential in Eq. (3.211) is only required up to at most $e^{-S} = 1 + S + \frac{1}{2}S^2$, where the Berezin integral over 1 vanishes, the term S leads to the contributions from the four-Grassmann number coupling, and the term S^2 generates the non-vanishing contributions stemming from the bilinear terms in S . The resulting expressions can be expressed using determinants in flavor space or evaluated directly.

We do not want to go into more details, but ultimately all expectation values as moments of $Z_t[\tilde{J}]$ and $Z_t[\tilde{J}]$ itself can be computed with only the integral over $\vec{\phi}$ or alternatively ρ remaining for numerical integration or symbolical evaluation for specific actions. One interesting observation is that at vanishing Grassmann-valued sources the generating functional evaluates to

$$Z_t[\vec{J}, 0, 0] = \mathcal{N} \int d\vec{\phi} \exp \left(-U(\rho) + \vec{J} \cdot \vec{\phi} + \ln \left(\frac{1}{4} [m^2(\rho) + 2\rho h^2(\rho) - g(\rho)] \right) \right), \quad (3.215)$$

with the Grassmann-valued components completely integrated out. This allows for the definition of a new effective potential

$$\tilde{U}(\rho) = U(\rho) - \ln \left(\frac{1}{4} [m^2(\rho) + 2\rho h^2(\rho) - g(\rho)] \right), \quad (3.216)$$

which can be used to derive restrictions on valid initial conditions for $U(\rho)$, $m(\rho)$, $h(\rho)$, and $g(\rho)$. Furthermore $\tilde{U}(\rho)$ could be used to study observables for the $SU(2)$ model using a completely bosonic flow. The latter could be very instructive to the study of the role of fermionic regulators in the zero-dimensional RG-scale-dependent generating functionals. A complete bosonization in the spirit of Eq. (3.216) shares some resemblance with the treatment of fermions in lattice (Monte Carlo) simulations and lattice field theory, see, *e.g.*, Refs. [79, 645–647] for an introduction. In these approaches the fermions/quarks are usually integrated out in the same fashion and appear as a shift of the action in a $\ln \det(M)$ -term. It is this term which causes the aforementioned, notorious QCD-sign-problem as real, non-zero quark chemical potentials render this determinant term complex. With such complex terms the action can no longer be considered as a probability distribution rendering the highly developed sampling algorithms of lattice QCD algorithmically completely ineffective. In FRG and large- N /MF fermions are usually not integrated out completely, beyond a HS transformation [452, 453] or dynamical hadronization of fermionic couplings, *cf.* subsections 2.3.3 and 4.1.1. The reason for this is that dealing with fermionic fluctuations – especially when considering bilinear actions – is comparatively simple and bosonic fluctuations are usually the harder problem to tackle.

Using $Z_t[\tilde{J}]$ from Eq. (3.211) we can define the corresponding EAA in the usual manner, *cf.* subsection 2.1.2 and subsection 3.1.3.2. The most general EAA, including all possible couplings/terms for the $SU(2)$ model reads

$$\bar{\Gamma}_t[\chi] = (m_t(\varrho)(t_0)^\alpha{}_\beta + i h_t(\varrho)(t_i)^\alpha{}_\beta \varphi_i) \bar{\vartheta}_\alpha \vartheta^\beta + \frac{1}{2} g_t(\varrho)(t_0)^\alpha{}_\beta (t_0)^\delta{}_\gamma \bar{\vartheta}_\alpha \vartheta^\beta \bar{\vartheta}_\delta \vartheta^\gamma + U_t(\varrho). \quad (3.217)$$

To derive explicit flow equation in the flowing subsection 3.3.2 it is necessary to evaluate the Wetterich Eq. (2.66) and its FS derivatives (2.68) and (2.70) on the QEOM, *viz.* projecting

on to $\chi_{\text{EoM}} = \underline{\chi}$. This means we have to decide on which field configuration $\underline{\chi}$ we want to compute the EAA, which in zero dimensions is again comparatively simple since we only need to consider Grassmann numbers and scalars. The issue of possible inhomogeneous phases, cf. subsection 2.4.1 and section 5.1, with their explicitly position-dependent condensates/mean-fields $\chi_{\text{EoM}} = \underline{\chi}(\vec{x})$ does not arise without the notion of space-time. Expectation values for an odd number of Grassmann numbers vanish, due to the rules (3.214) of Berezin integration, when evaluating the expectation values at vanishing sources $\tilde{J}^\theta = \tilde{J}^{\bar{\theta}}$, i.e., on the QEOM. This means, following the discussion of the symmetry breaking pattern of subsection 3.3.1, that the only non-vanishing expectation value to consider is $\langle \vec{\phi} \rangle = \underline{\vec{\phi}} = (0, 0, \sigma)$, while $\langle \theta \rangle = \underline{\vartheta} = 0$ and $\langle \bar{\theta} \rangle = \underline{\bar{\vartheta}} = 0$. For the multi-field this entails

$$\chi_{\text{EoM}} = \underline{\chi} \equiv (\underline{\vec{\phi}}, \underline{\vartheta}, \underline{\bar{\vartheta}}) = ((0, 0, \sigma), 0, 0). \quad (3.218)$$

3.3.2. System of FRG flow equations

This subsection contains some material from Apps. B–D of the draft [7] but the complete set of flow equations in the form presented here is original to this work.

In this subsection we will derive flow equations for all four field and RG-scale-dependent couplings, $u_t(\sigma)$, $m_t(\sigma)$, $h_t(\sigma)$, and $g_t(\sigma)$. In the spirit of our computations for the zero-dimensional $O(N)$ model of subsection 3.2.2 we will reformulate the resulting flow equations in σ instead of the invariant $\varrho = \frac{1}{2}\sigma$, which for a coupling $C_t(\varrho)$ entails

$$C_t(\varrho) \rightarrow C_t(\sigma), \quad (3.219a)$$

$$\partial_\varrho C_t(\varrho) \equiv C_t^{(1)}(\varrho) \rightarrow \frac{\partial_\sigma C_t(\sigma)}{\sigma} \equiv \frac{C_t^{(1)}(\sigma)}{\sigma}, \quad (3.219b)$$

$$\partial_\varrho^2 C_t(\varrho) \equiv C_t^{(2)}(\varrho) \rightarrow \frac{\partial_\sigma^2 C_t(\sigma)}{\sigma^2} - \frac{\partial_\sigma C_t(\sigma)}{\sigma^3} \equiv \frac{C_t^{(2)}(\sigma)}{\sigma^2} - \frac{C_t^{(1)}(\sigma)}{\sigma^3}. \quad (3.219c)$$

Furthermore, we use the so-called (fermionic) mass term

$$Y_t(\sigma) \equiv \frac{1}{2}\sigma h_t(\varrho) \quad (3.220)$$

instead of the Yukawa coupling $h_t(\sigma)$ in expressions.

The expressions for the vertices, propagators, and regulator insertions of App. D.2.1, have been computed programmatically, using our MATHEMATICA codes [299, 642]. Using them and the flow equations from subsection 2.1.5, the subsequent derivations reduce to straightforward computations involving just sums/traces.

Flow equation for the self-interaction potential $U_t(\sigma)$

We derive the following flow equation for the self-interaction potential by tracing over the

Wetterich Eq. (2.66) and evaluating on $\underline{\chi}$ from Eq. (3.218). The result of this computation is

$$\partial_t U_t(\sigma) = \partial_t \bar{\Gamma}_t = \mathcal{F}_t^U[\sigma; U_t^{(1,2)}(\sigma), m_t(\sigma), Y_t(\sigma)] \quad (3.221)$$

$$= +\frac{1}{2} \underline{G}_{t;\vartheta^\alpha \bar{\vartheta}_\beta} \partial_t \underline{R}_t^{;\bar{\vartheta}_\beta \vartheta^\alpha} + \frac{1}{2} \underline{G}_{t;\bar{\vartheta}_\alpha \vartheta^\beta} \partial_t \underline{R}_t^{;\vartheta^\beta \bar{\vartheta}_\alpha} + \frac{1}{2} \underline{G}_{t;\pi_i \pi_i} \partial_t \underline{R}_t^{;\pi_i \pi_i} + \frac{1}{2} \underline{G}_{t;\sigma\sigma} \partial_t \underline{R}_t^{;\sigma\sigma} \quad (3.222)$$

$$= -\frac{1}{2} \text{diag}_1 - \frac{1}{2} \text{diag}_2 + \frac{1}{2} \text{diag}_3 + \frac{1}{2} \text{diag}_4, \quad (3.222')$$

$$= -\underline{G}_{t;\vartheta^\alpha \bar{\vartheta}_\beta} \partial_t \underline{R}_t^{;\vartheta^\alpha \bar{\vartheta}_\beta} + \frac{1}{2} \underline{G}_{t;\pi_i \pi_i} \partial_t \underline{R}_t^{;\pi_i \pi_i} + \frac{1}{2} \underline{G}_{t;\sigma\sigma} \partial_t \underline{R}_t^{;\sigma\sigma} \quad (3.223)$$

$$= -\text{diag}_1 + \frac{1}{2} \text{diag}_3 + \frac{1}{2} \text{diag}_4, \quad (3.223')$$

$$= -\frac{(m_t(\sigma) + 2r_f(t))\partial_t r_f(t)}{Y_t(\sigma)^2 + (r_f(t) + m_t(\sigma)/2)^2} + 2\frac{\frac{1}{2}\partial_t r_b(t)}{r_b(t) + u(t,\sigma)/\sigma} + \frac{\frac{1}{2}\partial_t r_b(t)}{r_b(t) + \partial_\sigma u(t,\sigma)}, \quad (3.224)$$

where we unified the fermionic contributions using a transposition in the second fermionic loop of Eq. (3.222) to obtain Eq. (3.223), in which we used

$$\underline{G}_{t;\vartheta^\alpha \bar{\vartheta}_\beta} \partial_t \underline{R}_t^{;\bar{\vartheta}_\beta \vartheta^\alpha} = -\underline{G}_{t;\vartheta^\alpha \bar{\vartheta}_\beta} \partial_t \underline{R}_t^{;\vartheta^\alpha \bar{\vartheta}_\beta}. \quad (3.225)$$

The involved regulator insertions and propagators can be found in App. D.2.1. In the following we will frequently flip Grassmann-valued regulator insertion indices in the spirit of Eq. (3.225) to have a consistent sign between the expressions for fermionic contributions and their diagrams, cf. Eqs. (3.223) and (3.223'). In the field space formalism of App. B.4 Grassmann-valued and ordinary field components are treated on equal footing and necessary sign factors are included in the propagators, see Eqs. (2.27) and (D.45). That being said however, in final expressions like Eq. (3.224), Grassmann-valued and scalar contributions manifest with different signs, which we already want to highlight on the diagrammatic level, cf. Eqs. (3.222') and (3.223'), motivating our sign convention for Grassmann-valued regulator insertions in Eqs. (D.44a) and (D.44b).

The flow Eq. (3.221) is derived in detail in Sec. 2.2 of our auxiliary notebook [642].

The flow equation for the RG-scale-dependent self-interaction potential $\partial_t U_t(\sigma)$ can, like in the $O(N)$ model, cf. subsection 3.2.2.3 and Eqs. (3.63), (3.74), and (3.75), be recast in a conservative form for $\partial_\sigma U_t(\sigma) \equiv u_t(\sigma) \equiv u(t, \sigma)$

$$\partial_t u_t(\sigma) = \partial_\sigma \mathcal{F}_t^U[\dots] \equiv \mathcal{F}_t^u[\sigma; u_t^{(0,1)}(\sigma), m_t(\sigma), Y_t(\sigma)] \quad (3.226)$$

by taking a derivative w.r.t. σ . This is possible since the the FRG flux $\mathcal{F}_t^U[\dots]$ from Eq. (3.221) and explicitly (3.224), does not depend on $U_t(\sigma)$ but only, through the scalar propagators, on $U_t^{(1)}(\sigma) \equiv \partial_\sigma U_t(\sigma) \equiv u_t(\sigma)$ and $U_t^{(2)}(\sigma) \equiv \partial_\sigma^2 U_t(\sigma) \equiv \partial_\sigma u_t(\sigma)$, indicated in Eq. (3.221) by $\mathcal{F}_t^U[\dots, U_t^{(1,2)}(\sigma), \dots]$ in a compact notation we will adopt throughout this subsection.

The contribution to $\mathcal{F}_t^u[\dots]$ from the Grassmann-valued components enters as a complicated source term – first term in Eq. (3.224) – which depends on the Grassmann-valued regulator (insertion), the mass term $Y_t(\sigma)$, and mass function $m_t(\sigma)$. As such the source term carries a complicated t - and σ -dependence. We mentioned the inclusion of such sources in conservation laws in our methodological introduction of CFD specifically in subsections 2.2.2 and 2.2.5. We will discuss fermionic source terms/contributions to LPA-flows in much more detail in subsection 4.2.2.

Flow equation for the mass term $Y_t(\sigma)$ and mass function $m_t(\sigma)$

The flow equations for the mass term $Y_t(\sigma)$ and mass function $m_t(\sigma)$ can be obtained from the flow equation for the Grassmann-valued two-point function

$$\begin{aligned}
\partial_t \bar{\Gamma}_t^{\vartheta_\alpha \vartheta^\beta} = & - \bar{\vartheta}_\alpha \left[\text{diagram 1} \right] \vartheta^\beta - \bar{\vartheta}_\alpha \left[\text{diagram 2} \right] \vartheta^\beta - \\
& - \bar{\vartheta}_\alpha \left[\text{diagram 3} \right] \vartheta^\beta - \bar{\vartheta}_\alpha \left[\text{diagram 4} \right] \vartheta^\beta - \\
& - \left[\text{diagram 5} \right] \vartheta^\beta - \frac{1}{2} \left[\text{diagram 6} \right] \vartheta^\beta - \frac{1}{2} \left[\text{diagram 7} \right] \vartheta^\beta, \tag{3.227}
\end{aligned}$$

by means of appropriate contractions:

$$\partial_t Y_t(\sigma) = i(t_3)^\beta_\alpha \partial_t \bar{\Gamma}_t^{\vartheta_\alpha \vartheta^\beta} = \mathcal{F}_t^Y[\sigma; u_t^{(0,1)}(\sigma), m_t^{(0,1)}(\sigma), Y_t^{(0,1,2)}(\sigma), g_t(\sigma)], \tag{3.228}$$

$$\partial_t m_t(\sigma) = -2(t_0)^\beta_\alpha \partial_t \bar{\Gamma}_t^{\vartheta_\alpha \vartheta^\beta} = \mathcal{F}_t^m[\sigma; u_t^{(0,1)}(\sigma), m_t^{(0,1,2)}(\sigma), Y_t^{(0,1)}(\sigma), g_t(\sigma)]. \tag{3.229}$$

The flow Eq. (3.227) follows directly from traces over Eq. (2.68). The resulting expressions for \mathcal{F}_t^Y and \mathcal{F}_t^m are rather lengthy and can be found in Sec. 2.4 of our auxiliary notebook [642].

An important structural difference between the FRG flows $\mathcal{F}_t^Y[\dots]$ and $\mathcal{F}_t^m[\dots]$ for the Grassmann-valued couplings and the one for the scalar self-interaction potential $\mathcal{F}_t^U[\dots]$ is, that $\mathcal{F}_t^Y[\dots]$ ($\mathcal{F}_t^m[\dots]$) includes a dependence on $Y_t(\sigma)$ ($m_t(\sigma)$) primarily – but not exclusively – due to the Grassmann-valued propagators, cf. App. D.2.1. This makes a naive conservation reformulation impossible.

The (re)formulation of conservative flow equations for field-dependent couplings like the Yukawa coupling $h_t(\sigma)$ and the associated mass term $Y_t(\sigma)$ is an open problem [162, 210]. We hope to gain new insights into the issue by further considering and massaging the the flow equations of zero-dimensional Grassmann-scalar models, like the $SU(2)$ model discussed here.

A rather interesting prospect in this context are alternative projections onto $Y_t^{(1)}(\sigma)$ and $m_t^{(1)}(\sigma)$. Using the flow for the corresponding three-point function $\partial_t \bar{\Gamma}_t^{\vartheta_\alpha \vartheta^\beta \sigma}$ from Eq. (2.69)

with appropriate contractions yields:

$$\begin{aligned}\partial_t Y_t^{(1)}(\sigma) &= i(t_3)^\beta \partial_t \bar{\Gamma}_t^{\bar{\vartheta}_\alpha \vartheta^\beta \sigma} = \\ &= \mathcal{F}_t^{\partial_\sigma Y} [\sigma; u_t^{(0,1)}(\sigma), m_t^{(0,1,2)}(\sigma), Y_t^{(0,1,2,3)}(\sigma), g_t^{(0,1)}(\sigma)],\end{aligned}\quad (3.230)$$

$$\begin{aligned}\partial_t m_t^{(1)}(\sigma) &= -2(t_0)^\beta \partial_t \bar{\Gamma}_t^{\bar{\vartheta}_\alpha \vartheta^\beta \sigma} = \\ &= \mathcal{F}_t^{\partial_\sigma m} [\sigma; u_t^{(0,1)}(\sigma), m_t^{(0,1,2,3)}(\sigma), Y_t^{(0,1,2)}(\sigma), g_t^{(0,1)}(\sigma)].\end{aligned}\quad (3.231)$$

These flow equations might contain additional constraints since

$$\partial_\sigma \mathcal{F}_t^Y [\dots] \neq \mathcal{F}_t^{\partial_\sigma Y} [\dots], \quad (3.232)$$

$$\partial_\sigma \mathcal{F}_t^m [\dots] \neq \mathcal{F}_t^{\partial_\sigma m} [\dots], \quad (3.233)$$

which one might be able to use to facilitate the construction of conservative flow equations for $Y_t^{(1)}(\sigma)$ and $m_t^{(1)}(\sigma)$. This is however still subject of ongoing research and development.

Flow equation for the four-Grassmann coupling $g_t(\sigma)$

The flow equations for the four-Grassmann coupling $g_t(\sigma)$ can be obtained from the flow Eq. (2.70) for the corresponding four-point function by means of appropriate contractions:

$$\begin{aligned}\partial_t g_t(\sigma) &= -8(t_0)^\gamma \beta (t_0)^\delta \partial_t \bar{\Gamma}_t^{\bar{\vartheta}_\delta \vartheta^\gamma \bar{\vartheta}_\beta \vartheta^\alpha} = \\ &= \mathcal{F}_t^g [\sigma; u_t^{(0,1)}(\sigma), m_t^{(0,1,2)}(\sigma), Y_t^{(0,1,2)}(\sigma), g_t^{(0,1,2)}(\sigma)]\end{aligned}\quad (3.234)$$

$$\begin{aligned}&= -4 \begin{array}{c} \vartheta^\alpha \\ \swarrow \quad \searrow \\ \text{---} \otimes \text{---} \\ \nwarrow \quad \nearrow \\ \bar{\vartheta}_\beta \end{array} + \langle\langle 1 \rangle\rangle -4 \begin{array}{c} \vartheta^\alpha \\ \swarrow \quad \searrow \\ \text{---} \otimes \text{---} \\ \nwarrow \quad \nearrow \\ \bar{\vartheta}_\alpha \end{array} + \langle\langle 3 \rangle\rangle -4 \begin{array}{c} \vartheta^\alpha \\ \swarrow \quad \searrow \\ \text{---} \otimes \text{---} \\ \nwarrow \quad \nearrow \\ \bar{\vartheta}_\alpha \end{array} + \langle\langle 1 \rangle\rangle - \\ &-4 \begin{array}{c} \bar{\vartheta}_\beta \\ \swarrow \quad \searrow \\ \text{---} \otimes \text{---} \\ \nwarrow \quad \nearrow \\ \vartheta^\beta \end{array} + \langle\langle 1 \rangle\rangle -4 \begin{array}{c} \bar{\vartheta}_\beta \\ \swarrow \quad \searrow \\ \text{---} \otimes \text{---} \\ \nwarrow \quad \nearrow \\ \vartheta^\alpha \end{array} + \langle\langle 3 \rangle\rangle -4 \begin{array}{c} \bar{\vartheta}_\beta \\ \swarrow \quad \searrow \\ \text{---} \otimes \text{---} \\ \nwarrow \quad \nearrow \\ \vartheta^\alpha \end{array} + \langle\langle 1 \rangle\rangle - \\ &-4 \begin{array}{c} \vartheta^\alpha \\ \swarrow \quad \searrow \\ \text{---} \otimes \text{---} \\ \nwarrow \quad \nearrow \\ \bar{\vartheta}_\alpha \end{array} + \langle\langle 1 \rangle\rangle -4 \begin{array}{c} \vartheta^\alpha \\ \swarrow \quad \searrow \\ \text{---} \otimes \text{---} \\ \nwarrow \quad \nearrow \\ \bar{\vartheta}_\alpha \end{array} + \langle\langle 1 \rangle\rangle -4 \begin{array}{c} \vartheta^\alpha \\ \swarrow \quad \searrow \\ \text{---} \otimes \text{---} \\ \nwarrow \quad \nearrow \\ \bar{\vartheta}_\alpha \end{array} + \langle\langle 1 \rangle\rangle - \\ &-4 \begin{array}{c} \vartheta^\alpha \\ \swarrow \quad \searrow \\ \text{---} \otimes \text{---} \\ \nwarrow \quad \nearrow \\ \bar{\vartheta}_\alpha \end{array} + \langle\langle 1 \rangle\rangle -2 \begin{array}{c} \vartheta^\alpha \\ \swarrow \quad \searrow \\ \text{---} \otimes \text{---} \\ \nwarrow \quad \nearrow \\ \bar{\vartheta}_\alpha \end{array} + \langle\langle 3 \rangle\rangle -2 \begin{array}{c} \vartheta^\alpha \\ \swarrow \quad \searrow \\ \text{---} \otimes \text{---} \\ \nwarrow \quad \nearrow \\ \bar{\vartheta}_\alpha \end{array} + \langle\langle 3 \rangle\rangle -\end{aligned}$$

$$\begin{aligned}
& -2 \begin{array}{c} \bar{\vartheta}_\alpha \\ \vartheta^\alpha \\ \vartheta^\beta \\ \bar{\vartheta}_\beta \end{array} + \langle\langle 2 \rangle\rangle -2 \begin{array}{c} \bar{\vartheta}_\alpha \\ \vartheta^\alpha \\ \vartheta^\beta \\ \bar{\vartheta}_\beta \end{array} + \langle\langle 2 \rangle\rangle + \begin{array}{c} \vartheta^\alpha \\ \bar{\vartheta}_\beta \\ \vartheta^\beta \\ \bar{\vartheta}_\alpha \end{array} \\
& -2 \begin{array}{c} \bar{\vartheta}_\alpha \\ \vartheta^\alpha \\ \vartheta^\beta \\ \bar{\vartheta}_\beta \end{array} + \langle\langle 2 \rangle\rangle -2 \begin{array}{c} \bar{\vartheta}_\alpha \\ \vartheta^\alpha \\ \vartheta^\beta \\ \bar{\vartheta}_\beta \end{array} + \langle\langle 2 \rangle\rangle + \begin{array}{c} \vartheta^\alpha \\ \bar{\vartheta}_\beta \\ \vartheta^\beta \\ \bar{\vartheta}_\alpha \end{array}, \tag{3.234'}
\end{aligned}$$

where the following six classes of diagrams vanish,

$$\begin{aligned}
0 &= -4 \begin{array}{c} \vartheta^\alpha \\ \bar{\vartheta}_\beta \\ \bar{\vartheta}_\alpha \\ \vartheta^\beta \end{array} + \langle\langle 1 \rangle\rangle = -4 \begin{array}{c} \vartheta^\alpha \\ \bar{\vartheta}_\beta \\ \bar{\vartheta}_\alpha \\ \vartheta^\beta \end{array} + \langle\langle 1 \rangle\rangle = \\
&= -2 \begin{array}{c} \vartheta^\alpha \\ \bar{\vartheta}_\beta \\ \bar{\vartheta}_\alpha \\ \vartheta^\beta \end{array} + \langle\langle 5 \rangle\rangle = -2 \begin{array}{c} \vartheta^\alpha \\ \bar{\vartheta}_\beta \\ \bar{\vartheta}_\alpha \\ \vartheta^\beta \end{array} + \langle\langle 2 \rangle\rangle = \\
&= +2 \begin{array}{c} \bar{\vartheta}_\alpha \\ \vartheta^\alpha \\ \bar{\vartheta}_\beta \\ \vartheta^\beta \end{array} + \langle\langle 3 \rangle\rangle = +2 \begin{array}{c} \bar{\vartheta}_\alpha \\ \vartheta^\alpha \\ \bar{\vartheta}_\beta \\ \vartheta^\beta \end{array} + \langle\langle 3 \rangle\rangle, \tag{3.235}
\end{aligned}$$

after tracing in flavor space. Thus from the 41 classes of diagrams in Eq. (3.234), 35 have non-vanishing contributions. The resulting expression for \mathcal{F}_t^g is very lengthy and can be found in Sec. 2.5 of our auxiliary notebook [642].

As for the flow Eqs. (3.228) and (3.229) a conservative formulation for the flow equation for the field-dependent four-Grassmann coupling $\partial_t g_t(\sigma)$ is also not obvious due to the dependence $\mathcal{F}_t^g[\dots, g_t(\sigma), \dots]$. An alternative projection onto $g_t^{(1)}(\sigma)$ by means of the flow for the corresponding five-point function with an appropriate contraction

$$\begin{aligned}
\partial_t g_t(\sigma) &= -8(t_1)^\gamma{}_\beta (t_0)^\delta{}_\alpha \bar{\Gamma}_t^{\bar{\vartheta}_\delta \vartheta^\gamma \bar{\vartheta}_\beta \vartheta^\alpha \sigma} = \\
&= \mathcal{F}_t^g[\sigma; u_t^{(0,1)}(\sigma), m_t^{(0,1,2,3)}(\sigma), Y_t^{(0,1,2,3)}(\sigma), g_t^{(0,1,2,3)}(\sigma)], \tag{3.236}
\end{aligned}$$

might again be worthwhile to consider, since

$$\partial_\sigma \mathcal{F}_t^g[\dots] \neq \mathcal{F}_t^{\partial_\sigma g}[\dots]. \tag{3.237}$$

We will refrain from further discussions at this point and refer to the following outlook 3.4.

3.4. Conclusion and outlook

This section has been compiled from Secs. VI, VI, and V of our series [1–3] respectively. The following discussion also includes conceptual ideas developed in the drafts [7, 8].

The time has come to conclude our discussions of zero-dimensional QFTs, by providing a concise summary and conclusion of our results so far and by giving an outlook into further research prospects in zero dimensions. After more than 130 pages of discussions regarding ordinary and Berezin integrals, we have to report that our research into this vast field is not concluded, especially with regard to Grassmann numbers in zero dimensions.

The functional renormalization group and (numerical) fluid dynamics

We set out to study zero-dimensional theories, predominantly within the FRG, to firmly develop an understanding of FRG flow equations in a robust CFD framework, *i.e.*, as flow equations in the true sense of the word. In a way this work is a rediscovery of well known concepts of the (F)RG: it is no accident that the evolution equations are called “flow equations”. Motivated by the work [163] of Jan Keitel and Lorenz Bartosch and triggered by the publication [162] of Eduardo Grossi and Nicolas Wink, we developed a detailed understanding of FRG flow equations for zero-dimensional $O(N)$ models as highly non-linear convection equations [1–3].

In section 3.1 we rigorously and didactically developed the FRG framework in the interesting limiting case of vanishing space-time dimensions for a theory of a single scalar, *viz.* the $O(N = 1)$ a simple \mathbb{Z}_2 -symmetric integral at its core. The fact that the theories under consideration are just theories of scalars, with ordinary integrals as their generating functionals, allows for a mathematically comparatively simple (but by no means trivial) development of the FRG as an integral deformation. The governing equation of this deformation – the Wetterich equation in zero dimensions – manifests directly as a PDE without the need for any truncations. Solving this equation in the following with the FRG and comparing to exact reference results has provided us with a vast testing ground.

After generalizing our earlier discussion to a model including N scalars and $O(N)$ symmetry, we discuss the conservative formulation of the FRG flow equation for scalar theories in zero dimensions in subsection 3.2.2. The absence of any truncation and the underlying integral expressions allow for a detailed discussion of initial and boundary conditions also in the context of RG consistency. The underlying problem – N -dimensional ordinary integrals with $O(N)$ symmetry, *viz.* effectively still one-dimensional integrals, manifests on the level of the FRG flow equation for the underlying integral transformation as a highly non-trivial task. For the accurate and explicit numerical solution of the involved convection equations, we employ the well established *Kurganov-Tadmor* (KT) finite volume (FV) scheme [167, 168]. The flow equations manifest as non-linear advection-diffusion equations, where we can attribute advective contributions $\propto (N - 1)$ to π -modes and diffusive contributions are directly linked to the radial σ -mode. This formal observation already allows for a refined understanding of bosonic fluctuations in the FRG framework.

The test cases I–IV: precision tests and fluid dynamics for the $O(N)$ model in $d = 0$

The underlying nature of the generating functionals as simple integrals in zero dimensions allows us to construct an infinite amount of solvable theories in form of integrals. We limit our discussion in subsection 3.2.3 to four families of test cases, *viz.* UV initial conditions/classical actions, chosen to study different aspects of the resulting explicit FRG flows.

We have demonstrated the applicability of the implemented KT scheme for FRG flow equations by comparing the results against exact solutions for the n -point functions of the $O(N)$ model as obtained from a direct integration of the partition function. We have performed several precision tests by quantifying discretization and boundary effects.

We have also discussed the advective and diffusive contributions to the FRG flow on a qualitative level by varying the number of scalars N in the $O(N)$ model. As expected from the general discussion of the flow equations, the system becomes advection-dominated for large N . Pionic modes dominate the flow through their non-linear, hyperbolic advection term in the flow equation. For small N the diffusive contribution of the radial σ -mode becomes the dominant (in the case $N = 1$ the system is purely diffusive) driving force.

The study of discontinuous ICs (test cases I and IV) in this context highlights the capability of our chosen numerics. This comes as no surprise to the CFD initiated since, FV volume methods like the KT scheme, are purpose-build as shock-capturing and flexible black-box solvers for large classes of complicated non-linear convection equations. The proper resolution of non-linear advective contributions is at the core of the construction of such schemes. This makes FV methods, like the KT, scheme extremely attractive for FRG studies of highly non-perturbative phenomena and phase transitions in the FRG framework, *cf.* Refs. [4, 162, 210, 247, 284, 355, 648] for recent work leveraging the newly developed CFD-perspective for FRG flow equations. In all test cases, we do not observe a violation of the CMWH theorem [550–552], *i.e.*, we find that there is no spontaneous symmetry breaking in $d = 0$ in the IR limit.

We have also performed quantitative studies of the dependence on the value of the IR cutoff r_{IR} . Moreover, we have discussed RG consistency, which is related to the proper choice of UV initial scale Λ for a given initial action \mathcal{S} . We find that computations in the FRG framework require sufficiently low IR cutoffs and sufficiently large UV initial scales in order to recover the exact n -point functions. As demonstrated by our results, the explicit values for k_{IR} and Λ depend on the initial action under consideration.

Discussing the FRG Taylor (vertex) expansion as a possible truncation scheme for the Wetterich equation in the context of zero-dimensional models, we have observed that the absence of momentum suppression in $d = 0$ leads to an extremely strong coupling in field space. In turn, this greatly limits the applicability of such local expansion schemes. These findings are supported by and directly related to our novel findings (rediscoveries) regarding the irreversibility of the (F)RG flows, which we will discuss in the next two paragraphs.

Irreversibility of of FRG flows, (numerical) entropy, and a \mathcal{C} -theorem for the $O(1)$ model in $d = 0$

In subsection 3.2.4 we mainly focus on the purely diffusive case $N = 1$, *viz.* studying zero-dimensional $O(1)$ models, which are ultimately the \mathbb{Z}_2 -symmetric integrals, we discussed at the beginning of this chapter.

Based on the formulation of FRG flows as advection and diffusion driven dissipative flows in the field space along RG scale, we argued already in subsection 3.2.2.3 on general ground that (F)RG flows “produce” entropy. The RG scale/time defines a rather natural “thermodynamic” arrow of time in this respect. We concluded that this dissipative character of the (F)RG, which causes irreversibility of FRG flows, is hard coded in the Wetterich equation. This implies that the irreversibility of Kadanoff’s block-spin picture is directly encoded in the PDEs (the field-dependent beta functions), which describe the FRG flows. Hereby, the IR solutions of FRG flows represent equilibrium solutions of fluid-dynamic equations. The impossibility of an unambiguous resolution of the microphysics (UV) from the macrophysics (IR) becomes apparent from this standpoint.

We make these general arguments specific in subsection 3.2.4 by studying zero-dimensional $O(1)$ models. Using such theories, we explicitly demonstrated that the entropy production and the irreversibility during the FRG flow from the UV to the IR are not only of abstract manner, but can be quantified for $O(1)$ models in $d = 0$. Our discussion is based on the manifestation of the flow equation as a non-linear diffusion/heat equation, which allows us to leverage CFD techniques and concepts developed for such parabolic systems. Thereby, we directly related the field theoretical entropy production to the numerical entropy production from the research field of PDEs and numerical fluid dynamics, viz. to the CFD notion of total variation (TV) and its non-increasing property (TVNI).

Making use of our established set of test cases from subsection 3.2.3, we demonstrate how numerical entropy is produced by diffusion in FRG flows and non-analyticities in the UV initial conditions. Furthermore, we related certain aspects of the (numeric) entropy production in FRG flows to the concept of \mathcal{C}/\mathcal{A} -theorems in RG theory since both manifestly encode the irreversible character of FRG flows. For the zero-dimensional $O(1)$ model we argue that the numerical entropy discussed and derived in this work is in fact a valid \mathcal{C}/\mathcal{A} -function. In the sense of a meaningful zero dimension analog fulfilling all properties of \mathcal{C}/\mathcal{A} -function, which in the zero-dimensional $O(1)$ model is also directly related to absence of admissible global fixed-point solutions [3, 8].

A generalization of this notion to $N > 1$ and especially $d > 0$ still eludes us but is a very interesting direction for further research. Although certain aspects of our discussion are still on an abstract level and could not yet be formalized in terms of explicit equations, we believe that our present work provides a fresh view on certain aspects of (F)RG theory, embellished with at least a few new insights.

Particularities of the $\frac{1}{N}$ -expansion and advection-dominated FRG flows for the $O(N)$ model at large N in $d = 0$

In the last subsection 3.2.5 of this chapter dealing exclusively with scalar zero-dimensional theories, we study the $O(N)$ model at large and even infinite N . This study of advection dominated – in the limit $N \rightarrow \infty$ purely advective – FRG flow completes our studies at variable (but mainly low) N of subsection 3.2.3 and our discussion of the opposite – purely diffusive limit – $N = 1$ of subsection 3.2.4

For our studies at large N we construct a new “test case” in the spirit of subsection 3.2.3, which we have coined [an instructive toy model](#). By inspecting this non-analytic piece-wise

quadratic potential, we elucidated on the restricted applicability and validity of the large- N expansion as well as the infinite- N limit. Thereby we approached the task of calculating expectation values $\langle(\vec{\phi}^2)^n\rangle$ and the respective 1PI correlation functions $\Gamma^{(n)}$ with different methods.

On the one hand, we studied the large- N and infinite- N limit within a saddle-point expansion of the partition function. On the other hand, we used the FRG and analyzed the same problem in terms of an exact untruncated FRG flow equation. The capabilities of our KT FV numerics to handle FRG flows involving different non-analyticities, like shock and rarefaction waves, was crucial to facilitate this study of advection dominated systems at large N .

We identified two main pitfalls when it comes to the applicability of the large- N expansion or large- N limit. The first pitfall is the drastically limited applicability of the large- N approximation within certain methods, like the saddle-point expansion, where analyticity of the expansion point needs to be guaranteed (which is *a priori* hardly ensured in higher-dimensional systems). The second pitfall is, that the infinite- N limit (only retaining the zeroth-order of the large- N expansion) may alter fundamental aspects of a QFT, like the convexity of (effective) potentials, while other observables, like specific correlation functions, might not be totally off the exact results. Both effects as well as the exact results can be adequately resolved within our maturing fluid-dynamic formulation of the FRG.

Interestingly we additionally found, that a formulation purely advective flow equation in the limit $N \rightarrow \infty$, in the invariant $\varrho \equiv \frac{1}{2}\sigma^2$, has the TV as a – in the field of CFD established – numerical entropy function. In comparison with our results in the opposite ($N = 1$)-limit, we have been able to link irreversibility of purely advective FRG flows with the interaction of shock- and rarefaction waves. This is a well known observation for non-linear advection equations, which in absence of internal source terms, *i.e.*, explicit position-dependencies, are TVNI and can become irreversible, see, *e.g.*, our discussion of the BBE (2.130) in subsection 2.2.3.2.

Grassmann numbers as fermionic contributions in $d = 0$

In section 3.3 we presented our very much ongoing research of zero-dimensional theories involving scalars and pairs of Grassmann numbers. We discuss the explicit construction of an $SU(2)$ -symmetric zero-dimensional theory including four Grassmann numbers and three scalars, which we constructed to study dynamic symmetry/breaking and restoration, *i.e.*, precondensation – the formation of a non-persistent, non-trivial minimum of the EAA or other involved couplings in zero dimensions. As a theory including a four-Grassmann-coupling and a Yukawa-type interaction, the model can in a sense be considered a zero-dimensional analog to NJL- and QM-type models. In terms of field content, couplings and a treatment within the FRG the model turned out to be surprisingly complicated. Nevertheless, it is completely solvable by means of ordinary and Berezin integration.

The derivation of the complete set of field-dependent FRG flow equations is rather lengthy. This promoted us to improve our existing MATHEMATICA code [299] for computations in field space by extending its capabilities. The MATHEMATICA code/notebook [642] used for the $SU(2)$ model has a very diverse set of capabilities (derivation, manipulation, and diagrammatic visualization – both in MATHEMATICA and L^AT_EX).

On the level of the flow equation for the scalar-self-interaction potential $U_t(\sigma)$ can be recast in conservative form using the same simple derivative used for the $O(N)$ model. A conservative formulation for the flow equations of the couplings associated to Grassmann numbers is still work in progress. We encounter the same difficulties, presenting in studies of the QM model with field-dependent Yukawa coupling $h_t(\sigma)$, *cf.* Refs. [162, 210]. The goal would be to find a formulation which allows a treatment of all field-dependent couplings on equal footing, *i.e.*, to derive a system of conservation laws like, *e.g.*, the Euler-Equations, *cf.* subsection 2.2.6. Grassmann-scalar models, like the $SU(2)$ model considered here could help to gain insight into the open problem of conservative systems of flow equations in higher truncations beyond the LPA. Further interesting, and as far as we know never addressed, topics are:

- Regulator choice, *i.e.*, non-unified regulator schemes for scalars and Grassmann numbers,
- The role of the Grassmann-valued regulator as a modification/deformation of the underlying theory,
- The aforementioned conservative formulation of systems of flow equations,
- Dynamical hadronization for zero-dimensional theories,

to name a few highly interesting open questions.

In summary we identify Grassmann-scalar models, like our $SU(2)$ model, a vast and very promising field.

Outlook and future research projects

So far, throughout this chapter, we have commented at several points on the implications and impact of our zero-dimensional studies for applications in non-vanishing space-time dimensions. We will reserve a summary of these comments and findings for the general summary and outlook of this thesis in chapter 6, following our explicit application in chapter 4. In chapter 4 we will apply the developed frame work of our zero-dimensional studies to the $(1+1)$ -dimensional Gross-Neveu(-Yukawa) model, focusing on the question of symmetry-breaking and restoration at a finite number of fermion flavors N .

Regarding further applications in $d = 0$ we want to formulate two projects, which we are interested in

- **Construction of a (numeric) entropy functional for the zero-dimensional $O(N)$ model at finite $N > 1$:**
This is closely related to the discussion of fixed-point solutions and zero-dimensional variants of \mathcal{C} -/ \mathcal{A} -functions.
- **Study of a GN-type two-Grassmann-one-scalar model:**
The $SU(2)$ model considered so far might be too complicated as a first approach towards interacting Grassmann numbers in $d = 0$. It might therefore be a good idea to take a step back and consider the simplest (yet as we expect still non-trivial) theory involving just two Grassmann numbers and a single scalar. Such a model might be sufficient to study a lot of the questions raised in the [last paragraph](#).

4. Gross-Neveu model in two dimensions

Large parts of this chapter are based on Refs. [4, 5]. The individual sections include more detailed disclaimers. The involved collaborators are J. Stoll, N. Zorbach, A. Koenigstein, and S. Rechenberger as well as L. Pannullo and M. Winstel.

Ref. [4] contains results from the Master's theses [649, 650] of J. Stoll and N. Zorbach and is also discussed in A. Koenigstein's dissertation [165]. J. Stoll, N. Zorbach, A. Koenigstein, and me contributed in equal shares to this work. S. Rechenberger was involved in early stages of this project before leaving academia and contributed to the final draft.

Preliminary analytical and numerical computations for Ref. [5] were performed by S. Rechenberger (see, e.g., Ref. [651]) before he left academia but prior to Ref. [5] they were not published. The authors of Ref. [5] completed the computations and wrote Ref. [5] as a “pedagogical and detailed supplement, and completion of existing literature”. All authors contributed in equal shares to this work.

The following introduction of this chapter has been compiled from the introductions and abstracts of Refs. [4, 5].

After our lengthy discussion of theories in zero space-time dimensions the time has finally come to discuss “real” QFT, *i.e.*, theories which have a notion of space-time and actually deal with fluctuating quantum fields rather than scalars and Grassmann numbers. We have chosen to study the $(1+1)$ -dimensional Gross-Neveu (GN) model [169] for its relative simplicity, at least when compared with QCD or even the QM model.

In theoretical high-energy physics the GN model has been studied extensively as a toy model or testing ground to study effects like asymptotic freedom, (chiral) symmetry breaking and restoration, and inhomogeneous phases. In this chapter we will study the GN model and its variants with the FRG in LPA within our developed CFD framework for FRG flow equations. We study the model at finite N , exploring the role of bosonic fluctuations, and at infinite N , where bosonic fluctuations are completely suppressed.

In section 4.1 we introduce the GN model and the GNY model as a partially bosonized variant, which we will study with the FRG. In section 4.2 we adapt the CFD methods, which we developed in chapter 3, to the LPA flow equation of the GNY model.

To set up our FRG study of the GNY model at finite N in section 4.5, we first study the model in the infinite- N /mean-field limit. We use the FRG in LPA to recover the well known results for the homogeneous phase diagram at infinite N in section 4.3. Renormalization and asymptotic freedom are discussed as important aspects for the subsequent analysis at finite N .

At infinite N the GN model is renowned for its robust inhomogeneous phase, *cf.* subsection 2.4.2 and figure 2.15a. We will use the established explicit, literature results of Michael

Thies *et al.* to study inhomogeneous phases indirectly in section 4.4 using a stability analysis of the homogeneous phase. Using the literature results as reference we assess the stability analysis and the related generalized Ginzburg-Landau (gGL) analysis both qualitatively and quantitatively.

We finish the discussions in this chapter with our FRG study of the GNY model at finite N in section 4.5. We employ our CFD numerics and perspective to discuss the role of fermionic and bosonic fluctuations in FRG flows at zero and non-zero temperature and chemical potential. With this explicit LPA study we address the long standing open research question: whether there is symmetry breaking at finite N in the GN model or not. There are a lot of literature results on this topic including, heuristic arguments, large- N studies, and even lattice results but the situation remained unclear. The main result of our explicit computations is that bosonic thermal fluctuations vaporize the chiral condensate at any finite N : we do not find symmetry breaking at non-zero temperature and arbitrary chemical potential.

In section 4.6 we summarize our key research results of our studies with the GN(Y) model. Extending the present discussion beyond the LPA is identified as the logical and necessary next step.

This chapter has two primary digital auxiliary files [652, 653]. The MATHEMATICA notebook [652] includes some of the symbolic and (semi-)analytic computations of this chapter, while the C++ code [653] was used for numerical computations in the infinite- N limit.

4.1. The Gross-Neveu(-Yukawa) model

This section follows the discussion presented in Secs. I and II of Ref. [4].

Since its original publication in 1974, the Gross-Neveu (GN) model [169] – a relativistic QFT of N massless Dirac fermions that are self-interacting via the scalar channel of the four-Fermi interaction – was subject of intensive research w.r.t. various aspects of strongly interacting systems. In $1 + 1$ space-time dimensions it was studied as a (perturbatively) renormalizable prototype model for asymptotic freedom [169–179], while for $2 + 1$ space-time dimensions it served as a toy model for asymptotically safe QFTs [612] and is renormalizable with non-perturbative methods [654–657]. In $3 + 1$ dimensions it mimics the dynamics of the important scalar channel of the NJL model [64, 65] and is non-renormalizable, but can be seen as being part of a low-energy effective model of QCD, *cf.* subsection 2.3.3. However, for the rest of this chapter, we exclusively focus on its formulation in $1 + 1$ space-time dimensions.

We will use the model as a testing ground to study the stability and generalized Ginzburg-Landau (gGL) analysis for inhomogeneous phases at large N and to apply our FRG CFD methods, developed so far in zero dimensions only, to a real QFT. As such we consider the GN model as a toy model in the context of theoretical high-energy physics but it has a multitude of applications beyond such a purely theoretical scope. We will briefly comment on some applications of the GN model in the next paragraph but as mentioned in [A disclaimer about physics](#) in chapter 1, we will not attempt to comment on the possible implications of our results for physical systems in this context. While certainly interesting and relevant, such a discussion is beyond the scope of the current work, since we are ultimately interested in studies in $3 + 1$ dimensions, *cf.* chapter 5,

and we consider the results of this chapter as a stepping stone towards applications in $3 + 1$ dimensions.

Applications of the GN model for physical systems

The GN has various connections to non-relativistic models in solid-state physics, see, *e.g.*, Refs. [181, 658]. GN-type four-fermi models can arise in the continuum limit (describing large distance physics) of one-dimensional solid-state systems. Examples of such one-dimensional systems are quantum antiferromagnets (described by spin- $\frac{1}{2}$ Heisenberg models [659]), interacting electrons in a one-dimensional conductor (described by a Tomonaga–Luttinger liquid [660, 661]), and polyacetylene polymer chains [505, 662] – $(\text{CH})_x$ – (described in the limit $x \rightarrow \infty$ with the Su-Schrieffer-Heeger model [663] or the subsequent Takayama-Lin-Liu-Maki model [664]). Recently, a one-dimensional probabilistic cellular automaton, where classical bits can be interpreted as Ising spins, was shown to be equivalent to a relativistic fermionic quantum field theory [665]. A central concept behind the emergence of fermionic QFTs in two dimensions from spin-systems in one dimension is the mapping of spin operators onto fermionic creation and annihilation operators by means of the Jordan–Wigner transformation [666], for a pedagogic discussion see Ref. [658]. GN-type models also arise naturally in the continuum limit of two-dimensional spin-systems like the Ashkin-Teller model [667], which is related to the well-known Potts model [668] and as such used to study various phenomena of solid-state physics, see, *e.g.*, Ref. [669] for a general overview. In the following, we will list some explicit connections between the GN model and models used in solid-state physics.

The lattice field theoretical formulation of the GN model in the limit $N \rightarrow \infty$ is equivalent to an Ising model [670].

At finite N the GN model can be considered as the continuum limit of the N -color (N Ising spin) Ashkin-Teller model [667, 671, 672], which describes N coupled Ising spins on a two-dimensional lattice [672].

For $N = 1$ the GN model is equivalent to the Thirring model [673, 674] due to Fierz identities, *cf.* Refs. [177, 178, 658]. In the continuum limit the one-dimensional spin- $\frac{1}{2}$ Heisenberg model is equivalent to a $N = 1$ GN (Thirring) model [658]. The Thirring model also arises in the infinite volume limit of the Luttinger model [661] with strictly local interactions [675], see Ref. [658] for further details. The massive Thirring model is equivalent to the sine-Gordon model [676, 677], which in turn is (among its other application in mathematical physics) the continuum-limit of the Frenkel–Kontorova model [678]. The latter is a simple model of a harmonic chain in a periodic potential known from solid-state physics [679]. The equivalence of the Thirring model and sine-Gordon model is based on an Abelian bosonization transformation, see Refs. [658, 677] and references therein, which connects equivalent bosonic and fermionic two-dimensional quantum field theories.

Apart from research efforts in high-energy and solid-state physics the GN model is also of interest in the context of holographic methods [631, 680] especially in the study of the AdS/CFT correspondence involving higher-spin fields, see Ref. [681] for a recent review.

Phenomenology of the Gross-Neveu model

A peculiar feature of the massless GN model is, that at leading order of an $\frac{1}{N}$ -expansion,

thus in the infinite- N limit (sometimes also referred to as 't Hooft limit), the GN model dynamically develops a mass gap for the fermions, which is associated with an anti-fermion-fermion condensate $\langle \tilde{\psi} \tilde{\psi} \rangle \neq 0$. In turn, this results in the breakdown of the discrete chiral symmetry of the initial microscopic UV theory. The formation of a mass gap is a purely non-perturbative effect, see, *e.g.*, the Refs. [176, 178] for details, and is a prime example for *dimensional transmutation* – the emergence of a dimensionful scale in a theory which has only dimensionless couplings in its UV classical action, see, *e.g.*, Refs. [177, 178, 682]. Hence, by summing up loop-contributions of all orders in the four-Fermi coupling in a $\frac{1}{N}$ -expansion the discrete chiral symmetry spontaneously breaks down and is absent in the macroscopic theory in the IR. In the partially bosonized version, this amounts to integrating out the fermion-loop contribution to the bosonic effective potential, which develops a non-trivial minimum in the IR – the condensate [171, 175, 176, 178, 179].

Shortly after D. J. Gross and A. Neveu had published their results [169] on χ SB, the question arose, to what extent condensate formation is stable against thermal effects due to non-zero temperature T or an increase in density, induced by a non-zero quark chemical potential μ . Within the infinite- N limit and allowing only for spatially homogeneous condensates, the answer to these questions was quickly settled and is remarkable [183–192]: The homogeneous phase diagram of the GN model consists of a region, where the discrete chiral symmetry is broken and a region of vanishing chiral condensate, *cf.* figure 4.2. The phase-transition line between these regions splits up into a second-order phase transition (starting at $\mu = 0$ and some critical temperature $T_C \neq 0$ and ending in a CP with $\mu_{CP} \neq 0$ and $T_{CP} \neq 0$) and a first-order phase transition (starting at the critical point and ending on the $T = 0$ axis and some non-zero chemical potential μ_1). The entire phase diagram solely depends on a single dimensionful parameter, which is related to a renormalization condition, and can be chosen freely. All other dimensionful quantities are fixed multiples of this parameter and choosing a different renormalization condition (fixing some other parameter) corresponds to simple rescalings of all dimensionful quantities, but does not change their ratios, the phenomenology and the phase diagram.

Notwithstanding these early successes, the discussion on the physics of the GN model did not stop. One of the assumptions, which has led to the above results, is the assumption of a spatially homogeneous condensation of the fermions. Relaxing this assumption, but retaining the $N \rightarrow \infty$ limit, it was shown in Refs. [180–182] that there are regions in the μ - T -plane, where a spatially inhomogeneous but static condensate $\langle \tilde{\psi} \tilde{\psi} \rangle(x) \neq \text{const.}$ is energetically favored over homogeneous condensation including a vanishing of the condensate, *cf.* subsection 2.4.2 and figure 2.15a. We will discuss those inhomogeneous condensates in more detail in section 4.3.

4.1.1. The models in vacuum and at non-zero T and μ

This subsection is compiled from Secs. II.A and B and App. B of Ref. [4] and Sec. II.A of Ref. [5].

In this subsection, we introduce the GN model, its bosonized counterpart and the GNY model

in Euclidean space-time. We comment on its symmetries and its in-medium generalization for non-zero chemical potentials μ and temperatures T .

In vacuum

The GN model in one spatial and one temporal dimension in Euclidean space-time is defined by its classical action, cf. Ref. [169],

$$S_{\text{GN}}[\tilde{\psi}, \tilde{\bar{\psi}}] = \int d^2x \left(\tilde{\bar{\psi}} \gamma^\nu \partial_\nu \tilde{\psi} - \frac{g^2}{2N} (\tilde{\bar{\psi}} \tilde{\psi})^2 \right), \quad (4.1)$$

where $\tilde{\psi}$ is a N -component object in flavor space ($f = 1, 2, \dots, N$ and $N > 1$)⁶⁹ and a two-component spinor in Dirac space. Our conventions for spinors in $d = 1+1$ can be found in App. B.6.1. The action (4.1) involves a kinetic term and a four-fermion-interaction term with the dimensionless positive coupling constant $g \in \mathbb{R}^+$.

Apart from the usual Euclidean space-time symmetries (translations and a rotation), the action (4.1) is invariant under transformations of the symmetry group $G = U(1) \times SU(N) \times \mathbb{Z}_2$. The group acts on the fermion fields as follows

$$G \times \mathbb{C}^{2N} \rightarrow \mathbb{C}^{2N}, \quad (4.2a)$$

$$((\alpha, \theta, n), \tilde{\psi}) \mapsto \alpha (\theta \gamma_+ + n \theta \gamma_-) \tilde{\psi}, \quad (4.2b)$$

with $n \in \{-1, +1\}$, left- and right-handed chiral projection operators γ_\mp from Eq. (B.80), and $\alpha \in U(1)$ and $\theta \in SU(N)$. The full group G is defined as the direct product of the groups $U(1)$, $SU(N)$, and \mathbb{Z}_2 . Hereby, the $SU(N)$ symmetry is usually called flavor or color symmetry and causes, according to Noether's theorem, the conservation of a vector current. The \mathbb{Z}_2 symmetry is called discrete chiral symmetry. The $U(1)$ symmetry is called phase symmetry and leads to a conserved Noether-charge density $\tilde{\bar{\psi}} \gamma^2 \tilde{\psi}/N$, which is usually called baryon number density, which is tuned by the chemical potential μ for the fermions [522, 683–685], see also App. C.1. It is also worth mentioning, that the $SU(N)$ symmetry group of the GN model in $1 + 1$ space-time dimensions is an $O(N)$ symmetry, which is why it is sometimes also denoted as an $O(N)$ -symmetric model [178, 187]. Furthermore the GN model in two dimensions has an additional hidden $O(2N)$ symmetry between Majorana components of the fermion fields [189] which prevents the appearance of different four-fermion interaction channels during renormalization [175].

The partition function of the GN model is equivalent to the partition function of a bosonized Gross-Neveu (bGN), which can be derived by means of a Hubbard-Stratonovich (HS) transformation [452, 453]. One introduces a Gaussian integral over a bosonic auxiliary field $\tilde{\xi}$ using

$$1 = \mathcal{N} \int \mathcal{D}[\tilde{\xi}] e^{-\int d^2x \frac{\tilde{\xi}^2}{2g^2}}, \quad (4.3)$$

⁶⁹We explicitly exclude $N = 1$, where the GN model is identical to the Thirring model [673, 674], which has a vanishing perturbative one-loop beta function and different phenomenology than the GN model at $N > 1$ [177, 178]. Some details and References concerning the Thirring model can be found in the [previous paragraph](#).

with a normalization factor \mathcal{N} . Combining this with the purely fermionic grand-canonical partition function, based on the action (4.1), cf. App. C.1, we find

$$\mathcal{Z} \propto \int \mathcal{D}[\tilde{\xi}, \tilde{\psi}, \tilde{\bar{\psi}}] e^{-\int d^2x [\tilde{\bar{\psi}} \gamma^\nu \partial_\nu \tilde{\psi} - \frac{g^2}{2N} (\tilde{\bar{\psi}} \tilde{\psi})^2 + \frac{\tilde{\xi}^2}{2g^2}]}. \quad (4.4)$$

Next, we shift the bosonic field integration variable

$$\tilde{\xi} = h\phi + \frac{g^2}{\sqrt{N}} \tilde{\bar{\psi}} \tilde{\psi}, \quad (4.5)$$

where we introduced the Yukawa coupling constant h in order to have bosonic fields ϕ ⁷⁰ with zero energy dimension, which is natural in two dimensions. The real scalar field ϕ usually called “auxiliary” or “constraint” field [175, 186, 187, 686]. Using

$$\frac{1}{2g^2} \tilde{\xi}^2 = \frac{h^2}{2g^2} \phi^2 + \frac{h}{\sqrt{N}} \tilde{\bar{\psi}} \phi \tilde{\psi} + \frac{g^2}{2N} (\tilde{\bar{\psi}} \tilde{\psi})^2, \quad (4.6)$$

we can completely eliminate the four-Fermi interaction term in favor of a Yukawa interaction term,

$$\mathcal{Z} \propto \int \mathcal{D}[\phi, \tilde{\psi}, \tilde{\bar{\psi}}] e^{-\int d^2x [\tilde{\bar{\psi}} (\gamma^\nu \partial_\nu + \frac{h}{\sqrt{N}} \phi) \tilde{\psi} + \frac{h^2}{2g^2} \phi^2]}. \quad (4.7)$$

This complete bosonization of the four-fermi interaction channel is reminiscent to the construction discussed in subsection 2.3.3 in the context of dynamical hadronization in composite FRG flows of QCD.

Using Eq. (4.7), we define the action of the bGN as

$$S_{\text{bGN}}[\phi, \tilde{\psi}, \tilde{\bar{\psi}}] = \int d^2x [\tilde{\bar{\psi}} (\gamma^\nu \partial_\nu + \frac{h}{\sqrt{N}} \phi) \tilde{\psi} + \frac{h^2}{2g^2} \phi^2], \quad (4.8)$$

which is equivalent to the action Eq. (4.1) of the original GN model. Equivalent in this context means, that both theories share the same correlation functions, see the discussion at the beginning of subsection 4.2.1 or the textbooks [177, 178] for additional details.

In the bosonized version (4.8), the four-Fermi interaction is replaced by a Yukawa interaction term with coupling constant h as well as a quadratic (mass) term h^2/g^2 for the auxiliary field ϕ . If we postulate

$$G \times \mathbb{R} \rightarrow \mathbb{R}, \quad (4.9a)$$

$$((\alpha, \theta, n), \phi) \mapsto n\phi, \quad (4.9b)$$

then the action (4.8) is invariant under the same symmetry group G as the original action (4.1). Within this work, we are especially interested in the discrete chiral symmetry transformation, which we understand as the group element $(\alpha, \theta, n) = (1, \mathbb{1}_N, -1) \in G$, i.e.,

$$\tilde{\psi} \mapsto \tilde{\psi}' = \gamma_{\text{ch}} \tilde{\psi}, \quad \tilde{\bar{\psi}} \mapsto \tilde{\bar{\psi}}' = -\tilde{\bar{\psi}} \gamma_{\text{ch}}, \quad \phi \mapsto \phi' = -\phi. \quad (4.10)$$

⁷⁰Following the convention used throughout chapter 3 we use ϕ to denote a fluctuating field (not $\tilde{\phi}$) since we use φ for the expectation value $\langle \phi \rangle = \varphi$.

It is this symmetry which prevents the GN model from perturbatively generating a mass gap, see, *e.g.*, Refs. [169, 178].

Correlation functions of the GN and bGN are linked through Ward-Takahashi identities. Most notably among them: the expectation value of the scalar field can be related to the fermionic expectation value $\langle \tilde{\psi} \psi \rangle$,

$$\langle \phi \rangle \equiv \varphi = -\frac{g^2}{hN} \langle \tilde{\psi} \tilde{\psi} \rangle, \quad (4.11)$$

see, *e.g.*, Ref. [687] for a derivation of this well known identity. For this expectation value the discrete symmetry transformation (4.10) is realized as follows,

$$\langle \tilde{\psi} \tilde{\psi} \rangle \mapsto -\langle \tilde{\psi} \tilde{\psi} \rangle \quad \Leftrightarrow \quad \varphi \mapsto -\varphi. \quad (4.12)$$

Since the expectation value of $\langle \phi \rangle \equiv \varphi$ is directly proportional to this condensate, a non-vanishing φ implies a spontaneous breaking of the discrete chiral symmetry.

By including an additional kinetic term for the bosonic field we obtain the Gross-Neveu-Yukawa (GNY) model [176, 178, 656]

$$S[\phi, \tilde{\psi}, \tilde{\psi}] = \int d^2x \left[\tilde{\psi} (\gamma^\nu \partial_\nu + \frac{h}{\sqrt{N}} \phi) \tilde{\psi} - \phi (\square \phi) + \frac{h^2}{2g^2} \phi^2 \right], \quad (4.13)$$

which we will use for practical computations in the FRG framework. We elaborate on the specific model choice and differences between the (b)GN and GNY model in subsection 4.2.1.

In medium

In this work, we are mainly interested in the in-medium properties of the GNY model. To work at non-zero baryon density, we fix the net baryon number density by introducing a quark chemical potential μ in the usual manner, *cf.* App. C.1, *viz.* by subtracting

$$\mu N \equiv \mu \int dx \int_0^\beta d\tau \tilde{\psi} \gamma^2 \tilde{\psi} \quad (4.14)$$

from the classical UV action, which yields the grand canonical partition function

$$\mathcal{Z} \propto \int \mathcal{D}[\phi, \tilde{\psi}, \tilde{\psi}] e^{-S[\phi, \tilde{\psi}, \tilde{\psi}] + \mu N}. \quad (4.15)$$

Furthermore, we introduce non-zero temperature via a compactification of the Euclidean time-direction in the usual manner, *cf.* Apps. C.1 and C.2 and specifically in this context App. C of Ref. [4].

The aforementioned steps lead us to the in-medium or thermal GNY model,

$$S[\phi, \tilde{\psi}, \tilde{\psi}] = \int dx \int_0^\beta d\tau \left[\tilde{\psi} (\gamma^\nu \partial_\nu - \mu \gamma^2 + \frac{h}{\sqrt{N}} \phi) \tilde{\psi} - \phi (\square \phi) + \frac{h^2}{2g^2} \phi^2 \right]. \quad (4.16)$$

4.2. The FRG in LPA for the Gross-Neveu-Yukawa model

This section follows the discussion presented in Secs. III and IV and App. G of Ref. [4].

After the introduction of the GN(Y) model on the level of the classical action, we will now focus on the application of the FRG to this model. We will use the FRG to investigate the research questions outlined in the introduction. The goals are to use the FRG to study the GN(Y) model both at finite and infinite N . Especially our study at finite N will serve as the first application of our developments of chapter 3 to higher-dimensional models. This study will be focused on developing a detailed understanding of both fermionic and bosonic quantum and thermal fluctuations in our CFD framework for the FRG.

We have introduced the FRG on a formal level in section 2.1 and we have discussed its application to zero-dimensional theories at length in the previous chapter 3. The major conceptual and practical challenge arising in FRG studies in non-zero dimensions is the fact that the Wetterich Eq. (2.37) manifests as a functional differential equation which can not be solved directly. As discussed in subsection 2.1.4.2, truncations are necessary to project from the functional flow equation onto a finite set of ODEs and/or PDEs.

We are aware that the FRG (at least in simple truncations like the LPA) is usually not the method of choice for quantitative high precision predictions. But it has several advantages when it comes to the research questions addressed in this work. The FRG naturally resolves fluctuation effects – including fermionic and bosonic quantum and thermal fluctuations – at different energy scales and provides direct access to our observables of interest (the condensate, the curvature masses and the effective potential) at all scales $k(t)$. The FRG as a continuum method can be used for direct computations in infinite volumes, incorporating quantum and thermal fluctuations non-perturbatively over a huge range of energies (wavelengths). Computations in finite volumes are also possible within the FRG framework. Actually, we plan to repeat the analysis of this work for the GNY model in a finite spatial volume along the lines of Refs. [688–692] elsewhere, in order to directly analyze the effects of a finite sized spatial volume and to compare our results to the ones obtained with lattice Monte-Carlo simulations [519–522, 693–695].

The advantages and shortcomings of our FRG setup for the GNY model will become clear within the following elaborations, where we introduce our truncation scheme and the explicit FRG flow equation. We will comment on the limitations of our approach, and discuss symmetry restoration/breaking within the FRG approach.

4.2.1. The GNY model in LPA truncation

In the context of this work, we use the local potential approximation (LPA), introduced in subsection 2.1.4.2, as a truncation for the Wetterich Eq. (2.37). For the GNY model this means that the EAA is approximated as

$$\bar{\Gamma}_t[\varphi, \psi, \bar{\psi}] = \int dx \int_0^\beta d\tau [\bar{\psi} (\gamma^\nu \partial_\nu - \mu\gamma^2 + \frac{\hbar}{\sqrt{N}} \varphi) \psi - \frac{1}{2} \varphi (\square\varphi) + U(t, \varphi)]. \quad (4.17)$$

In this ansatz exclusively the RG-scale-dependent effective potential $U(t, \varphi)$ is evolving with RG time t (along RG scale $k(t)$), while all other couplings (e.g., the Yukawa coupling h) are kept constant.

Although being a rather simplistic ansatz, the LPA is established as a common and powerful truncation scheme and is widely – arguably sometimes wildly – used in the FRG community, especially in the context of strongly interacting systems, e.g., low-energy effective models, cf. Ref. [231] and references therein. In the absence of fermions, the LPA can be viewed as the lowest-order contribution of a derivative expansion, cf. subsection 2.1.4.2 and references therein. The LPA is assumed to be (and is for certain setups proven to be [1–3, 162, 163, 247, 632]) a good option for systems that are strongly coupled in field space and systems, where interactions with low-momentum transfer dominate the dynamics. For further discussions on the quality or the comparison of truncation schemes, see, subsection 2.1.4.2 and in this context also Refs. [105–108, 696].

When dealing with the effects of long-range interactions (low momenta) in a low-dimensional model at non-zero μ and T (strong coupling and complicated dynamics in field space), that we are heading at, the LPA presents as a natural starting point for an analysis beyond the mean-field approximation. We are aware, that the inclusion of scale-dependent and potentially even field-dependent wave-function renormalizations and couplings (especially a scale- and potentially field-dependent Yukawa coupling $h(t, \varphi)$) would result in a significantly improved truncation. We will come back to this in subsection 4.2.1. For the moment we will just start off with the LPA, which is already an improvement compared to the commonly used mean-field approximations for the GN(Y) model, where the effects of bosonic quantum fluctuations are usually completely ignored or compared to “improved” mean-field approximations, see, e.g., Ref. [188], which include only specific (effects of) bosonic modes.

The FRG flow equation for the effective potential in the LPA is obtained, by inserting the ansatz (4.17) for $\bar{\Gamma}_t[\varphi, \psi, \bar{\psi}]$ into the Wetterich Eq. (2.37) followed by a projection onto a suited (here constant) background field configuration

$$\chi_{\text{EoM}} = \underline{\chi} \equiv (\underline{\varphi}, \underline{\psi}, \underline{\bar{\psi}}) = (\sigma, 0, 0), \quad (4.18)$$

analogous to our discussion in subsection 3.3.1.1 of the zero-dimensional $SU(2)$ model, see also Chap. 23 of Ref. [682]. Additionally one has to specify proper, explicit regulators. For a discussion on suitable choice and influences of different regulators on the FRG flow and the IR results within a truncation, we refer to Refs. [256, 259, 260, 263] and the discussion in the [next paragraph](#). In the context of our work, we use a one-dimensional LPA-optimized momentum-space regulator for fermions and bosons [259, 260], see subsection 2.1.4.1 for general remarks and App. E.1 for specifics.

Additionally and analogously to mean-field studies, we perform a rescaling of the bosonic (background) field and the scale-dependent effective potential,

$$\varphi \mapsto \tilde{\varphi} = \frac{1}{\sqrt{N}} \varphi, \quad (4.19a)$$

$$U(t, \varphi) \mapsto \tilde{U}(t, \tilde{\varphi}) = \frac{1}{N} U(t, \varphi). \quad (4.19b)$$

This rescaling allows for a comparison of calculations at different finite values of N and the infinite- N limit. In the following we are exclusively working in rescaled quantities $\tilde{\varphi}$ and $\tilde{U}(t, \tilde{\varphi})$, such that we do not maintain the “tilde” in our notation.

Using the propagators and regulator insertions of App. E.1, we obtain the LPA flow equation for the scale-dependent effective potential $U(t, \sigma)$ in rescaled quantities, by performing all traces in field and internal spaces:

$$\partial_t U(t, \sigma) = \frac{1}{N} \left(\frac{1}{2} \text{[diagram: blue dashed circle with cross]} - \text{[diagram: green solid circle with cross]} \right) \quad (4.20)$$

$$\begin{aligned} &= -\frac{1}{\pi N} \frac{k^3(t)}{2E_b(t, \partial_\sigma^2 U)} [1 + 2n_b(\beta E_b(t, \partial_\sigma^2 U))] + \\ &\quad + \frac{d_\gamma}{\pi} \frac{k^3(t)}{2E_f(t, \sigma)} [1 - n_f(\beta[E_f(t, \sigma) + \mu]) - n_f(\beta[E_f(t, \sigma) - \mu])], \end{aligned} \quad (4.21)$$

with $d_\gamma \equiv 2$, cf. App. B.6, and where we introduced the abbreviations

$$E_b(t, \partial_\sigma^2 U) \equiv \sqrt{k^2(t) + \partial_\sigma^2 U(t, \sigma)}, \quad (4.22a)$$

$$E_f(t, \sigma) \equiv \sqrt{k^2(t) + (h\sigma)^2}, \quad (4.22b)$$

for the Euclidean bosonic and fermionic “energies” (dispersion relations) and used the distribution functions of App. C.2. Note that the prefactor $1/N$ of the bosonic contributions (the first term on the r.h.s. of Eq. (4.21)) realizes the aforementioned suppression of bosonic fluctuations in the large- N limit. For the sake of completeness, all further details on the derivation of the flow equation are provided in App. E.2. Structurally this equation is (apart from the missing pion contribution) reminiscent of the flow Eq. (3.224) for the self-interaction potential of the zero-dimensional $SU(2)$ model. We will comment on this further in subsection 4.2.2.

Before we continue our main discussion, we present the zero-temperature limit of the FRG flow equation (4.21),

$$\partial_t U(t, \sigma) = -\frac{1}{\pi N} \frac{k^3(t)}{2E_b(t, \sigma)} + \frac{d_\gamma}{\pi} \frac{k^3(t)}{2E_f(t, \sigma)} \Theta\left(1 - \frac{\mu^2}{E_f^2(t, \sigma)}\right) \quad (4.23)$$

as well as the vacuum limit for $T \rightarrow 0$ and $\mu \rightarrow 0$,

$$\partial_t U(t, \sigma) = -\frac{1}{\pi N} \frac{k^3(t)}{2E_b(t, \sigma)} + \frac{d_\gamma}{\pi} \frac{k^3(t)}{2E_f(t, \sigma)}. \quad (4.24)$$

The FRG flow equation in vacuum is needed to fix the IC.

Note that Eq. (4.24) differs from the popular LPA flow equation of the effective potential for the $d = 2$ GNY model in vacuum, cf. Refs. [612, 656],

$$\partial_t U(t, \sigma) = -\frac{1}{4\pi N} \frac{k^4(t)}{2E_b^2(t, \sigma)} + \frac{d_\gamma}{4\pi} \frac{k^4(t)}{2E_f^2(t, \sigma)}, \quad (4.25)$$

due to the fact that we are using one-dimensional purely spatial LPA-optimized regulators in Eq. (4.24). Whereas Eq. (4.25) is the flow equation for two-dimensional LPA-optimized regulators. We will comment on possible implications of this difference and the explicit breaking of Euclidean Poincaré invariance in the [next paragraph](#), subsection 4.5.3.6 and App. F of Ref. [4].

Comment on regulators

At this point we ought to comment on the choice of our regulators and the caveats that go hand in hand with this choice. The regulator shape functions (E.8) which parametrize the employed regulators, cf. Eq. (E.3), only regulate the spatial momentum (direction). Hence, if the spatial (loop) momenta are smaller than the RG scale k , they are suppressed. However, the Matsubara sums are not affected by the regulator at all and frequencies of all orders of magnitude enter the FRG flow at all scales $k(t)$. This has several direct consequences.

Although regulators should in principle be in accordance with the symmetries of the theory, the employed regulators explicitly break (Euclidean) Poincaré invariance. Hence, we cannot expect to recover full (Euclidean) Poincaré symmetry in the limits $\mu \rightarrow 0$ and $T \rightarrow 0$, without the introduction of counter-terms (Ward identities) to account for this discrepancy, e.g., Refs. [102, 262] and subsection 5.2.1. This means that the IR results of the FRG flow equation (4.24) do not necessarily coincide with IR results of the vacuum LPA flow equation (4.25) that can be derived with two-dimensional LPA optimized regulators, if one uses exactly the same UV IC. Whether or not these differences manifest in physical observables in vacuum or even medium, since computations at non-zero T and μ usually use an UV IC fixated in vacuum, depends on the observable, model, and truncation under consideration, see, e.g., Refs. [102, 262] and subsection 5.2.1. Within the scope of this work we performed some test comparing results obtained with a two-dimensional LPA-optimized regulator to results obtained using the one-dimensional LPA-optimized regulator in vacuum using identical ICs. For a brief discussion see App. E of Ref. [4]. The situation for the GN(Y) model might be discussed elsewhere in more detail especially regarding regulator-dependencies at non-zero temperature [650].

One might ask now, why we are – regardless of these facts – using one-dimensional LPA-optimized regulators? The answer to this question has several aspects:

A first drawback of using two-dimensional regulators is that large classes of those regulators cause problems in the presence of chemical potentials and violate the so-called *Silver-Blaze* property [308, 697–699]. However, we are especially interested in calculations at non-zero μ . Coping with this challenge is part of state of the art research, see, e.g., Refs. [262, 263, 445], and we do not want to enter this discussion within this work.

Secondly, the analytic evaluation of the Matsubara sums or the loop-momentum integrals in Eq. (E.7) might become impossible or at least extremely challenging, which drastically complicates numerical computations. The presence of numerical sums and integrals in the flow equation would significantly increase computation time and hinder an in-depth discussion at variable T , μ and N .

Note that for non-zero temperature and chemical potential (Euclidean) Poincaré invariance is broken anyhow, such that explicitly breaking this symmetry via the regulators might not

spoil the results too drastically.

Mainly to facilitate, speed up numerical computations, and to avoid any conceptual issues at $\mu > 0$ we decided to use one-dimensional, spatial Litim regulators within this work as a first significant step beyond mean-field computations.

Interestingly, the approach of exclusively regulating spatial momenta is similar to the common strategy employed in conventional mean-field studies at non-zero temperature including the mean-field computations for the GN(Y) model [184, 186–190]. There Matsubara summations are usually executed analytically before momentum integrals are regulated at all. Divergent contributions (usually associated with vacuum quantum fluctuations) to expressions are separated from convergent (usually thermal) contributions and only the divergent parts are regulated. Both approaches include all thermal/Matsubara modes independent of RG scale or in case of mean-field studies of the chosen regularization scheme.

Truncations and ICs – Differences and similarities of GN, bGN and GNY models

In section 4.1 we introduced three distinct models by specifying their actions: the GN model defined by S_{GN} in Eq. (4.1), the bGN model defined by S_{bGN} in Eq. (4.8) and ultimately the GNY model defined by S in Eq. (4.13). In this paragraph we will elaborate on their differences and similarities in the FRG framework with special focus on the, in this context, central issues of truncations and ICs for their respective EAAs $\bar{\Gamma}_t[\varphi, \psi, \bar{\psi}]$. As for all FRG flows (and PDEs in general) their respective solutions depend on the corresponding initial and possible BC(s). We discuss the (numerical) BCs in field space at length in subsection 3.2.2.4 and solely focus on the IC for the moment.

The GN model and its bosonized version – the bGN model – have an identical partition function and are thus physically equivalent. The bosonization procedure/HS transformation is merely a technical reformulation with the goal to eliminate the four-Fermi coupling term $\propto (\tilde{\psi}\tilde{\psi})^2$ of the GN model by introducing the auxiliary field ϕ with a mass term $\propto \phi^2$ and a Yukawa-Coupling term $\propto \phi\tilde{\psi}\tilde{\psi}$. This reformulation facilitates computations especially for non-vanishing condensates $\varphi \equiv \langle \phi \rangle \propto \langle \tilde{\psi}\tilde{\psi} \rangle$, as discussed in the context of dynamical hadronization in composite FRG flows for QCD in subsection 2.3.3. The IC for $\bar{\Gamma}_t[\chi]$ for the Wetterich Eq. (2.37) is the classical action $S[\chi]$. Within the LPA truncation the only scale-dependent quantity is the potential $U(t, \sigma)$ for which an appropriate IC at $k(t=0) = \Lambda$ can be read off directly from the classical action,

$$U(0, \sigma) = \frac{h^2}{2g^2} \sigma^2, \quad (4.26)$$

while the Yukawa coupling h keeps its initial value throughout the FRG flow in the LPA. Note that the two rescalings in Eq. (4.19) cancel for the rescaled initial potential (4.26). This IC $U(0, \sigma)$ is valid both for the bGN and GNY model and will be discussed further in subsection 4.5.2.

The only difference between the bGN (and by proxy the GN) model and the GNY model is the kinetic term $-\phi(\square\phi)$ in the latter. A corresponding contribution $-\varphi(\square\varphi)$ (in terms of classical/mean-fields $\varphi = \langle \phi \rangle$) is of course also present in the LPA ansatz (4.17) for $\bar{\Gamma}_t[\varphi, \psi, \bar{\psi}]$ of the GNY model to establish the proper IC $\bar{\Gamma}_{t=0} = S$. Such a kinetic term is needed in the FRG framework to study the effect of bosonic quantum fluctuations of ϕ at finite N . In consequence,

the LPA to the GNY model for $\bar{\Gamma}_t[\varphi, \psi, \bar{\psi}]$ seems incapable of resembling the bGN model (GN model by proxy) in the UV. One might argue that the results, which are obtained from the FRG flow equation (4.21) with IC (4.26), are consequently not directly transferable to the GN model. It seems, as if bosonic quantum fluctuations, which are linked to the kinetic term, are artificially enhanced already at the beginning of the FRG flow, while they should actually be strongly suppressed (strictly speaking vanishing directly in the UV when considering the limit $\Lambda \rightarrow \infty$) in the bGN model (4.8), which starts without the kinetic term in the UV and generates the term and bosonic fluctuations dynamically during the FRG flow.

From the FRG perspective, the intuitive way to cure this problem is the introduction of a bosonic wave-function renormalization in the kinetic term,

$$-\varphi(\square\varphi) \rightarrow -Z_\varphi(t) \varphi(\square\varphi), \quad (4.27)$$

and initializing $1 \gg Z_\varphi(0) > 0$ in the UV to make direct contact with the action (4.8) of the bGN model. Initializing $Z_\varphi(0)$ at exactly zero in the UV would lead to complications in practical computation since, e.g., the renormalized mass term $\frac{1}{Z_\varphi(t)} \partial_\sigma^2 U(t, \sigma)$ in the dispersion relation (4.22a) would diverge. Besides technical problems $Z_\varphi(0) = 0$ at a finite UV initial scale Λ would also weakly violate RG-consistency, cf. subsection 2.1.7, since fluctuations (especially fermionic ones) at scales $k > \Lambda$ would have already generated a small wave-function renormalization. Initializing the wave-function renormalization with $1 \gg Z_\varphi(0) > 0$ in the UV at a sufficiently large UV initial scale Λ – large enough at the initial scale and in doing so realizing RG consistency – leads to a direct suppression of bosonic fluctuations at the beginning of the FRG flow. This is directly seen on the level of $\bar{\Gamma}_t[\varphi, \psi, \bar{\psi}]$, where the bosonic kinetic term is suppressed by its small prefactor $Z_\varphi(t=0)$ in the UV. During the FRG flow $Z_\varphi(t)$ will turn non-zero already by its fermionic loop contribution, cf. Refs. [612, 686] and especially the corresponding discussion in subsection 4.4.2.

Hence, we already conclude at this point that a natural generalization of the LPA truncation in this work is the inclusion of a bosonic wave-function renormalization, such that the UV IC for $\bar{\Gamma}_t[\varphi, \psi, \bar{\psi}]$ in the GNY model really resembles the bGN and GN model. First steps of such a generalization/improvement are discussed in Ref. [165].

Finally, we have to briefly comment on another issue, which also stems from the truncation scheme and the mismatch of the ICs for the bGN and GNY models. The original GN action (4.1) as well as its bosonized counterpart in Eq. (4.8) without the kinetic term $-\phi(\square\phi)$ have only a single coupling constant g^2 . The artificial Yukawa coupling h introduced during the bosonization procedure can actually be absorbed in the bosonic field. In mean-field calculations, see below, this is evident, because all observables can be fixed via a single dimensionful parameter (e.g., the IR bosonic curvature mass, the IR fermion mass, the critical temperature etc.) for $\Lambda \rightarrow \infty$ and can be mapped into each other, if different renormalization schemes were chosen. Including bosonic fluctuations, i.e. the kinetic term for the bosons, the Yukawa coupling h can no longer be completely absorbed via appropriate substitutions. Hence, the model involves an additional parameter that needs to be fixed via some renormalization condition [178] – even if we stick to quadratic initial potentials (4.26).

We will comment on our specific choice of initial condition and implications on the suppression of bosonic fluctuations in the UV in subsection 4.5.2 after our discussions at infinite- N .

Dynamical symmetry breaking in FRG flows

Since the FRG is formulated in terms of the effective (average) action, we set the following criteria for (spontaneous) symmetry breaking.

The vacuum/ground state of a QFT is defined as the field configuration with least energy, which has to be a field configuration that minimizes the IR effective action $\Gamma[\chi]$, cf. Refs. [229, 240]. Hence it has to be a solution to the QEOM (2.20) for the mean-fields $\chi \equiv (\varphi, \psi, \bar{\psi})$,

$$0 \stackrel{!}{=} \left. \frac{\delta\Gamma[\chi]}{\delta\varphi} \right|_{\chi=\chi_{\text{EoM}}}, \quad (4.28a)$$

$$0 \stackrel{!}{=} \left. \frac{\delta\Gamma[\chi]}{\delta\psi} \right|_{\chi=\chi_{\text{EoM}}}, \quad (4.28b)$$

$$0 \stackrel{!}{=} \left. \frac{\delta\Gamma[\chi]}{\delta\bar{\psi}} \right|_{\chi=\chi_{\text{EoM}}}, \quad (4.28c)$$

Within our truncation (4.17), these equations reduce to the following three PDEs

$$0 = \square \varphi - \partial_\varphi U(t_{\text{IR}}, \varphi) - \frac{\hbar}{N} \bar{\psi} \psi. \quad (4.29a)$$

$$0 = (\gamma^\nu \partial_\nu - \mu \gamma^2 + \hbar \varphi) \psi, \quad (4.29b)$$

$$0 = (\partial_\nu \bar{\psi}) \gamma^\nu + \bar{\psi} (\mu \gamma^2 - \hbar \varphi), \quad (4.29c)$$

Given their nature as Grassmann-valued, fermionic fields it is natural to consider the trivial solutions $\psi(x, \tau) = 0$ and $\bar{\psi}(x, \tau) = 0$. In this chapter we do not consider explicit inhomogeneous condensation and hence assume $\varphi(x, \tau) = \text{const.} \equiv \sigma$ such that Eq. (4.29a) simply reduces to

$$0 \stackrel{!}{=} \partial_\sigma U(t_{\text{IR}}, \sigma). \quad (4.30)$$

In order to ensure that this extremum condition defines a minimum and not a maximum, we need the additional sufficient condition $\partial_\sigma^2 U(t_{\text{IR}}, \sigma) > 0$ at the extremum, viz. a positive IR curvature mass for σ .

Consequently, in the FRG framework a minimum σ_{min} of the scale-dependent effective potential $U(t, \sigma)$ in the IR (for $t \rightarrow \infty$) is considered to be a (translational invariant) ground state of our system. The system is said to be in the symmetry broken phase, if $\sigma_{\text{min}} \neq 0$, and in the symmetric phase if $\sigma_{\text{min}} = 0$, because non-trivial σ_{min} break the \mathbb{Z}_2 symmetry of the vacuum as discussed in subsection 4.1.1.

4.2.2. LPA flow equation as non-linear diffusion-source/sink equation

In this subsection we discuss the numerical implementation and manifestation in a CFD context of the LPA flow Eq. (4.21) of the GNY model. We already noted a striking resemblance between the LPA flow Eq. (4.21) of the GNY model in $d = 1+1$ and the flow Eq. (3.224) of the $SU(2)$ model in $d = 0$. In this regard the bosonic contributions in Eq. (4.21) are structurally similar to the ones encountered in the flow Eqs. (3.36) and (3.105) for the zero-dimensional $O(1)/\mathbb{Z}_2$

model. Informed by our studies in $d = 0$ of chapter 3 we take a derivative w.r.t. σ to arrive at a conservative form for the flow equation of $\partial_t \partial_\sigma U(t, \sigma) \equiv \partial_t u(t, \sigma)$:

$$\partial_t u(t, \sigma) = \frac{d}{d\sigma} Q(t, \partial_\sigma u) + S(t, \sigma), \quad (4.31)$$

where we introduced the non-linear diffusion flux

$$Q(t, \partial_\sigma u) \equiv -\frac{1}{\pi N} \frac{k^3(t)}{2E_b(t, \partial_\sigma u)} [1 + 2n_b(\beta E_b(t, \partial_\sigma u))], \quad (4.32)$$

and the non-linear source/sink term

$$S(t, \sigma) \equiv \frac{d}{d\sigma} \left(\frac{d_\gamma}{\pi} \frac{k^3(t)}{2E_f(t, \sigma)} [1 - n_f(\beta[E_f(t, \sigma) + \mu]) - n_f(\beta[E_f(t, \sigma) - \mu])] \right). \quad (4.33)$$

In primitive form the parabolic diffusive contribution in Eq. (4.31) reads

$$\frac{d}{d\sigma} Q(t, \partial_\sigma u) = \alpha(t, \partial_\sigma u) \partial_\sigma^2 u(t, \sigma), \quad (4.34)$$

We have arrived at a non-linear heat equation with a complicated source term. This formulation allows for a direct application of our CFD framework of chapter 3 and section 2.2. We have discussed diffusive contributions of the kind of Eq. (4.32) at length in subsection 3.2.4 and in our methodological introduction of diffusion equations in subsection 2.2.4. It turns out that we can apply the numerical tools and the CFD framework developed in $d = 0$ directly to the LPA flow equation in $d = 1 + 1$. Therefore we completely refrain from commenting on boundary conditions, spatial discretization, and a discussion of numerical entropy at this point since we have already discussed those aspects at length in subsections 3.2.2.3 and 3.2.2.4 and subsection 3.2.4. The only novel aspect, compared to the numerical studies in section 3.2, is the interesting source/sink term (4.33) on which we will comment in the next paragraph.

Fermionic (thermodynamic) fluctuations as sinks and sources

Formulating the FRG flow equation on the level of the derivative of the scale-dependent effective potential $u(t, \sigma) = \partial_\sigma U(t, \sigma)$ allows for a refined understanding of the dynamics induced by a non-vanishing chemical potential μ and fermionic fluctuations in general. The interpretation of the purely fermionic contribution $S(t, \sigma)$ in terms of a time-dependent source/sink term emerges naturally in the CFD framework. From Eq. (4.33) we find that the “fluid” $u(t, \sigma)$ does not explicitly enter $S(t, \sigma)$ and the contribution to the flow of $u(t, \sigma)$ solely depends on the time t and position in the spatial direction σ . Actually it presents on a formal level in our flow equation as a classical potential (similar to a Newtonian gravitational potential) of a conservative (external) force field acting on the fluid, *cf.* subsection 2.2.5 and Ref. [167]. Executing the σ -derivative in Eq. (4.33) one finds that the term enters the flow equation (4.31) for $u(t, \sigma)$ with negative sign for $\mu = 0$, which explains the denotation as a “sink” for $\sigma > 0$ and “source” for $\sigma < 0$ and is responsible for symmetry breaking during the flow at $\mu = 0$. Note that the dynamics of $u(t, \sigma)$ is antisymmetric in σ . Due to this antisymmetry and w.l.o.g., we focus

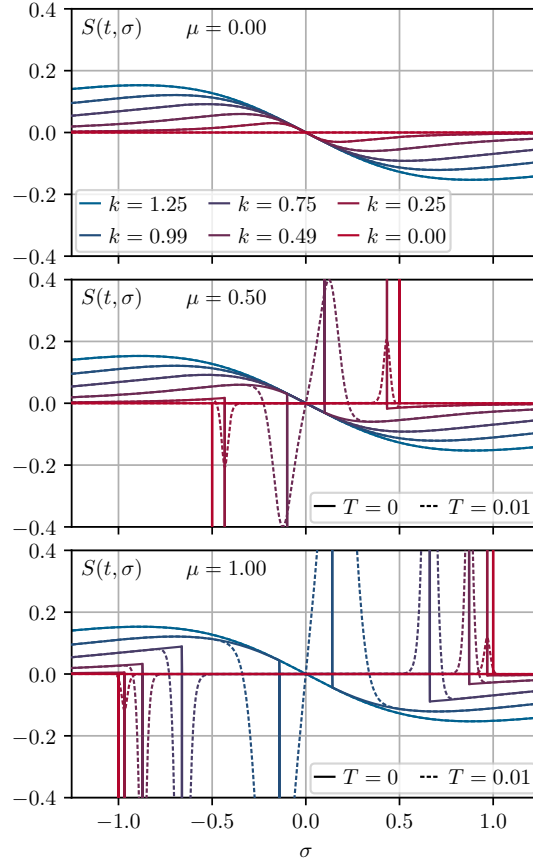


Figure 4.1.: Source/sink term of Eq. (4.33) at zero (solid lines) and small temperature $T = 0.01$ (dashed lines) at various RG scales k (close to and below the model scales) between $k = 1.25$ in blue and $k = 0$ in red at $\mu = 0$ (upper panel), $\mu = 0.5$ (middle panel) and $\mu = 1.0$ (lower panel). All dimensional quantities are measured in multiples of the Yukawa coupling h . From Fig. 1 of Ref. [4].

our discussion on $\sigma \in [0, \infty)$, where the “sink” interpretation is more natural. For negative σ the dynamics has of course opposite sign. The bosonic contributions in terms of non-linear diffusion tend to fill the “sink” or distribute the “source” that is caused by the fermions and work against symmetry breaking. At non-zero μ the sink/source term (4.33) is not always manifest negative/positive: it has a rather intricate dynamic (especially at low and zero temperature) and manifests as either source or sink depending on the value for σ at a given μ and t for both – negative and positive σ . We will spend the rest of this paragraph illuminating this interesting manifestation of chemical potential as externally induced shock waves/discontinuities in field space.

It turns out that the chemical potential induces discontinuities in $u(t, \sigma)$ in field space. For the sake of simplicity, we analyze the FRG flow Eq. (4.21) at vanishing (and small) temperature, viz. Eqs. (4.24) and (4.23), but on the level of $u(t, \sigma)$, cf. Eq. (4.31). We find that the difference between the $T = 0$ flow equations for $u(t, \sigma)$ at vanishing and non-vanishing chemical potential

is the contributions stemming from the derivative of the Heaviside function $\Theta(1 - \mu^2/E_f^2(t, \sigma))$ in the source/sink term. The sink/source term at different RG scales and chemical potentials is plotted in figure 4.1 for $T = 0$ and also small $T = 0.01$ to support and illustrate the following discussion. The approximate signs in the rest of this subsection hold at small temperatures and become exact for $T = 0$.

As long as $E_f^2 \gtrsim \mu^2$, effects due the chemical potential do not manifest in the FRG flow, because μ does not show up in the source/sink term, see figure 4.1. However, when $E_f^2 \approx \mu^2$, the chemical potential becomes relevant and distinguishes FRG flows with $\mu = 0$ and $\mu \neq 0$. Therefore, it is important to understand when (in terms of RG time t), where (in field space σ), and how this is going to happen. This can be done by analyzing the estimate

$$E_f^2 = k^2 + (h\sigma)^2 \approx \mu^2 \quad (4.35)$$

for different positions in field space.

The first time during the FRG flow, at which μ is going to influence the dynamics is, when $k^2(t) \approx \mu^2$, cf. figure 4.1 at $k = 0.99$ and $k = 0.49$ in the middle and lower panel. At this RG scale, we find that the chemical potential will influence the dynamics at positions in field space close to $\sigma = 0$. At slightly later RG times, when t is larger and the RG scale $k(t)$ is lowered a little, also field space positions at slightly larger $|\sigma|$ will be influenced by μ . The largest $|\sigma|$ that are directly affected by μ in the PDE are of the order $h^2\sigma^2 \approx \mu^2$. This is the case when $t \rightarrow \infty$ and $k(t) \rightarrow 0$ in Eq. (4.35), cf. figure 4.1 at $k = 0.0$ in the middle and lower panel. The peaks induced by the chemical potential are located at $\sigma \approx \pm \frac{1}{h} \sqrt{\mu^2 - k(t)^2}$ for $\mu \gtrsim k(t)$ and change the character of the sink/source term around their respective position. For $\sigma > 0$ ($\sigma < 0$) the peak presents as a source (sink).

Of course, the diffusive character of the σ -loop contribution will transport the effects of and the information about the chemical potential via diffusion also to larger $|\sigma|$. The same holds true for the non-zero temperature version of the FRG flow Eq. (4.31), where the Heaviside function is smeared out in terms of a Fermi-Dirac distribution function (C.18). However, overall the RG time t and scale $k(t)$ as well as the relevant positions in field space σ for the dynamics induced by the chemical potential are very similar at low temperatures where the dynamics is dominated by the chemical potential, cf. figure 4.1 for $T = 0.01$.

The remaining question, that needs to be answered is, how the chemical potential μ – through the source term $S(t, \sigma)$ – influences the dynamics of the FRG flow. We have argued before, that the fermionic contributions to the FRG flow of $u(t, \sigma)$ enter as local time-dependent sink terms. Now we found that the “sinking” stops suddenly at certain positions in field space and at certain RG times during the FRG flow due to the chemical potential. Hence, we expect that the chemical potential introduces a sharp edge in $u(t, \sigma)$ at $\sigma \approx 0$, when $k^2(t) \approx \mu^2$. This edge will “move” in field space like a shock wave towards larger $|\sigma|$ until it reaches $|\sigma| \approx |\mu/h|$, where it comes to a halt. This dynamics is imprinted by the underlying dynamics of the sink/source term (4.33) visualized and discussed earlier.

As already said before, this discontinuity is smeared by the diffusion and washed out right from the beginning at non-zero temperatures. However, its dynamics is clearly underlying all diffusive processes. In order to visualize the drastic effects of this discontinuity, we plot and contrast mean-field FRG flows with FRG flows involving bosonic fluctuations in subsection 4.5.3.2.

In mean-field, only the fermions are active (the sink term), such that the induced shock wave is not subject to diffusive effects and thus clearly visible.

In fact, it is the chemical potential that introduces a jump (mean-field) or cusp (finite N) discontinuity in $u(t, \sigma)$, which seems to render practical calculations at zero temperature involving bosonic fluctuations of the σ -mode impossible: The discontinuity in $u(t, \sigma)$ corresponds to a large jump in the derivative $\partial_\sigma u(t, \sigma)$ with negative sign. However, this happens at rather small $k^2(t) \approx \mu^2$, such that the bosonic energy function,

$$E_b^2(t, \partial_\sigma u(t, \sigma)) = k^2(t) + \partial_\sigma u(t, \sigma), \quad (4.36)$$

turns negative and one overshoots the pole of the bosonic propagator $\frac{1}{E_b}$ in the FRG flow equations. Preventing further numerical evolution towards the IR.

When considering a model involving also Goldstone modes, which enter the FRG flow as advective contributions, *cf.* subsections 3.2.3 and 3.2.5 and Refs. [1, 3, 162, 247], the huge gradients introduced via the chemical potential induce a shock wave that propagates towards smaller $|\sigma|$.

A possible reason, why this subtle dynamics in field space was not discussed in detail in the past within FRG studies might be that it is hardly visible and understandable on the level of the scale-dependent effective potential $U(t, \sigma)$ itself, because it is the integral of $u(t, \sigma)$, where jumps might only show up as tiny cusps, *cf.* subsection 4.5.3.2. Additionally, a lot of previous studies did not perform calculations at sufficiently low temperatures, where this effect is not completely washed out by the thermal distribution functions (C.18). At this point the underlying reason for and resolution of this practical problem are not clear to the author. The disconnection between the fermionic sector and the dynamics of $u(t, \sigma)$ in LPA, the regulator choice or the formulation⁷¹ of the flow equation could be possible reasons for this intricate problem. Solving this problem is beyond the scope of the current work. Consequently, we claim that understanding and/or capturing this effect correctly will be one of the central challenges in FRG at non-zero μ within the next years – independent of the specific models. For related discussions on these novel findings, we also refer to Refs. [162, 210, 284].

Numerical implementation within our CFD framework

In this paragraph we present the explicit numeric implementation of the FRG flow equation (4.31). To this end we adapt our developed and tested methods from sections 2.2 and 3.2.

To adequately capture highly non-linear diffusive effects as well as the position-dependent source/sink terms, we adapt our implementation of the KT scheme. We use the scheme in its semi-discrete form (2.113) and for this chapter without the advective numerical fluxes, since we do not have advective contributions in the flow Eq. (4.31). Within this chapter, we use the time-stepper `solve_ivp` with the `LSODA` option using an Adams/BDF method with automatic stiffness detection and switching from the `SciPy 1.0` library [354]. For further details, see App. F of Ref. [4]. We also cross-checked selected results with the `MATHEMATICA` codebase [325, 364–366] of chapter 3.

⁷¹A formal classification and proper weak formulation of the PDEs (4.21) and (4.31) might be paramount to understand the nature of the arising discontinuities and weak/physical solutions in their presence.

The explicit discretization of Eq. (4.31), *i.e.*, the diffusion flux (4.32) and sink term (4.33) is as follows. We consider a compact computational domain $[0, \sigma_{\max}]$, with boundary conditions according to subsection 3.2.2.4, subdivided into $n \in \mathbb{N}$ equally sized (finite) volume cells of size $\Delta\sigma$ centered at positions σ_i , $i = 0, 1, \dots, n-1$. The zeroth volume cell is centered at $\sigma = \sigma_0 = 0$, while the last cell is centered at $\sigma_{n-1} = \sigma_{\max}$. Within a single volume cell σ_i , the cell average of the “fluid” $u(t, \sigma)$ is denoted as $\bar{u}_i(t)$. The actual computation and scheme is entirely formulated via these cell averages as discussed in sections 2.2 and 3.2. For the explicit implementation of boundary conditions one ghost cell is required at each interval boundary when considering a problem involving solely diffusive contributions in the semi-discrete KT-scheme. The ghost cells are of size $\Delta\sigma$ and centered at $\sigma_{-1} = -\Delta\sigma$ and $\sigma_n = \sigma_{\max} + \Delta\sigma$. As described in subsection 3.2.2.4 we use the antisymmetry of $u(t, \sigma)$ as boundary condition to fix the cell averages of the zeroth cell and first ghost cell to $\bar{u}_0(t) = 0$ and $\bar{u}_{-1}(t) = -\bar{u}_1(t)$ for all times t respectively. For the ghost cell at σ_n we use linear extrapolation, thus for the cell average $\bar{u}_n(t) = 2\bar{u}_{n-1}(t) - \bar{u}_{n-2}(t)$ for all t . Additionally, we consider as usual the grid of cell interfaces, which are positioned at $\sigma_{i+\frac{1}{2}} \equiv \sigma_i + \frac{\Delta\sigma}{2}$.

Within this setup, the semi-discrete scheme for the non-linear diffusion-sink equation (4.31) and the evolution of the cell averages $\bar{u}_i(t)$ reads [167]

$$\partial_t \bar{u}_i = \frac{1}{\Delta\sigma} (P_{i+\frac{1}{2}} - P_{i-\frac{1}{2}}) + S_i, \quad (4.37)$$

with the sink/source term $S_i = S(t, \sigma_i)$ from Eq. (4.33) and the numerical diffusion flux (2.112) for the parabolic GNY model diffusion term (4.32).

We conclude this brief discussion of the numerical implementation of Eq. (4.31) with a comment on different discretization schemes for the sink/source term (4.33).

We want to put forward two possible discretization schemes for the source/sink term. To arrive at these schemes, we return to the initial idea of the finite volume discretization outlined in subsection 2.2.1. Consider the integral form (2.95) of the flow equation (4.31) for the i^{th} cell

$$\int_{\sigma_i - \frac{\Delta\sigma}{2}}^{\sigma_i + \frac{\Delta\sigma}{2}} d\sigma \partial_t u(t, \sigma) = \int_{\sigma_i - \frac{\Delta\sigma}{2}}^{\sigma_i + \frac{\Delta\sigma}{2}} d\sigma \left[\frac{d}{d\sigma} Q(t, \partial_\sigma u) + S(t, \sigma) \right]. \quad (4.38)$$

Keeping the control volumes fixed, one identifies the integral on the l.h.s. with the t -derivative of the cell averages of the fluid $\partial_t \bar{u}_i(t)$ times $\Delta\sigma$. The integral over the σ -derivative of the diffusion flux on the r.h.s. is approximated using the numerical diffusion flux of the KT scheme, *cf.* subsection 2.2.2. For the integral over the source/sink term $S(t, \sigma)$ we basically consider two options.

1. The first option is an approximation. One approximates the source/sink term with $S(t, \sigma_i)$ at the cell center times the cell-volume $\Delta\sigma$. Omitting the diffusive contribution, the semi-discrete flow equation for the cell averages $\bar{u}_i(t)$ reads,

$$\partial_t \bar{u}_i(t) = S(t, \sigma_i), \quad (4.39)$$

where we divided by $\Delta\sigma$.

2. The second option, which is due to a special feature of our FRG flow equation, is, to make use of the fact that the source/sink term in the flow Eq. (4.31) presents as a spatial derivative of some function $s(t, \sigma)$, which solely depends on t and σ ,

$$S(t, \sigma) = \frac{d}{d\sigma} s(t, \sigma). \quad (4.40)$$

This means that the integral on the r.h.s. of Eq. (4.38) can be calculated exactly, by evaluating $s(t, \sigma)$ on the cell surfaces $\sigma_{i+\frac{1}{2}}$. This results in,

$$\partial_t \bar{u}_i(t) = \frac{1}{\Delta\sigma} [s(t, \sigma_{i+\frac{1}{2}}) - s(t, \sigma_{i-\frac{1}{2}})], \quad (4.41)$$

where we again omitted the diffusion flux for the sake of the present discussion and divided by $\Delta\sigma$.

At first sight, it seems better to use the second exact version. However, during our calculations, we did not experience any differences in precision between both versions for $T \neq 0$, as long as $\Delta\sigma$ is not too large. Nevertheless, concerning the runtime, the first version turned out preferable in practical computations. Eventually, this might be related to the fact, that, ignoring bosonic fluctuations (no diffusion), the first version reduces exactly to the mean-field calculation for $u(t, \sigma)$ at positions σ_i , which can be directly seen from Eq. (4.39), where the PDE reduces into decoupled differential equations at the σ_i .

Though, for $T = 0$ the analytic evaluation of the σ -derivative would produce Dirac-delta distributions through the derivative of the Heaviside function, see Eq. (4.23). Delta-peaks are extremely complicated to implement in a numerical setup, but they are important at $T = 0$ and should not be disregarded. We therefore suggest to use the second version (4.41) (although it can only be used for FRG-mean-field calculations at $T = 0$ for $u(t, \sigma)$, which do not suffer from the problems described in subsection 4.2.2 and eluded to earlier in this paragraph).

We believe that there is some need for further investigations on the best discretization schemes for such fermionic contributions, see also Refs. [162, 210, 284].

4.3. Infinite- N analysis of homogeneous phases

This section follows the discussion presented in Sec. V of Ref. [4].

The results for the homogeneous phase diagram in figure 4.2 were obtained with my C++ code [653], computing 39887 points in the μ - T -plane in about an hour CPU time on an AMD Ryzen[®] 9 3900X processor (6 minutes wall time on 12 cores). The results of the Ginzburg–Landau analysis of the homogeneous phase diagram took only a few minutes to compute on an Intel[®] Core™ i7-8750H processor with the MATHEMATICA notebook [652].

In this section, we will rediscover some of the well-known results for the infinite- N (mean-field) limit of the GN(Y) model. We will demonstrate that the FRG in LPA is capable of reproducing the latter results analytically and numerically. Additionally, these mean-field calculations are

used to motivate a proper UV IC for the flow equation (4.21) in subsection 4.5.2, but also serve as a consistency check of our numerical implementation in the limit $N \rightarrow \infty$ in subsection 4.5.2.

Within subsection 4.3.1 we will discuss the effective potential of the GN(Y) model in vacuum and the related notion of asymptotic freedom in this context. In subsection 4.3.2 we present results for the homogeneous phase diagram at infinite N . We conclude this section with subsection 4.3.3, discussing the Ginzburg–Landau (GL) analysis for the GN(Y) model and Landau’s theory of phase transitions.

Mean-field, infinite- N , and FRG

Within the FRG framework (arguably even in general), the term “mean-field approximation” has no universal, agreed upon formal definition. Usually performing calculations on “mean-field level” in the context of fermionic models refers to computations including only fermionic fluctuations, while disregarding bosonic ones. Whether this includes fermionic vacuum fluctuations and/or fermionic contributions beyond the effective potential usually depends on the work under consideration. In the FRG one way to define a mean-field approximation is the usage of a LPA truncation disregarding the bosonic fluctuations. This can be formally achieved by taking the infinite- N limit for the LPA flow equation under consideration, in this chapter Eq. (4.21), after appropriate rescalings, like the ones introduced in Eq. (4.19).

However, it can be shown that in general the infinite- N limit and “ignoring the bosonic loop in a LPA truncation” is not the same procedure. In fact, if starting with a more advanced FRG truncation scheme, like LPA’, which also includes wave-function renormalizations, one finds, that even in the infinite- N limit, there are fermionic loop contributions to the bosonic wave-function renormalization, see, *e.g.*, Refs. [612, 686] and especially the corresponding discussion in subsection 4.4.2. Hence, in general the order of “limits” plays a crucial role and “choosing a truncation scheme in FRG” and “taking the infinite- N limit” do not necessarily commute. We will also mention some subtleties when it comes to variants of the mean-field approximation in section 5.2. Furthermore in models including Goldstone bosons/pions a large- N limit for fermions, *e.g.*, in the large- N_f limit for chiral fermion flavors, does not lead to the desired suppression of bosonic modes, because the Goldstone modes/pions do not form as flavor singlets – pionic contributions to the LPA flow equation are usually proportional to $N_f^2 - 1$, *cf.* Eq. (3.63). Another degree of freedom, *e.g.*, the number of colors N_c , has to be used to facilitate the large- N limit and the desired suppression of bosonic fluctuations.

For our purposes in this chapter, we simply start by definition on the level of the LPA and take all limits like the infinite- N limit or the zero- T and zero- μ limit afterwards. Hence, within our truncation, the mean-field limit and the infinite- N limit are considered to be identical, which simplifies the discussion and allows to make direct contact with established conventional mean-field computations for the GN model, *cf.* Refs. [190, 505], which consider only fermionic fluctuations on the level of the effective potential.

Performing the large- N limit for the flow equation (4.21), yields

$$\lim_{N \rightarrow \infty} \partial_t U(t, \sigma) = \frac{d_\gamma}{\pi} \frac{k^3(t)}{2E_f(t, \sigma)} (1 - n_f[\beta(E_f(t, \sigma) + \mu)] - n_f[\beta(E_f(t, \sigma) - \mu)]). \quad (4.42)$$

We find that the former PDE decouples in field space and reduces to a first-order ODE in t at each point in σ -direction. In the fluid-dynamic picture, on the level of $u(t, \sigma) = \partial_\sigma U(t, \sigma)$, this is rather intuitive, since the fermionic contribution to the flow equation (4.31) presents as a local time-dependent source/sink term (4.33) and the spatial movement of the fluid (via diffusion in field space) is totally suppressed. On a mathematical and also technical level this changes and in fact simplifies the flow equation drastically. We are no longer dealing with a non-linear parabolic PDE including a sink/source term, we are just left with a comparatively simple ODE which can be integrated directly. The notion of irreversibility of FRG flows is completely lost in this limit.

When disregarding bosonic fluctuations completely in mean-field approximation all three model variants – GN, bGN and GNY model – introduced in subsection 4.1.1 are equivalent. The bGN and GNY model are identical in mean-field approximation and the bGN model as the bosonized version of the GN model is in general physically equivalent to the latter as already discussed in subsection 4.1.1. This is the reason for us using the collective term GN(Y) model so far in this section but for the remainder of the section we will just use the term GN model.

4.3.1. The mean-field vacuum potential and asymptotic freedom

Due to the decoupling in field space, the differential equation (4.42) can be integrated analytically in $k(t)$. Using the definition of the RG time (2.12), which implies $\partial_t = -k \partial_k$, we find

$$U_{k=0}(\sigma) = U_{k=\Lambda}(\sigma) + \frac{d_\gamma}{\pi} \int_0^\Lambda dk \frac{k^2}{2E_f} (1 - n_f[\beta(E_f + \mu)] - n_f[\beta(E_f - \mu)]) \equiv \quad (4.43a)$$

$$U_0(\sigma) = U_\Lambda(\sigma) + \frac{d_\gamma}{\pi} \left[\frac{k}{2} (E_f + \frac{1}{\beta} \ln [1 + e^{-\beta(E_f + \mu)}] + \frac{1}{\beta} \ln [1 + e^{-\beta(E_f - \mu)}]) \right]_0^\Lambda - \frac{d_\gamma}{2\pi} \int_0^\Lambda dk (E_f + \frac{1}{\beta} \ln [1 + e^{-\beta(E_f + \mu)}] + \frac{1}{\beta} \ln [1 + e^{-\beta(E_f - \mu)}]), \quad (4.43b)$$

where the UV IC for this trivial integrable “FRG-flow” is given by the classical UV potential, see subsection 4.1.1,

$$U_\Lambda(\sigma) \equiv U(t=0, \sigma) = \frac{1}{2g^2} (h\sigma)^2 \quad (4.44)$$

and where we introduced the notation⁷²

$$U_k(\sigma) \equiv U_{k(t)}(\sigma) \equiv U(t, \sigma) \quad (4.45)$$

for the potential at a given RG scale k and the corresponding RG time t .

In the second line of Eq. (4.43) we integrated by parts in order to recover the usual expression for the grand canonical potential density for $\Lambda \rightarrow \infty$ (up to an infinite constant $\sim k E_f|_{k=\Lambda}$), cf.

⁷²This chapter does not share the at times lenient approach of section 2.1 and chapter 3 when it comes to when, where, and how to denote RG-scale- and -time-dependencies. We will consistently use $U_k(\sigma)$ and $U(t, \sigma)$ – i.e., the given notation of Ref. [4].

Refs. [186, 187, 190, 505]. The first terms of the integrands of Eq. (4.43) lead to divergences. These divergences have to be canceled by “renormalizing” the coupling g^2 such that the IR observables are finite and could in principle be matched with experimental observations. The renormalized version of this so-called *vacuum contribution* (the only contribution, that does not depend on μ and T) is directly linked to the IC of our FRG-flows, when solving the PDE (4.21) and ODE (4.42) (numerically), see subsection 4.5.2 and subsection 4.5.2.

For renormalization, we turn to the ($\mu = 0$)- and ($\beta \rightarrow \infty \Leftrightarrow T \rightarrow 0$)-limit of Eq. (4.43),

$$U_{0;\text{vac}}(\sigma) \equiv \lim_{\mu, T \rightarrow 0} U_0(\sigma) = \frac{h^2 \sigma^2}{2g^2} + \frac{d_\gamma}{2\pi} \int_0^\Lambda dk \frac{k^2}{\sqrt{k^2 + h^2 \sigma^2}}, \quad (4.46)$$

and study the corresponding gap equation

$$0 \stackrel{!}{=} \frac{1}{h^2 \sigma_0} \partial_\sigma U_{0;\text{vac}}(\sigma) \Big|_{\sigma=\sigma_0} = \frac{1}{g^2} - \frac{d_\gamma}{2\pi} \int_0^\Lambda dk \frac{k^2}{(k^2 + h^2 \sigma_0^2)^{\frac{3}{2}}} \quad (4.47a)$$

$$= \frac{1}{g^2} + \frac{d_\gamma}{2\pi} \left[\frac{k}{\sqrt{k^2 + h^2 \sigma_0^2}} \Big|_0^\Lambda - \int_0^\Lambda dk \frac{1}{\sqrt{k^2 + h^2 \sigma_0^2}} \right] \quad (4.47b)$$

$$= \frac{1}{g^2} + \frac{d_\gamma}{2\pi} \left[\left[1 + \left(\frac{h\sigma_0}{\Lambda} \right)^2 \right]^{-\frac{1}{2}} - \text{artanh} \left(\left[1 + \left(\frac{h\sigma_0}{\Lambda} \right)^2 \right]^{-\frac{1}{2}} \right) \right]. \quad (4.47c)$$

at possible non-trivial minima $\sigma_0 \neq 0$, cf. Refs. [171, 190, 505]. Hence, as a first result, assuming that σ_0 is non-zero and finite, we can study the asymptotic behavior of Eq. (4.47) for $\Lambda \gg h$,

$$\frac{1}{g^2} = \frac{d_\gamma}{2\pi} \left[-1 + \frac{1}{2} \ln \left(\left(\frac{2\Lambda}{h\sigma_0} \right)^2 \right) \right] + \mathcal{O} \left(\left(\frac{h\sigma_0}{\Lambda} \right)^2 \right). \quad (4.48)$$

This reflects the asymptotically free behavior of the four-Fermi coupling [169, 177, 178] of the original Gross-Neveu model (4.1), since

$$\lim_{\frac{\Lambda}{h} \rightarrow \infty} g^2 = 0. \quad (4.49)$$

Furthermore, we can use (4.48) and solve for σ_0 ,

$$\sigma_0 = \pm \frac{2\Lambda}{h} e^{-\frac{4\pi}{d_\gamma g^2} - \frac{1}{2}}. \quad (4.50)$$

Hence, due to the asymptotic free behavior of g^2 , there is \mathbb{Z}_2 (discrete chiral) symmetry breaking via two non-trivial minima for all non-zero g^2 in vacuum and for infinite- N – a central result for the GN model [169].

Furthermore, we can insert the results from the gap equation (4.47) in Eq. (4.44) and solve for the UV potential

$$U_\Lambda(\sigma) = \frac{d_\gamma}{4\pi} (h\sigma)^2 \left[\text{artanh} \left(\left[1 + \left(\frac{h\sigma_0}{\Lambda} \right)^2 \right]^{-\frac{1}{2}} \right) - \left[1 + \left(\frac{h\sigma_0}{\Lambda} \right)^2 \right]^{-\frac{1}{2}} \right]. \quad (4.51)$$

In the limit $\frac{\Lambda}{h} \rightarrow \infty$ we approach the Gaussian fixed point (UV fixed point) for the bGN model (4.8), which becomes clear when considering dimensionless quantities

$$\tilde{h} = \frac{1}{\Lambda} h, \quad \tilde{U}_\Lambda(\sigma) = \frac{1}{\Lambda^2} U_\Lambda(\sigma). \quad (4.52)$$

Both, \tilde{h} and $\tilde{U}_\Lambda(\sigma)$, vanish in the limit $\frac{\Lambda}{h} \rightarrow \infty$. This implies – as expected – that the bGN model (4.8) in vacuum in the infinite- N limit, is also asymptotically free.

Turning now to the IR mean-field potential (4.46) and using the previous results, we find

$$U_{0;\text{vac}}(\sigma) = \frac{d_\gamma}{4\pi} (h\sigma)^2 \left[\text{artanh} \left(\left[1 + \left(\frac{h\sigma_0}{\Lambda} \right)^2 \right]^{-\frac{1}{2}} \right) - \left[1 + \left(\frac{h\sigma_0}{\Lambda} \right)^2 \right]^{-\frac{1}{2}} - \text{artanh} \left(\left[1 + \left(\frac{h\sigma}{\Lambda} \right)^2 \right]^{-\frac{1}{2}} \right) \right] + \frac{d_\gamma}{4\pi} \Lambda^2 \sqrt{1 + \left(\frac{h\sigma}{\Lambda} \right)^2}. \quad (4.53)$$

Considering the first derivative of Eq. (4.53) one can verify $0 = \partial_\sigma U_{0;\text{vac}}(\sigma)|_{\sigma_0}$ which has to hold by construction and we note that

$$\partial_\sigma^2 U_{0;\text{vac}}(\sigma)|_{\sigma_0} = \frac{d_\gamma}{2\pi} \frac{\Lambda^3}{[\Lambda^2 + (h\sigma_0)^2]^{3/2}} h^2, \quad (4.54)$$

which is manifest positive – again consistent with the notion of σ_0 as a non-trivial minimum by construction – and corresponds to the squared curvature mass m_σ^2 of the σ -mode in vacuum.

Considering the limit $\frac{\Lambda}{h} \rightarrow \infty$ in Eq. (4.53), the divergent contributions of the two artanh cancel exactly. For the last term, we use

$$\Lambda^2 \sqrt{1 + \left(\frac{h\sigma}{\Lambda} \right)^2} = \Lambda^2 + \frac{1}{2} (h\sigma)^2 + \mathcal{O}\left(\left(\frac{h\sigma}{\Lambda}\right)^2\right), \quad (4.55)$$

which results in an unobservable infinite constant and a finite contribution. In total we find the well-known renormalized vacuum IR effective potential, cf. Refs. [190, 505],

$$U_{0;\text{vac}}(\sigma) = \frac{d_\gamma}{8\pi} (h\sigma)^2 \left(\ln \left(\frac{h\sigma}{h\sigma_0} \right)^2 - 1 \right) + \frac{d_\gamma}{4\pi} \Lambda^2 + \mathcal{O}\left(\left(\frac{h\sigma}{\Lambda}\right)^2\right), \quad (4.56)$$

with its global minimum at $\pm\sigma_0$ and with a corresponding squared curvature mass of

$$m_\sigma^2 = \frac{d_\gamma}{2\pi} h^2, \quad (4.57)$$

cf. Ref. [169].

Finally, the result (4.56) can be used to also simplify the full IR potential in medium (4.43) by replacing the vacuum contributions,

$$U_0(\sigma) = \frac{d_\gamma}{8\pi} (h\sigma)^2 \left(\left[\ln \left(\frac{h\sigma}{h\sigma_0} \right)^2 \right] - 1 \right) + \frac{d_\gamma}{4\pi} \Lambda^2 + \mathcal{O}\left(\left(\frac{h\sigma}{\Lambda}\right)^2\right) - \frac{d_\gamma}{2\pi} \int_0^\Lambda dp \left(\frac{1}{\beta} \ln [1 + e^{-\beta(E_f + \mu)}] + \frac{1}{\beta} \ln [1 + e^{-\beta(E_f - \mu)}] \right). \quad (4.58)$$

For $\Lambda \rightarrow \infty$ we can read off from Eq. (4.56) that the model contains only a single internal dimensionful parameter, for instance h , because the bosonic field σ is dimensionless and h and σ only appear in combination. All other dimensionful quantities (μ , T , Λ , U) can be expressed via this single parameter and results for different specifications of the reference parameter can be mapped into each other via simple rescaling. A direct consequence is that also the mean-field phase diagram is unique, as is discussed in the next subsection 4.3.2.

4.3.2. The mean-field phase diagram in the renormalized limit $\Lambda \rightarrow \infty$

In this subsection we will discuss the mean-field potential $U_0(\sigma)$ of Eq. (4.58) in the limit $\Lambda \rightarrow \infty$. We will compare our analytical results of this subsection with the existing renormalized mean-field results of specifically Refs. [190, 505] for the Gross-Neveu model at vanishing bare fermion mass. Of special interest is the phase-diagram (see Figure 1 of Ref. [505] or Fig. 3 of the preceding publication [190]) and the underlying renormalized grand canonical potential density, see, e.g., Eq. (4) of Ref. [505]. The results of this section will serve as a reference in the consistence check of our numerical implementation in subsection 4.5.2.

Consider the mean-field potential $U_0(\sigma)$ of Eq. (4.58) in the renormalized limit $\Lambda \rightarrow \infty$,

$$\lim_{\Lambda \rightarrow \infty} U_0(\sigma) - \frac{d_\gamma}{4\pi} \Lambda^2 = \frac{d_\gamma}{8\pi} (h\sigma)^2 \left(\ln \left[\left(\frac{h\sigma}{h\sigma_0} \right)^2 \right] - 1 \right) - \frac{d_\gamma}{4\pi} \int_{-\infty}^{+\infty} dk \left(\frac{1}{\beta} \ln [1 + e^{-\beta(E_f + \mu)}] + \frac{1}{\beta} \ln [1 + e^{-\beta(E_f - \mu)}] \right), \quad (4.59)$$

where we used the symmetry ($k \rightarrow -k$) of the remaining integral. We identify several noteworthy terms in Eq. (4.59):

- the remaining integral is the canonical one-loop, convergent medium contribution of fermions in 1+1 dimensions, cf. Eq. (C.56),
- the vacuum contribution carries a, for 1 + 1 dimensions typical [700–702], term proportional to $(h\sigma)^2 \ln(h\sigma)$,
- and we subtracted a (in σ , μ and β) constant but otherwise divergent contribution proportional Λ^2 to perform the limit $\Lambda \rightarrow \infty$. In observables this divergent but constant contribution cancels (since $U_0(\sigma)$ is only defined up to a constant) and therefore it can be subtracted from $U_0(\sigma)$ without further consequences.

For the following we therefore consider the effective potential

$$\mathcal{V}(\mu, T; \sigma) \equiv \lim_{\Lambda \rightarrow \infty} U_0(\sigma) - \frac{d_\gamma}{4\pi} \Lambda^2 = \frac{1}{4\pi} \sigma^2 \left[\ln(\sigma^2) - 1 \right] + \mathcal{V}_{\text{f,med}}(\mu, T; \sigma) \quad (4.60)$$

where we used $d_\gamma = 2$ as well as w.l.o.g. $h = 1$ and $\sigma_0 = 1$ and abbreviate the medium contribution with

$$\mathcal{V}_{\text{f,med}}(\mu, T; \sigma) \equiv -\frac{T}{2\pi} \int_{-\infty}^{+\infty} dk \ln [1 + e^{-\frac{1}{T}(E_f + \mu)}] - \frac{T}{2\pi} \int_{-\infty}^{+\infty} dk \ln [1 + e^{-\frac{1}{T}(E_f - \mu)}]. \quad (4.61)$$

For a given μ and T the physical value of the condensate σ is found by minimization of $\mathcal{V}(\mu, T; \sigma)$, according to subsection 4.2.1, App. C.1, and especially the discussion surrounding Eq. (C.15). When evaluated at its global minimum $\mathcal{V}(\mu, T; \sigma)$ is the renormalized grand canonical potential per spatial volume Ω , cf. Eq. (C.8). The renormalized (FRG) mean-field result of Eq. (4.60) for $\mathcal{V}(\mu, T; \sigma)$ obtained in the infinite- N limit of the LPA flow equation with a one-dimensional LPA-optimized regulator (4.42) coincides with the renormalized mean-field

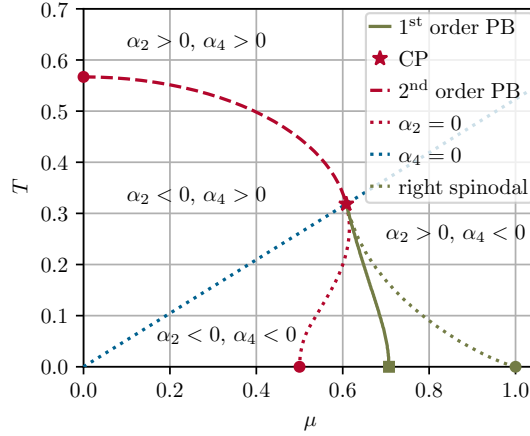


Figure 4.2.: Phase diagram of the renormalized GN model in the infinite- N limit. The critical point (red star) separates the second-order phase boundary (red-dashed line) from the first-order phase boundary (solid green line). The red-dotted line and the green-dotted line are the left and right spinodal lines. The blue ($\alpha_4 = 0$) and red ($\alpha_2 = 0$) lines are obtained from the Ginzburg-Landau expansion of subsection 4.3.3. The critical temperature T_C is marked on the T -axis with a red disk, while the end points at μ_L and μ_R of the spinodal lines are marked on the μ -axis with red and green disks respectively. The first-order phase transition at zero temperature is marked with a green square at μ_1 . From Fig. 2 of Ref. [4].

results in literature, see, *e.g.*, Refs. [190, 505], and explicitly Eq. (4) of Ref. [505]. In the rest of this subsection we derive and recapitulate known MF results for the homogeneous phase diagram of the GN model, see, *e.g.*, Refs. [190, 505].

The phase diagram of figure 4.2 identical to the one presented in Fig. 1 of Ref. [505]. The first-order phase boundary and the right spinodal have been obtained by explicit numerical integration [703] and subsequent repeated, local, numerical minimization [704] of the renormalized grand canonical potential per spatial volume (4.60) using my C++ code [653]. The phase boundaries and the spinodal region have been obtained with the help of a block-structured adaptive mesh refinement algorithm, which I implemented for the efficient computation of phase diagrams and the precise detection of lines of interest, without the need of explicit bisection. Details can be found in the C++ code [653] and its documentation – including a very instructive example using the Mandelbrot set – and in my group seminar talk [705].

By construction – due to the renormalization condition of Eq. (4.47) – discrete chiral symmetry is broken with $\sigma = \sigma_0 = 1$ in the vacuum at $T = \mu = 0$. At high chemical potentials and temperatures the discrete chiral symmetries is restored and therefore $\sigma = 0$. At intermediate temperatures and chemical potentials one observes a first-order phase transition line starting at zero temperature and non-zero chemical potential μ_1 and ending in a critical point at (μ_{CP}, T_{CP}) . Above T_{CP} discrete chiral symmetry is restored across a second-order phase transition line starting at the critical point and ending on the ($\mu = 0$)-axis at a non-zero temperature T_C .

The position of the critical point (μ_{CP}, T_{CP}) as well as μ_L , μ_1 , μ_R , and T_C can be computed with the help of known functions without the need of numerical minimization of the potential

$\mathcal{V}(\mu, T; \sigma)$. The determination of the location of the critical point and the value for the critical temperature will be discussed in the next subsection 4.3.3. We devote the remainder of this subsection to considerations at zero temperature.

For $T \rightarrow 0$ the integral in $\mathcal{V}_{\text{f;med}}(\mu, T; \Delta)$ can be performed analytically – as discussed in App. C.5 – with the result

$$\mathcal{V}_{\text{f;med}}(\mu, 0; \sigma) = \frac{1}{2\pi} \left(\sigma^2 \operatorname{arsinh} \left[\sqrt{\left(\frac{\mu}{\sigma}\right)^2 - 1} \right] - \mu^2 \sqrt{1 - \left(\frac{\sigma}{\mu}\right)^2} \right) \Theta \left[\left(\frac{\mu}{\sigma}\right)^2 - 1 \right], \quad (4.62)$$

cf. Eq. (C.77), with $\Delta \equiv h\sigma$ and $h = 1$ in the present setting. We note $\mathcal{V}_{\text{f;med}}(0, 0; \sigma) = 0$ as all vacuum contributions are already integrated out and included in Eq. (4.60). An analysis of Eq. (4.62) reveals, that the extremum at $\sigma = 0$ becomes a local minimum for $\mu > \mu_L = \frac{1}{2}$. The potential has only a trivial minimum at $\sigma = 0$ for $\mu > \mu_R = 1$. For $\mu \in [\mu_L, \mu_R]$ the potential has three minima (one at $\sigma = 0$ and two at $\sigma = \pm 1$) and at $\mu_1 = \frac{1}{\sqrt{2}} \simeq 0.707107$ all local minima become global minima signaling a first-order phase transition at μ_1 . The notable chemical potentials μ_L , μ_1 and μ_R are marked on the ($T = 0$)-axis in figure 4.2.

4.3.3. Ginzburg-Landau analysis and Landau's theory of phase transitions

We will conclude our discussion of the homogeneous phase diagram of the GN model in the infinite- N limit by considering a Ginzburg–Landau (GL) expansion/analysis of the effective potential $\mathcal{V}(\mu, T; \sigma)$ of Eq. (4.60). A GL analysis in this context is an expansion of $\mathcal{V}(\mu, T; \sigma)$ around $\sigma = 0$, resulting in a Ginzburg–Landau type theory/potential [706]. Details on such expansions in the context of theoretical physics can be found in, e.g., Refs. [63, 198, 495, 702, 707–711]. We will use this expansion to comment on first and second-order phase transitions in the spirit of Landau's theory of phase transitions [712]. A discussion of the latter in the context of the zero-dimensional theories of chapter 3 can be found in App. B of Ref. [1]. We have decided to not include this part of our studies in zero dimensions in favor of the present discussion, which is much more illuminating for the applications of this chapter and the next chapter 5.

For the medium part $\mathcal{V}_{\text{f;med}}(\mu, T; \sigma)$ of Eq. (4.62) a GL analysis is discussed in App. C.4 with the relevant results in one spatial dimensions listed in App. C.4.1 and specifically Eqs. (C.64)–(C.67). Note that these results are also included and in fact derived in the digital auxiliary MATHEMATICA notebook [713], which also includes the code employed in chapter 2 of the MATHEMATICA notebook [652], used to create the plots and results of this subsection. For the discussion in this subsection we will adopt the notation of App. C.4 and discuss the effective potential as a function of the fermion mass term $\Delta = \sigma h$. For the remainder of this subsection all dimensionful quantities are assumed to be expressed in multiples of the fermion mass term in vacuum $\Delta_0 \equiv h\sigma_0$ which has dimensions of energy. We consider an expansion up to at most order six, viz.

$$\mathcal{V}^{(6)}[\mu, T; \Delta] = \sum_{m=0}^3 \alpha_{2m}(\mu, T) \Delta^{2m}, \quad (4.63)$$

with $\alpha_{2m}(\mu, T) = \alpha_{2m}^{s=1}(\mu, T)$. For $2m \in \{0, 4, 6\}$ explicit expressions can be found in Eqs. (C.64), (C.66), and (C.67). $\alpha_2(\mu, T)$ gains a vacuum contribution from Eq. (4.56) additional to the medium contribution $\alpha_2^{(s=1)}(\mu, T)$ from Eq. (C.65) and thus reads

$$\alpha_2(\mu, T) = -\frac{1}{4\pi} + \frac{1}{2\pi} \ln \Delta + \alpha_2^{(s=1)}(\mu, T), \quad (4.64)$$

where the $(\ln \Delta)$ -term of the vacuum contribution cancels with the potential IR divergence – in form of exactly such a $(\ln \Delta)$ -term – in $\alpha_2^{(s=1)}(\mu, T)$.

The expansion (4.63) around $\sigma = 0$ can be used to compute the second-order phase-boundary in terms of known functions including the critical point. The second-order phase transition between the restored and a broken phase with small $\sigma > 0$ occurs at $\alpha_2 = 0$ while $\alpha_4 > 0$. In the vicinity of a second-order phase transition one finds $\alpha_2 > 0$ and $\alpha_4 > 0$ in the restored phase while $\alpha_2 < 0$ and $\alpha_4 > 0$ holds in the broken phase in this context. Using Eqs. (4.64) and (C.65) we find the transition temperature at $\mu = 0$

$$T_C = \frac{e^\gamma}{\pi} \simeq 0.566933. \quad (4.65)$$

The curvature κ of the second-order phase boundary $T_C(\frac{\mu}{T}) = T_C [1 - \kappa (\frac{\mu}{T})^2 + \dots]$ at $\mu = 0$ can be computed using Eq. (C.65) and is given by $\kappa = \frac{7\zeta(3)}{4\pi^2} \simeq 0.213139$. For comparison recall $\kappa' = 0.1584(9)$ from Eq. (2.180) for $N_f = 2$ QCD.

The critical point is located at the intersection of the $\alpha_2 = 0$ and $\alpha_4 = 0$ lines, see, *e.g.*, Refs. [63, 198].

Using Eq. (C.66), we determine $\frac{\mu_{\text{CP}}}{T_{\text{CP}}} \simeq 1.910669$ from the only root $z_{2,1}$ of $\text{DLi}_2(z)$ from Eq. (C.60). Having the ratio $\frac{\mu_{\text{CP}}}{T_{\text{CP}}}$ fixed, we determine

$$(\mu_{\text{CP}}, T_{\text{CP}}) \simeq (0.608221, 0.318329), \quad (4.66)$$

using Eq. (4.64). Above T_{CP} we have the second-order phase transition with $\alpha_4 > 0$, while below T_{CP} we have the spinodal region with $\alpha_4 < 0$ and $\alpha_6 > 0$ in the vicinity of the critical point. $\alpha_2 > 0$, $\alpha_4 < 0$, and $\alpha_6 > 0$ allows for three local minima in the Ginzburg-Landau potential (4.63) when considered up to $m = 3$, which indicates a first-order phase transition below T_{CP} . At the critical point ($\alpha_2 = \alpha_4 = 0$ and $\alpha_6 > 0$) the non-trivial minima from the ($\alpha_2 > 0$, $\alpha_4 < 0$)-scenario and ($\alpha_2 < 0$, $\alpha_4 > 0$)-scenario merge in $\sigma = 0$. The $\alpha_2 = 0$ line below T_{CP} signals the appearance of a local minimum at $\sigma = 0$ and is called the left spinodal line ending in μ_L at $T = 0$, in accordance with the results at $T = 0$ discussed earlier in the previous subsection 4.3.2. The $\alpha_2 = 0$ and $\alpha_4 = 0$ lines are displayed in figure 4.2.

Before discussing Landau's theory of phase transitions in the present context in the next paragraph, we will comment on the GL expansion up to order $m = 3$ and the corresponding results for the first-order phase-boundary and the right spinodal line. In the following discussion the dimensionless ratio

$$\eta_2 \equiv \frac{\alpha_2 \alpha_6}{\alpha_4^2}, \quad (4.67)$$

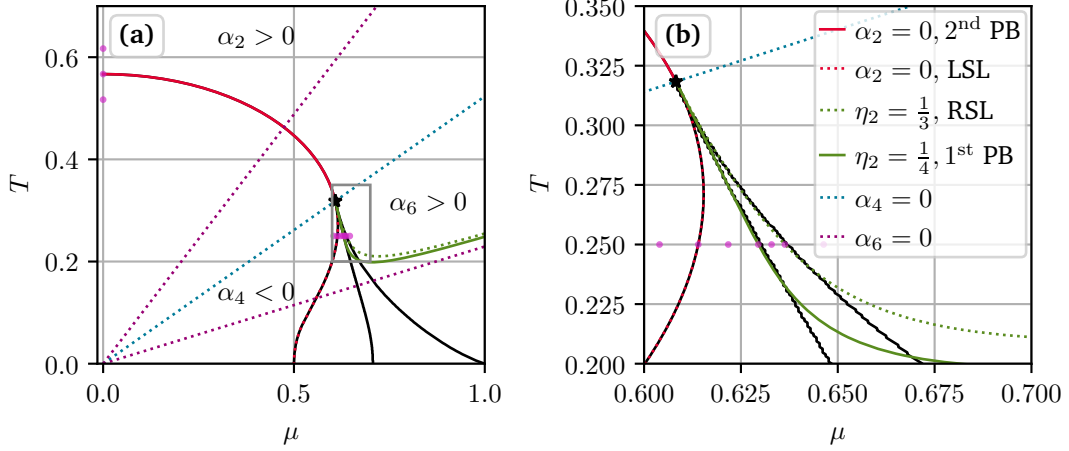


Figure 4.3.: Phase diagram of the renormalized GN model in the infinite- N limit based on the GL expansion with the right figure (b) being just a zoom-in (marked on the left (a) with a gray rectangle) around the CP. The black lines are the numerical reference lines from figure 4.2 with the finite resolution of $0.1 \cdot 2^{-7} = 7.8125 \cdot 10^{-4}$ in both μ and T visible on the right. The GL phase boundaries and lines are marked in the figure caption including their defining equation in the GL expansion. The transparent purple dots are relevant for the following discussion of phase transitions.

will be particularly useful. A simple curve discussion of $\mathcal{V}^{(6)}(\mu, T; \Delta)$ of Eq. (4.63), see subsection 5.1 of Ref. [713], reveals a spinodal region for $1 - 3\eta_2 > 0$, *i.e.*, $\mathcal{V}^{(6)}$ develops five extrema in Δ . $\eta_2 = \frac{1}{3}$ marks the right spinodal line. Further analysis reveals that at $\eta_2 = \frac{1}{4}$ the non-trivial minima at $\Delta = \pm \frac{|\alpha_4|}{2\alpha_6}$ become global minima, signaling a first-order phase transition at that point.

We are now in a position to compute the full GL-based phase diagram by means of simple contour plots [713]. In figure 4.3 we confront the results of the GL expansion with the numerical results of figure 4.2. Unsurprisingly we find a perfect agreement for the second-order phase boundary, the left spinodal line, and the critical point, since for those the GL expansion is perfectly justified. For the first-order phase transition and right spinodal line we find a good agreement in the immediate vicinity around the critical point and quickly loose predictive power as we approach $\mu/T = z_{4,2} \simeq 4.359$, where α_6 becomes negative and the expansion based on $\mathcal{V}^{(6)}$ breaks down. It should however be stressed that around the critical point the GL expansion has both qualitative and also quantitative power for both first- and second-order phase transitions.

Landau's theory of phase transitions

In the following we will discuss second- and first-order phase transitions using the GL effective potentials to fourth- and sixth-order ($\mathcal{V}^{(4)}(\mu, T; \Delta)$ and $\mathcal{V}^{(6)}(\mu, T; \Delta)$) respectively. This discussion is based on the websites [710, 711], which not only provide an excellent explanation of Landau's theory of phase transitions but also interactive tools to study them. We adapted the discussion of Refs. [710, 711] to the GN model at infinite N . To discuss second-order phase

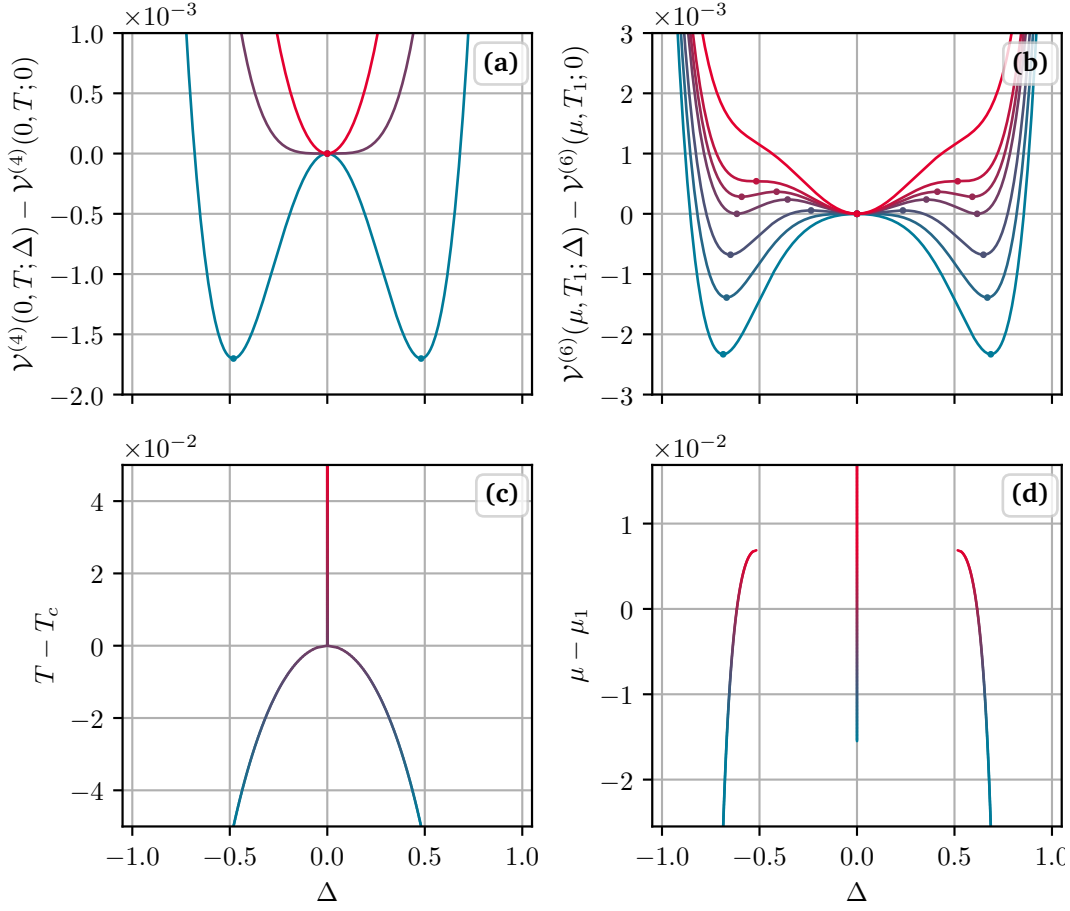


Figure 4.4.: $\mathcal{V}^{(4)}(0, T; \Delta)$ in (a) and corresponding evolution of its minima in temperature in (c). $\mathcal{V}^{(6)}(\mu, 0.25; \Delta)$ in (b) and corresponding evolution of its minima in chemical potential in (d). The extrema of the potentials are marked as dots in (a) and (b). The colors change from lower temperatures/chemical potentials in blue to higher ones in red.

transitions we follow the phase diagram at $\mu = 0$ across the second-order phase transition. To discuss first-order phase transitions we track through the spinodal region at a constant temperature $T = 0.25$. The respective relevant points for the following discussion are marked in figure 4.3 in purple.

In figures 4.4a and 4.4c we can observe symmetry restoration across a second-order phase transition, where the order parameter changes smoothly from $\Delta^2 > 0$ to $\Delta^2 = 0$. As we approach T_C from below, the non-trivial minima located at $\Delta^2 = -\frac{\alpha_2}{2\alpha_4}$ (note that $\alpha_2 < 0$ in the broken phase) melt away, *i.e.*, they continuously merge into $\Delta = 0$ as we approach $\alpha_2 = 0$ at the second-order phase boundary.

In figures 4.4b and 4.4d we can observe symmetry restoration across a first-order phase transition, where the order parameter changes discontinuously from $\Delta^2 > 0$ to $\Delta^2 = 0$. The spinodal region, where five extrema and three minima coexist, is clearly visible in figure 4.4b.

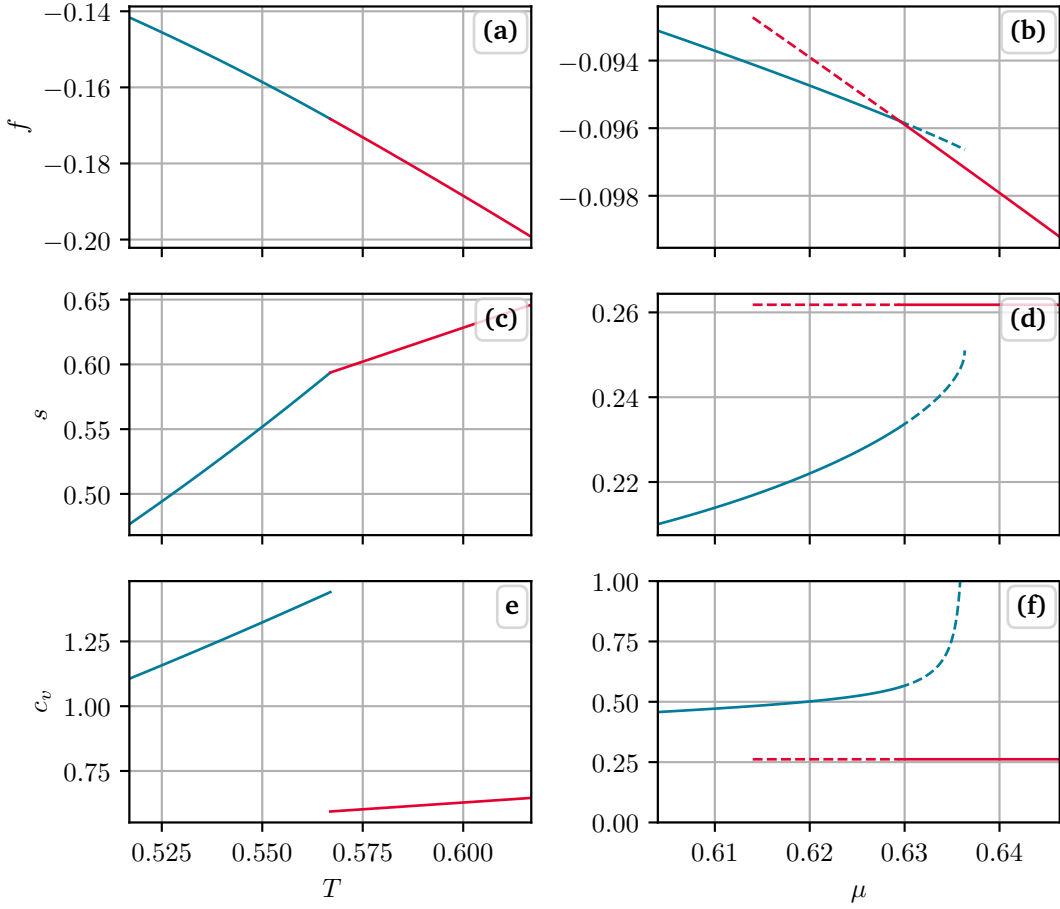


Figure 4.5.: Landau free energy density f , the entropy density s , and volumetric heat capacity c_v across the second-order (first-order) phase transition in (a), (c), and (e) ((b), (d), and (f)) respectively plotted over temperature T at $\mu = 0$ (chemical potential μ at $T = 0.25$).

At the first-order phase boundary the three minima (at $\Delta = 0$ and $\Delta = \pm \frac{|\alpha_4|}{2\alpha_6}$) become degenerate and a discontinuous jump in Δ from the broken to the restored phase takes place.

This dynamics in the effective potential also imprints itself into thermodynamic observables. Using the expressions provided in App. C.1, *i.e.*, Eqs. (C.9), (C.11), and (C.12), we can compute the Landau free energy density f , the entropy density s , and the mean quark number density n with

$$f = \mathcal{V}(\mu, T; \Delta_{\min}), \quad s = - \left(\frac{\partial f}{\partial T} \right)_{\mu}, \quad n = - \left(\frac{\partial f}{\partial \mu} \right)_T. \quad (4.68)$$

Additionally we consider the first moments of entropy and mean quark number-density, *viz.*

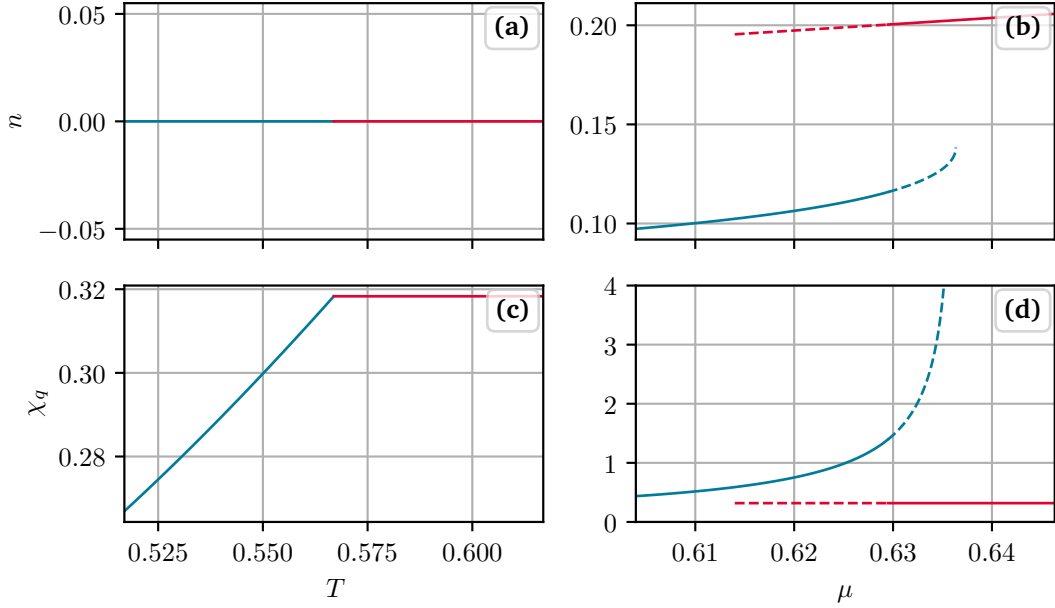


Figure 4.6.: Mean quark number-density n and quark number susceptibility χ_q across the second-order (first-order) phase transition in (a) and (c) ((b) and (d)) respectively plotted over temperature T at $\mu = 0$ (chemical potential μ at $T = 0.25$). Note that χ_q is not the slope of n in the T direction but in μ direction.

the volumetric heat capacity⁷³ c_v and quark number susceptibility χ_q with

$$c_v = T \left(\frac{\partial s}{\partial T} \right)_\mu, \quad \chi_q = \left(\frac{\partial n}{\partial \mu} \right)_T. \quad (4.69)$$

Note that the absolute value of the Landau free energy density f computed with Eq. (4.63) is not meaning full since we have not subtracted/accounted for the vacuum contribution, cf. Eq. (C.14). This is simply not possible using just the GL expansion, since the vacuum is too far out of the range of validity of the expansion for a meaningful subtraction in the sense of Eq. (C.14). That being said, the changes/differences in $f(\mu, T)$ and the derived quantities are meaningful.

We plotted the aforementioned thermodynamic quantities in figures 4.5 and 4.6 across the second- and first-order phase transition. The Landau free energy stays constant at the phase

⁷³Strictly speaking the expression (4.69) for the volumetric heat capacity is incomplete, see footnote 38 and Eq. (4.97) of Ref. [59] for details (I thank Michael Buballa for pointing this out – who in turn thanks Igor Shovkovy, who alerted him to this subtlety some time ago). The physical volumetric heat capacity is defined as the temperature dependence of the internal energy, cf. Eq. (C.13), at fixed spatial volume and fixed particle number. In the expression (4.69) we evaluate at fixed spatial volume and fixed chemical potential – not at fixed particle number. When working with the chemical potential the expression (4.69) would have to include a correction $\left(\frac{\partial^2 f}{\partial \mu^2} \right)^{-1} \left(\frac{\partial^2 f}{\partial T \partial \mu} \right)^2$ to be equivalent to the physical volumetric heat capacity. This subtlety/correction has no impact on the brief discussion of c_v in this subsection.

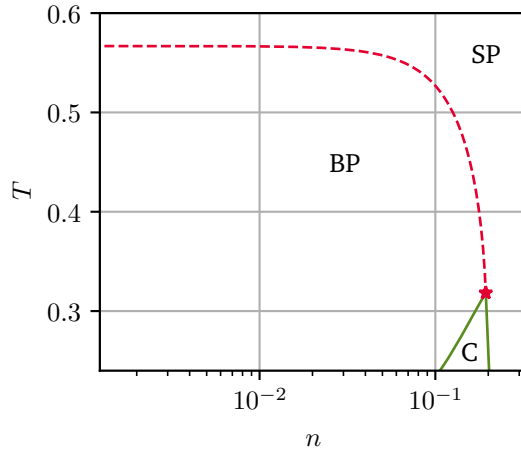


Figure 4.7.: Phase diagram in the n - T -plane of the renormalized GN model in the infinite- N limit based on the GL expansion. With BP marking the symmetry-broken phase, SP marking the symmetry-restored phase, and C marking the region of phase coexistence associated with the first-order phase transition. Note that we have plotted only down to $T = 0.25$ since the GL expansion only gives meaningful results for the first-order phase transition in the vicinity of the critical point, *cf.* figure 4.3b for a detailed plot of the analogous situation in the μ - T -plane.

transitions, *cf.* figures 4.5a and 4.5b, since the point at which the phase transitions occur is given by the point at which the energies of the trivial and non-trivial minima are degenerate.

The entropy and number density across the second-order phase transition remain constant, *cf.* figures 4.5c and 4.6a. The first discontinuity of thermodynamic variables manifests in the volumetric heat capacity, *cf.* figure 4.5e. This is consistent with the Ehrenfest classification of phase transitions [571].

For the first-order phase transition on the other hand, discontinuities arise already in first derivatives, *viz.* in the entropy and number density, *cf.* figures 4.5d and 4.6b, again in accordance with the Ehrenfest classification. This particular first-order phase transition has a latent heat per unit volume of $L = T\Delta s \simeq 7.2 \cdot 10^{-3}$. The discontinuities in entropy and number density are clear signals for a disorder-broadened first-order transition exhibiting phase coexistence. We will close this subsection with figure 4.7 – the phase diagram in the n - T -plane of the renormalized GN model in the infinite- N limit based on the GL expansion. The phase coexistence region below the critical point is clearly visible.

4.4. Infinite- N analysis of inhomogeneous phases

This section follows in large parts the discussion presented in Ref. [5]. The plots of Ref. [5] were produced by L. Pannullo.

The following introduction of this section is based on Sec. I of Ref. [5].

In this section we examine and cross-check the functionality of a stability analysis [5, 80, 87, 180, 182, 193–208] of a spatially homogeneous ground state and the closely related generalized Ginzburg-Landau (gGL) analysis [197, 493, 495, 526, 527], *cf.* our introductory remarks of subsection 2.4.1. Both present as very appealing indirect methods to study inhomogeneous phases without the need to explicitly compute with inhomogeneous condensates, thus avoiding the related major technical challenges commented on in subsection 2.4.1.

Arguably the most prominent examples for spatially inhomogeneous condensation in relativistic QFTs are observed in 1+1 dimensions. In the (1+1)-dimensional GN model in MF spatially oscillating condensates have been proven to be the true absolute ground states in some regions of the phase diagram [180, 181, 500–505], as already mentioned in our introduction of literature results in subsection 2.4.2. In this section we will examine the results, shown and discussed around figure 2.15a in detail. In the (1+1)-dimensional GN model at infinite N the exact spatial modulation of the inhomogeneous condensate was derived analytically in terms of known functions [181, 504] deploying in parts semi-analytic techniques of supersymmetric quantum mechanics [496, 499]. Also more involved (1+1)-dimensional models with more complicated symmetry breaking patterns exhibit an inhomogeneous phase (IP) [201, 497, 498, 506, 507]. For a general review regarding IPs in the context of high-energy physics, we refer again to Ref. [63] and our overview in the introduction of section 2.4.

In subsection 2.4.1 we commented on the various direct and indirect methods to study inhomogeneous phases. The stability analysis and the closely related gGL analysis as indirect methods are based on the idea to determine the ground state assuming a spatially homogeneous condensate and to study position-dependent perturbations of this state in a second step. Hence, one expands the full quantum effective action in the IR in powers of the perturbation in a functional series. By inspecting the two-point function, which is basically the curvature of the action at its homogeneous minimum (the homogeneous ground state), one can classify stable and unstable directions in field space from the sign of the two-point function. Thus, one is performing a functional curve sketching and searches for expansion points that are saddle-points of the action. A non-trivial minimum of the two-point function at non-zero external spatial momentum q signals the instability of the homogeneous phase against inhomogeneous condensation, since the ground state energy can be lowered by forming an inhomogeneous condensate with relative momentum q .

This relatively simple concept allows to examine a sufficient, but not necessary condition for an IP, *i.e.*, if the homogeneous ground state is unstable w.r.t. inhomogeneous perturbations, the ground state must be inhomogeneous. In simple terms, stability of the homogeneous condensate can be found, but the true global minimum of the action can still be an inhomogeneous field configuration located outside the range of validity of the stability analysis around the homogeneous ground state – which is of course a limitation of this approach. We discuss this limitation at length in subsection 4.4.2.2.

The gGL analysis can be seen as a variant of the stability analysis since it is basically an expansion of the stability analysis in powers of the homogeneous condensate and external momentum q . It manifests as a gradient expansion of the effective action and as such is more limited when it comes to qualitative and especially quantitative predictive power as we will discuss in subsection 4.4.3.

Howsoever, the great advantage of these techniques is, that they are basically applicable to all kinds of models and theories. They work independent of the technical method and approximation that is used to compute the underlying “expansion coefficients”.

For example, the stability analysis has been applied in mean-field studies of a broad range of models but is also used in FRG calculations or in the context of lattice field theory. There are multiple studies, see, *e.g.*, Refs. [87, 182, 193, 194, 198, 200, 202, 203, 205, 495, 526], which are based on a stability analysis or directly related approaches.

To the best of our knowledge, there has not been a significant attempt to discuss the limitations and successes of these method in great detail using a fully-understood/solved model, where the exact solution is well-known. Hence, our goal is to revisit the $(1+1)$ -dimensional GN model, as it has been solved analytically in Refs. [181, 504] with an exact solution for the ground state for all temperatures T and chemical potentials μ , and extend earlier “stability analyses”⁷⁴ within this and closely related models [180, 195, 196, 201] and the gGL analysis put forward in Ref. [495]. In this sense the present discussion is in the spirit of chapter 3: we again use exact reference values (now be it much more involved ones than just mere integrals) to rigorously test and evaluate computational methods (now the stability and gGL analysis instead of the FRG in a CFD formulation).

At this point we emphasize that the work discussed in this section is explicitly not about groundbreaking new results or a concept that is original to this work. It is merely a recapitulation and combination of existing literature results in a form that is meant to allow for a keener insight into the quantitative and qualitative predictive power of the stability analysis and related gGL analysis as indirect methods to study inhomogeneous condensates.

This section is structured as follows: In subsection 4.4.1, we briefly recapitulate the phenomenology of the GN model in the infinite- N limit, *viz.* its inhomogeneous phase diagram at (non-)zero baryon densities and (non-)zero temperature.

In subsection 4.4.2 we discuss the stability analysis. First we introduce the formalism for the stability analysis of bosonic two-point functions w.r.t. inhomogeneous perturbations. After this technical introduction we discuss explicit results for the renormalized GN model at infinite N in the subsequent subsections. In subsection 4.4.2.1 we discuss numerical results for the two-point function. The results for the detection of inhomogeneous condensation in the phase diagram via the stability analysis are presented and compared to the analytical solution of the model in subsection 4.4.2.2. In two additional subsections, namely subsections 4.4.2.3 and 4.4.2.4, we compare the dominant mode of the exact inhomogeneous condensate with the dominant wave vector from the stability analysis and further comment on the values of the bosonic wave-function renormalization and its implications.

In subsection 4.4.3 we confront the results obtained with a gGL analysis [495] with the analytical solution of the model.

⁷⁴In these works the term “almost degenerate perturbation theory (ADPT)” is used instead of “stability analysis”. However, the approach is quite similar.

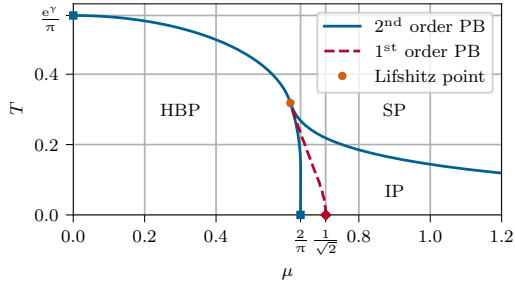


Figure 4.8.: The phase diagram of the GN model in the infinite- N limit. The dashed red curve corresponds to the first-order phase boundary that is obtained if spatially homogeneous condensation is assumed [190, 497]. The solid blue lines correspond to second-order phase transitions, if spatially inhomogeneous condensation is taken into account [181, 197, 502, 504]. From Fig. 1 of Ref. [5].

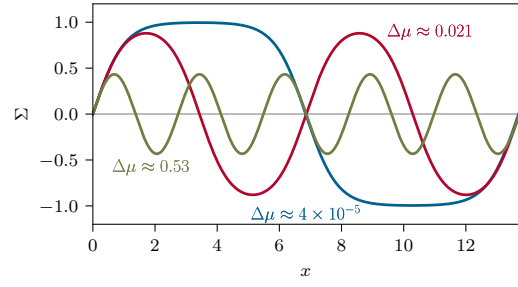


Figure 4.9.: Spatial inhomogeneous chiral condensate $\Sigma(\mu, T, x)$ at $T = 0$ for various chemical potentials μ with $\Delta\mu = (\mu - \mu_c)/\bar{\Sigma}_0$ in the IP (where $\mu_c/\bar{\Sigma}_0 = 2/\pi$). The curves are calculated using expressions of Refs. [180, 181, 504]. This figure is inspired by Fig. 2 of Ref. [180]. From Fig. 2 of Ref. [5].

4.4.1. The inhomogeneous phase diagram of the Gross-Neveu model

The inhomogeneous phase diagram of the GN model for $N \rightarrow \infty$ is well-known, which makes it an ideal testing ground for methods in QFTs. Therefore, we will briefly summarize the established phenomenology of the GN in the μ - T -plane as benchmark and reference values.

For related (and more comprehensive) discussions and original works of the rich large- N phenomenology and physics of the GN model we refer to Refs. [170–174, 179–183, 185–192, 194–197, 497, 498, 500–506, 621, 662, 670, 672, 683, 684, 693–695, 709, 714–730].

Enforcing the ground state (the $\langle \tilde{\psi}\tilde{\psi} \rangle$ -condensate) of the auxiliary field to be constant (homogeneous) in space-time, thus $\sigma(x) = \bar{\sigma} = \text{const.}$, we are in the setting of the previous section 4.3, where we discussed the homogeneous phase diagram 4.2 at length in subsection 4.3.2. We recall the following findings in the language and notation⁷⁵ used in this section: We find a homogeneously broken phase (HBP) with a condensate $\bar{\Sigma}(\mu, T) \neq 0$ (broken \mathbb{Z}_2 symmetry) at small μ and T and the symmetric phase (SP) with $\bar{\Sigma}(\mu, T) = 0$ with restored \mathbb{Z}_2 symmetry in the rest of the μ - T -plane. The phase transition is of second-order at $(\mu, T_c)/\bar{\Sigma}_0 = (0, e^\gamma/\pi) \simeq (0, 0.567)$ and ranges from $\mu = 0$ to the critical point (CP) at $(\mu_{\text{CP}}, T_{\text{CP}})/\bar{\Sigma}_0 \simeq (0.608, 0.318)$. At this point the phase transition becomes first-order and continues to lower temperatures until it finally terminates at $(\mu_{c,\text{hom}}, T)/\bar{\Sigma}_0 = (1/\sqrt{2}, 0.0) \simeq (0.707, 0.0)$.

⁷⁵In this subsection we denote the homogeneous condensate/fermion mass with $\bar{\Sigma}(\mu, T) \equiv \sigma(\mu, T)h \equiv \Delta(\mu, T)$ with its value in vacuum $\bar{\Sigma}_0 \equiv \bar{\Sigma}(0, 0) \equiv \sigma(0, 0)h \equiv \sigma_0 h \equiv \Delta_0$. At this point I have to apologize for the wealth of different – but at least not contradictory – notations for the same quantities in this part of my thesis. Since this chapter is based on published results [4, 5] involving different collaborators, the notations of Refs. [4, 5] are slightly different. Unifying the notations would require changing the plot labels and legends, which I deemed too time consuming and cumbersome when it comes to referencing the figure sources.

Relaxing the restrictive assumption of homogeneous condensation and allowing for a spatially varying background field $\varphi = \varphi = \sigma(x)$, a modified phase diagram is obtained. Here, one finds an inhomogeneous phase (IP) where the ground state $\Sigma(\mu, T) = \Sigma(\mu, T, x)$ is an oscillating function in space. This phase emerges for temperatures $T < T_L \simeq 0.318 \bar{\Sigma}_0$ and moderate chemical potentials $\mu > \mu_L \simeq 0.608 \bar{\Sigma}_0$ and grows in μ -direction for decreasing temperature, cf. figure 4.8 and Refs. [180, 181, 501, 502, 504, 505]. The former homogeneous first-order phase boundary is completely engulfed by the IP. The novel phase transition between the IP and the HBP is of second-order and ranges from $(\mu_c, T)/\bar{\Sigma}_0 = (2/\pi, 0.0) \simeq (0.637, 0.0)$ to a Lifshitz point (LP) which is located at the position $(\mu_L, T_L)/\bar{\Sigma}_0 \simeq (0.608, 0.318)$ of the former CP. At the LP three phases – a homogeneously broken, an inhomogeneously broken, and a restored phase – meet.

At the HBP \leftrightarrow IP phase boundary, the phase transition is not linked to the \mathbb{Z}_2 symmetry breaking/restoration, but rather to the breaking/restoration of spatial translational invariance, because discrete chiral symmetry is always (periodically) broken by the condensate. The other phase boundary from the IP to the SP is also of second-order and thus all phase boundaries of the *correct/revised* mean-field phase diagram correspond to second-order phase transitions. Crossing the SP \leftrightarrow IP phase boundary the discrete chiral symmetry as well as spatial translational invariance are broken/restored. This crucial difference between discrete chiral symmetry and translational invariance breaking/restoration is of great importance for the remainder of this work and the limitations of the stability analysis.

The spatially inhomogeneous chiral condensate in the IP is described by Jacobi elliptic functions⁷⁶

$$\Sigma = M_0 \sqrt{\nu} \operatorname{sn}(M_0 x, \nu), \quad (4.70)$$

and for increasing chemical potential

- its shape evolves from a kink-antikink shape ($\nu \rightarrow 1$) to a sine-like shape ($\nu \rightarrow 0$),
- its amplitude $M_0 \sqrt{\nu}$ decreases – mainly due to the aforementioned decrease of ν ,
- its wave vector $q = \frac{2\pi}{M_0 K(\nu)}$ increases,

as shown in figure 4.9 for zero temperature, see also Refs. [181, 504]. The general behavior of the condensate is very similar at non-zero temperature, see Ref. [181] for details.

4.4.2. Stability analysis of the spatially homogeneous \mathbb{Z}_2 -symmetric phase

This subsection is based on Sec. II.D of Ref. [5]. The four included subsections closely follow the discussions of Secs. III.A–D of Ref. [5].

The numerical results for the stability analysis in the μ - T -plane, cf. figures 4.16 and 4.18, were obtained with my C++ code [653], computing 49875 points in the μ - T -plane in about two hours CPU time on an AMD Ryzen[®] 9 3900X processor (14 minutes wall time on 12 cores). The references values discussed in subsection 4.4.1, see also figure 4.8, were computed by L. Pannullo in a few hours of wall time.

⁷⁶For definitions, properties, and relations of the involved Jacobi elliptic functions, see, e.g., Chap. 22 of Ref. [302].

In this subsection we turn to the theoretical considerations behind the stability analysis to detect spatially inhomogeneous phases and discuss numerical results in the following subsections 4.4.2.1–4.4.2.4, where we confront the results obtained from the stability analysis with the reference values discussed in subsection 4.4.1. The following discussion is in parts based on Ref. [651], but similar discussions can be found in Refs. [193, 198, 199, 202]. We further deviate a bit from the presentation chosen in Ref. [5], since we consider a computation of the homogeneous effective potential and the bosonic two-point function using the FRG framework.

In order to relax the assumption of spatially homogeneous condensation and to search for a spatially IP, one has to find the global x -dependent minima $\Sigma(\mu, T, x)$ of the functional $\Gamma[\sigma(x)]$ for all possible field configurations $\sigma(x)$. Generically – as was already discussed in section 2.4 – this is an extremely challenging task, both analytically and numerically.

Due to these challenges, the idea of an indirect detection of inhomogeneous condensation arose, which is based on analyzing the stability of the spatially homogeneous ground state against inhomogeneous perturbations. This was already discussed and/or applied in various contexts [80, 198, 200, 202, 204] and to some extent also in the context of the (chiral) GN model [180, 201]. The proposed approach allows to search for a sufficient condition for an IP, *i.e.*, if $\bar{\Sigma}(\mu, T)$ is unstable against spatially inhomogeneous perturbation, the true ground state has to be inhomogeneous. In general, $\bar{\Sigma}(\mu, T)$ could, however, be stable against inhomogeneous perturbations, but by a functional minimization of $\Gamma[\sigma(x)]$ one may still find an inhomogeneous ground state. In this scenario the local, homogeneous and the global, inhomogeneous minimum are separated by a “potential barrier”, which prevents a stability analysis and calls for global minimization approaches. This implies that the stability analysis is expected to work properly in the vicinity of second-order phase boundaries between homogeneous and inhomogeneous phases. Nonetheless, this model and approximation independent method is still a powerful tool for the search of exotic phases of matter. Note that the construction/expansion is technically not limited to the trivial homogeneous minimum $\bar{\Sigma}(\mu, T) = 0$.

On a formal level the stability analysis is based on a functional (Taylor) expansion of the effective action $\Gamma[\sigma]$ about a spatially homogeneous background field $\bar{\sigma}$ in powers of an inhomogeneous perturbation $\delta\sigma(x)$. A spatially homogeneous ground state is considered to be unstable, if the second-order coefficient of this expansion exhibits some unstable direction in field space, if it is evaluated on the spatially homogeneous minimum $\bar{\Sigma}(\mu, T)$. Note that the first-order coefficient in this expansion vanishes due to the QEOM Eq. (2.20) when evaluated on the IR minimum $\bar{\Sigma}(\mu, T)$. On a mean-field/large- N level this is encoded by the homogeneous gap Eq. (4.47).

The second-order Taylor coefficient is the bosonic two-point function $\Gamma^{(2)}$, which is analyzed in momentum space. An unstable direction in field space corresponds to a negative value $\Gamma^{(2)}$ for external spatial momentum q , which can be associated to the wave vector of a spatially oscillating energetically preferred ground state. This implies a lower ground state energy for the inhomogeneous phase when compared to the homogeneous one assuming the higher-order contributions of the expansion beyond the second-order are either positive or negligible.

Whether or not these assumptions are met depends on the model, the expansion point and the magnitude of the inhomogeneous oscillations as we will discuss in detail in the following. Hence, the stability analysis corresponds to searching for a sign change in $\Gamma^{(2)}$ at some external momentum q in the μ - T -plane.

Ref. [5] includes a derivation of this two-point function and the corresponding expansion of $\Gamma[\sigma]$ in a conventional mean-field/large- N setting [193, 198, 199, 202] using the effective classical action $\mathcal{S}_{\text{eff}}[\sigma]$. For details using this approach we refer to the corresponding discussion in Sec. II.D of Ref. [5]. We are in this work in the comfortable position that we have the FRG at our disposal which allows us to compute n -point functions – including the bosonic two-point function required for the following discussion. We have introduced the flow equations for higher-order n -point functions in subsection 2.1.5 and have already encountered flow equations for two-point functions in the context of our zero-dimensional $SU(2)$ model, cf. subsection 3.3.2. Details for the computation of the bosonic two-point function in the limit $N \rightarrow \infty$ can be found in App. E.3. It should also be noted that in the renormalized limit $\Lambda \rightarrow \infty$ results of (fermionic) one-loop computations are in general completely regularization-scheme-independent. At this point we just want to give the result of the computations outlined in App. E.3, viz. the bosonic two-point function for the GN model in the renormalized limit at infinite N :

$$\Gamma^{(2)}(\bar{\sigma}, \mu, T, q) = \frac{1}{2\pi} \ln \left(\frac{\bar{\sigma}^2}{\bar{\Sigma}_0^2} \right) - \ell_2(\bar{\sigma}, \mu, T, q) + \frac{1}{\pi} \int_0^\infty dp \frac{1}{E_p} (n_f(\beta[E_p + \mu]) + n_f(\beta[E_p - \mu])), \quad (4.71)$$

with the energies $E_p = \sqrt{p^2 + \bar{\sigma}^2}$ and the integral

$$\ell_2(\bar{\sigma}, \mu, T, q) = - \left(\frac{q^2}{2} + \bar{\sigma}^2 \right) \frac{2}{\pi} \int_0^\infty dp \frac{1}{E_p} \left(\frac{1}{E_{p+q}^2 - E_p^2} + \frac{1}{E_{p-q}^2 - E_p^2} \right) \times \left(1 - n_f(\beta[E_p + \mu]) - n_f(\beta[E_p - \mu]) \right). \quad (4.72)$$

The result Eq. (4.71) can be further simplified, if at least one of the four arguments $\bar{\sigma}$, μ , T , or q is zero. All possible cases and the respective simplifications of $\Gamma^{(2)}$ are listed in Tab. I of Ref. [5] with corresponding symbolic expressions in App. A of Ref. [5]. A detailed derivation and discussion of the different cases is presented in Ref. [165].

Negative values of $\Gamma^{(2)}(\bar{\Sigma}(\mu, T), \mu, T, q)$ indicate an instability of the homogeneous minimum $\bar{\Sigma}(\mu, T)$ w.r.t. inhomogeneous perturbations of momentum q . Consequently, the two-point function can be used to search for inhomogeneous ground states for arbitrary μ and T . This can be done by analyzing $\Gamma^{(2)}(\bar{\Sigma}(\mu, T), \mu, T, q)$ as a function of q for each point (μ, T) in the phase diagram. In practice one searches for regions where $\Gamma^{(2)}(q)$ is negative.

The wave-function renormalization

In the past it was speculated, if it might be sufficient to study the curvature of $\Gamma^{(2)}(\bar{\Sigma}(\mu, T), \mu, T, q)$ at $q = 0$, i.e., the second-order coefficient of a Taylor expansion of the two-point function in

momentum space about $q = 0$, *viz.* the wave-function renormalization,

$$Z(\bar{\sigma}, \mu, T) \equiv \frac{1}{2} \frac{d^2}{dq^2} \Gamma^{(2)}(\bar{\sigma}, \mu, T, q) \Big|_{q=0}. \quad (4.73)$$

It was speculated that a negative bosonic wave-function renormalization might be sufficient to destabilize spatially homogeneous ground states and to energetically favor gradients in the spatial profile of the ground state over a spatially uniform ground state field configuration.

As pointed out, *e.g.*, in Refs. [80, 510], a negative wave-function renormalization is only indicative towards the possibility for spatial modulations of the ground state. It is not a sufficient or even necessary criterion, because higher-order momentum-dependencies of the bosonic two-point function might again disfavor spatially inhomogeneous condensation over homogeneous condensation. Consequently, a study of the full momentum structure of the two-point function is necessary.

Nevertheless, the wave-function renormalization is still an extremely important quantity, as it directly enters the dispersion relations [731, 732], see also our discussion in subsection 4.2.1. Explicit expressions for $Z(\bar{\sigma}, \mu, T)$, where $\bar{\sigma}$, μ , and T take either non-vanishing or vanishing values, can be found in App. B of Ref. [5] with an overview in table II of the aforementioned publication. The physically relevant wave-function renormalization is again obtained, if Eq. (4.73) is ultimately evaluated at the homogeneous ground state $\bar{\sigma} = \Sigma(\mu, T)$.

Finally, we turn to the actual results and the promised proof of concept. We start in subsection 4.4.2.1 by presenting the q -dependence of the bosonic two-point function at various points in the μ - T -plane. The discussion of this momentum structure provides deeper insights in the (physical pairing) mechanisms and the operating principle behind the stability analysis. Furthermore, we come back to these results, when we comment on recent calculations in the GN model beyond the mean-field approximation [519–522] including implications for our research in the next section 4.5. Based on the analysis in subsection 4.4.2.1 the actual stability analysis of the homogeneous phase in the μ - T -plane can be performed and results are presented in subsection 4.4.2.2. Here, we demonstrate that this method is actually able to detect the well-known second-order phase-transition line between the IP and the SP, but also comment on its shortcomings. Afterwards in subsection 4.4.2.3, the momentum profile of the bosonic two-point function, *i.e.*, the dominant wave vector, is compared with the analytic solutions (4.70) from Ref. [181]. Finally, we close the discussion of our results by presenting results for bosonic wave-function renormalization in the μ - T -plane in subsection 4.4.2.4. We again comment on the insufficiency of the wave-function renormalization as a single measure for the detection of spatially inhomogeneous condensates. Furthermore, we discuss possible implications on the quality of the mean-field approximation based on our quantitative calculations.

4.4.2.1. The momentum structure of the bosonic two-point function

The entire idea of the stability analysis is based on the momentum structure/dispersion of the bosonic two-point function (4.71). Therefore, this subsection contains a detailed discussion of the various possible shapes of $\Gamma^{(2)}$, which occur in the GN model at different points (μ, T) in

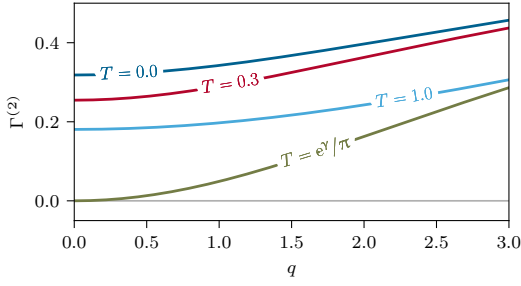


Figure 4.10.: The bosonic two-point function $\Gamma^{(2)}(\bar{\sigma}, \mu, T, q)$ as a function of the external momentum q at vanishing chemical potential $\mu = 0$ and fixed temperatures $T/\bar{\Sigma}_0 \in \{0.0, 0.3, e^\gamma/\pi, 1.0\}$ evaluated at the respective homogeneous minimum $\bar{\sigma} = \bar{\Sigma}(\mu, T)$. From Fig. 3 of Ref. [5].

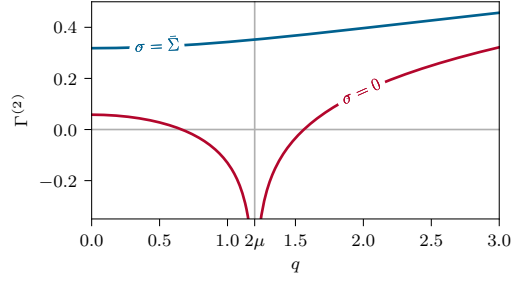


Figure 4.11.: The bosonic two-point function $\Gamma^{(2)}(\bar{\sigma}, \mu, T, q)$ as a function of the external momentum q at constant chemical potential $\mu/\bar{\Sigma}_0 = 0.6$ and vanishing temperature $T = 0$ evaluated at the homogeneous global minimum $\bar{\sigma} = \bar{\Sigma}(\mu, 0) \neq 0$ and the homogeneous local minimum $\bar{\sigma} = 0$. The unphysical red curve (stemming from an evaluation away from the homogeneous ground state, viz. $\bar{\sigma} = 0$) has a pole at $q = 2\mu$. From Fig. 4 of Ref. [5].

the phase diagram. Our discussion is based on figures 4.10–4.13 and 4.15, which were directly produced by (numeric) evaluation of Eq. (4.71) or its simplified versions, see Tab. I and App. A of Ref. [5]. If needed, the corresponding spatially homogeneous ground state $\bar{\Sigma}(\mu, T)$ was determined (numerically) by minimization of Eq. (4.59).

We begin our discussion at vanishing chemical potential $\mu = 0$. The corresponding plots for $\Gamma^{(2)}(\bar{\Sigma}(0, T), 0, T, q)$ are presented in figure 4.10. One finds that the bosonic two-point function is always positive and convex for all external momenta at $\mu = 0$. This is the case for zero and non-zero temperature, in the \mathbb{Z}_2 symmetry broken and symmetric phase respectively. Consequently, the spatially homogeneous minimum is stable against inhomogeneous perturbations. Furthermore, this might also imply that a low order derivative expansion of the bosonic effective action, e.g., in the context of the following computation at finite N in section 4.5, should be a decent approximation and capture the relevant momentum-dependencies. Additionally, this confirms that it is unlikely to generate crystalline like ground states at zero density. Only at the phase transition at $T/\bar{\Sigma}_0 = e^\gamma/\pi$ the curve for $\Gamma^{(2)}$ has a single root at $q = 0$, which is expected, since the bosonic curvature mass vanishes at this phase transition [180, 184, 186, 733].

Next, figure 4.11 is discussed, where we plot $\Gamma^{(2)}(\bar{\sigma}, \mu, T, q)$ at constant chemical potential $\mu/\bar{\Sigma}_0 = 0.6$ and vanishing temperature $T = 0$ for two evaluation points $\bar{\sigma}$ in the constant background field space. As can be seen from figure 4.8 this μ - T -point lies in the HBP implying that the true homogeneous ground state has $\bar{\Sigma}(\mu, 0) \neq 0$. The two curves in figure 4.11 show that it is crucial to evaluate $\Gamma^{(2)}(\bar{\sigma}, \mu, T, q)$ at the correct homogeneous minimum $\bar{\sigma} = \bar{\Sigma}(\mu, 0) \neq 0$ as the evaluation at $\bar{\sigma} = 0$ leads to negative values of $\Gamma^{(2)}$ giving a false signal of instability. This seems somewhat obvious, especially for the rather simple GN model in mean-field approx-

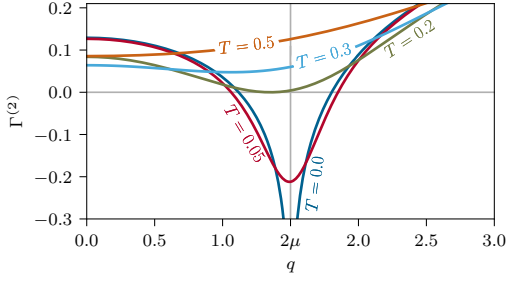


Figure 4.12.: The bosonic two-point function $\Gamma^{(2)}(\bar{\sigma}, \mu, T, q)$ as a function of the external momentum q at constant chemical potential $\mu/\bar{\Sigma}_0 = 0.75$ and fixed temperatures $T/\bar{\Sigma}_0 \in \{0.0, 0.05, 0.2, 0.3, 0.5\}$ evaluated at the respective homogeneous minimum $\bar{\sigma} = \bar{\Sigma}(\mu, T) = 0$. The curve for $T = 0.0$ has a pole at $q = 2\mu$, cf. Eq. (A15) of Ref. [5]. From Fig. 5 of Ref. [5].

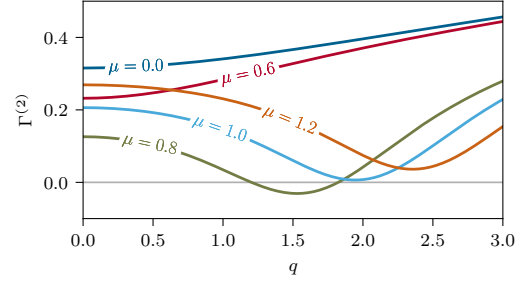


Figure 4.13.: The bosonic two-point function $\Gamma^{(2)}(\bar{\sigma}, \mu, T, q)$ as a function of the external momentum q at constant temperature $T/\bar{\Sigma}_0 = 0.15$ and fixed chemical potentials $\mu/\bar{\Sigma}_0 \in \{0.0, 0.6, 0.8, 1.0, 1.2\}$ evaluated at the respective homogeneous minimum $\bar{\sigma} = \bar{\Sigma}(\mu, T)$. From Fig. 6 of Ref. [5].

imation. However, for example in more involved FRG model calculations as in Refs. [87, 96, 105–108, 150, 151, 162, 231, 734] and especially for advanced truncations, it is sometimes not obvious to determine the correct evaluation point in field space for correlation functions – at least during the RG flow.

After covering the simple scenarios, we turn to figure 4.12, where we plot the behavior of $\Gamma^{(2)}$ for different temperatures but constant chemical potential $\mu/\bar{\Sigma}_0 = 0.75$. As discussed in subsection 4.4.1 and figure 4.8, these μ - T -points are located in the SP and in the IP, such that the correct evaluation point in background field space is always the trivial homogeneous minimum $\bar{\sigma} = \bar{\Sigma}(\mu, T) = 0$. As expected we find a manifestly positive and convex $\Gamma^{(2)}$ at high temperatures, where thermal fluctuations are likely to vaporize any kind of crystal like structures and condensates, because the temperature T and not the chemical potential μ is the dominating external energy scale. On the other hand, for moderate temperatures one finds that $\Gamma^{(2)}$ develops a non-trivial minimum at some non-zero q , which indicates that the energy scale set by μ gains in importance. However, this non-trivial minimum does not destabilize the spatially homogeneous ground state if $\Gamma^{(2)}$ stays manifestly positive. Only below a certain threshold for the temperature (here $T/\bar{\Sigma}_0 \approx 0.2$), where the minimum of $\Gamma^{(2)}$ turns negative, an instability is observed implying a breaking of the \mathbb{Z}_2 symmetry and translational invariance by some lower lying ground state $\Sigma(\mu, T, x)$. Exactly at the temperature threshold the new x -dependent ground state $\Sigma(\mu, T, x)$ is anticipated to exhibit a single wave vector Q , namely the single touching root of $\Gamma^{(2)}$. The latter is equal to the minimum of the two-point function. This is discussed in detail in subsection 4.4.2.3. In the following, Q generically denotes the location of the minimum of $\Gamma^{(2)}$ in q -direction, *i.e.*,

$$Q \equiv \operatorname{argmin}_q \Gamma^{(2)}(\bar{\Sigma}(\mu, T), \mu, T, q). \quad (4.74)$$

Further decreasing the temperature, we observe in figure 4.12 that the q -range where $\Gamma^{(2)}$ is negative initially grows. Additionally, the minimum of $\Gamma^{(2)}$ gets more and more negative and ultimately turns into a pole at $q = 2\mu$ for $T = 0$. The roots of $\Gamma^{(2)}$ which are poles of the propagator $1/\Gamma^{(2)}$ signal a resonance in the respective anti-fermion-fermion two-point function $\langle \bar{\psi} \psi \rangle$. This resonance is associated with an anti-fermion-fermion bound state in which an anti-fermion and a fermion of opposite chirality are paired with a non-zero total momentum forming an inhomogeneous chiral condensate. More details and qualitative as well as quantitative discussions of this pairing mechanism can be found in Refs. [63, 735, 736]. The preferred momenta for the anti-fermion-fermion pairs are from the momentum range of negative $\Gamma^{(2)}(q)$ with the dominant frequency Q typically associated with the minimum of $\Gamma^{(2)}$, see Eq. (4.74). The dominant frequency of $Q \sim 2\mu$ at low and especially zero temperature is typical for such inhomogeneous condensates as the anti-fermion-fermion pairs are formed in vicinity of the Fermi surface [63, 735, 736]. Apart from the identification of the dominant frequency Q the course of $\Gamma^{(2)}(q)$ for $\Gamma^{(2)} < 0$ between the roots (including the pole at $q = 2\mu$ for $T = 0$) is not very instructive because the employed stability analysis using a homogeneous expansion point is incapable of capturing the full physics of the inhomogeneous chiral condensate in this momentum regime. A notable exception occurs when we have a single touching root, in figure 4.12 the case for $T \approx 0.2$, signaling the onset of instability of the homogeneous phase in favor of an inhomogeneous phase with an explicit single momentum mode Q instead of a spectrum. We will discuss this further in the following subsection 4.4.2.2.

Lastly, figure 4.13 is considered, where again $\Gamma^{(2)}$ is presented at different points in the phase diagram. In contrast to the previous discussion, we do not vary the temperature at constant chemical potential, but fix $T/\bar{\Sigma}_0 = 0.15$ and study curves at various chemical potentials. As can be seen from figure 4.8 the slice through the phase diagram at $T/\bar{\Sigma}_0 = 0.15$ is chosen, because of its rich phenomenology at different μ . Starting from zero density at $\mu = 0$, a convex and manifestly positive function course of $\Gamma^{(2)}$ is observed. Increasing μ the bosonic curvature mass (the value of $\Gamma^{(2)}$ at $q = 0$) is lowered, but $\Gamma^{(2)}$ stays convex. As soon as one leaves the HBP and crosses the first-order phase boundary to the \mathbb{Z}_2 -symmetric phase (for spatially homogeneous condensates), cf. figure 4.8, $\Gamma^{(2)}$ immediately develops a non-trivial negative minimum (for $\mu/\bar{\Sigma}_0 = 0.8$ at $q/\bar{\Sigma}_0 \approx 1.6$ in figure 4.13), which indicates that spatially inhomogeneous condensation is energetically favorable and μ completely dominates the dynamics as an external energy scale, *i.e.*, one enters the IP. However, further increasing μ at non-zero T ultimately shifts the $\Gamma^{(2)}$ -profile to larger values, such that at $\mu/\bar{\Sigma}_0 \approx 1.0$ the minimal value of $\Gamma^{(2)}$ turns positive again, see figure 4.13. This means that by further increasing μ we again cross a phase transition line and enter ultimately the \mathbb{Z}_2 -symmetric and translation invariant phase.

At this point we remark, that the q -profiles for $\Gamma^{(2)}$ in figures 4.10–4.13 are very similar to courses of $\Gamma^{(2)}$ that were sketched in Fig. 5 of Ref. [510] or the ones calculated and displayed in different contexts in Fig. 5 of Ref. [87], Fig. 2 of Ref. [198], and Fig. 8 of Ref. [193].

We conclude this subsection with a discussion of a shortcoming of the stability analysis. To do so, a point in the phase diagram is studied that is located extremely close to the first-order phase transition line in figure 4.8, but still only just corresponds to the HBP, if only spatially

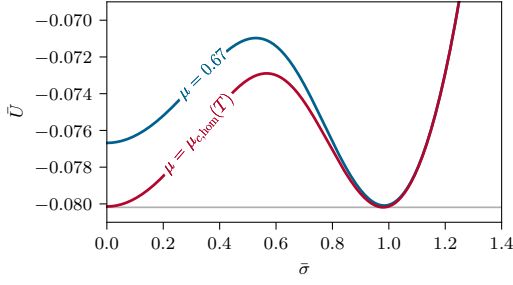


Figure 4.14.: The homogeneous effective potential $\bar{U}(\bar{\sigma}, \mu, T)$ as a function of the homogeneous background field $\bar{\sigma}$ at constant temperature $T/\bar{\Sigma}_0 = 0.1$ and fixed chemical potentials $\mu/\bar{\Sigma}_0 \in \{0.67, \mu_{c,\text{hom}}(T)\}$, where $\mu_{c,\text{hom}}(T) \approx 0.686$ is the critical chemical potential of the homogeneous phase transition at this temperature. *From Fig. 7 of Ref. [5].*

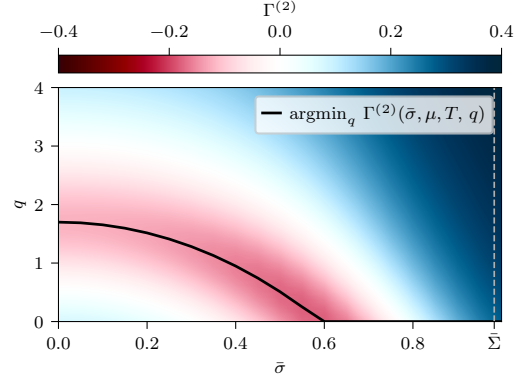


Figure 4.15.: The bosonic two-point function $\Gamma^{(2)}(\bar{\sigma}, \mu, T, q)$ in the $\bar{\sigma}$ - q -plane for the point $(\mu, T)/\bar{\Sigma}_0 = (0.67, 0.1)$ in the phase diagram. The solid black line marks the non-trivial minima. *From Fig. 8 of Ref. [5].*

homogeneous condensation is considered. At $(\mu, T)/\bar{\Sigma}_0 = (0.67, 0.1)$ the correct homogeneous minimum of the effective potential \bar{U} is located at $\bar{\sigma} = \bar{\Sigma}/\bar{\Sigma}_0 \approx 1.0$, while the point $\bar{\sigma} = 0$ corresponds to a local minimum, which is of similar depth, see figure 4.14.

However, it is known from the exact solution [181, 502, 504], see figure 4.8, that this point in the μ - T -plane actually corresponds to the IP, if one allows for spatial modulations of the ground state. For selected sample points we experienced during this subsection that the stability analysis seems to work well, if the expansion point is the trivial homogeneous minimum of the effective potential in the \mathbb{Z}_2 -symmetric phase, thus $\bar{\Sigma}(\mu, T) = 0$. Naturally the question arises whether or not the stability analysis maintains its predictive power even with non-trivial spatially homogeneous expansion points $\bar{\Sigma}(\mu, T) \neq 0$ are considered. Hence, we present $\Gamma^{(2)}(\bar{\sigma}, \mu, T, q)$ at $(\mu, T)/\bar{\Sigma}_0 = (0.67, 0.1)$ as a function of $\bar{\sigma}$ and q in figure 4.15.

Evaluating $\Gamma^{(2)}$ at large values of $\bar{\sigma}$, e.g., at the correct homogeneous minimum and expansion point $\bar{\Sigma}/\bar{\Sigma}_0 \approx 1$, the bosonic two-point function is manifestly positive and does not signal any instability. The reason is that the non-trivial homogeneous minimum and the spatially oscillating minimum are separated by a kind of “potential barrier”, as the effective potential increases when studying small perturbations about the homogeneous minima. Formally, the correct expansion point is no longer unique. There are two degenerate homogeneous minima and therefore two possible expansion points with the trivial minimum and a potential barrier in between, see figure 4.14 upper curve. We observe that the two homogeneous minima are no longer saddle-points with an unstable direction in momentum space, when studying inhomogeneous perturbations. In fact the analytic solution for the ground state in the IP in terms of Jacobi elliptic functions turns into rather pronounced kinks close to the correct second-order phase transition to the HBP. This means that the condensate almost oscillates between the two homogeneous minima $\pm \bar{\Sigma}(\mu, T)$ and cannot be described as a small perturbation/oscillation around just one of the two non-trivial minima. Finding an instability with large oscillations about $\bar{\sigma} = 0$ would require even larger $\delta\sigma(x)$ when expanding around one of the two homogeneous minima.

However, having large perturbations $\delta\sigma(x)$ about $\pm\bar{\Sigma}(\mu, T)$ would require to always change the expansion point during an oscillation. Furthermore, large $\delta\sigma(x)$ would call for the inclusion of basically all higher-order coefficients in the expansion, see Ref. [737]. The reason is the increase in the effective potential when perturbing around the homogeneous minima with small $\delta\sigma(x)$ before the effective potential decreases in the vicinity of the inhomogeneous ground state when studying large $\delta\sigma(x)$. Due to this behavior, coefficients of progressively higher orders are required in the expansion in order to reproduce this behavior when moving in the μ - T -plane towards the phase boundary between the IP and the HBP, as described in Refs. [509, 737].

In summary, we observe that for this model the stability analysis fails to detect the inhomogeneous phase as long as the correct expansion point $\bar{\Sigma}(\mu, T) \neq 0$. This was already partially discussed in Ref. [180] and observed in Ref. [182], where a similar analysis of the GN was done on a finite lattice. In the latter reference, it was stated that this “potential barrier” was a result of the finite volume, but our present results in an infinite volume suggest that this is a generic problem of the stability analysis independent of the considered volume.

4.4.2.2. The phase diagram from the stability analysis

Based on our previous discussion, we turn to the central result of this subsection. Within the following paragraphs it is demonstrated and briefly discussed that the stability analysis correctly detects the well-known phase transition line between the SP and the IP, but fails in the region between the HBP \leftrightarrow IP phase boundary and the homogeneous first-order phase transition, *cf.* figure 4.8 and the related discussion in Ref. [180].

As we argued before, we can trust this method in the regions of the phase diagram where the minimum and correct expansion point in field space is at $\bar{\sigma} = \bar{\Sigma}(\mu, T) = 0$ and especially where the inhomogeneous condensate oscillates with a small amplitude about the expansion point. This is the case in the GN model at the phase boundary between the IP and the SP. Thus, it is expected that the exact phase boundary and the line of instability obtained via the stability analysis match. This is supported by our (numerical) results that are plotted in figure 4.16. The solid black line is the line where $\Gamma^{(2)}$ has a single root at $q = Q$ in the external momentum, *i.e.*, $\Gamma^{(2)}(\bar{\Sigma}(\mu, T), \mu, T, Q) = 0$ only for one wave vector $q = Q$, see also Ref. [193]. The line extends from the LP to larger μ and is numerically identical to the exact phase boundary, which is shown in figure 4.8.

Interestingly (but actually not really surprisingly) also the second-order phase boundary between the SP and HBP is correctly detected using $\Gamma^{(2)}$. The reason is that the bosonic curvature mass vanishes along this phase transition line [180, 184, 186, 733]. The curvature mass, however, is defined as $\Gamma^{(2)}(\bar{\Sigma}(\mu, T), \mu, T, q)$ evaluated at vanishing external momentum $q = 0$. The minimum of $\Gamma^{(2)}$ in q -direction is located at $q = 0$ above the LP, *viz.* for $T \geq T_L$, as discussed in the previous subsection 4.4.2.1, which explains the recovery of the SP \leftrightarrow HBP phase boundary from the employed two-point function.

Nonetheless, at the phase boundary of the HBP and IP the amplitude of the inhomogeneous condensate is large and the inhomogeneous condensate almost oscillates between the values of the homogeneous minima, *i.e.*, between $\pm\bar{\Sigma}(\mu, T)$, *cf.* figure 4.9. As soon as one crosses the first-order phase transition and needs to switch to one of these minima as the formal correct

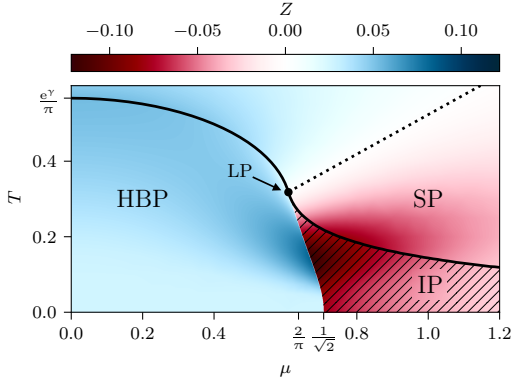


Figure 4.16.: The bosonic wave-function renormalization $Z(\bar{\Sigma}(\mu, T), \mu, T)$ (heat map), line of vanishing wave-function renormalization $Z(\bar{\Sigma}(\mu, T), \mu, T) = 0$ (thick black dashed line), and the line of vanishing bosonic two-point function $\Gamma^{(2)}(\bar{\Sigma}(\mu, T), \mu, T, Q) = 0$ (thick, black solid line) in the μ - T -plane. In the region marked by the diagonal hatching using thin black solid lines (bottom-right corner) we find $\Gamma^{(2)}(\bar{\Sigma}(\mu, T), \mu, T, Q) < 0$, i.e., the homogeneous minimum is unstable w.r.t. an inhomogeneous perturbation. From Fig. 9 of Ref. [5].

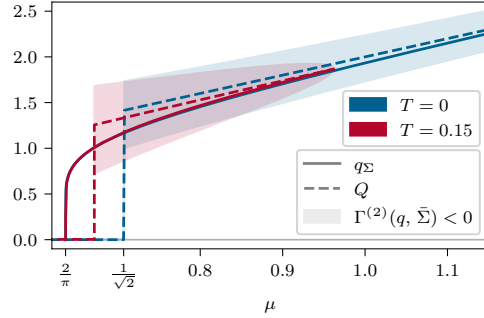


Figure 4.17.: The minimum of the bosonic two-point function $Q(\mu)$ and the dominating wave vector of the true inhomogeneous condensate $q_{\Sigma}(\mu)$ as a function of the chemical potential at constant temperatures $T/\bar{\Sigma}_0 \in \{0.0, 0.15\}$. The colored regions mark the range of momenta q , where $\Gamma^{(2)}(\bar{\Sigma}(\mu, T), \mu, T, q) < 0$. From Fig. 10 of Ref. [5].

expansion point, the initial assumption of the stability analysis of small perturbations about the expansion point is violated and one finds a deviation from the exact result.

The additional color map in figure 4.16 shows the value of the wave-function renormalization $Z(\bar{\sigma}, \mu, T)$, Eq. (4.73), evaluated at the true homogeneous minimum $\bar{\sigma} = \bar{\Sigma}(\mu, T)$. It is calculated numerically using the appropriate formulae from App. B of Ref. [5].

We also cross-checked that these results coincide with results, which are obtained by a numeric evaluation of the q -derivatives of $\Gamma^{(2)}$ in Eq. (4.73). In the SP the wave-function renormalization is given by

$$Z(0, \mu, T) = -\frac{1}{8\pi} \frac{1}{T^2} \text{DLi}_2\left(\frac{\mu}{T}\right), \quad (4.75)$$

according to Eq. (B3) of Ref. [5], which entails that the $(Z = 0)$ -line is given by $z_{2,1} \simeq 1.910$ from Eq. (C.60). It therefore coincides with the $(\alpha_4 = 0)$ -line from subsection 4.3.3. This is well known in the context of the gGL analysis and is encountered frequently in the study of inhomogeneous phases in different models. It implies that the locations of the LP of the inhomogeneous phase and of the CP of the homogeneous phase coincide, see, e.g., Refs. [63, 493, 495] for details.

It is immediately clear that a negative $Z(\bar{\Sigma}(\mu, T), \mu, T)$ can only be an indication that an inhomogeneous perturbation might lower the action, because negative curvature of $\Gamma^{(2)}$ at $q = 0$

does not guarantee that the function has a root. This scenario is found in the region between the ($Z = 0$)-line and the $SP \leftrightarrow IP$ phase boundary right of the LP, where the wave-function renormalization is negative, but the spatially homogeneous ground state is stable.

Regions with $Z < 0$: Moat/Lifshitz regimes

We have already encountered such regions with $Z < 0$ in subsection 2.4.2 as an indicator/precursor for inhomogeneous phases in the context of the FRG QCD computations of Ref. [80], cf. figure 2.13a and specifically figure 2.17.

Regions with $Z < 0$ and the corresponding modified dispersion relation for bosons are discussed in Refs. [731, 732, 738, 739] and referred to as moat and Lifshitz regimes. Moat or Lifshitz regimes are regions of negative wave-function renormalization, which signals a dispersion relation with a minimum at a non-zero momentum [731, 732, 738, 739]. The expression moat regime [731, 732] goes back to the dispersion relations encountered in these phases, cf. figure 4.12, resembling the deep, broad ditch – the moat – in front of a castle wall.

Regions of inhomogeneous phases can be included in such moat regimes, like in the present study, but they do not have to be present since $Z < 0$ is not a necessary condition for instability of the homogeneous phase in favor of inhomogeneous condensation. Other exotic phases of matter, like a quantum spin liquid [739], might be possible and energetically preferred over a typical homogeneous static ground state in the moat regime – if the particle content and space-time dimensionality of the model is more involved.

In summary, an inhomogeneous field configuration with momentum q that lowers the effective action can only be indirectly detected in the present analysis, when $\Gamma^{(2)}(\bar{\Sigma}(\mu, T), \mu, T, q) < 0$ and $\bar{\Sigma}(\mu, T) = 0$, which corresponds to the hatched region (bottom, right) in figure 4.16. The fact that $\bar{\Sigma}(\mu, T) = 0$ is required in the present context to find $\Gamma^{(2)}(\bar{\Sigma}(\mu, T), \mu, T, q) < 0$ is an *a posteriori* observation rather than an *a priori* requirement and is related to the potential barrier discussed in the previous subsection 4.4.2.1.

4.4.2.3. The wave vector of the inhomogeneous perturbation and the wave vector of the true inhomogeneous condensate

Even though the stability analysis is expected to work only for very small perturbations about a vanishing homogeneous condensate, we found that it even correctly predicts inhomogeneous condensation at points to the right of the homogeneous first-order phase transition at extremely small temperatures which are far away from the second-order $SP \leftrightarrow IP$ phase transition line. At these points one still uses the appropriate expansion point $\bar{\Sigma}(\mu, T) = 0$, but the perturbations are no longer small and the true condensate has a spectrum of wave vectors instead of a single frequency/wave vector, cf. figure 4.9.

One might thus wonder, if the single wave vector Q at the phase transition line actually matches the wave vector of the true solution, *i.e.*, the dominating wave vector of the Jacobi elliptic functions. Therefore, we compare the dominating wave vector of the correct inhomogeneous condensate minimizing the effective action

$$q_{\Sigma} \equiv \operatorname{argmax}_q \tilde{\Sigma}(\mu, T, q) \quad (4.76)$$

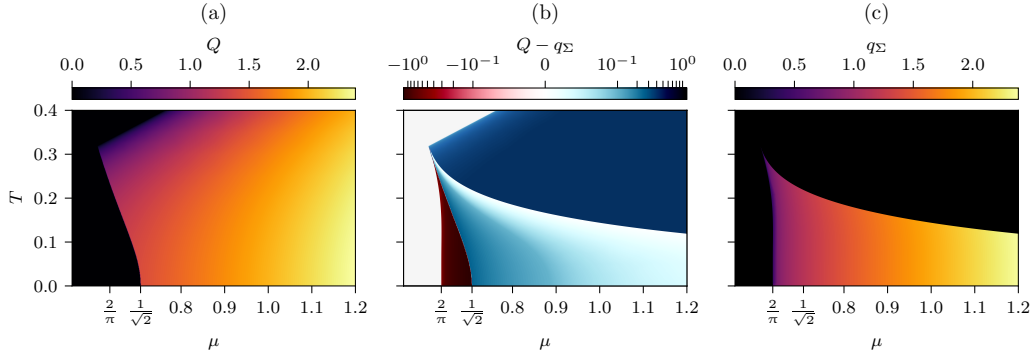


Figure 4.18.: Wave vector Q predicted by the stability analysis in (a), dominating wave vector of the reference solution q_Σ in (c), and their difference $Q - q_\Sigma$ in (b) in the (μ, T) -plane. Note that the colormap in (b) is linear around 0 and logarithmic for values $|(Q - q_\Sigma)/\bar{\Sigma}_0| > 0.1$. From Fig. 11 of Ref. [5].

with the wave vector that minimizes the two-point function Q as defined in Eq. (4.74). While Q is the direction of the largest curvature of the action at the saddle-point, it does not necessarily coincide with q_Σ . In figure 4.17 these two quantities are plotted for two different temperatures. At $T = 0$, Q approaches q_Σ for increasing chemical potential⁷⁷ and at $T/\bar{\Sigma}_0 = 0.15$ the two momenta match at the phase boundary. This is expected as the amplitude of the inhomogeneous condensate $\Sigma(\mu, T, x)$ at this point is infinitesimal and therefore the stability analysis becomes exact. At small chemical potential – as already discussed before – the stability analysis does not detect an inhomogeneous phase unless $\bar{\Sigma}(\mu, T) = 0$ and thus fails left of the homogeneous first-order phase transition. At intermediate chemical potential, Q and q_Σ do not agree. However, q_Σ is within the interval where $\Gamma^{(2)} < 0$ is predicted by the stability analysis, which means that the latter at least captures the dominating wave vectors.

In figure 4.18 we again compare Q and q_Σ . This time we plot Q , $Q - q_\Sigma$, and q_Σ in the μ - T -plane using different color maps. The previously discussed trend extends to the whole temperature range. The difference $Q - q_\Sigma$ approaches zero close to the IP \leftrightarrow SP boundary and its magnitude is the largest close to the HBP \leftrightarrow IP boundary, where Q is zero (because the stability analysis is ill-conditioned) and q_Σ is minimal. On the other hand, Q is also non-zero in the region of $Z < 0$ above the phase transition line, but does not correspond to an inhomogeneous perturbation that lowers the action, since $\Gamma^{(2)}$ is manifestly positive. We want to emphasize that this does not mark a failure of the employed method, but is rather just an effect of the negative wave-function renormalization Z . A discussion similar to our elaboration on figure 4.18 can be found in a different context in Ref. [193].

⁷⁷Plots similar to figure 4.17 of the wave vector of some inhomogeneous condensate plotted over baryon density (chemical potential), can be found in, e.g., Fig. 2 of Ref. [484], Fig. 2 of Ref. [740], Figs. 6 & 7 of Ref. [741].

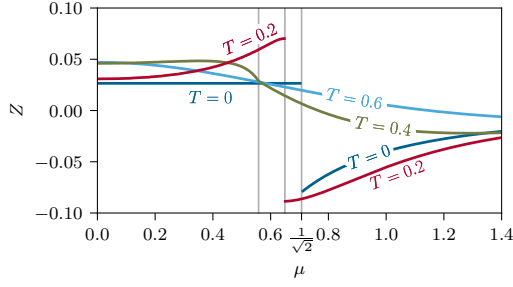


Figure 4.19.: The bosonic wave-function renormalization $Z(\bar{\sigma}, \mu, T)$ as a function of the chemical potential at fixed temperatures $T \in \{0.0, 0.2, 0.4, 0.6\}$ evaluated at the homogeneous minimum $\bar{\sigma} = \bar{\Sigma}(\mu, T)$. From Fig. 12 of Ref. [5].

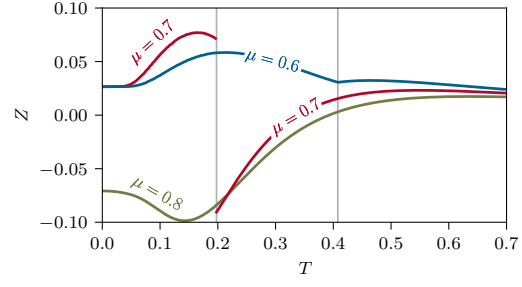


Figure 4.20.: The bosonic wave-function renormalization $Z(\bar{\sigma}, \mu, T)$ as a function of temperature at fixed chemical potentials $\mu \in \{0.55, 0.65, 0.75\}$ evaluated at the homogeneous minimum $\bar{\sigma} = \bar{\Sigma}(\mu, T)$. From Fig. 13 of Ref. [5].

4.4.2.4. The bosonic wave-function renormalization

Before closing our discussion of this subsection, we shortly return to our results for the bosonic wave-function renormalization and their implications.

In figure 4.16 the bosonic wave-function renormalization $Z(\bar{\Sigma}(\mu, T), \mu, T)$ was already presented in the entire μ - T -plane. We stress again that negative values of Z are not a sufficient or even necessary criterion for instabilities of the homogeneous phase. However, in regions of the phase diagram where the stability analysis is expected to work, *i.e.*, regions with $\bar{\Sigma}(\mu, T) = 0$, a negative wave-function renormalization presents as a strong indicator for an inhomogeneous phase. In regions where $\Gamma^{(2)}(q)$ is dominated by low-momentum contributions – *i.e.*, around the CP/LP – $Z < 0$ is a necessary condition for an inhomogeneous phase if contributions of $\mathcal{O}(q^6)$ to $\Gamma^{(2)}(q)$ can be neglected, *cf.* the following discussion of the gGL analysis in subsection 4.4.3.

Apart from this, one can learn a lot from the values of the wave-function renormalization alone. In a first rather rough approximation, we can use Z as a measure for the importance of bosonic quantum fluctuations, because it accompanies the trivial quadratic momentum-dependence of the bosonic field in the action – the kinetic term – which drives fluctuations. Inspecting the classical UV action of the GN model, we find that it lacks by construction a term like $\frac{Z}{2} (\partial_\mu \phi)^2$ – which is included in the GNY model with $Z = 1$ – and also all other bosonic higher-order derivative terms, which could partially be associated to the higher-order Taylor coefficients/moments of $\Gamma^{(2)}$ in momentum space. Hence, in the classical action of the GN model all these coefficients are initially zero, because there are no bosonic fluctuations in the UV – there are only non-interacting fermions – and ϕ is only introduced as an auxiliary field. However, by integrating out all fermionic quantum fluctuations and interactions one finds that the system gets strongly coupled and anti-fermion-fermion pairs are bosonized and eventually condense, if the external energy scales (μ and/or T) are not too large [186, 188, 190]. Ultimately, also all of the bosonic derivative couplings are generated by integrating out the fermion fluctuations, as can be seen from our results for Z and $\Gamma^{(2)}$. From an FRG perspective this is a rather natural finding, see Ref. [231] and references therein. Though, the generation

of all these bosonic kinetic couplings actually implies that the system tends to drive bosonic quantum fluctuations by itself, which is only hindered by the artificial suppression of the infinite- N limit. Therefore, one might conclude that our results for the bosonic wave-function renormalization (and the bosonic two-point function) in the infinite- N limit may – at least to some extent – predict the insufficiency of the mean-field approximation at finite N . In consequence one might state, that at least in those areas of the phase diagram, where the bosonic wave-function renormalization significantly deviates from zero and rapidly changes its value (and sign) with μ and T , bosonic quantum fluctuations will play an important role, if the infinite- N approximation is relaxed and calculations are performed at finite N . Interestingly, such values are indeed observed, especially close to the first-order phase transition and right below the LP. This is actually expected, since in these regions correlation lengths usually diverge and fluctuations of all orders become relevant.

To better visualize the behavior of Z , we additionally plot slices through the color map of figure 4.16 in a way to cover all interesting regions of the phase diagram. In figures 4.19 and 4.20 we can observe that the wave-function renormalization increases (decreases) close to the phase transition line⁷⁸ and then jumps from positive to negative values at the phase transition. The region of drastically rising Z is exactly the region adjacent to the first-order phase transition, where the stability analysis fails. Thus, it seems as if the wave-function renormalization already signals that fluctuations and gradient driven bosonic field configurations are of great importance in this region.

4.4.3. Generalized Ginzburg-Landau analysis

This subsection is not based on Ref. [5] and the discussion is original to this work. However the presented results are basically just a projection of the results [495] of H. Abuki et al. into the μ - T -plane using the expressions of subsection 4.3.3 and App. C.4.1. In that sense the presented results are just a comparison of existing literature results.

The results for this gGL analysis of the inhomogeneous phase diagram took only a few minutes to compute on an Intel® Core™ i7-8750H processor with the MATHEMATICA notebook [652].

In this subsection we want to briefly introduce the generalized Ginzburg-Landau (gGL) analysis as another indirect method to study inhomogeneous phases. To this end we will follow Ref. [495] but additional details can be found in Refs. [197, 493, 495, 526, 527] and Ref. [742].

The gGL analysis can be seen as an extension of the conventional GL analysis outlined in subsection 4.3.3. The idea is to expand the effective potential or equivalently the effective action in a gradient expansion. Up to sixth-order such an expansion for a model like the GN model reads,

$$\mathcal{V}[\mu, T; \Sigma(x)] \equiv \langle \omega[\mu, T; \Sigma(x)] \rangle_{\text{WS}} \quad (4.77)$$

⁷⁸Except for $T = 0$, where $Z(\bar{\Sigma}(\mu, 0), \mu, 0)$ is independent of μ for $\bar{\Sigma}(\mu, 0)^2 > \mu^2 \Leftrightarrow \mu < \frac{1}{\sqrt{2}}$, see Eq. (B5) of Ref. [5]. This is a notion of the silver blaze property.

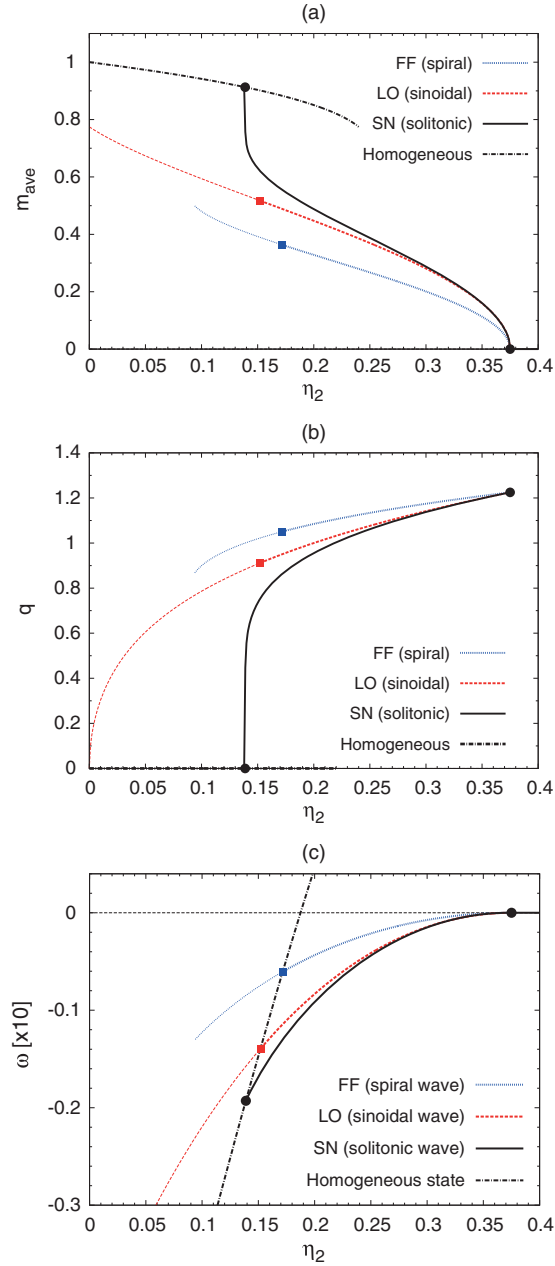


Figure 4.21.: Average mass $m_{\text{ave}} \equiv (\langle \Sigma(x)^2 \rangle_{\text{ws}})^{1/2}$ in (a), wave vector q in (b), and associated energy $\omega \equiv \mathcal{V}[\mu, T; \Sigma(x)]$ in (c) for various inhomogeneous modulations as a function of η_2^A . Note that H. Abuki *et al.* use a different convention for the pre-factors of their gGL coefficients in Eq. (2) of Ref. [495] and thus $\eta_2 = \frac{4}{3}\eta_2^A$. From Fig. 4 of Ref. [495]. Publication under CC BY-SA 4.0 license with the permission of H. Abuki.

as the volume average over the Wigner-Seitz cell of the generalized GL functional

$$\begin{aligned} \omega[\mu, T; \Sigma(x)] \equiv & \alpha_2(\mu, T)\Sigma(x)^2 + \alpha_4(\mu, T) (\Sigma(x)^4 + (\nabla\Sigma(x))^2) + \\ & + \alpha_6(\mu, T)(\Sigma(x)^6 + 5\Sigma(x)^2(\nabla\Sigma(x))^2 + \frac{1}{2}(\Delta\Sigma(x))^2) \end{aligned} \quad (4.78)$$

according to Eqs. (2) and (6) in Ref. [495]. When rescaling all quantities appropriately with α_6 and setting the scale with $|\alpha_2|$, the r.h.s. of Eq. (4.78) has only $\eta_2 \equiv \alpha_2 \alpha_6 / \alpha_4^2$ from Eq. (4.67) as a parameter left. The great advantage of this expansion is that it allows the study of various condensate shapes without the need of any complicated field-theoretical computation. A condensate shape $\Sigma(x)$ gets inserted into Eq. (4.78) and with Eq. (4.77) the corresponding energy can be computed just by taking a suitable volume average. Additionally it is possible to consider Euler-Lagrange equations for $\mathcal{V}[\mu, T; \Sigma(x)]$ which, when limited to one-dimensional modulations, yield the solitonic solutions (4.70) of the GN model as a self-consistent solution. For further details we refer to Refs. [495, 742].

In figure 4.21 results for several one-dimensional modulations are shown over η_2 , with the solitonic wave of the GN model as the energetically most favored solution. Furthermore $\eta_2 = 5/27 (1/2)^{79}$ can be identified as the location of the HBP \leftrightarrow IP (IP \leftrightarrow SP) second-order phase transition. We can use those results with our GL coefficients of subsection 4.3.3 to project the results [495] of H. Abuki *et al.* in terms of η_2 into the μ - T -plane. The result is shown in figure 4.22 together with the reference values of subsection 4.4.1. As one might expect from an expansion basically around the restored/trivial solution $\Sigma(x) = 0$ the gGL expansion loses predictive power when leaving the vicinity of the LP. But it should be noted that around the LP it has both qualitative and quantitative predictive power and might be one of the most promising options when it comes to the search of the preferred condensate shape in models, where the solution to this question is not known. Which basically includes all models in $d > 2$.

We close this discussion by noting, that the stability analysis via the bosonic two-point function, as it is presented in the last subsection 4.4.2, goes beyond the gGL expansion discussed here. The bosonic two-point function Eq. (4.71) retains its full momentum structure, which makes the stability analysis suited for wave vectors q of all magnitudes without the limitation to small q . Comparing figures 4.18b and 4.22 clearly shows the difference in predictive power. Additionally, $\Gamma^{(2)}$ does not even need to be analytic for all q . This was already pointed out in Ref. [199] and such a non-analyticity can be seen in figure 4.12 for $T = 0$. It is also the reason, why the stability analysis is still predicting instabilities of the homogeneous condensate correctly for extremely small and even vanishing temperatures.

It should however be noted that there exist several improved versions, see, *e.g.*, Refs. [495, 526, 527], of the simple expansion up to order six discussed here.

⁷⁹Note that H. Abuki *et al.* use a different convention for the pre-factors of their gGL coefficients in Eq. (2) of Ref. [495] and thus $\eta_2 = \frac{4}{3}\eta_2^A$, *i.e.*, the values on the horizontal axis of figure 4.21 have to be rescaled by a factor $\frac{4}{3}$ to be consistent with the discussion in the text here.

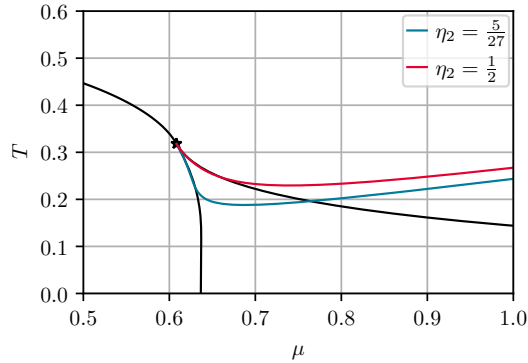


Figure 4.22.: Results for the HBP \leftrightarrow IP and IP \leftrightarrow SP second-order phase transitions with the gGL analysis ($\eta_2 = 5/27$ and $\eta_2 = 1/2$) compared to the reference solution of figure 4.8.

4.5. The Gross-Neveu-Yukawa model at finite N

In this section we mainly follow the discussion of results presented in Sec. VI of Ref. [4].

The plots of Ref. [4] and the majority of underlying numerical data were produced by N. Zorbach. Selected results have been cross-checked by J. Stoll, A. Koenigstein, and me. The single thread wall time on various consumer processors for the numeric results of Ref. [4] is around 80 days, with most of it spend on the computation of the phase diagram 4.35a.

After our discussions in the infinite- N limit of sections 4.3 and 4.4 it is time to use our adapted CFD FRG formalism of section 4.2 to study the GNY model at finite N . To this end we will first give a brief overview of the literature concerning the GN(Y) model at finite N in subsection 4.5.1. Even though there seem to be a lot of indications and notions, that there should not be any symmetry breaking in the GN(Y) model at finite N and $T > 0$, the question is still unsettled and will be at the heart of our research in this section.

So far we have not specified a specific UV initial condition for our LPA flow Eq. (4.21)/(4.31) of the GNY model. In subsection 4.5.2 we will continue the discussion of subsection 4.2.1 by incorporating our findings/rediscoversies of subsection 4.3.1 to construct a UV initial condition viable for flows at finite and infinite N , which is based on the notion of asymptotic freedom. As a first step we will use this IC and our CFD numerics to recover the renormalized, infinite- N phase diagram figure 4.2.

We conclude this section with our FRG study of the GNY model at finite N in subsection 4.5.3. We employ our CFD numerics and perspective to discuss the role of fermionic and bosonic fluctuations in FRG flows at zero and non-zero temperature and chemical potential. The main result of our explicit computations, summarized by the phase diagram 4.35a of the GNY model at $N = 2$, is that bosonic thermal fluctuations vaporize the chiral condensate at any finite N and $T > 0$. This finding is in line with the vague consensus of arguments in subsection 4.5.1, which predict such an outcome but usually are not based on explicit computations at finite N . The CFD perspective of FRG flows developed in chapter 3 allows for a unique and detailed understanding of the role the different fluctuations at finite N .

4.5.1. To break or not to break – \mathbb{Z}_2 symmetry at finite N

This subsection has been copied from Sec. I.B of Ref. [4] with only small adaptations to the presentation in this thesis. While I am the author of a first draft of this subsection, I do not claim sole authorship, since it went through iterations during the preparation of the manuscript for Ref. [4].

The big question that immediately comes to mind if one relaxes the infinite- N limit and studies the GN model for finite N is, if spontaneous symmetry breaking (SSB) and condensation still takes place, especially when medium effects (non-zero μ and/or T) are included.

At first sight, it seems as if already the Coleman-Mermin-Wagner-Hohenberg (CMWH) theorem [550–552] forbids the formation of a condensate at non-zero temperatures. Though, the theorem strongly relies on the presence of massless Nambu-Goldstone bosons [441, 442, 563], which are only included in extensions of the GN model, e.g., the chiral GN model [197, 497, 743] with continuous chiral symmetry or other related models [171, 674]. We therefore believe that one should exercise caution, when arguing directly with this theorem.

Nevertheless, a qualitative argumentation was put forward already by L. D. Landau in 1950 [744], which should in principle forbid also discrete chiral symmetry breaking in one-spatial dimension at non-zero temperature. L. D. Landau and E. M. Lifshitz argue in Chap. 163 of Ref. [744] that for systems in one dimension of infinite extent only one phase can exist at $T > 0$, since coexistence of more than one phase is energetically disfavored. To be concrete, they considered a bistable system in one dimension of infinite extent at non-zero temperature with n interfaces between the two possible phases per length L and showed that the thermodynamic potential of the system can be decreased by increasing the concentration of interfaces n/L , which is directly related to the entropy, assuming a finite interface energy. Thus the system breaks down into a macroscopic number of domains, which rendered macroscopic phase coexistence at non-zero temperature impossible. Landau’s argument can be applied to a broad range of effectively one-dimensional systems including the Ising model in one spatial dimension [561] at $T \neq 0$, which is always in its \mathbb{Z}_2 -symmetric phase, cf. Refs. [171, 178]. A dedicated discussion of Landau’s argument in the context of one-dimensional systems can be found in Ref. [745].

In their study [188] of the GN model based on a large- N expansion R. F. Dashen, S. Ma, and R. Rajaraman were able to confirm Landau’s argument, see also Ref. [714]. They found no SSB for any small but non-zero temperature and finite N . Using in parts heuristic arguments, they showed that the entropic gain of a field configuration of alternating kinks is large enough at finite N and $1/T$ to be energetically preferred over a homogeneous configuration⁸⁰. Those field configurations alternating in kinks have a vanishing chiral condensate $\langle \tilde{\psi} \tilde{\psi} \rangle = 0$. In the infinite- N -limit (mean-field), the energy per kink becomes infinite and consequently the density of kinks approaches zero realizing a homogeneous field configuration compatible with

⁸⁰Homogeneous and inhomogeneous field configurations in this context refer to the configurations used to evaluate the partition function in a saddle-point approximation, see Ref. [188] for details on their computation, and they are not to be confused with homogeneous and inhomogeneous classical/mean field configurations $\langle \tilde{\psi} \tilde{\psi} \rangle(x)$ discussed in the previous section 4.1.

$\langle \tilde{\psi} \tilde{\psi} \rangle > 0$ allowing for SSB. This is no contradiction to Landau’s argument since the latter only holds assuming finite interface energies [744, 745]. Although R. F. Dashen, S. Ma, and R. Rajaraman argue that $T_C = 0$ at finite N , they do not discuss the situation for $T = 0$ and $\mu \geq 0$ for finite N in Ref. [188].

Another discussion on the absence of symmetry breaking in one-spatial dimension at non-zero T can be found in Ref. [674] by E. Witten, which discusses the absence of a phase with spontaneous symmetry breaking and long-range order in accordance with the CMWH theorem [550–552] and the related possibility for a phase of Berezinski-Kosterlitz-Thouless type [746, 747] with quasi long-range order for the $SU(N)$ Thirring model [673, 674].

Other authors, *e.g.*, U. Wolff [190], argue based on the duality of the spatial and Euclidean time direction in 1+1 dimensions for $T > 0$ and $\mu = 0$: The thermal GN model in 1+1 dimensions is equivalent to a QFT with a finite spatial volume (but infinite Euclidean time-direction) and hence no SSB takes place since it is canonically considered as an effect only present in systems with infinite volumes, see, *e.g.*, Ref. [240]. While this reasoning – the general absence of SSB in finite systems – might strictly speaking be sound, sufficiently large volumes, the inclusion of small (possibly infinitesimal) explicit symmetry breaking, or subtleties of the thermodynamic and/or infinite volume limit, *cf.* Ref. [748], can lead to signatures reminiscent of SSB.

Indeed, only recently some of our colleagues and collaborators found some indications via numerical lattice Monte-Carlo simulations [519–522], that some (inhomogeneous) condensation phenomena in the massless bGN model at finite N and non-zero μ and T still seem to be present. Similar results were already found in earlier lattice Monte-Carlo studies [693–695] at finite N . However, in all of these works, the above arguments by Landau *et al.* against condensation at non-zero T could neither be completely ruled out nor be confirmed. In fact, most of the results suffer from the facts that proper continuum and infinite volume extrapolations were not performed. Consequently finite volume effects and discretization artifacts limit the predictive power of those results for the continuum theory in an infinite volume. The finite sized spatial domain (and the related BCs) might have prevented a sufficient resolution of long-range fluctuations, which are however of uttermost importance for condensation and in this context especially vaporization phenomena in low-dimensional systems.

Recent lattice results presented in Refs. [519–522] have sparked further lattice studies of four-Fermi models in 1 + 1 dimensions: We are aware of these parallel developments and computations using lattice Monte Carlo simulations in the GN model and related models (especially the chiral GN model) in Refs. [749, 750], which are however not completed yet and therefore omitted in the following discussion. For the chiral GN model, we expect some interesting dynamics at finite N due to competing effects from the CMWH theorem and a $U(1)_A$ anomaly [743].

All of this lead us to the idea to study the phenomenon of \mathbb{Z}_2 symmetry breaking and/or restoration in the GN model at finite N , $T \geq 0$, and also $\mu \geq 0$ but in an infinite spatial volume

within a different framework – namely within our CFD frame work for FRG flow equations.⁸¹ We wanted to find out, if it is possible to (numerically) confirm the arguments by Landau *et al.* against symmetry breaking in the GN model or if there are some other competing effects, which are not captured in the aforementioned mostly qualitative/heuristic discussions, that allow for symmetry breaking or some long-range ordering.

4.5.2. UV initial condition for FRG flows at variable N

This subsection is based on Secs. V.D and E of Ref. [5].

We again turn to the UV IC for the effective potential and continue the discussion of subsection 4.2.1. For practical calculations within the FRG framework, where the flow is not integrable analytically, we can not initialize the FRG flow directly at $\Lambda = \infty$. But rather we have to choose a sufficiently large and but finite Λ to specify the initial values for the flow via $\bar{\Gamma}_\Lambda[\chi] = \mathcal{S}[\chi]$. For a general discussion in the context of RG consistency we refer to subsection 2.1.6 and our specific, explicit discussion of the issue in zero dimensions in subsection 3.2.3.1.

From the previous discussion in subsection 4.3.1, it is obvious, how to specify the IC for a numeric solution of Eq. (4.42) or rather Eq. (4.31) with $Q(t, \partial_\sigma u) = 0$, *i.e.*, in the mean-field approximation:

In our discussion on asymptotic freedom, we were able to eliminate g^2 from the IC (4.44) in favor of the UV scale Λ and the combination $\Delta_0 \equiv h\sigma_0$. Hence, we can simply use Eq. (4.51) as the initial potential at some large scale Λ . Initializing the (numeric) mean-field version of the FRG flow (4.31) with the σ -derivative of (4.51) and an arbitrary value for h at some scale $\Lambda \gg h$, one always finds that the IR minimum in vacuum is located at σ_0 . Consequently and w.l.o.g. we can rescale all dimensionful quantities in terms of h and express the dimensionless field space variable σ in multiples of σ_0 . On the level of the equations, this amounts to setting $\sigma_0 = 1$ and $h = 1$. Other choices for h and σ_0 correspond to different renormalization conditions, but all results are unique and can be transformed into each other via simple rescaling – as already mentioned. However, we still have to ensure that other IR observables do not depend on the UV scale Λ , which is realized by choosing Λ much larger than all internal and external model scales. This checked numerically in the following paragraph discussing figure 4.23.

Including bosonic quantum fluctuations, it is less obvious, how to choose the IC for the FRG flow, that means how to choose a meaningful value for $\frac{h^2}{g^2}$ in Eq. (4.26). When performing calculations at finite N , each individual choice of N represents a single model on its own. Hence, even if there is symmetry breaking for the vacuum flow equation (4.24) including bosonic quantum fluctuations, the IR physics for different N is not necessarily directly comparable. Thus, setting a unique renormalization condition for all N in the IR, like fixing the position of

⁸¹After completing Ref. [4], we became aware of Ref. [715], where next-to-leading order corrections of the $\frac{1}{N}$ -expansion to the effective potential of the GN model were calculated. Finding that this expansion breaks down in the vicinity of mean-field critical temperature T_C the authors also suggest to analyze the GN model within the FRG framework, which is the main focus of this section and one main purpose of this whole chapter. We thank J. Braun for drawing our attention to this interesting publication.

the IR minimum and/or the IR curvature mass by tuning the various UV ICs, is – to the best of our knowledge – not useful.

We think that it is natural to use exactly the same IC for all FRG flows, namely Eq. (4.51), with and without bosons and to fix the renormalization condition for the bosonic FRG flows in the UV. This might be counter-intuitive, because in a lot of FRG studies for effective models of strongly correlated systems, the physics is fixed in the IR and the UV IC is tuned, in such a way that the FRG flow ends up with an IR effective action having observables compatible with desired numerical values. We are however using the GN model in our studies with the same top-down approach, used in the FRG studies of QCD, discussed in subsection 2.3.3. We make use of asymptotic freedom and RG consistency to fix our initial condition and associated UV initial scale Λ in the following way.

Using the same UV IC for all finite and infinite N allows for a direct comparison of calculations at different N . This is the case, because the $\frac{1}{N}$ -rescaled UV potential (4.51) always describes a theory of N asymptotically free fermions and a σ -mode that decouples from the system at the UV initial scale. Choosing $\Lambda \gg h$ naturally leads to a large curvature mass $\partial_\sigma^2 U(t, \sigma)$ and suppression of fluctuations of the σ -mode in the UV, which can be directly seen in Eq. (4.51). On a formal level this can be seen by inspecting the fluid-dynamic formulation of the FRG flow equation (4.31) and especially its bosonic contribution in terms of a highly non-linear diffusion equation (4.34). One finds that the large curvature mass $\partial_\sigma^2 U(t, \sigma) = \partial_\sigma u(t, \sigma)$ in the propagators $\frac{1}{E_\sigma}$ yields a small diffusion coefficient $\alpha(t, \partial_\sigma u)$ and therefore a suppression of the diffusion along field space – the bosonic contribution to the FRG flow.

Though, the more drastic argument, why bosonic fluctuations are actually totally absent in the UV, is a fundamental property of all diffusion equations of type $\partial_t u(t, \sigma) \propto \partial_\sigma^2 u(t, \sigma)$. Independent of the finite diffusion coefficient the term $\partial_\sigma^2 u(t, \sigma)$ vanishes exactly for spatially linear $u(t, \sigma) \propto \sigma$ and the diffusion and dynamics stops, cf. subsection 2.2.4 and especially the discussion surrounding Eq. (2.139c') as an equilibrium solution to the HE (2.138) with Dirichlet BCs. In the context of this work, it follows from the quadratic UV potential (4.26) that $u(0, \sigma) \propto \sigma$ and consequently the contribution from the σ -mode to the FRG flow vanishes exactly. Bosonic fluctuations will be suppressed as long as the fermionic source/sink contributions to the FRG flow do not alter the linear shape of $u(t, \sigma)$, which is approximately the case until $k^2(t) \approx (h\sigma)^2$ for small σ . We conclude that the FRG trajectories in theory space for FRG flows including fermions and bosons at finite N will approximately follow the mean-field FRG trajectories for infinite N , as long as the UV initial potential is quadratic in σ . This behavior is indeed observed in our numeric computations in subsection 4.5.3.

It also gives merit to our choice of setting $Z_\varphi(t=0) = 1$ in the UV and we expect to resemble the dynamics of the GN model with the GNY model in LPA to a certain extent. Even though $Z_\varphi(t=0) = 1$ would allow for contributions of bosonic fluctuations to the FRG flow at the initial scale, our choice of UV IC leads to a vanishing contribution of the corresponding diffusion flux. Given our discussion in subsection 4.4.2.4 fermionic fluctuations will eventually generate a non-vanishing $Z_\varphi(t)$ at non-zero t , so initializing the wave-function renormalization for the bosons with a non-zero value is certainly justified especially from an RG consistency perspective. So our flows in the GNY model at early RG times are completely dominated by fermionic

contributions and only after their sink/source dynamics leave a significant imprint on $u(t, \sigma)$ bosonic contributions become relevant. This is very reminiscent of the sequential decoupling, in composite FRG flows for hadronized QCD, described in subsection 2.3.3. However, as we will see in subsection 4.5.3, the decoupling is even more clear and pronounced in the GNY model.

Our last formal argument is based on the previous discussion and concerns regarding the UV-scale-independence, *i.e.*, RG consistency, of IR observables for FRG flows at finite N . Because the FRG trajectories at finite N will approximately follow the mean-field FRG trajectories at infinite N , we expect that choices of Λ , which are sufficiently large to ensure UV-scale-independence at infinite N , should also suffice to ensure RG consistency for FRG flows at finite N , if the same UV initial potential is used. This is explicitly demonstrated in App. F.3 of Ref. [4], where we numerically demonstrate UV scale independence of the calculations presented in subsection 4.5.3 in the spirit of our related test in zero dimensions, *cf.* figures 3.11 and 3.24c.

In summary, as a first approach to enable a comparison of FRG flows within the GNY with bosonic quantum fluctuations at different N , we choose exactly the same UV IC (4.51) with $h = 1$ and $\sigma_0 = 1$ for all FRG flows. Hence, all dimensionful quantities are measured in terms of the UV value of the Yukawa coupling h (which stays constant in our truncation anyhow), while field space is measured in multiples of the mean-field minimum σ_0 , which has turned into a free additional parameter. Including bosonic fluctuations σ_0 is no longer the position of the vacuum IR minimum, but modifies the ratio of the Yukawa coupling h and Λ in the UV, *cf.* Eq. (4.51). Of course, this ratio will still influence the dimensionless position of the vacuum IR minimum even in the presence of bosons. Hence, it is most convenient for us to choose $\sigma_0 = 1$ in the IC (4.51) to recover the infinite- N results directly for $N \rightarrow \infty$, without trivial rescalings. Still, we also performed calculations for $\sigma_0 \neq 1$, which did not alter the qualitative results.

Overall this implies that we do not perform computations for different N on lines of “constant IR physics”. We compute on “constant UV physics” for different N , which is no problem for us, since we are not interested in specific values for IR observables anyway. Again, as mentioned in [A disclaimer about physics](#) in chapter 1, we do not use the GN(Y) model to describe physical systems, we use it as a testing ground.

(Numeric) consistency check with the renormalized, infinite- N results

This paragraph is dedicated to a consistency check of our numeric implementation of the fermionic contribution to the FRG flow. Furthermore, we comment on the concept of RG consistency in the context of the discussed mean-field calculations, as a direct application of the first scenario described in subsubsection 2.1.6.1.

For the consistency checks in this section we use the numerical implementation presented in subsection 4.2.2 and manually switch off the bosonic contribution (the diffusion) in the flow equation (4.31). Since Eq. (4.31) is formulated for $u(t, \sigma) = \partial_\sigma U(t, \sigma)$, we used the σ -derivative of Eq. (4.51) as the IC for $u(t, \sigma)$. Furthermore, as already done in the previous section 4.3, we work in rescaled quantities. This means that σ is measured in multiples of σ_0 and dimensionful quantities are measured in multiples of the Yukawa coupling h – implying

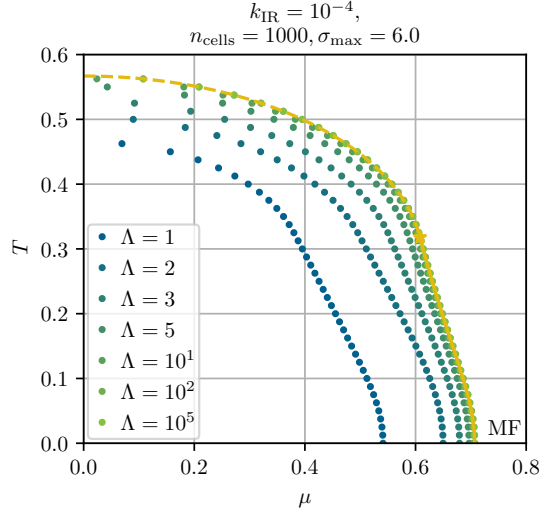


Figure 4.23.: Phase transition lines (equally colored dots) in the μ - T -plane of the GNY model (4.8) in the mean-field approximation for different values of the UV scale Λ . The curves are extracted from numerical solutions of the FRG flows of $u(t, \sigma)$ with the methods presented in subsection 4.2.2. As a reference curve, we also plot the exact phase transition line (in yellow) in the renormalized limit $\Lambda \rightarrow \infty$ below the data points, cf. figure 4.2. FRG flows for larger cutoffs Λ are closer to the renormalized reference result. From Fig. 3 of Ref. [4].

w.l.o.g. $h = 1$ and $\sigma_0 = 1$ on the level of the equations. Thus, the UV IC for the (numeric) FRG flow in dimensionless variables explicitly reads

$$u(t = 0, \sigma) = \frac{d_\gamma}{2\pi} \sigma \left[\operatorname{artanh} \left(\left[1 + \left(\frac{1}{\Lambda} \right)^2 \right]^{-\frac{1}{2}} \right) - \left[1 + \left(\frac{1}{\Lambda} \right)^2 \right]^{-\frac{1}{2}} \right]. \quad (4.79)$$

The explicit dependence on Λ of $u(t = 0, \sigma)$ realizes non-trivial IR minima at $\pm\sigma_0$ independent of the UV initial scale by a RG-consistent construction in vacuum.

One way to ensure RG consistency in medium is to choose Λ significantly larger than all external scales of the problem under consideration. We will discuss this on mean-field level in this subsection while dedicating subsection 4.5.3 to a similar discussion at finite N .

While the condensate is fixed in the IR in vacuum by construction, the corresponding sigma curvature mass, see Eq. (4.54), is not. Comparing the expression (4.54) at finite Λ to the renormalized result of Eq. (4.57) we conclude that a relative difference of for example 10^{-3} (10^{-6}) between m_σ^2 at finite and infinite Λ requires an UV initial scale of around 40 (1200). Considerations like this in vacuum give insight into internal model scales.

Studying the Λ -dependence of observables at $\mu > 0$ and/or $T > 0$ we can assess the relation between Λ and the external model scales. To this end we plot the phase transition lines in the μ - T -plane, which we obtain via the numerical solution of the purely fermionic FRG flow equation for various Λ in figure 4.23. The phase boundaries are extracted via the bisection method [554, 555] in the μ - T -plane, by extracting the minimum of the IR potential from the cell averages $\{\bar{u}_i(t_{\text{IR}})\}$.

As reference values for the mean-field phase boundaries in figure 4.23, we use the exact results of the previous section, which are also plotted in figure 4.2. We observe a dependence of the phase boundary between the restored and broken phase on Λ . Increasing Λ beyond 10^2 we observe an apparent convergence of the numerically obtained phase boundaries, which eventually for $\Lambda \approx 10^5$ approaches the phase boundary of the renormalized mean-field computation. The general UV initial scale dependence at non-zero chemical potential and temperature is easily understood when considering the expression (4.43) of the underlying IR potential. In FRG based mean-field computations with the Litim regulator the UV initial scale acts basically like a sharp momentum cutoff (with an additional surface term, see also App. E.2).

We find that our numeric implementation of the source term in the FRG flow equation (4.31) is capable of reproducing the conventional mean-field results. Furthermore, we already obtain some estimate for decent UV-cutoffs Λ for computations involving bosonic quantum fluctuations. At this point we can close all our preliminary discussions and finally turn our attention to bosonic quantum fluctuations at finite N .

4.5.3. Bosonic quantum fluctuations in the GNY model

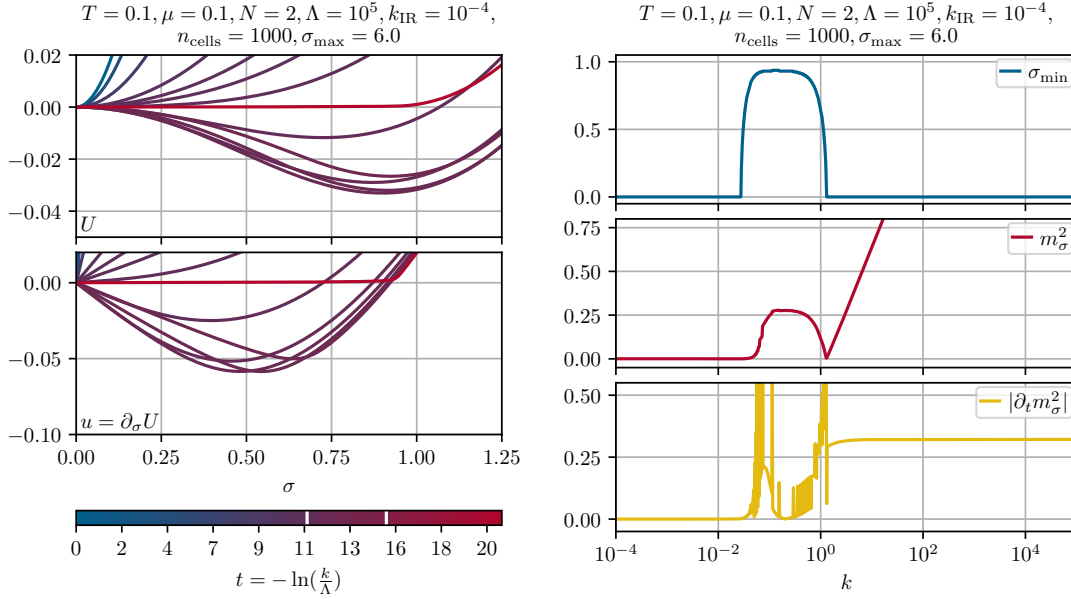
In this subsection we closely follow the discussion of results presented in Sec. VI of Ref. [4].

In this subsection, we present our (numeric) results for FRG flows of the GNY model at non-zero μ and T including bosonic quantum fluctuations in the LPA. Thereby we proceed as follows: First, we discuss the dynamics, which take place during a single FRG flow at some fixed finite N , μ , and T , cf. the similar discussion in subsection 3.2.3.1 for the zero-dimensional $O(N)$ model. This sets the stage for a detailed discussion of the effects that are induced by the chemical potential at low temperatures. Here we support our conceptual discussion of subsection 4.2.2 with explicit numerical computations. Afterward, we turn to our central result – the absence of spontaneous \mathbb{Z}_2 symmetry breaking at finite N and $T > 0$. We thereby present details on dependencies on μ , T , and N of the restoration scale k_{res} , where the discrete chiral symmetry is restored, as well as a phase diagram during the FRG flow.

4.5.3.1. Symmetry breaking and restoration during the FRG flow

This subsection is dedicated to an instructive discussion of symmetry breaking and restoration during FRG flows in the framework developed within section 3.2. To get a better intuition on how this realizes during the FRG flow and how the typical setup and dynamics looks like, we picked a single point in the μ - T -plane, namely $\mu = 0.1$ and $T = 0.1$, where we at least expect some non-trivial condensation and vaporization phenomena and typical dynamics in the FRG flow. We also fixed the number of fermions to $N = 2$. The computational parameters used for the computations in this subsection are $\sigma_{\text{max}} = 6$, $n_{\text{cells}} = 1000$, $\Lambda = 10^5$, and $k_{\text{IR}} = 10^{-4}$. They have been validated with the methodology developed in subsection 3.2.3 and the detailed checks and numerical tests can be found in App. F of Ref. [4]. As UV initial condition, we directly use Eq. (4.79), as discussed in subsection 4.5.2, with $h = 1$ and $\sigma_0 = 1$.

Using this setup, we obtain the numeric results for the FRG flow of $u(t, \sigma)$ and $U(t, \sigma)$.



(a) FRG flow of the scale-dependent effective potential $U(t, \sigma)$ (upper panel) and its σ -derivative (the fluid) $u(t, \sigma) = \partial_\sigma U(t, \sigma)$ (lower panel) from the UV (blue) to the IR (red). For the sake of simplicity (and using the (anti-)symmetry in σ) the functions $u(t, \sigma)$ and $U(t, \sigma)$ are plotted for positive σ only. The different RG times are encoded via the colored bar-legend below the plots. The white vertical lines in the colored bar-legend denote the RG times (scales) when the \mathbb{Z}_2 symmetry is broken (condensation) and restored (vaporization).

(b) FRG flow of the minimum $\sigma_{\min}(k)$ (upper panel), the squared curvature mass $m_\sigma^2(k) = \partial_\sigma^2 U(t, \sigma)|_{\sigma_{\min}(t)}$ at the moving minimum $\sigma_{\min}(t)$ (middle panel), and the relative change of the squared curvature mass $|\partial_t m_\sigma^2(k)|$ (lower panel) according to Eq. (4.81) plotted as functions of the RG scale $k(t)$. Note, that the curvature mass at the moving minimum in the IR is non-zero, $m_\sigma^2(t_{\text{IR}}) \approx 4.60 \cdot 10^{-4}$.

Figure 4.24.: FRG flow of the potential $U(t, \sigma)$ and its derivative on the left (a) and corresponding evolution of $\sigma_{\min}(k)$, $m_\sigma^2(k)$ and changing rate $|\partial_t m_\sigma^2(k)|$ on the right (b) for $N = 2$ at $T = 0.1$ and $\mu = 0.1$. From Figs. 4 and 5 of Ref. [4].

The latter is reconstructed from the cell averages $\{\bar{u}_i(t)\}$ by direct Riemann summation, cf. Eq. (3.96) and the corresponding discussion in subsection 3.2.3.1. The FRG flow of the potential is depicted in figure 4.24a with figure 4.24b showing the associated evolution of the scale-dependent minimum $\sigma_{\min}(t)$ and the scale-dependent curvature mass,

$$m_\sigma^2(t) = \partial_\sigma^2 U(t, \sigma)|_{\sigma_{\min}(t)} = \partial_\sigma u(t, \sigma)|_{\sigma_{\min}(t)}, \quad (4.80)$$

which is evaluated at the moving scale-dependent minimum. We determine the position of the scale-dependent minimum $\sigma_{\min}(t) = \Delta\sigma \cdot i_{\min}(t)$, by searching for the position $i_{\min}(t)$ of cells next to zero-crossings in the list $\{u(t, \sigma_i)\}$ combined with a check of the list $\{U(t, \sigma_i)\}$ for its smallest entry. The curvature mass is calculated at this minimum via a simple right-derivative stencil, hence $\partial_\sigma u(t, \sigma)|_{\sigma_{\min}(t)} = \frac{1}{\Delta\sigma} [\bar{u}_{i_{\min}+1}(t) - \bar{u}_{i_{\min}}(t)]$. For optical guidance and better detection, when the plateau in IR is reached, we also introduce the changing rate of the

curvature mass

$$\partial_t m_\sigma^2(k_j) \equiv -k_j \frac{m_\sigma^2(k_{j+1}) - m_\sigma^2(k_j)}{k_{j+1} - k_j}, \quad (4.81)$$

which we evaluated for the plots at $j \in \{0, 1, \dots, 998\}$ intermediate RG scales k_j between $k = \Lambda$ and $k = k_{\text{IR}}$, such that the belonging RG times are equidistantly distributed.

In figure 4.24 we observe the following dynamics: The flow for $u(t, \sigma)$ starts with the UV initial condition that is linear in σ . At the beginning of the flow the fermions are active and clearly dominate the dynamics, according to the sink/source contribution in the fluid-dynamic language. We find that this sink/source contribution causes the \mathbb{Z}_2 symmetry breaking and generation of a non-trivial minimum at $k(t \approx 11.2) \approx 1.31$, which is roughly at the order of the model scales, which are of order 1 (cf. position of the intermediate minimum or value of h). Shortly after the non-trivial minimum has formed, the sink (source) is still active, but the diffusion caused by the bosonic contributions sets in, due to the negative gradients $\partial_\sigma u(t, \sigma)$ close to $\sigma = 0$, which enhance the diffusion coefficient. Interestingly, when the position of the minimum (the value of the condensate) has settled, it is approximately of the same order of magnitude as for the mean-field calculations, even though $N = 2$ is everything but close to $N \rightarrow \infty$. As a matter of fact, this signals that the diffusion is weak at $\sigma > \sigma_{\min}(t)$. Subsequently, for approximately another two orders of magnitude in RG scale $k(t)$, the minimum keeps its position $\sigma_{\min} \approx 0.93$. Also the bosonic curvature mass seems to freeze at $m_\sigma^2 \approx 0.28$ and the potential $U(t, \sigma)$ is not changing much. However, having a closer look at $u(t, \sigma)$, we find that the diffusion in field space direction σ causes some highly non-linear dynamics, especially close to the point, where the gradient $\partial_\sigma u(t, \sigma)$ changes its sign. Suddenly, at $k(t \approx 15.1) \approx 2.76 \cdot 10^{-2}$, we observe a destabilization of the condensate $\sigma_{\min}(t)$ and also $m_\sigma^2(t)$ starts changing drastically. The inclusion of IR modes in a small momentum range leads to a complete vaporization of the condensate. Additionally, inspecting $U(t, \sigma)$, we find that meanwhile the potential turned convex – as it should be the case in the IR. This flattening of the potential is completely driven by the highly non-linear diffusion, cf. subsection 3.2.4. Finally, we find that the dynamics completely freezes and that we indeed integrated out all fermionic and bosonic quantum fluctuations. This can be seen best by looking at the absolute value of the changing rate of the squared curvature mass $|\partial_t m_\sigma^2(t)|$, but also directly from $m_\sigma^2(t)$ or $\sigma_{\min}(t)$. Note, that $m_\sigma^2(t_{\text{IR}}) \approx 4.60 \cdot 10^{-4}$, which is not visible from the plot, while $\sigma_{\min}(t) = 0$ already shortly after $k(t \approx 15.1) \approx 2.76 \cdot 10^{-2}$.

Overall, we observed that the fermions were indeed able to form a condensate, which however does not survive the long-range bosonic quantum fluctuations in the deep IR. This dynamics might also be referred to as precondensation [273, 510, 699, 751–753].

4.5.3.2. The role of the chemical potential in the fluid-dynamic setup

Before we come to our discussion on symmetry breaking and restoration in FRG flows for arbitrary N and arbitrary points in the μ - T -plane, we briefly return to the discussion in subsection 4.2.2 on the role of the chemical potential in the fluid-dynamic formulation of the FRG flow equation (4.31). We therefore accentuate our theoretical discussion with explicit

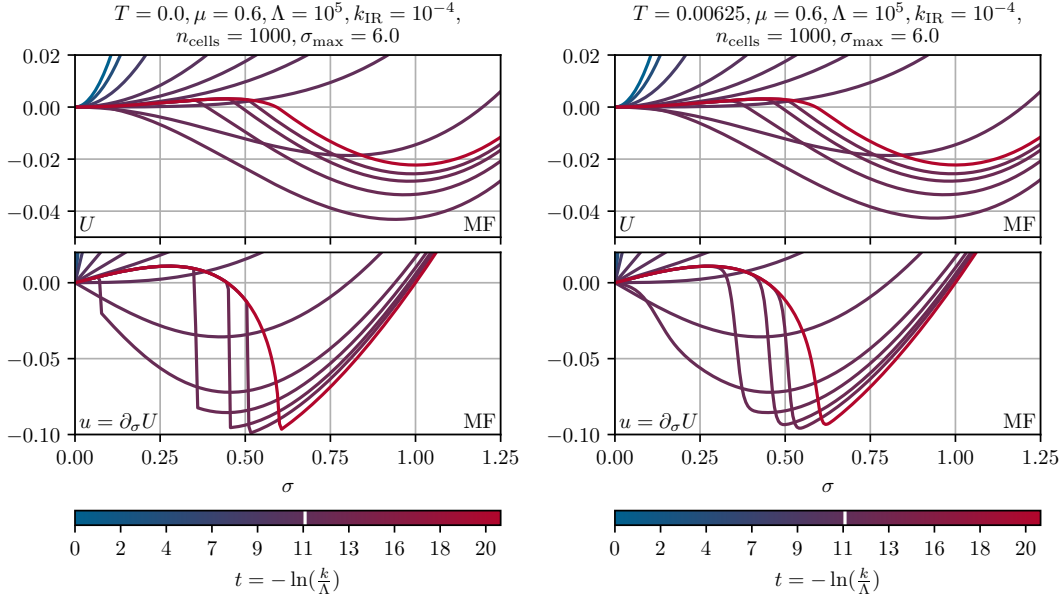


Figure 4.25.: Mean-field (infinite- N) FRG flow (sink term only) of the scale-dependent effective potential $U(t, \sigma)$ (upper panel) and its σ -derivative (the fluid) $u(t, \sigma)$ (lower panel) from the UV (blue) to the IR (red). For $T = 0$ on the left (a) and $T = 0.00625$ on the right (b) both at $\mu = 0.6$. The white vertical line in the colored bar-legend denotes the RG time (scales) when the \mathbb{Z}_2 symmetry is broken (condensation). There is no symmetry restoration at these points in the phase diagram in MF. *From Figs. 6 and 7 of Ref. [4].*

calculations and plots of FRG flows at very low as well as vanishing temperature and moderate chemical potential. W.l.o.g. we choose $\mu = 0.6$ and $T = 0.00625$ or $T = 0$.

Therefore we present figure 4.25a as the reference plot of our discussion. It shows the mean-field FRG flow for $u(t, \sigma)$ and $U(t, \sigma)$ at $T = 0$ and $\mu = 0.6$. As predicted the chemical potential enters the FRG flow of $u(t, \sigma)$, which is entirely described via the source/sink equation, suddenly as a discontinuity of $u(t, \sigma)$ in field space. This discontinuity appears at $\sigma = 0$ when $k^2(t) \approx \mu^2$ and moves towards larger $|\sigma|$ until $\sigma^2 \approx \frac{\mu^2}{h^2}$ ($h = 1$). Formally, this discontinuity leads to infinite negative gradients $\partial_\sigma u(t, \sigma)$ and impedes the following study of bosonic quantum fluctuations at $T = 0$, $\mu \neq 0$ and finite N . This is, because $E_b^2(t, \partial_\sigma u) = k^2(t) + \partial_\sigma u(t, \sigma) \approx \mu^2 + \partial_\sigma u(t, \sigma) < 0$, which leads to an abrupt overshooting over the poles of the bosonic propagators $\frac{1}{E_b}$ and drives the diffusion coefficient $\alpha(t, \partial_\sigma u)$ from Eq. (4.34) negative.

After spatial integration of $u(t, \sigma)$ the remnant of the discontinuity is clearly visible in $U(t, \sigma)$ in terms of a moving cusp. Additionally, it is worth mentioning that the potential $U(t, \sigma)$ is in the symmetry broken phase and everything but flat for small $|\sigma|$ in the IR, which violates a fundamental property of thermodynamic potentials and $\Gamma[\varphi, \psi, \bar{\psi}]$, namely convexity. This is a typical mean-field/infinite- N artifact.

In order to study, how the chemical potential influences the bosonic FRG flows, hence the diffusion in field space, we first slightly increase the temperature of the mean-field calculation

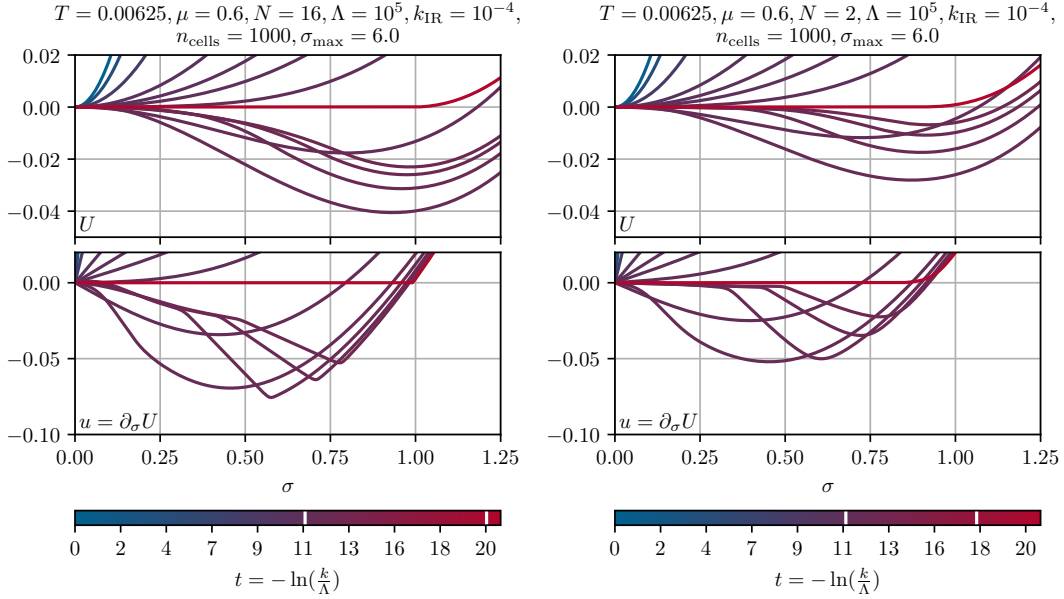


Figure 4.26.: Same FRG flow as in figure 4.25b but $N = 16$ on the left (a) and $N = 2$ on the right (b) instead $N \rightarrow \infty$, thus involving the effects of bosonic quantum fluctuations (diffusion). From Figs. 8 and 9 of Ref. [4].

to $T = 0.00625$, while keeping the same chemical potential $\mu = 0.6$. In figure 4.25b it is clearly visible that the huge negative gradients $\partial_\sigma u(t, \sigma)$ are still present and the overall shape and flows of $u(t, \sigma)$ and $U(t, \sigma)$ do not change much compared to figure 4.25a.

Though, already very small temperatures are able to smear out the sharp edges of the jumps, which smoothens $u(t, \sigma)$ significantly already without any diffusive contributions from the bosons. This effect stemming from the Fermi-Dirac distribution function (C.18) enables the inclusion of bosons, since gradients are still large, but finite.

The next question is, what happens, if the number of fermions is finite and bosonic fluctuations enter the FRG flow as non-linear diffusion on the level of $u(t, \sigma)$. To this end, we plot the same FRG flows as before at $T = 0.00625$ and $\mu = 0.6$ for $N = 16$ fermions in figure 4.26a.

Even though the number of fermions seems to be rather large, the overall picture changes drastically when compared to the situation in the limit $N \rightarrow \infty$. We observe that the chemical potential is still clearly visible on the level of $u(t, \sigma)$ in terms of rather large gradients and cusps. But it is hardly visible in $U(t, \sigma)$. The highly non-linear character of the diffusion does not really smear out the cusps, but results in the somewhat strange movement of the straight part of $u(t, \sigma)$ between the two pronounced edges. Finally, the greatest difference to the mean-field calculations is that the diffusion vaporizes the condensate and fully restores the \mathbb{Z}_2 symmetry in the IR⁸². Additionally, the potential $U(t, \sigma)$ turns convex in the IR, as

⁸²We have checked numerically that there is indeed only a trivial minimum at $\sigma = 0$, which is hardly visible, because $u(t_{\text{IR}}, \sigma)$ and $U(t_{\text{IR}}, \sigma)$ are extremely close to the σ -axis in the relevant region. For details, we refer to the discussions within the next subsections.

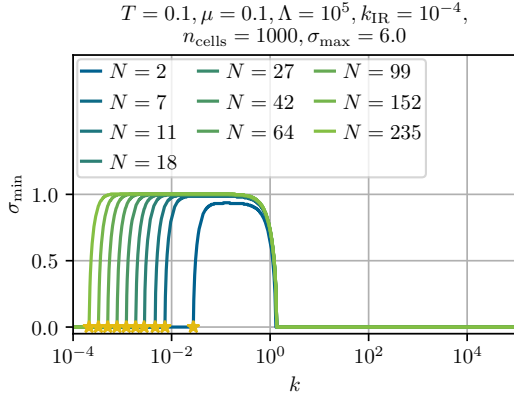


Figure 4.27.: FRG flows of the value of the condensate (the position of the minimum) $\sigma_{\min}(k)$ for various N as functions of the RG scale k at $T = 0.1$ and $\mu = 0.1$. The yellow stars mark the RG scales k_{res} , where the \mathbb{Z}_2 symmetry is restored, signaled by a vanishing condensate. From Fig. 10 of Ref. [4].

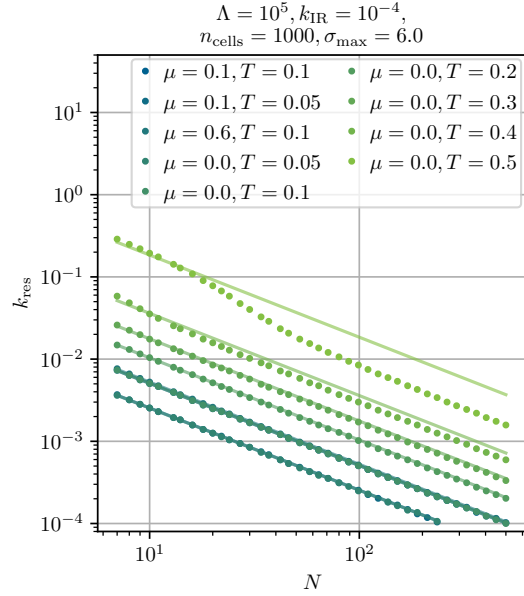


Figure 4.28.: Restoration scale k_{res} , where the \mathbb{Z}_2 symmetry is restored during the FRG flow, as a function of the number of fermions N at various points in the μ - T -plane, where the \mathbb{Z}_2 symmetry was dynamically broken at $k > k_{\text{res}}$ by the fermions. For $\mu = 0.1$ and $T = 0.1$ the data points correspond to the yellow stars in figure 4.27. For the various (μ, T) -tuples we include $k_{\text{res}}(N) \propto N^{-1}$ fits ought to be used for optical guidance. Note, that the points for equal temperatures but different chemical potentials are lying on top of each other. In subsection 4.5.3.5 we will discuss this in detail. From Fig. 11 of Ref. [4].

expected in the case of finite N . Already from this calculation it is obvious that large but finite numbers of N yields entirely different results than the $N \rightarrow \infty$ limit, as prominently stated in various publications [171, 178, 674] and exemplified in great detail in subsection 3.2.5 for the zero-dimensional $O(N)$ model at large N .

Finally, we further decrease the number of fermions to $N = 2$ and again study the FRG flows at $T = 0.00625$ and $\mu = 0.6$. In the corresponding figure 4.26b we observe that the diffusion via the σ -mode sets in much earlier during the FRG flow and the intermediate symmetry breaking is less drastic. The reason is rather obvious: Changing N in Eq. (4.23) changes the relative strength between bosonic and fermionic interactions (fluctuations). On the level of the fluid-dynamic equation (4.31) this implies that the flow is either more diffusion (for small N) or more source/sink (for large N) dominated. Still, even for $N = 2$ the chemical potential is

clearly visible in form of a slightly smeared and moving cusp in $u(t, \sigma)$. Apart from this, the qualitative picture is similar to the $N = 16$ scenario.

4.5.3.3. Varying the number of flavors N

Next, we turn to a more systematic analysis of our previous findings regarding FRG flows at different numbers of flavors. We start by analyzing the relation between the RG scale k_{res} , where the \mathbb{Z}_2 symmetry is restored (if it was initially broken by fermionic quantum fluctuation) and the number of fermionic flavors N .

As a first step to get an overall impression, we again fix $\mu = 0.1$ and $T = 0.1$ and look at the condensate $\sigma_{\text{min}}(t)$ as a function of the RG scale $k(t)$ for various selected values of N . The numeric results are depicted in figure 4.27.

The results are rather intuitive. The RG time period, in which we find a non-zero condensate $\sigma_{\text{min}}(t) \neq 0$, strongly depends on N . For small N , the \mathbb{Z}_2 symmetry restores almost at model scales, which are set by $h = 1$, while for larger N one finds that the restoration scale k_{res} moves several orders of magnitude on the RG scale towards the IR⁸³. Furthermore, we observe that in the time periods with broken \mathbb{Z}_2 symmetry, the position of the minimum $\sigma_{\text{min}}(t)$ is approaching its mean-field value $\sigma_{\text{min}} = 1$ rapidly while increasing N in figure 4.27. The reason for this behavior is that the precondensation – the formation of a non-persistent non-trivial minimum during the FRG flow – due to fermionic quantum fluctuations does not depend on N .

The direct follow up question is, if there is some fixed relation between k_{res} and N and if we can expect to recover the mean-field result for $N \rightarrow \infty$, where $k_{\text{res}} = 0$, which is not reachable in practical computations at finite N involving bosonic fluctuations. Therefore, we calculate and plot k_{res} as a function of N for different combinations of μ and T in figure 4.28 in a double logarithmic plot. The values for μ and T in figure 4.28 lie in the symmetry broken phase of the MF phase diagram and consequently precondensation occurs during the FRG flow, which is necessary to define and discuss the restoration scale k_{res} .

Already from the numeric data points, it seemed as if we found some power law behavior for $k_{\text{res}}(N)$, which was confirmed for all combinations of μ and T , as long as T is sufficiently small⁸⁴. The straight lines are fits of the function

$$k_{\text{res}}(N) \propto N^{-1} \quad (4.82)$$

to our data points. This strongly supports the hypothesis that for all finite N the discrete chiral symmetry is never broken in the IR for $T > 0$, while for $N \rightarrow \infty$, the mean-field result is recovered. In the following discussions we will mainly focus on $N = 2$. Nevertheless, we

⁸³This is the reason, why we cannot choose arbitrarily large N for numeric calculations. If N is too large, we have to integrate to too small RG scales to find symmetry restoration. However, this is numerically not possible, due to general limitations of the numerical precision during numerical RG time evolution.

⁸⁴For $\mu = 0.0$ and $T = 0.5$ the relation $k_{\text{res}}(N)$ does not obey a strict power law (4.82) but slightly deviates. We believe that the reason for this behavior is the fact that for sufficiently large T one is already close to the second-order phase transition, where the \mathbb{Z}_2 symmetry is restored by thermal fluctuations (also in mean-field) and not primary by bosonic quantum fluctuations.

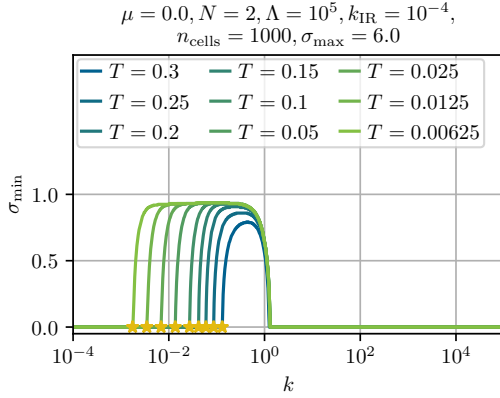


Figure 4.29.: Value of the condensate (the position of the minimum) $\sigma_{\min}(k)$ for various T as a function of the RG scale $k(t)$. The yellow stars mark the RG scales k_{res} , where the \mathbb{Z}_2 symmetry is restored, signaled by a vanishing condensate. *From Fig. 12 of Ref. [4].*

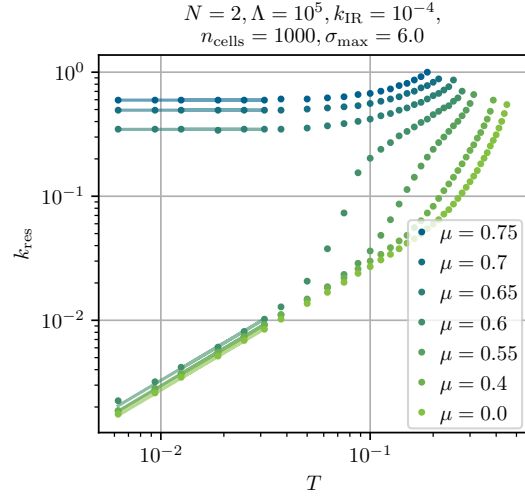


Figure 4.30.: Restoration scale k_{res} , where the \mathbb{Z}_2 symmetry is restored during the FRG flow, as a function of temperature T for a constant number of fermionic flavors $N = 2$ and various values of μ . The points corresponding to $\mu = 0.65$, $\mu = 0.7$, and $\mu = 0.75$ correspond to regions in the μ - T -plane, where the \mathbb{Z}_2 symmetry is restored by the chemical potential, already before bosonic fluctuations are active, cf. figure 4.35a. For temperatures larger than the points, which are shown in the plot, there is never symmetry breaking throughout the entire FRG flow. For $T \lesssim 0.03$ we plot $k_{\text{res}}(T) \propto T^0$ for $\mu > 0.6$ and $k_{\text{res}}(T) \propto T$ for $\mu < 0.6$ ought to be used for optical guidance. *From Fig. 13 of Ref. [4].*

checked for various other values of N that our overall findings are similar for general finite $N > 1$.

4.5.3.4. Varying the temperature T

In this subsection we focus on the relation between the restoration scale k_{res} and the temperature T . This relation is exemplified for $N = 2$.

We start by setting $\mu = 0$ and solely focusing on the evolution of $\sigma_{\min}(t)$ along the RG scale $k(t)$ for different temperatures T . This is plotted in figure 4.29.

We find, that by decreasing the temperature, the RG time period of broken \mathbb{Z}_2 symmetry becomes longer and one has to go deeper into the IR to find symmetry restoration for smaller temperatures. Additionally, we observe remnants of the mean-field second-order phase tran-

sition, because for larger temperatures the value of the intermediate condensate $\sigma_{\min}(t)$ is smaller than for smaller temperatures. In general we observe no SSB in the IR for all $T > 0$ and $\mu = 0$. For temperatures above the mean-field critical temperature $T_C \simeq 0.567$, see Eq. (4.65), symmetry restoration is driven by thermal fluctuations while for $0 < T < T_C$ bosonic quantum fluctuations seem to drive symmetry restoration at finite N and $\mu = 0$.

In figure 4.30 we present results for the temperature-dependence of the symmetry restoration scale $k_{\text{res}}(T)$ for various chemical potentials. We observe that for large temperatures, which are already close to the mean-field critical temperature, the influence of the thermal fluctuations, also in the fermionic loop contribution is too large to have a simple relation between k_{res} and T . For $T \gtrsim 0.03$ we find that $k_{\text{res}}(T)$ depends non-trivially on μ indicating a complicated interplay of thermal, density, and quantum fluctuations that leads to symmetry restoration.

For low temperatures we can identify two distinct trends in figure 4.30. On the one hand, the points $k_{\text{res}}(T)$ for $\mu > 0.6$ become insensitive to T for $T \lesssim 0.03$ while showing a clear dependence on μ : $k_{\text{res}}(T) = c(\mu) T^0$. In this regime it is not the bosonic quantum fluctuations that restore the symmetry, but rather density fluctuations related to the chemical potential. This is already the case in the limit $N \rightarrow \infty$ (mean-field). In the fluid-dynamical interpretation of fermions as a source/sink term, symmetry gets restored at large chemical potentials due to the manifestation as a source in this scenario, cf. subsection 4.2.2.

On the other hand, the points $k_{\text{res}}(T)$ for $\mu < 0.6$ become rather insensitive to μ for $T \lesssim 0.03$ while showing a clear linear dependence on T , viz. $k_{\text{res}}(T) = c(\mu) T$, where the constant $c(\mu)$ depends only very weakly on μ . This implies that for small T the fermionic contributions to the flow are almost negligible and predominantly the first non-zero Matsubara mode $2\pi T$ controls k_{res} , which also explains the linear relation between k_{res} and T .

For $T < 0.3$ and $\mu < 0.6$ we find symmetry restoration at a finite k_{res} – consequently no SSB in the IR – at finite $N = 2$, which is in direct contrast to the $N \rightarrow \infty$ (mean-field) results, where symmetry is still broken in this regime. Assuming that the functional trends identified in figure 4.30 at low T hold in the limit $T \rightarrow 0$, the linear relations $k_{\text{res}}(T) \propto T^1$ suggest SSB in the IR at $T = 0$ even at finite N . We will come back to this possibility in subsection 4.5.3.7 when discussing the phase diagram after we explore the situation in vacuum in subsection 4.5.3.6.

Before we turn to further discussion concerning the chemical potential, we conclude this subsection on temperature-dependencies with another plot, namely figure 4.31. With this figure we study the dependence of the temperature T_{pc} on N . T_{pc} is the precondensation temperature [273, 510, 699, 751–753], which is defined in our work as the threshold temperature above which the system is always in the symmetric phase for all $k(t)$ at $\mu = 0$ and \mathbb{Z}_2 symmetry is never broken during the FRG flow. We observe that T_{pc} approaches the mean-field value for the critical temperature $T_C \simeq 0.567$ while increasing N . It should however be stressed, that for finite N T_{pc} is not a critical temperature associated with a second-order phase transition to a symmetry broken phase in the IR. While symmetry breaking occurs for $T < T_{\text{pc}}(N)$ during the FRG flow, bosonic fluctuations restore symmetry in the IR for all finite N . Only in the limit $N \rightarrow \infty$ the mean-field result of a second-order phase transition at $\lim_{N \rightarrow \infty} T_{\text{pc}}(N) = T_C$ is recovered, which again qualitatively confirms the consistency of our numeric results.

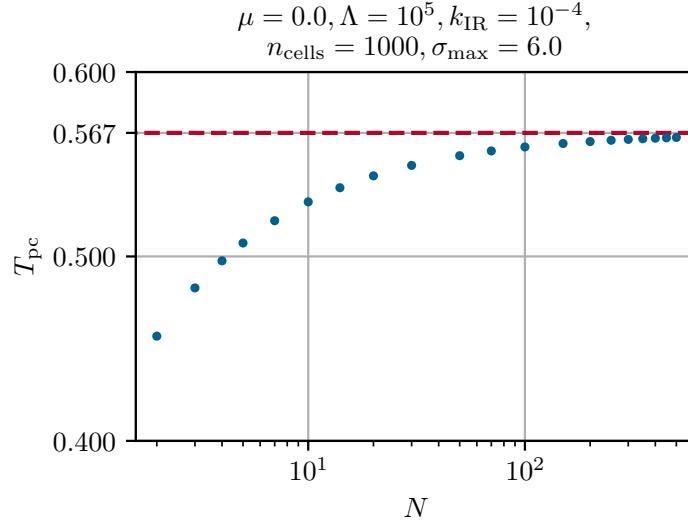


Figure 4.31.: Precondensation temperature $T_{\text{pc}}(N)$ as a function of the number of fermions N at $\mu = 0$. Hereby $T_{\text{pc}}(N)$ is defined as the temperature that is needed to keep the system in the \mathbb{Z}_2 -symmetric phase over the entire FRG flow, meaning that $\sigma_{\text{min}}(k) = 0$ at all scales k . The red-dashed line marks the critical temperature $T_C \simeq 0.567$ from mean-field calculations, see Eq. (4.65). From Fig. 14 of Ref. [4].

4.5.3.5. Varying the chemical potential μ

To further study the relation between k_{res} and μ , we proceed as follows. First, we fix $N = 2$ and $T = 0.1$ and again look at $\sigma_{\text{min}}(t)$ plotted over the RG scale $k(t)$ in figure 4.32.

Here, we observe that for large $\mu > 0.6$ the fermionic density fluctuations restore the symmetry during the FRG flow, signaled by a k_{res} which is slightly smaller than μ but of the same order of magnitude. The strip at $T = 0.1$ with $\mu > 0.6$ is in the restored phase of the mean-field phase diagram and the dynamics at finite and infinite N are dominated by fermionic density fluctuations mediated by the chemical potential. Small values of $\mu < 0.6$ cannot influence a large region in field space. The source contributions at small μ are insufficient to restore the symmetry (compare with our previous discussions). For $\mu < 0.6$ the restoration scale k_{res} is always the same and is set by the temperature.

This behavior is visualized even better in figure 4.33, where we plot $k_{\text{res}}(\mu)$ for various T . Note that $k_{\text{res}}(\mu)$ becomes insensitive to μ for small chemical potentials. We observe remnants – the jump/large gradient in $k_{\text{res}}(\mu)$ at $\mu \approx 0.6$ around $T \approx 0.3$ – of the mean-field first-order phase transition below the mean-field critical point $(\mu_{\text{CP}}, T_{\text{CP}}) \simeq (0.6, 0.3)$.

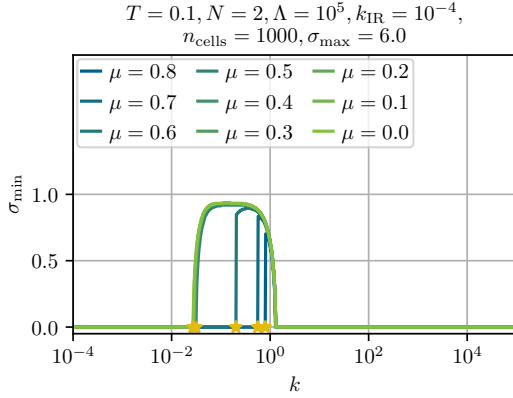


Figure 4.32.: Value of the condensate (position of the minimum) $\sigma_{\min}(k)$ for various μ as a function of the RG scale $k(t)$ at constant temperature $T = 0.1$ and constant $N = 2$. The yellow stars mark the RG scales, where the \mathbb{Z}_2 symmetry is restored, signaled by a vanishing condensate. From Fig. 15 of Ref. [4].

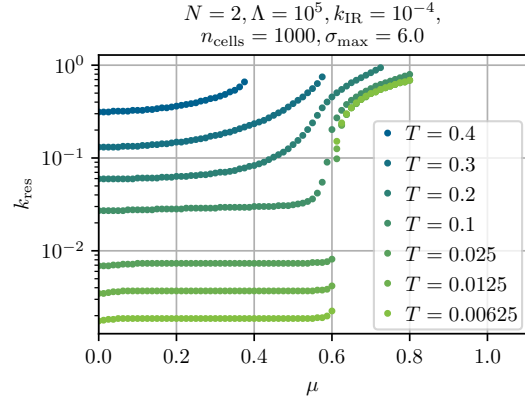
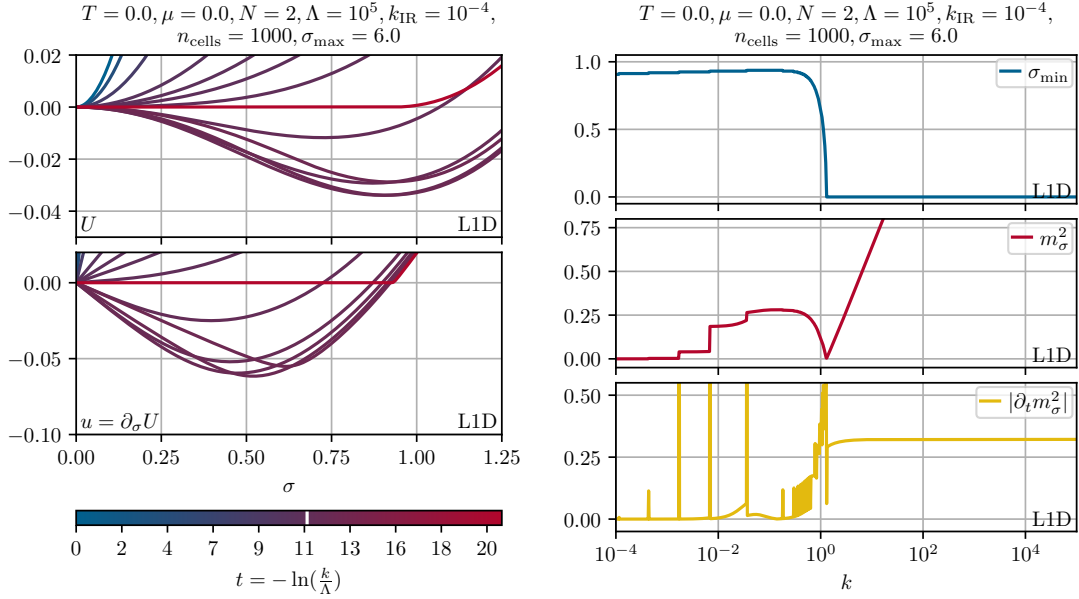


Figure 4.33.: Restoration scale k_{res} , where the \mathbb{Z}_2 symmetry gets restored during the FRG flow, as a function of the chemical potential μ for different temperatures for constant $N = 2$. From Fig. 16 of Ref. [4].

4.5.3.6. Computations in vacuum

Before we conclude this subsection with the discussion of the phase diagram at finite N we turn to selected results in vacuum at vanishing temperature and chemical potential. Direct numerical computations at $T = 0$ and $\mu > 0$ and finite N were not possible within this work as discussed at length in the previous subsections. Computations at $T = 0$ and vanishing chemical potential $\mu = 0$ are however possible at finite N . In this subsection we discuss a specific vacuum flow at $N = 2$ obtained by numerical solution of the vacuum flow Eq. (4.24) (strictly speaking the σ -derivative of Eq. (4.24)) with the one-dimensional Litim regulator also used for the previous computations at $T > 0$.

The vacuum FRG flow for $N = 2$ is displayed in figure 4.34a, showing the scale evolution from the UV and the initial condition (4.79) towards the IR. The corresponding flows of the running minimum $\sigma_{\min}(k)$, the squared curvature mass $m_\sigma^2(k) = \partial_\sigma u(t, \sigma)$ at the IR minimum $\sigma_{\min} > 0$ with the corresponding changing rate $|\partial_t m_\sigma^2(k)|$ according to Eq. (4.81) are plotted in figure 4.34b. We observe SSB in the IR indicated by the non-zero minimum $\sigma_{\min} > 0$. The value of $\sigma_{\min} \approx 0.907$ for $N = 2$ is slightly smaller than the mean-field value in the limit $N \rightarrow \infty$ of $\sigma_{\min} = \sigma_0 = 1$. The curvature mass squared for $N = 2$ is extremely small with $m_\sigma^2 \approx 1.04 \cdot 10^{-5}$, significantly smaller than the mean-field value of $m_\sigma^2 = \frac{1}{\pi} \approx 0.318$, see Eq. (4.57), in the limit $N \rightarrow \infty$. The changing rate $|\partial_t m_\sigma^2(k)|$ indicates an extremely long dynamical range in RG scale k . The IR cutoff of $k_{\text{IR}} = 10^{-4}$ is arguably not low enough and integration deeper into the IR should be performed to ensure that all relevant long-range bosonic vacuum fluctuations are included. However the computations in vacuum are numerically extremely demanding. Lower IR cutoffs would require better spatial resolution and potentially even higher numerical



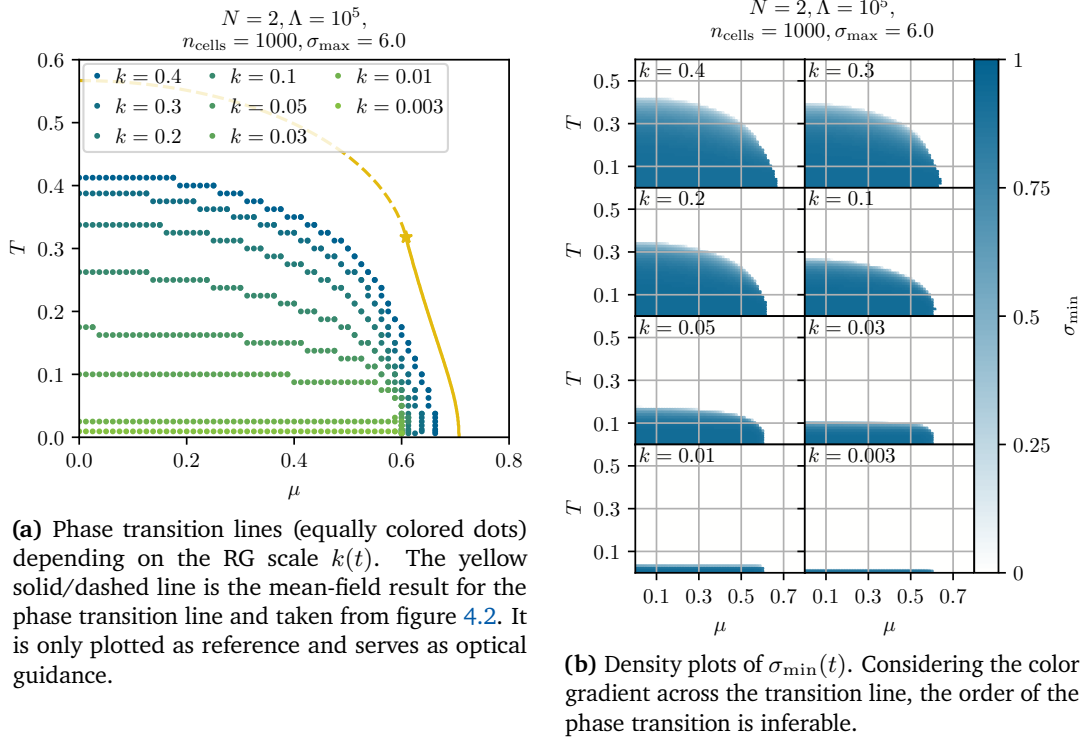
(a) FRG flow of the scale-dependent effective potential $U(t, \sigma)$ (upper panel) and its σ -derivative (the fluid) $u(t, \sigma)$ (lower panel). The white vertical line in the colored bar-legend denotes the RG time (scales) when the \mathbb{Z}_2 symmetry is broken (condensation). We do not find symmetry restoration in vacuum for finite $N = 2$ within the FRG flow for $k \geq k_{\text{IR}} = 10^{-4}$.

(b) FRG flow of the minimum $\sigma_{\text{min}}(k)$ (upper panel), the squared curvature mass $m_\sigma^2(k) = \partial_\sigma u(t, \sigma)$ (middle panel), and the relative change of the squared curvature mass $|\partial_t m_\sigma^2(k)|$ (lower panel) according to Eq. (4.81) plotted as functions of the RG scale $k(t)$ in vacuum ($T = \mu = 0$).

Figure 4.34.: FRG flow of the potential $U(t, \sigma)$ and its derivative on the left (a) and corresponding evolution of $\sigma_{\text{min}}(k)$, $m_\sigma^2(k)$ and changing rate $|\partial_t m_\sigma^2(k)|$ on the right (b) for $N = 2$ in vacuum. Results were obtained using the conventional one-dimensional, spatial LPA-optimized (Litim) regulator. Corresponding results with the two-dimensional LPA-optimized (Litim) regulator can be found in App. E of Ref. [4]. From Figs. 17 and 18 of Ref. [4].

precession for numerical RG time evolution. Both increase the computational time significantly. Computations with lower IR cutoffs were infeasible within the scope of this work. This limitation also implicitly excludes studies at significantly higher finite N since the dynamics get shifted to even lower RG scales for $N > 2$ as discussed in subsection 4.5.3.3.

The result of SSB in the IR for finite $N = 2$ at $T = \mu = 0$ is supported by the results discussed in App. E of Ref. [4] obtained from vacuum flows using two-dimensional Litim regulators. A non-vanishing σ_{min} in vacuum is also supported by the results at finite but low temperature of subsection 4.5.3.4 and especially the results presented in figure 4.30.



(a) Phase transition lines (equally colored dots) depending on the RG scale $k(t)$. The yellow solid/dashed line is the mean-field result for the phase transition line and taken from figure 4.2. It is only plotted as reference and serves as optical guidance.

(b) Density plots of $\sigma_{\text{min}}(t)$. Considering the color gradient across the transition line, the order of the phase transition is inferable.

Figure 4.35.: Phase diagram of the GNY model in the μ - T -plane with $N = 2$ at selected RG scales $k(t)$ during the FRG flow, where condensation is present. Phase transition lines on the left (a) and corresponding density plots on the right (b). The plots are extracted from 3432 independent FRG flows at points (μ_i, T_j) with $\mu_i = 0.0125 \cdot i, i \in \{0, \dots, 65\}$ and $T_j = 0.0125 \cdot j, j \in \{1, \dots, 48\}$. For better resolution at small temperatures, we also included calculations at points with $T_j = 0.00625 \cdot j, j \in \{1, \dots, 4\}$ and the same μ_i as before. From Figs. 19 and 20 of Ref. [4].

4.5.3.7. The phase diagram

With this subsection we finally turn to a discussion of the phase diagram in the μ - T -plane at finite N . We focus explicitly on $N = 2$ but the qualitative statements should, following subsection 4.5.3.3, generalize to finite $N > 2$.

In figure 4.35a we plot the phase transition lines in the μ - T -plane for different $k(t)$. For slightly larger and smaller values of $k(t)$ – including the physical point in the IR – than those that are presented, there is no phase with \mathbb{Z}_2 symmetry breaking at finite temperature. For $k(t) > 0.4$ not enough momentum modes are included to allow for the formation of a non-trivial minimum by fermionic fluctuations, while for scales $k(t) < 0.003$ bosonic long-range fluctuations already vaporized the condensate. With figure 4.35b, we present complementary density plots for the condensate at the selected $k(t)$ of figure 4.35a.

We find that when symmetry breaking sets in, the phase transition line looks similar to its infinite- N counter part (yellow line in figure 4.35a). However, the region of broken \mathbb{Z}_2

symmetry is smaller at its formation at $k(t) \approx 0.4$, since thermal bosonic fluctuations work against the symmetry breaking induced by the fermions. As soon as one further decreases $k(t)$, the symmetry broken regime shrinks drastically. Interestingly, we can observe directly, that for small T and late RG times the phase boundary is almost independent of μ . This was already discussed in the previous subsections. Ultimately, the entire \mathbb{Z}_2 symmetry broken phase vanishes for $T > 0$, such that plotting a “phase diagram” in the μ - T -plane at the physical point in the IR is kind of pointless. Still, figure 4.35 clearly shows the region in the μ - T -plane, where the precondensation phenomenon [273, 510, 699, 751–753] takes place.

It is also noteworthy, that the time period during the FRG flow, hence the range of RG scales, where we find \mathbb{Z}_2 symmetry breaking, is rather small (approximately $k \in [0.4, 0.003]$ spanning over roughly two orders of magnitude), if compared to the total flow time, respectively the nine-orders of magnitude between the UV scale $k_{\text{UV}} = \Lambda = 10^5$ and the IR scale $k_{\text{IR}} = 10^{-4}$. A dynamical range of roughly two orders of magnitude starting at around $k(t) \approx 1$ was also observed in the previous subsections for computations at $T > 0$ and $N = 2$.

We conclude this subsection with a few remarks regarding the situation at zero temperature and finite N . From the $N = 2$ computations in vacuum, presented in the previous subsection 4.5.3.6, we have strong reasons to believe that \mathbb{Z}_2 symmetry breaking persists in vacuum for finite N at low RG scales in the IR. The results obtained by direct computations at low temperatures and $\mu \geq 0$ discussed in subsection 4.5.3.4 support this notion and suggest that \mathbb{Z}_2 symmetry breaking persists at non-zero μ until a chemical potential of $\mu \approx 0.6$ is reached. For $\mu \gtrsim 0.6$ at $T = 0$ and $N = 2$ we do not expect symmetry breaking in the IR. In order to give a more definite and refined picture of the situation at $T = 0$ and $\mu \geq 0$ further computations as well as research and development are required including computations at even lower RG scales as well as direct computations at $T = 0$ and $\mu > 0$ for finite N .

A phase transition at zero temperature driven by an external parameter (or field) rather than thermal fluctuation is called a quantum phase transition [754]. In the context of the GN(Y) model at zero temperature the chemical potential acts as such an external parameter. Fermionic vacuum fluctuations are responsible for symmetry breaking in vacuum and low μ , while density fluctuations induced by a non-zero chemical potential (at finite and infinite N) as well as bosonic quantum fluctuations (at finite N only) drive the system towards symmetry restoration. For a general pedagogic discussion of quantum phase transitions we refer to the textbook [754] as well as the review article [755]. There are multiple systems known to exhibit a quantum phase transition, see, *e.g.*, Refs. [754, 755] and references therein.

4.6. Conclusion and outlook

This section has been compiled from Secs. VII and IV of Refs. [4, 5] respectively.

In the introduction of this chapter, in subsection 4.4.1, and with our literature review in subsection 4.5.1 – regarding the fate of \mathbb{Z}_2 symmetry breaking at finite N , we provided a broad phenomenological overview of the GN model. Nevertheless, we have considered the GN model within this chapter just as our next testing ground in $d = 1+1$ after leaving the roam of $d = 0$. Within this chapter we have studied the GN model at infinite- N and the GNY model – as a closely related bosonized variant of the GN model – at finite N . Identifying the GNY model as a suitable candidate for an LPA FRG study of the partially bosonized GN model we considered its formulation in our CFD frame work for the FRG

The LPA flow equation of the GNYM as a highly non-linear diffusion-source/sink equation

Setting up the framework for numerical computation with the LPA flow equation of the GNY model, included as a first step the reformulation of the flow equation in conservative form. Using the previously established methodology we formulate the LPA flow equation as a non-linear diffusion equation with a source/sink term. The diffusive contributions can be clearly attributed to bosonic quantum fluctuations, of a massive radial mode, which we studied at length already in $d = 0$. While we already encountered source/sink-like contributions from Grassmann numbers, the manifestation of the source/sink term in the GNY model as a real QFT with a chemical potential is novel to our discussion. We have dedicated subsection 4.2.2 to a discussion of its dynamic: depending on RG scale, location in field space, chemical potential, and temperature it can either act like a source or a sink. Fermionic fluctuations can therefore both act towards a breaking and a restoration of \mathbb{Z}_2 symmetry.

The homogeneous phase at infinite N

For infinite N the bosonic fluctuations are completely suppressed within the GNY model, which is then equivalent to the GN model. Within the FRG framework in the limit $N \rightarrow \infty$ we recover well-known infinite- N (mean-field) results for the homogeneous phase diagram of the GN model. The discrete chiral \mathbb{Z}_2 symmetry is spontaneously broken at small chemical potentials and temperatures and gets restored at high temperatures and chemical potentials across a second-order (first-order) phase transition for high temperatures (low temperatures). The restoration of \mathbb{Z}_2 symmetry in the infinite- N limit is purely driven by fermionic thermal and density fluctuations.

The inhomogeneous phases at infinite N

Before turning our attention to the FRG studies at finite N . We make use of the well established explicit results for the inhomogeneous phase in the GN model to benchmark the stability analysis as one of the most popular indirect detection methods for inhomogeneous condensation.

It was shown in subsection 4.4.2.2 that the stability analysis is able to accurately predict the second-order phase transition between the IP and SP as the amplitude of the inhomogeneous

condensate Σ at this phase boundary becomes infinitesimal and its functional form is described by a harmonic wave. Matching the initial expectation, the stability analysis fails to correctly detect the phase boundary between the HBP and IP, because large perturbations would be required. Such perturbations can not be captured within the present expansion scheme. Therefore, the region of the IP, where $\bar{\Sigma}(\mu, T) \neq 0$, is completely undetected by the stability analysis.

Moreover, we compared the wave vector that minimizes the bosonic two-point function Q with the dominating wave vector of the inhomogeneous condensate q_Σ in subsection 4.4.2.3. Inside the IP close to the phase boundary between the SP and IP these two quantities agree very well. Further away from this phase boundary, the amplitude of the inhomogeneous condensate is large, thus violating an assumption of the stability analysis. This is reflected in a small but finite tension of Q and q_Σ .

Also, the bosonic wave-function renormalization Z was investigated. The existence of a region where the wave-function renormalization is negative and the homogeneous minimum is stable under inhomogeneous perturbations, *i.e.*, $Z < 0$ and $\forall q, \Gamma^{(2)}(\bar{\Sigma}(\mu, T), \mu, T, q) > 0$, explicitly shows that a negative Z is only a necessary condition for an inhomogeneous phase.

In summary, these findings show that the stability analysis can indeed be an appropriate tool in the search for second-order phase boundaries of inhomogeneous phases. By using the (1+1)-dimensional GN model as a test ground the shortcomings of this methods were quantified and it was demonstrated that it can also give a reasonable estimate of quantities within the inhomogeneous phase like the dominating wave vector of the condensate.

In subsection 4.4.3 we briefly discuss the related gGL analysis and identify it as a very simple jet potent tool in the vicinity of LPs.

The Gross-Neveu-Yukawa model at finite N

Using the FRG framework and the established finite volume methods for it, we have performed computations for the GNY model at finite and infinite number of flavor N at finite temperature $T \geq 0$ and quark chemical potential $\mu \geq 0$.

At finite N the GNY and GN model are not equivalent in LPA truncation. We argue however that, due to our specific choice for the classical action of the GNY model, the phenomenology of both at least on LPA level should be similar. Direct computations with the GN model in LPA truncation within the FRG framework are not feasible. A proper resolution of the differences between the two models at finite N would be possible by improving the truncation scheme. Especially the addition of a scale-dependent wave-function renormalization for the scalar σ -channel is a natural next step in this direction. First results in this direction are discussed in Ref. [165] and indicate that due to the intricate dynamics on the level of the two-point function, discussed here in the context of the stability analysis, higher orders in the derivative expansion might indeed be crucial to properly resolve the underlying FRG flow.

Numerical results for various finite N and especially $N = 2$ at non-zero temperature and/or chemical potential were presented and discussed in subsection 4.5.3 and have revealed that there is no spontaneous \mathbb{Z}_2 symmetry breaking at non-zero temperature for finite N . This

binary result is in agreement with heuristic arguments of L. D. Landau *et al.* [744] and in the context of the GN model of R. F. Dashen *et al.* [188], which were summarized and discussed in subsection 4.5.1. The situation at vanishing temperature is not completely settled yet.

Direct computations in vacuum are numerically challenging but possible and suggest spontaneous \mathbb{Z}_2 symmetry breaking even for finite N at $T = \mu = 0$. Computations at zero and very low temperatures and non-zero chemical potentials within the used LPA flow equation are also challenging and arguably, see subsection 4.2.2, impossible at zero temperature. This novel aspect of LPA flow equations arising in the CFD framework certainly warrants further research and development. Direct computations beyond very low temperatures are however possible without conceptual or numerical challenges even at non-zero chemical potentials. Considering the vacuum results and an extrapolation from results at low temperatures we have strong reasons to believe that a quantum phase transition between a phase of broken \mathbb{Z}_2 symmetry at low chemical potentials and a restored phase at higher chemical potentials is a highly likely scenario at $T = 0$ and finite N .

Outlook

Beyond the aforementioned further research directions in regards to truncation and a more refined understanding of the involved sources, studies in related models in 1+1 dimensions might be very interesting. Another extremely interesting research direction is the study of the GN(Y) model in finite volumes.

Further remarks regarding the application of the more and more refined CFD framework for FRG flow equations will be made in chapter 6.

5. Quark meson model in four dimensions

Large parts of this chapter are based on the unpublished and so far unfinished manuscript [6] and related work which has been done in close collaboration with M. Buballa and B.-J. Schaefer. The manuscript [6] is based on research done for this dissertation. The draft for [6] is in its early stages and so far I am the sole contributor to the document in terms of explicit computations and text. Parts of subsection 5.2.1 discuss results done in collaboration with L. Kurth.

The numerical results discussed in section 5.2, were obtained with various versions of my C++ code [756], computing the phase diagrams in the μ - T -plane in a few hours of wall time using various consumer processors.

The role of bosonic thermal and quantum fluctuations on the stability of inhomogeneous chiral condensates remains unclear. Recent FRG studies, *cf.* subsection 2.4.2 and especially the discussion surrounding figures 2.13a, 2.17, and 2.18, have shown indications, that inhomogeneous chiral condensation might be possible beyond the mean-field/large- N_c limit. Both FRG studies [80, 87] used indirect methods, related to the stability analysis discussed in subsection 4.4.2, to infer information about the possibility of inhomogeneous condensation. We plan to contribute to this research in two ways.

With the methodological developments regarding both the numerics for FRG flow equations, mainly discussed in chapter 3 and sections 4.2 and 4.5, and the stability analysis, discussed in section 4.3, we plan to study inhomogeneous phases by means of a FRG based stability analysis. We believe, that we now have the proper tools and understanding to apply our conceptual developments to LEFTs of QCD in the spirit of subsection 2.3.3. With the developed CFD framework for FRG flow equations it should be possible to continue the discussion started in Ref. [87] to answer the question whether there is an instability towards inhomogeneous condensation in the QM model in LPA. The main point of interest of Ref. [87] were thermodynamic instabilities/artifacts of the QM model in LPA and inhomogeneous condensates were not the focus of the discussion in Ref. [87]. A review of the issues discussed in Ref. [87] can be found in Sec. III.B of the recent review [109]. Very recent results [210] have brought significant progress with a combination of improvements regarding regulator choice, truncation but also importantly a robust CFD formulation of the underlying flow equation.

The second way in which we want to contribute to the research into inhomogeneous phases beyond mean-field is to the best of our knowledge original to our work [6] and this thesis. We plan to supplement the indirect detection methods with a direct method. To this end we

developed a way to incorporate an explicit inhomogeneous condensate into the FRG treatment of LEFTs like the QM model. We will spend the rest of this chapter discussing this development.

In the next section 5.1 we will discuss the central result of this chapter, *viz.* our successful derivation of a LPA flow equation for a specific inhomogeneous condensate – the chiral density wave (CDW) – in the QM model. This derivation is based on two related analytical/symbolic ideas, which we will discuss in detail, and a subsequent rather tedious but straight forward symbolic computation. We will include the latter only in the digital auxiliary file [757].

In the second and last section 5.2 of this chapter, we will discuss a series of mean-field results we obtained using the derived flow equation. Here we will just focus on the obtained results rather than the technical details given the already substantial scope of the present work. Details regarding the implementation and the involved expressions can be found in the C++ code [756], in the digital auxiliary file [757], and will eventually be discussed in Ref. [6]. These studies do not include any bosonic fluctuations and the derived flow equation can be integrated in RG scale symbolically. We will focus on RG-consistent mean-field computations to study the QM model as a LEFT rather than a renormalizable model.

We will not conclude this chapter with its own, separated conclusion and outlook, since it is the last chapter of the main part of this thesis. We will include our concluding remarks and outlook regarding this part of our research, in the following final summary and outlook in chapter 6.

5.1. Deriving a LPA flow equation for the chiral density wave

Considering the QM model of subsection 2.3.3.1 in LPA entails the ansatz (2.184) for the EAA:

$$\bar{\Gamma}_k[\chi] \equiv \int_x \left(\bar{\psi}(\gamma^\nu \partial_\nu - \gamma^4 \mu + h\varphi_i \tau^i)\psi + \frac{1}{2}(\partial_\mu \varphi)^2 + U_k(\varrho) \right). \quad (5.1)$$

For the condensates – the possible solutions of the QEOM – we consider in this section exclusively

$$\chi_{\text{EoM}} = \underline{\chi} = (\varphi(\vec{x}), 0, 0), \quad (5.2)$$

with “the” chiral density wave (CDW)

$$\varphi(\vec{x}) \equiv \Delta(\cos(\vec{q} \cdot \vec{x}), 0, 0, \sin(\vec{q} \cdot \vec{x})), \quad (5.3)$$

with wave vector \vec{q} and amplitude Δ . Due to its specific analytic properties this is one of the most commonly studied inhomogeneous modulations, see, *e.g.*, Refs. [83–86, 88, 193, 484–486, 514] and section 2.4. A crucial and unique property of this inhomogeneous modulation is the fact that, its related $O(4)$ invariant is constant:

$$\frac{1}{2} \varphi(\vec{x})^2 = \frac{1}{2} \Delta^2 = \text{const.} \quad (5.4)$$

on account of the Pythagorean identity. Another closely related property is a variant of Euler’s formula

$$\forall O^2 = \mathbb{1} \quad \varphi_0(\vec{x}) \pm iO\varphi_3(\vec{x}) = \Delta \exp(\pm iO\vec{q} \cdot \vec{x}). \quad (5.5)$$

A third very nice property is, that in the limit $\vec{q} = 0$ the CDW becomes the ordinary homogeneous condensate

$$\underline{\chi} \xrightarrow{\vec{q}=0} \underline{\chi} = ((\Delta, 0, 0, 0), 0, 0). \quad (5.6)$$

When evaluating the Wetterich equation on the CDW background, Eq. (5.4) allows for a simple and conventional treatment of the LPA potential on the r.h.s. of the Wetterich equation (2.37). The r.h.s. involves the fermionic and bosonic two-point functions

$$\overline{\Gamma}_k^{\bar{\psi}\psi}(x, y) = \delta^{(4)}(x - y) [\gamma^\nu \partial_{x^\nu} - \gamma^4 \mu + \frac{\hbar\Delta}{2} (\cos(\vec{q} \cdot \vec{x}) + 2i\gamma^{\text{ch}} t_3 \sin(\vec{q} \cdot \vec{x}))], \quad (5.7)$$

$$\overline{\Gamma}_k^{\varphi_i \varphi_j}(x, y) = \delta^{(4)}(x - y) [(-\delta_x^2 + U'_k(\Delta^2/2))\delta_{i,j} + U''_k(\Delta^2/2)\varphi_i(\vec{x})\varphi_j(\vec{x})], \quad (5.8)$$

which are manifest position-dependent for $q \equiv |\vec{q}| \neq 0$. In momentum space this amounts to a non-diagonal coupling of momenta, which is a characteristic feature of inhomogeneous phases. As mentioned in section 2.4, this non-diagonal structure in momentum space makes an inversion – necessary for the computation of propagators – of the involved two-point functions impossible with standard techniques.

The unique analytical properties of the CDW however, here notably Eq. (5.5), make a symbolic inversion possible. Noting that $(2\gamma^{\text{ch}} t_3)^2 = \mathbb{1}$, we may rewrite Eq. (5.7) as

$$\overline{\Gamma}_k^{\bar{\psi}\psi}(x, y) = \delta^{(4)}(x - y) [\gamma^\nu \partial_{x^\nu} + \gamma^4 \mu + \frac{\hbar\Delta}{2} \exp(+i(2\gamma^{\text{ch}} t_3)\vec{q} \cdot \vec{x})]. \quad (5.9)$$

Given this form F. Dautry and E. M. Nyman realized in their pioneering work [484] that the unitary transformation

$$U_\psi(\vec{x}) = \exp(-i\gamma^{\text{ch}} t_3 \vec{q} \cdot \vec{x}) \quad (5.10)$$

eliminates the explicit position dependency in Eq. (5.9), when considering

$$\overline{\Gamma}_{k;U}^{\bar{\psi}\psi} \equiv U_\psi^\dagger \gamma^4 \overline{\Gamma}_k^{\bar{\psi}\psi} U_\psi, \quad (5.11)$$

since $U_\psi^\dagger \gamma^4 = \gamma^4 U_\psi$, which can be easily verified and is ultimately rooted in the fact that γ^{ch} anticommutes with all other γ -matrices, including γ^4 . In momentum space this translates to a diagonalization of $\gamma^4 \overline{\Gamma}_k^{\bar{\psi}\psi}$ using U_ψ , with only the small price of a slightly more complicated matrix structure. We can follow F. Dautry and E. M. Nyman and can invert the fermionic two-point function by transforming it and the fermionic regulator according to (5.11). This can be formalized by inserting identities $U_\psi^\dagger U_\psi = \mathbb{1}$ and $\gamma^4 \gamma^4 = \mathbb{1}$ into the r.h.s. of the Wetterich equation and using the cyclic property of the trace. As mentioned in the introduction, details regarding this step can be found in Ref. [757].

Motivated by this approach we started working on a similar unitary transformation for the bosonic two-point function $\overline{\Gamma}_k^{\varphi_i \varphi_j}$. By studying the term $\varphi_i(\vec{x})\varphi_j(\vec{x})$ we ultimately were able to construct such a transformation

$$U_\phi(\vec{x})_{ij} = \frac{1}{2} \begin{pmatrix} 1 - \exp(-2i\vec{q} \cdot \vec{x}) & 0 & 0 & 1 + \exp(-2i\vec{q} \cdot \vec{x}) \\ 0 & 2 & 0 & 0 \\ 0 & 0 & 2 & 0 \\ -i(1 + \exp(-2i\vec{q} \cdot \vec{x})) & 0 & 0 & i(\exp(-2i\vec{q} \cdot \vec{x}) - 1) \end{pmatrix}_{ij}. \quad (5.12)$$

The transformed two-point functions $\bar{\Gamma}_{k;U}^{\bar{\psi}\psi}$, $\bar{\Gamma}_{k;U}^{\varphi\varphi}$, and the corresponding transformed regulators gain complexity in terms of their matrix structure but the conceptually challenging inversion problem in momentum space is solved. Performing the involved matrix inversions and traces one can derive the following LPA flow equation, assuming spatial regulators in a unified regulator scheme:

$$\begin{aligned} \partial_k U_k(\varrho) = 12 \int \frac{d^3 p}{(2\pi)^3} \sum_{\pm} \left(-1 + n_f(\beta(E_{\psi;k}^{\pm} + \mu)) + n_f(\beta(E_{\psi;k}^{\pm} - \mu)) \right) \partial_k E_{\psi;k}^{\pm} + \\ + \int \frac{d^3 p}{(2\pi)^3} \sum_{i=0}^3 \left(\frac{1}{2} + n_b(\beta E_{\phi;k}^i) \right) \tilde{\partial}_k E_{\phi;k}^i, \end{aligned} \quad (5.13)$$

with the two fermionic CDW eigenvalues $E_{\psi;k}^{\pm}$, four bosonic CDW eigenvalues $E_{\phi;k}^i$, and the invariant $\varrho = \Delta^2/2$. The aforementioned fermionic eigenvalues are given by

$$(E_k^{\pm})^2 = M^2 + \frac{(\vec{p}_k^{+q})^2}{2} + \frac{(\vec{p}_k^{-q})^2}{2} \pm \sqrt{M^2 \left(\vec{p}_k^{+q} - \vec{p}_k^{-q} \right)^2 + \frac{1}{4} \left((\vec{p}_k^{+q})^2 - (\vec{p}_k^{-q})^2 \right)^2} \quad (5.14a)$$

$$\stackrel{q=0}{=} M^2 + (\vec{p}_k)^2 \quad (5.14b)$$

with the mass term $M^2 \equiv \frac{1}{4} h^2 \Delta^2 = \frac{h^2}{2} \varrho$ and the shifted regulated momenta, cf. Eq. (C.55),

$$\vec{p}_k^q = (\vec{p} + \vec{q}/2) \lambda_k(|\vec{p} + \vec{q}/2|). \quad (5.15)$$

We may distinguish the four bosonic eigenvalues in two pairs:

$$(E_{\phi;k}^1)^2 = (E_{\phi;k}^2)^2 = (\vec{p}_k)^2 + U_k'(\varrho) \stackrel{q=0}{=} (\vec{p}_k)^2 + U_k'(\varrho) \quad (5.16)$$

are the ones always associated with the massless π -modes, cf. Eq. (3.63) from section 3.2 for the related discussion in the zero-dimensional $O(N)$ model. While

$$\begin{aligned} (E_{\phi;k}^{0,3})^2 = \frac{1}{2} (\vec{p}_k)^2 + \frac{1}{2} (\vec{p}_k^{+4q})^2 + U_k'(\varrho) + \varrho U_k''(\varrho) \pm \\ \pm \sqrt{\varrho^2 U_k''(\varrho)^2 + \frac{1}{4} \left((\vec{p}_k^{+4q})^2 - (\vec{p}_k)^2 \right)^2} \end{aligned} \quad (5.17a)$$

$$\stackrel{q=0}{=} (\vec{p}_k)^2 + U_k'(\varrho) + \varrho (U_k''(\varrho) \pm |U_k''(\varrho)|) \quad (5.17b)$$

are associated with the CDW continuously rotating its chiral symmetry breaking between the σ - and π_3 -direction. Only in the limit $q = 0$ can we recover the notion of another mass-less and just one massive mode in Eq. (5.17b).

In the limit $q = 0$ we overall recover the conventional LPA flow equation of the QM model, using a so far not specified regulator shape function.

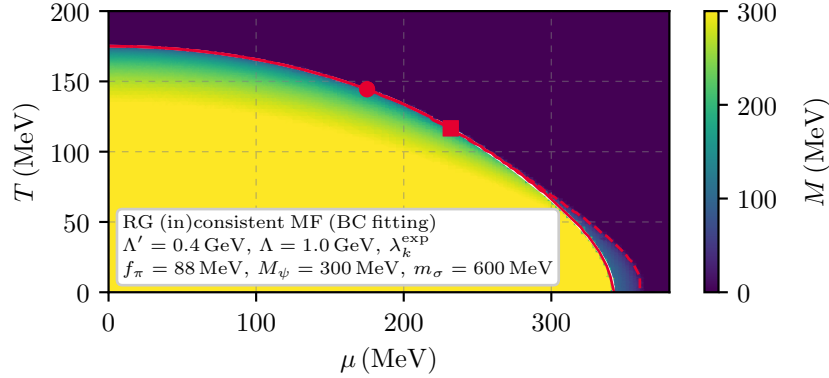


Figure 5.1.: QM model phase diagram at $\Lambda = 1$ GeV with inhomogeneous window marked in red and homogeneous phase boundary (in white), which would occur if one were to disregard inhomogeneous condensation. Solid (dashed/dash-dotted) lines mark first-order (second-order) phase transitions. The dot marks the inhomogeneous LP while the square marks the homogeneous CP. All model parameters are included in the figure and the color map shows the magnitude of the quark mass parameter M .

5.2. RG-consistent mean-field results

As discussed in chapter 1 at the time we derived Eq. (5.13), we did not have the appropriate tools to numerically solve it. So in a first step we focused, before we got “distracted” by our studies in $d = 0$ and $d = 1+1$, on mean-field studies with this flow equation. Disregarding the novel contributions of the bosons the equation becomes an integral equation, *cf.* our discussion in chapter 4, which can be integrated in RG scale at wish symbolically. This allows for a direct application of the construction principles outlined in subsection 2.1.6.1.

We chose the exponential regulator (2.47) for explicit numerical integration [703] and subsequent repeated, local, numerical minimization [704] of the integrated flow equation Eq. (5.13) using my C++ code [756]. The phase boundaries have been obtained with the help of a block-structured adaptive mesh refinement algorithm, which I implemented for the efficient computation of these phase diagrams and the precise detection of lines of interest, without the need of explicit bisection. Details can be found in the C++ code [756] and its documentation.

While we are ultimately interested in an application of the QM model as a LEFT theory in the context of subsection 2.3.3, for this work we did not consider such a setup. We choose the standard bottom-up approach of many mean-field and FRG studies a like and fitted IR observables to fix our model parameters. We choose a “sombbrero”-type (symmetric double-well) potential, *cf.* subsection 3.2.3.2, as initial condition. Tuning its two parameters and the Yukawa coupling h in vacuum to fix the bare pion decay constant f_π to its common reference value in the chiral limit, *viz.* $f_\pi = 88$ MeV, the curvature mass of the σ -meson to $m_\sigma = 600$ MeV and the quark mass parameter $M_\psi = 300$ MeV. We did so in an RG-consistent setting fixing those parameters at a relatively low model reference scale $\Lambda' = 0.4$ GeV and used the FRG flow as described in subsection 2.1.6.1 to construct a UV completion – hence allow for a

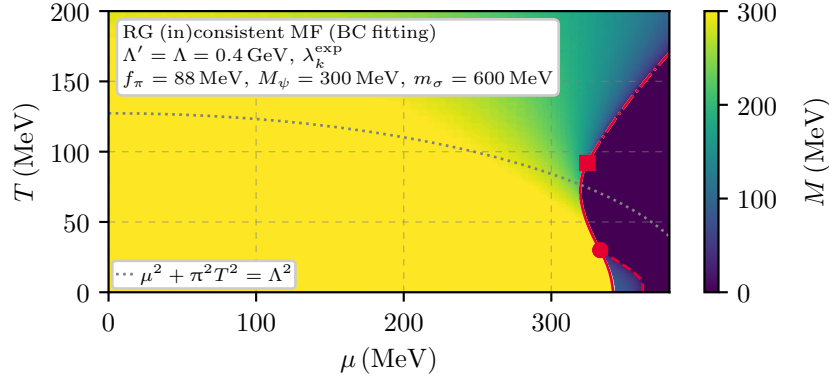


Figure 5.2.: Same as figure 5.1 but for lower $\Lambda' = \Lambda = 0.4$ GeV. With the gray-dotted line $\mu^2 + \pi^2 T^2 = \Lambda^2$ we mark an *a posteriori* estimate for the range of validity of this computation.

study not plagued by regularization artifacts. The resulting phase diagram constructing the completion up to $\Lambda = 1$ GeV is shown in figure 5.1

With figure 5.2 we show the corresponding situation using $\Lambda' = \Lambda = 0.4$ GeV and thus a situation without a proper UV completion. As one would expect we find an extreme violation of RG consistency at $T > 0$ and the results basically loose complete predictive power for $\mu^2 + \pi^2 T^2 > \Lambda^2$ which we made out as a rough estimate. At these large external scales the initial scale $\Lambda = 0.4$ GeV is just too low in this case. This highlights the need for a proper RG-consistent UV completion when using small Λ' .

We summarize the situation with figure 5.3 overlaying four results ranging from $\Lambda = 0.4$ GeV up to $\Lambda = 5$ GeV all the while keeping $\Lambda' = 0.4$ GeV. The difference between the results at 1 GeV and 5 GeV is rather small signaling that we are approaching RG consistency in the entire thermodynamic range considered. We find a stable, persistent but rather small inhomogeneous phase ending in a LP where HBP, IP, and SP meet and beyond which we observe a second-order phase transition between HBP and SP as usual in the chiral limit in such models.

Using RG consistency as a guiding principle to construct proper UV completions in MF computations is a very elegant way to remove cutoff artifacts and focus on other issues, like, *e.g.*, renormalization and/or parameter fitting.

Before discussing issues related to renormalization in the present approach, we want to comment on one particular limit. In a RG-consistent MF computation it is technically possible to set $\Lambda' = 0$ and thus – from an FRG perspective – fixing the EA in the IR without considering any vacuum fluctuations from the flow whatsoever. When doing this with the classical initial condition this effectively entails disregarding all fermionic quantum fluctuations, only allowing for thermodynamic ones. With a sufficiently large Λ or even $\Lambda \rightarrow \infty$ we are thus able to recover the *standard mean-field* result of figure 2.16a in figure 5.4⁸⁵.

⁸⁵The only small quantitative difference stemming from the fact that in Ref. [86] $f_\pi = 93$ MeV is used while we fix $f_\pi = 88$ MeV.

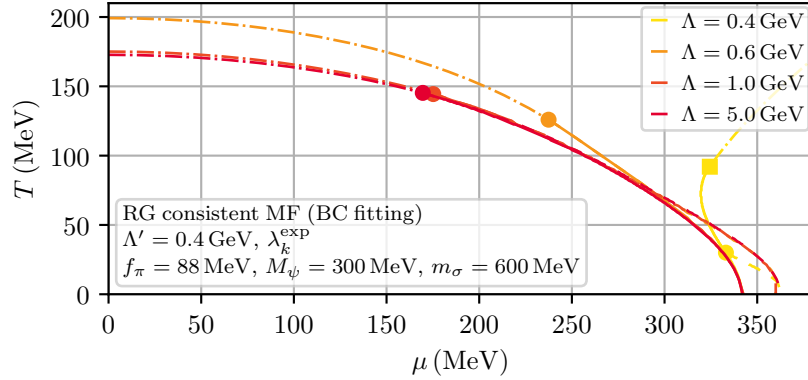


Figure 5.3.: Same as figure 5.1 but for increasing Λ : moving towards RG consistency from $\Lambda = 0.4$ GeV up to $\Lambda = 5$ GeV all the while keeping $\Lambda' = 0.4$ GeV.

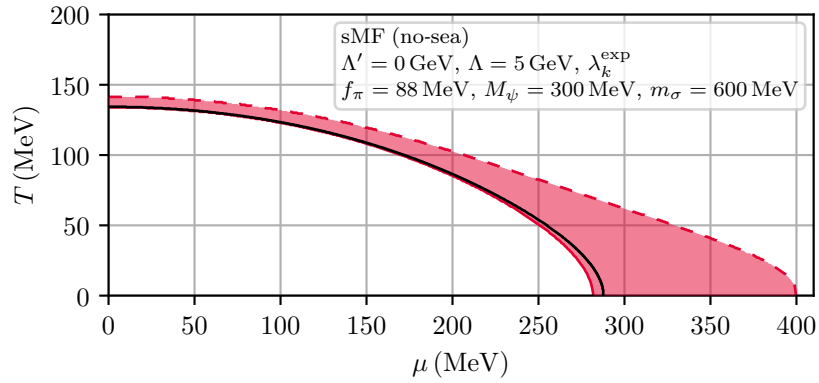


Figure 5.4.: Recovering the *standard mean-field/no-sea* (sMF) result of figure 2.16a with a RG-consistent reconstruction with $\Lambda' = 0$ and $\Lambda = 5$ GeV. The black line is the homogeneous phase boundary, the red lines and shaded area mark the inhomogeneous phase, and the solid (dashed) lines are first-(second-)order phase transitions.

5.2.1. Renormalized mean-field, parameter fitting, and Poincaré invariance

Within this subsection we want to comment on important observations when it comes to renormalization in the present MF context. One can consider the QM model as a renormalizable QFT on its own and it is possible to renormalize it, *i.e.*, remove all cutoffs and for these simple fermionic one-loop computations even all scheme-dependencies. The result for the inhomogeneous phase diagram in such a scenario is presented in figure 2.16b, which was computed using dimensional regularization in the original Ref. [86], but can be exactly reproduced by other regularization schemes like Pauli-Villars, see, *e.g.*, Ref. [85].

From the present perspective of the QM model as a LEFT such a renormalization with a quartic potential in the limit $\Lambda \rightarrow \infty$ makes little sense. It would however seem dishonest not to comment on the renormalization of the QM model in the present setup as a consistency check in the spirit of all the other consistency checks discussed in this thesis.

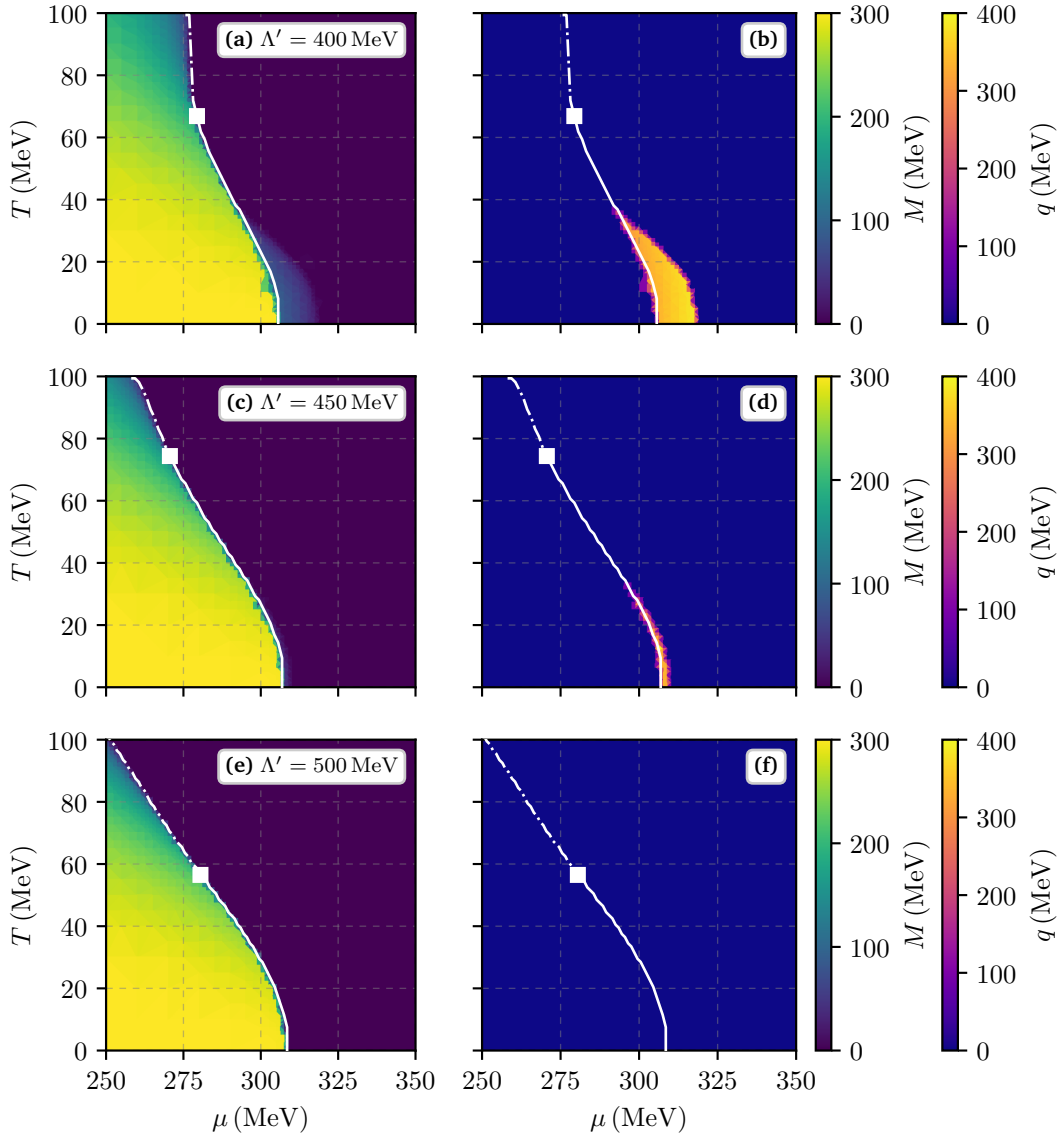


Figure 5.5.: Starting at $\Lambda' = 0.4$ GeV, *cf.* figure 5.2, we increase Λ' in increments of 0.05 GeV from top to bottom and observe the disappearance of the inhomogeneous window while fixing $\Lambda' = \Lambda$. The color map on the right (left) shows the magnitude of the quark mass parameter M (CDW wave vector q).

Figure 5.5 shows the immediate failure of this consistency check as we do not find any inhomogeneous phases for $\Lambda' \gtrsim 500$ MeV. The reason for this is however understood, see, *e.g.*, Ref. [758] for the specific context here, and is quite general. When we fit our parameters to bare quantities, while considering fluctuations in the effective potential we incorporate fluctuations in an inconsistent way. For some observables and applications this might not be an issue, for the renormalized inhomogeneous phase diagram it is however a massive

one [85, 758]. One has to fit renormalized quantities: for the QM model the renormalized pion decay constant and the pole mass of the sigma meson not its curvature mass. These can be computed on LPA-level (mean-field being one further simplification) by evaluating the flow of the corresponding two-point functions, *cf.* our related discussion in section 4.4 and App. E.3. While the flow of the two-point function has no direct feedback into the LPA flow it generates non-trivial contributions to the two-point functions.

In an attempt to sufficiently improve our parameter fitting a new issue arose, which we also wondered about in subsection 4.2.1 for the GNY model. Our choice of regulator breaks (Euclidean) Poincaré invariance explicitly for all finite Λ , which is especially apparent in vacuum, where we are now trying to fit observables by computing wave-function renormalization factors and pole masses. We observe a splitting in the wave-function renormalization due to our regulator choice which spoils our results. We however found a solution for this problem by introducing appropriate counter terms in the UV to account and correct for this splitting in the IR, see, *e.g.*, Refs. [102, 262] for comments on such Ward identities. Using two counter terms and fixing $1 = Z_\pi^{\parallel} = Z_\pi^{\perp}$ in the IR seems to yield the best results at finite Λ . Preliminary tests show that one approaches the reference values of the renormalized limit as Λ is increased. It seems however that with our exponential regulator this approach is rather slow. We have chosen this regulator to increase the performance of our numerical integration of the CDW eigenvalues, which worked out well but especially for considerations of renormalization one should probably explore other options, *cf.* Ref. [265].

With a remark in this direction we will finish this chapter: the flow Eq. (5.13) for the CDW for arbitrary regulator shape functions involves genuine two-dimensional integrals which is the main contributor to the numerical cost of these MF computations. Numerical evaluating these integrals when studying the FRG flow with bosonic fluctuations in our developed CFD context, seems like a daunting task: we have our volume cells in field direction, our flow in RG time, the wave vector of the CDW as an additional minimization parameter and the μ - T -plane to raster. A careful consideration of the angle-dependence in the eigenvalues (5.14a) and (5.17a) of the CDW might allow for an analytic evaluation for Litim-type regulators, which should definitely be considered when implementing the LPA flow Eq. (5.13).

6. Summary and outlook

We have already summarized the findings of our studies in $d = 0$ and $d = 1+1$ in section 3.4 and section 4.6 respectively. At this point, we want comment on overarching concepts and key findings with a special focus on applications in $d = 3+1$.

Our work and research has been focused on technical developments within the framework of the FRG. With our research in zero and two dimensions we have developed a firm understanding of FRG flow equations, particularly of the LPA flow equation, as conservation laws. Within the framework of (numerical) fluid dynamics we have established an understanding of pionic modes and fluctuations as non-linear advective contributions. While we identified radial/massive modes and fluctuations with non-linear diffusive contributions. Fermionic quantum and thermodynamic fluctuations are understood as sources and sinks on the level of the LPA flow. We have observed highly non-linear dynamics during our studies of FRG flows both driven by internal and external factors.

The field of CFD did not only provide the powerful and robust FV method of our choosing, namely the KT scheme, but it also provided a potent language to concisely describe the dynamics and interplay of different fluctuations on the level of the flow equation. Especially the notion of (numerical) entropy and characteristic curves can provide quite unique insights. We established a connection between numerical entropy and the inherent irreversible nature of the FRG, which manifests itself clearly on the level of the flow equation.

We have further developed and studied tools for both the direct and indirect detection of inhomogeneous phases. We find ourselves in a very promising position. With a firm understanding of the stability analysis as an indirect method and a LPA flow equation for an explicit inhomogeneous condensate as a direct method, we hope to use them in conjunction to gain novel insights into inhomogeneous phases beyond mean-field. The adaptation of the developed CFD approach for the LPA flow equation to the QM model seems to be the logical next step. First one would establish contact with recent results, *e.g.*, Ref. [210], using the FV method as an alternative to the employed discontinuous Galerkin methods [162, 210, 247]. This would provide a valuable cross-check of both approaches. Hopefully gaining control over the homogeneous computations to a sufficient level one could turn towards inhomogeneous phases using both the homogeneous stability analysis and the explicitly inhomogeneous CDW condensate. The latter, in particular, will still involve more research and development especially when it comes to the involved momentum integrals.

Our developments with RG-consistent MF studies, parameter fitting, and Poincaré invariance deserve more attention and space than we gave them in this work. They are a rather unique combination and culmination of different results from the field of mean-field studies in the

context of the FRG. We plan to finish Ref. [6] in the near future before any further new developments as it has been put of for too long already. Even for this thesis the plan was a more detailed discussion of the involved concepts but again the preceding discussions in zero and two dimensions took the space.

Talking about space it seems only appropriate to come back to zero-dimensional theories at this point. I want to again stress the wealth of knowledge hidden in these simple theories. Our work with Grassmann numbers in zero-dimensions is still in its infancy. I personally have high hopes when it comes to the study of Grassmann numbers with the FRG. I think there is a lot of potential for developments for fermion-boson systems using just Grassmann numbers and scalars in zero dimensions.



Appendices



A. Digital auxiliary files and used software

A.1. Digital auxiliary files and online repository

The following digital auxiliary files

- [299] M. J. Steil, “Field space and FRG flow equations”, fs_20231206.nb, Mathematica notebook (2023), digital auxiliary file,
- [325] M. J. Steil, “Computational fluid dynamic”, cfd_20231111.nb, Mathematica notebook (2023), digital auxiliary file,
- [399] M. J. Steil, “Quantum chromodynamics and low-energy effective models”, qcd_20231129.nb, Mathematica notebook (2023), digital auxiliary file,
- [364] M. J. Steil, “Zero dimensional $O(N)$ model”, 00N_20231205.nb, Mathematica notebook (2023), digital auxiliary file,
- [365] M. J. Steil, “Zero dimensional $O(1)$ model”, 0d01_20231120.nb, Mathematica notebook (2023), digital auxiliary file,
- [366] M. J. Steil, “Zero dimensional $O(N)$ model at large N ”, 0d0NLargeN_20231111.nb, Mathematica notebook (2023), digital auxiliary file,
- [642] M. J. Steil, “Zero dimensional $SU(2)$ model”, 0dSU2_20230806.nb, Mathematica notebook (2023), digital auxiliary file,
- [652] M. J. Steil, “Gross-Neveu model in $d = 1 + 1$ ”, gn_20240701.nb, Mathematica notebook (2024), digital auxiliary file,
- [653] M. J. Steil, “Gross-Neveu model at infinite N ”, GNcpp_20231207.zip, C++ code (2023), digital auxiliary files,
- [742] M. J. Steil, “Generalized Ginzburg-Landau analysis”, gg1_20200227.nb, Mathematica notebook (2020), digital auxiliary file,
- [757] M. J. Steil, “QMM LPA CDW flow equation”, qmmcdw_20231210.nb, Mathematica notebook (2023), digital auxiliary file,
- [756] M. J. Steil, “Quark-Meson model inhomogeneous MF”, QMcpp_20231209.zip, C++ code (2023), digital auxiliary files,
- [705] M. J. Steil, “BSAM for phase diagrams”, bsamPD_20201115.pdf, Group seminar talk (2020), digital auxiliary file,

[713] M. J. Steil, “Thermal quantum field theory”, tqft_20231122.nb, Mathematica notebook (2023), digital auxiliary file

are referenced throughout this work. They serve as digital appendices of this thesis and they include related derivations and computations which are either too lengthy to be presented in this print document directly or they benefit immensely from a digital format. In the latter category are MATHEMATICA notebooks and packages, C++ codes, and related files.

Files for figures, underlying data, bibliographic references, additional material, my disputation presentation, and the L^AT_EX code for this thesis are also included in the following repository.

The digital material is available in the online repository

<https://github.com/MJSteil/PhD-Thesis>.

A.2. Used software

This document has been created with the use of several software tools and packages.

The document itself is typeset in L^AT_EX [759, 760] using a slightly modified version of the *TUDa-CI* [761, 762]. For bibliography management and citation formatting we use the BibL^AT_EX [763] package with the *biber* backend [764]. A multitude of other L^AT_EX packages are used for various applications, e.g., *axodraw2* [53, 54] for Feynman diagrams, *glossaries/glossaries-extra* [765, 766] for acronyms, *cleveref* [767] for intelligent cross-referencing, and *amsmath* [768] for improved mathematical typesetting to name a few notable ones.

Parts of this thesis have been manually spell-checked using the dictionaries of T_EXNIC CENTER [769], NOTEPAD++ [770], and the language model CHATGPT 4 [771]. Note that the latter has not been used to generate text passages. The text in this document has been compiled in accordance with the affidavit – [Erklärungen laut Promotionsordnung](#) – and the disclaimers throughout this work, see also section 1.2.

Plots and figures in this document have been created with *Matplotlib* [56] and MATHEMATICA [166, 353].

The software and code used for symbolic and numeric computations is described and referenced in the main part of this work, see also App. A.1.

B. Units, conventions, and notations

B.1. Compact notations

Throughout this work, we employ various compact notations to improve readability.

Compact notations and abbreviations related to computations in field space and in position/momentum space are discussed separately in App. B.4 and App. B.5. Summation/integration over repeated internal indices/variables is implied in the usual manner. When abbreviating elements of large sums or products, we adopt the *Skeleton* notation of MATHEMATICA [166] where $\langle\langle n \rangle\rangle$ is used to represent a sequence of n omitted elements.

B.2. Units

For equations and numerical computations in this work we use a natural units (NU) system in which the units are defined such that the Boltzmann constant k_B , the reduced Planck constant \hbar , and the speed of light in vacuum c are dimensionless and exactly unity, *i.e.*,

$$(k_B)_{\text{NU}} \equiv (\hbar)_{\text{NU}} \equiv (c)_{\text{NU}} \equiv 1. \quad (\text{B.1})$$

This NU system simplifies equations and numerical computations and it is realized by using energy as dimension for the quantities mass and temperature and reciprocal energy as dimensions for time and length. We chose electronvolt (eV) as the base unit of energy in our NU system. For discussions and figures which benefit/require the use of units, we usually adopt units common in high-energy physics which are obtained from results in NU by multiplication with appropriate powers of the conversion factor

$$\hbar c = 197.328\,980\,4\dots \text{MeVfm}, \quad (\text{B.2})$$

see, *e.g.*, Eqs. (B.8) and (B.9).

Selected conversion factors to SI units and derived units are

$$(1 \text{ MeV})_{\text{NU}} = 1 \text{ MeV} \cdot c^{-2} = 1.782\,661\,9\dots \times 10^{-30} \text{ kg}, \quad (\text{B.3})$$

$$(1 \text{ MeV}^{-1})_{\text{NU}} = 1 \text{ MeV}^{-1} \cdot \hbar c = 1.973\,269\,8\dots \times 10^{-13} \text{ m}, \quad (\text{B.4})$$

$$(1 \text{ MeV}^{-1})_{\text{NU}} = 1 \text{ MeV}^{-1} \cdot \hbar = 6.582\,119\,5\dots \times 10^{-22} \text{ s}, \quad (\text{B.5})$$

$$(1 \text{ MeV})_{\text{NU}} = 1 \text{ MeV} \cdot 1 = 1.602\,176\,6\dots \times 10^{-13} \text{ J}, \quad (\text{B.6})$$

$$(1 \text{ MeV})_{\text{NU}} = 1 \text{ MeV} \cdot k_B^{-1} = 1.160\,451\,8\dots \times 10^{+10} \text{ K}, \quad (\text{B.7})$$

$$(1 \text{ MeV}^3)_{\text{NU}} = 1 \text{ MeV}^3 \cdot (\hbar c)^{-3} = 1.301 489 2 \dots \times 10^{-7} \text{ fm}^{-3}, \quad (\text{B.8})$$

$$(1 \text{ MeV}^4)_{\text{NU}} = 1 \text{ MeV}^4 \cdot (\hbar c)^{-3} = 1.301 489 2 \dots \times 10^{-7} \text{ MeV fm}^{-3}, \quad (\text{B.9})$$

for mass, length, time, energy, temperature, number density, and energy density respectively. Depending on the context pressure and density are typically expressed in units of MeV fm^{-3} in high-energy physics with the following conversion factors

$$1 \text{ MeV fm}^{-3} \hat{=} 1.602 176 6 \dots \times 10^{+32} \text{ Pa} \hat{=} 1.782 661 9 \dots \times 10^{+15} \text{ kg m}^{-3} \quad (\text{B.10})$$

to the respective (derived) SI units.

For the exact SI values of the fundamental constants – *viz.* k_{B} , \hbar , c , and the electronvolt in joules – used in our numerical computations we use the recommended values of CODATA [772].

B.3. The (special) unitary group

The Lie algebra $\mathfrak{su}(N)$ of the group $\text{SU}(N)$ – the Lie-group of unitary matrices U of rank N and determinant one – has in its N -dimensional fundamental representation $N^2 - 1$ generators $T_a \equiv T^a$ (traceless, hermitian $N \times N$ matrices) obeying

$$T_a T_b = \frac{1}{2N} \delta_{a,b} \mathbb{1}_N + \frac{1}{2} \sum_{c=1}^{N^2-1} (i f_{abc} + d_{abc}) T^c, \quad (\text{B.11})$$

and thus implementing the (anti-)commutator relations

$$\{T_a, T_b\} \equiv T_a T_b + T_b T_a = \frac{1}{N} \delta_{a,b} \mathbb{1}_N + \sum_{c=1}^{N^2-1} d_{abc} T^c, \quad (\text{B.12})$$

$$[T_a, T_b] \equiv T_a T_b - T_b T_a = i \sum_{c=1}^{N^2-1} f_{abc} T^c, \quad (\text{B.13})$$

with the antisymmetric structure constants f_{abc} , the symmetric d -coefficients, and the normalization

$$\text{Tr}(T_a T_b) = \frac{1}{2} \delta_{a,b}. \quad (\text{B.14})$$

The elements of the group $\text{SU}(N)$ are given by

$$\mathcal{U} = \exp(i\theta_a T^a), \quad (\text{B.15})$$

with the generators T^a and the real parameters θ_a .

The $(N^2 - 1)$ -dimensional adjoint representation is given by

$$(\tilde{T}^a)^{bc} = -i f^{abc}. \quad (\text{B.16})$$

B.3.1. SU(2) and U(2) algebras

The special unitary group of degree two SU(2) is of particular importance for several parts of this work therefore we elaborate on this special case of the group SU(N) in this appendix.

The Lie algebra $\mathfrak{su}(2)$ of the group SU(2) consists of 2×2 hermitian matrices with vanishing trace. The three two-dimensional generators $t_a \equiv t^a$ of the fundamental representation are given by

$$t_1 = \frac{1}{2}\sigma_1 = \frac{1}{2} \begin{pmatrix} 0 & 1 \\ 1 & 0 \end{pmatrix}, \quad t_2 = \frac{1}{2}\sigma_2 = \frac{1}{2} \begin{pmatrix} 0 & -i \\ i & 0 \end{pmatrix}, \quad t_3 = \frac{1}{2}\sigma_3 = \frac{1}{2} \begin{pmatrix} 1 & 0 \\ 0 & -1 \end{pmatrix}, \quad (\text{B.17})$$

with the canonical Pauli matrices σ_i . The structure constants f_{abc} are given by the totally antisymmetric Levi-Civita symbol ε_{abc} and the symmetric d -coefficients vanish for the generators of SU(2) and consequently Eq. (B.11) manifests as

$$t_a t_b = \frac{1}{4} \delta_{a,b} \mathbb{1}_2 + \frac{i}{2} \varepsilon^{abc} t_c, \quad (\text{B.18})$$

where Latin indices run from 1 to 3 and summation over repeating indices implied as usual. Using Eq. (B.18) and contraction identities for the Levi-Civita symbol repeatedly one can show

$$t_a t_b t_c = \frac{i}{8} \varepsilon_{abc} \mathbb{1}_2 + \frac{1}{4} (\delta_{b,c} t_a - \delta_{a,c} t_b + \delta_{a,b} t_c), \quad (\text{B.19})$$

$$t_a t_b t_c t_d = \frac{i}{8} \varepsilon_{abcd} t_a + \frac{1}{16} (\delta_{a,d} \delta_{b,c} - \delta_{a,c} \delta_{b,d} + \delta_{a,b} \delta_{c,d}) \mathbb{1}_2 + \frac{i}{8} (\delta_{b,c} \varepsilon_{ad}^m - \delta_{b,d} \varepsilon_{ac}^m + \delta_{c,d} \varepsilon_{ab}^m) t_m, \quad (\text{B.20})$$

and consequently the following identities for traces hold

$$\text{Tr}(t_a) = 0, \quad (\text{B.21})$$

$$\text{Tr}(t_a t_b) = \frac{1}{2} \delta_{a,b}, \quad (\text{B.22})$$

$$\text{Tr}(t_a t_b t_c) = \frac{i}{4} \varepsilon^{abc}, \quad (\text{B.23})$$

$$\text{Tr}(t_a t_b t_c t_d) = \frac{1}{8} (\delta_{a,d} \delta_{b,c} - \delta_{a,c} \delta_{b,d} + \delta_{a,b} \delta_{c,d}). \quad (\text{B.24})$$

Further product and trace identities can be derived by further repeated use of Eq. (B.18).

The three-dimensional adjoint representation is defined by the structure constants $f_{abc} = \varepsilon_{abc}$ and given by

$$\tilde{t}^1 = \begin{pmatrix} 0 & 0 & 0 \\ 0 & 0 & -i \\ 0 & i & 0 \end{pmatrix}, \quad \tilde{t}^2 = \begin{pmatrix} 0 & 0 & i \\ 0 & 0 & 0 \\ -i & 0 & 0 \end{pmatrix}, \quad \tilde{t}^3 = \begin{pmatrix} 0 & -i & 0 \\ i & 0 & 0 \\ 0 & 0 & 0 \end{pmatrix}. \quad (\text{B.25})$$

The Lie algebra $\mathfrak{u}(2)$ of the group $U(2)$ of unitary matrices of rank N has four two-dimensional generators $\{t_0, t_1, t_2, t_3\}$, where t_1, t_2 are t_3 shared with $\mathfrak{su}(2)$, see Eq. (B.17), and

$$t_0 = \frac{1}{2}\mathbb{1}_2 = \frac{1}{2} \begin{pmatrix} 1 & 0 \\ 0 & 1 \end{pmatrix}. \quad (\text{B.26})$$

B.4. Field space notation

The field space notation introduced in this appendix is based on the one put forward in Refs. [104, 222, 226] and allows for a unified treatment of fermionic (Grassmann-valued) and bosonic (non-Grassmann-valued) fields.

In the following we collect all Grassmann-valued fields of the theory under consideration in $\hat{\psi}$ and $\hat{\bar{\psi}}$ and all other fields in $\hat{\phi}$. In the FS notation introduced in this appendix, we will suppress all discrete and continuous internal indices of those fields and collect all fields in one multi-field $\hat{\chi}$. FS indices, related to components of the multi-field $\hat{\chi}$, are typeset as bold roman indices. The multi-field $\hat{\chi}$ includes all fundamental fields of the theory as well as all optional composite fields under consideration. The FS components of this multi-field

$$(\hat{\chi}_{\mathbf{a}}) \equiv (\hat{\phi}, \hat{\psi}, \hat{\bar{\psi}})^\top, \quad (\text{B.27})$$

$$(\hat{\chi}^{\mathbf{a}}) \equiv (\hat{\phi}, \hat{\bar{\psi}}, -\hat{\psi}), \quad (\text{B.28})$$

are chosen to implement the contraction

$$\hat{\chi}^{\mathbf{m}}\hat{\chi}_{\mathbf{m}} = \gamma^{\mathbf{mn}}\hat{\chi}_{\mathbf{n}}\hat{\chi}_{\mathbf{m}} = \hat{\chi}^{\mathbf{m}}\hat{\chi}^{\mathbf{n}}\gamma_{\mathbf{nm}} = \hat{\phi}^2 + \hat{\bar{\psi}}\hat{\psi} - \hat{\psi}\hat{\bar{\psi}} = \hat{\phi}^2 + 2\hat{\bar{\psi}}\hat{\psi}, \quad (\text{B.29})$$

where we introduced the FS metric⁸⁶

$$(\gamma^{\mathbf{ab}}) \equiv (\gamma_{\mathbf{ab}}) \equiv \begin{pmatrix} 1 & 0 & 0 \\ 0 & 0 & 1 \\ 0 & -1 & 0 \end{pmatrix} \quad (\text{B.30})$$

and the Northwest-Southeast (NW-SE) convention: FS indices are always raised (N) from the left (W), $\hat{\chi}^{\mathbf{a}} = \gamma^{\mathbf{am}}\hat{\chi}_{\mathbf{m}}$, and lowered (S) from the right (E), $\hat{\chi}_{\mathbf{a}} = \hat{\chi}^{\mathbf{m}}\gamma_{\mathbf{ma}}$. Summation over FS and discrete internal indices as well as integration over continuous internal variables is implied for contractions.

⁸⁶Our FS metric of Eq. (B.30) is consistent with the sign conventions used in Refs. [104, 226] while in Ref. [222] the signs in the FS metric of Eq. (A.1) should be switched for Eqs. (A.2) and (A.7) of Ref. [222] to be consistent. The ± 1 for the components of the FS metric related to Grassmann-valued fields are just convention (∓ 1 is also possible) but they affect the relation between $(\hat{\chi}_{\mathbf{a}})$ and $(\hat{\chi}^{\mathbf{a}})$, see Eqs. (B.27) and (B.28), and consequently signs in contractions like the one in Eq. (B.29).

The FS metric is non-diagonal in FS, which is necessary to take the Grassmann nature of some field components into account. In all, in our notation currently suppressed, internal spaces the metric is trivial and the respective identity. The FS metric introduced above has the following properties

$$\gamma_{\mathbf{a}}^{\mathbf{b}} = \gamma_{\mathbf{am}}\gamma^{\mathbf{bm}} = \gamma_{\mathbf{ma}}\gamma^{\mathbf{mb}} = \delta_{\mathbf{a}}^{\mathbf{b}}, \quad (\text{B.31})$$

$$\gamma_{\mathbf{b}}^{\mathbf{a}} = \gamma^{\mathbf{am}}\gamma_{\mathbf{mb}} = \gamma^{\mathbf{ma}}\gamma_{\mathbf{bm}} = (-1)^{\mathbf{ab}}\delta_{\mathbf{b}}^{\mathbf{a}}, \quad (\text{B.32})$$

where we introduced the generalized sign factor

$$(-1)^{\mathbf{ab}} \equiv \begin{cases} -1 & \text{if the components } \mathbf{a} \text{ and } \mathbf{b} \text{ are Grassmann-valued} \\ +1 & \text{otherwise} \end{cases}, \quad (\text{B.33})$$

which tracks possible sign flips due to the commutation of FS components \mathbf{a} and \mathbf{b} . Products of such sign factors appear frequently in practical computations therefore we introduce the compact notation

$$(-1)^{\mathbf{ab,cd,ef}} \equiv (-1)^{\mathbf{ab}}(-1)^{\mathbf{cd,ef}} \equiv (-1)^{\mathbf{ab,\langle\langle 2 \rangle\rangle}}. \quad (\text{B.34})$$

The defined metric together with the NW-SE convention implements the anticommutation of Grassmann-valued fields properly, *e.g.*,

$$\hat{\chi}^{\mathbf{m}}\hat{\chi}_{\mathbf{m}} = \gamma^{\mathbf{mn}}\hat{\chi}_{\mathbf{n}}\hat{\chi}^{\mathbf{l}}\gamma_{\mathbf{lm}} = \hat{\chi}_{\mathbf{n}}\hat{\chi}^{\mathbf{l}}\gamma_{\mathbf{ln}}^{\mathbf{m}} = (-1)^{\mathbf{nl}}\delta_{\mathbf{l}}^{\mathbf{n}}\hat{\chi}_{\mathbf{n}}\hat{\chi}^{\mathbf{l}} = (-1)^{\mathbf{mm}}\hat{\chi}_{\mathbf{m}}\hat{\chi}^{\mathbf{m}}, \quad (\text{B.35})$$

which is of course consistent with Eq. (B.29).

Sources related to components of $\hat{\chi}$ can also be treated in the introduced notation

$$(\hat{J}_{\mathbf{a}}) \equiv (J_{\hat{\varphi}}, J_{\hat{\psi}}, J_{\hat{\psi}}), \quad (\text{B.36})$$

$$(\hat{J}^{\mathbf{a}}) = (\gamma^{\mathbf{am}}\hat{J}_{\mathbf{m}}) = (J_{\hat{\varphi}}, J_{\hat{\psi}}, -J_{\hat{\psi}}), \quad (\text{B.37})$$

which implements

$$\hat{J}^{\mathbf{m}}\hat{\chi}_{\mathbf{m}} = (-1)^{\mathbf{mm}}\hat{\chi}^{\mathbf{m}}\hat{J}_{\mathbf{m}} = J_{\hat{\varphi}}\hat{\varphi} + J_{\hat{\psi}}\hat{\psi} - J_{\hat{\psi}}\hat{\psi} = J_{\hat{\varphi}}\hat{\varphi} + J_{\hat{\psi}}\hat{\psi} + \hat{\psi}J_{\hat{\psi}}. \quad (\text{B.38})$$

Functional derivatives in FS are always taken from the left. The order of those derivatives is important since derivatives w.r.t. Grassmann-valued fields or sources anticommute with Grassmann-valued components. For the product rule this implies

$$\frac{\delta}{\delta\hat{J}^{\mathbf{b}}} \left(\frac{\delta f[\hat{J}]}{\delta\hat{J}^{\mathbf{a}}} g[\hat{J}] \right) = \left(\frac{\delta}{\delta\hat{J}^{\mathbf{b}}} \frac{\delta f[\hat{J}]}{\delta\hat{J}^{\mathbf{a}}} \right) g[\hat{J}] + (-1)^{\mathbf{ab}} \frac{\delta f[\hat{J}]}{\delta\hat{J}^{\mathbf{a}}} \frac{\delta g[\hat{J}]}{\delta\hat{J}^{\mathbf{b}}}, \quad (\text{B.39})$$

while for the chain rule

$$\frac{\delta}{\delta\hat{J}^{\mathbf{a}}} f[g[\hat{J}]] = f'[g[\hat{J}]] \frac{\delta g[\hat{J}]}{\delta\hat{J}^{\mathbf{a}}} \quad (\text{B.40})$$

applies in the usual manner.

For functional derivatives we frequently adopt the compact notations

$$\bar{\Gamma}_k^{\mathbf{xm}_n \dots \mathbf{m}_2 \mathbf{m}_1}[\chi] \equiv \frac{\delta}{\delta \chi_{\mathbf{x}}} \bar{\Gamma}_k^{\mathbf{m}_n \dots \mathbf{m}_2 \mathbf{m}_1}[\chi] \equiv \frac{\delta}{\delta \chi_{\mathbf{x}}} \frac{\delta}{\delta \chi_{\mathbf{m}_n}} \dots \frac{\delta}{\delta \chi_{\mathbf{m}_2}} \frac{\delta}{\delta \chi_{\mathbf{m}_1}} \bar{\Gamma}_k[\chi], \quad (\text{B.41})$$

$$W_{k, \mathbf{xm}_n \dots \mathbf{m}_2 \mathbf{m}_1}[\hat{J}] \equiv \frac{\delta}{\delta \hat{J}_{\mathbf{x}}} W_{k, \mathbf{m}_n \dots \mathbf{m}_2 \mathbf{m}_1}[\chi] \equiv \frac{\delta}{\delta \hat{J}_{\mathbf{x}}} \frac{\delta}{\delta \hat{J}_{\mathbf{m}_n}} \dots \frac{\delta}{\delta \hat{J}_{\mathbf{m}_2}} \frac{\delta}{\delta \hat{J}_{\mathbf{m}_1}} W_k[\hat{J}], \quad (\text{B.42})$$

where additional derivatives are attached from the left, derivatives to the right are performed first, taking derivatives w.r.t. upper (lower) FS indices lowers (raises) the index in question and functional derivatives are understood as derivatives w.r.t. the argument of the functional in question.

For FS components of operators which are not directly related to functional derivatives and which already carry sub- or superscript characters we use a semicolon as separator, *e.g.*, $\hat{\chi}_{k; \mathbf{a}}[\tilde{\chi}]$ and $G_{k; \mathbf{ab}}[\chi]$.

B.5. Fourier transformations and functional derivatives

For d -dimensional Euclidean QFTs at zero temperature and the corresponding ($d = s+1$)-dimensional theories at non-zero temperature $T = 1/\beta$, see also App. C, we use the following conventions for Fourier transformations of bosonic (φ) and fermionic ($\psi, \bar{\psi}$) fields

$$\varphi(x) = \int_{-\infty}^{+\infty} \frac{d^d p}{(2\pi)^d} \varphi(p) e^{+ip \cdot x}, \quad \varphi(\vec{x}, \tau) = \frac{1}{\beta} \sum_{n=-\infty}^{\infty} \int_{-\infty}^{+\infty} \frac{d^s p}{(2\pi)^s} \varphi(\vec{p}, \omega_n) e^{+i(\vec{p} \cdot \vec{x} + \omega_n \tau)}, \quad (\text{B.43})$$

$$\psi(x) = \int_{-\infty}^{+\infty} \frac{d^d p}{(2\pi)^d} \psi(p) e^{+ip \cdot x}, \quad \psi(\vec{x}, \tau) = \frac{1}{\beta} \sum_{n=-\infty}^{\infty} \int_{-\infty}^{+\infty} \frac{d^s p}{(2\pi)^s} \psi(\vec{p}, \nu_n) e^{+i(\vec{p} \cdot \vec{x} + \nu_n \tau)}, \quad (\text{B.44})$$

$$\bar{\psi}(x) = \int_{-\infty}^{+\infty} \frac{d^d p}{(2\pi)^d} \bar{\psi}(p) e^{-ip \cdot x}, \quad \bar{\psi}(\vec{x}, \tau) = \frac{1}{\beta} \sum_{n=-\infty}^{\infty} \int_{-\infty}^{+\infty} \frac{d^s p}{(2\pi)^s} \bar{\psi}(\vec{p}, \nu_n) e^{-i(\vec{p} \cdot \vec{x} + \nu_n \tau)}. \quad (\text{B.45})$$

The corresponding inverse transformations are given by

$$\varphi(p) = \int_{V_d} d^d x \varphi(x) e^{-ip \cdot x}, \quad \varphi(\vec{p}, \omega_n) = \int_0^\beta d\tau \int_{V_s} d^s x \varphi(\vec{x}, \tau) e^{-i(\vec{p} \cdot \vec{x} + \omega_n \tau)}, \quad (\text{B.46})$$

$$\psi(p) = \int_{V_d} d^d x \psi(x) e^{-ip \cdot x}, \quad \psi(\vec{p}, \nu_n) = \int_0^\beta d\tau \int_{V_s} d^s x \psi(\vec{x}, \tau) e^{-i(\vec{p} \cdot \vec{x} + \nu_n \tau)}, \quad (\text{B.47})$$

$$\bar{\psi}(p) = \int_{V_d} d^d x \bar{\psi}(x) e^{+ip \cdot x}, \quad \bar{\psi}(\vec{p}, \nu_n) = \int_0^\beta d\tau \int_{V_s} d^s x \bar{\psi}(\vec{x}, \tau) e^{+i(\vec{p} \cdot \vec{x} + \nu_n \tau)}. \quad (\text{B.48})$$

Appropriate boundary conditions for the fields – (anti-)periodic ones for fermionic/bosonic fields – in position space at non-zero temperature are implemented by series using discrete bosonic $\omega_n = 2n \frac{\pi}{\beta}$ and fermionic $\nu_n = (2n + 1) \frac{\pi}{\beta}$ Matsubara frequencies, *cf.* Apps. C.1 and C.2.

Throughout this work we usually abbreviate momentum and position space integrals and sums over internal indices with a single \int or $\int\!\!\!\int$. Appropriate factors of $1/\beta$ for Matsubara sums and powers of $1/(2\pi)$ for momentum-space integrals are included in the $\int\!\!\!\int$ - and \int -symbols:

$$\int_{V_d} d^d x_1 \dots d^d x_m \rightarrow \int_{x_1, \dots, x_m}, \quad (\text{B.49})$$

$$\int_{-\infty}^{+\infty} \frac{d^d p_1}{(2\pi)^d} \dots \frac{d^d p_m}{(2\pi)^d} \rightarrow \int_{p_1, \dots, p_m}, \quad (\text{B.50})$$

$$\int_0^\beta d\tau_1 \dots d\tau_m \int_{V_s} d^s x_1 \dots d^s x_m \rightarrow \int_{\substack{\tau_1, \dots, \tau_m \\ x_1, \dots, x_m}}, \quad (\text{B.51})$$

$$\frac{1}{\beta^m} \sum_{n_1, \dots, n_m = -\infty}^{\infty} \int_{-\infty}^{+\infty} \frac{d^s p_1}{(2\pi)^s} \dots \frac{d^s p_m}{(2\pi)^s} \rightarrow \int\!\!\!\int_{\substack{n_1, \dots, n_m \\ p_1, \dots, p_m}}. \quad (\text{B.52})$$

Conventions for Fourier transformations of operators follow from the identities for the fields, *e.g.*,

$$\bar{\Gamma}_k^{\varphi_1 \varphi_2}(p_1, p_2) = \int_{x_1, x_2} e^{-ip_1 \cdot x_1} \bar{\Gamma}_k^{\varphi_1 \varphi_2}(x_1, x_2) e^{-ip_2 \cdot x_2}, \quad (\text{B.53})$$

$$\bar{\Gamma}_k^{\bar{\psi}_1 \psi_2}(p_1, p_2) = \int_{x_1, x_2} e^{+ip_1 \cdot x_1} \bar{\Gamma}_k^{\bar{\psi}_1 \psi_2}(x_1, x_2) e^{-ip_2 \cdot x_2}, \quad (\text{B.54})$$

$$\bar{\Gamma}_k^{\psi_1 \bar{\psi}_2}(p_1, p_2) = \int_{x_1, x_2} e^{-ip_1 \cdot x_1} \bar{\Gamma}_k^{\psi_1 \bar{\psi}_2}(x_1, x_2) e^{+ip_2 \cdot x_2}. \quad (\text{B.55})$$

Apart from the introduced conventions for (inverse) Fourier transformations of fields and operators the following identities for delta distributions are very useful in practical computations

$$\int_{V_d} d^d x e^{+ip \cdot x} = (2\pi)^d \delta^{(d)}(p), \quad (\text{B.56})$$

$$\int_0^\beta d\tau \int_{V_s} d^s x e^{+i(\vec{p} \cdot \vec{x} + v\tau)} = \beta (2\pi)^s \delta^{(s)}(\vec{p}) \delta(v), \quad (\text{B.57})$$

where v usually manifests as a sum/difference of Matsubara frequencies, *e.g.*, $\omega_{n_1} + \omega_{n_2} = \omega_{n_1+n_2}$ or $\nu_{n_1} - \nu_{n_2} = \omega_{n_1-n_2}$ in which case $\delta(v)$ manifests as $\delta_{0, n_1 \pm n_2} = \delta_{n_1, \mp n_2}$ and is strictly speaking not understood as a distribution. Note that Eqs. (B.56) and (B.57) are the identity operators in momentum space, given our conventions for momentum integrals and Matsubara sums. In the expressions and computations of App. E we will routinely encounter expressions like

$$(2\pi)^s \delta^{(s)}(\vec{p}_1 \pm \vec{p}_2) \equiv \tilde{\delta}_{\vec{p}_1 \pm \vec{p}_2}^{(s)}, \quad (\text{B.58})$$

$$\beta \delta_{0, n_1 \pm n_2} (2\pi)^s \delta^{(s)}(\vec{p}_1 \pm \vec{p}_2) \equiv \tilde{\delta}_{\substack{n_1 \pm n_2 \\ \vec{p}_1 \pm \vec{p}_2}}^{(s)}, \quad (\text{B.59})$$

where we introduced the compact notations using $\tilde{\delta}$. This entails in momentum space

$$\int_{-\infty}^{+\infty} \frac{d^d p}{(2\pi)^d} (2\pi)^d \delta^{(d)}(p) \equiv \int_p \tilde{\delta}_p^{(d)} = 1 \quad (\text{B.60})$$

$$\frac{1}{\beta} \sum_{n=-\infty}^{\infty} \int_{-\infty}^{+\infty} \frac{d^s p}{(2\pi)^s} \beta \delta_{0,n} (2\pi)^s \delta^{(s)}(p) \equiv \sum_{n;p} \tilde{\delta}_n^{(s)} = 1 \quad (\text{B.61})$$

summarizing the previously introduced compact notations in momentum space.

Functional derivatives in position space are understood as

$$\frac{\delta \varphi_1(x_1)}{\delta \varphi_2(x_2)} = \delta_{a_1 a_2} \delta^{(d)}(x_1 - x_2), \quad \frac{\delta \varphi_1(\vec{x}_1, \tau_1)}{\delta \varphi_2(\vec{x}_2, \tau_2)} = \delta_{a_1 a_2} \delta^{(s)}(\vec{x}_1 - \vec{x}_2) \delta(\tau_1 - \tau_2), \quad (\text{B.62})$$

$$\frac{\delta \psi_1(x_1)}{\delta \psi_2(x_2)} = \delta^{\alpha_1 \alpha_2} \delta^{(d)}(x_1 - x_2), \quad \frac{\delta \psi_1(\vec{x}_1, \tau_1)}{\delta \psi_2(\vec{x}_2, \tau_2)} = \delta^{\alpha_1 \alpha_2} \delta^{(s)}(\vec{x}_1 - \vec{x}_2) \delta(\tau_1 - \tau_2), \quad (\text{B.63})$$

$$\frac{\delta \bar{\psi}_1(x_1)}{\delta \bar{\psi}_2(x_2)} = \delta^{\alpha_2 \alpha_1} \delta^{(d)}(x_1 - x_2), \quad \frac{\delta \bar{\psi}_1(\vec{x}_1, \tau_1)}{\delta \bar{\psi}_2(\vec{x}_2, \tau_2)} = \delta^{\alpha_2 \alpha_1} \delta^{(s)}(\vec{x}_1 - \vec{x}_2) \delta(\tau_1 - \tau_2), \quad (\text{B.64})$$

where discrete bosonic indices are collected in a and discrete fermionic indices are collected in α . Corresponding functional derivatives in momentum space are given by

$$\frac{\delta \varphi_1(p_1)}{\delta \varphi_2(p_2)} = \delta_{a_1 a_2} \delta^{(d)}(p_1 - p_2), \quad \frac{\delta \varphi_1(\vec{p}_1, \omega_{n_1})}{\delta \varphi_2(\vec{p}_2, \omega_{n_2})} = \delta_{a_1 a_2} \delta^{(s)}(\vec{p}_1 - \vec{p}_2) \delta_{n_1 n_2}, \quad (\text{B.65})$$

$$\frac{\delta \psi_1(p_1)}{\delta \psi_2(p_2)} = \delta^{\alpha_1 \alpha_2} \delta^{(d)}(p_1 - p_2), \quad \frac{\delta \psi_1(\vec{p}_1, \nu_{n_1})}{\delta \psi_2(\vec{p}_2, \nu_{n_2})} = \delta^{\alpha_1 \alpha_2} \delta^{(s)}(\vec{p}_1 - \vec{p}_2) \delta_{n_1 n_2}, \quad (\text{B.66})$$

$$\frac{\delta \bar{\psi}_1(p_1)}{\delta \bar{\psi}_2(p_2)} = \delta^{\alpha_2 \alpha_1} \delta^{(d)}(p_1 - p_2), \quad \frac{\delta \bar{\psi}_1(\vec{p}_1, \nu_{n_1})}{\delta \bar{\psi}_2(\vec{p}_2, \nu_{n_2})} = \delta^{\alpha_2 \alpha_1} \delta^{(s)}(\vec{p}_1 - \vec{p}_2) \delta_{n_1 n_2}, \quad (\text{B.67})$$

which in combination with the transformations of Eqs. (B.43)–(B.45) lead to the rather useful identities for mixed functional derivatives

$$\frac{(2\pi)^d \delta \varphi_1(x_1)}{\delta \varphi_2(p_2)} = \delta_{a_1 a_2} e^{+i p_2 \cdot x_1}, \quad \frac{\beta (2\pi)^s \delta \varphi_1(\vec{x}_1, \tau_1)}{\delta \varphi_2(\vec{p}_2, \omega_{n_2})} = \delta_{a_1 a_2} e^{+i(\vec{p}_2 \cdot \vec{x}_1 + \omega_{n_2} \tau_1)}, \quad (\text{B.68})$$

$$\frac{(2\pi)^d \delta \psi_1(x_1)}{\delta \psi_2(p_2)} = \delta^{\alpha_1 \alpha_2} e^{+i p_2 \cdot x_1}, \quad \frac{\beta (2\pi)^s \delta \psi_1(\vec{x}_1, \tau_1)}{\delta \psi_2(\vec{p}_2, \nu_{n_2})} = \delta^{\alpha_1 \alpha_2} e^{+i(\vec{p}_2 \cdot \vec{x}_1 + \nu_{n_2} \tau_1)}, \quad (\text{B.69})$$

$$\frac{(2\pi)^d \delta \bar{\psi}_1(x_1)}{\delta \bar{\psi}_2(p_2)} = \delta^{\alpha_2 \alpha_1} e^{-i p_2 \cdot x_1}, \quad \frac{\beta (2\pi)^s \delta \bar{\psi}_1(\vec{x}_1, \tau_1)}{\delta \bar{\psi}_2(\vec{p}_2, \nu_{n_2})} = \delta^{\alpha_2 \alpha_1} e^{-i(\vec{p}_2 \cdot \vec{x}_1 + \nu_{n_2} \tau_1)}. \quad (\text{B.70})$$

B.6. Spinor degrees of freedom

In this work, we perform computations involving spinors in two and four dimensions using a Euclidean metric $g_{\mu\nu} \equiv \delta_{\mu\nu}$. In this appendix we present the relevant conventions for Euclidean and Minkowski signature, where the latter is not used in practical computations through out this work and is presented here for completeness sake. The notation and conventions we introduce below are partly based on the ones put forward in Ref. [422] therefore we refer the interested reader to this article for further details especially regarding discrete and continuous symmetries and aspects of analytic continuation⁸⁷.

We consider the Clifford algebra

$$\{\gamma^\mu, \gamma^\nu\} = 2g^{\mu\nu} \mathbb{1} \quad (\text{B.71})$$

for the d -dimensional inverse diagonal metric $g^{\mu\nu}$ with \tilde{s} eigenvalues -1 such that $\tilde{s} = 0$ amounts to Euclidean and $\tilde{s} = d - 1$ to Minkowski signature. In this work we only consider d even, *viz.* $d = 2$ and $d = 4$, and $(\gamma^\mu)^\dagger = \pm\gamma^\mu$ for $g^{\mu\mu} = \pm 1$. When considering Euclidean space Greek (Lorentz) indices run from 1 to d while we use $\mu \in \{1, \dots, d-1, 0\}$ when considering Minkowski signature. We use $(d_\gamma \equiv 2^{\lfloor d/2 \rfloor})$ -dimensional Dirac spinors for chiral fermions described by two associated elements ψ and $\bar{\psi}$ of a Grassmann algebra which transform under infinitesimal $\text{SO}(\tilde{s}, d - \tilde{s})$ transformations of the generalized Lorentz group as

$$\delta\psi^{\bar{\alpha}} = -\frac{1}{2}\epsilon_{\mu\nu}(\Sigma^{\mu\nu})^{\bar{\alpha}}_{\bar{\beta}}\psi^{\bar{\beta}}, \quad (\text{B.72})$$

$$\delta\bar{\psi}_{\bar{\alpha}} = \frac{1}{2}\epsilon_{\mu\nu}\bar{\psi}_{\bar{\beta}}(\Sigma^{\mu\nu})^{\bar{\beta}}_{\bar{\alpha}}, \quad (\text{B.73})$$

with $\epsilon_{\mu\nu} = -\epsilon_{\nu\mu} = \epsilon_{\mu\nu}^*$, the spinor indices $\bar{\alpha}$ and $\bar{\beta}$ and where we suppressed the corresponding transformations of the generalized Lorentz group of coordinates or momenta in our notation. Conventions for (inverse) Fourier transformations for fermionic components can be found in App. B.5. The generators $\Sigma^{\mu\nu}$ of the $\text{SO}(\tilde{s}, d - \tilde{s})$ group can be constructed using the elements γ^μ of the matrix representation of the Clifford algebra (B.71)

$$\Sigma^{\mu\nu} = \frac{1}{4}[\gamma^\mu, \gamma^\nu]. \quad (\text{B.74})$$

Dirac spinors in even dimensions can be decomposed into Weyl spinors using an additional gamma matrix

$$\gamma^{\text{ch}} \equiv -(-i)^{\frac{d}{2}-\tilde{s}}\gamma^1 \dots \gamma^{d-1}\gamma^{d/0} \quad (\text{B.75})$$

for Euclidean ($\tilde{s} = 0$) and Minkowski ($\tilde{s} = d - 1$) signature respectively⁸⁸. With γ^{ch} defined according to Eq. (B.75) the following identities hold

$$(\gamma^{\text{ch}})^2 = \mathbb{1}, \quad (\text{B.76})$$

⁸⁷Our conventions for analytic continuation from Minkowski signature ($s = 1$) to Euclidean signature ($s = 0$), implied by the conventions of Apps. B.6.1 and B.6.2, are based on the usual continuation of the time coordinate and not on the formulation using a vielbein used in Ref. [422].

⁸⁸We use a different sign convention for γ^{ch} when compared to Eq. (2.14) of Ref. [422].

$$(\gamma^{\text{ch}})^\dagger = \gamma^{\text{ch}}, \quad (\text{B.77})$$

$$\{\gamma^\mu, \gamma^{\text{ch}}\} = 0, \quad (\text{B.78})$$

$$[\Sigma^{\mu\nu}, \gamma^{\text{ch}}] = 0. \quad (\text{B.79})$$

Because of the property (B.76) one can define the “right”- and “left”-handed projection operators

$$\gamma_\pm \equiv \frac{1}{2}(\mathbb{1} \pm \gamma^{\text{ch}}), \quad (\text{B.80})$$

which can be used to decompose the Dirac spinors into two Weyl spinors ψ_\pm ($\bar{\psi}_\pm$) of opposite “chirality” denoted by the subscript \pm :

$$\psi_\pm = \gamma_\pm \psi, \quad \bar{\psi}_\pm = \bar{\psi} \gamma_\mp. \quad (\text{B.81})$$

Boosts and rotations do not mix between Weyl spinors of opposite “chirality” and while rotations act similarly on ψ_+ ($\bar{\psi}_+$) and ψ_- ($\bar{\psi}_-$), boosts act differently on ψ_+ ($\bar{\psi}_+$) and ψ_- ($\bar{\psi}_-$), which when considering $d = 4$ and Minkowski signature $\tilde{s} = 3$ gives rise to the notion of chirality in this context.

Using the objects introduced in this appendix it is possible to define the bilinears $\bar{\psi}\mathbb{1}\psi$, $\bar{\psi}\gamma^{\text{ch}}\psi$, $\bar{\psi}\gamma^\mu\psi$, $\bar{\psi}\gamma^{\text{ch}}\gamma^\mu\psi$ and $\bar{\psi}\Sigma^{\mu\nu}\psi$, which transform under Lorentz transformations as scalars, pseudoscalars, vectors, pseudovectors, and antisymmetric second rank tensors respectively. Those bilinears can be used to construct Lorentz-invariant actions including spinor degrees of freedom.

For lengthy (partial) Dirac traces in d dimension we use the functionalities of the *FormTracer* package [773, 774] for MATHEMATICA [166] as well as the explicit representations of the following two subsections.

B.6.1. Clifford algebra in two dimensions

For computations in $d = 2$ and Euclidean signature ($\tilde{s} = 0$) requiring an explicit representation we use hermitian gamma matrices in Weyl basis

$$\gamma^1 = -\sigma^2 = \begin{pmatrix} 0 & \text{i} \\ -\text{i} & 0 \end{pmatrix}, \quad \gamma^2 = \sigma^1 = \begin{pmatrix} 0 & 1 \\ 1 & 0 \end{pmatrix}, \quad \gamma^{\text{ch}} = -\sigma^3 = \begin{pmatrix} -1 & 0 \\ 0 & 1 \end{pmatrix}, \quad (\text{B.82})$$

as basis elements of the Clifford algebra in accordance to the representation-independent definitions of App. B.6. Corresponding matrices for computations in Minkowski signature ($\tilde{s} = 1$) are given by

$$\gamma_{\text{M}}^0 = \gamma^2, \quad \gamma_{\text{M}}^1 = -\text{i}\gamma^1, \quad \text{and} \quad \gamma_{\text{M}}^{\text{ch}} = \gamma^{\text{ch}}. \quad (\text{B.83})$$

B.6.2. Clifford algebra in four dimensions

For computations in $d = 4$ and Euclidean signature ($\tilde{s} = 0$) requiring an explicit representation we use hermitian gamma matrices in Weyl basis⁸⁹

$$\gamma^i = \begin{pmatrix} \mathbf{0}_{2 \times 2} & i\sigma^i \\ -i\sigma^i & \mathbf{0}_{2 \times 2} \end{pmatrix}, \quad \gamma^4 = \begin{pmatrix} \mathbf{0}_{2 \times 2} & \mathbf{1}_{2 \times 2} \\ \mathbf{1}_{2 \times 2} & \mathbf{0}_{2 \times 2} \end{pmatrix}, \quad \gamma^{\text{ch}} = \begin{pmatrix} -\mathbf{1}_{2 \times 2} & \mathbf{0}_{2 \times 2} \\ \mathbf{0}_{2 \times 2} & \mathbf{1}_{2 \times 2} \end{pmatrix}, \quad (\text{B.84})$$

with $i \in \{1, 2, 3\}$ as basis elements of the Clifford algebra in accordance to the representation-independent definitions of App. B.6. Corresponding matrices for computations in Minkowski signature ($\tilde{s} = 3$) are given by

$$\gamma_{\text{M}}^0 = \gamma^4, \quad \gamma_{\text{M}}^i = -i\gamma^i, \quad \text{and} \quad \gamma_{\text{M}}^{\text{ch}} = \gamma^{\text{ch}}. \quad (\text{B.85})$$

⁸⁹We use a different sign for γ^i and γ^{ch} in Weyl basis when compared to Eq. (A.1) of Ref. [422].

C. Thermal quantum field theory

In this appendix, we will briefly discuss the Matsubara formalism [775] used in this work, for computations in thermal equilibrium (at non-zero temperature). We will focus mainly on technical aspects and refer the interested reader to Refs. [558, 776–781] for a comprehensive introduction of thermal (quantum) field theory. An introduction to FRG flows at non-zero temperature can be found, *e.g.*, Refs. [226, 782]. This appendix has a corresponding digital auxiliary file [713].

C.1. Grand canonical partition function

Throughout this work we use the grand canonical ensemble to study equilibrium bulk properties of thermodynamic systems at non-zero temperature T , chemical potentials μ ⁹⁰ and in our applications constant spatial volume V_s . The latter is usually assumed to be asymptotically large/infinite and we limit the discussion to appropriate densities of thermodynamic quantities, *cf.* Eqs. (C.9)–(C.12). The partition function of the grand canonical ensemble is given by

$$\mathcal{Z} = \text{Tr } \hat{\rho} = \text{Tr } e^{-\beta \hat{\mathcal{H}}} = \sum_n e^{-\beta E_n}, \quad (\text{C.1})$$

with the density matrix $\hat{\rho}$, the Hamiltonian $\hat{\mathcal{H}}$, and corresponding energy eigenvalues E_n with $\hat{\mathcal{H}}|n\rangle = E_n|n\rangle$. The Hamiltonian $\hat{\mathcal{H}}$ includes a Lagrange multiplier $\mu \hat{N}$ realizing the conservation of the associated mean quark number density $n = \langle \hat{N} \rangle$ with the corresponding quark chemical potential μ . The latter is a measure of the change in the energy of the system when the number of quarks, *i.e.*, quark-anti-quark-asymmetry, is changed. The associated mean quark number density n measures the number of quarks minus the number of anti-quarks per unit volume. The ensemble average of an observable represented by the operator \hat{O} is given by

$$\langle \hat{O} \rangle = \frac{1}{\text{Tr } \hat{\rho}} \text{Tr}(\hat{\rho} \hat{O}) = \frac{1}{\mathcal{Z}} \text{Tr}(\hat{O} e^{-\beta \hat{\mathcal{H}}}). \quad (\text{C.2})$$

The traces in Eqs. (C.1) and (C.2) can be expressed as

$$\mathcal{Z} = \text{Tr } e^{-\beta \hat{\mathcal{H}}} = \int d^s \tilde{\chi} \langle \tilde{\chi} | e^{-\beta \hat{\mathcal{H}}} | \tilde{\chi} \rangle, \quad (\text{C.3})$$

$$\langle \hat{O} \rangle = \frac{1}{\mathcal{Z}} \int d^s \tilde{\chi} \langle \tilde{\chi} | \hat{O} e^{-\beta \hat{\mathcal{H}}} | \tilde{\chi} \rangle, \quad (\text{C.4})$$

⁹⁰Through this work we consider only one chemical potential, *viz.* the quark chemical potential. Expressions in this appendix however can trivially be extended to incorporate multiple chemical potentials.

using field eigenstates. In this context the density matrix $\hat{\rho}$ – the operator $e^{-\beta\hat{H}}$ – can be interpreted as an evolution operator on a compact imaginary time axis with $0 \leq t \leq i\beta$. This allows a computation – in the Matsubara formalism [775] – of such traces as expectation values of Euclidean QFTs with a compact Euclidean time-direction $0 \leq \tau \leq \beta$ and on account of the governing traces (anti-)periodic boundary conditions

$$\tilde{\chi}(\vec{x}, \tau) = \mp \tilde{\chi}(\vec{x}, \tau + \beta), \quad (\text{C.5})$$

for (fermionic) bosonic fields. In momentum space this periodicity amounts to a replacement of continuous frequencies $p_d \equiv p_{s+1}$ associated with the Euclidean time direction with discrete bosonic $\omega_n = 2n\frac{\pi}{\beta}$ or fermionic $\nu_n = (2n+1)\frac{\pi}{\beta}$ Matsubara frequencies. Related conventions for fields, operators, and functional derivatives are presented in App. B.5. Identities for computations involving Matsubara frequencies are presented in the next App. C.2.

In the context of subsection 2.1.1 the thermodynamic partition function \mathcal{Z} is given by the Euclidean generating functional in the IR ($k=0$) and at vanishing source ($\hat{J}=0$): $\mathcal{Z} = Z_0[0]$. This allows for an identification of the EAA $\bar{\Gamma}_0[\chi_{\text{EoM}}]$ in the IR evaluated on the QEOM,

$$\chi_{\text{EoM};\mathbf{a}} = \left. \frac{\delta W_0[\hat{J}]}{\delta \hat{\mathbf{J}}\mathbf{a}} \right|_{\hat{J}=0} \Leftrightarrow \left. \frac{\delta \bar{\Gamma}_0[\chi]}{\delta \chi\mathbf{a}} \right|_{\chi=\chi_{\text{EoM}}} = 0, \quad (\text{C.6})$$

viz. Eqs. (2.11) and (2.20), with the so called *grand potential* $\tilde{\Omega}$:

$$\tilde{\Omega}(\mu, T) = -T \ln \mathcal{Z} = T \bar{\Gamma}_0[\chi_{\text{EoM}}; \mu, T]. \quad (\text{C.7})$$

Therefore $\bar{\Gamma}_0[\chi]$ does not only carry the information of all 1PI correlation function in its moments, it also encodes the thermodynamics of the system when evaluated on the QEOM (C.6). Explicit solutions for χ_{EoM} depend on temperature and chemical potential. In the context of symmetry breaking and phase transitions the QEOM (C.6) might have multiple solutions. The physical ground state of the system is in this case given by the solution χ_{EoM} which minimizes $\bar{\Gamma}_0[\chi]$. Explicit examples are discussed in chapters 4 and 5 including both homogeneous $\chi_{\text{EoM}} = \text{const.}$ and inhomogeneous $\chi_{\text{EoM}}(\vec{x})$ solutions of the QEOM.

For our explicit computations at constant and implicitly infinite spatial volume V_s it is convenient to work with the *grand potential density* Ω

$$\Omega \equiv \frac{1}{V_s} \tilde{\Omega} = -\frac{T}{V_s} \ln \mathcal{Z} = \frac{T}{V_s} \bar{\Gamma}_0[\chi_{\text{EoM}}], \quad (\text{C.8})$$

from which one can derive densities of thermodynamic quantities in the usual manner:

$$f = -\frac{T}{V_s} \ln \mathcal{Z} = \Omega, \quad (\text{C.9})$$

$$p = \frac{\partial T \ln \mathcal{Z}}{\partial V} = -\Omega, \quad (\text{C.10})$$

$$s = \frac{1}{V_s} \frac{\partial T \ln \mathcal{Z}}{\partial T} = -\frac{\partial \Omega}{\partial T}, \quad (\text{C.11})$$

$$n = -\frac{1}{V_s} \frac{\partial T \ln \mathcal{Z}}{\partial \mu} = -\frac{\partial \Omega}{\partial \mu}, \quad (\text{C.12})$$

with the Landau free energy density f , the pressure p , the entropy density s , and the mean quark number density n . The energy density ε follows with the Gibbs-Duhem relation as

$$\varepsilon = -p + Ts + \mu n. \quad (\text{C.13})$$

Eq. (C.10) holds only if the EAA in the IR is normalized such that $\Omega(0, 0) = 0$ reproduces a vanishing pressure in vacuum. Such a normalization is not very practical and in fact not necessary since $\Omega(0, 0) = 0$ can be realized for any sensible normalization by modifying Eq. (C.10):

$$p = -(\Omega(\mu, T) - \Omega(0, 0)) = \frac{T}{V_s} \left(\bar{\Gamma}_0[0, 0; \chi_{\text{EoM}}] - \bar{\Gamma}_0[\mu, T; \chi_{\text{EoM}}] \right). \quad (\text{C.14})$$

For the study of phase transitions and symmetry breaking it is convenient to define the effective potential

$$\mathcal{V}[\mu, T; \chi] \equiv \frac{T}{V_s} \bar{\Gamma}_0[\mu, T; \chi], \quad (\text{C.15})$$

which entails for the extremum χ_{EoM}

$$\left. \frac{\delta \mathcal{V}[\mu, T; \chi]}{\delta \chi_{\mathbf{a}}} \right|_{\chi=\chi_{\text{EoM}}} = 0, \quad (\text{C.16})$$

as a variant of Eq. (C.6). The grand potential density Ω is found by minimizing $\mathcal{V}[\mu, T; \chi]$ w.r.t. χ and $\Omega(\mu, T) = \mathcal{V}[\mu, T; \chi_{\text{EoM}}]$. When studying homogeneous condensation, the effective potential becomes a function (not a functional) of the homogeneous/constant expectation values χ and the effective potential can be identified with the local potential $\mathcal{V}(\mu, T; \chi) = U_0(\mu, T; \chi)$, cf. chapters 4 and 5 for explicit applications.

C.2. Selected Matsubara sums and identities for distribution functions

Symbolic expressions arising in computations in the Matsubara formalism involve so called Matsubara sums

$$\frac{1}{\beta} \sum_{n=-\infty}^{\infty} f(\omega_n) \quad \text{or} \quad \frac{1}{\beta} \sum_{n=-\infty}^{\infty} g(\nu_n) \quad (\text{C.17})$$

involving bosonic $\omega_n = 2n\frac{\pi}{\beta}$ or fermionic $\nu_n = (2n+1)\frac{\pi}{\beta}$ Matsubara frequencies. Such sums can usually be computed by means of the residue theorem using bosonic (Bose-Einstein [783])

$$n_b(x) \equiv \frac{1}{e^x - 1} = \frac{1}{2} \coth\left(\frac{x}{2}\right) - \frac{1}{2} \quad (\text{C.18})$$

or fermionic (Fermi-Dirac [784–786])

$$n_f(x) \equiv \frac{1}{e^x + 1} = \frac{1}{2} - \frac{1}{2} \tanh\left(\frac{x}{2}\right) \quad (\text{C.19})$$

distribution functions, which have poles at $i\omega_n$ and $i\nu_n$ respectively. Using the residue theorem the sums in Eq. (C.17) can be expressed as contour integrals using the distributions functions with the initial contour enclosing all poles of the distribution functions. When considering sums involving well-behaved functions f or g , which decay sufficiently fast for arguments with a large absolute value, the contours can be deformed to include the poles of f or g instead of the poles of the distributions functions without changing the result of the integrals. The remaining contour integrals can be evaluated using the residue theorem backwards to express the contour integrals as sums over the poles of f or g . Explicit computations for typical sums can be found in, e.g., Ref. [779]. After presenting useful relations and identities for the distribution functions we will present results for selected explicit Matsubara sums relevant for this work. The following expressions and corresponding computations can be found in the chapter *Distribution functions* of the digital auxiliary file [713].

Using the definitions (C.19) and (C.18) for $n_b(x)$ and $n_f(x)$ the following identities for powers and derivatives of the distribution functions are straightforward to derive

$$\begin{aligned} n'_b(x) &= -\frac{1}{4} \sinh^{-2}\left(\frac{x}{2}\right) = \\ &= -n_b(x)^2 - n_b(x), \end{aligned} \quad (\text{C.20})$$

$$\begin{aligned} n''_b(x) &= \frac{1}{4} \coth\left(\frac{x}{2}\right) \sinh^{-2}\left(\frac{x}{2}\right) = \\ &= 2n_b(x)^3 + 3n_b(x)^2 + n_b(x), \end{aligned} \quad (\text{C.21})$$

$$\begin{aligned} n'''_b(x) &= -\frac{1}{8} \sinh^{-4}\left(\frac{x}{2}\right) - \frac{1}{4} \coth^2\left(\frac{x}{2}\right) \sinh^{-2}\left(\frac{x}{2}\right) = \\ &= -6n_b(x)^4 - 12n_b(x)^3 - 7n_b(x)^2 - n_b(x), \end{aligned} \quad (\text{C.22})$$

$$n_b(x)^2 = -n'_b(x) - n_b(x), \quad (\text{C.23})$$

$$n_b(x)^3 = \frac{1}{2}n''_b(x) + \frac{3}{2}n'_b(x) + n_b(x), \quad (\text{C.24})$$

$$n_b(x)^4 = -\frac{1}{6}n'''_b(x) - n''_b(x) - \frac{11}{6}n'_b(x) - n_b(x), \quad (\text{C.25})$$

$$\begin{aligned} n'_f(x) &= -\frac{1}{4} \coth^{-2}\left(\frac{x}{2}\right) = \\ &= n_f(x)^2 - n_f(x), \end{aligned} \quad (\text{C.26})$$

$$\begin{aligned} n''_f(x) &= \frac{1}{4} \tanh\left(\frac{x}{2}\right) \coth^{-2}\left(\frac{x}{2}\right) = \\ &= 2n_f(x)^3 - 3n_f(x)^2 + n_f(x), \end{aligned} \quad (\text{C.27})$$

$$\begin{aligned} n'''_f(x) &= \frac{1}{8} \coth^{-4}\left(\frac{x}{2}\right) - \frac{1}{4} \tanh^2\left(\frac{x}{2}\right) \coth^{-2}\left(\frac{x}{2}\right) = \\ &= 6n_f(x)^4 - 12n_f(x)^3 + 7n_f(x)^2 - n_f(x), \end{aligned} \quad (\text{C.28})$$

$$n_f(x)^2 = n'_f(x) + n_f(x), \quad (\text{C.29})$$

$$n_f(x)^3 = \frac{1}{2}n''_f(x) + \frac{3}{2}n'_f(x) + n_f(x), \quad (\text{C.30})$$

$$n_f(x)^4 = \frac{1}{6}n_f'''(x) + n_f''(x) + \frac{11}{6}n_f'(x) + n_f(x). \quad (\text{C.31})$$

Additionally relations for the indefinite parity

$$n_b(-x) = -1 - n_b(x), \quad (\text{C.32})$$

$$n_f(-x) = 1 - n_f(x), \quad (\text{C.33})$$

and transmutations

$$n_b(\beta(E + i\omega_n)) = n_b(\beta E), \quad n_b(\beta(E + i\nu_n)) = -n_f(\beta E), \quad (\text{C.34})$$

$$n_f(\beta(E + i\omega_n)) = n_f(\beta E), \quad n_f(\beta(E + i\nu_n)) = -n_b(\beta E), \quad (\text{C.35})$$

of distribution functions are again direct consequences of the definitions (C.19) and (C.18). In the limit of vanishing temperature ($\beta = 1/T \rightarrow \infty$) we find

$$\forall E > 0 \quad \lim_{\beta \rightarrow \infty} n_b(\beta E) = \lim_{\beta \rightarrow \infty} \frac{1}{e^{\beta E} - 1} = 0, \quad (\text{C.36})$$

$$\forall E > 0, \mu \geq 0 \quad \lim_{\beta \rightarrow \infty} n_f(\beta(E + \mu)) = \lim_{\beta \rightarrow \infty} \frac{1}{e^{\beta(E+\mu)} - 1} = 0, \quad (\text{C.37})$$

$$\forall E > 0, \mu \geq 0 \quad \lim_{\beta \rightarrow \infty} n_f(\beta(E - \mu)) = \lim_{\beta \rightarrow \infty} \frac{1}{e^{\beta(E-\mu)} - 1} = \Theta(\mu - E) \equiv \begin{cases} 1 & E < \mu \\ \frac{1}{2} & E = \mu \\ 0 & E > \mu \end{cases}, \quad (\text{C.38})$$

with the Heaviside step function $\Theta(x)$ in half-maximum convention with $\Theta(0) = \frac{1}{2}$.

In the computation of (non-perturbative) one-loop diagrams involving a single propagator the bosonic sum

$$\mathcal{M}_b^1(\mu, \beta; E) \equiv \mathcal{M}_b^1(\beta; E) \equiv \frac{1}{\beta} \sum_{n=-\infty}^{\infty} \frac{1}{\omega_n^2 + E^2} = \frac{1}{2E} + \frac{n_b(\beta E)}{E} \quad (\text{C.39})$$

and the fermionic sum

$$\mathcal{M}_f^1(\mu, \beta; E) \equiv \frac{1}{\beta} \sum_{n=-\infty}^{\infty} \frac{1}{(\nu_n + i\mu)^2 + E^2} = \frac{1}{2E} - \frac{n_f(\beta(E + \mu))}{2E} - \frac{n_f(\beta(E - \mu))}{2E} \quad (\text{C.40})$$

are frequently encountered. The identities

$$\begin{aligned} \mathcal{M}_b^0(\mu, \beta; E) &\equiv \mathcal{M}_b^0(\beta; E) \equiv \frac{1}{\beta} \sum_{n=-\infty}^{\infty} \ln[\beta^2(\omega_n^2 + E^2)] = \\ &= -E - \frac{2}{\beta} \ln[n_b(\beta E)] + \text{const.} \end{aligned} \quad (\text{C.41})$$

$$= E + \frac{2}{\beta} \ln[1 + e^{-\beta E}] + \text{const.}, \quad (\text{C.42})$$

$$\begin{aligned}\mathcal{M}_f^0(\mu, \beta; E) &\equiv \frac{1}{\beta} \sum_{n=-\infty}^{\infty} \ln[\beta^2((\nu_n + i\mu)^2 + E^2)] = \\ &= -E - \frac{1}{\beta} \ln[n_f(\beta(E + \mu))] - \frac{1}{\beta} \ln[n_f(\beta(E - \mu))] + \text{const.}\end{aligned}\quad (\text{C.43})$$

$$= E + \frac{1}{\beta} \ln[1 + e^{-\beta(E+\mu)}] + \frac{1}{\beta} \ln[1 + e^{-\beta(E-\mu)}] + \text{const.}, \quad (\text{C.44})$$

containing divergent but in E , β , and μ constant contributions follow directly from the identities (C.39) and (C.40) when applying $\frac{1}{2E} \frac{\partial}{\partial E}$ to them. $\mathcal{M}_{b/f}^0$ appear in the study of zero-point functions – effective/thermodynamic potentials – and naturally in (partial) integrals involving expressions containing $\mathcal{M}_{b/f}^1$.

In the computation of computation of two-point functions Matsubara sums involving multiple energies appear frequently. The simplest sums of this type are

$$\begin{aligned}\mathcal{M}_b^{1,1}(\mu, \beta; E_1, E_2) &\equiv \mathcal{M}_b^{1,1}(\beta; E_1, E_2) \equiv \frac{1}{\beta} \sum_{n=-\infty}^{\infty} \frac{1}{\omega_n^2 + E_1^2} \frac{1}{\omega_n^2 + E_2^2} = \\ &= \frac{1}{2E_1(E_2^2 - E_1^2)} (1 + 2n_b(\beta E_1)) + 1 \leftrightarrow 2,\end{aligned}\quad (\text{C.45})$$

$$\begin{aligned}\mathcal{M}_f^{1,1}(\mu, \beta; E_1, E_2) &\equiv \frac{1}{\beta} \sum_{n=-\infty}^{\infty} \frac{1}{(\nu_n + i\mu)^2 + E_1^2} \frac{1}{(\nu_n + i\mu)^2 + E_2^2} = \\ &= \frac{1}{2E_1(E_2^2 - E_1^2)} (1 + n_f(\beta(E_1 + \mu)) + n_f(\beta(E_1 - \mu))) + 1 \leftrightarrow 2.\end{aligned}\quad (\text{C.46})$$

Related sums involving higher powers of $(\omega_n^2 + E_i^2)$ or $((\nu_n + i\mu)^2 + E_i^2)$ can be readily computed by applying $-\frac{1}{2E_i} \frac{\partial}{\partial E_i}$ to $\mathcal{M}_b^{1,1}(\mu, \beta; E_1, E_2)$ or $\mathcal{M}_f^{1,1}(\mu, \beta; E_1, E_2)$ potentially repeatedly.

The zero-temperature limits of the presented Matsubara sums can be obtained with the help of the limits of Eqs. (C.36)–(C.38). For renormalization and regularization it is often advantageous to split (if possible) the Matsubara sums into vacuum and medium parts in the following way

$$\mathcal{M}(\mu, \beta) \equiv \mathcal{M}_{\text{vac}} + \mathcal{M}_{\text{med}}(\mu, \beta), \quad (\text{C.47})$$

where

$$\mathcal{M}_{\text{vac}} \equiv \lim_{\beta \rightarrow \infty} \mathcal{M}(\mu = 0, \beta), \quad (\text{C.48})$$

$$\mathcal{M}_{\text{med}}(\mu, \beta) \equiv \mathcal{M}(\mu, \beta) - \mathcal{M}_{\text{vac}}. \quad (\text{C.49})$$

For the Matsubara sums presented in this appendix this split can be read of the given expressions directly when noting that both the bosonic and fermionic distribution functions vanish in the zero-temperature limit at vanishing chemical potential μ . For the sums $\mathcal{M}_{b/f}^0(\mu, \beta; E)$ the alternative expressions (C.42) and (C.44) should be considered to directly read of the zero-temperature limit and/or the split in vacuum and medium parts.

C.3. Momentum integrals and related notations

Throughout this work and in QFT in general we are frequently faced with momentum-space integrals – often referred to as loop integrals. Before commenting on their evaluation (especially in the FRG context) note and recall the following identities between RG time t , RG scale k , the dimensionless ration y , and spatial momentum p ,

$$y \equiv \frac{p^2}{k^2} \quad \longrightarrow \quad dp \rightarrow \frac{k^2}{2p} dy, \quad (\text{C.50})$$

$$k \equiv \Lambda e^{-t} \quad \longrightarrow \quad \partial_t = -k\partial_k = 2y\partial_y, \quad (\text{C.51})$$

cf. Eqs. (2.12) and (2.41).

For s -dimensional momentum-space integrals with spherical symmetry, *i.e.*, their integrands depend only on the absolute value/square the spatial momentum, we employ hyperspherical coordinates

$$\int \frac{d^s p}{(2\pi)^s} f(|\vec{p}|) = \frac{a_s}{(2\pi)^s} \int_0^\infty dp p^{s-1} f(p) = sA_s \int_0^\infty dp p^{s-1} f(p), \quad (\text{C.52})$$

with hypervolume a_s of the $s - 1$ unit sphere (area of the boundary of the s -dimensional unit ball) and the related factor A_s :

$$a_s \equiv \frac{2\pi^{\frac{s}{2}}}{\Gamma(\frac{s}{2})}, \quad \text{with } a_1 = 2, \quad \text{and } a_3 = 4\pi, \quad (\text{C.53})$$

$$A_s \equiv \frac{a_s}{s(2\pi)^s} = \frac{2^{1-s}\pi^{-\frac{s}{2}}}{s\Gamma(\frac{s}{2})}, \quad \text{with } A_1 = \frac{1}{\pi}, \quad \text{and } A_3 = \frac{1}{6\pi^2}. \quad (\text{C.54})$$

Note that one-dimensional hyperspherical coordinates ($s = 1$) are trivial in the sense that they just entail using the \mathbb{Z}_2 symmetry of the one-dimensional momentum integral (hence $a_1 = 2$) and three-dimensional hyperspherical coordinates ($s = 3$) are just canonical spherical coordinates (hence $a_3 = 4\pi$, *viz.* the surface area of the 2-sphere).

The following compact notation for regulated spatial momenta

$$\vec{p}_k \equiv \vec{p} \sqrt{\lambda(\vec{p}^2/k^2)}, \quad (\text{C.55})$$

with $\lambda(y) \equiv r(y) + 1 \equiv r_b(y) + 1 \equiv (r_f(y) + 1)^2$ from Eq. (2.49), is particularly useful for our FRG computations in chapters 4 and 5 and the corresponding App. E.

C.4. Series expansion for the medium part of the MF thermodynamic potential

The medium contribution to the effective potential in MF approximation of a fermionic theory $\mathcal{V}_{\text{f;med}}(\mu, T; \Delta)$ in $d = s + 1$ dimensions involves the s -momentum integral over the medium

part of the Matsubara sum \mathcal{M}_f^0 , cf. Eq. (C.44),

$$\mathcal{V}_{\text{f;med}}(\mu, T; \Delta) \equiv -\frac{d_\gamma N}{2} \int \frac{d^s p}{(2\pi)^s} \mathcal{M}_{\text{f;med}}^0(\mu, \beta; \sqrt{p^2 + \Delta^2}), \quad (\text{C.56})$$

with the dimension $d_\gamma = \text{Tr}(\mathbb{1}_\gamma)$ of the matrix representation of the Clifford algebra (B.71) (in even dimensions typically $d_\gamma \equiv 2^{\lfloor d/2 \rfloor}$) used for the fermions, N the number of different fermion species, and the quark mass Δ associated with homogeneous, spontaneous (chiral) symmetry breaking.

The Ginzburg–Landau expansions discussed in subsection 4.3.3 require an expansion of Eq. (C.56) around $\Delta = 0$. Such an expansion can be computed by expressing the integral in Eq. (C.56) with a series of modified Bessel function of the second kind $K_n(x)$ [166, 787] following Ref. [702] one can derive:

$$\mathcal{V}_{\text{f;med}}(\mu, T; \Delta) = \frac{2^{1-n} d_\gamma N}{\pi^n} (\beta \Delta)^n \beta^{-2n} \sum_{m=1}^{\infty} (-1)^m K_n(m\beta \Delta) \cosh(m\beta \mu), \quad (\text{C.57})$$

with the inverse temperature $\beta = 1/T$ and $n = \frac{s+1}{2}$. A detailed derivation of this and the following expressions of this section can be found in the chapter 4 of the digital auxiliary file [713].

Using the *ascending Series for $K_n(x)$ for integer n* from Eq. (9.6.11) of Ref. [787] it is possible to split the sum in Eq. (C.57) and rewrite it in terms of a modified power series in Δ for odd spatial dimensions s (integer n):

$$\begin{aligned} \mathcal{V}_{\text{f;med}}(\mu, T; \Delta) = & 2^{-n} d_\gamma N \sum_{k=0}^{n-1} \frac{(-1)^k}{2^{2k+1-n} \pi^n} \frac{(n-k-1)!}{k!} \beta^{2k-2n} \Delta^{2k} \times \\ & \times \left(\text{Li}_{2n-2k}(-e^{-\beta\mu}) + \text{Li}_{2n-2k}(-e^{\beta\mu}) \right) + \\ & + 2^{-n} d_\gamma N \frac{(-1)^n}{(2\pi)^n n!} \Delta^{2n} \left(\gamma - \frac{H_n}{2} + \ln\left(\frac{\beta\Delta}{2}\right) + \text{DLi}_0(\beta\mu) \right) + \\ & + 2^{-n} d_\gamma N \sum_{k=1}^{\infty} \frac{(-1)^n}{2^{2k+n} \pi^n k! (k+n)!} \beta^{2k} \Delta^{2(k+n)} \text{DLi}_{2n}(\beta\mu), \end{aligned} \quad (\text{C.58})$$

involving the Euler-Mascheroni constant $\gamma \simeq 0.577216$, the harmonic number H_n ($H_1 = 1$ and $H_2 = 3/2$), and (derivatives of) the polylogarithm function $\text{Li}_n(z)$ ⁹¹

$$\text{DLi}_{2n}(z) \equiv \left[\frac{\partial}{\partial m} \text{Li}_m(-e^z) + \frac{\partial}{\partial m} \text{Li}_m(-e^{-z}) \right]_{m=-2n} = \quad (\text{C.59a})$$

$$= -\delta_{0,n} (\ln(2\pi) + \gamma) + (-1)^{1+n} (2\pi)^{-2n} \Re \psi^{(2n)}\left(\frac{1}{2} + \frac{i}{2\pi} z\right). \quad (\text{C.59b})$$

⁹¹At this point we have to apologize for the differing definitions for the subscript of $\text{DLi}_{2n}(z)$ across our publications [4, 5]. Throughout this work we exclusively and consistently use the definitions of Eqs. (C.59a) and (C.59b) which can be translated by switching sign in the subscript $\text{DLi}_{2n}(z) \leftrightarrow \text{DLi}_{-2n}(z)$ in Refs. [4, 5].

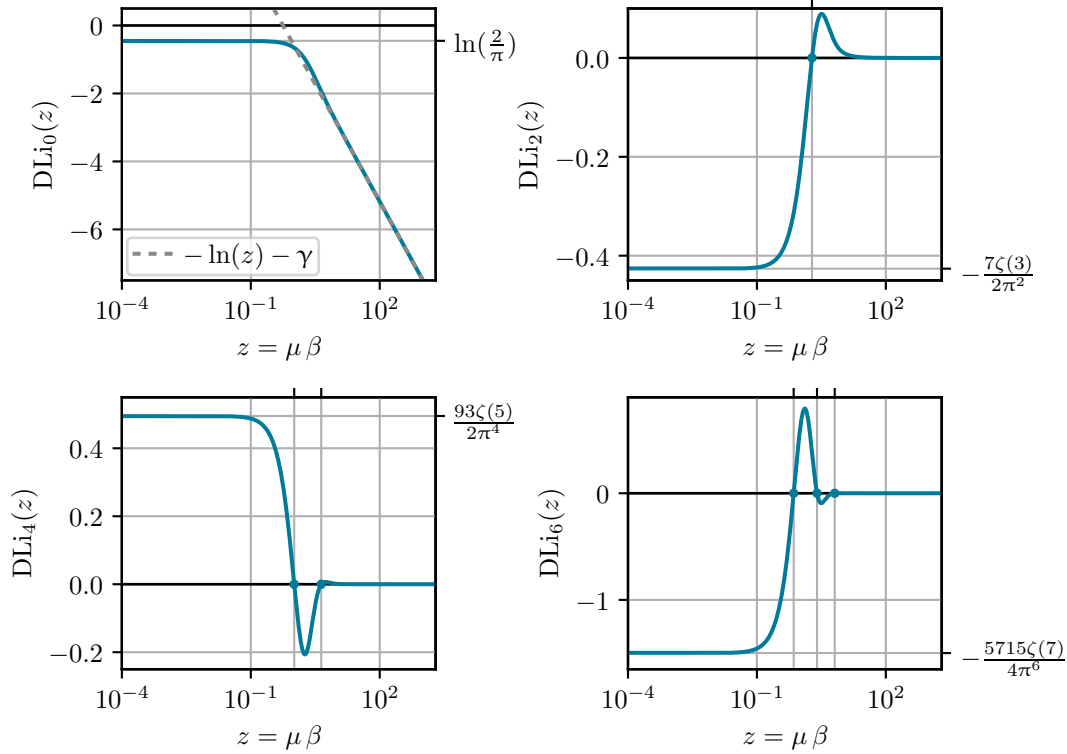


Figure C.1.: First four functions $DLi_{2n}(z)$ for $n = 0, 1, 2, 3$ plotted log-linearly over $z = \mu\beta$. The roots of $DLi_{2n}(z)$ for $n = 1, 2, 3$ are marked with solid dots and additional grid lines while the corresponding numerical values (in double precision – 16 decimal digits) for the roots can be found in Eqs. (C.60), (C.61), and (C.62). $DLi_{2n}(z)$ decay asymptotically for large z with z^{-2n} for $n > 0$ while $DLi_0(z)$ diverges logarithmically. The asymptotics of $DLi_0(z)$ for $z \rightarrow \infty$ is plotted in the corresponding panel (upper left) as a gray-dashed line.

The representation⁹² (C.59b) for $DLi_{2n}(z)$ is based on identities for the polygamma function $\psi^{(2n)}$, see, e.g., Refs. [166, 302, 787], and a relation with the Hurwitz zeta function, cf. identity 25.11.12 of Ref. [302]. Eq. (C.59b) is better suited for numerical computations of $DLi_{2n}(z)$ when compared to the defining expression (C.59a).

Figure C.1 displays the first four $DLi_{2n}(z)$ with their asymptotics and roots. For positive integer n $DLi_{2n}(z)$ are smooth, “well behaved”, and their roots can be computed numerically to arbitrary precision using MATHEMATICA [166]. $DLi_0(z)$ has no root, $DLi_2(z)$ has a single root located at

$$z_{2,1} = 1.910668692586341, \quad (\text{C.60})$$

⁹²Expressions involving $\Re\psi^{(2n)}(\frac{1}{2} + \frac{i}{2\pi}z)$ appear throughout analytic work for limits, expansion, and evaluations involving fermionic distribution functions. We do not claim that the expression (C.59b) in conjunction with Eq. (C.58) is original to this work but we do not have an explicit reference for this formulation either. A similar expansion to Eq. (C.58) can be found in Ref. [788] which is referenced in Ref. [709].

$\text{DLi}_4(z)$ has two roots located at

$$z_{4,1} = 1.024174392948833, \quad (\text{C.61a})$$

$$z_{4,2} = 4.359150199084925, \quad (\text{C.61b})$$

and $\text{DLi}_6(z)$ has three roots located at

$$z_{6,1} = 0.717273524934982, \quad (\text{C.62a})$$

$$z_{6,2} = 2.505674421545387, \quad (\text{C.62b})$$

$$z_{6,3} = 6.473624182009944. \quad (\text{C.62c})$$

Evaluating Eq. (C.58) explicitly for $s = 1$ and $s = 3$ ($n = 1$ and $n = 2$) we arrive at Ginzburg–Landau expansions for $\mathcal{V}_{\text{f;med}}$ in form of modified power series in Δ presented in Apps. C.4.1 and C.4.2. Modified in the sense that $\alpha_2^{s=1}(\mu, T)$ and $\alpha_4^{s=3}(\mu, T)$ contain logarithmic divergencies $\ln \Delta$, which are however highly relevant and in fact physical rather than artificial, see, e.g., Eq. (4.64). The zero temperature limit ($\beta \rightarrow \infty$) in the following equations is computed using the appropriate expansions (6.3.18) and (6.4.11) of Ref. [787] for the polygamma function and they are cross-checked using the explicit computations at $T = 0$ of App. C.5 [713].

C.4.1. Ginzburg-Landau series for $\mathcal{V}_{\text{f;med}}^{s=1}(\mu, T; \Delta)$ in one spatial dimension

$$\mathcal{V}_{\text{f;med}}^{s=1}(\mu, T; \Delta) = \frac{d_\gamma N}{2} \sum_{m=0}^{\infty} \alpha_{2m}^{s=1}(\mu, T) \Delta^{2m}, \quad (\text{C.63})$$

with the first six non-vanishing medium Ginzburg-Landau coefficients

$$\alpha_0^{s=1}(\mu, T) = -\frac{\mu^2}{2\pi} - \frac{\pi T^2}{6}, \quad (\text{C.64})$$

$$\alpha_2^{s=1}(\mu, T) = -\frac{1}{2\pi} \left(\text{DLi}_0\left(\frac{\mu}{T}\right) + \ln\left(\frac{\Delta}{2T}\right) + \gamma - \frac{1}{2} \right) = \begin{cases} -\frac{1}{2\pi} \left(-\Re\psi^{(0)}\left(\frac{i\mu}{2\pi T} + \frac{1}{2}\right) + \ln\left(\frac{\Delta}{4\pi T}\right) - \frac{1}{2} \right) & \text{for } \mu > 0 \wedge T > 0 \\ -\frac{1}{2\pi} \left(\ln\left(\frac{\Delta}{\pi T}\right) + \gamma - \frac{1}{2} \right) & \text{for } \mu = 0 \wedge T \geq 0, \\ -\frac{1}{2\pi} \left(\ln\left(\frac{\Delta}{2\mu}\right) - \frac{1}{2} \right) & \text{for } \mu \geq 0 \wedge T = 0 \end{cases}, \quad (\text{C.65})$$

$$\alpha_4^{s=1}(\mu, T) = -\frac{\text{DLi}_2\left(\frac{\mu}{T}\right)}{16\pi T^2} = \begin{cases} \frac{1}{64\pi^3 T^2} \Re\psi^{(2)}\left(\frac{i\mu}{2\pi T} + \frac{1}{2}\right) & \text{for } \mu > 0 \wedge T > 0 \\ \frac{7\zeta(3)}{32\pi^3 T^2} & \text{for } \mu = 0 \wedge T \geq 0, \\ -\frac{1}{16\pi\mu^2} & \text{for } \mu \geq 0 \wedge T = 0 \end{cases}, \quad (\text{C.66})$$

$$\alpha_6^{s=1}(\mu, T) = -\frac{\text{DLi}_4\left(\frac{\mu}{T}\right)}{384\pi T^4} = \begin{cases} \frac{1}{6114\pi^5 T^4} \Re\psi^{(4)}\left(\frac{i\mu}{2\pi T} + \frac{1}{2}\right) & \text{for } \mu > 0 \wedge T > 0 \\ -\frac{31\zeta(5)}{256\pi^5 T^4} & \text{for } \mu = 0 \wedge T \geq 0, \\ -\frac{1}{64\pi\mu^4} & \text{for } \mu \geq 0 \wedge T = 0 \end{cases}, \quad (\text{C.67})$$

which can also be found in Ref. [709] for $\mu > 0 \wedge T > 0$. The adept reader might recognize the Stefan-Boltzmann pressure of a massless free Fermi gas in 1 + 1 dimensions, see, e.g., Ref. [709] and the textbooks [682, 778], in Eq. (C.64) for $-\alpha_0^{s=1}(\mu, T)$.

C.4.2. Ginzburg-Landau series for $\mathcal{V}_{f;\text{med}}^{s=3}(\mu, T; \Delta)$ in three spatial dimension

$$\mathcal{V}_{f;\text{med}}^{s=3}(\mu, T; \Delta) = \frac{d_\gamma N}{4} \sum_{m=0}^{\infty} \alpha_{2m}^{s=3}(\mu, T) \Delta^{2m}, \quad (\text{C.68})$$

with the first six non-vanishing medium Ginzburg-Landau coefficients

$$\alpha_0^{s=3}(\mu, T) = -\frac{\mu^4}{12\pi^2} - \frac{\mu^2 T^2}{6} - \frac{7\pi^2 T^4}{180}, \quad (\text{C.69})$$

$$\alpha_2^{s=3}(\mu, T) = \frac{\mu^2}{4\pi^2} + \frac{T^2}{12}, \quad (\text{C.70})$$

$$\begin{aligned} \alpha_4^{s=3}(\mu, T) &= \frac{1}{8\pi^2} \left(\text{DLi}_0\left(\frac{\mu}{T}\right) + \ln\left(\frac{\Delta}{2T}\right) + \gamma - \frac{3}{4} \right) = \\ &= \begin{cases} \frac{1}{8\pi^2} \left(-\Re\psi^{(0)}\left(\frac{i\mu}{2\pi T} + \frac{1}{2}\right) + \ln\left(\frac{\Delta}{4\pi T}\right) - \frac{3}{4} \right) & \text{for } \mu > 0 \wedge T > 0 \\ \frac{1}{8\pi^2} \left(\ln\left(\frac{\Delta}{\pi T}\right) + \gamma - \frac{3}{4} \right) & \text{for } \mu = 0 \wedge T \geq 0, \\ \frac{1}{8\pi^2} \left(\ln\left(\frac{\Delta}{2\mu}\right) - \frac{3}{4} \right) & \text{for } \mu \geq 0 \wedge T = 0 \end{cases} \end{aligned} \quad (\text{C.71})$$

$$\alpha_6^{s=3}(\mu, T) = \frac{\text{DLi}_2\left(\frac{\mu}{T}\right)}{96\pi^2 T^2} = \begin{cases} \frac{1}{384\pi^4 T^2} \Re\psi^{(2)}\left(\frac{i\mu}{2\pi T} + \frac{1}{2}\right) & \text{for } \mu > 0 \wedge T > 0 \\ -\frac{7\zeta(3)}{192\pi^4 T^2} & \text{for } \mu = 0 \wedge T \geq 0. \\ \frac{1}{96\pi^2 \mu^2} & \text{for } \mu \geq 0 \wedge T = 0 \end{cases} \quad (\text{C.72})$$

The adept reader might recognize the Stefan-Boltzmann pressure of a massless free Fermi gas in 3 + 1 dimensions, see, e.g., Ref. [789] and the textbooks [682, 778], in Eq. (C.69) for $-\alpha_0^{s=3}(\mu, T)$.

C.5. Zero temperature limit of the medium part of the MF thermodynamic potential

Using Eq. (C.38) we can compute $\mathcal{V}_{f;\text{med}}(\mu, T = 0; \Delta)$ from Eq. (C.56) directly for $\mu > 0$

$$\mathcal{V}_{f;\text{med}}(\mu, T = 0; \Delta) = -\frac{d_\gamma N}{2} \lim_{\beta \rightarrow \infty} \int \frac{d^s p}{(2\pi)^s} \mathcal{M}_{f;\text{med}}^0(\mu, \beta; \sqrt{p^2 + \Delta^2}) \quad (\text{C.73})$$

$$= -\frac{d_\gamma N}{2} \frac{a_s}{(2\pi)^s} \int_0^\infty dp p^{s-1} \left(\mu - \sqrt{p^2 + \Delta^2} \right) \Theta \left(\mu - \sqrt{p^2 + \Delta^2} \right) \quad (\text{C.74})$$

$$= \int_0^\infty dE \rho_s(E) (\mu - E) \Theta(\mu - E), \quad (\text{C.75})$$

where we used hyperspherical coordinates, see App. C.3 and specifically Eq. (C.53), and in Eq. (C.75) the density of states

$$\rho_s(E) = \frac{d_\gamma N}{2^s \pi^{\frac{s}{2}} \Gamma(\frac{s}{2})} E(E^2 - \Delta^2)^{\frac{s}{2}-1} \Theta(E - \Delta). \quad (\text{C.76})$$

Evaluating the integrals in Eq. (C.75) explicitly for $s = 1$ and $s = 3$ we arrive at

$$\mathcal{V}_{\text{f;med}}^{s=1}(\mu, T = 0; \Delta) = \frac{d_\gamma N}{4\pi} \left(\Delta^2 \sinh^{-1} \left(\sqrt{\frac{\mu^2}{\Delta^2} - 1} \right) - \mu \sqrt{\mu^2 - \Delta^2} \right) \Theta(\mu - \Delta), \quad (\text{C.77})$$

$$\begin{aligned} \mathcal{V}_{\text{f;med}}^{s=3}(\mu, T = 0; \Delta) = \frac{d_\gamma N}{96\pi^2} & \left(\mu \left(5\Delta^2 - 2\mu^2 \right) \sqrt{\mu^2 - \Delta^2} - \right. \\ & \left. - 3\Delta^4 \sinh^{-1} \left(\sqrt{\frac{\mu^2}{\Delta^2} - 1} \right) \right) \Theta(\mu - \Delta), \quad (\text{C.78}) \end{aligned}$$

which are used in Eq. (4.46) and for the validation of the $T = 0$ expressions in Apps. C.4.1 and C.4.2 using the series expansion (4.6.31) of Ref. [787] for the inverse hyperbolic sine in Eqs. (C.77) and (C.78) [713].

D. Models in zero dimensions

D.1. $O(N)$ model

D.1.1. Selected vertices, propagators, and regulator insertions

In this appendix we will present the for section 3.2 relevant two-point functions, regulator insertions, propagators, and vertices. Those are obtained by taking functional derivatives of the EAA (3.58) and evaluating the resulting expressions on the QEOM, *viz.* projecting on to $\varphi_{\text{EoM}} = \varphi \equiv (0, \dots, 0, \sigma)$:

$$(A^{\dots})_{\varphi=\varphi_{\text{EoM}}=\varphi} \equiv \underline{A}^{\dots}. \quad (\text{D.1})$$

We will mark uncontracted, external indices with an underscore, in the spirit of subsection 2.1.5, and the involved and $SO(N-1)$ flavor indices are $i \in 1, \dots, N-1$. Note that traces in flavour space lead to the $N-1$ multiplicity of the pion loop contributions, *cf.* Eq. (3.63).

The non-vanishing two-point functions are

$$\underline{\Gamma}_t^{;\pi_j \pi_i} \equiv \pi_i \text{---} \circ \text{---} \pi_j = \delta_{i,j} \frac{U_t^{(1)}(\sigma)}{\sigma} = \delta_{i,j} \frac{u(t,\sigma)}{\sigma}, \quad (\text{D.2a})$$

$$\underline{\Gamma}_t^{;\sigma\sigma} \equiv \sigma \text{---} \circ \text{---} \sigma = U_t^{(2)}(\sigma) = \partial_\sigma u(t, \sigma). \quad (\text{D.2b})$$

The regulator insertions – marked as usual with a crossed circle (\otimes) – are given by

$$\partial_t \underline{R}_t^{;\pi_j \pi_i} \equiv \pi_i \text{---} \otimes \text{---} \pi_j = \delta_{i,j} \partial_t r(t), \quad (\text{D.3a})$$

$$\partial_t \underline{R}_t^{;\sigma\sigma} \equiv \sigma \text{---} \otimes \text{---} \sigma = \partial_t r(t), \quad (\text{D.3b})$$

and follow directly from Eq. (3.61).

Splitting radial and transversal modes in the unified propagator (3.62) leads to

$$\underline{G}_{t;\pi_j \pi_i} = \pi_i \text{---} \dots \text{---} \pi_j = \frac{1}{r_b(t) + u(t, \sigma)/\sigma} \delta_{i,j}, \quad (\text{D.4a})$$

$$\underline{G}_{t;\sigma\sigma} = \sigma \text{---} \dots \text{---} \sigma = \frac{1}{r_b(t) + \partial_\sigma u(t, \sigma)}, \quad (\text{D.4b})$$

for the pion- and sigma-propagator⁹³ respectively.

The flow for the sigma-one-point function in Eq. (3.75) includes the following vertices,

$$\bar{\Gamma}_t^{\sigma} = \text{diagram} \sigma = U_t^{(1)}(\sigma) = u(t, \sigma), \quad (\text{D.5a})$$

$$\bar{\Gamma}_t^{\pi_j \pi_i \sigma} = \text{diagram} \pi_i \pi_j \sigma = \partial_\sigma \left[\frac{U_t^{(1)}(\sigma)}{\sigma} \right] \delta_{i,j} = \partial_\sigma \left[\frac{1}{\sigma} u(t, \sigma) \right] \delta_{i,j}, \quad (\text{D.5b})$$

$$\bar{\Gamma}_t^{\sigma\sigma\sigma} = \text{diagram} \sigma \sigma \sigma = U_t^{(3)}(\sigma) = \partial_\sigma^2 u(t, \sigma). \quad (\text{D.5c})$$

D.1.2. Numerical derivatives

This appendix has been copied from App. A of Ref. [1] with only small adaptations to the presentation in this thesis.

Throughout section 3.2 and subsections 3.2.4 and 3.2.5 we need to extract the 1PI vertex functions $\Gamma_{\varphi_{i_1} \dots \varphi_{i_{2n}}}^{(2n)}$ at the physical point $\sigma = 0$ from the IR results of the FRG flows (or respectively the coefficients $\Gamma^{(2n)}$, which contain the same information). To this end, we compute numerical derivatives of the discrete values of the derivative of the effective potential $u(t_{\text{IR}}, \sigma) = \partial_\sigma U(t_{\text{IR}}, \sigma)$, which were calculated via the FV method. In this work, the following FD approximations [787, 790] are used,

$$f_{i,c}^{(1,2)} = \frac{-f_{i-1} + f_{i+1}}{2 \Delta x} + \mathcal{O}(\Delta x^2), \quad (\text{D.6})$$

$$f_{i,c}^{(1,4)} = \frac{f_{i-2} - 8 f_{i-1} + 8 f_{i+1} - f_{i+2}}{12 \Delta x} + \mathcal{O}(\Delta x^4), \quad (\text{D.7})$$

$$f_{i,f}^{(1,2)} = \frac{-3 f_i + 4 f_{i+1} - f_{i+2}}{2 \Delta x} + \mathcal{O}(\Delta x^2), \quad (\text{D.8})$$

$$f_{i,c}^{(3,2)} = \frac{-f_{i-2} + 2 f_{i-1} - 2 f_{i+1} + f_{i+2}}{2 \Delta x^3} + \mathcal{O}(\Delta x^2), \quad (\text{D.9})$$

$$f_{i,c}^{(3,4)} = \frac{f_{i-3} - 8 f_{i-2} + 13 f_{i-1} - 13 f_{i+1} + 8 f_{i+2} - f_{i+3}}{8 \Delta x^3} + \mathcal{O}(\Delta x^4), \quad (\text{D.10})$$

$$f_{i,f}^{(3,2)} = \frac{-5 f_i + 18 f_{i+1} - 24 f_{i+2} + 14 f_{i+3} - 3 f_{i+4}}{2 \Delta x^3} + \mathcal{O}(\Delta x^2), \quad (\text{D.11})$$

$$f_{i,c}^{(5,2)} = \frac{-f_{i-3} + 4 f_{i-2} - 5 f_{i-1} + 5 f_{i+1} - 4 f_{i+2} + f_{i+3}}{2 \Delta x^5} + \mathcal{O}(\Delta x^2), \quad (\text{D.12})$$

$$f_{i,c}^{(5,4)} = \frac{f_{i-4} - 9 f_{i-3} + 26 f_{i-2} - 29 f_{i-1} + 29 f_{i+1} - 26 f_{i+2} + 9 f_{i+3} - f_{i+4}}{6 \Delta x^5} + \mathcal{O}(\Delta x^4), \quad (\text{D.13})$$

⁹³The term “propagator” is of course misleading for a QFT in a single point, where “propagation” in the true sense of the word is not possible. Nevertheless, we again adopt the notation from higher-dimensional QFT and statistical mechanics for the zero-dimensional analog expressions.

where $f_i \equiv f(x_i)$, $f^{(n,m)}$ denotes the n^{th} derivative of f to order $\mathcal{O}(\Delta x^m)$, and the subscripts c/f stand for central/forward stencil approximations. The scaling order m of the error is indicated by $\mathcal{O}(\Delta x^m)$. In our numerical implementation, the central-scheme approximations are further simplified by exploiting the antisymmetry property $u(t, -\sigma) = -u(t, \sigma)$ of the derivative of the effective potential. In consequence, the central stencils are effectively forward stencils. Furthermore, at the same order of accuracy, the anti-symmetrized central stencils need one point less than the actual forward stencils of same error order of accuracy. In figure 3.8 we find that this property singles out the central stencils as the most favorable choice, because the accumulation of errors in the derivative stencil, which originally derive from the numerical solution of the flow equation, can be reduced this way, by including as few points as possible in the numerical derivative approximations.

We stress that the use of low-order finite-difference approximations to the derivative is only justified because the effective IR potential $U(t_{\text{IR}}, \sigma)$ has to be smooth, which is discussed at length in App. B of Ref. [1]. For higher-dimensional models, the use of finite-difference approximations to extract information from the IR effective potential $U(t_{\text{IR}}, \sigma)$ might not always be justified due to the possibility of non-analyticities in the vicinity of the physical point, where the 1PI n -point functions have to be calculated. Further investigation is needed.

D.1.3. Additional expressions for the $\mathcal{O}(N)$ model in the $N \rightarrow \infty$ limit

This appendix is compiled from Apps. A–D of Ref. [3] with only minor adaptations to the presentation in this thesis.

D.1.3.1. Analytical solution for the instructive toy model

Within this appendix we present results for the integral $I_n^N[V]$ of Eq. (3.148) for the potential (3.149),

$$I_n^N[V] = N^{-(\frac{N}{2}+n)} \left(\Gamma\left(\frac{N}{2} + n\right) - \Gamma\left(\frac{N}{2} + n, 2N\right) + e^{6N(a+1)} \Gamma\left(\frac{N}{2} + n, 8N\right) + (-a)^{-(\frac{N}{2}+n)} e^{-2N(a+1)} \left[\Gamma\left(\frac{N}{2} + n, -2Na\right) - \Gamma\left(\frac{N}{2} + n, -8Na\right) \right] \right), \quad (\text{D.14})$$

and in the special case $a = 0$,

$$I_n^N[V] = N^{-(\frac{N}{2}+n)} \left[\Gamma\left(\frac{N}{2} + n\right) - \Gamma\left(\frac{N}{2} + n, 2N\right) + e^{6N} \Gamma\left(\frac{N}{2} + n, 8N\right) + e^{-2N} \frac{(4^{\frac{N}{2}+n} - 1) (2N)^{\frac{N}{2}+n}}{\frac{N}{2} + n} \right], \quad (\text{D.15})$$

where

$$\Gamma(a, z) \equiv \int_z^\infty dt t^{a-1} e^{-t}, \quad \Gamma(z) \equiv \Gamma(z, 0), \quad (\text{D.16})$$

is the (incomplete) gamma function. To determine the leading order contribution to $\langle(\vec{\phi}^2)^n\rangle$ in the limit $N \rightarrow \infty$ assuming finite n , we employ the asymptotic series, see, e.g., Secs. 6.1.41 and 6.5.32 of Ref [787] or Secs. 5.11 and 8.11 of Ref. [302],

$$\Gamma(z) = e^{-z} \sqrt{\frac{2\pi}{z}} z^z \left(1 + \frac{1}{12z} + \frac{1}{288z^2} + \dots\right), \quad (\text{D.17a})$$

$$\Gamma(a, z) = e^{-z} z^{a-1} \left(1 + \frac{a-1}{z} + \frac{(a-2)(a-1)}{z^2} + \dots\right), \quad (\text{D.17b})$$

valid for large real z and in case of $\Gamma(a, z)$ for $a \simeq \mathcal{O}(z)$ [791].

For $a = 0$ we find

$$\lim_{N \rightarrow \infty} \frac{1}{N^n} \langle(\vec{\phi}^2)^n\rangle = \lim_{N \rightarrow \infty} \frac{2^n I_n^N[V]}{I_0^N[V]} \Big|_{a=0} = 1, \quad (\text{D.18})$$

while for $a > 0$

$$\lim_{N \rightarrow \infty} \frac{1}{N^n} \langle(\vec{\phi}^2)^n\rangle = \lim_{N \rightarrow \infty} \frac{2^n I_n^N[V]}{I_0^N[V]} = \quad (\text{D.19a})$$

$$= \lim_{N \rightarrow \infty} \frac{17 e^{6Na} 16^{\frac{N}{2}+n} + 256 \sqrt{N\pi} e^{\frac{n^2}{N} + \frac{3N}{2}}}{17 e^{6Na} 4^N + 256 \sqrt{N\pi} e^{\frac{3N}{2}}} = \quad (\text{D.19b})$$

$$= \begin{cases} 1 & \text{for } a \leq a_c, \\ 16^n & \text{for } a > a_c, \end{cases} \quad (\text{D.19c})$$

where $a_c \equiv \frac{1}{4} - \frac{1}{3} \ln(2) \simeq 0.018951$. For $a > a_c$ the first terms in the denominator and numerator of Eq. (D.19b) dominate, while for $a < a_c$ the second terms dominate. For $a = a_c$ Eq. (D.19b) can be simplified ultimately to $e^{\frac{n^2}{N}}$ under the limit $N \rightarrow \infty$ and thus yielding 1 in the limit.

D.1.3.2. Saddle-point expansion at large N

In this appendix we present the so-called saddle-point expansion for integrals of the type

$$I^N[f, g] \equiv \int_0^\infty dy g(y) e^{-Nf(y)}. \quad (\text{D.20})$$

Assuming that $f(y)$ has a unique global minimum at y_0 and further assuming analyticity (expandability to arbitrary order) of $f(y)$ and also $g(y)$ in y_0 , it is possible to derive an asymptotic series of $I^N[f, g]$ for large N if the series expansions of $f(y)$ and $g(y)$ around y_0 grow like polynomials. We focus here on the one-dimensional integral (D.20) see, e.g., Ref. [634] for further details and generalizations.

For large N the integrand of Eq. (D.20) is peaked around y_0 and we therefore consider an expansion around y_0 using the computational coordinate z defined by

$$y = y_0 + \frac{z}{\sqrt{N}}. \quad (\text{D.21})$$

We proceed with the computation of $I^N[f, g]$ at large N :

$$I^N[f, g] = \int_0^\infty dy g(y) e^{-Nf(y)} = \quad (\text{D.22a})$$

$$= \frac{1}{\sqrt{N}} \int_{-y_0\sqrt{N}}^\infty dz g(y_0 + \frac{z}{\sqrt{N}}) \exp\left[-Nf\left(y_0 + \frac{z}{\sqrt{N}}\right)\right] = \quad (\text{D.22b})$$

$$= \frac{1}{\sqrt{N}} \int_{-y_0\sqrt{N}}^\infty dz g\left(y_0 + \frac{z}{\sqrt{N}}\right) \exp\left[-Nf^{(0)} - \frac{1}{2}f^{(2)}z^2 - \frac{1}{6\sqrt{N}}f^{(3)}z^3 - \frac{1}{24N}f^{(4)}z^4 - \mathcal{O}(z^5)\right] \simeq \quad (\text{D.22c})$$

$$\simeq e^{-Nf^{(0)}} \frac{1}{\sqrt{N}} \int_{-\infty}^{+\infty} dz e^{-\frac{1}{2}f^{(2)}z^2} g\left(y_0 + \frac{z}{\sqrt{N}}\right) \left(1 - \frac{1}{6\sqrt{N}}f^{(3)}z^3 + \frac{1}{72N}[(f^{(3)})^2z^6 - 3f^{(4)}z^4] + \mathcal{O}(N^{-\frac{3}{2}})\right) = \quad (\text{D.22d})$$

$$= e^{-Nf^{(0)}} \frac{1}{\sqrt{N}} \int_{-\infty}^{+\infty} dz e^{-\frac{1}{2}f^{(2)}z^2} \left(g^{(0)} + \frac{1}{\sqrt{N}}[g^{(1)} - \frac{1}{6}g^{(0)}f^{(3)}z^2]z + \frac{1}{N}[\frac{1}{2}g^{(2)} - \frac{1}{6}g^{(1)}f^{(3)}z^2 + \frac{1}{72}g^{(0)}(f^{(3)})^2z^4 - \frac{1}{24}g^{(0)}f^{(4)}z^2]z^2 + \mathcal{O}(N^{-\frac{3}{2}})\right) = \quad (\text{D.22e})$$

$$= e^{-Nf^{(0)}} \sqrt{\frac{2\pi}{Nf^{(2)}}} \sum_{i=0}^{\infty} C_i[f, g] N^{-i}, \quad (\text{D.22f})$$

where we abbreviated n^{th} derivatives of f and g evaluated at y_0 with superscripts (n). In the preceding set of equalities we first expanded the exponent in powers of N after switching to the coordinate z . We split of the contributions of $\mathcal{O}(N^1)$ and $\mathcal{O}(N^0)$ in the exponent and then expanded the exponential in an asymptotic series in N , while shifting the lower integration bound⁹⁴. Afterwards, we continued by expanding g and collecting terms of $\mathcal{O}(N^{-\frac{n}{2}})$. Ultimately, we were left with a sum over Gaussian integrals of $\mathcal{O}(N^{-n})$ and vanishing contributions of odd integrands of $\mathcal{O}(N^{-\frac{2n+1}{2}})$ in Eq. (D.22e) and performed those integrals, which left us with the desired power series (D.22f) with coefficients $C_i[f, g]$ of $\mathcal{O}(N^0)$, e.g.,

$$C_0[f, g] = g^{(0)}, \quad (\text{D.23a})$$

$$C_1[f, g] = \frac{g^{(2)}}{2f^{(2)}} - \frac{g^{(1)}f^{(3)}}{2(f^{(2)})^2} + \frac{5g^{(0)}(f^{(3)})^2}{24(f^{(2)})^3} - \frac{g^{(0)}f^{(4)}}{8(f^{(2)})^2}. \quad (\text{D.23b})$$

The computation of higher-order coefficients is straightforward and tedious by hand, but is easy to implement in computer algebra systems like MATHEMATICA [353], cf. the digital auxiliary file [366].

⁹⁴Since we are interested in an asymptotic power series for large N shifting the lower integration bound in line (D.22b) is valid since contributions stemming from this shift decay exponentially and as such faster than any power.

The presented saddle-point expansion of $I^N[f, g]$ can be used in combination with Eq. (3.147) for a large- N expansion of the expectation values $\langle(\vec{\phi}^2)^n\rangle$

$$\begin{aligned} \frac{1}{N^n} \langle(\vec{\phi}^2)^n\rangle &= \frac{2^n I^N[V(y) - \frac{1}{2} \ln(y), y^{n-1}]}{I^N[V(y) - \frac{1}{2} \ln(y), y^{-1}]} = \\ &= 2^n y_0^n + \frac{1}{N} \frac{n 2^n y_0^n [2(n-3) y_0^2 V^{(2)}(y_0) + n - 2y_0^3 V^{(3)}(y_0) - 1]}{[2y_0^2 V^{(2)}(y_0) + 1]^2} + \mathcal{O}(N^{-2}), \end{aligned} \quad (\text{D.24})$$

which is valid for $V(y) - \frac{1}{2} \ln(y)$ which are analytic around their respective unique global minimum y_0 . Corresponding expressions for the 1PI correlation functions can be derived using the relations between $\Gamma^{(n)}$ and $\langle(\vec{\phi}^2)^n\rangle$, see, e.g., Eqs. (70)-(75) of Ref. [1] or Ref. [163].

D.1.3.3. Results from the method of characteristics

In this appendix we derive the expressions for the characteristic curves of Eq. (3.167) and (3.169) using the method of characteristics and to be specific the Lagrange–Charpit Eqs. (2.120) introduced in subsection 2.2.3.1.

We proceed with the solution of the characteristic Eqs. (2.120) for the FRG flow Eq. (3.167) and (3.169) of the zero-dimensional $O(N)$ model in the limit $N \rightarrow \infty$. Since the equations in x and y are related by the coordinate transformation $y = \frac{1}{2} x^2$, the solutions and also characteristic curves are directly related. For simplicity we solve the characteristic equations for the flow equation (3.169) in the rescaled invariant y and then compute the corresponding curves in x using the coordinate transformation. A direct solution of the characteristic equations for the flow equation (3.167) in x is also possible and shares a lot of computations with the slightly simpler computation in y . After performing the y derivative in Eq. (3.169) comparing coefficients with Eq. (2.119) yields for the Eqs. (2.120) explicitly

$$\frac{\partial t(\tau)}{\partial \tau} = 1, \quad (\text{D.25a})$$

$$\frac{\partial y(\tau)}{\partial \tau} = - \frac{\Lambda e^{-t(\tau)}}{2 [\Lambda e^{-t(\tau)} + v(\tau)]^2}, \quad (\text{D.25b})$$

$$\frac{\partial v(\tau)}{\partial \tau} = 0, \quad (\text{D.25c})$$

with the UV ICs

$$t(\tau = 0) = 0, \quad (\text{D.26a})$$

$$y(\tau = 0) = y_0 \geq 0, \quad (\text{D.26b})$$

$$v(\tau = 0) = v(0, y_0), \quad (\text{D.26c})$$

specifying the characteristic curves. The ODEs for $t(\tau)$ and $v(\tau)$ decouple and can be trivially integrated

$$t(\tau) = \tau, \quad (\text{D.27})$$

$$v(\tau) = v(0, y_0). \quad (\text{D.28})$$

Due to the direct equivalence of t and τ we continue by using the RG time t as the curve-parameter in the following. The ODE (D.25b) for $y(\tau)$ is independent of y itself and can be integrated directly after inserting the solutions (D.27) and (D.28) for t and v . The solution for $y(t)$ follows as

$$y(t) = y_0 - \int_0^t d\tau \frac{\Lambda e^{-\tau}}{2[\Lambda e^{-\tau} + v(0, y_0)]^2} = \quad (\text{D.29a})$$

$$= y_0 - \frac{1}{2[\Lambda e^{-t} + v(0, y_0)]} + \frac{1}{2[\Lambda + v(0, y_0)]}. \quad (\text{D.29b})$$

Using the coordinate transformation $y = \frac{1}{2}x^2$ and the associated relation for the first derivative $\partial_y V(t, y) = \frac{1}{x} \partial_x V(t, x)$ we can compute the characteristic curves $x(t)$ and $v(t)$ for the flow Eq. (3.167) from Eq. (D.29) and (D.28),

$$x(t) = \pm \sqrt{2y(t)} = \pm \sqrt{x_0^2 - \frac{1}{\Lambda e^{-t} + \frac{v(0, x_0)}{x_0}} + \frac{1}{\Lambda + \frac{v(0, x_0)}{x_0}}}, \quad (\text{D.30})$$

$$v(t) = \frac{v(0, x_0)}{x_0} x(t). \quad (\text{D.31})$$

A particularity of the flow equation in x is that the conserved quantity $v(t, x)$ (the derivative $\partial_x V(t, x)$) is not constant along the characteristics, $\frac{dv}{dt} \neq 0$, due to the contribution stemming from $x(t)$ in Eq. (D.31).

D.1.3.4. Rankine-Hugoniot condition and shock position

The Riemann problems posed by the IC (3.150) with the flow Eq. (3.169) include a shock discontinuity in the UV ($t = 0$) at $y = 2$, since $v(2^-) > v(2^+)$ and $G[t, v] < 0$. For a discussion see subsection 3.2.5.4. This appendix is dedicated to the computation of the position of the shock as a function of flow time t using the Rankine-Hugoniot condition [368, 369] introduced in subsection 2.2.3.1. A computation in the invariant y for a structurally identical flow equation and IC can be found in App. C.1 of Ref. [247]. We present a derivation for the complementary problem – IC (3.178) with the flow Eq. (3.167) – in x for the sake of completeness in the following.

Assume that there is a single shock wave (discontinuity) at the position $\xi_s(t)$ between $x_L(t) < \xi_s(t) < x_R(t)$. Integration over the conservation law (3.167) yields

$$\begin{aligned} \int_{x_L(t)}^{x_R(t)} dx \partial_t v(t, x) &= \int_{x_L(t)}^{x_R(t)} dx \frac{d}{dx} F[t, x, v(t, x)] = \\ &= - (F[t, x_R(t), v(t, x_R(t))] - F[t, x_L(t), v(t, x_L(t))]). \end{aligned} \quad (\text{D.32})$$

For the l.h.s., we split the integral about the shock $\xi_s(t)$

$$\begin{aligned} \int_{x_L(t)}^{x_R(t)} dx \partial_t v(t, x) &= \int_{x_L(t)}^{\xi_s(t)} dx \partial_t v(t, x) + \int_{\xi_s(t)}^{x_R(t)} dx \partial_t v(t, x) = \\ &= -v(t, \xi_s(t)) \partial_t \xi_s(t) + v(t, x_L(t)) \partial_t x_L(t) + \frac{d}{dt} \int_{x_L(t)}^{\xi_s(t)} dx v(t, x) - \\ &\quad - v(t, x_R(t)) \partial_t x_R(t) + v(t, \xi_s(t)) \partial_t \xi_s(t) + \frac{d}{dt} \int_{\xi_s(t)}^{x_R(t)} dx v(t, x), \end{aligned} \quad (\text{D.33})$$

where we used Leibniz integral rule in the last equality. Next, we study the limits $x_L(t) \rightarrow \xi_s^-(t)$ and $x_R(t) \rightarrow \xi_s^+(t)$. We find that the two integrals with the total time derivatives vanish and by defining

$$v_L(t) = \lim_{x_L(t) \rightarrow \xi_s^-(t)} v(t, x_L(t)), \quad (\text{D.34a})$$

$$F_L(t) = \lim_{x_L(t) \rightarrow \xi_s^-(t)} F[t, x_L(t), v(t, x_L(t))], \quad (\text{D.34b})$$

$$v_R(t) = \lim_{x_R(t) \rightarrow \xi_s^+(t)} v(t, x_R(t)), \quad (\text{D.35a})$$

$$F_R(t) = \lim_{x_R(t) \rightarrow \xi_s^+(t)} F[t, x_R(t), v(t, x_R(t))], \quad (\text{D.35b})$$

the equation for the shock speed according to the Rankine–Hugoniot (jump) condition (2.122) reads

$$\partial_t \xi_s(t) = \frac{F_R(t) - F_L(t)}{v_R(t) - v_L(t)}. \quad (\text{D.36})$$

For the explicit problem under consideration the initial positions at $t = 0$ of the two shocks are $x = 2$ and $x = -2$. W.l.o.g. we consider the shock at $x = 2$ since the discussion for the shock at $x = -2$ follows from the symmetry of the problem. Consider the characteristic curves (D.30) and $v(t, x(t))$, thus Eq. (D.31), left and right of the shock we find

$$v_L(t) = \frac{v_{UV,L}}{x_{UV,L}} x_L(t) = \xi_s^-(t), \quad (\text{D.37a})$$

$$v_R(t) = \frac{v_{UV,R}}{x_{UV,R}} x_R(t) = -a \xi_s^+(t), \quad (\text{D.37b})$$

and for the corresponding fluxes Eq. (3.167) yields

$$F_L(t) = -\frac{\frac{1}{2} \partial_t r(t)}{r(t) + \frac{v_L(t)}{x_L(t)}} = -\frac{\frac{1}{2} \partial_t r(t)}{r(t) + 1}, \quad (\text{D.38a})$$

$$F_R(t) = -\frac{\frac{1}{2} \partial_t r(t)}{r(t) + \frac{v_R(t)}{x_R(t)}} = -\frac{\frac{1}{2} \partial_t r(t)}{r(t) - a}. \quad (\text{D.38b})$$

Inserting those explicit results into the Rankine–Hugoniot (jump) condition (2.122) results in

$$\partial_t \xi_s(t) = \frac{F_R(t) - F_L(t)}{v_R(t) - v_L(t)} = \frac{1}{\xi_s(t)} \frac{1}{a+1} \left[\frac{\frac{1}{2} \partial_t r(t)}{r(t) - a} - \frac{\frac{1}{2} \partial_t r(t)}{r(t) + 1} \right], \quad (\text{D.39})$$

where we are allowed to set $\xi_s^+(t) = \xi_s^-(t) = \xi_s(t)$. Using the monotonicity of the regulator shape function $r(t)$, see Eq. (3.8), we find

$$\partial_r (\xi_s^2(r)) = \frac{1}{a+1} \left(\frac{1}{r-a} - \frac{1}{r+1} \right), \quad (\text{D.40})$$

which can be integrated from the UV ($r = \Lambda$) down to an arbitrary value $r(t) \geq 0$ yielding

$$\xi_s(t) = \sqrt{\xi_{s,\text{UV}}^2 + \frac{1}{a+1} \left[\ln \left(\frac{r(t) - a}{\Lambda - a} \right) - \ln \left(\frac{r(t) + 1}{\Lambda + 1} \right) \right]}, \quad (\text{D.41})$$

with $\xi_{s,\text{UV}}^2 = 2^2 = 4$.

For $a \geq 0$ (and $\Lambda \gg a$) we find $\xi_s(t_0) = 0$ for a finite $t_0 > 0$, which indicates that the shocks originating from -2 and $+2$ in the UV annihilate at $x = 0$ at the RG time t_0 based on the discussion of this appendix. The applicability of the construction discussed in this appendix is however limited as outlined in subsection 3.2.5.3.

D.2. $SU(2)$ model

D.2.1. Selected vertices, propagators, and regulator insertions

In this appendix we will present the for section 3.3 relevant two-point functions, regulator insertions, propagators, and vertices. Those are obtained by taking functional derivatives of the EAA (3.217) and regulator term (3.210) and evaluating the resulting expressions on the QEOM, *viz.* projecting on to $\chi_{\text{EoM}} = \underline{\chi} \equiv ((0, 0, \sigma), 0, 0)$ from Eq. (3.218):

$$(A^{\dots})_{\chi=\chi_{\text{EoM}}=\underline{\chi}} \equiv \underline{A}^{\dots}. \quad (\text{D.42})$$

We will mark uncontracted, external indices with an underscore, in the spirit of subsection 2.1.5, and the involved $SU(2)$ and $SO(2)$ flavor indices are $\alpha \in 1, 2$ and $i \in 1, 2$.

This appendix has a corresponding digital auxiliary file [642], which includes all the following expressions and their explicit, programmatic derivation, making use of the functionalities of our MATHEMATICA code [299].

The non-vanishing two-point functions are

$$\underline{\Gamma}_t^{\bar{\vartheta}_\alpha \vartheta^\beta} \equiv \bar{\vartheta}_\alpha \rightarrow \text{O} \rightarrow \vartheta^\beta = -m_t(\sigma)(t_0)^\alpha_\beta - 2iY_t(\sigma)(t_3)^\alpha_\beta, \quad (\text{D.43a})$$

$$\underline{\Gamma}_t^{\vartheta^\alpha \bar{\vartheta}_\beta} \equiv \vartheta^\alpha \leftarrow \text{O} \leftarrow \bar{\vartheta}_\beta = m_t(\sigma)(t_0)^\beta_\alpha + 2iY_t(\sigma)(t_3)^\beta_\alpha, \quad (\text{D.43b})$$

$$\bar{\Gamma}_t^{\pi_j \pi_i} \equiv \pi_i \cdots \circ \cdots \pi_j = \delta_{i,j} \frac{U_t^{(1)}(\sigma)}{\sigma} = \delta_{i,j} \frac{u(t,\sigma)}{\sigma}, \quad (\text{D.43c})$$

$$\bar{\Gamma}_t^{\sigma\sigma} \equiv \sigma \text{---}\circ\text{---}\sigma = U_t^{(2)}(\sigma) = \partial_\sigma u(t,\sigma). \quad (\text{D.43d})$$

The regulator insertions are given by

$$-\partial_t R_t^{\bar{\vartheta}_\alpha \vartheta^\beta} \equiv \bar{\vartheta}_\alpha \text{---}\otimes\text{---}\vartheta^\beta = \partial_t r_f(t) (\mathbb{1}_t)_{\alpha\beta}^{\alpha\beta} = 2\partial_t r_f(t) (t_0)_{\alpha\beta}^{\alpha\beta}, \quad (\text{D.44a})$$

$$-\partial_t R_t^{\vartheta^\alpha \bar{\vartheta}_\beta} \equiv \vartheta^\alpha \text{---}\otimes\text{---}\bar{\vartheta}_\beta = -\partial_t r_f(t) (\mathbb{1}_t)_{\alpha\beta}^{\beta\alpha} = -2\partial_t r_f(t) (t_0)_{\alpha\beta}^{\beta\alpha}, \quad (\text{D.44b})$$

$$\partial_t R_t^{\pi_j \pi_i} \equiv \pi_i \cdots \otimes \cdots \pi_j = \delta_{i,j} \partial_t r_b(t), \quad (\text{D.44c})$$

$$\partial_t R_t^{\sigma\sigma} \equiv \sigma \text{---}\otimes\text{---}\sigma = \partial_t r_b(t), \quad (\text{D.44d})$$

where we introduced a minus sign for the Grassmann-valued insertions such that diagrams with Grassmann-valued regulator insertions appear with their more conventional minus sign. We discussed this in subsection 3.3.2 following Eq. (3.225).

Recall Eq. (2.27):

$$G_{t;\mathbf{a}\mathbf{m}}[\chi] \left(\bar{\Gamma}_t^{\mathbf{m}\mathbf{b}}[\chi] + R_t^{\mathbf{m}\mathbf{b}} \right) = \gamma_{\mathbf{a}}^{\mathbf{b}} = (-1)^{\mathbf{a}\mathbf{b}} \delta_{\mathbf{b}}^{\mathbf{a}}, \quad (\text{D.45})$$

with which we can derive the propagators

$$\underline{G}_{t;\bar{\vartheta}_\alpha \vartheta^\beta} = \bar{\vartheta}_\alpha \text{---}\leftarrow\vartheta^\beta = \frac{-(m_t(\sigma) + 2r_f(t))(t_0)_{\alpha\beta}^{\beta\alpha} + 2iY_t(\sigma)(t_3)_{\alpha\beta}^{\beta\alpha}}{Y_t(\sigma)^2 + (r_f(t) + m_t(\sigma)/2)^2}, \quad (\text{D.46a})$$

$$\underline{G}_{t;\vartheta^\alpha \bar{\vartheta}_\beta} = \vartheta^\alpha \text{---}\rightarrow\bar{\vartheta}_\beta = \frac{(m_t(\sigma) + 2r_f(t))(t_0)_{\alpha\beta}^{\alpha\beta} - 2iY_t(\sigma)(t_3)_{\alpha\beta}^{\alpha\beta}}{Y_t(\sigma)^2 + (r_f(t) + m_t(\sigma)/2)^2}, \quad (\text{D.46b})$$

$$\underline{G}_{t;\pi_j \pi_i} = \pi_i \cdots \text{---}\pi_j = \frac{1}{r_b(t) + u(t,\sigma)/\sigma} \delta_{i,j}, \quad (\text{D.46c})$$

$$\underline{G}_{t;\sigma\sigma} = \sigma \text{---}\text{---}\sigma = \frac{1}{r_b(t) + \partial_\sigma u(t,\sigma)}, \quad (\text{D.46d})$$

by inverting

$$(\underline{\Gamma}_t^{\mathbf{a}\mathbf{b}} + \underline{R}_t^{\mathbf{a}\mathbf{b}}) = (\underline{\Gamma}_t^{\mathbf{a}\mathbf{b}}), \quad (\text{D.47})$$

and carefully keeping track of the sign factors $(-1)^{\mathbf{a}\mathbf{b}}$ for the Grassmann numbers. Note that

$$(\underline{G}_{t;\bar{\vartheta}\vartheta})_{\alpha\beta}^{\beta\alpha} + (\underline{G}_{t;\vartheta\bar{\vartheta}})_{\alpha\beta}^{\alpha\beta} = 0, \quad (\text{D.48a})$$

$$(\underline{R}_{t;\bar{\vartheta}\vartheta})_{\alpha\beta}^{\beta\alpha} + (\underline{R}_{t;\vartheta\bar{\vartheta}})_{\alpha\beta}^{\alpha\beta} = 0, \quad (\text{D.48b})$$

i.e., they are directly related by transposition. This usually allows for a unification of Grassmann-valued contributions in the traces of the Wetterich equation, *viz.* the elimination of one class of propagators and insertions in favor of the other one, *cf.* Eqs. (3.222) and (3.223) in subsection 3.3.2. We will usually eliminate $\underline{G}_{t;\bar{\vartheta}_\alpha \vartheta^\beta}$ in favor of $\underline{G}_{t;\vartheta^\alpha \bar{\vartheta}_\beta}$ by transposition (and by using

the invariance of the involved traces under such an operation). For complicated diagrams, like the box-diagrams in the flow equation (3.234) for $g_t(\sigma)$, such a simple elimination by transposition is not possible while maintaining the simple order of elements on the loop, *cf.* ref a mixed diagram, and we maintain diagrams and expressions involving both propagator types.

The flow Eq. (3.227) for the Grassmann-valued two-point function includes the following three- and four-point vertices,

$$\bar{\Gamma}_t^{\bar{\vartheta}_\beta \vartheta^\alpha \pi_i} \equiv \begin{array}{c} \pi_i \\ \vdots \\ \vartheta^\alpha \\ \swarrow \quad \searrow \\ \bar{\vartheta}_\beta \end{array} = -2i \frac{Y_t(\sigma)}{\sigma} (t_i)_{\underline{\alpha}}^\beta, \quad (\text{D.49})$$

$$\bar{\Gamma}_t^{\bar{\vartheta}_\beta \vartheta^\alpha \sigma} \equiv \begin{array}{c} \sigma \\ \vdots \\ \vartheta^\alpha \\ \swarrow \quad \searrow \\ \bar{\vartheta}_\beta \end{array} = -m_t^{(1)}(\sigma) (t_0)_{\underline{\alpha}}^\beta - 2i Y_t^{(1)}(\sigma) (t_3)_{\underline{\alpha}}^\beta, \quad (\text{D.50})$$

$$\bar{\Gamma}_t^{\bar{\vartheta}_\delta \vartheta^\gamma \bar{\vartheta}_\beta \vartheta^\alpha} \equiv \begin{array}{c} \vartheta^\alpha \quad \bar{\vartheta}_\beta \\ \swarrow \quad \searrow \\ \bar{\vartheta}_\delta \quad \vartheta^\gamma \end{array} = g_t(\sigma) [(t_0)_{\underline{\alpha}}^\beta (t_0)_{\underline{\gamma}}^\delta - (t_0)_{\underline{\gamma}}^\beta (t_0)_{\underline{\alpha}}^\delta], \quad (\text{D.51})$$

$$\bar{\Gamma}_t^{\bar{\vartheta}_\beta \vartheta^\alpha \pi_j \pi_i} \equiv \begin{array}{c} \pi_i \quad \pi_j \\ \vdots \\ \vartheta^\alpha \\ \swarrow \quad \searrow \\ \bar{\vartheta}_\beta \end{array} = -\delta_{i,j} \left[\frac{m_t^{(1)}(\sigma)}{\sigma} (t_0)_{\underline{\alpha}}^\beta + 2i \partial_\sigma \left(\frac{Y_t(\sigma)}{\sigma} \right) (t_3)_{\underline{\alpha}}^\beta \right], \quad (\text{D.52})$$

$$\bar{\Gamma}_t^{\bar{\vartheta}_\beta \vartheta^\alpha \sigma \sigma} \equiv \begin{array}{c} \sigma \quad \sigma \\ \vdots \\ \vartheta^\alpha \\ \swarrow \quad \searrow \\ \bar{\vartheta}_\beta \end{array} = -m_t^{(2)}(\sigma) (t_0)_{\underline{\alpha}}^\beta - 2i Y_t^{(2)}(\sigma) (t_3)_{\underline{\alpha}}^\beta, \quad (\text{D.53})$$

while the flow equation for the Grassmann-valued four-point function in subsection 3.3.2 includes, furthermore, the following mixed four-, five-, and six-point vertices,

$$\bar{\Gamma}_t^{\bar{\vartheta}_\beta \vartheta^\alpha \pi_i \sigma} \equiv \begin{array}{c} \sigma \quad \pi_i \\ \vdots \\ \vartheta^\alpha \\ \swarrow \quad \searrow \\ \bar{\vartheta}_\beta \end{array} = -2i \partial_\sigma \left(\frac{Y_t(\sigma)}{\sigma} \right) (t_i)_{\underline{\alpha}}^\beta, \quad (\text{D.54})$$

$$\bar{\Gamma}_t^{\bar{\vartheta}_\delta \vartheta^\gamma \bar{\vartheta}_\beta \vartheta^\alpha \sigma} \equiv \begin{array}{c} \sigma \quad \vartheta^\alpha \\ \vdots \\ \bar{\vartheta}_\beta \\ \swarrow \quad \searrow \\ \bar{\vartheta}_\delta \quad \vartheta^\gamma \end{array} = g_t^{(1)}(\sigma) [(t_0)_{\underline{\alpha}}^\beta (t_0)_{\underline{\gamma}}^\delta - (t_0)_{\underline{\gamma}}^\beta (t_0)_{\underline{\alpha}}^\delta], \quad (\text{D.55})$$

$$\bar{\Gamma}_t^{\bar{\vartheta}_\delta \vartheta^\gamma \bar{\vartheta}_\beta \vartheta^\alpha \pi_j \pi_i} \equiv \begin{array}{c} \pi_i \quad \pi_j \\ \vdots \\ \vartheta^\alpha \\ \swarrow \quad \searrow \\ \bar{\vartheta}_\beta \\ \swarrow \quad \searrow \\ \bar{\vartheta}_\delta \quad \vartheta^\gamma \end{array} = \delta_{i,j} \frac{g_t^{(1)}(\sigma)}{\sigma} [(t_0)_{\underline{\alpha}}^\beta (t_0)_{\underline{\gamma}}^\delta - (t_0)_{\underline{\gamma}}^\beta (t_0)_{\underline{\alpha}}^\delta], \quad (\text{D.56})$$

$$\bar{\Gamma}_t^{\bar{\vartheta}_\delta \vartheta^\gamma \bar{\vartheta}_\beta \vartheta^\alpha \sigma \sigma} \equiv \begin{array}{c} \sigma \quad \sigma \\ \vdots \\ \vartheta^\alpha \\ \swarrow \quad \searrow \\ \bar{\vartheta}_\beta \\ \swarrow \quad \searrow \\ \bar{\vartheta}_\delta \quad \vartheta^\gamma \end{array} = g_t^{(2)}(\sigma) [(t_0)_{\underline{\alpha}}^\beta (t_0)_{\underline{\gamma}}^\delta - (t_0)_{\underline{\gamma}}^\beta (t_0)_{\underline{\alpha}}^\delta]. \quad (\text{D.57})$$

E. Gross-Neveu model in two dimensions

E.1. Selected vertices, propagators, and regulator insertions

In this appendix we will present the for chapter 4 relevant two-point functions, regulator insertions, propagators, and vertices. Those are obtained by taking functional derivatives of the EAA (4.17) and the corresponding, canonical regulator term (2.7) and evaluating the resulting expressions on the QEOM, *viz.* projecting on to $\chi_{\text{EoM}} = \underline{\chi} \equiv (\sigma, 0, 0)$ from Eq. (4.18):

$$(A^{\dots})_{\chi=\chi_{\text{EoM}}=\underline{\chi}} \equiv \underline{A}^{\dots}. \quad (\text{E.1})$$

We will mark uncontracted, external indices with an underscore, in the spirit of subsection 2.1.5. We will use f as flavor index and a for spinor indices.

This appendix has a corresponding digital auxiliary file [652].

The non-vanishing two-point functions are

$$\bar{\Gamma}_t^{\bar{\psi}_I \psi_{II}} \equiv \bar{\psi}_I \xrightarrow{\text{O}} \psi_{II} = -\tilde{\delta}_{n_I - n_{II}} \frac{f_I f_{II}}{p_I - p_{II}} \left(i(\nu_{n_I} + i\mu)\gamma^2 + ip_I \gamma^1 + \frac{h\sigma}{\sqrt{N}} \mathbb{1}_2 \right)^{a_I}_{a_{II}}, \quad (\text{E.2a})$$

$$\bar{\Gamma}_t^{\sigma_I \sigma_{II}} \equiv \sigma_I \xrightarrow{\text{O}} \sigma_{II} = \tilde{\delta}_{n_I + n_{II}} \frac{\omega_{n_I}^2 + p_I^2 + u_t^{(1)}(\sigma)}{p_I + p_{II}}. \quad (\text{E.2b})$$

The regulator insertions are given by

$$-\partial_t \underline{R}_t^{\bar{\psi}_I \psi^{\perp}} \equiv \psi^{\perp} \xrightarrow{\text{O}} \bar{\psi}_I = \tilde{\delta}_{n_I - n_{II}} \frac{f_I f_{II}}{p_I - p_{II}} \left(ip_I \gamma^1 \partial_t r_f(t, p_I) \right)^{a_I}_{a_{II}}, \quad (\text{E.3a})$$

$$\partial_t \underline{R}_t^{\sigma_I \sigma_{II}} \equiv \sigma_I \xrightarrow{\text{O}} \sigma_{II} = \tilde{\delta}_{n_I + n_{II}} \frac{\omega_{n_I}^2 + p_I^2 \partial_t r_b(t, p_I)}{p_I + p_{II}}, \quad (\text{E.3b})$$

where we follow the diagrammatic conventions of App. D.2.1, momentum-space conventions of App. B.5, and only consider the one class of fermionic contributions and unify the other by means of transposition as discussed in App. D.2.1.

The propagators are given by

$$\underline{G}_{t; \psi_I \bar{\psi}_{II}} = \psi^{\perp} \xrightarrow{\text{O}} \bar{\psi}_{II} = -\tilde{\delta}_{n_I - n_{II}} \frac{f_I f_{II}}{p_I - p_{II}} \frac{\left(i(\nu_{n_I} + i\mu)\gamma^2 + ip_I \gamma^1 - \frac{h\sigma}{\sqrt{N}} \mathbb{1}_2 \right)^{a_I}_{a_{II}}}{(\nu_{n_I} + i\mu)^2 + p_{I,k(t)}^2 + \frac{h^2 \sigma^2}{N}}, \quad (\text{E.4a})$$

$$\underline{G}_{t; \sigma_I \sigma_{II}} = \sigma_I \xrightarrow{\text{O}} \sigma_{II} = \tilde{\delta}_{n_I + n_{II}} \frac{1}{p_I + p_{II} \omega_{n_I}^2 + p_{I,k(t)}^2 + u_t^{(1)}(\sigma)}, \quad (\text{E.4b})$$

where we used the compact notation for the regulated spatial momenta $p_{;k}$ of Eq. (C.55).

For the flow equation discussed in App. E.3 we additionally require the vertex

$$\bar{\Gamma}_t^{\psi_I \sigma_{II} \bar{\psi}^{III}} \equiv \begin{array}{c} \psi^{III} \\ \swarrow \\ \text{---} \sigma_{II} \\ \nwarrow \\ \bar{\psi}_I \end{array} = \tilde{\delta}_{\substack{n_{II}+n_{III}-n_I \\ p_{II}+p_{III}-p_I}} \frac{\hbar}{\sqrt{N}} (\mathbb{1}_2)^{a_I} a_{III} (\mathbb{1}_N)^{f_I} f_{III}. \quad (\text{E.5})$$

E.2. The LPA flow equation

In this appendix we present a derivation of the FRG flow equation (4.21) of the effective potential $U(t, \sigma)$ at non-zero μ and T in LPA truncation for the sake of completeness. Tracing the Wetterich Eq. (2.37) in field space using the propagators and regulator insertions of App. E.1 and projecting onto $\chi_{\text{EoM}} = \underline{\chi} = (\sigma, 0, 0)$, cf. Eq. (4.18), yields

$$\beta(2\pi) \delta(0) \partial_t U(t, \sigma) = \partial_t \bar{\Gamma}_t = \frac{1}{2} \left(\text{blue loop} - \text{green loop} \right), \quad (\text{E.6})$$

with an infinite volume factor $V \equiv \beta(2\pi) \delta(0)$, which also appears in the loops on the r.h.s. and thus ultimately cancels. Plugging in the explicit expressions of App. E.1, we can perform the traces in Dirac and flavor space and are left with the traces in momentum space with manifest as one-dimensional momentum-space integrals and Matsubara sums. The flow equation ultimately reads

$$\begin{aligned} \partial_t U(t, \sigma) = & \frac{1}{2} \int_{n;p} \frac{p^2 \partial_t r(t, p)}{\omega_n^2 + p^2 [1 + r(t, p)] + \partial_\sigma^2 U(t, \sigma)} - \\ & - \int_{n;p} \frac{N p^2 \partial_t r(t, p)}{(\nu_n + i\mu)^2 + p^2 [1 + r(t, p)] + \frac{(\hbar \sigma)^2}{N}}, \end{aligned} \quad (\text{E.7})$$

where we assumed a unified scheme for the regulator shape functions, according to Eq. (2.49):

$$r(t, p) + 1 \equiv r_b(t, p) + 1 \equiv (r_f(t, p) + 1)^2. \quad (\text{E.8})$$

With the flat (LPA optimized Litim) regulator shape function (2.45) the momentum integral can be evaluated analytically, see, e.g., Refs. [4, 652] for the involved subtleties, and we arrive at

$$\partial_t U(t, \sigma) = -\frac{1}{\pi} \frac{1}{\beta} \sum_n \frac{k^3(t)}{\omega_n^2 + E_b^2(t, \sigma)} + \frac{2N}{\pi} \frac{1}{\beta} \sum_n \frac{k^3(t)}{(\nu_n + i\mu)^2 + E_f^2(t, \sigma)}. \quad (\text{E.9})$$

The Matsubara sums can be evaluated analytically, as discussed in App. C.2. The relevant expressions for this case are given in Eqs. (C.39) and (C.40). After the $\frac{1}{N}$ -rescalings of Eq. (4.19) we finally obtain FRG flow equation (4.21) for the scale-dependent effective potential in LPA at non-zero T and non-zero μ .

The corresponding expression in the large- N limit with the sharp regulator shape function of Eq. (2.46) relevant for some specifics of the discussion in section 4.4 will be included in Ref. [652].

E.3. The bosonic two-point function in the limit $N \rightarrow \infty$

The bosonic two-point function discussed in the stability analysis of Eq. (4.71) can be computed from the flow equation

$$\partial_t \bar{\Gamma}_t^{\sigma_I \sigma_{II}} = -\frac{1}{2} \sigma_I \text{---} \text{---} \text{---} \text{---} \text{---} \text{---} \text{---} \text{---} \text{---} \text{---} \text{---} \text{---} \sigma_{II} - \frac{1}{2} \sigma_I \text{---} \text{---} \text{---} \text{---} \text{---} \text{---} \text{---} \text{---} \text{---} \text{---} \text{---} \sigma_{II}, \quad (\text{E.10})$$

which in turn can be obtained by tracing Eq. (2.68) in field space with the expressions from App. E.1. Evaluating Eq. (E.10) at vanishing external frequency $n_I = n_{II} = 0$ and external momenta $p_I = -p_{II} = q$ yields the required flow equation $\partial_t \bar{\Gamma}_t^{(2)}(\bar{\sigma}, \mu, T, q)$, which can be integrated directly in the large- N limit. Choosing the sharp regulator shape function of Eq. (2.46) or equivalently a sharp momentum cut-off in the unregularized variant of the flow equation, one can isolate the involved divergencies and equate them with the corresponding divergencies from the vacuum contribution. Careful consideration in a consistent regularization scheme allows for the computation of the renormalized result presented in Eq. (4.71). Additional details can be found in App. A of Ref. [5] and Ref. [165].



Backmatter



Bibliography

- [1] A. Koenigstein *et al.*, “Numerical fluid dynamics for FRG flow equations: Zero-dimensional QFTs as numerical test cases. I. The $O(N)$ model”, *Phys. Rev. D* **106** (2022) 065012, arXiv: 2108.02504 [[cond-mat.stat-mech](#)].
- [2] A. Koenigstein *et al.*, “Numerical fluid dynamics for FRG flow equations: Zero-dimensional QFTs as numerical test cases. II. Entropy production and irreversibility of RG flows”, *Phys. Rev. D* **106** (2022) 065013, arXiv: 2108.10085 [[cond-mat.stat-mech](#)].
- [3] M. J. Steil and A. Koenigstein, “Numerical fluid dynamics for FRG flow equations: Zero-dimensional QFTs as numerical test cases. III. Shock and rarefaction waves in RG flows reveal limitations of the $N \rightarrow \infty$ limit in $O(N)$ -type models”, *Phys. Rev. D* **106** (2022) 065014, arXiv: 2108.04037 [[cond-mat.stat-mech](#)].
- [4] J. Stoll *et al.*, “Bosonic fluctuations in the $(1 + 1)$ -dimensional Gross-Neveu(-Yukawa) model at varying μ and T and finite N ” (2021), arXiv: 2108.10616 [[hep-ph](#)].
- [5] A. Koenigstein *et al.*, “Detecting inhomogeneous chiral condensation from the bosonic two-point function in the $(1 + 1)$ -dimensional Gross-Neveu model in the mean-field approximation*”, *J. Phys. A* **55** (2022) 375402, arXiv: 2112.07024 [[hep-ph](#)].
- [6] M. J. Steil, M. Buballa, and B.-J. Schaefer, “Inhomogeneous chiral condensates in the quark-meson model with the functional renormalization group”, Draft, 2024, in preparation.
- [7] M. J. Steil, A. Koenigstein, and J. Braun, “Numerical fluid dynamics for FRG flow equations: Zero-dimensional QFTs as numerical test cases - Part IV: A fermion-boson model”, Draft, 2021, in preparation.
- [8] A. Koenigstein and M. J. Steil, “Absence of global fixed-point solutions in the zero-dimensional $O(N)$ -model”, 2021, unpublished notes, private communication.
- [9] A. Koenigstein and M. J. Steil, “Comment on the “grid methods” and other numerical schemes”, 2021, unpublished notes, private communication.
- [10] M. Gell-Mann, “The Eightfold Way: A theory of strong interaction symmetry” (1961), DOI: [10.2172/4008239](#).
- [11] Y. Ne’eman, “Derivation of strong interactions from a gauge invariance”, *Nucl. Phys.* **26** (1961) 222–229.
- [12] M. Gell-Mann, “Symmetries of baryons and mesons”, *Phys. Rev.* **125** (1962) 1067–1084.
- [13] G. Zweig, “An SU(3) model for strong interaction symmetry and its breaking. Version 1”, [CERN-TH-401 \(1964\)](#) .
- [14] G. Zweig, “An SU(3) model for strong interaction symmetry and its breaking. Version 2”, [CERN-TH-412 \(1964\) 22–101](#), in: *Developments in the Quark Theory of Hadrons, Vol. 1, 1964 - 1978*, ed. by D. B. Lichtenberg and S. P. Rosen.
- [15] B. J. Björken and S. L. Glashow, “Elementary particles and SU(4)”, *Phys. Lett.* **11** (1964) 255–257.
- [16] S. L. Glashow, J. Iliopoulos, and L. Maiani, “Weak Interactions with Lepton-Hadron Symmetry”, *Phys. Rev. D* **2** (1970) 1285–1292.
- [17] M. Kobayashi and T. Maskawa, “CP-Violation in the Renormalizable Theory of Weak Interaction”, *Prog. Theor. Phys.* **49** (1973) 652–657.

-
- [18] O. W. Greenberg, “Spin and Unitary-Spin Independence in a Paraquark Model of Baryons and Mesons”, *Phys. Rev. Lett.* **13** (1964) 598–602.
- [19] M. Y. Han and Y. Nambu, “Three-Triplet Model with Double SU(3) Symmetry”, *Phys. Rev.* **139** (1965) B1006–B1010.
- [20] W. A. Bardeen, H. Fritzsch, and M. Gell-Mann, “Light cone current algebra, π^0 decay, and e^+e^- annihilation”, in: *Topical Meeting on the Outlook for Broken Conformal Symmetry in Elementary Particle Physics* (1972), arXiv: [hep-ph/0211388](https://arxiv.org/abs/hep-ph/0211388).
- [21] H. Fritzsch, M. Gell-Mann, and H. Leutwyler, “Advantages of the color octet gluon picture”, *Phys. Lett. B* **47** (1973) 365–368.
- [22] C. J. Horowitz, J. Piekarewicz, and B. Reed, “Insights into nuclear saturation density from parity-violating electron scattering”, *Phys. Rev. C* **102** (2020) 044321.
- [23] N. Ramberg and L. Visinelli, “Probing the Early Universe with Axion Physics and Gravitational Waves”, *Phys. Rev. D* **99** (2019) 123513, arXiv: [1904.05707](https://arxiv.org/abs/1904.05707) [[astro-ph.CO](https://arxiv.org/abs/1904.05707)].
- [24] A. Arbey and F. Mahmoudi, “Dark matter and the early Universe: a review”, *Prog. Part. Nucl. Phys.* **119** (2021) 103865, arXiv: [2104.11488](https://arxiv.org/abs/2104.11488) [[hep-ph](https://arxiv.org/abs/2104.11488)].
- [25] J. J. Aubert *et al.*, “Experimental Observation of a Heavy Particle J ”, *Phys. Rev. Lett.* **33** (1974) 1404–1406.
- [26] J.-E. Augustin *et al.*, “Discovery of a Narrow Resonance in e^+e^- Annihilation”, *Phys. Rev. Lett.* **33** (1974) 1406–1408.
- [27] S. W. Herb *et al.*, “Observation of a Dimuon Resonance at 9.5 GeV in 400-GeV Proton-Nucleus Collisions”, *Phys. Rev. Lett.* **39** (1977) 252–255.
- [28] CDF Collaboration *et al.*, “Observation of Top Quark Production in $\bar{p}p$ Collisions with the Collider Detector at Fermilab”, *Phys. Rev. Lett.* **74** (1995) 2626–2631.
- [29] D0 Collaboration *et al.*, “Observation of the Top Quark”, *Phys. Rev. Lett.* **74** (1995) 2632–2637.
- [30] R. Brandelik *et al.*, “Evidence for planar events in e^+e^- annihilation at high energies”, *Phys. Lett. B* **86** (1979) 243–249.
- [31] J. Ellis and I. Karliner, “Measuring the spin of the gluon in e^+e^- annihilation”, *Nucl. Phys. B* **148** (1979) 141–147.
- [32] T. Collaboration *et al.*, “Evidence for a spin-1 gluon in three-jet events”, *Phys. Lett. B* **97** (1980) 453–458.
- [33] P. Collaboration *et al.*, “A study of multi-jet events in e^+e^- annihilation”, *Phys. Lett. B* **97** (1980) 459–464.
- [34] O. Collaboration *et al.*, “Measurement of three-jet distributions sensitive to the gluon spin in e^+e^- annihilations at GeV”, *Z. Phys. C* **52** (1991) 543–550.
- [35] Y. Saito *et al.*, *Deep Inelastic Scattering*, 4 (Oxford University Press, Oxford, England, UK, 2004), ISBN: 978-0-19170956-2, DOI: [10.1603/0013-8746\(2004\)097\[0635:ROTGSB\]2.0.CO;2](https://doi.org/10.1603/0013-8746(2004)097[0635:ROTGSB]2.0.CO;2).
- [36] Particle Data Group *et al.*, “Review of Particle Physics”, *Prog. Theor. Exp. Phys.* **2022** (2022) 083C01, URL: <https://pdg.lbl.gov/2023/>.
- [37] *The CBM physics book: Compressed baryonic matter in laboratory experiments*, ed. by B. Friman *et al.* (2011), DOI: [10.1007/978-3-642-13293-3](https://doi.org/10.1007/978-3-642-13293-3).
- [38] N. Collaboration, “NA61/SHINE facility at the CERN SPS: beams and detector system”, *JINST* **9** (2014) P06005, arXiv: [1401.4699](https://arxiv.org/abs/1401.4699) [[physics.ins-det](https://arxiv.org/abs/1401.4699)].
- [39] T. Ablyazimov *et al.*, “Challenges in QCD matter physics –The scientific programme of the Compressed Baryonic Matter experiment at FAIR”, *Eur. Phys. J. A* **53** (2017) 60, arXiv: [1607.01487](https://arxiv.org/abs/1607.01487) [[nucl-ex](https://arxiv.org/abs/1607.01487)].
- [40] Meehan, Kathryn C. and STAR Collaboration, “Fixed Target Collisions at STAR”, *Nucl. Phys. A* **956** (2016) 878–881.

-
- [41] A. Aparin, “STAR Experiment Results From Beam Energy Scan Program”, *Phys. Atom. Nucl.* **86** (2023) 758–766.
- [42] Z. Sweger, “Recent Results and Future Prospects from the STAR Beam Energy Scan Program”, in: *57th Rencontres de Moriond on QCD and High Energy Interactions* (2023), arXiv: 2305.07139 [nucl-ex].
- [43] J. M. Lattimer and M. Prakash, “The Equation of State of Hot, Dense Matter and Neutron Stars”, *Phys. Rept.* **621** (2016) 127–164, arXiv: 1512.07820 [astro-ph.SR].
- [44] G. Baym *et al.*, “From hadrons to quarks in neutron stars: a review”, *Rept. Prog. Phys.* **81** (2018) 056902, arXiv: 1707.04966 [astro-ph.HE].
- [45] G. Raaijmakers *et al.*, “Constraints on the Dense Matter Equation of State and Neutron Star Properties from NICER’s Mass–Radius Estimate of PSR J0740+6620 and Multimessenger Observations”, *Astrophys. J. Lett.* **918** (2021) L29, arXiv: 2105.06981 [astro-ph.HE].
- [46] G. Raaijmakers *et al.*, “A NICER view of PSR J0030+0451: Implications for the dense matter equation of state”, *Astrophys. J. Lett.* **887** (2019) L22, arXiv: 1912.05703 [astro-ph.HE].
- [47] C.-N. Yang and R. L. Mills, “Conservation of Isotopic Spin and Isotopic Gauge Invariance”, *Phys. Rev.* **96** (1954) 191–195, ed. by J.-P. Hsu and D. Fine.
- [48] F.-K. Thielemann *et al.*, “Neutron Star Mergers and Nucleosynthesis of Heavy Elements”, *Ann. Rev. Nucl. Part. Sci.* **67** (2017) 253–274, arXiv: 1710.02142 [astro-ph.HE].
- [49] G. Aarts, “Introductory lectures on lattice QCD at nonzero baryon number”, *J. Phys. Conf. Ser.* **706** (2016) 022004, arXiv: 1512.05145 [hep-lat].
- [50] K. Fukushima and T. Hatsuda, “The phase diagram of dense QCD”, *Rept. Prog. Phys.* **74** (2011) 014001, arXiv: 1005.4814 [hep-ph].
- [51] A. Maire, *Production des baryons multi-étranges au LHC dans les collisions proton-proton avec l’expérience ALICE*, PhD thesis, Strasbourg University, 2011, URL: <https://cds.cern.ch/record/1490315>.
- [52] R. Sahoo and T. K. Nayak, “Possible early universe signals in proton collisions at the Large Hadron Collider”, *Curr. Sci.* **121** (2021) 1403, arXiv: 2201.00202 [hep-ph].
- [53] J. C. Collins and J. A. Vermaseren, “Axodraw version 2” (2016), arXiv: 1606.01177 [cs.OH].
- [54] J. C. Collins and J. A. Vermaseren, “CTAN: Package axodraw2 v2.1.1c” (2021), URL: <https://ctan.org/pkg/axodraw2>.
- [55] OpenAI, “DALL-E 2” (2023), URL: <https://chat.openai.com>, [Online; accessed 2023 through ChatGPT-4].
- [56] J. D. Hunter, “Matplotlib: A 2D graphics environment”, *Comput. Sci. Eng.* **9** (2007) 90–95.
- [57] Adobe Systems, “Adobe Photoshop CS6,” Computer software, *Adobe Creative Suite 6 Design Standard Student and Teacher* (2012), URL: <https://www.adobe.com/>.
- [58] E. V. Shuryak, “Quantum Chromodynamics and the Theory of Superdense Matter”, *Phys. Rept.* **61** (1980) 71–158.
- [59] M. Buballa, “NJL model analysis of quark matter at large density”, *Phys. Rept.* **407** (2005) 205–376, arXiv: hep-ph/0402234.
- [60] R. Alkofer and J. Greensite, “Quark Confinement: The Hard Problem of Hadron Physics”, *J. Phys. G* **34** (2007) S3, arXiv: hep-ph/0610365.
- [61] M. G. Alford *et al.*, “Color superconductivity in dense quark matter”, *Rev. Mod. Phys.* **80** (2008) 1455–1515, arXiv: 0709.4635 [hep-ph].
- [62] P. Braun-Munzinger and J. Wambach, “The Phase Diagram of Strongly-Interacting Matter”, *Rev. Mod. Phys.* **81** (2009) 1031–1050, arXiv: 0801.4256 [hep-ph].
- [63] M. Buballa and S. Carignano, “Inhomogeneous chiral condensates”, *Prog. Part. Nucl. Phys.* **81** (2015) 39–96, arXiv: 1406.1367 [hep-ph].

-
- [64] Y. Nambu and G. Jona-Lasinio, “Dynamical model of elementary particles based on an analogy with superconductivity. I”, *Phys. Rev.* **122** (1961) 345–358, ed. by T. Eguchi.
- [65] Y. Nambu and G. Jona-Lasinio, “Dynamical model of elementary particles based on an analogy with superconductivity. II”, *Phys. Rev.* **124** (1961) 246–254, ed. by T. Eguchi.
- [66] D. J. Gross and F. A. Wilczek, “Ultraviolet behavior of non-Abelian gauge theories”, *Phys. Rev. Lett.* **30** (1973) 1343–1346, ed. by J. C. Taylor.
- [67] H. D. Politzer, “Reliable perturbative results for strong interactions?”, *Phys. Rev. Lett.* **30** (1973) 1346–1349, ed. by J. C. Taylor.
- [68] S. Coleman and D. J. Gross, “Price of Asymptotic Freedom”, *Phys. Rev. Lett.* **31** (1973) 851–854.
- [69] Clay Mathematics Institute, “Yang-Mills & The Mass Gap” (2023), URL: <https://www.claymath.org/millennium/yang-mills-the-maths-gap/>, [Online; accessed 2023.11.17].
- [70] L. Adamczyk *et al.*, “Bulk Properties of the Medium Produced in Relativistic Heavy-Ion Collisions from the Beam Energy Scan Program”, *Phys. Rev. C* **96** (2017) 044904, arXiv: 1701.07065 [nucl-ex].
- [71] P. Alba *et al.*, “Freeze-out conditions from net-proton and net-charge fluctuations at RHIC”, *Phys. Lett. B* **738** (2014) 305–310, arXiv: 1403.4903 [hep-ph].
- [72] A. Andronic *et al.*, “Decoding the phase structure of QCD via particle production at high energy”, *Nature* **561** (2018) 321–330, arXiv: 1710.09425 [nucl-th].
- [73] F. Becattini *et al.*, “Hadronization conditions in relativistic nuclear collisions and the QCD pseudo-critical line”, *Phys. Lett. B* **764** (2017) 241–246, arXiv: 1605.09694 [nucl-th].
- [74] V. Vovchenko, V. V. Begun, and M. I. Gorenstein, “Hadron multiplicities and chemical freeze-out conditions in proton-proton and nucleus-nucleus collisions”, *Phys. Rev. C* **93** (2016) 064906, arXiv: 1512.08025 [nucl-th].
- [75] V. V. Sagun *et al.*, “Hadron Resonance Gas Model with Induced Surface Tension”, *Eur. Phys. J. A* **54** (2018) 100, arXiv: 1703.00049 [hep-ph].
- [76] K. G. Wilson, “Confinement of Quarks”, *Phys. Rev. D* **10** (1974) 2445–2459, ed. by J. C. Taylor.
- [77] R. Bellwied *et al.*, “The QCD phase diagram from analytic continuation”, *Phys. Lett. B* **751** (2015) 559–564, arXiv: 1507.07510 [hep-lat].
- [78] A. Bazavov *et al.*, “Chiral crossover in QCD at zero and non-zero chemical potentials”, *Phys. Lett. B* **795** (2019) 15–21, arXiv: 1812.08235 [hep-lat].
- [79] P. de Forcrand, “Simulating QCD at finite density”, *PoS LAT2009* (2009) 010, ed. by C. Liu and Y. Zhu, arXiv: 1005.0539 [hep-lat].
- [80] W.-j. Fu, J. M. Pawłowski, and F. Rennecke, “QCD phase structure at finite temperature and density”, *Phys. Rev. D* **101** (2020) 054032, arXiv: 1909.02991 [hep-ph].
- [81] B.-J. Schaefer and J. Wambach, “The phase diagram of the quark meson model”, *Nucl. Phys. A* **757** (2005) 479–492, arXiv: nucl-th/0403039.
- [82] M. Asakawa and K. Yazaki, “Chiral Restoration at Finite Density and Temperature”, *Nucl. Phys. A* **504** (1989) 668–684.
- [83] W. Broniowski, A. Kotlorz, and M. Kutschera, “Quarks with a pion condensate. A new phase of matter”, *Acta Phys. Polon. B* **22** (1991) 145–166, ed. by W. Czyz.
- [84] M. Sadzikowski and W. Broniowski, “Nonuniform chiral phase in effective chiral quark models”, *Phys. Lett. B* **488** (2000) 63–67, arXiv: hep-ph/0003282.
- [85] S. Carignano, M. Buballa, and B.-J. Schaefer, “Inhomogeneous phases in the quark-meson model with vacuum fluctuations”, *Phys. Rev. D* **90** (2014) 014033, arXiv: 1404.0057 [hep-ph].

-
- [86] P. Adhikari, J. O. Andersen, and P. Kneschke, “Inhomogeneous chiral condensate in the quark-meson model”, *Phys. Rev. D* **96** (2017) 016013, arXiv: [1702.01324 \[hep-ph\]](#), [Erratum: *Phys.Rev.D* 98, 099902 (2018)].
- [87] R.-A. Tripolt *et al.*, “Low-temperature behavior of the quark-meson model”, *Phys. Rev. D* **97** (2018) 034022, arXiv: [1709.05991 \[hep-ph\]](#).
- [88] W. Broniowski, “Chiral waves in quark matter”, *Acta Phys. Polon. Supp.* **5** (2012) 631, ed. by L. Turko, arXiv: [1110.4063 \[nucl-th\]](#).
- [89] S. Bornholdt *et al.*, “Flow of the coarse grained free energy for crossover phenomena”, *Int. J. Mod. Phys. A* **14** (1999) 899–918, arXiv: [cond-mat/9603129](#).
- [90] D.-U. Jungnickel and C. Wetterich, “Nonperturbative flow equations, low-energy QCD and the chiral phase transition”, in: *NATO Advanced Study Institute on Confinement, Duality and Nonperturbative Aspects of QCD* (1997), arXiv: [hep-ph/9710397](#).
- [91] B.-J. Schaefer and H.-J. Pirner, “Renormalization group flow and equation of state of quarks and mesons”, *Nucl. Phys. A* **660** (1999) 439–474, arXiv: [nucl-th/9903003](#).
- [92] G. Papp *et al.*, “On the convergence of the expansion of renormalization group flow equation”, *Phys. Rev. D* **61** (2000) 096002, arXiv: [hep-ph/9909246](#).
- [93] J. Berges, N. Tetradis, and C. Wetterich, “Nonperturbative renormalization flow in quantum field theory and statistical physics”, *Phys. Rept.* **363** (2002) 223–386, arXiv: [hep-ph/0005122](#).
- [94] L. Canet *et al.*, “Optimization of the derivative expansion in the nonperturbative Renormalization Group”, *Phys. Rev. D* **67** (2003) 065004, arXiv: [hep-th/0211055](#).
- [95] B. Delamotte, “An introduction to the nonperturbative Renormalization Group”, *Lect. Notes Phys.* **852** (2012) 49–132, arXiv: [cond-mat/0702365](#).
- [96] J. M. Pawłowski and F. Rennecke, “Higher order quark-mesonic scattering processes and the phase structure of QCD”, *Phys. Rev. D* **90** (2014) 076002, arXiv: [1403.1179 \[hep-ph\]](#).
- [97] J. Braun *et al.*, “From Quarks and Gluons to Hadrons: Chiral Symmetry Breaking in Dynamical QCD”, *Phys. Rev. D* **94** (2016) 034016, arXiv: [1412.1045 \[hep-ph\]](#).
- [98] W.-j. Fu and J. M. Pawłowski, “Relevance of matter and glue dynamics for baryon number fluctuations”, *Phys. Rev. D* **92** (2015) 116006, arXiv: [1508.06504 \[hep-ph\]](#).
- [99] F. Rennecke and B.-J. Schaefer, “Fluctuation-induced modifications of the phase structure in $(2 + 1)$ -flavor QCD”, *Phys. Rev. D* **96** (2017) 016009, arXiv: [1610.08748 \[hep-ph\]](#).
- [100] H. Zhang *et al.*, “Functional renormalization group study of the quark-meson model with ω meson”, *Phys. Rev. D* **96** (2017) 114029, arXiv: [1709.05654 \[hep-ph\]](#).
- [101] J. Riebesell, *Functional Renormalization Analytically Continued*, Master’s thesis, 2017, arXiv: [1712.09863 \[hep-th\]](#).
- [102] J. M. Pawłowski, N. Strodthoff, and N. Wink, “Finite temperature spectral functions in the $O(N)$ -model”, *Phys. Rev. D* **98** (2018) 074008, arXiv: [1711.07444 \[hep-th\]](#).
- [103] G. Almasi, R. Pisarski, and V. Skokov, “Volume dependence of baryon number cumulants and their ratios”, *Phys. Rev. D* **95** (2017) 056015, arXiv: [1612.04416 \[hep-ph\]](#).
- [104] F. Rennecke, *The chiral phase transition of QCD*, PhD thesis, University of Heidelberg, 2015, DOI: [10.11588/heidok.00019205](#).
- [105] J. Eser *et al.*, “Low-energy limit of the $O(4)$ quark-meson model from the functional renormalization group approach”, *Phys. Rev. D* **98** (2018) 014024, arXiv: [1804.01787 \[hep-ph\]](#).
- [106] J. Eser, F. Divotgey, and M. Mitter, “Low-energy limit of the $O(4)$ quark-meson model”, *PoS CD2018* (2019) 060, arXiv: [1902.04804 \[hep-ph\]](#).

-
- [107] F. Divotgey, J. Eser, and M. Mitter, “Dynamical generation of low-energy couplings from quark-meson fluctuations”, *Phys. Rev. D* **99** (2019) 054023, arXiv: 1901.02472 [hep-ph].
- [108] N. Cichutek, F. Divotgey, and J. Eser, “Fluctuation-induced higher-derivative couplings and infrared dynamics of the quark-meson-diquark model”, *Phys. Rev. D* **102** (2020) 034030, arXiv: 2006.12473 [hep-ph].
- [109] W.-j. Fu, “QCD at finite temperature and density within the fRG approach: an overview”, *Commun. Theor. Phys.* **74** (2022) 097304, arXiv: 2205.00468 [hep-ph].
- [110] J. A. Adams *et al.*, “Solving nonperturbative flow equations”, *Mod. Phys. Lett. A* **10** (1995) 2367–2380, arXiv: hep-th/9507093.
- [111] N. Tetradis, “The Electroweak phase transition through the renormalization group”, *Nucl. Phys. B* **488** (1997) 92–140, arXiv: hep-ph/9608272.
- [112] J. Berges and C. Wetterich, “Equation of state and coarse grained free energy for matrix models”, *Nucl. Phys. B* **487** (1997) 675–720, arXiv: hep-th/9609019.
- [113] J. Berges, N. Tetradis, and C. Wetterich, “Coarse graining and first order phase transitions”, *Phys. Lett. B* **393** (1997) 387–394, arXiv: hep-ph/9610354.
- [114] N. Tetradis, “Comparison of renormalization group and lattice studies of the electroweak phase transition”, *Phys. Lett. B* **409** (1997) 355–362, arXiv: hep-ph/9611461.
- [115] N. Tetradis, “Renormalization group study of weakly first order phase transitions”, *Phys. Lett. B* **431** (1998) 380–386, arXiv: hep-th/9706088.
- [116] N. Rius, “Symmetry nonrestoration at high temperature”, in: *International Workshop on Physics Beyond the Standard Model: From Theory to Experiment (Valencia 97)* (1997), DOI: 10.1142/9789814447263_0068, arXiv: hep-ph/9801313.
- [117] B. Bergerhoff, “Critical behavior of ϕ^4 theory from the thermal renormalization group”, *Phys. Lett. B* **437** (1998) 381–389, arXiv: hep-ph/9805493.
- [118] A. Strumia and N. Tetradis, “Bubble nucleation rates for radiatively induced first order phase transitions”, *Nucl. Phys. B* **554** (1999) 697–718, arXiv: hep-ph/9811438.
- [119] B. Bergerhoff and J. Reingruber, “Thermal renormalization group equations and the phase transition of scalar $O(N)$ theories”, *Phys. Rev. D* **60** (1999) 105036, arXiv: hep-ph/9809251.
- [120] K. Ogure and J. Sato, “Critical exponents and critical amplitude ratio of the scalar model from finite temperature field theory”, *Phys. Rev. D* **57** (1998) 7460–7466, arXiv: hep-ph/9801439.
- [121] A. S. Kapoyannis and N. Tetradis, “Quantum mechanical tunneling and the renormalization group”, *Phys. Lett. A* **276** (2000) 225–232, arXiv: hep-th/0010180.
- [122] B.-J. Schaefer, O. Bohr, and J. Wambach, “Renormalization group flow equations for the scalar $O(N)$ theory”, *Int. J. Mod. Phys. A* **16** (2001) 2119–2124, ed. by S. Arnone *et al.*, arXiv: hep-ph/0011371.
- [123] O. Bohr, B.-J. Schaefer, and J. Wambach, “Renormalization group flow equations and the phase transition in $O(N)$ -models”, *Int. J. Mod. Phys. A* **16** (2001) 3823–3852, arXiv: hep-ph/0007098.
- [124] B.-J. Schaefer, O. Bohr, and J. Wambach, “Finite temperature gluon condensate with renormalization group flow equations”, *Phys. Rev. D* **65** (2002) 105008, arXiv: hep-th/0112087.
- [125] B.-J. Schaefer and J. Wambach, “Susceptibilities near the QCD (tri)critical point”, *Phys. Rev. D* **75** (2007) 085015, arXiv: hep-ph/0603256.
- [126] E. Nakano *et al.*, “Fluctuations and isentropes near the chiral critical endpoint”, *Phys. Lett. B* **682** (2010) 401–407, arXiv: 0907.1344 [hep-ph].
- [127] K. Fukushima, K. Kamikado, and B. Klein, “Second-order and Fluctuation-induced First-order Phase Transitions with Functional Renormalization Group Equations”, *Phys. Rev. D* **83** (2011) 116005, arXiv: 1010.6226 [hep-ph].

-
- [128] M. Drews *et al.*, “Thermodynamic phases and mesonic fluctuations in a chiral nucleon-meson model”, *Phys. Rev. D* **88** (2013) 096011, arXiv: 1308.5596 [hep-ph].
- [129] R.-A. Tripolt *et al.*, “Spectral functions for the Quark-Meson Model phase diagram from the Functional Renormalization Group”, *Phys. Rev. D* **89** (2014) 034010, arXiv: 1311.0630 [hep-ph].
- [130] M. Drews *et al.*, “Dense nucleonic matter and the renormalization group”, *EPJ Web Conf.* **66** (2014) 04008, ed. by S. Lunardi *et al.*, arXiv: 1307.6973 [nucl-th].
- [131] R.-A. Tripolt *et al.*, “Finite-Temperature Spectral Functions from the Functional Renormalization Group”, *PoS LATTICE2013* (2014) 457, arXiv: 1311.4304 [hep-lat].
- [132] J. Wambach *et al.*, “Spectral Functions from the Functional Renormalization Group”, *Nucl. Phys. A* **928** (2014) 156–167, ed. by J. M. Lattimer, E. Shuryak, and A. Gal, arXiv: 1404.7312 [hep-ph].
- [133] R.-A. Tripolt *et al.*, “Spectral functions from the functional renormalization group”, *Nucl. Phys. A* **931** (2014) 790–795, ed. by P. Braun-Munzinger, B. Friman, and J. Stachel, arXiv: 1407.8387 [hep-ph].
- [134] M. Drews and W. Weise, “From asymmetric nuclear matter to neutron stars: a functional renormalization group study”, *Phys. Rev. C* **91** (2015) 035802, arXiv: 1412.7655 [nucl-th].
- [135] R.-A. Tripolt, *Spectral Functions and Transport Coefficients from the Functional Renormalization Group*, PhD thesis, Technische Universität Darmstadt, 2015, URL: <https://tuprints.ulb.tu-darmstadt.de/4578/>.
- [136] R.-A. Tripolt, L. von Smekal, and J. Wambach, “Spectral functions and in-medium properties of hadrons”, *Int. J. Mod. Phys. E* **26** (2017) 1740028, arXiv: 1605.00771 [hep-ph].
- [137] C. Jung *et al.*, “In-Medium Spectral Functions of Vector- and Axial-Vector Mesons from the Functional Renormalization Group”, *Phys. Rev. D* **95** (2017) 036020, arXiv: 1610.08754 [hep-ph].
- [138] M. Drews and W. Weise, “Functional renormalization group studies of nuclear and neutron matter”, *Prog. Part. Nucl. Phys.* **93** (2017) 69–107, arXiv: 1610.07568 [nucl-th].
- [139] J. Wambach *et al.*, “Spectral Functions from the Functional Renormalization Group”, *PoS CPOD2017* (2018) 077, arXiv: 1712.02093 [hep-ph].
- [140] D. Hou *et al.*, “Functional renormalization group study on the phase structure in the Quark-Meson model with ω meson”, *PoS CPOD2017* (2018) 060.
- [141] M. Reichert, *Towards a UV-complete Standard Model: From baryogenesis to asymptotic safety*, PhD thesis, Heidelberg University, 2018, DOI: 10.11588/heidok.00024469.
- [142] B. Qin *et al.*, “Nonperturbative renormalization group for the Landau–de Gennes model”, *Phys. Rev. B* **98** (2018) 014102, arXiv: 1803.03683 [cond-mat.stat-mech].
- [143] R.-A. Tripolt *et al.*, “In-medium spectral functions and dilepton rates with the Functional Renormalization Group”, *Nucl. Phys. A* **982** (2019) 775–778, ed. by F. Antinori *et al.*, arXiv: 1807.04952 [hep-ph].
- [144] R.-A. Tripolt *et al.*, “Vector and axial-vector mesons in nuclear matter”, *Phys. Rev. D* **104** (2021) 054005, arXiv: 2105.00861 [hep-ph].
- [145] N. Strodthoff, B.-J. Schaefer, and L. von Smekal, “Quark-meson-diquark model for two-color QCD”, *Phys. Rev. D* **85** (2012) 074007, arXiv: 1112.5401 [hep-ph].
- [146] T. K. Herbst *et al.*, “Exploring the Phase Structure and Thermodynamics of QCD”, *PoS QCD-TNT-III* (2013) 030, arXiv: 1401.1735 [hep-ph].
- [147] M. Mitter and B.-J. Schaefer, “Fluctuations and the axial anomaly with three quark flavors”, *Phys. Rev. D* **89** (2014) 054027, arXiv: 1308.3176 [hep-ph].
- [148] T. K. Herbst *et al.*, “Thermodynamics of QCD at vanishing density”, *Phys. Lett. B* **731** (2014) 248–256, arXiv: 1308.3621 [hep-ph].
- [149] S. Resch, F. Rennecke, and B.-J. Schaefer, “Mass sensitivity of the three-flavor chiral phase transition”, *Phys. Rev. D* **99** (2019) 076005, arXiv: 1712.07961 [hep-ph].

-
- [150] K. Otto, M. Oertel, and B.-J. Schaefer, “Hybrid and quark star matter based on a nonperturbative equation of state”, *Phys. Rev. D* **101** (2020) 103021, arXiv: 1910.11929 [hep-ph].
- [151] K. Otto, M. Oertel, and B.-J. Schaefer, “Nonperturbative quark matter equations of state with vector interactions”, *Eur. Phys. J. ST* **229** (2020) 3629–3649, arXiv: 2007.07394 [hep-ph].
- [152] K. Otto, C. Busch, and B.-J. Schaefer, “Regulator scheme dependence of the chiral phase transition at high densities”, *Phys. Rev. D* **106** (2022) 094018, arXiv: 2206.13067 [hep-ph].
- [153] C. S. Fischer and H. Gies, “Renormalization flow of Yang-Mills propagators”, *JHEP* **10** (2004) 048, arXiv: hep-ph/0408089.
- [154] J. Borchardt and B. Knorr, “Global solutions of functional fixed point equations via pseudospectral methods”, *Phys. Rev. D* **91** (2015) 105011, arXiv: 1502.07511 [hep-th], [Erratum: Phys.Rev.D 93, 089904 (2016)].
- [155] J. Borchardt and B. Knorr, “Solving functional flow equations with pseudo-spectral methods”, *Phys. Rev. D* **94** (2016) 025027, arXiv: 1603.06726 [hep-th].
- [156] G. G. Barnafoldi, A. Jakovac, and P. Posfay, “Harmonic expansion of the effective potential in a functional renormalization group at finite chemical potential”, *Phys. Rev. D* **95** (2017) 025004, arXiv: 1604.01717 [hep-th].
- [157] J. Borchardt, *From condensed matter to higgs physics : solving functional renormalization group equations globally in field space*, PhD thesis, Friedrich Schiller University Jena, 2017, URL: https://www.db-thueringen.de/receive/dbt_mods_00032014.
- [158] G. A. Almasi, B. Friman, and K. Redlich, “Baryon number fluctuations in chiral effective models and their phenomenological implications”, *Phys. Rev. D* **96** (2017) 014027, arXiv: 1703.05947 [hep-ph].
- [159] G. A. Almasi, *Properties of hot and dense strongly interacting matter*, PhD thesis, Technische Universität Darmstadt, 2017, URL: <https://tuprints.ulb.tu-darmstadt.de/6748/>.
- [160] Y.-r. Chen, R. Wen, and W.-j. Fu, “Critical behaviors of the $O(4)$ and $Z(2)$ symmetries in the QCD phase diagram”, *Phys. Rev. D* **104** (2021) 054009, arXiv: 2101.08484 [hep-ph].
- [161] M. Planck, “*Auch eine Enttäuschung, wenn sie nur gründlich und endgültig ist, bedeutet einen Schritt vorwärts, und die mit der Resignation verbundenen Opfer würden reichlich aufgewogen werden durch den Gewinn an Schätzen neuer Erkenntnis.*” (1910), URL: <https://beruhmte-zitate.de/zitate/124247-max-planck-auch-eine-enttaeuschung-wenn-sie-nur-gruendlich-und/>, [Online; accessed 2021.11.23].
- [162] E. Grossi *et al.*, “Shocks and quark-meson scatterings at large density”, *Phys. Rev. D* **104** (2021) 016028, arXiv: 2102.01602 [hep-ph].
- [163] J. Keitel and L. Bartosch, “The zero-dimensional $O(N)$ vector model as a benchmark for perturbation theory, the large- N expansion and the functional renormalization group”, *J. Phys. A* **A45** (2012) 105401, arXiv: 1109.3013 [cond-mat.stat-mech].
- [164] M. J. Steil and A. Koenigstein, “Solving ~~QFT~~ convection–diffusion equations with finite volume methods – Kurganov and Tadmor (KT) $O(x^2)$ central scheme - An appetizer”, Slides (Heidelberg: Mini-Workshop “QCD & beyond with the FRG”, 2019), URL: https://mjsteil.github.io/talks/20190717-KT-Heidelberg_handout.pdf, [Online; accessed 2023.11.17].
- [165] A. Koenigstein, *Non-perturbative aspects of (low-dimensional) quantum field theories*, PhD thesis, Universitätsbibliothek Johann Christian Senckenberg, 2023, p. 441, DOI: 10.21248/gups.74658.
- [166] Wolfram Research, Inc., “Mathematica, Version 13.0” (Champaign, IL, 2023), URL: <https://www.wolfram.com/mathematica>.
- [167] A. Kurganov and E. Tadmor, “New High-Resolution Central Schemes for Nonlinear Conservation Laws and Convection–Diffusion Equations”, *J. Comput. Phys.* **160** (2000) 241–282.
- [168] A. Kurganov, S. Noelle, and G. Petrova, “Semidiscrete Central-Upwind Schemes for Hyperbolic Conservation Laws and Hamilton–Jacobi Equations”, *SIAM J. Sci. Comput.* **23** (2001) 707–740.

-
- [169] D. J. Gross and A. Neveu, “Dynamical Symmetry Breaking in Asymptotically Free Field Theories”, *Phys. Rev. D* **10** (1974) 3235.
- [170] W. Wetzel, “Two Loop Beta Function for the Gross-Neveu Model”, *Phys. Lett. B* **153** (1985) 297–299.
- [171] B. Rosenstein, B. J. Warr, and S. H. Park, “Dynamical symmetry breaking in four Fermi interaction models”, *Phys. Rept.* **205** (1991) 59–108.
- [172] J. A. Gracey, “Three loop calculations in the $O(N)$ Gross-Neveu model”, *Nucl. Phys. B* **341** (1990) 403–418.
- [173] J. A. Gracey, “Calculation of exponent η to $O(1/N^{**2})$ in the $O(N)$ Gross-Neveu model”, *Int. J. Mod. Phys. A* **6** (1991) 395–408, [Erratum: *Int.J.Mod.Phys.A* **6**, 2755 (1991)].
- [174] J. A. Gracey, “Computation of the three loop Beta function of the $O(N)$ Gross-Neveu model in minimal subtraction”, *Nucl. Phys. B* **367** (1991) 657–674.
- [175] C. Luperini and P. Rossi, “Three-loop β function(s) and effective potential in the Gross-Neveu model”, *Annals Phys.* **212** (1991) 371–401.
- [176] J. Zinn-Justin, “Four fermion interaction near four-dimensions”, *Nucl. Phys. B* **367** (1991) 105–122.
- [177] M. E. Peskin and D. V. Schroeder, *An introduction to quantum field theory* (Addison-Wesley, Reading, USA, 1995), ISBN: 978-0-201-50397-5.
- [178] J. Zinn-Justin, *Quantum field theory and critical phenomena*, 4th ed., Int. Ser. Monogr. Phys. (Oxford University Press, 2002), A Clarendon Press Publication, pp. 1–1054, ISBN: 9780198509233, DOI: [10.1093/acprof:oso/9780198509233.001.0001](https://doi.org/10.1093/acprof:oso/9780198509233.001.0001).
- [179] A. G. Quinto, R. Vega Monroy, and A. F. Ferrari, “Renormalization group improvement of the effective potential in a $(1 + 1)$ dimensional Gross-Neveu model”, *Nucl. Phys. B* **984** (2022) 115959, arXiv: [2108.04079](https://arxiv.org/abs/2108.04079) [hep-th].
- [180] M. Thies and K. Urlichs, “Revised phase diagram of the Gross-Neveu model”, *Phys. Rev. D* **67** (2003) 125015, arXiv: [hep-th/0302092](https://arxiv.org/abs/hep-th/0302092).
- [181] O. Schnetz, M. Thies, and K. Urlichs, “Phase diagram of the Gross-Neveu model: Exact results and condensed matter precursors”, *Annals Phys.* **314** (2004) 425–447, arXiv: [hep-th/0402014](https://arxiv.org/abs/hep-th/0402014).
- [182] P. de Forcrand and U. Wenger, “New baryon matter in the lattice Gross-Neveu model”, *PoS LAT2006* (2006) 152, ed. by T. Blum *et al.*, arXiv: [hep-lat/0610117](https://arxiv.org/abs/hep-lat/0610117).
- [183] F. Karbstein and M. Thies, “How to get from imaginary to real chemical potential”, *Phys. Rev. D* **75** (2007) 025003, arXiv: [hep-th/0610243](https://arxiv.org/abs/hep-th/0610243).
- [184] L. A. Dolan and R. W. Jackiw, “Symmetry behavior at finite temperature”, *Phys. Rev. D* **9** (1974) 3320–3341.
- [185] B. J. Harrington and A. Yildiz, “Chiral Symmetry Behavior at Large Densities”, *Phys. Rev. D* **11** (1975) 1705.
- [186] B. J. Harrington and A. Yildiz, “Restoration of Dynamically Broken Symmetries at Finite Temperature”, *Phys. Rev. D* **11** (1975) 779.
- [187] L. Jacobs, “Critical behavior in a class of $O(N)$ -invariant field theories in two dimensions”, *Phys. Rev. D* **10** (1974) 3956.
- [188] R. F. Dashen, S.-k. Ma, and R. Rajaraman, “Finite temperature behavior of a relativistic field theory with dynamical symmetry breaking”, *Phys. Rev. D* **11** (1975) 1499.
- [189] R. F. Dashen, B. Hasslacher, and A. Neveu, “Semiclassical Bound States in an Asymptotically Free Theory”, *Phys. Rev. D* **12** (1975) 2443.
- [190] U. Wolff, “The phase diagram of the infinite- N Gross-Neveu model at finite temperature and chemical potential”, *Phys. Lett. B* **157** (1985) 303–308.
- [191] T. F. Treml, “Dynamical mass generation in the Gross-Neveu model at finite temperature and density”, *Phys. Rev. D* **39** (1989) 679–682.

-
- [192] R. Pausch, M. Thies, and V. L. Dolman, “Solving the Gross-Neveu model with relativistic many body methods”, *Z. Phys. A* **338** (1991) 441–453.
- [193] E. Nakano and T. Tatsumi, “Chiral symmetry and density wave in quark matter”, *Phys. Rev. D* **71** (2005) 114006, arXiv: [hep-ph/0411350](#).
- [194] M. Wagner, “Fermions in the pseudoparticle approach”, *Phys. Rev. D* **76** (2007) 076002, arXiv: [0704.3023 \[hep-lat\]](#).
- [195] C. Boehmer, M. Thies, and K. Urlichs, “Tricritical behavior of the massive chiral Gross-Neveu model”, *Phys. Rev. D* **75** (2007) 105017, arXiv: [hep-th/0702201](#).
- [196] C. Boehmer *et al.*, “Phase structure of the massive chiral Gross-Neveu model from Hartree-Fock”, *Phys. Rev. D* **78** (2008) 065043, arXiv: [0807.2571 \[hep-th\]](#).
- [197] G. Basar, G. V. Dunne, and M. Thies, “Inhomogeneous condensates in the thermodynamics of the chiral NJL₂ model”, *Phys. Rev. D* **79** (2009) 105012, arXiv: [0903.1868 \[hep-th\]](#).
- [198] M. Buballa and S. Carignano, “Inhomogeneous chiral phases away from the chiral limit”, *Phys. Lett. B* **791** (2019) 361–366, arXiv: [1809.10066 \[hep-ph\]](#).
- [199] S. Carignano and M. Buballa, “Inhomogeneous chiral condensates in three-flavor quark matter”, *Phys. Rev. D* **101** (2020) 014026, arXiv: [1910.03604 \[hep-ph\]](#).
- [200] M. Winstel, J. Stoll, and M. Wagner, “Lattice investigation of an inhomogeneous phase of the 2 + 1-dimensional Gross-Neveu model in the limit of infinitely many flavors”, *J. Phys. Conf. Ser.* **1667** (2020) 012044, ed. by M. Destefanis *et al.*, arXiv: [1909.00064 \[hep-lat\]](#).
- [201] M. Thies, “Phase structure of the (1 + 1)-dimensional Nambu-Jona-Lasinio model with isospin”, *Phys. Rev. D* **101** (2020) 014010, arXiv: [1911.11439 \[hep-th\]](#).
- [202] M. Buballa *et al.*, “Regulator dependence of inhomogeneous phases in the (2 + 1)-dimensional Gross-Neveu model”, *Phys. Rev. D* **103** (2021) 034503, arXiv: [2012.09588 \[hep-lat\]](#).
- [203] M. Buballa, S. Carignano, and L. Kurth, “Inhomogeneous phases in the quark-meson model with explicit chiral-symmetry breaking”, *Eur. Phys. J. ST* **229** (2020) 3371–3385, arXiv: [2006.02133 \[hep-ph\]](#).
- [204] M. Winstel, L. Pannullo, and M. Wagner, “Phase diagram of the 2+1-dimensional Gross-Neveu model with chiral imbalance”, *PoS LATTICE2021* (2022) 381, arXiv: [2109.04277 \[hep-lat\]](#).
- [205] L. Pannullo, M. Wagner, and M. Winstel, “Inhomogeneous Phases in the Chirally Imbalanced 2 + 1-Dimensional Gross-Neveu Model and Their Absence in the Continuum Limit”, *Symmetry* **14** (2022) 265, arXiv: [2112.11183 \[hep-lat\]](#).
- [206] L. Pannullo, M. Wagner, and M. Winstel, “Inhomogeneous phases in the 3+1-dimensional Nambu-Jona-Lasinio model and their dependence on the regularization scheme”, *PoS LATTICE2022* (2023) 156, arXiv: [2212.05783 \[hep-lat\]](#).
- [207] T. F. Motta, M. Buballa, and C. S. Fischer, “Towards a Stability Analysis of Inhomogeneous Phases in the QCD Phase Diagram”, *Acta Phys. Polon. Supp.* **16** (2023) 8–A12.
- [208] T. F. Motta *et al.*, “Towards a Stability Analysis of Inhomogeneous Phases in QCD” (2023), arXiv: [2306.09749 \[hep-ph\]](#).
- [209] W.-j. Fu *et al.*, “Four-quark scatterings in QCD I”, *SciPost Phys.* **14** (2023) 069, arXiv: [2209.13120 \[hep-ph\]](#).
- [210] F. Ihssen *et al.*, “Towards quantitative precision for QCD at large densities” (2023), arXiv: [2309.07335 \[hep-th\]](#).
- [211] C. Wetterich, “The average action for scalar fields near phase transitions”, *Z. Phys. C* **57** (1993) 451–470.
- [212] C. Wetterich, “Exact evolution equation for the effective potential”, *Phys. Lett. B* **301** (1993) 90–94, arXiv: [1710.05815 \[hep-th\]](#).

-
- [213] M. Reuter and C. Wetterich, “Effective average action for gauge theories and exact evolution equations”, *Nucl. Phys. B* **417** (1994) 181–214.
- [214] T. R. Morris, “The Exact Renormalization Group and approximate solutions”, *Int. J. Mod. Phys. A* **09** (1994) 2411–2450, arXiv: [hep-ph/9308265](#).
- [215] N. Tetradis and C. Wetterich, “Critical exponents from effective average action”, *Nucl. Phys. B* **422** (1994) 541–592, arXiv: [hep-ph/9308214](#).
- [216] U. Ellwanger, “Flow equations for N point functions and bound states”, *Z. Phys. C* **62** (1994) 503–510, arXiv: [hep-ph/9308260](#).
- [217] F. J. Dyson, “The S matrix in quantum electrodynamics”, *Phys. Rev.* **75** (1949) 1736–1755.
- [218] J. S. Schwinger, “On the Green’s functions of quantized fields. 1.”, *Proc. Nat. Acad. Sci.* **37** (1951) 452–455.
- [219] J. S. Schwinger, “On the Green’s functions of quantized fields. 2.”, *Proc. Nat. Acad. Sci.* **37** (1951) 455–459.
- [220] J. Berges, “N-particle irreducible effective action techniques for gauge theories”, *Phys. Rev. D* **70** (2004) 105010, arXiv: [hep-ph/0401172](#).
- [221] J. Berges *et al.*, “Nonperturbative renormalization for 2PI effective action techniques”, *Annals Phys.* **320** (2005) 344–398, arXiv: [hep-ph/0503240](#).
- [222] J. M. Pawłowski, “Aspects of the functional renormalisation group”, *Annals Phys.* **322** (2007) 2831–2915, arXiv: [hep-th/0512261](#).
- [223] M. E. Carrington and Y. Guo, “Techniques for n-Particle Irreducible Effective Theories”, *Phys. Rev. D* **83** (2011) 016006, arXiv: [1010.2978 \[hep-ph\]](#).
- [224] J.-P. Blaizot, J. M. Pawłowski, and U. Reinosa, “Functional renormalization group and 2PI effective action formalism”, *Annals Phys.* **431** (2021) 168549, arXiv: [2102.13628 \[hep-th\]](#).
- [225] J. Berges, “Introduction to nonequilibrium quantum field theory”, *AIP Conf. Proc.* **739** (2004) 3–62, ed. by M. Bracco *et al.*, arXiv: [hep-ph/0409233](#).
- [226] J. M. Pawłowski *et al.*, “The functional renormalization group - applications to gauge theories and gravity”, 2019, URL: <https://www.thphys.uni-heidelberg.de/~pawlawski/NPgauge18-19.php>, Lecture Notes, in preparation.
- [227] H. Gies, “Introduction to the Functional RG and applications to gauge theories”, *Lect. Notes Phys.* **852** (2012) 287–348, arXiv: [hep-ph/0611146](#).
- [228] P. Kopietz, L. Bartosch, and F. Schütz, *Introduction to the Functional Renormalization Group*, Lecture Notes in Physics (Springer-Verlag Berlin Heidelberg, 2010), ISBN: 978-3-642-05093-0, DOI: [10.1007/978-3-642-05094-7](#).
- [229] C. Wetterich, “Effective average action in statistical physics and quantum field theory”, *Int. J. Mod. Phys. A* **16** (2001) 1951–1982, ed. by Z. Horvath and L. Palla, arXiv: [hep-ph/0101178](#).
- [230] O. J. Rosten, “Fundamentals of the Exact Renormalization Group”, *Phys. Rept.* **511** (2012) 177–272, arXiv: [1003.1366 \[hep-th\]](#).
- [231] N. Dupuis *et al.*, “The nonperturbative functional renormalization group and its applications”, *Phys. Rept.* **910** (2021) 1–114, arXiv: [2006.04853 \[cond-mat.stat-mech\]](#).
- [232] C. S. Fischer, “QCD at finite temperature and chemical potential from Dyson–Schwinger equations”, *Prog. Part. Nucl. Phys.* **105** (2019) 1–60, arXiv: [1810.12938 \[hep-ph\]](#).
- [233] K. G. Wilson, “Renormalization group and critical phenomena. 1. Renormalization group and the Kadanoff scaling picture”, *Phys. Rev. B* **4** (1971) 3174–3183.
- [234] K. G. Wilson, “Renormalization group and critical phenomena. 2. Phase space cell analysis of critical behavior”, *Phys. Rev. B* **4** (1971) 3184–3205.

-
- [235] K. G. Wilson, “Problems in physics with many scales of length”, *Sci. Am.* **241** (1979) 158–179.
- [236] L. P. Kadanoff, “Scaling laws for Ising models near T_c ”, *Phys. Phys. Fiz.* **2** (1966) 263–272.
- [237] R. Alkofer *et al.*, “Bound state properties from the functional renormalization group”, *Phys. Rev. D* **99** (2019) 054029, arXiv: 1810.07955 [hep-ph].
- [238] D. F. Litim and J. M. Pawłowski, “Completeness and consistency of renormalisation group flows”, *Phys. Rev. D* **66** (2002) 025030, arXiv: hep-th/0202188.
- [239] J. Iliopoulos, C. Itzykson, and A. Martin, “Functional methods and perturbation theory”, *Rev. Mod. Phys.* **47** (1975) 165.
- [240] S. Weinberg, *The quantum theory of fields: Modern applications* (Cambridge University Press, Cambridge, England, UK, 1996), DOI: 10.1017/CB09781139644174.
- [241] J. Polchinski, “Renormalization and Effective Lagrangians”, *Nucl. Phys. B* **231** (1984) 269–295.
- [242] D. F. Litim, “Universality and the renormalisation group”, *JHEP* **07** (2005) 005, arXiv: hep-th/0503096.
- [243] S. Yabunaka and B. Delamotte, “Why Might the Standard Large N Analysis Fail in the $O(N)$ Model: The Role of Cusps in the Fixed Point Potentials”, *Phys. Rev. Lett.* **121** (2018) 231601, arXiv: 1807.04681 [cond-mat.stat-mech].
- [244] D. F. Litim and M. J. Trott, “Asymptotic safety of scalar field theories”, *Phys. Rev. D* **98** (2018) 125006, arXiv: 1810.01678 [hep-th].
- [245] J. Cotler and S. Rezhikov, “Renormalization Group Flow as Optimal Transport” (2022), arXiv: 2202.11737 [hep-th].
- [246] D. F. Litim, J. M. Pawłowski, and L. Vergara, “Convexity of the effective action from functional flows” (2006), arXiv: hep-th/0602140.
- [247] E. Grossi and N. Wink, “Resolving phase transitions with Discontinuous Galerkin methods” (2019), arXiv: 1903.09503 [hep-th].
- [248] F. Ihssen and J. M. Pawłowski, “Flowing fields and optimal RG-flows” (2023), arXiv: 2305.00816 [hep-th].
- [249] A. K. Cyrol *et al.*, “Nonperturbative quark, gluon, and meson correlators of unquenched QCD”, *Phys. Rev. D* **97** (2018) 054006, arXiv: 1706.06326 [hep-ph].
- [250] F. J. Wegner and A. Houghton, “Renormalization Group equation for critical phenomena”, *Phys. Rev. A* **8** (1973) 401–412.
- [251] K. Symanzik, “Small-distance behaviour in field theory”, in: *Proceedings, KfK Summer School 81 on Quarks and Nuclear Forces: Bad Liebenzell, Germany, September 27-October 3, 1981*, ed. by D. Fries and B. Zeitnitz, vol. 57 (1971), pp. 222–236, DOI: 10.1007/BFb0041355.
- [252] K. Symanzik, “Small-distance-behaviour analysis and Wilson expansions”, *Commun. Math. Phys.* **23** (1971) 49–86.
- [253] J. Alexandre and J. Polonyi, “Functional Callan-Symanzik equation”, *Annals Phys.* **288** (2001) 37–51, arXiv: hep-th/0010128.
- [254] C. G. Callan, “Broken Scale Invariance in Scalar Field Theory”, *Phys. Rev. D* **2** (1970) 1541–1547, URL: <https://link.aps.org/doi/10.1103/PhysRevD.2.1541>.
- [255] K. Symanzik, “Small distance behavior in field theory and power counting”, *Commun. Math. Phys.* **18** (1970) 227–246.
- [256] J. M. Pawłowski *et al.*, “Physics and the choice of regulators in functional renormalisation group flows”, *Annals Phys.* **384** (2017) 165–197, arXiv: 1512.03598 [hep-th].
- [257] J. Braun, M. Leonhardt, and J. M. Pawłowski, “Renormalization group consistency and low-energy effective theories”, *SciPost Phys.* **6** (2019) 056, arXiv: 1806.04432 [hep-ph].

-
- [258] J. Braun *et al.*, “Renormalised spectral flows”, *SciPost Phys. Core* **6** (2023) 061, arXiv: [2206.10232 \[hep-th\]](#).
- [259] D. F. Litim, “Optimization of the exact renormalization group”, *Phys. Lett. B* **486** (2000) 92–99, arXiv: [hep-th/0005245](#).
- [260] D. F. Litim, “Optimized renormalization group flows”, *Phys. Rev. D* **64** (2001) 105007, arXiv: [hep-th/0103195](#).
- [261] H. Osborn and D. E. Twigg, “Remarks on Exact RG equations”, *Annals Phys.* **327** (2012) 29–73, arXiv: [1108.5340 \[hep-th\]](#).
- [262] J. Braun, M. Leonhardt, and M. Pospiech, “Fierz-complete NJL model study: Fixed points and phase structure at finite temperature and density”, *Phys. Rev. D* **96** (2017) 076003, arXiv: [1705.00074 \[hep-ph\]](#).
- [263] J. Braun *et al.*, “Renormalization group studies of dense relativistic systems”, *Phys. Rev. D* **104** (2021) 096002, arXiv: [2008.05978 \[hep-ph\]](#).
- [264] G. De Polsi and N. Wschebor, “Regulator dependence in the functional renormalization group: A quantitative explanation”, *Phys. Rev. E* **106** (2022) 024111, arXiv: [2204.09170 \[cond-mat.stat-mech\]](#).
- [265] N. Zorbach, J. Stoll, and J. Braun, “Optimization and Stabilization of Functional Renormalization Group Flows” (2024), arXiv: [2401.12854 \[hep-ph\]](#).
- [266] J.-P. Blaizot, R. Mendez Galain, and N. Wschebor, “A New method to solve the non perturbative renormalization group equations”, *Phys. Lett. B* **632** (2006) 571–578, arXiv: [hep-th/0503103](#).
- [267] J.-P. Blaizot, R. Mendez Galain, and N. Wschebor, “Non perturbative renormalization group, momentum dependence of n-point functions and the transition temperature of the weakly interacting Bose gas”, *EPL* **72** (2005) 705–711, arXiv: [cond-mat/0412481](#).
- [268] J.-P. Blaizot, R. Mendez-Galain, and N. Wschebor, “Non perturbative renormalization group and momentum dependence of n-point functions. II.”, *Phys. Rev. E* **74** (2006) 051117, arXiv: [hep-th/0603163](#).
- [269] J.-P. Blaizot, R. Mendez-Galain, and N. Wschebor, “Non-perturbative renormalization group calculation of the scalar self-energy”, *Eur. Phys. J. B* **58** (2007) 297–309, arXiv: [hep-th/0605252](#).
- [270] S. Ledowski, N. Hasselmann, and P. Kopietz, “Self-energy and critical temperature of weakly interacting bosons”, *Phys. Rev. A* **69** (2004) 061601, arXiv: [cond-mat/0311043](#).
- [271] A. Sinner, N. Hasselmann, and P. Kopietz, “Functional renormalization group in the broken symmetry phase: Momentum dependence and two-parameter scaling of the self-energy”, *J. Phys. Condens. Matter* **20** (2008) 075208, arXiv: [0707.4110 \[cond-mat.stat-mech\]](#).
- [272] F. Benitez *et al.*, “Solutions of renormalization group flow equations with full momentum dependence”, *Phys. Rev. E* **80** (2009) 030103, arXiv: [0901.0128 \[cond-mat.stat-mech\]](#).
- [273] I. Boettcher, J. M. Pawłowski, and S. Diehl, “Ultracold atoms and the Functional Renormalization Group”, *Nucl. Phys. B Proc. Suppl.* **228** (2012) 63–135, ed. by B.-J. Schaefer, R. Alkofer, and C. S. Fischer, arXiv: [1204.4394 \[cond-mat.quant-gas\]](#).
- [274] W. Metzner *et al.*, “Functional renormalization group approach to correlated fermion systems”, *Rev. Mod. Phys.* **84** (2012) 299–352, arXiv: [1105.5289 \[cond-mat.str-el\]](#).
- [275] C. Wetterich, “Integrating out gluons in flow equations”, *Z. Phys. C* **72** (1996) 139–162, arXiv: [hep-ph/9604227](#).
- [276] H. Gies, “Running coupling in Yang-Mills theory: A flow equation study”, *Phys. Rev. D* **66** (2002) 025006, arXiv: [hep-th/0202207](#).
- [277] M. Reuter, “Nonperturbative evolution equation for quantum gravity”, *Phys. Rev. D* **57** (1998) 971–985, arXiv: [hep-th/9605030](#).
- [278] N. Christiansen *et al.*, “Local Quantum Gravity”, *Phys. Rev. D* **92** (2015) 121501, arXiv: [1506.07016 \[hep-th\]](#).

-
- [279] J. Meibohm, J. M. Pawłowski, and M. Reichert, “Asymptotic safety of gravity-matter systems”, *Phys. Rev. D* **93** (2016) 084035, arXiv: 1510.07018 [hep-th].
- [280] A. Eichhorn *et al.*, “Effective universality in quantum gravity”, *SciPost Phys.* **5** (2018) 031, arXiv: 1804.00012 [hep-th].
- [281] M. Reuter, N. Tetradis, and C. Wetterich, “The Large N limit and the high temperature phase transition for the ϕ^4 theory”, *Nucl. Phys. B* **401** (1993) 567–590, arXiv: hep-ph/9301271.
- [282] T. R. Morris, “On truncations of the exact renormalization group”, *Phys. Lett. B* **334** (1994) 355–362, arXiv: hep-th/9405190.
- [283] F. J. Ihssen, *Low-energy effective models of QCD at finite temperatures and densities*, Master’s thesis, University of Heidelberg, 2020, DOI: 10.11588/heidok.00033504.
- [284] F. Ihssen *et al.*, “Local Discontinuous Galerkin for the Functional Renormalisation Group” (2022), arXiv: 2207.12266 [hep-th].
- [285] J. P. Boyd, *Chebyshev and Fourier spectral methods*, 2nd ed. (Dover Publications, Mineola, New York, 2001), 1st ed. in 1969 by Springer-Verlag, Berlin Heidelberg, in the series *Lecture Notes in Engineering*, Vol. 49, ISBN: 978-0486411835.
- [286] H. Wilbraham, “On a certain periodic function”, *Cambridge and Dublin Mathematical Journal* **3** (1848) 198–201.
- [287] J. W. Gibbs, “Fourier’s series”, *Nature* **59** (1898) 200.
- [288] J. W. Gibbs, “Fourier’s series”, *Nature* **59** (1899) 606.
- [289] T. Papenbrock and C. Wetterich, “Two-loop results from improved one loop computations”, *Z. Phys. C* **65** (1995) 519–535, arXiv: hep-th/9403164.
- [290] J. Braun, “Introduction to the Functional Renormalization Group Approach”, Slides for a lecture given at the 2021 CRC-TR 211 retreat 2021 (2021), URL: https://crc-tr211.org/internal/files/retreat2021/2021-03-31_lqcd_braun.pdf, [Online; accessed 2023.10.18].
- [291] U. Ellwanger, “The Running gauge coupling in the exact renormalization group approach”, *Z. Phys. C* **76** (1997) 721–727, arXiv: hep-ph/9702309.
- [292] P. Kopietz, “Two loop beta function from the exact renormalization group”, *Nucl. Phys. B* **595** (2001) 493–518, arXiv: hep-th/0007128.
- [293] A. Codello *et al.*, “Computing the Effective Action with the Functional Renormalization Group”, *Eur. Phys. J. C* **76** (2016) 226, arXiv: 1505.03119 [hep-th].
- [294] A. Codello *et al.*, “Functional perturbative RG and CFT data in the ϵ -expansion”, *Eur. Phys. J. C* **78** (2018) 30, arXiv: 1705.05558 [hep-th].
- [295] M. Q. Huber, A. K. Cyrol, and J. M. Pawłowski, “DoFun 3.0: Functional equations in Mathematica”, *Comput. Phys. Commun.* **248** (2020) 107058, arXiv: 1908.02760 [hep-ph].
- [296] M. Q. Huber and A. K. Cyrol, “DoFun v3.0.1”, *GitHub repository* (GitHub, 2023), URL: <https://github.com/markusqh/DoFun>.
- [297] J. M. Pawłowski, C. S. Schneider, and N. Wink, “QMeS-Derivation: Mathematica package for the symbolic derivation of functional equations”, *Comput. Phys. Commun.* **287** (2023) 108711, arXiv: 2102.01410 [hep-ph].
- [298] C. S. Schneider and N. Wink, “QMeS-Derivation v1.2”, *GitHub repository* (GitHub, 2023), URL: <https://github.com/QMeS-toolbox/QMeS-Derivation>.
- [299] M. J. Steil, “Field space and FRG flow equations”, fs_20231206.nb, Mathematica notebook (2023), digital auxiliary file.
- [300] J. H. Conway, “Sequence A000670: Fubini numbers”, *The On-Line Encyclopedia of Integer Sequences* (2021), URL: <https://oeis.org/A000670>, [Online; accessed 2021.03.16].

-
- [301] N. J. A. Sloane and M. Goebel, “Sequence A019538: Triangle of numbers”, The On-Line Encyclopedia of Integer Sequences (2021), URL: <https://oeis.org/A019538>, [Online; accessed 2021.03.16].
- [302] F. W. J. Olver *et al.*, “NIST Digital Library of Mathematical Function”, Release 1.1.2 of 2021-06-15 (2021), URL: <http://dlmf.nist.gov/>, [Online; accessed 2020.06.24].
- [303] J. P. Barthelemy, “An asymptotic equivalent for the number of total preorders on a finite set”, *Discrete Math.* **29** (1980) 311–313.
- [304] R. Simion, “Convex Polytopes and Enumeration”, *Adv. Appl. Math.* **18** (1997) 149–180.
- [305] G. M. Ziegler, *Lectures on Polytopes* (Springer-Verlag, New York, NY, USA, 1995), ISBN: 978-0-387-94329-9, DOI: [10.1007/978-1-4613-8431-1](https://doi.org/10.1007/978-1-4613-8431-1).
- [306] J. Braun, K. Schwenzer, and H.-J. Pirner, “Linking the quark meson model with QCD at high temperature”, *Phys. Rev. D* **70** (2004) 085016, arXiv: [hep-ph/0312277](https://arxiv.org/abs/hep-ph/0312277).
- [307] P. Springer *et al.*, “QCD-inspired determination of NJL model parameters”, *EPJ Web Conf.* **137** (2017) 03022, ed. by Y. Foka, N. Brambilla, and V. Kovalenko, arXiv: [1611.06020](https://arxiv.org/abs/1611.06020) [hep-ph].
- [308] M. Leonhardt, *Phase Structure and Equation of State of Dense Strong-Interaction Matter*, PhD thesis, Technische Universität Darmstadt, 2019, URL: <http://tuprints.ulb.tu-darmstadt.de/9255/>.
- [309] L. M. Haas *et al.*, “Improved Polyakov-loop potential for effective models from functional calculations”, *Phys. Rev. D* **87** (2013) 076004, arXiv: [1302.1993](https://arxiv.org/abs/1302.1993) [hep-ph].
- [310] D. C. Brydges and T. Kennedy, “Mayer expansions and the Hamilton-Jacobi equation”, *J. Stat. Phys.* **48** (1987) 19–49.
- [311] G. Zumbach, “The Local Potential Approximation of the Renormalization Group and its applications”, *Phys. Lett. A* **190** (1994) 225–230.
- [312] D. Skinner, “Lecture notes: Quantum Field Theory II” (Cambridge, United Kingdom: Department of Applied Mathematics and Theoretical Physics, Centre for Mathematical Sciences, 2018), URL: <http://www.damtp.cam.ac.uk/user/dbs26/AQFT.html>, [Online; accessed 2021.01.12].
- [313] M. Salmhofer, “Rigorous Renormalization Group”, Talk at the 10th International Conference on Exact Renormalization Group 2020 (ERG2020) (Kyoto, Japan (online conference): Yukawa Institute for Theoretical Physics, Kyoto University, 2020), URL: https://www2.yukawa.kyoto-u.ac.jp/~erg2020/ERG2020_slides/Salmhofer.pdf, [Online; accessed 2021.01.12].
- [314] J. R. Cannon, *The one-dimensional heat equation* (Cambridge University Press, 1984), ISBN: 9781139086967, DOI: [10.1017/CB09781139086967](https://doi.org/10.1017/CB09781139086967).
- [315] R. J. LeVeque, *Numerical methods for conservation laws*, 2nd ed. (Birkhäuser, Basel, 1992), ISBN: 978-3-7643-2723-1, DOI: [10.1007/978-3-0348-8629-1](https://doi.org/10.1007/978-3-0348-8629-1).
- [316] R. Eymard, T. Gallouët, and R. Herbin, “Finite volume methods”, in: *Handbook of Numerical Analysis*, vol. 7 (Elsevier, Waltham, MA, USA, 2000), pp. 713–1018, DOI: [10.1016/S1570-8659\(00\)07005-8](https://doi.org/10.1016/S1570-8659(00)07005-8).
- [317] R. J. LeVeque, *Finite-volume methods for hyperbolic problems*, Cambridge Texts in Applied Mathematics (Cambridge University Press, 2002), ISBN: 9780511791253, DOI: [10.1017/CB09780511791253](https://doi.org/10.1017/CB09780511791253).
- [318] J. S. Hesthaven and T. Warburton, *Nodal Discontinuous Galerkin Methods: Algorithms, Analysis, and Applications*, 1st (Springer Publishing Company, Incorporated, 2007), DOI: [10.5555/1557392](https://doi.org/10.5555/1557392).
- [319] L. Rezzolla and O. Zanotti, *Relativistic hydrodynamics* (Oxford University Press, Oxford, England, UK, 2018), ISBN: 9780198807599, DOI: [10.1093/acprof:oso/9780198528906.001.0001](https://doi.org/10.1093/acprof:oso/9780198528906.001.0001).
- [320] J. K. Hunter, “Notes on Partial Differential Equations” (Davis, California, United States: University of California at Davis, 2014), URL: <https://www.math.ucdavis.edu/~hunter/pdes/pdes.html>, [Online; accessed 2023.11.03].
- [321] S. Mishra, U. S. Fjordholm, and R. Abgrall, “Numerical methods for conservation laws and related equations” (ETH Zürich, 2015), URL: https://metaphor.ethz.ch/x/2019/hs/401-4671-00L/literature/mishra_hyperbolic_pdes.pdf, Lecture Notes.

-
- [322] M. E. Vázquez-Cendón, *Solving Hyperbolic Equations with Finite Volume Methods* (Springer International Publishing, Cham, Switzerland, 2015), ISBN: 978-3-319-14784-0, DOI: [10.1007/978-3-319-14784-0](https://doi.org/10.1007/978-3-319-14784-0).
- [323] A. Polyanin and V. Zaitsev, *Handbook of Nonlinear Partial Differential Equations, Second Edition*, 2. ed., A Chapman & Hall book (CRC Press, Florida, USA, 2016), DOI: [10.1201/b11412](https://doi.org/10.1201/b11412).
- [324] L. Rezzolla, “Numerical Methods for the Solution of Partial Differential Equations”, Lecture notes (Frankfurt, Germany: Institute for Theoretical Physics, 2020), URL: https://itp.uni-frankfurt.de/~rezzolla/lecture_notes/2010/fd_evolution_pdes_lnotes.pdf, [Online; accessed 2023.11.03].
- [325] M. J. Steil, “Computational fluid dynamic”, `cfD_20231111.nb`, Mathematica notebook (2023), digital auxiliary file.
- [326] E. F. Toro, *Riemann Solvers and Numerical Methods for Fluid Dynamics*, 3rd ed. (Springer-Verlag, Berlin, Germany, 2009), ISBN: 978-3-540-25202-3, DOI: [10.1007/978-3-540-49834-6](https://doi.org/10.1007/978-3-540-49834-6).
- [327] P. D. Lax, “1. Hyperbolic Systems of Conservation Laws and the Mathematical Theory of Shock Waves”, in: *Hyperbolic Systems of Conservation Laws and the Mathematical Theory of Shock Waves* (Society for Industrial and Applied Mathematics, 1973), pp. 1–48, DOI: [10.1137/1.9781611970562.ch1](https://doi.org/10.1137/1.9781611970562.ch1).
- [328] W. F. Ames, *Numerical Methods for Partial Differential Equations*, 3. ed., 1. [Dr.], Computer science and scientific computing (Academic Press, Boston [u.a.], 1992), ISBN: 012056761X.
- [329] P. L. Roe, “Approximate Riemann solvers, parameter vectors, and difference schemes”, *J. Comput. Phys.* **135** (1997) 250–258.
- [330] A. Harten, P. D. Lax, and B. van Leer, “On upstream differencing and Godunov-type schemes for hyperbolic conservation laws”, *SIAM Rev.* **25** (1983) 35–61.
- [331] B. Einfeldt, “On Godunov-type Methods for Gas Dynamics”, *SIAM J. Numer. Anal.* **25** (1988) 294–318.
- [332] H. Nessyahu and E. Tadmor, “Non-oscillatory central differencing for hyperbolic conservation laws”, *J. Comput. Phys.* **87** (1990) 408–463.
- [333] B. van Leer, “Towards the ultimate conservative difference scheme. V. A second-order sequel to Godunov’s method”, *J. Comput. Phys.* **32** (1979) 101–136.
- [334] P. D. Lax, “Weak solutions of nonlinear hyperbolic equations and their numerical computation”, *Commun. Pure Appl. Math.* **7** (1954) 159–193.
- [335] K. O. Friedrichs, “Symmetric hyperbolic linear differential equations”, *Commun. Pure Appl. Math.* **7** (1954) 345–392.
- [336] H. Tang and T. Tang, “Adaptive Mesh Methods for One- and Two-Dimensional Hyperbolic Conservation Laws”, *SIAM J. Numer. Anal.* **41** (2003) 487–515.
- [337] P. Lakaschus, M. Buballa, and D. H. Rischke, “Competition of inhomogeneous chiral phases and two-flavor color superconductivity in the NJL model”, *Phys. Rev. D* **103** (2021) 034030, arXiv: [2012.07520 \[hep-ph\]](https://arxiv.org/abs/2012.07520).
- [338] G. Fejős and A. Patkós, “Field dependence of the Yukawa coupling in the three flavor quark-meson model”, *Phys. Rev. D* **103** (2021) 056015, arXiv: [2011.08387 \[hep-ph\]](https://arxiv.org/abs/2011.08387).
- [339] A. Harten, “High resolution schemes for hyperbolic conservation laws”, *J. Comput. Phys.* **49** (1983) 357–393.
- [340] Wikipedia contributors, “Flux limiter” (2020), URL: https://en.wikipedia.org/wiki/Flux_limiter, [Online; accessed 2020.10.15].
- [341] P. L. Roe, “Characteristic-Based Schemes for the Euler Equations”, *Annu. Rev. Fluid Mech.* **18** (1986) 337–365.
- [342] X.-D. Liu, S. Osher, and T. Chan, “Weighted Essentially Non-oscillatory Schemes”, *J. Comput. Phys.* **115** (1994) 200–212.
- [343] D. Levy, G. Puppo, and G. Russo, “Central WENO Schemes for hyperbolic systems of conservation laws”, *ESAIM: Math. Model. Numer. Anal.* **33** (1999) 547–571.

-
- [344] D. Levy, G. Puppo, and G. Russo, “Compact Central WENO Schemes for Multidimensional Conservation Laws”, *SIAM J. Sci. Comput.* **22** (2000) , arXiv: [math/9911089](https://arxiv.org/abs/math/9911089) [cs.NA].
- [345] A. Kurganov and D. Levy, “A Third-Order Semi-Discrete Central Scheme for Conservation Laws and Convection-Diffusion Equations”, *SIAM J. Sci. Comput.* **22** (2000) , arXiv: [math/0002133](https://arxiv.org/abs/math/0002133) [math.NA].
- [346] G.-S. Jiang and C.-W. Shu, “Efficient Implementation of Weighted ENO Schemes”, *J. Comput. Phys.* **126** (1996) 202–228.
- [347] J. Shi, C. Hu, and C.-W. Shu, “A Technique of Treating Negative Weights in WENO Schemes”, *J. Comput. Phys.* **175** (2002) 108–127.
- [348] A. Kurganov, G. Petrova, and B. Popov, “Adaptive Semidiscrete Central-Upwind Schemes for Nonconvex Hyperbolic Conservation Laws”, *SIAM J. Sci. Comput.* **29** (2007) 2381–2401.
- [349] A. Suresh and H. T. Huynh, “Accurate Monotonicity-Preserving Schemes with Runge–Kutta Time Stepping”, *J. Comput. Phys.* **136** (1997) 83–99.
- [350] T. Jourdan *et al.*, “An accurate scheme to solve cluster dynamics equations using a Fokker–Planck approach”, *Comput. Phys. Commun.* **207** (2016) 170–178.
- [351] X.-d. Liu and E. Tadmor, “Third Order Nonoscillatory Central Scheme For Hyperbolic Conservation Laws”, *Numer. Math.* **79** (2000) .
- [352] G.-s. Jiang and E. Tadmor, “Non-oscillatory Central Schemes for Multidimensional Hyperbolic Conservation Laws”, *SIAM J. Sci. Comput.* **19** (1997) 1892–1917.
- [353] Wolfram Research, Inc., “Mathematica, Version 12.1” (Champaign, IL, 2020), URL: <https://www.wolfram.com/mathematica>.
- [354] P. Virtanen *et al.*, “SciPy 1.0: Fundamental Algorithms for Scientific Computing in Python”, *Nat. Methods* **17** (2020) 261–272.
- [355] F. Ihssen, F. R. Sattler, and N. Wink, “Numerical RG-time integration of the effective potential: Analysis and benchmark”, *Phys. Rev. D* **107** (2023) 114009, arXiv: [2302.04736](https://arxiv.org/abs/2302.04736) [hep-th].
- [356] R. M. Redheffer and W. Walter, “The total variation of solutions of parabolic differential equations and a maximum principle in unbounded domains”, *Math. Ann.* **209** (1974) 57–67.
- [357] A. Chertock, A. Kurganov, and P. Rosenau, “On degenerate saturated-diffusion equations with convection”, *Nonlinearity* **18** (2005) 609–630.
- [358] L. Monthé, “A study of splitting scheme for hyperbolic conservation laws with source terms”, *J. Comput. Appl. Math.* **137** (2001) 1–12.
- [359] R. D. Beneito and A. M. Gavara, “A ‘TVD-like’ Scheme for Conservation Laws with Source Terms”, in: *Numerical Mathematics and Advanced Applications* (Springer, Berlin, Germany, 2008), pp. 265–272, DOI: [10.1007/978-3-540-69777-0_31](https://doi.org/10.1007/978-3-540-69777-0_31).
- [360] R. Chen and D.-k. Mao, “Entropy-TVD Scheme for Nonlinear Scalar Conservation Laws”, *J. Sci. Comput.* **47** (2011) 150–169.
- [361] M. Bessemoulin-Chatard and F. Filbet, “A Finite Volume Scheme for Nonlinear Degenerate Parabolic Equations”, *SIAM J. Sci. Comput.* **34** (2012) B559–B583, URL: <http://dx.doi.org/10.1137/110853807>.
- [362] A. C. Hindmarsh *et al.*, “SUNDIALS: Suite of nonlinear and differential/algebraic equation solvers”, *ACM Trans. Math. Softw.* **31** (2005) 363–396.
- [363] D. J. Gardner *et al.*, “Enabling new flexibility in the SUNDIALS suite of nonlinear and differential/algebraic equation solvers”, *ACM Trans. Math. Softw.* (2022) .
- [364] M. J. Steil, “Zero dimensional $O(N)$ model”, `00N_20231205.nb`, Mathematica notebook (2023), digital auxiliary file.

-
- [365] M. J. Steil, “Zero dimensional $O(1)$ model”, 0d01_20231120.nb, Mathematica notebook (2023), digital auxiliary file.
- [366] M. J. Steil, “Zero dimensional $O(N)$ model at large N ”, 0d0NLargeN_20231111.nb, Mathematica notebook (2023), digital auxiliary file.
- [367] M. Delgado, “Classroom Note: The Lagrange–Charpit Method”, *SIAM Rev.* (2006) .
- [368] W. J. M. Rankine, “On the thermodynamic theory of waves of finite longitudinal disturbance”, *Phil. Trans. R. Soc.* **160** (1870) 277–288.
- [369] P.-H. Hugoniot, “On the propagation of motion in bodies and in perfect gases in Particular – I”, in: *Classic papers in shock compression science*, translation of: Hugoniot, Pierre-Henri, Journal de l’École Polytechnique, Vol. **57**, pp. 3 – 97 (1887) (Springer, New York, 1998), pp. 161–243, ISBN: 978-1-4612-2218-7, DOI: [10.1007/978-1-4612-2218-7_7](https://doi.org/10.1007/978-1-4612-2218-7_7).
- [370] D. L. Bernstein, *Existence Theorems in Partial Differential Equations. (AM-23), Volume 23* (Princeton University Press, Princeton, NJ, USA, 1951), ISBN: 978-0-69109580-6.
- [371] H. Bateman, “Some recent researches on the motion of fluids”, *Mon. Weather Rev.* **43** (1915) 163–170.
- [372] J. M. Burgers, “A mathematical model illustrating the theory of turbulence”, *Adv. Appl. Mech.* **1** (1948) 171–199, ed. by R. von Mises and T. von Kármán, URL: <http://www.sciencedirect.com/science/article/pii/S0065215608701005>.
- [373] H. Nessayahu and E. Tadmor, “The Convergence Rate of Approximate Solutions for Nonlinear Scalar Conservation Laws”, *SIAM J. Numer. Anal.* **29** (1992) 1505–1519.
- [374] N. V. Krylov, *Nonlinear Elliptic and Parabolic Equations of the Second Order* (Springer Netherlands, 1987), ISBN: 978-1-4020-0334-9.
- [375] G. M. Lieberman, *Second Order Parabolic Differential Equations* (World Scientific, Singapore, 1996), ISBN: 978-981-022883-5.
- [376] J. B. J. Fourier and A. Freeman, *The Analytical Theory of Heat* (Cambridge University Press, Cambridge, England, UK, 2009), English translation (1878) by Alexander Freeman of Joseph J. B. Fourier’s *Théorie analytique de la chaleur* (1822), ISBN: 978-1-10800178-6, DOI: [10.1017/CB09780511693205](https://doi.org/10.1017/CB09780511693205).
- [377] V. Casalegno *et al.*, “Measurement of thermal properties of a ceramic/metal joint by laser flash method”, *J. Nucl. Mater.* **407** (2010) 83–87.
- [378] L. Euler, “Principes généraux du mouvement des fluides”, *Scholarly Commons* (1757) 274–315.
- [379] T. A. Handy and M. J. Steil, “ToroExact v1.3.0”, *GitHub repository* (GitHub, 2023), URL: <https://github.com/MJSteil/ToroExact>.
- [380] G. A. Sod, “A survey of several finite difference methods for systems of nonlinear hyperbolic conservation laws”, *J. Comput. Phys.* **27** (1978) 1–31.
- [381] X. C. Coll, “Studying Shock Wave Phenomena with a Shock Tube Application”, *COMSOL Blog post* (2018), URL: <https://www.comsol.com/blogs/studying-shock-wave-phenomena-with-a-shock-tube-application/>, [Online; accessed 2023.10.05].
- [382] The Engineering ToolBox, “Dry Air - Thermodynamic and Physical Properties” (2005), URL: https://www.engineeringtoolbox.com/dry-air-properties-d_973.html, [Online; accessed 2023.10.05].
- [383] V. Springel and C. P. Dullemond, “Numerische Strömungsmechanik” (Ruprecht-Karls-Universität Heidelberg, 2012), URL: https://www.ita.uni-heidelberg.de/~dullemond/lectures/num_fluid_2011/, Lecture Notes.
- [384] Y. Xing and C.-W. Shu, “High Order Well-Balanced WENO Scheme for the Gas Dynamics Equations Under Gravitational Fields”, *J. Sci. Comput.* **54** (2013) 645–662.
- [385] R. Touma, U. Koley, and C. Klingenberg, “Well-Balanced Unstaggered Central Schemes for the Euler Equations with Gravitation”, *SIAM J. Sci. Comput.* **38** (2016) B773–B807.

-
- [386] S. Qian *et al.*, “High order well-balanced discontinuous Galerkin methods for Euler equations at isentropic equilibrium state under gravitational fields”, *Appl. Math. Comput.* **329** (2018) 23–37, URL: <https://www.sciencedirect.com/science/article/pii/S0096300318300882>.
- [387] R. Käppeli and S. Mishra, “A well-balanced finite volume scheme for the Euler equations with gravitation - The exact preservation of hydrostatic equilibrium with arbitrary entropy stratification”, *Astron. Astrophys.* **587** (2016) A94.
- [388] G.-Q. Chen, “Global Solutions to the Compressible Navier–Stokes Equations for a Reacting Mixture”, *SIAM J. Math. Anal.* **23** (1992) 609–634.
- [389] J. Berg and J. Nordström, “Using the compressible Navier-Stokes equations as a model for heat transfer in solids”, *CTR Annual Research Briefs* (2011) .
- [390] S. Li, “On one-dimensional compressible Navier–Stokes equations for a reacting mixture in unbounded domains”, *Z. Angew. Math. Phys.* **68** (2017) 106–24.
- [391] Clay Mathematics Institute, “Navier-Stokes Equation” (2023), URL: <https://www.claymath.org/millennium/navier-stokes-equation>, [Online; accessed 2023.10.05].
- [392] L. H. Ryder, *Quantum Field Theory* (Cambridge University Press, Cambridge, England, UK, 1996), ISBN: 978-0-51181390-0, DOI: [10.1017/CB09780511813900](https://doi.org/10.1017/CB09780511813900).
- [393] C. Burgess and G. Moore, *The Standard Model: A Primer* (Cambridge University Press, Cambridge, England, UK, 2006), ISBN: 978-0-52186036-9, DOI: [10.1017/CB09780511819698](https://doi.org/10.1017/CB09780511819698).
- [394] W. Greiner, S. Schramm, and E. Stein, *Quantum Chromodynamics*, 3rd ed. (Springer, Berlin, Germany, 2007), ISBN: 978-3-540-48535-3.
- [395] M. D. Schwartz, *Quantum Field Theory and the Standard Model* (Cambridge University Press, Cambridge, England, UK, 2013), ISBN: 978-1-10898503-1, DOI: [10.1017/9781139540940](https://doi.org/10.1017/9781139540940).
- [396] J. M. Pawłowski and P. Tilman, “Lecture notes: QCD” (Cambridge, United Kingdom: Institute for Theoretical Physics, University of Heidelberg, 2018), URL: https://www.thphys.uni-heidelberg.de/~pawłowski/qcd_17-18.php, [Online; accessed 2024.05.18].
- [397] F. Gao and J. M. Pawłowski, “QCD phase structure from functional methods”, *Phys. Rev. D* **102** (2020) 034027, arXiv: [2002.07500](https://arxiv.org/abs/2002.07500) [hep-ph].
- [398] N. Wink, *Towards the spectral properties and phase structure of QCD*, PhD thesis, University of Heidelberg, 2020, DOI: [10.11588/heidok.00028503](https://doi.org/10.11588/heidok.00028503).
- [399] M. J. Steil, “Quantum chromodynamics and low-energy effective models”, `qcd_20231129.nb`, Mathematica notebook (2023), digital auxiliary file.
- [400] F. J. Ynduráin, “Limits on the mass of the gluon”, *Phys. Lett. B* **345** (1995) 524–526.
- [401] W. Pauli, “Über den Einfluß der Geschwindigkeitsabhängigkeit der Elektronenmasse auf den Zeemaneffekt”, *Z. Phys.* **31** (1925) 373–385.
- [402] W. Pauli, “Über den Zusammenhang des Abschlusses der Elektronengruppen im Atom mit der Komplexstruktur der Spektren”, *Z. Phys.* **31** (1925) 765–783.
- [403] W. Pauli, “The Connection Between Spin and Statistics”, *Phys. Rev.* **58** (1940) 716–722.
- [404] R. Mills, “Gauge fields”, *Am. J. Phys.* **57** (1989) 493–507.
- [405] L. D. Faddeev and V. N. Popov, “Feynman diagrams for the Yang-Mills field”, *Phys. Lett. B* **25** (1967) 29–30.
- [406] A. Deur, S. J. Brodsky, and G. F. de Teramond, “The QCD Running Coupling”, *Nucl. Phys.* **90** (2016) 1, arXiv: [1604.08082](https://arxiv.org/abs/1604.08082) [hep-ph].
- [407] A. M. Polyakov, “Compact gauge fields and the infrared catastrophe”, *Phys. Lett. B* **59** (1975) 82–84, ed. by J. C. Taylor.
- [408] V. N. Gribov, “Quantization of Nonabelian Gauge Theories”, *Nucl. Phys. B* **139** (1978) 1, ed. by J. Nyiri.

-
- [409] T. Kugo and I. Ojima, “Local Covariant Operator Formalism of Non-Abelian Gauge Theories and Quark Confinement Problem”, *Prog. Theor. Phys.* **66** (1979) 1–130.
- [410] D. Zwanziger, “Nonperturbative Faddeev-Popov formula and infrared limit of QCD”, *Phys. Rev. D* **69** (2004) 016002, arXiv: [hep-ph/0303028](#).
- [411] J. Braun, H. Gies, and J. M. Pawłowski, “Quark confinement from color confinement”, *Phys. Lett. B* **684** (2010) 262–267, arXiv: [0708.2413 \[hep-th\]](#).
- [412] F. Marhauser and J. M. Pawłowski, “Confinement in Polyakov Gauge” (2008), arXiv: [0812.1144 \[hep-ph\]](#).
- [413] J. Braun *et al.*, “On the Nature of the Phase Transition in SU(N), Sp(2) and E(7) Yang-Mills theory”, *Eur. Phys. J. C* **70** (2010) 689–702, arXiv: [1007.2619 \[hep-ph\]](#).
- [414] L. Fister and J. M. Pawłowski, “Confinement from Correlation Functions”, *Phys. Rev. D* **88** (2013) 045010, arXiv: [1301.4163 \[hep-ph\]](#).
- [415] T. K. Herbst, J. Luecker, and J. M. Pawłowski, “Confinement order parameters and fluctuations” (2015), arXiv: [1510.03830 \[hep-ph\]](#).
- [416] G. Eichmann, C. S. Fischer, and C. A. Welzbacher, “Baryon effects on the location of QCD’s critical end point”, *Phys. Rev. D* **93** (2016) 034013, arXiv: [1509.02082 \[hep-ph\]](#).
- [417] B.-J. Schaefer, J. M. Pawłowski, and J. Wambach, “The Phase Structure of the Polyakov–Quark-Meson Model”, *Phys. Rev. D* **76** (2007) 074023, arXiv: [0704.3234 \[hep-ph\]](#).
- [418] P. M. Lo *et al.*, “Polyakov loop fluctuations in SU(3) lattice gauge theory and an effective gluon potential”, *Phys. Rev. D* **88** (2013) 074502, arXiv: [1307.5958 \[hep-lat\]](#).
- [419] J. Braun *et al.*, “Crystalline ground states in Polyakov-loop extended Nambu–Jona-Lasinio models”, *Phys. Rev. D* **93** (2016) 014032, arXiv: [1510.04012 \[hep-ph\]](#).
- [420] K. Fukushima and V. Skokov, “Polyakov loop modeling for hot QCD”, *Prog. Part. Nucl. Phys.* **96** (2017) 154–199, arXiv: [1705.00718 \[hep-ph\]](#).
- [421] W.-j. Fu, J. M. Pawłowski, and F. Rennecke, “Strangeness Neutrality and QCD Thermodynamics”, *SciPost Phys. Core* **2** (2020) 002, arXiv: [1808.00410 \[hep-ph\]](#).
- [422] C. Wetterich, “Spinors in euclidean field theory, complex structures and discrete symmetries”, *Nucl. Phys. B* **852** (2011) 174–234, arXiv: [1002.3556 \[hep-th\]](#).
- [423] E. Noether, “Invariant Variation Problems”, *Gott. Nachr.* **1918** (1918) 235–257, arXiv: [physics/0503066](#), M. A. Tavel’s English translation of Noether’s Theorems (1918), reproduced by Frank Y. Wang.
- [424] E. Noether, “Invarianten beliebiger Differentialausdrücke.”, German, *Nachr. Ges. Wiss. Göttingen, Math.-Phys. Kl.* **1918** (1918) 37–44.
- [425] S. L. Adler, “Axial vector vertex in spinor electrodynamics”, *Phys. Rev.* **177** (1969) 2426–2438.
- [426] S. L. Adler and W. A. Bardeen, “Absence of higher order corrections in the anomalous axial vector divergence equation”, *Phys. Rev.* **182** (1969) 1517–1536.
- [427] J. S. Bell and R. Jackiw, “A PCAC puzzle: $\pi^0 \rightarrow \gamma\gamma$ in the σ model”, *Nuovo Cim. A* **60** (1969) 47–61.
- [428] W. A. Bardeen, “Anomalous Ward identities in spinor field theories”, *Phys. Rev.* **184** (1969) 1848–1857.
- [429] G. ’t Hooft, “Symmetry breaking through Bell-Jackiw anomalies”, *Phys. Rev. Lett.* **37** (1976) 8–11, ed. by M. A. Shifman.
- [430] G. ’t Hooft, “Computation of the quantum effects due to a four-dimensional pseudoparticle”, *Phys. Rev. D* **14** (1976) 3432–3450, ed. by M. A. Shifman, [Erratum: *Phys.Rev.D* 18, 2199 (1978)].
- [431] J. M. Pawłowski, “Exact flow equations and the U(1) problem”, *Phys. Rev. D* **58** (1998) 045011, arXiv: [hep-th/9605037](#).
- [432] M. Kobayashi and T. Maskawa, “Chiral symmetry and eta-x mixing”, *Prog. Theor. Phys.* **44** (1970) 1422–1424.

-
- [433] M. Kobayashi, H. Kondo, and T. Maskawa, “Symmetry breaking of the chiral $u(3) \times u(3)$ and the quark model”, *Prog. Theor. Phys.* **45** (1971) 1955–1959.
- [434] L. Del Debbio, L. Giusti, and C. Pica, “Topological susceptibility in the $SU(3)$ gauge theory”, *Phys. Rev. Lett.* **94** (2005) 032003, arXiv: [hep-th/0407052](https://arxiv.org/abs/hep-th/0407052).
- [435] M. Luscher and F. Palombi, “Universality of the topological susceptibility in the $SU(3)$ gauge theory”, *JHEP* **09** (2010) 110, arXiv: [1008.0732](https://arxiv.org/abs/1008.0732) [[hep-lat](https://arxiv.org/abs/hep-lat)].
- [436] M. Cè *et al.*, “Testing the Witten-Veneziano mechanism with the Yang-Mills gradient flow on the lattice”, *PoS LATTICE2014* (2014) 353, arXiv: [1410.8358](https://arxiv.org/abs/1410.8358) [[hep-lat](https://arxiv.org/abs/hep-lat)].
- [437] V. Koch, “Aspects of chiral symmetry”, *Int. J. Mod. Phys. E* **6** (1997) 203–250, arXiv: [nuc1-th/9706075](https://arxiv.org/abs/nuc1-th/9706075).
- [438] J. R. Pelaez, “From controversy to precision on the sigma meson: a review on the status of the non-ordinary $f_0(500)$ resonance”, *Phys. Rept.* **658** (2016) 1, arXiv: [1510.00653](https://arxiv.org/abs/1510.00653) [[hep-ph](https://arxiv.org/abs/hep-ph)].
- [439] V. Jamieson, “Physics Nobel snubs key researcher”, *New Sci.* (2008) , [Online; accessed 2023.11.28].
- [440] “The Nobel Prize in Physics 2008”, *Nobelprize.org* (2008), URL: <https://www.nobelprize.org/prizes/physics/2008/nambu/lecture>, [Online; accessed 2023.11.28].
- [441] Y. Nambu, “Quasiparticles and gauge invariance in the theory of superconductivity”, *Phys. Rev.* **117** (1960) 648–663, ed. by J. C. Taylor.
- [442] J. Goldstone, “Field theories with superconductor solutions”, *Nuovo Cim.* **19** (1961) 154–164.
- [443] J. Braun, “The QCD Phase Boundary from Quark-Gluon Dynamics”, *Eur. Phys. J. C* **64** (2009) 459–482, arXiv: [0810.1727](https://arxiv.org/abs/0810.1727) [[hep-ph](https://arxiv.org/abs/hep-ph)].
- [444] M. Mitter, J. M. Pawłowski, and N. Strodthoff, “Chiral symmetry breaking in continuum QCD”, *Phys. Rev. D* **91** (2015) 054035, arXiv: [1411.7978](https://arxiv.org/abs/1411.7978) [[hep-ph](https://arxiv.org/abs/hep-ph)].
- [445] J. Braun, M. Leonhardt, and M. Pospiech, “Fierz-complete NJL model study. II. Toward the fixed-point and phase structure of hot and dense two-flavor QCD”, *Phys. Rev. D* **97** (2018) 076010, arXiv: [1801.08338](https://arxiv.org/abs/1801.08338) [[hep-ph](https://arxiv.org/abs/hep-ph)].
- [446] J. Braun, M. Leonhardt, and M. Pospiech, “Fierz-complete NJL model study III: Emergence from quark-gluon dynamics”, *Phys. Rev. D* **101** (2020) 036004, arXiv: [1909.06298](https://arxiv.org/abs/1909.06298) [[hep-ph](https://arxiv.org/abs/hep-ph)].
- [447] M. Sadzikowski, “Coexistence of pion condensation and color superconductivity in two flavor quark matter”, *Phys. Lett. B* **553** (2003) 45–50, arXiv: [hep-ph/0210065](https://arxiv.org/abs/hep-ph/0210065).
- [448] R. Casalbuoni and G. Nardulli, “Inhomogeneous superconductivity in condensed matter and QCD”, *Rev. Mod. Phys.* **76** (2004) 263–320, arXiv: [hep-ph/0305069](https://arxiv.org/abs/hep-ph/0305069).
- [449] M. Sadzikowski, “Comparison of the non-uniform chiral and 2SC phases at finite temperatures and densities”, *Phys. Lett. B* **642** (2006) 238–243, arXiv: [hep-ph/0609186](https://arxiv.org/abs/hep-ph/0609186).
- [450] R. Anglani *et al.*, “Crystalline color superconductors”, *Rev. Mod. Phys.* **86** (2014) 509–561, arXiv: [1302.4264](https://arxiv.org/abs/1302.4264) [[hep-ph](https://arxiv.org/abs/hep-ph)].
- [451] D. Nowakowski and S. Carignano, “Color-superconductivity and inhomogeneous chiral symmetry breaking in isospin-asymmetric quark matter”, *PoS MPC2015* (2016) 010, arXiv: [1602.04798](https://arxiv.org/abs/1602.04798) [[hep-ph](https://arxiv.org/abs/hep-ph)].
- [452] R. L. Stratonovich, “On a Method of Calculating Quantum Distribution Functions”, *Sov. Phys. Dokl.* **2** (1957) 416.
- [453] J. Hubbard, “Calculation of partition functions”, *Phys. Rev. Lett.* **3** (1959) 77–80.
- [454] H. Yukawa, “On the Interaction of Elementary Particles I”, *Proc. Phys. Math. Soc. Jap.* **17** (1935) 48–57.
- [455] P. Boucaud *et al.*, “Discretization effects on renormalized gauge-field Green’s functions, scale setting, and the gluon mass”, *Phys. Rev. D* **98** (2018) 114515, arXiv: [1809.05776](https://arxiv.org/abs/1809.05776) [[hep-ph](https://arxiv.org/abs/hep-ph)].
- [456] S. Borsanyi *et al.*, “QCD Crossover at Finite Chemical Potential from Lattice Simulations”, *Phys. Rev. Lett.* **125** (2020) 052001, arXiv: [2002.02821](https://arxiv.org/abs/2002.02821) [[hep-lat](https://arxiv.org/abs/hep-lat)].

-
- [457] C. S. Fischer, J. Luecker, and C. A. Welzbacher, “Phase structure of three and four flavor QCD”, *Phys. Rev. D* **90** (2014) 034022, arXiv: 1405.4762 [hep-ph].
- [458] F. Gao *et al.*, “Phase diagram and thermal properties of strong-interaction matter”, *Phys. Rev. D* **93** (2016) 094019, arXiv: 1507.00875 [nucl-th].
- [459] M. Leonhardt *et al.*, “Symmetric nuclear matter from the strong interaction”, *Phys. Rev. Lett.* **125** (2020) 142502, arXiv: 1907.05814 [nucl-th].
- [460] U. Ellwanger and C. Wetterich, “Evolution equations for the quark - meson transition”, *Nucl. Phys. B* **423** (1994) 137–170, arXiv: hep-ph/9402221.
- [461] M. D. Scadron, G. Rupp, and R. Delbourgo, “The quark-level linear σ model”, *Fortsch. Phys.* **61** (2013) 994–1027, arXiv: 1309.5041 [hep-ph].
- [462] B.-J. Schaefer and M. Wagner, “The Three-flavor chiral phase structure in hot and dense QCD matter”, *Phys. Rev. D* **79** (2009) 014018, arXiv: 0808.1491 [hep-ph].
- [463] S. Carignano, *Inhomogeneous chiral symmetry breaking phases*, PhD thesis, Technische Universität Darmstadt, 2012, URL: <https://tuprints.ulb.tu-darmstadt.de/3149>.
- [464] M. Buballa, D. H. Rischke, and M. Wagner, “CRC-TR 211 Project A03: Inhomogeneous phases at high density”, Proposal for the Establishment and Funding (2016), URL: <https://crc-tr211.org/>.
- [465] M. Buballa, D. H. Rischke, and M. Wagner, “CRC-TR 211 Project A03: Inhomogeneous phases at high density”, Proposal for the Second Funding Period (2021), URL: <https://crc-tr211.org/>.
- [466] F. Wilczek, “Quantum Time Crystals”, *Phys. Rev. Lett.* **109** (2012) 160401, arXiv: 1202.2539 [quant-ph].
- [467] A. Shapere and F. Wilczek, “Classical Time Crystals”, *Phys. Rev. Lett.* **109** (2012) 160402, arXiv: 1202.2537 [cond-mat.other].
- [468] K. Sacha and J. Zakrzewski, “Time crystals: a review”, *Rept. Prog. Phys.* **81** (2018) 016401, arXiv: 1704.03735 [quant-ph].
- [469] P. Bruno, “Impossibility of Spontaneously Rotating Time Crystals: A No-Go Theorem”, *Phys. Rev. Lett.* **111** (2013) 070402, arXiv: 1306.6275 [quant-ph].
- [470] H. Watanabe and M. Oshikawa, “Absence of Quantum Time Crystals”, *Phys. Rev. Lett.* **114** (2015) 251603, arXiv: 1410.2143 [cond-mat.stat-mech].
- [471] J. Nissinen and G. E. Volovik, “Effective Minkowski-to-Euclidean signature change of the magnon BEC pseudo-Goldstone mode in polar ^3He ”, *Sov. Phys. JETP* **106** (2017) 234–241, arXiv: 1707.00905 [cond-mat.other].
- [472] S. Kinoshita, K. Murata, and T. Oka, “Holographic Floquet states II: Floquet condensation of vector mesons in nonequilibrium phase diagram”, *JHEP* **06** (2018) 096, arXiv: 1712.06786 [hep-th].
- [473] A. Gorsky and A. Grekov, “Flavored extended instanton in QCD”, *JHEP* **01** (2020) 074, arXiv: 1910.06304 [hep-th].
- [474] R. Arouca, E. C. Marino, and C. M. Smith, “Non-Hermitian quantum gases: a platform for imaginary time crystals”, *Quant. Front* **1** (2022) 2, arXiv: 2108.01747 [cond-mat.quant-gas].
- [475] R. E. Peierls, *Quantum Theory of Solids* (Oxford University Press, Oxford, England, UK, 1996), ISBN: 978-0-19267017-5.
- [476] P. Fulde and R. A. Ferrell, “Superconductivity in a Strong Spin-Exchange Field”, *Phys. Rev.* **135** (1964) A550–A563.
- [477] A. I. Larkin and Y. N. Ovchinnikov, “Nonuniform state of superconductors”, *Zh. Eksp. Teor. Fiz.* **47** (1964) 1136–1146, also published in *Sov. Phys. JETP* **20** (1965) 762.
- [478] G. Gruner, “The dynamics of spin-density waves”, *Rev. Mod. Phys.* **66** (1994) 1–24.
- [479] P. Monceau, “Electronic crystals: an experimental overview”, *Adv. Phys.* **61** (2012) 325–581, URL: <http://dx.doi.org/10.1080/00018732.2012.719674>.

-
- [480] J.-P. Pouget, “The Peierls instability and charge density wave in one-dimensional electronic conductors”, *C. R. Phys.* **17** (2016) 332–356.
- [481] A. W. Overhauser, “Structure of Nuclear Matter”, *Phys. Rev. Lett.* **4** (1960) 415–418.
- [482] A. B. Migdal, “ π Condensation in Nuclear Matter”, *Phys. Rev. Lett.* **31** (1973) 257–260.
- [483] A. B. Migdal, “Pion fields in nuclear matter”, *Rev. Mod. Phys.* **50** (1978) 107–172.
- [484] F. Dautry and E. M. Nyman, “Pion condensation and the σ -model in liquid neutron matter”, *Nucl. Phys. A* **319** (1979) 323–348.
- [485] D. V. Deryagin, D. Y. Grigoriev, and V. A. Rubakov, “Standing wave ground state in high density, zero temperature QCD at large N_c ”, *Int. J. Mod. Phys. A* **7** (1992) 659–681.
- [486] E. Shuster and D. T. Son, “On finite density QCD at large $N(c)$ ”, *Nucl. Phys. B* **573** (2000) 434–446, arXiv: [hep-ph/9905448](https://arxiv.org/abs/hep-ph/9905448).
- [487] M. G. Alford, J. A. Bowers, and K. Rajagopal, “Crystalline color superconductivity”, *Phys. Rev. D* **63** (2001) 074016, arXiv: [hep-ph/0008208](https://arxiv.org/abs/hep-ph/0008208).
- [488] J. A. Bowers *et al.*, “A Diagrammatic approach to crystalline color superconductivity”, *Phys. Rev. D* **64** (2001) 014024, arXiv: [hep-ph/0101067](https://arxiv.org/abs/hep-ph/0101067).
- [489] A. K. Leibovich, K. Rajagopal, and E. Shuster, “Opening the Crystalline Color Superconductivity Window”, *Phys. Rev. D* **64** (2001) 094005, arXiv: [hep-ph/0104073](https://arxiv.org/abs/hep-ph/0104073).
- [490] I. Giannakis, J. T. Liu, and H.-c. Ren, “Angular momentum mixing in crystalline color superconductivity”, *Phys. Rev. D* **66** (2002) 031501, arXiv: [hep-ph/0202138](https://arxiv.org/abs/hep-ph/0202138).
- [491] M. Mannarelli, K. Rajagopal, and R. Sharma, “Testing the Ginzburg-Landau approximation for three-flavor crystalline color superconductivity”, *Phys. Rev. D* **73** (2006) 114012, arXiv: [hep-ph/0603076](https://arxiv.org/abs/hep-ph/0603076).
- [492] R. Anglani *et al.*, “Superfluid and pseudo-goldstone modes in three flavor crystalline color superconductivity”, *Phys. Rev. D* **76** (2007) 054007, arXiv: [0706.1781 \[hep-ph\]](https://arxiv.org/abs/0706.1781).
- [493] D. Nickel, “How many phases meet at the chiral critical point?”, *Phys. Rev. Lett.* **103** (2009) 072301, arXiv: [0902.1778 \[hep-ph\]](https://arxiv.org/abs/0902.1778).
- [494] D. Nickel, “Inhomogeneous phases in the Nambu-Jona-Lasino and quark-meson model”, *Phys. Rev. D* **80** (2009) 074025, arXiv: [0906.5295 \[hep-ph\]](https://arxiv.org/abs/0906.5295).
- [495] H. Abuki, D. Ishibashi, and K. Suzuki, “Crystalline chiral condensates off the tricritical point in a generalized Ginzburg-Landau approach”, *Phys. Rev. D* **85** (2012) 074002, arXiv: [1109.1615 \[hep-ph\]](https://arxiv.org/abs/1109.1615).
- [496] G. V. Dunne and J. Feinberg, “Self isospectral periodic potentials and supersymmetric quantum mechanics”, *Phys. Rev. D* **57** (1998) 1271–1276, arXiv: [hep-th/9706012](https://arxiv.org/abs/hep-th/9706012).
- [497] V. Schön and M. Thies, “2-D model field theories at finite temperature and density”, in: *At The Frontier of Particle Physics: Handbook of QCD, Boris Ioffe Festschrift*, vol. 3 (World Scientific, 2000), chap. 33, pp. 1945–2032, DOI: [10.1142/9789812810458_0041](https://doi.org/10.1142/9789812810458_0041), arXiv: [hep-th/0008175](https://arxiv.org/abs/hep-th/0008175).
- [498] V. Schön and M. Thies, “Emergence of Skyrme crystal in Gross-Neveu and ’t Hooft models at finite density”, *Phys. Rev. D* **62** (2000) 096002, arXiv: [hep-th/0003195](https://arxiv.org/abs/hep-th/0003195).
- [499] F. Cooper, A. Khare, and U. Sukhatme, *Supersymmetry and quantum mechanics* (World Scientific, 2001), DOI: [10.1142/4687](https://doi.org/10.1142/4687).
- [500] A. Brzoska and M. Thies, “No first order phase transition in the Gross-Neveu model?”, *Phys. Rev. D* **65** (2002) 125001, arXiv: [hep-th/0112105](https://arxiv.org/abs/hep-th/0112105).
- [501] M. Thies, “Analytical solution of the Gross-Neveu model at finite density”, *Phys. Rev. D* **69** (2004) 067703, arXiv: [hep-th/0308164](https://arxiv.org/abs/hep-th/0308164).
- [502] O. Schnetz, M. Thies, and K. Urlichs, “The Phase diagram of the massive Gross-Neveu model, revisited” (2005), arXiv: [hep-th/0507120](https://arxiv.org/abs/hep-th/0507120).

-
- [503] M. Thies and K. Urlichs, “From non-degenerate conducting polymers to dense matter in the massive Gross-Neveu model”, *Phys. Rev. D* **72** (2005) 105008, arXiv: [hep-th/0505024](#).
- [504] O. Schnetz, M. Thies, and K. Urlichs, “Full phase diagram of the massive Gross-Neveu model”, *Annals Phys.* **321** (2006) 2604–2637, arXiv: [hep-th/0511206](#).
- [505] M. Thies, “From relativistic quantum fields to condensed matter and back again: Updating the Gross-Neveu phase diagram”, *J. Phys. A* **39** (2006) 12707–12734, arXiv: [hep-th/0601049](#).
- [506] A. Heinz *et al.*, “Inhomogeneous condensation in effective models for QCD using the finite-mode approach”, *Phys. Rev. D* **93** (2016) 014007, arXiv: [1508.06057 \[hep-ph\]](#).
- [507] M. Thies, “Duality study of the chiral Heisenberg-Gross-Neveu model in 1+1 dimensions”, *Phys. Rev. D* **102** (2020) 096006, arXiv: [2008.13119 \[hep-th\]](#).
- [508] R. Ciccone, L. Di Pietro, and M. Serone, “Inhomogeneous Phase of the Chiral Gross-Neveu Model”, *Phys. Rev. Lett.* **129** (2022) 071603, arXiv: [2203.07451 \[hep-th\]](#).
- [509] D. Roscher, J. Braun, and J. E. Drut, “Inhomogeneous phases in one-dimensional mass- and spin-imbalanced Fermi gases”, *Phys. Rev. A* **89** (2014) 063609, arXiv: [1311.0179 \[cond-mat.quant-gas\]](#).
- [510] D. Roscher, J. Braun, and J. E. Drut, “Phase structure of mass- and spin-imbalanced unitary Fermi gases”, *Phys. Rev. A* **91** (2015) 053611, arXiv: [1501.05544 \[cond-mat.quant-gas\]](#).
- [511] K. Maeda, T. Hatsuda, and G. Baym, “Antiferromagnetic ground state of two-component dipolar Fermi gases: An analog of meson condensation in nuclear matter”, *Phys. Rev. A* **87** (2013) 021604, arXiv: [1205.1086 \[cond-mat.quant-gas\]](#).
- [512] A. C. Loheac, J. Braun, and J. E. Drut, “Polarized fermions in one dimension: density and polarization from complex Langevin calculations, perturbation theory, and the virial expansion”, *Phys. Rev. D* **98** (2018) 054507, arXiv: [1804.10257 \[cond-mat.quant-gas\]](#).
- [513] L. Rammelmüller, J. E. Drut, and J. Braun, “Pairing patterns in one-dimensional spin- and mass-imbalanced Fermi gases”, *SciPost Phys.* **9** (2020) 014, arXiv: [2003.06853 \[cond-mat.quant-gas\]](#).
- [514] D. Müller, M. Buballa, and J. Wambach, “Dyson-Schwinger study of chiral density waves in QCD”, *Phys. Lett. B* **727** (2013) 240–243, arXiv: [1308.4303 \[hep-ph\]](#).
- [515] L. Pannullo and M. Winstel, “Absence of inhomogeneous chiral phases in (2+1)-dimensional four-fermion and Yukawa models”, *Phys. Rev. D* **108** (2023) 036011, arXiv: [2305.09444 \[hep-ph\]](#).
- [516] L. Pannullo, “Inhomogeneous condensation in the Gross-Neveu model in noninteger spatial dimensions $1 \leq d < 3$ ”, *Phys. Rev. D* **108** (2023) 036022, arXiv: [2306.16290 \[hep-ph\]](#).
- [517] W. Broniowski and M. Kutschera, “Ambiguities in Effective Chiral Models With Cutoff”, *Phys. Lett. B* **242** (1990) 133–138.
- [518] T. L. Partyka and M. Sadzikowski, “Phase diagram of the non-uniform chiral condensate in different regularization schemes at $T=0$ ”, *J. Phys. G* **36** (2009) 025004, arXiv: [0811.4616 \[hep-ph\]](#).
- [519] L. Pannullo *et al.*, “Inhomogeneous phases in the 1+1 dimensional Gross-Neveu model at finite number of fermion flavors”, *Acta Phys. Polon. Supp.* **13** (2020) 127, arXiv: [1902.11066 \[hep-lat\]](#).
- [520] L. Pannullo *et al.*, “Lattice investigation of the phase diagram of the 1+1 dimensional Gross-Neveu model at finite number of fermion flavors”, *PoS LATTICE2019* (2019) 063, arXiv: [1909.11513 \[hep-lat\]](#).
- [521] J. Lenz *et al.*, “Inhomogeneous phases in the Gross-Neveu model in 1+1 dimensions at finite number of flavors”, *Phys. Rev. D* **101** (2020) 094512, arXiv: [2004.00295 \[hep-lat\]](#).
- [522] J. J. Lenz *et al.*, “Baryons in the Gross-Neveu model in 1+1 dimensions at finite number of flavors”, *Phys. Rev. D* **102** (2020) 114501, arXiv: [2007.08382 \[hep-lat\]](#).
- [523] J. J. Lenz and M. Mandl, “Remnants of large- N_f inhomogeneities in the 2-flavor chiral Gross-Neveu model”, *PoS LATTICE2021* (2022) 415, arXiv: [2110.12757 \[hep-lat\]](#).

-
- [524] J. J. Lenz, M. Mandl, and A. Wipf, “Inhomogeneities in the two-flavor chiral Gross-Neveu model”, *Phys. Rev. D* **105** (2022) 034512, arXiv: 2109.05525 [hep-lat].
- [525] M. Winstel and L. Pannullo, “Stability of homogeneous chiral phases against inhomogeneous perturbations in 2+1 dimensions”, *PoS LATTICE2022* (2023) 195, arXiv: 2211.04414 [hep-ph].
- [526] H. Abuki, “Ginzburg-Landau phase diagram of QCD near chiral critical point - chiral defect lattice and solitonic pion condensate”, *Phys. Lett. B* **728** (2014) 427–432, arXiv: 1307.8173 [hep-ph].
- [527] S. Carignano *et al.*, “Crystalline phases by an improved gradient expansion technique”, *Phys. Rev. D* **97** (2018) 036009, arXiv: 1711.08607 [hep-ph].
- [528] R. D. Pisarski, V. V. Skokov, and A. M. Tselik, “A Pedagogical Introduction to the Lifshitz Regime”, *Universe* **5** (2019) 48, arXiv: 2202.01036 [hep-ph].
- [529] S. Hikami and E. Brezin, “Large order behavior of the $1/N$ expansion in zero and one dimensions”, *J. Phys. A* **12** (1979) 759–770.
- [530] D. Bessis, C. Itzykson, and J.-B. Zuber, “Quantum field theory techniques in graphical enumeration”, *Adv. Appl. Math.* **1** (1980) 109–157.
- [531] S. Nishigaki and T. Yoneya, “A nonperturbative theory of randomly branching chains”, *Nucl. Phys. B* **348** (1991) 787–807.
- [532] P. Di Vecchia, M. Kato, and N. Ohta, “Double scaling limit in $O(N)$ vector models”, *Nucl. Phys. B* **357** (1991) 495–520.
- [533] S. Schelstraete and H. Verschelde, “Large N limit of $O(N)$ vector models”, *Phys. Lett. B* **332** (1994) 36–43, arXiv: hep-th/9405158.
- [534] J. Zinn-Justin, “Vector models in the large N limit: A Few applications”, in: *11th Taiwan Spring School on Particles and Fields* (1998), arXiv: hep-th/9810198.
- [535] S. Flörchinger, “Functional Renormalization and Ultracold Quantum Gases”, *Springer Theses* (2010), URL: <http://dx.doi.org/10.1007/978-3-642-14113-3>.
- [536] S. Moroz, *Few-body physics with functional renormalization*, PhD thesis, University of Heidelberg, 2011, DOI: 10.11588/heidok.00011602.
- [537] S. Kemler and J. Braun, “Towards a Renormalization Group approach to density functional theory – general formalism and case studies”, *J. Phys. G* **40** (2013) 085105, arXiv: 1304.1161 [nucl-th].
- [538] F. Strocchi, *An introduction to non-perturbative foundations of quantum field theory* (Oxford University Press, Oxford, 2013), ISBN: 978-0-19-967157-1, DOI: 10.1093/acprof:oso/9780199671571.001.0001.
- [539] J. M. Pawłowski, “Solving integrals with flow equations”, Slides for the lecture *Non-perturbative aspects of gauge theories* winter term 2012/2013 (2013), URL: <https://www.thphys.uni-heidelberg.de/~pawowski/NPgauge12/bonus/idea.pdf>, [Online; accessed 2020.10.29].
- [540] J. F. Rentrop, S. G. Jakobs, and V. Meden, “Two-particle irreducible Functional Renormalization Group schemes – a comparative study”, *J. Phys. A* **48** (2015) 145002.
- [541] D. S. Rosa, R. L. S. Farias, and R. O. Ramos, “Reliability of the optimized perturbation theory in the 0-dimensional $O(N)$ scalar field model”, *Physica A* **464** (2016) 11–26, arXiv: 1604.00537 [hep-ph].
- [542] H. Liang, Y. Niu, and T. Hatsuda, “Functional Renormalization Group and Kohn-Sham scheme in density functional theory”, *Phys. Lett. B* **779** (2018) 436–440, arXiv: 1710.00650 [cond-mat.str-el].
- [543] A. G. Catalano, *Application of renormalization group techniques to the solution of integrals and Schrödinger eigenvalue equations*, Master’s thesis, Politecnico di Torino, 2019, URL: <http://webthesis.biblio.polito.it/id/eprint/18673>.
- [544] P. Millington and P. M. Saffin, “Visualising quantum effective action calculations in zero dimensions”, *J. Phys. A* **52** (2019) 405401, arXiv: 1905.09674 [hep-th].

-
- [545] E. Alexander *et al.*, “Alternative flow equation for the functional renormalization group”, *Phys. Rev. D* **100** (2019) 101702, arXiv: 1907.06503 [hep-th].
- [546] P. Millington, “An alternative flow equation from the regulator-sourced 2PI effective action”, Talk at the 10th International Conference on Exact Renormalization Group 2020 (ERG2020) (Kyoto, Japan (online conference): Yukawa Institute for Theoretical Physics, Kyoto University, 2020), URL: https://www2.yukawa.kyoto-u.ac.jp/~erg2020/ERG2020_slides/Millington.pdf, [Online; accessed 2021.01.12].
- [547] K. Fraboulet, *Path-integral approaches to strongly-coupled quantum many-body systems*, PhD thesis, LPMC - Palaiseau - IJCLab, Orsay, 2021.
- [548] L. Kades *et al.*, “Monte Carlo sampling of complex actions in extended state spaces”, *Phys. Rev. E* **105** (2022) 045315, arXiv: 2106.09367 [hep-lat].
- [549] P. Millington and P. M. Saffin, “Benchmarking regulator-sourced 2PI and average 1PI flow equations in zero dimensions”, *J. Phys. A* **54** (2021) 465401, arXiv: 2107.12914 [hep-th].
- [550] N. D. Mermin and H. Wagner, “Absence of ferromagnetism or antiferromagnetism in one- or two-dimensional isotropic Heisenberg models”, *Phys. Rev. Lett.* **17** (1966) 1133–1136.
- [551] P. C. Hohenberg, “Existence of long-range order in one and two dimensions”, *Phys. Rev.* **158** (1967) 383–386.
- [552] S. R. Coleman, “There are no Goldstone bosons in two-dimensions”, *Commun. Math. Phys.* **31** (1973) 259–264.
- [553] H. Kleinert, *Path integrals in quantum mechanics, statistics, polymer physics, and financial markets*, 5th ed. (World Scientific, 2004), p. 1624, ISBN: 978-981-4273-55-8, DOI: 10.1142/7305.
- [554] W. H. Press *et al.*, *Numerical recipes in FORTRAN: The art of scientific computing*, 2nd ed. (Cambridge University Press, Cambridge, USA, 1992), ISBN: 0-521-43064-X.
- [555] W. H. Press *et al.*, *Numerical Recipes in C: The art of scientific computing*, 2nd ed. (Cambridge University Press, Cambridge, USA, 1992), ISBN: 0-521-43108-5.
- [556] P. McCullagh and J. Kolassa, “Cumulants”, *Scholarpedia* **4** (2009) 4699, revision #137322.
- [557] Y. Fujimoto, L. O’Raifeartaigh, and G. Parravicini, “Effective potential for non-convex potentials”, *Nucl. Phys. B* **212** (1983) 268–300.
- [558] A. Wipf, *Statistical Approach to Quantum Field Theory*, Lect. Notes Phys. 864 (Springer-Verlag, Berlin, Germany, 2013), ISBN: 978-3-642-33104-6, DOI: 10.1007/978-3-642-33105-3.
- [559] B. S. DeWitt, *Dynamical theory of groups and fields* (Gordon and Breach, New York, USA, 1965).
- [560] L. F. Abbott, “Introduction to the Background Field Method”, *Acta Phys. Polon. B* **13** (1982) 33–50.
- [561] E. Ising, “Beitrag zur Theorie des Ferromagnetismus”, *Z. Phys.* **31** (1925) 253–258.
- [562] L. Canet *et al.*, “Nonperturbative Renormalization Group approach to the Ising model: A derivative expansion at order ∂^4 ”, *Phys. Rev. B* **68** (2003) 064421, arXiv: hep-th/0302227.
- [563] J. Goldstone, A. Salam, and S. Weinberg, “Broken symmetries”, *Phys. Rev.* **127** (1962) 965–970.
- [564] A. M. Bonanno and G. Lacagnina, “Spontaneous symmetry breaking and proper time flow equations”, *Nucl. Phys. B* **693** (2004) 36–50, arXiv: hep-th/0403176.
- [565] K.-I. Aoki, S.-I. Kumamoto, and M. Yamada, “Phase structure of NJL model with weak renormalization group”, *Nucl. Phys. B* **931** (2018) 105–131, arXiv: 1705.03273 [hep-th].
- [566] N. Tetradis and D. F. Litim, “Analytical solutions of exact renormalization group equations”, *Nucl. Phys. B* **464** (1996) 492–511, arXiv: hep-th/9512073.
- [567] V. Pangon *et al.*, “Onset of symmetry breaking by the Functional RG method”, *Int. J. Mod. Phys. A* **26** (2011) 1327–1345, arXiv: 0907.0144 [hep-th].

-
- [568] V. Pangon, “Structure of the broken phase of the sine-Gordon model using Functional Renormalization”, *Int. J. Mod. Phys. A* **27** (2012) 1250014, arXiv: 1008.0281 [hep-th].
- [569] N. Wink, “Resolving phase transitions with Discontinuous Galerkin methods”, Talk at the EMMI Workshop Functional Methods in Strongly Correlated Systems (Hirschegg, Austria, 2019), URL: <https://indico.gsi.de/event/8375/contributions/36534/>, [Online; accessed 2020.11.24].
- [570] M. J. Steil *et al.*, “Numerical fluid dynamics for FRG-flow equations: Zero-dimensional QFTs as numerical test cases”, Slides for the 10th International Conference on Exact Renormalization Group 2020 (ERG2020) (Kyoto, Japan (online conference): Yukawa Institute for Theoretical Physics, Kyoto University, 2020), URL: https://www2.yukawa.kyoto-u.ac.jp/~erg2020/ERG2020_slides/steil_koenigstein.pdf, [Online; accessed 2021.02.01].
- [571] P. Ehrenfest, “Phasenumwandlungen im ueblichen und erweiterten Sinn, classifiziert nach den entsprechenden Singularitaeten des thermodynamischen Potentiales”, *Proc. Royal Acad. Amsterdam* **36** (1933) 153–157, Supplement No 75b zu den Mitteilungen aus dem Kamerlingh Onnes-Institute, Leiden.
- [572] S. R. Coleman, *Aspects of Symmetry: Selected Erice Lectures* (Cambridge University Press, Cambridge, U.K., 1985), ISBN: 978-0-521-31827-3, DOI: 10.1017/CB09780511565045.
- [573] D. J. Wallace and R. K. P. Zia, “Gradient flow and the Renormalization Group”, *Phys. Lett. A* **48** (1974) 325.
- [574] D. J. Wallace and R. K. P. Zia, “Gradient properties of the Renormalization Group Equations in multicomponent systems”, *Annals Phys.* **92** (1975) 142.
- [575] A. B. Zamolodchikov, “Irreversibility of the flux of the Renormalization Group in a 2D field theory”, *JETP Lett.* **43** (1986) 730–732.
- [576] G. Zumbach, “The Renormalization Group in the Local Potential Approximation and its applications to the $O(N)$ model”, *Nucl. Phys. B* **413** (1994) 754–770.
- [577] G. Felder, “Renormalization Group in the local potential approximation”, *Comm. Math. Phys.* **111** (1987) 101–121.
- [578] A. Hasenfratz and P. Hasenfratz, “Renormalization Group study of scalar field theories”, *Nucl. Phys. B* **270** (1986) 687–701.
- [579] J. L. Lebowitz, “Time’s arrow and Boltzmann’s entropy”, *Scholarpedia* **3** (2008) 3448, revision #137152, [Online; accessed 2021.02.01].
- [580] G. Zumbach, “Almost second order phase transitions”, *Phys. Rev. Lett.* **71** (1993) 2421–2424.
- [581] D. J. Gross and F. A. Wilczek, “Asymptotically free gauge theories I”, *Phys. Rev. D* **8** (1973) 3633–3652.
- [582] D. J. Gross and F. A. Wilczek, “Asymptotically free gauge theories II”, *Phys. Rev. D* **9** (1974) 980–993.
- [583] T. Banks and E. J. Martinec, “The Renormalization Group and String Field Theory”, *Nucl. Phys. B* **294** (1987) 733–746.
- [584] J. L. Cardy, “Is there a c -theorem in four dimensions?”, *Phys. Lett. B* **215** (1988) 749–752.
- [585] H. Osborn, “Derivation of a four dimensional c -theorem for renormalisable quantum field theories”, *Phys. Lett. B* **222** (1989) 97–102.
- [586] I. Jack and H. Osborn, “Analogues for the c -theorem for four-dimensional renormalizable field theories”, *Nucl. Phys. B* **343** (1990) 647–688.
- [587] Z. Komargodski and A. Schwimmer, “On Renormalization Group flows in four dimensions”, *JHEP* **12** (2011) 099, arXiv: 1107.3987 [hep-th].
- [588] T. L. Curtright, X. Jin, and C. K. Zachos, “RG flows, cycles, and c -theorem folklore”, *Phys. Rev. Lett.* **108** (2012) 131601, arXiv: 1111.2649 [hep-th].
- [589] P. E. Haagensen *et al.*, “Gradient flows from an approximation to the Exact Renormalization Group”, *Phys. Lett. B* **323** (1994) 330–338, arXiv: hep-th/9310032.

-
- [590] J. Generowicz, C. Harvey-Fros, and T. R. Morris, “ C function representation of the Local Potential Approximation”, *Phys. Lett. B* **407** (1997) 27–32, arXiv: [hep-th/9705088](#).
- [591] S. Forte and J. I. Latorre, “A proof of the irreversibility of Renormalization Group flows in four-dimensions”, *Nucl. Phys. B* **535** (1998) 709–728, arXiv: [hep-th/9805015](#).
- [592] A. Codello, G. D’Odorico, and C. Pagani, “A Functional RG equation for the c -function”, *JHEP* **07** (2014) 040, arXiv: [1312.7097 \[hep-th\]](#).
- [593] A. Codello, G. D’Odorico, and C. Pagani, “Functional and local Renormalization Groups”, *Phys. Rev. D* **91** (2015) 125016, arXiv: [1502.02439 \[hep-th\]](#).
- [594] D. Becker and M. Reuter, “Towards a C -function in 4D quantum gravity”, *JHEP* **03** (2015) 065, arXiv: [1412.0468 \[hep-th\]](#).
- [595] D. Becker, *Asymptotically safe quantum gravity: Bimetric actions, boundary terms, & a C-function*, PhD thesis, Johannes Gutenberg University Mainz, 2016, DOI: [10.25358/openscience-2831](#).
- [596] P. Lakaschus, *Inhomogeneous chiral condensates in low-energy color-superconductivity models of QCD*, PhD thesis, Universitätsbibliothek Johann Christian Senckenberg, 2021, p. 155, DOI: [10.21248/gups.62534](#).
- [597] J. D. Jackson, *Classical electrodynamics*, 3rd ed. (Wiley, 1998), ISBN: [978-0-471-30932-1](#).
- [598] S. Buckley and M. C. Leverett, “Mechanism of fluid displacement in sands”, *Trans.* **146** (1942) 107–116.
- [599] R. Rajaraman, *Solitons and instantons. An introduction to solitons and instantons in quantum field theory* (North-Holland, Amsterdam, 1987), ISBN: [9780444870476](#).
- [600] *Instantons in gauge theories*, ed. by M. A. Shifman (World Scientific Publishing Co. Pt. Ltd., 1994), ISBN: 981-02-1681-5.
- [601] S. Weinberg, *Gravitation and Cosmology: Principles and Applications of the General Theory of Relativity* (John Wiley and Sons, New York, 1972), ISBN: [978-0-471-92567-5](#).
- [602] C. W. Misner, K. S. Thorne, and J. A. Wheeler, *Gravitation* (W. H. Freeman, San Francisco, 1973), ISBN: [978-0-7167-0344-0](#).
- [603] L. Ryder, *Introduction to general relativity* (Cambridge University Press, 2009), ISBN: 9780511809033, DOI: [10.1017/CB09780511809033](#).
- [604] J.-M. Caillol, “The non-perturbative renormalization group in the ordered phase”, *Nucl. Phys. B* **855** (2012) 854–884, arXiv: [1109.4024 \[cond-mat.stat-mech\]](#).
- [605] T. W. Baumgarte and S. L. Shapiro, *Numerical Relativity* (Cambridge University Press, Cambridge, England, UK, 2010), ISBN: 978-0-52151407-1, DOI: [10.1017/CB09781139193344](#).
- [606] M. Alcubierre, *Introduction to 3+1 Numerical Relativity* (Oxford University Press, Oxford, England, UK, 2008), ISBN: 978-0-19170937-1, DOI: [10.1093/acprof:oso/9780199205677.001.0001](#).
- [607] P. Grandclement and J. Novak, “Spectral methods for numerical relativity”, *Living Rev. Rel.* **12** (2009) 1, arXiv: [0706.2286 \[gr-qc\]](#).
- [608] E.ourgoulhon, “3+1 formalism and bases of numerical relativity” (2007), arXiv: [gr-qc/0703035](#).
- [609] G.-Q. G. Chen, “Shock capturing and related numerical methods in computational fluid dynamics”, *Acta Math. Univ. Comen.* **1** (2001) 51–73.
- [610] M. Peláez and N. Wschebor, “Ordered phase of the $O(N)$ model within the nonperturbative renormalization group”, *Phys. Rev. E* **94** (2016) 042136, arXiv: [1510.05709 \[cond-mat.stat-mech\]](#).
- [611] D. F. Litim, “Critical exponents from optimized renormalization group flows”, *Nucl. Phys. B* **631** (2002) 128–158, arXiv: [hep-th/0203006](#).
- [612] J. Braun, H. Gies, and D. D. Scherer, “Asymptotic safety: a simple example”, *Phys. Rev. D* **83** (2011) 085012, arXiv: [1011.1456 \[hep-th\]](#).

-
- [613] P. Deligne *et al.*, *Quantum fields and strings: a course for mathematicians* (American Mathematical Society Providence, 1999), ISBN: 978-0-82182012-4.
- [614] S. Weinberg, “Critical Phenomena for Field Theorists”, in: *14th International School of Subnuclear Physics: Understanding the Fundamental Constituents of Matter* (1976), DOI: 10.1007/978-1-4684-0931-4_1.
- [615] S. Weinberg, “What is quantum field theory, and what did we think it is?”, in: *Conference on Historical Examination and Philosophical Reflections on the Foundations of Quantum Field Theory* (1996), arXiv: hep-th/9702027.
- [616] R. Percacci, “Asymptotic Safety”, in: *Approaches to Quantum Gravity: Toward a New Understanding of Space, Time and Matter*, ed. by D. Oriti (Cambridge University Press, Cambridge, 2007), chap. 8, pp. 111–128, arXiv: 0709.3851 [hep-th].
- [617] S. Weinberg, “Living with Infinities”, in (2009), arXiv: 0903.0568 [hep-th].
- [618] M. Niedermaier and M. Reuter, “The Asymptotic Safety Scenario in Quantum Gravity”, *Living Rev. Rel.* **9** (2006) 5–173.
- [619] A. Bonanno *et al.*, “Critical reflections on asymptotically safe gravity”, *Front. in Phys.* **8** (2020) 269, arXiv: 2004.06810 [gr-qc].
- [620] A. Jakovác, A. Patkós, and P. Pósfay, “Non-Gaussian fixed points in fermionic field theories without auxiliary Bose-fields”, *Eur. Phys. J. C* **75** (2015) 2, arXiv: 1406.3195 [hep-th].
- [621] J. Zinn-Justin, “Critical Phenomena: field theoretical approach”, *Scholarpedia* **5** (2010) 8346, revision #148508.
- [622] M. A. Virasoro, “Subsidiary conditions and ghosts in dual resonance models”, *Phys. Rev. D* **1** (1970) 2933–2936.
- [623] L. Boltzmann, “Further Studies on the Thermal Equilibrium of Gas Molecules”, in: *The Kinetic Theory of Gases*, [Originally published under the title “Weitere Studien über das Wärmegleichgewicht unter Gasmolekülen”, in *Sitzungsberichte Akad. Wiss.*, Vienna, part II, 66, 275–370 (1872); reprinted in Boltzmann’s *Wissenschaftliche Abhandlungen*, Vol. I, Leipzig, J. A. Barth, 1909, pp. 316–402]. (2003), pp. 262–349, DOI: 10.1142/9781848161337_0015.
- [624] J. W. Gibbs, *Elementary Principles in Statistical Mechanics: Developed with Especial Reference to the Rational Foundation of Thermodynamics* (Cambridge University Press, Cambridge, England, UK, 2010), ISBN: 978-1-10801702-2, DOI: 10.1017/CB09780511686948.
- [625] R. C. Tolman, *The Principles of Statistical Mechanics (Dover Books on Physics)* (Dover Publications Inc., Mineola, NY, USA, 1979), ISBN: 978-0-48663896-6.
- [626] E. Witt, “Treue Darstellung Liescher Ringe.”, *De Gruyter* **1937** (1937) 152–160.
- [627] G. ’t Hooft, “A planar diagram theory for strong interactions”, *Nucl. Phys. B* **72** (1974) 461–473, ed. by J. C. Taylor.
- [628] G. Veneziano, “ $U(1)$ Without Instantons”, *Nucl. Phys. B* **159** (1979) 213–224.
- [629] E. Witten, “Current Algebra Theorems for the $U(1)$ Goldstone Boson”, *Nucl. Phys. B* **156** (1979) 269–283.
- [630] E. Witten, “Baryons in the $1/N$ expansion”, *Nucl. Phys. B* **160** (1979) 57–115.
- [631] J. M. Maldacena, “The large N limit of superconformal field theories and supergravity”, *Int. J. Theor. Phys.* **38** (1999) 1113–1133, arXiv: hep-th/9711200.
- [632] M. D’Attanasio and T. R. Morris, “Large N and the renormalization group”, *Phys. Lett. B* **409** (1997) 363–370, arXiv: hep-th/9704094.
- [633] M. Moshe and J. Zinn-Justin, “Quantum field theory in the large N limit: A Review”, *Phys. Rept.* **385** (2003) 69–228, arXiv: hep-th/0306133.
- [634] G. B. Arfken and H. J. Weber, *Mathematical Methods for Physicists*, 6. ed. (Elsevier Academic Press, California, 2005), DOI: 10.1016/C2009-0-30629-7.

-
- [635] D. Litim and N. Tetradis, “Approximate solutions of exact renormalization group equations” (1995), arXiv: [hep-th/9501042](#).
- [636] G. Fejos, “Chiral symmetry breaking patterns in the $U_L(n) \times U_R(n)$ meson model”, *Phys. Rev. D* **87** (2013) 056006, arXiv: [1212.3415 \[hep-ph\]](#).
- [637] D. F. Litim and E. Marchais, “Critical $O(N)$ models in the complex field plane”, *Phys. Rev. D* **95** (2017) 025026, arXiv: [1607.02030 \[hep-th\]](#).
- [638] S. Yabunaka and B. Delamotte, “Surprises in $O(N)$ Models: Nonperturbative Fixed Points, Large N Limits, and Multicriticality”, *Phys. Rev. Lett.* **119** (2017) 191602, arXiv: [1707.04383 \[cond-mat.stat-mech\]](#).
- [639] S. Yabunaka, C. Fleming, and B. Delamotte, “Incompleteness of the large- N analysis of the $O(N)$ models: Nonperturbative cuspy fixed points and their nontrivial homotopy at finite N ”, *Phys. Rev. E* **106** (2022) 054105, arXiv: [2104.02744 \[hep-th\]](#).
- [640] K.-I. Aoki, S.-I. Kumamoto, and D. Sato, “Weak solution of the non-perturbative renormalization group equation to describe dynamical chiral symmetry breaking”, *PTEP* **2014** (2014) 043B05, arXiv: [1403.0174 \[hep-th\]](#).
- [641] A. Kurganov *et al.*, “Adaptive Moving Mesh Central-Upwind Schemes for Hyperbolic System of PDEs: Applications to Compressible Euler Equations and Granular Hydrodynamics”, *Commun. Appl. Math. Comput.* (2020) 1–35.
- [642] M. J. Steil, “Zero dimensional $SU(2)$ model”, `0dsu2_20230806.nb`, Mathematica notebook (2023), digital auxiliary file.
- [643] F. A. Berezin, *The Method of Second Quantization*, Pure and applied physics : a series of monographs and textbooks. 24 (Academic Press, London, England, UK, 1966), ISBN: [978-0-12089450-5](#).
- [644] W. Greiner and J. Reinhardt, *Field quantization* (Springer, Berlin Heidelberg, 1996), ISBN: 978-3-540-78048-9, DOI: [10.1007/978-3-642-61485-9](#).
- [645] R. Gupta, “Introduction to lattice QCD: Course”, in: *Les Houches Summer School in Theoretical Physics, Session 68: Probing the Standard Model of Particle Interactions* (1997), pp. 83–219, arXiv: [hep-lat/9807028](#).
- [646] C. Gattringer and C. B. Lang, *Quantum Chromodynamics on the Lattice* (Springer, Berlin, Germany, 2010), ISBN: [978-3-642-01850-3](#).
- [647] O. Philipsen, “The QCD equation of state from the lattice”, *Prog. Part. Nucl. Phys.* **70** (2013) 55–107, arXiv: [1207.5999 \[hep-lat\]](#).
- [648] F. Murgana, A. Koenigstein, and D. H. Rischke, “Reanalysis of critical exponents for the $O(N)$ model via a hydrodynamic approach to the Functional Renormalization Group” (2023), arXiv: [2303.16838 \[hep-th\]](#).
- [649] J. Stoll, *Das $(1 + 1)$ -dimensionale Gross-Neveu-(Yukawa)-Modell jenseits des large- N -Limes*, Master thesis, Goethe University Frankfurt, 2021.
- [650] N. Zorbach, *Bosonische Fluktuationen im $(1 + 1)$ -dimensionalen Gross-Neveu-Yukawa-Modell mit endlichen N* , Master thesis, Goethe University Frankfurt, 2021.
- [651] S. Rechenberger, “Inhomogeneous phases at high density: In Search for Instabilities”, Talk at the 1st retreat of the CRC-TR 211 presented by D. H. Rischke, March 12-16, ZiF Bielefeld and corresponding private notes (2018).
- [652] M. J. Steil, “Gross-Neveu model in $d = 1 + 1$ ”, `gn_20240701.nb`, Mathematica notebook (2024), digital auxiliary file.
- [653] M. J. Steil, “Gross-Neveu model at infinite N ”, `Gncpp_20231207.zip`, C++ code (2023), digital auxiliary files.
- [654] B. Rosenstein, B. J. Warr, and S. H. Park, “The Four Fermi Theory Is Renormalizable in $(2+1)$ -Dimensions”, *Phys. Rev. Lett.* **62** (1989) 1433–1436.

-
- [655] B. Rosenstein, B. J. Warr, and S. H. Park, “Thermodynamics of (2+1)-dimensional Four Fermi Models”, *Phys. Rev. D* **39** (1989) 3088.
- [656] L. Rosa, P. Vitale, and C. Wetterich, “Critical exponents of the Gross-Neveu model from the effective average action”, *Phys. Rev. Lett.* **86** (2001) 958–961, arXiv: [hep-th/0007093](https://arxiv.org/abs/hep-th/0007093).
- [657] F. Hofling, C. Nowak, and C. Wetterich, “Phase transition and critical behavior of the $D = 3$ Gross-Neveu model”, *Phys. Rev. B* **66** (2002) 205111, arXiv: [cond-mat/0203588](https://arxiv.org/abs/cond-mat/0203588).
- [658] E. Fradkin, *Field Theories of Condensed Matter Physics*, 2nd ed. (Cambridge University Press, Cambridge, 2013), DOI: [10.1017/CB09781139015509](https://doi.org/10.1017/CB09781139015509).
- [659] W. Heisenberg, “Zur Theorie des Ferromagnetismus”, *Z. Phys.* **49** (1928) 619–636.
- [660] S.-i. Tomonaga, “Remarks on Bloch’s Method of Sound Waves applied to Many-Fermion Problems”, *Prog. Theor. Exp. Phys.* **5** (1950) 544–569.
- [661] J. M. Luttinger, “An Exactly Soluble Model of a Many Fermion System”, *J. Math. Phys.* **4** (1963) 1154–1162.
- [662] A. Chodos and H. Minakata, “The Gross-Neveu model as an effective theory for polyacetylene”, *Phys. Lett. A* **191** (1994) 39.
- [663] W. P. Su, J. R. Schrieffer, and A. J. Heeger, “Solitons in polyacetylene”, *Phys. Rev. Lett.* **42** (1979) 1698–1701.
- [664] H. Takayama, Y. R. Lin-Liu, and K. Maki, “Continuum model for solitons in polyacetylene”, *Phys. Rev. B* **21** (1980) 2388–2393.
- [665] C. Wetterich, “Quantum fermions from classical bits”, *Phil. Trans. A. Math. Phys. Eng. Sci.* **380** (2021) 20210066, arXiv: [2106.15517](https://arxiv.org/abs/2106.15517) [quant-ph].
- [666] P. Jordan and E. P. Wigner, “Über das Paulische Äquivalenzverbot”, *Z. Phys.* **47** (1928) 631–651.
- [667] J. Ashkin and E. Teller, “Statistics of Two-Dimensional Lattices with Four Components”, *Phys. Rev.* **64** (1943) 178–184.
- [668] R. B. Potts, “Some generalized order - disorder transformations”, *Proc. Cambridge Phil. Soc.* **48** (1952) 106–109.
- [669] F. Y. Wu, “The Potts model”, *Rev. Mod. Phys.* **54** (1982) 235–268.
- [670] I. K. Affleck, “Phase Transition in the Lattice Gross-Neveu Model”, *Phys. Lett. B* **109** (1982) 307–310.
- [671] E. Fradkin, “ N -Color Ashkin-Teller Model in Two Dimensions: Solution in the Large- N Limit”, *Phys. Rev. Lett.* **53** (1984) 1967–1970.
- [672] R. Shankar, “Ashkin-Teller and Gross-Neveu models: New relations and results”, *Phys. Rev. Lett.* **55** (1985) 453–456.
- [673] W. E. Thirring, “A soluble relativistic field theory”, *Annals Phys.* **3** (1958) 91–112.
- [674] E. Witten, “Chiral Symmetry, the $1/n$ Expansion, and the $SU(N)$ Thirring Model”, *Nucl. Phys. B* **145** (1978) 110–118.
- [675] R. Heidenreich, R. Seiler, and D. A. Uhlenbrock, “The Luttinger model”, *J. Stat. Phys.* **22** (1980) 27–57.
- [676] S. R. Coleman, “The Quantum Sine-Gordon Equation as the Massive Thirring Model”, *Phys. Rev. D* **11** (1975) 2088, ed. by M. Stone.
- [677] D. Delepine, R. Gonzalez Felipe, and J. Weyers, “Equivalence of the sine-Gordon and massive Thirring models at finite temperature”, *Phys. Lett. B* **419** (1998) 296–302, arXiv: [hep-th/9709039](https://arxiv.org/abs/hep-th/9709039).
- [678] Y. Frenkel and T. Kontorova, “On the theory of plastic deformation and twinning”, *Izv. Akad. Nauk, Ser. Fiz.* **1** (1939) 137–149.
- [679] Y. S. Kivshar, H. Benner, and O. M. Braun, “Nonlinear Models for the Dynamics of Topological Defects in Solids”, in: *Nonlinear Science at the Dawn of the 21st Century*, ed. by P. L. Christiansen, M. P. Sørensen, and A. C. Scott, vol. 542 (Springer Berlin Heidelberg, Berlin, Heidelberg, 2000), pp. 265–291.

-
- [680] E. Witten, “Anti-de Sitter space and holography”, *Adv. Theor. Math. Phys.* **2** (1998) 253–291, arXiv: [hep-th/9802150](#).
- [681] S. Giombi, “Higher Spin — CFT Duality”, in: *Theoretical Advanced Study Institute in Elementary Particle Physics: New Frontiers in Fields and Strings* (2016), DOI: [10.1142/9789813149441_0003](#), arXiv: [1607.02967](#) [hep-th].
- [682] H. Kleinert, *Particles and Quantum Fields*, 2nd ed. (World Scientific Publishing Company, Singapore, 2016).
- [683] C. Fitzner and M. Thies, “Exact solution of N baryon problem in the Gross-Neveu model”, *Phys. Rev. D* **83** (2011) 085001, arXiv: [1010.5322](#) [hep-th].
- [684] G. V. Dunne, C. Fitzner, and M. Thies, “Baryon-baryon scattering in the Gross-Neveu model: the large N solution”, *Phys. Rev. D* **84** (2011) 105014, arXiv: [1108.5888](#) [hep-th].
- [685] M. Thies, “Beyond integrability: Baryon-baryon backward scattering in the massive Gross-Neveu model”, *Phys. Rev. D* **96** (2017) 076012, arXiv: [1706.06382](#) [hep-th].
- [686] J. Braun, “Fermion Interactions and Universal Behavior in Strongly Interacting Theories”, *J. Phys. G* **39** (2012) 033001, arXiv: [1108.4449](#) [hep-ph].
- [687] L. Pannullo, *Inhomogeneous Phases in the 1 + 1-Dimensional Gross-Neveu Model at Finite Number of Fermion Flavors*, Updated version from June 30, 2020 with minor corrections., Master thesis, Goethe University Frankfurt, 2020, URL: https://itp.uni-frankfurt.de/~mwagner/theses/MA_Pannullo.pdf.
- [688] J. Braun, B. Klein, and H.-J. Pirner, “Volume dependence of the pion mass in the quark-meson-model”, *Phys. Rev. D* **71** (2005) 014032, arXiv: [hep-ph/0408116](#).
- [689] J. Braun, B. Klein, and H.-J. Pirner, “Influence of quark boundary conditions on the pion mass in finite volume”, *Phys. Rev. D* **72** (2005) 034017, arXiv: [hep-ph/0504127](#).
- [690] J. Braun *et al.*, “Volume and quark mass dependence of the chiral phase transition”, *Phys. Rev. D* **73** (2006) 074010, arXiv: [hep-ph/0512274](#).
- [691] J. Braun, B. Klein, and B.-J. Schaefer, “On the Phase Structure of QCD in a Finite Volume”, *Phys. Lett. B* **713** (2012) 216–223, arXiv: [1110.0849](#) [hep-ph].
- [692] J. Braun, S. Diehl, and M. M. Scherer, “Finite-size and Particle-number Effects in an Ultracold Fermi Gas at Unitarity”, *Phys. Rev. A* **84** (2011) 063616, arXiv: [1109.1946](#) [cond-mat.quant-gas].
- [693] Y. Cohen, S. Elitzur, and E. Rabinovici, “Monte Carlo Study of Chiral Structure: The Gross-Neveu Model”, *Phys. Lett. B* **104** (1981) 289–293.
- [694] Y. Cohen, S. Elitzur, and E. Rabinovici, “A Monte Carlo study of the Gross-Neveu model”, *Nucl. Phys. B* **220** (1983) 102–118.
- [695] F. Karsch, J. B. Kogut, and H. W. Wyld, “The Gross-Neveu Model at finite temperature and density”, *Nucl. Phys. B* **280** (1987) 289–303.
- [696] I. Balog *et al.*, “Convergence of nonperturbative approximations to the Renormalization Group”, *Phys. Rev. Lett.* **123** (2019) 240604, arXiv: [1907.01829](#) [cond-mat.stat-mech].
- [697] T. D. Cohen, “Functional integrals for QCD at nonzero chemical potential and zero density”, *Phys. Rev. Lett.* **91** (2003) 222001, arXiv: [hep-ph/0307089](#).
- [698] G. Markó, U. Reinosa, and Z. Szép, “Bose-Einstein condensation and Silver Blaze property from the two-loop Φ -derivable approximation”, *Phys. Rev. D* **90** (2014) 125021, arXiv: [1410.6998](#) [hep-ph].
- [699] N. Khan *et al.*, “The Phase Diagram of QC2D from Functional Methods” (2015), arXiv: [1512.03673](#) [hep-ph].
- [700] A. Actor, “Compactification at finite temperature in noncompact electrodynamics”, *Annals Phys.* **159** (1985) 445–466.
- [701] A. Actor, “Chemical potentials in gauge theories”, *Phys. Lett. B* **157** (1985) 53–56.

-
- [702] A. Actor, “Zeta Function Regularization of High Temperature Expansions in Field Theory”, *Nucl. Phys. B* **265** (1986) 689–719.
- [703] S. G. Johnson, “Cubature v1.0.4”, *GitHub repository* (GitHub, 2020), URL: <https://github.com/steven-gj/cubature>.
- [704] J. A. Nelder and R. Mead, “A Simplex Method for Function Minimization”, *Comput. J.* **7** (1965) 308–313.
- [705] M. J. Steil, “BSAM for phase diagrams”, `bsamPD_20201115.pdf`, Group seminar talk (2020), digital auxiliary file.
- [706] V. L. Ginzburg and L. D. Landau, “On the Theory of superconductivity”, *Zh. Eksp. Teor. Fiz.* **20** (1950) 1064–1082, ed. by D. ter Haar.
- [707] S. P. Klevansky, “The Nambu-Jona-Lasinio model of quantum chromodynamics”, *Rev. Mod. Phys.* **64** (1992) 649–708.
- [708] P. C. Hohenberg and A. P. Krekhov, “An introduction to the Ginzburg-Landau theory of phase transitions and nonequilibrium patterns”, *Phys. Rep.* **572** (2015) 1–42, arXiv: 1410.7285 [cond-mat.stat-mech].
- [709] A. Ahmed, “Ginzburg-Landau Type Approach to the 1+1 Gross Neveu Model - Beyond Lowest Non-Trivial Order” (2018), arXiv: 1802.09095 [hep-th].
- [710] P. Hadley, “Advanced Solid State Physics – Landau theory of second order phase transitions”, Course material (2022), URL: http://lampx.tugraz.at/~hadley/ss2/landau/second_order.php, [Online; accessed 2023.11.16].
- [711] P. Hadley, “Landau theory of a first order phase transition”, Course material (2022), URL: http://lampx.tugraz.at/~hadley/ss2/landau/first_order.php, [Online; accessed 2023.11.16].
- [712] L. D. Landau, “On the theory of phase transitions”, *Zh. Eksp. Teor. Fiz.* **7** (1937) 19–32.
- [713] M. J. Steil, “Thermal quantum field theory”, `tqft_20231122.nb`, Mathematica notebook (2023), digital auxiliary file.
- [714] A. Barducci *et al.*, “Thermodynamics of the massive Gross-Neveu model”, *Phys. Rev. D* **51** (1995) 3042–3060, arXiv: hep-th/9406117.
- [715] J.-P. Blaizot, R. Mendez-Galain, and N. Wschebor, “The Gross-Neveu model at finite temperature at next to leading order in the 1/N expansion”, *Annals Phys.* **307** (2003) 209–271, arXiv: hep-ph/0212084.
- [716] M. Thies, “Duality between quark quark and quark anti-quark pairing in 1+1 dimensional large N models”, *Phys. Rev. D* **68** (2003) 047703, arXiv: hep-th/0303026.
- [717] M. Thies and K. Urlichs, “Baryons in massive Gross-Neveu models”, *Phys. Rev. D* **71** (2005) 105008, arXiv: hep-th/0502210.
- [718] F. Karbstein and M. Thies, “Integrating out the Dirac sea: Effective field theory approach to exactly solvable four-fermion models”, *Phys. Rev. D* **77** (2008) 025008, arXiv: 0708.3176 [hep-th].
- [719] F. Karbstein and M. Thies, “Divergence of the axial current and fermion density in Gross-Neveu models”, *Phys. Rev. D* **76** (2007) 085009, arXiv: 0706.0424 [hep-th].
- [720] G. Basar and G. V. Dunne, “Self-consistent crystalline condensate in chiral Gross-Neveu and Bogoliubov-de Gennes systems”, *Phys. Rev. Lett.* **100** (2008) 200404, arXiv: 0803.1501 [hep-th].
- [721] W. Brendel and M. Thies, “Covariant boost and structure functions of baryons in Gross-Neveu models”, *Phys. Rev. D* **81** (2010) 085002, arXiv: 0910.5351 [hep-th].
- [722] C. Fitzner and M. Thies, “Evidence for factorized scattering of composite states in the Gross-Neveu model”, *Phys. Rev. D* **85** (2012) 105015, arXiv: 1202.0648 [hep-th].
- [723] C. Fitzner and M. Thies, “Breathers and their interaction in the massless Gross-Neveu model”, *Phys. Rev. D* **87** (2013) 025001, arXiv: 1210.4423 [hep-th].
- [724] G. V. Dunne and M. Thies, “Full time-dependent Hartree-Fock solution of large N Gross-Neveu models”, *Phys. Rev. D* **89** (2014) 025008, arXiv: 1309.2443 [hep-th].

-
- [725] M. Thies, “Integrable Gross-Neveu models with fermion-fermion and fermion-antifermion pairing”, *Phys. Rev. D* **90** (2014) 105017, arXiv: 1408.5506 [hep-th].
- [726] M. Thies, “Untwisting twisted NJL₂-kinks by a bare fermion mass”, *Phys. Rev. D* **96** (2017) 116018, arXiv: 1709.01269 [hep-th].
- [727] A. Bermudez *et al.*, “Gross-Neveu-Wilson model and correlated symmetry-protected topological phases”, *Annals Phys.* **399** (2018) 149–180, arXiv: 1807.03202 [cond-mat.quant-gas].
- [728] R. Narayanan, “Phase diagram of the large N Gross-Neveu model in a finite periodic box”, *Phys. Rev. D* **101** (2020) 096001, arXiv: 2001.09200 [hep-th].
- [729] G. Roose *et al.*, “Lattice regularisation and entanglement structure of the Gross-Neveu model”, *JHEP* **21** (2020) 207, arXiv: 2010.03441 [hep-lat].
- [730] N. Lopes, M. A. Continentino, and D. G. Barci, “Excitonic insulators and Gross-Neveu models” (2021), arXiv: 2112.07362 [cond-mat.str-el].
- [731] R. D. Pisarski and F. Rennecke, “Signatures of Moat Regimes in Heavy-Ion Collisions”, *Phys. Rev. Lett.* **127** (2021) 152302, arXiv: 2103.06890 [hep-ph].
- [732] F. Rennecke and R. D. Pisarski, “Moat Regimes in QCD and their Signatures in Heavy-Ion Collisions”, in: *International Conference on Critical Point and Onset of Deconfinement* (2021), arXiv: 2110.02625 [hep-ph].
- [733] S. Weinberg, “Gauge and Global Symmetries at High Temperature”, *Phys. Rev. D* **9** (1974) 3357–3378.
- [734] J. Eser and J.-P. Blaizot, “S-wave pion-pion scattering lengths from nucleon-meson fluctuations”, *Phys. Rev. D* **105** (2022) 074031, arXiv: 2112.14579 [hep-ph].
- [735] T. Kojo *et al.*, “Quarkyonic Chiral Spirals”, *Nucl. Phys. A* **843** (2010) 37–58, arXiv: 0912.3800 [hep-ph].
- [736] T. Kojo *et al.*, “Interweaving Chiral Spirals”, *Nucl. Phys. A* **875** (2012) 94–138, arXiv: 1107.2124 [hep-ph].
- [737] J. Braun *et al.*, “Search for inhomogeneous phases in fermionic models”, *Phys. Rev. D* **91** (2015) 116006, arXiv: 1410.8181 [hep-ph].
- [738] R. D. Pisarski *et al.*, “The Lifshitz Regime and its Experimental Signals”, *Nucl. Phys. A* **1005** (2021) 121910, ed. by F. Liu *et al.*, arXiv: 2005.00045 [nucl-th].
- [739] R. D. Pisarski, A. M. Tselik, and S. Valgushev, “How transverse thermal fluctuations disorder a condensate of chiral spirals into a quantum spin liquid”, *Phys. Rev. D* **102** (2020) 016015, arXiv: 2005.10259 [hep-ph].
- [740] M. Kutschera, W. Broniowski, and A. Kotlorz, “Quark matter with neutral pion condensate”, *Phys. Lett. B* **237** (1990) 159–163.
- [741] M. Kutschera, W. Broniowski, and A. Kotlorz, “Quark matter with pion condensate in an effective chiral model”, *Nucl. Phys. A* **516** (1990) 566–588.
- [742] M. J. Steil, “Generalized Ginzburg-Landau analysis”, gg1_20200227.nb, Mathematica notebook (2020), digital auxiliary file.
- [743] K. Furuya, R. E. Gamboa Saravi, and F. A. Schaposnik, “Path Integral Formulation of Chiral Invariant Fermion Models in Two-dimensions”, *Nucl. Phys. B* **208** (1982) 159–181.
- [744] L. D. Landau and E. M. Lifshitz, *Statistical Physics, Part 1 & 2*, Course of Theoretical Physics (Butterworth-Heinemann, Oxford, 1980).
- [745] N. Theodorakopoulos, “Phase transitions in one dimension: Are they all driven by domain walls?”, *Physica D* **216** (2006) 185–190.
- [746] V. L. Berezinskii, “Destruction of Long-range Order in One-dimensional and Two-dimensional Systems having a Continuous Symmetry Group I. Classical Systems”, *Sov. Phys. JETP* **32** (1971) 493.
- [747] J. M. Kosterlitz and D. J. Thouless, “Ordering, metastability and phase transitions in two-dimensional systems”, *J. Phys. C* **6** (1973) 1181–1203.

-
- [748] N. P. Landsman, “Spontaneous symmetry breaking in quantum systems: Emergence or reduction?”, *Stud. Hist. Philos. Sci.* **44** (2013) 379–394, arXiv: 1305.4473 [math-ph].
- [749] M. Mandl, A. Wipf, and J. Lenz, “Inhomogeneous phases in 1+1 dimensional Gross-Neveu models at finite number of flavors on the lattice”, Talk at the 38th international Symposium on Lattice Field Theory (2021), URL: <https://indico.cern.ch/event/1006302/contributions/4371097/>, [Online; accessed 2021.07.28].
- [750] C. Nonaka and K. Horie, “Inhomogeneous phases in the chiral Gross-Neveu model on the lattice”, Talk at the 38th international Symposium on Lattice Field Theory (2021), URL: <https://indico.cern.ch/event/1006302/contributions/4371153/>, [Online; accessed 2021.07.28].
- [751] I. Boettcher *et al.*, “Tan contact and universal high momentum behavior of the fermion propagator in the BCS-BEC crossover”, *Phys. Rev. A* **87** (2013) 023606, arXiv: 1209.5641 [cond-mat.quant-gas].
- [752] I. Boettcher, J. M. Pawłowski, and C. Wetterich, “Critical temperature and superfluid gap of the Unitary Fermi Gas from Functional Renormalization”, *Phys. Rev. A* **89** (2014) 053630, arXiv: 1312.0505 [cond-mat.quant-gas].
- [753] I. Boettcher *et al.*, “Phase structure of spin-imbalanced unitary Fermi gases”, *Phys. Rev. A* **91** (2015) 013610, arXiv: 1409.5070 [cond-mat.quant-gas].
- [754] S. Sachdev, *Quantum Phase Transitions*, 2nd ed. (Cambridge University Press, Cambridge, 2011), DOI: 10.1017/CBO9780511973765.
- [755] A. Dutta *et al.*, “Quantum phase transitions in transverse field spin models: from statistical physics to quantum information” (2010), arXiv: 1012.0653 [cond-mat.stat-mech].
- [756] M. J. Steil, “Quark-Meson model inhomogeneous MF”, QMcpp_20231209.zip, C++ code (2023), digital auxiliary files.
- [757] M. J. Steil, “QMM LPA CDW flow equation”, qmmcdw_20231210.nb, Mathematica notebook (2023), digital auxiliary file.
- [758] S. Carignano, M. Buballa, and W. Elkamhawy, “Consistent parameter fixing in the quark-meson model with vacuum fluctuations”, *Phys. Rev. D* **94** (2016) 034023, URL: <https://link.aps.org/doi/10.1103/PhysRevD.94.034023>.
- [759] L^AT_EX Project Team, “L^AT_EX v3.141592653-2.6-1.40.25” (2023), URL: <https://www.latex-project.org>.
- [760] MiK_TE_X Project, “MiK_TE_X v23.5” (2023), URL: <https://miktex.org>.
- [761] M. Peischl *et al.*, “TUDa-CI – Corporate Design L^AT_EX-Templates for TU Darmstadt v3.30”, *GitHub repository* (2023), URL: https://github.com/tudace/tuda_latex_templates.
- [762] M. J. Steil, M. Peischl, *et al.*, “TUDa-CI – Modified Corporate Design L^AT_EX-Templates for TU Darmstadt”, *GitHub repository* (2024), URL: https://github.com/MJSteil/tuda_latex_templates/releases/tag/PhDThesisPublication.
- [763] P. Kime *et al.*, “CTAN: Package BibL^AT_EX v3.19” (2023), URL: <https://ctan.org/pkg/biblatex>.
- [764] F. Charette and P. Kime, “CTAN: Package biber v2.19” (2023), URL: <https://ctan.org/pkg/biber>.
- [765] N. Talbot, “CTAN: Package glossaries v4.53” (2023), URL: <https://ctan.org/pkg/glossaries>.
- [766] N. Talbot, “CTAN: Package glossaries-extra v1.53” (2023), URL: <https://ctan.org/pkg/glossaries-extra>.
- [767] T. Cubitt, “CTAN: Package cleveref v0.21.4” (2018), URL: <https://ctan.org/pkg/cleveref>.
- [768] L^AT_EX Project Team, “CTAN: Package amsmath v2.17” (2023), URL: <https://ctan.org/pkg/amsmath>.
- [769] The T_EXnicCenter Team, “T_EXnicCenter v2.02” (2013), URL: <https://www.texniccenter.org>.
- [770] D. Ho, “Notepad++ v8.5.8” (2023), URL: <https://notepad-plus-plus.org>.
- [771] OpenAI, “ChatGPT 4” (2023), URL: <https://chat.openai.com>, [Online; accessed 2023].

-
- [772] E. Tiesinga *et al.*, “CODATA Recommended Values of the Fundamental Physical Constants: 2018” (2021), URL: <https://physics.nist.gov/cuu/Constants/>.
- [773] A. K. Cyrol, M. Mitter, and N. Strodthoff, “FormTracer - A Mathematica Tracing Package Using FORM”, *Comput. Phys. Commun.* **219** (2017) 346–352, arXiv: 1610.09331 [hep-ph].
- [774] A. K. Cyrol *et al.*, “FormTracer v2.3.7”, *GitHub repository* (GitHub, 2021), URL: <https://github.com/FormTracer/FormTracer>.
- [775] T. Matsubara, “A new approach to quantum statistical mechanics”, *Prog. Theor. Phys.* **14** (1955) 351–378.
- [776] A. Das, *Finite Temperature Field Theory* (World Scientific, Singapore, 1997), ISBN: 978-981-022856-9, DOI: 10.1142/3277.
- [777] J. Zinn-Justin, “Quantum field theory at finite temperature: An Introduction” (2000), arXiv: hep-ph/0005272.
- [778] J. I. Kapusta and C. Gale, *Finite-temperature field theory: Principles and applications*, Cambridge Monographs on Mathematical Physics (Cambridge University Press, 2011), ISBN: 978-0-52182082-0, DOI: 10.1017/CB09780511535130.
- [779] M. Laine and A. Vuorinen, *Basics of Thermal Field Theory*, Lect. Notes Phys. 925 (Springer, 2016), pp. 1–281, DOI: 10.1007/978-3-319-31933-9, arXiv: 1701.01554 [hep-ph].
- [780] M. G. Mustafa, “An introduction to thermal field theory and some of its application”, *Eur. Phys. J. ST* **232** (2023) 1369–1457, arXiv: 2207.00534 [hep-ph].
- [781] D. H. Rischke, “Lecture notes on: Statistische Feldtheorie” (2022), URL: https://itp.uni-frankfurt.de/~drischke/Skript_SFT.pdf, [Online; accessed 2022.03.23].
- [782] D. F. Litim and J. M. Pawłowski, “Non-perturbative thermal flows and resummations”, *JHEP* **11** (2006) 026, arXiv: hep-th/0609122.
- [783] S. N. Bose, “Planck’s law and light quantum hypothesis”, *Z. Phys.* **26** (1924) 178–181.
- [784] E. Fermi, “Sulla quantizzazione del gas perfetto monoatomico”, *Rend. Lincei* **3** (1926) 145–149.
- [785] E. Fermi, “On the Quantization of the Monoatomic Ideal Gas”, trans. by A. Zannoni (1999), arXiv: cond-mat/9912229.
- [786] P. A. M. Dirac, “On the theory of quantum mechanics”, *Proc. Roy. Soc. Lond. A* **112** (1926) 661–677.
- [787] M. Abramowitz and I. A. Stegun, *Handbook of Mathematical Functions with Formulas, Graphs, and Mathematical Tables*, ninth Dover printing, tenth GPO printing (Dover Publications Inc., Mineola, NY, USA, 1964).
- [788] S. I. Blinnikov and M. A. Rudzskii, “New representations of the thermodynamic functions of fermi gases”, *Astrophysics* **29** (1988) 644–651.
- [789] T. K. Herbst, J. M. Pawłowski, and B.-J. Schaefer, “Phase structure and thermodynamics of QCD”, *Phys. Rev. D* **88** (2013) 014007, arXiv: 1302.1426 [hep-ph].
- [790] B. Fornberg, “Generation of finite difference formulas on arbitrarily spaced grids”, *Math. Comput.* **51** (1988) 699–706.
- [791] N. M. Temme, “Uniform asymptotic expansions of the incomplete gamma functions and the incomplete beta function”, *Math. Comput.* **29** (1975) 1109–1114.

Acronyms

List of acronyms including their meaning and the page number of their first use:

- (F)RG** (functional) renormalization group 15
 χ SB chiral symmetry breaking 1
 n PI n -particle irreducible 14
1PI one-particle irreducible 19
2PI two-particle irreducible 14
BBE Bateman-Burgers equation 59
BC boundary condition 45
bGN bosonized Gross-Neveu 234
CDW chiral density wave 4
CEP critical endpoint 85
CFD computational fluid dynamics 6
CMWH Coleman-Mermin-Wagner-Hohenberg 96
CP critical point 4
CSC color superconducting 90
DE derivative expansion 30
DSEs Dyson-Schwinger equations 14
EA effective action 19
EAA effective average action 15
ERG exact renormalization group 14
FD finite difference 5
FRG functional renormalization group 3
FS field space 16
FV finite volume 6
gGL generalized Ginzburg-Landau 231
GL Ginzburg-Landau 250
GN Gross-Neveu 9
GNY Gross-Neveu-Yukawa 9
HBP homogeneously broken phase 85
HE heat equation 64
HRSC high-resolution shock-capturing 45
HS Hubbard-Stratonovich 83
IC initial condition 23
IP inhomogeneous phase 263
IR infrared 4
IVP initial value problem 46
KNP Kurganov-Noelle-Petrova 47
KT Kurganov-Tadmor 8
l.h.s. left-hand side 63
LAE linear advection equation 57
LEFT low-energy effective theory 3
LP Lifshitz point 266
LPA local potential approximation 4
LPA' local potential approximation prime 31
LxF Lax-Friedrichs 47
MF mean-field 4
MUSCL Monotonic Upstream-centered Scheme for Conservation Laws 47
NJL Nambu-Jona-Lasinio 3
NT Nessyahu-Tadmor 47
NU natural units 320
ODE ordinary differential equation 7
PCAC partially conserved axial current 80
PDE partial differential equation 5
PQM model Polyakov loop enhanced quark-meson model 87
QCD quantum chromodynamics 1
QED quantum electrodynamics 72
QEOM quantum equation of motion 19
QFT quantum field theory 4
QGP quark-gluon plasma 3
QM quark-meson 4
r.h.s. right-hand side 22
RG renormalization group 3

SP symmetric phase 85
SSB spontaneous symmetry breaking 283
TV total variation 51
TVD total variation-diminishing 48
TVNI total variation non-increasing 48

UV ultraviolet 4
w.l.o.g. without loss of generality 116
w.r.t. with respect to 7
YM Yang–Mills 74

Curriculum vitae

Personal information

Name	Martin Jakob Steil
Date of birth	October 23, 1991
Place of birth	Offenbach am Main, Germany
Nationality	German

Languages

German	fluent	<i>mother tongue</i>
English	fluent	<i>oral and written</i>

Education

08/2017–10/2024	PhD in Physics , <i>Technische Universität Darmstadt</i> Dissertation “From zero-dimensional theories to inhomogeneous phases with the functional renormalization group” under the supervision of Priv.-Doz. Dr. Michael Buballa
02/2015–07/2017	Master of Science in Physics , <i>Technische Universität Darmstadt</i> Master’s thesis “Structure of slowly rotating magnetized neutron stars in a perturbative approach” under supervision of Priv.-Doz. Dr. Michael Buballa
10/2011–02/2015	Bachelor of Science in Physics , <i>Technische Universität Darmstadt</i> Bachelor’s thesis “Hadron-quark crossover and massive hybrid stars” under supervision of Priv.-Doz. Dr. Michael Buballa
05/2011	Abitur , <i>Claus-von-Stauffenberg-Schule</i> , Rodgau

Professional experience

- 08/2017–12/2021 **Research associate**, Institute for Nuclear Physics, Technische Universität Darmstadt
Study of inhomogeneous chiral condensates within the Functional Renormalization Group (26h/week)
- 04/2016–09/2016 **Student assistant**, Central Student Advisory and Orientation Office (ZSB), Technische Universität Darmstadt
- 10/2011–10/2015 IT Support, webmaster, print- and web-design (15h/week)

Publications and preprints

- 09/2022 A. Koenigstein, M. J. Steil, N. Wink, E. Grossi, J. Braun, M. Buballa, and D. H. Rischke, “Numerical fluid dynamics for FRG flow equations: Zero-dimensional QFTs as numerical test cases. I. The $O(N)$ model”, *Phys. Rev. D* **106** (2022) 065012, arXiv: [2108.02504](#) [[cond-mat.stat-mech](#)]
- 09/2022 A. Koenigstein, M. J. Steil, N. Wink, E. Grossi, and J. Braun, “Numerical fluid dynamics for FRG flow equations: Zero-dimensional QFTs as numerical test cases. II. Entropy production and irreversibility of RG flows”, *Phys. Rev. D* **106** (2022) 065013, arXiv: [2108.10085](#) [[cond-mat.stat-mech](#)]
- 09/2022 M. J. Steil and A. Koenigstein, “Numerical fluid dynamics for FRG flow equations: Zero-dimensional QFTs as numerical test cases. III. Shock and rarefaction waves in RG flows reveal limitations of the $N \rightarrow \infty$ limit in $O(N)$ -type models”, *Phys. Rev. D* **106** (2022) 065014, arXiv: [2108.04037](#) [[cond-mat.stat-mech](#)]
- 08/2022 A. Koenigstein, L. Pannullo, S. Rechenberger, M. J. Steil, and M. Winstel, “Detecting inhomogeneous chiral condensation from the bosonic two-point function in the $(1 + 1)$ -dimensional Gross–Neveu model in the mean-field approximation*”, *J. Phys. A* **55** (2022) 375402, arXiv: [2112.07024](#) [[hep-ph](#)]
- 08/2021 J. Stoll, N. Zorbach, A. Koenigstein, M. J. Steil, and S. Rechenberger, “Bosonic fluctuations in the $(1 + 1)$ -dimensional Gross-Neveu(-Yukawa) model at varying μ and T and finite N ” (2021), arXiv: [2108.10616](#) [[hep-ph](#)]



Teaching

10/2017–03/2020

Teaching assistant, Department of Physics, Technische Universität Darmstadt

- “*Quantum Field Theory II*” (winter term 2019/20)
- “*Quantum Field Theory I*” (summer term 2019)
- “*Classical Particles and Fields for Teachers*” (winter term 2018/19)
- “*Classical Particles and Fields for Teachers*” (winter term 2017/18)

08/2017–12/2021

Supervision of bachelor theses, Department of Physics, Technische Universität Darmstadt

Second referee and co-supervision of two bachelor theses



Awards, distinctions & grants

10/2019

Giersch-Excellence-Grant: in recognition of outstanding achievements in the doctoral thesis project “*Inhomogeneous Chiral Condensates within the Functional Renormalization Group*”



Academic associations

08/2017–10/2024

Junior member of the *Collaborative Research Center TransRegio 211* (funded by the *Deutsche Forschungsgemeinschaft*)

01/2018–07/2024

Member of the *Helmholtz Graduate School for Hadron and Ion Research (HGS-HIRe)*

since 08/2017

Member of the *Deutsche Physikalische Gesellschaft e. V.*

Acknowledgments

To start off the rather long list of people, collaborations, and institutions I want to acknowledge, I want to thank my supervisor, Michael Buballa, for his years of continuous support dating back to the days of my Bachelor's thesis. I am very grateful to him for his immense knowledge, excellent physical intuition, seemingly infinite patience, and his friendly and appreciative demeanor. I also want to thank him for giving me the opportunity to conduct my research very freely and interest-driven, resulting in this thesis and the accompanying publications.

I want to thank Jens Braun for his support throughout my research. Especially his expertise regarding the (F)RG, continued interest, support, and encouragement have been invaluable. As a member of my PhD committee, collaborator, and second referee of this thesis he made immense contributions to my research.

Furthermore, I want to thank Tetyana Galatyuk and Michael Vogel for joining my examination committee as the third and fourth examiner, respectively.

Dirk Rischke in his role as external supervisor in my PhD committee and principal investigator in the A03 project of the CRC-TR 211 has supervised my research from the start of my PhD project. Especially his input regarding numerical schemes for conservation laws and CFD has led to successful research efforts adapting the KT/MUSCL scheme to FRG flow equations.

I want to thank Guy D. Moore for his support and various interesting conversations ranging from physics over particularities of the German and English languages to interesting trivia.

I acknowledge support by the *Deutsche Forschungsgemeinschaft* (DFG, German Research Foundation) through the CRC-TR 211 "Strong-interaction matter under extreme conditions" – project number 315477589 – TRR 211. I am grateful to the *Helmholtz Graduate School for Hadron and Ion Research* for their interesting and stimulating scientific program, the excellent soft skill courses, and the travel funds I was able to enjoy due to my membership in the graduate school. Moreover, I acknowledge the support of *Stiftung Giersch* through the Giersch Excellence Grant and I want to thank Michael Buballa for the respective recommendation.

I want to explicitly acknowledge various collaborators and colleagues. First among them is Adrian Koenigstein, to whom I am immensely grateful. Our close and very productive collaboration over the years is among the aspects of my PhD studies I cherish most. His immense knowledge and his patience to share and explain at length improved my understanding of theoretical physics tremendously. His keen perception and attention to detail makes learning and researching together very rewarding. Our joint talks and contributions at various seminars, colloquia, and conferences have been a joy to prepare and present. The trips together to CRC events and conferences, and our brief research stay in Poland are among the most memorable moments of my time as a PhD student.

I want to thank Bernd-Jochen Schaefer and Michael Buballa for their work, input, and patience regarding our collaboration dealing with inhomogeneous chiral condensates in the QM model with the FRG framework.

I am very thankful to Eduardo Grossi and Nicolas Wink for various discussions regarding the (F)RG, numerics, and hydrodynamics and their contributions to our joint project studying the FRG and numerics for it with zero-dimensional models.

The discussions and joint work on the FRG treatment of the GN model with Niklas Zorbach, Jonas Stoll, Stefan Rechenberger, and Adrian Koenigstein have been very fulfilling. Especially the critical and at times persistent questions and discussions coming up in this collaboration have pushed my own understanding of the (F)RG and the large- N /MF approximation.

I want to thank Adrian Koenigstein, Laurin Pannullo, Stefan Rechenberger, and Marc Winstel for their work and fruitful discussions regarding our collaboration and publication dealing with the stability analysis in the GN model on MF level.

I am very thankful to Lennart Kurth for various discussions and critical questions regarding the (F)RG, the MF approximation, and (thermal) QFT in general. Our discussions and computations dealing with the QM model and the FRG have been extremely educational and productive.

I want to thank Deniz Nitt for his expertise in C/C++, his input at various group meetings, our unforgettable week in Schleiden, and his active participation in our “Codenames+” online activities during the COVID-19 pandemic.

The years at the Theoriezentrum as a member of the NHQ group have been the most enjoyable out of my years at the TU Darmstadt. I want to thank all my colleges at the Theoriezentrum for creating a great working and research environment and for all the great memories of lunch together, evening activities, Christmas parties, and joint trips. I am especially grateful to my past office mates of Room 306 – particularly Marc Barroso, Max Eller, Thomas Jahn, Parikshit Junnarkar, Vincent Klaer, Daniel Robaina, and Niels Schlusser – for countless hours of not only work and physics but also fun.

As member of the A03 project of the CRC-TR 211, I want to thank my colleagues in this project and the participants of our regular seminar meetings. Our discussions about inhomogeneous phases, low-dimensional and low-energy-effective models, the FRG, and physics as well as numerics in general have been very enlightening and productive.

I want to thank all members of the CRC-TR 211 for providing me with a stimulating research environment. Our colloquia and retreats and especially the possibility to present my research at those events has been immensely educational and helpful. I am especially grateful to Alessandro Sciarra for his immense engagement in the activities of the CRC-TR 211 and his expertise regarding good practices in coding, scientific data management, and \LaTeX .

During my PhD studies, I was able to visit the universities in Bielefeld, Frankfurt, Gießen, and Heidelberg on numerous occasions. I want to thank the colleagues from the respective institutes for their hospitality and interesting discussions. In this context, I want to explicitly thank Bernd-Jochen Schaefer, Lorenz von Smekal, Konstantin Otto, Christopher Busch, Jan M. Pawłowski, Eduardo Grossi, Nicolas Wink, and Friederike J. Ihssen explicitly.

I want to thank the multitude of people who have proofread parts of this manuscript for their comments and keen eyes concerning spelling, grammar, and commas. I am very grateful to all the participants of my “PhD Thesis Spellcheckers” group chat. Especially Michael Buballa, Jens Braun, Hanna Kniss, Sebastian Reinig, and Rebekka Allahyar Parsa deserve special recognition and thanks in this context.

To conclude, I want to express my heartfelt gratitude to all my friends and family. I thank Oliver Reinig, Simon Amann, and Sebastian Reinig for over twenty years of close friendship. They, together with my friends Sebastian Arncken and Kalina Nikolaeva, have been and still are an invaluable support and a source of joy and happiness.

Last but most certainly not least, I would like to thank my family. Without their ongoing support and encouragement this work would have been impossible. Their unconditional love – in some painful cases transcending death – has been and is a constant source of strength and safety throughout my life. I am especially grateful to all the (extended) members of the Kniss family – Herta & Erhard, Annina & Torsten, Hanna & Luca, Teresa & Ole, and Hannes. I am also profoundly thankful to my sister Rebekka, brother-in-law Ehsan, stepmother Gerda, father Winfried, and my beloved late mother Renate.